NASA/CR-97-206242/PT2

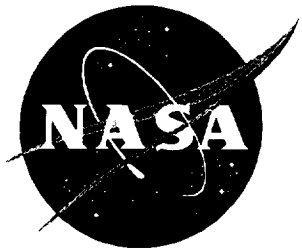

Magnetohydrodynamics Accelerator Research Into Advanced Hypersonics (MARIAH)

Final Report

Jack A. Baughman, David A. Micheletti, Gordon L. Nelson, and Gloyd A. Simmons
MSE Technology Applications, Inc., Butte, Montana

National Aeronautics and
Space Administration

Langley Research Center
Hampton, Virginia 23681-2199

Prepared for the National Aeronautics and Space Administration under Purchase Order A45416D and for the U.S. Department of Energy under Contract DE-AC22-96EW96405

October 1997

Acknowledgments

MSE Technology Applications, Inc., wishes to acknowledge the contributions to the MARIAH Project made by the following organizations:

University of Texas at Arlington
Ohio State University
Princeton University
NASA Ames Research Center
Bluesky Research, Inc.
Pulsatron
Russian Central Aerohydrodynamic Institute
ENGO

Available from the following:

NASA Center for AeroSpace Information (CASI)
800 Elkridge Landing Road
Linthicum Heights, MD 21090-2934
(301) 621-0390

National Technical Information Service (NTIS)
5285 Port Royal Road
Springfield, VA 22161-2171
(703) 487-4650

TABLE OF CONTENTS
*** Part I (Included Under Separate Cover)**

TABLE OF CONTENTS (Cont'd)

TABLE OF CONTENTS
Part II

FIGURES

TABLE OF CONTENTS (Cont'd)

TABLE OF CONTENTS (Cont'd)

TABLE OF CONTENTS (Cont'd)

Page

TABLES

TABLE OF CONTENTS (Cont'd)

ACRONYMS

1-D	one-dimensional
2-D	two-dimensional
3-D	three-dimensional
ACCEL	MSE 1-D MHD Accelerator Code
ADI	alternating direction implicit
AEDC	Arnold Engineering Development Center
AEDC-VKF	AEDC von Karman Facility
AERL	Avco Everett Research Laboratory
AIAA	American Institute of Aeronautics and Astronautics
CEA	Chemical equilibrium with applications computer code (NASA, 1994)
CET89	Chemical equilibrium computer code (NASA, 1989)
CDIF	Component Development and Integration Facility
CFD	computational fluid dynamics
CPU	central processing unit
dc	direct current
DOE	U.S. Department of Energy
DOE-FETC	DOE Federal Energy Technology Center
e^-	electrons
e-beam	electron beam
EEDF	electron energy distribution function
ENGO	a private Russian consortium comprised of researchers from a number of Russian scientific, academic, and technical agencies (also known as ENERGYGO)
ERDA	U.S. Energy Research and Development Administration
FHO	forced harmonic oscillator
GASL	General Applied Sciences Laboratory
GE	General Electric Company
HiRho	high density MHD accelerator test program at AEDC
HPDE	High Performance Demonstration Experiment
HST	Chemical equilibrium computer code (Outokumpu Research, Finland)

ACRONYMS (Cont'd)

IMACON™	image converter camera
LANL	Los Alamos National Laboratory
LBI	linearized block implicit
LINACCS	linear accelerators
LoRho	low density MHD accelerator test program at AEDC
LSODE	ordinary differential equation system solver
LTE	local thermodynamic equilibrium
MARIAH	Magnetohydrodynamics Accelerator Research Into Advanced Hypersonics
MHD	magnetohydrodynamics
MIT	Massachusetts Institute of Technology
MSE	MSE Technology Applications, Inc.
NASA	National Aeronautics and Space Administration
NASA Ames	NASA Ames Research Center
NASA Ames EAST	NASA Ames Electric Arc-Driven Shock Tube
NASA-LaRC	NASA Langley Research Center
NASA-MSFC	NASA Marshall Space Flight Center
NSSK	North-South Station Keeping
ODE	ordinary differential equations
OSU	Ohio State University
PAC91	computer program for calculating and fitting thermodynamic functions (NASA, 1991)
PDE	pulse detonation engine
PGU	piston gasdynamic unit
PI	Principal Investigator
PM/SIC	pre-mixed, shock-induced combustor
POC	proof of concept
R&D	research and development
RCC	reinforced carbon-carbon
RDHWT	Radiatively Driven Hypersonic Wind Tunnel
rf	radio frequency

ACRONYMS (Cont'd)

RIME	rocket-induced MHD ejector
SAB	Scientific Advisory Board (USAF)
SOW	statement of work
SSTO	single-stage-to-orbit
T&E	testing and evaluation
TAV	transatmospheric vehicle
TEOS	Tetraethyl-Ortho Silicate
TPS	thermal protection systems
TsAGI	The Russian Central Aerohydrodynamic Institute
UHP	ultrahigh pressure
USAF	United States Air Force
UTA	University of Texas at Arlington
UTSI	University of Tennessee Space Institute
UV	ultraviolet
V-T	vibrational-translational
V-V	vibration-vibration

APPENDIX B

CONTENTS

SECTION B.1

FIGURES

TABLES

SECTION B.2

FIGURES

TABLES

SECTION B.3

FIGURES

TABLES

APPENDIX B. COMPUTATIONAL STUDIES

Three computational studies have been accomplished for the Magnetohydrodynamics Accelerator Research Into Advanced Hypersonics (MARIAH) Project. A one-dimensional (1-D) magnetohydrodynamics (MHD) accelerator design and analysis computer code named ACCEL was previously developed at MSE and has been modified for modeling accelerator channels for hypervelocity wind tunnel applications. Two other modeling codes were developed through a subcontract with Ohio State University (OSU). These codes were a 1-D code and a two-dimensional (2-D) code, respectively. These codes were used to conduct parametric studies on both equilibrium and nonequilibrium MHD flow trains. The same computer codes were also used to analyze and interpret the experimental data collected in the NASA Ames Research Center (NASA Ames) testing program. The results of these analytical studies are documented in Sections B.2 and B.3.

APPENDIX B, SECTION B.1

B.1 MSE ONE-DIMENSIONAL MHD ACCELERATOR CODE (ACCEL)

A parametric study of MHD performance examined the effect of inlet conditions, maximum plasma temperature, magnetic field strength, and electrode current density, and each varied independently. Guided by the results of the parametric study, an optimization analysis was then performed to evaluate the performance of an MHD accelerator using the best combination of design variables. These analyses were performed using a modified version of the 1-D MHD Accelerator Code, ACCEL. The following sections discuss the accelerator code, including its validation and verification and the results of the parametric and optimization analyses.

B.1.1 Overview

An MHD accelerator design and analysis computer code named ACCEL (Ref. 1) has been modified to enhance its capabilities for modeling high performance accelerator channels currently being evaluated for hypervelocity wind tunnel driver applications. As presently configured, this code is a 1-D, supersonic flow, gasdynamics model for design or analysis of Faraday-connected MHD accelerator channels. Accelerator channels operating in either an ionizational equilibrium or nonequilibrium mode can be modeled. Since MHD often requires the addition of an easily ionized "seed" material to enhance ionization and increase performance, this code can model either seeded or unseeded flow.

Section B.1.2.1 describes the 1-D equations of motion on which the gas dynamic model is based as well as the various design options available in the code. Models for wall heat transfer and friction are also described. In Section B.1.2.2, the segmented Faraday electrical model is discussed along with electrode and boundary layer voltage drop models. The two-temperature, nonequilibrium ionization model, which allows elevation of the electron temperature by the local electric field or by an external source, is discussed in Section B.1.2.3. Finally, Section B.1.3 contains a verification and validation of the ACCEL code.

The results of an MHD parametric analysis are presented in Section B.1.4. In this study, MHD accelerator entrance conditions, accelerator gas temperatures, electrical current density, and magnetic field strength are each independently varied. Finally, the results of an optimization study are given in Section B.1.5. The selected parameters were varied one at a time, and the values resulting in the highest overall performance were selected.

B.1.2 Model Description

NOMENCLATURE

a,A	-	Parameters used in heat transfer calculation, [see Eq. (B.1- 5)]
A	-	Cross-sectional area, m^2
b,B	-	Parameters used in heat transfer calculation, [see Eq. (B.1- 5)]
B	-	Magnetic field strength, Tesla
$BndryVff$	-	Boundary layer voltage fudge factor
c_e	-	Mean random thermal velocity of electrons, m/s
$C_{1,2}$	-	Constants in the Nottingham equations, Eq. (B.1- 35)
C_f	-	Compressible skin-friction coefficient
C_p	-	Constant pressure specific heat, J/kg-K.
D	-	Hydraulic diameter, $(4A/\psi)$, m
$D_{1,2}$	-	Constants in the Nottingham equations, Eq. (B.1- 36)
e	-	Electron charge, 1.602×10^{-19} C
E	-	Electric field, V/m
E_{max}	-	Constraint on maximum electric field, V/m
f	-	Accommodation coefficient for thermal energy transfer from ions
g_i	-	Statistical weight for ground state of ions
g_0	-	Statistical weight for ground state of neutral atoms
h	-	Enthalpy, J/kg
h	-	Planck's constant, 6.6242×10^{-34}, J-s
h	-	Channel height or electrode pair separation, m
j	-	Current density, A/m^2
j_i	-	Ion current density at the cathode surface, A/m^2
k	-	Boltzmann's constant, 1.38047×10^{-23}, J/K
k_s	-	Equivalent sand grain roughness height, m
L	-	Channel length, m, Eq. (B.1- 20)
L	-	Arc length, Nottingham model, Equations (B.1- 35)(B.1- 36)
$\dot{m}$	-	Mass flow rate, kg/s
m_e	-	Rest mass of an electron, 9.110×10^{-31}kg
m_g	-	Average mass of heavy particles, kg
M	-	Mach number
n	-	Number density, $\#/m^3$
n	-	Exponent in the Nottingham Equations, Eq. (B.1- 35)(B.1- 36)
n_s	-	Total species concentration, $\#/m^3$
p	-	Pressure, Pa
P_e	-	Electrical Power, W
P_{reqd}	-	Power density input required to maintain elevated electron temperature, W/m^3, see Equation (B.1- 55)
Pr	-	Prandtl number
q	-	Wall heat flux, W/m^2
Q_w	-	Total heat rate to the channel walls, W
Q	-	Cross-section for collisions between electrons and heavy particles, m^2
Q_k	-	Collision cross section for the k^{th} neutral species, m^2
s	-	Electrode axial spacing, m
St	-	Stanton number
T	-	Temperature, K
u	-	Fluid velocity, m/s
v	-	Specific volume, m^3/kg
V	-	Channel volume, m^3
V_{ca}	-	Cathode voltage drop
V_{an}	-	Anode voltage drop

w - Channel width, m
W - Energy loss from an electron per collision, J/collision
x - Distance in axial direction, m

Greek Variable Names

$\psi_{1,2,3}$ - Constants in the Nottingham Equations, Eq. (B.1- 36)
β - Hall parameter
β_{crit} - Critical Hall Parameter
δ - Average fractional energy loss from electrons per collision with the heavy particles, see Equation (B.1- 62)
δ^{l} - Fractional energy loss factor for electron collisions with the heavy particles, see Equation (B.1- 62)
ϵ_0 - Permittivity of free space, 8.85525×10^{-12} F/m
ϵ_i - Ionization potential, eV
ϵ_{an} - Material work function, anode, eV
ϵ_{ca} - Material work function, cathode, eV
Λ - Ratio of Debye length to average impact parameter, see Equation (B.1- 58)
ρ - Mass density, kg/m^3
σ - Electrical conductivity, S/m
τ_w - Wall shear stress, N/m^2
ψ - Perimeter, 2×(height + width), m
γ - Specific Heat ratio

Subscripts

[Note: thermodynamic properties and flow properties with no subscript (e.g. p, T, u, h, etc.) refer to the local 1-D average value of that property.]

an - Anode
aw - Adiabatic wall
c - Channel core
ca - Cathode
bl - Boundary layer conditions
e - Electron
g - Gas (heavy particle)
I - Ion
k - kth species
k - Parameter based on roughness
ref - Reference value
s - Species
w - Wall
x - Axial coordinate direction
y - Transverse coordinate direction
z - Coordinate direction perpendicular to the axial and transverse directions

B.1.2.1 Gas Dynamic Model

Gas dynamic temperature and pressure are determined in the ACCEL code from the solution of the 1-D equations of motion and mass continuity, including the effects of wall friction and heat transfer. This section discusses the design features available in the code and describes the principles and equations on which the gasdynamic model is based. This code also allows the user to chose between four design variable options, which are discussed below.

B.1.2.1.1 *Fluid Dynamic Equations of Motion*

The gas dynamic equations of motion have been adapted from Rosa (Ref. 2) to include wall friction and heat transfer and are given by:

Momentum Equation:

$$\rho u \frac{du}{dx} + \frac{dp}{dx} = j_y B_z - \frac{4\tau_w}{D} \tag{B.1- 1}$$

Energy Equation:

$$\rho u \frac{d}{dx}\left(\frac{u^2}{2} + h\right) = j_y E_y - \frac{4q_w}{D} \tag{B.1- 2}$$

Mass Continuity Equation:

$$\dot{m} = \rho u A \tag{B.1- 3}$$

B.1.2.1.2 *Wall Friction and Heat Transfer*

The wall shear stress in the momentum equation is calculated from:

$$\tau_w = \frac{1}{2} C_f \rho u^2 \tag{B.1- 4}$$

where the compressible skin-friction coefficient C_f, is determined from the theory of van Driest (Ref. 3, Equation 7-140)

$$\frac{\sin^{-1} A + \sin^{-1} B}{\sqrt{C_f\,(T_{aw}/T - 1)}} \approx 5.79 + 4.15 \log\left(\frac{x}{k_s}\sqrt{C_f}\right) \tag{B.1- 5}$$

In this equation, "x" is the distance from leading edge, and k_s is the equivalent sand grain roughness height. The adiabatic wall temperature for turbulent flow T_{aw}, is given by:

$$T_{aw} = T\left(1 + \mathrm{Pr}_{ref}^{\frac{1}{3}} \frac{\gamma - 1}{2} M^2\right) \tag{B.1- 6}$$

where Pr_{ref} is the Prandtl number evaluated at the reference temperature. T_{ref} is determined from:

$$T_{ref} = \frac{T + T_w}{2} + 0.022\left(T_{aw} - T\right) \tag{B.1- 7}$$

Kays and Crawford (Ref. 4) note this reference temperature provides satisfactory correlations with high-speed turbulent flow data. The parameters "A" and "B" in Eq. (B.1- 5) are given by:

$$A = \frac{2a^2 - b}{\left(b^2 + 4a^2\right)^{1/2}} \tag{B.1- 8}$$

and

$$B = \frac{b}{\left(b^2 + 4a^2\right)^{1/2}} \tag{B.1- 9}$$

where the coefficients "a" and "b" are:

$$a = \left(\frac{\gamma - 1}{2} M^2 \frac{T}{T_w}\right)^{\frac{1}{2}} \tag{B.1- 10}$$

and

$$b = \frac{T_{aw}}{T_w} - 1 \tag{B.1- 11}$$

Convective heat transfer in the ACCEL code is calculated by a model from Kays and Crawford, which includes the effects of surface roughness and the effects of temperature recovery and variable properties in the boundary layer. Additional terms have been added to the model to

account for the increased heat transfer due to the anode and cathode sheaths. The convective heat transfer to the wall is given by:

$$q_{conv} = \rho\, u\, C_p\, St_{ref}\, \left(T_{aw} - T_w\right) \tag{B.1- 12}$$

where the Stanton number based on roughness is given by:

$$St_k = \mathrm{Re}_k^{-0.2}\ \mathrm{Pr}^{-0.44} \tag{B.1- 13}$$

The Reynolds number based on roughness height is given by:

$$Re_k = \frac{\mathrm{Re}_D \sqrt{C_f/2}}{D/k_s} \tag{B.1- 14}$$

and Re_D is the Reynolds number based on the hydraulic diameter:

$$Re_D = \frac{\rho_{ref}\, u\, D}{\mu_{ref}} \tag{B.1- 15}$$

The reference values in these equations are evaluated at the reference temperature T_{ref}, [Eq. (B.1-7)]. The overall Stanton number based on the reference property values and corrected for roughness effects is then given by:

$$St = \frac{C_f/2}{Pr_t + \sqrt{C_f/2}/St_k} \tag{B.1- 16}$$

where Pr_t is the turbulent Prandtl number, which is approximated by a value of 0.9 for air as suggested by Kays and Crawford.

Heat transfer to the anode and cathode surfaces due to the power dissipated in the sheath are approximated by Reference 5, Equations 36 and 37:

Anode Heat Transfer:

$$q_{anode} = j\left(\frac{5kT_e}{2e} + V_{an} + \epsilon_{an}\right) \tag{B.1- 17}$$

Cathode Heat Transfer:

$$q_{cathode} = j_i \left[\epsilon_i + f\left(\frac{5\,k\,T_i}{2e} + V_{ca} \right) \right] - j\,\epsilon_{ca} \qquad \text{(B.1- 18)}$$

where a value of 4.5 electron volts (eV) for copper (Ref. 6) was used for the material work functions for the anode and cathode, ϵ_{an} and ϵ_{ca}, during all studies in this report. Values for the electron temperature T_e and the ion temperature T_i were set equal to the gas temperature, T, since equilibrium was assumed for these studies.

The average heat flux to the wall is the sum of the heat fluxes due to convection and electrode sheath effects:

$$q_w = q_{conv} + \left(q_{anode} + q_{cathode} \right) \frac{w}{\psi} \qquad \text{(B.1- 19)}$$

The total heat transfer rate to the channel walls is then:

$$Q_w = \int_0^L q_w \psi \, d\,x \qquad \text{(B.1- 20)}$$

B.1.2.1.3 *Design Variable Options and Differential Equations*

Three design options and one off-design analysis option are available in the ACCEL code. For each of these options, the user must specify an axial distribution of the design variable. Axial variations of velocity, static temperature, or static pressure can be specified for the design options, or an area distribution can be specified for the off-design analysis option. For each option, the value of the design variable is specified at discrete axial locations along the accelerator channel. Linear interpolation between these locations determines the values at other locations during the computations.

Differential equations for the compressible MHD flow models with heat transfer and friction have been derived for each design option from the momentum, energy, and mass continuity equations [Equations (B.1- 1), (B.1- 2), (B.1- 3)] and are given below:

Velocity Distribution Option:

$$\frac{dh}{dx} = j_y E_y \frac{A}{\dot{m}} - u\frac{du}{dx} - \frac{q_w \psi}{\dot{m}} \tag{B.1-21}$$

$$\frac{dp}{dx} = j_y B_z - \frac{\dot{m}}{A}\frac{du}{dx} - \frac{\tau_w \psi}{A} \tag{B.1-22}$$

Temperature Distribution Option:

$$u\frac{du}{dx} = \frac{j_y E_y \frac{A}{\dot{m}} - \frac{q\psi}{\dot{m}} - C_p \frac{dT}{dx} - \frac{1}{\rho}\left[1 - \left(\frac{\partial \ln \nu}{\partial \ln T}\right)_p\right]\left(j_y B_z - \frac{\tau_w \psi}{A}\right)}{\left(\frac{\partial \ln \nu}{\partial \ln T}\right)_p} \tag{B.1-23}$$

$$\frac{dp}{dx} = j_y B_z - \rho u \frac{du}{dx} - \frac{\tau_w \psi}{A} \tag{B.1-24}$$

Pressure Distribution Option:

$$\frac{dh}{dx} = j_y E_y \frac{A}{\dot{m}} - u\frac{du}{dx} - \frac{q\psi}{A} \tag{B.1-25}$$

$$u\frac{du}{dx} = \frac{1}{\rho}\left[j_y B_z - \frac{dp}{dx} - \frac{\tau_w \psi}{A}\right] \tag{B.1-26}$$

Area Distribution Option:

$$\frac{dH}{dx} = \frac{1}{\rho u}\left(j_y E_y - \frac{q\psi}{A}\right) \tag{B.1-27}$$

$$\frac{dp}{dx} = \frac{\left[j_y B_z - \frac{\tau_w \psi}{A}\right]\left[1 + \frac{u^2}{C_p T}\left(\frac{\partial \ln v}{\partial \ln T}\right)_p\right] - \frac{\rho u^2}{C_p T}\left(\frac{\partial \ln v}{\partial \ln T}\right)_p \frac{dH}{dx} + \frac{\rho u^2}{A}\frac{dA}{dx}}{1 + \frac{\rho u^2}{P}\left(\frac{\partial \ln v}{\partial \ln P}\right)_T + \frac{u^2}{C_p T}\left(\frac{\partial \ln v}{\partial \ln T}\right)_p^2} \qquad \text{(B.1-28)}$$

Integration of the differential equations is accomplished with a fifth-order, adaptive step size, Runge-Kutta integrator (Ref. 7).

Solution of the differential equations associated with the chosen design option requires the initial conditions be specified for the integration variables. Table B.1- 1 lists the required inlet conditions for each design option.

Table B.1- 1. Specified inlet conditions for each design option.

Design Option	Inlet Conditions
Velocity Distribution	Enthalpy and Pressure
Temperature Distribution	Velocity and Pressure
Pressure Distribution	Velocity and Enthalpy
Area Distribution	Stagnation Enthalpy and Pressure

B.1.2.2 Segmented Faraday Electrical Model

In a Faraday configured MHD accelerator, power is applied by a source connected to opposing electrodes; therefore, the resulting electrical current flow through the plasma is mutually perpendicular to the velocity of the flow and the magnetic field. A segmented Faraday MHD channel requires the electrode walls consist of numerous electrodes designed to prevent current flow in the axial direction. In a segmented channel, the electrodes are paired on opposing walls and connected to independent power supplies, as illustrated in Figure B.1- 1. When a magnetic field is imposed on the channel, the transverse current flow (applied by the Faraday power supplies) produces an axial body force that increases the momentum of the flow; however, it also produces an axial electric field, E_x, that can be detrimental to the channel performance. If an internal or external current path is available, the axial electric field will result in an axial current flow that will reduce the performance of the accelerator. For this reason, segmented electrodes are typically designed to be narrow in the axial direction and are separated by electrical insulators to prevent or reduce axial eddy currents.

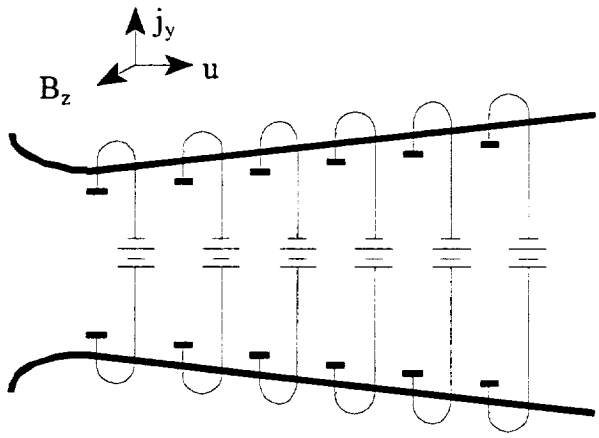

Figure B.1- 1. Segmented Faraday accelerator.

This section describes the Ohm's Law equations, critical Hall parameter limit, finite segmentation model, boundary layer voltage drop, and electrode voltage drop for a 1-D, segmented Faraday model.

B.1.2.2.1 *Ohm's Law Equations*

For the 1-D electrical model, variations of velocity, electrical conductivity, current density, and electric field are assumed to occur only in the axial direction. These parameters are assumed to be constant on any cross-section perpendicular to the channel axis, or they must be represented by an appropriate average in the Ohm's Law equations. Axial current density, j_x, is assumed to be zero for the segmented Faraday model (no axial current). The 1-D Ohm's Law for a segmented Faraday model is given by the following equations:

$$\textit{Transverse:} \qquad E_y = \frac{j_y}{\sigma} + u B_z \tag{B.1- 29}$$

$$\textit{Axial:} \qquad E_x = \beta\left(E_y - u B_z\right) \tag{B.1- 30}$$

B.1.2.2.2 *Electrical Conductivity and Hall Parameter*

Two models are provided for determining the electrical properties of the MHD plasma. Chemical and ionizational equilibrium can usually be assumed for seeded, thermally ionized, MHD plasmas, where an alkali metal seed material is added to the flow to enhance ionization.

For this type of flow, the thermodynamic and transport properties, including the electrical conductivity and Hall parameter, can be determined from a chemical equilibrium analysis at a given thermodynamic state. However, in some circumstances, chemical and ionizational equilibrium cannot be assumed, and a nonequilibrium model must be used except in a very specific nonequilibrium situation where the bulk of the flow can be assumed to be in chemical equilibrium. Nonequilibrium ionization occurs due to an elevated electron temperature; consequently, the electrical conductivity and Hall parameter can be determined using the model discussed in Section B.1.2.3. Other nonequilibrium flows are not presently supported by this code. Only equilibrium models are discussed in this section with the exception of the nonequilibrium ionization instability model, which may limit the Hall parameter in either the equilibrium or nonequilibrium models.

Nonequilibrium ionization instability can occur in a plasma when the Hall parameter is large. Rosa indicates that in atomic gases, observed data "show a wide departure from ideal behavior" when the Hall parameter is greater than 2 (Ref. 2). It is believed that molecular gases can maintain stability over a much larger range of Hall parameter values; however, the limits are presently unknown.

The effects of a nonequilibrium ionization instability phenomenon can be modeled as a reduction in the apparent values of the Hall parameter and electrical conductivity in the region where it occurs. A simple model to account for this phenomenon has been included in this accelerator code. This algorithm limits the ceiling on the Hall parameter to a maximum or "critical" value and reduces the electrical conductivity proportional to the reduction in the apparent Hall parameter. Therefore, Hall parameter is limited by:

$$\beta \leq \beta_{crit} \tag{B.1-31}$$

and electrical conductivity is adjusted when the equilibrium Hall parameter, β_0, exceeds the critical value by multiplying the conductivity by the Hall parameter ratio to give:

$$\sigma = \sigma_0 \frac{\beta}{\beta_0} \tag{B.1-32}$$

where the subscript "0" indicates the unadjusted values of conductivity and Hall parameter calculated by either the equilibrium chemistry model or the nonequilibrium model of Section B.1.2.3. Rosa indicates that "good performance seems to have been obtained in segmented-electrode channels up to a Hall parameter approaching 4 in combustion product gases, but only 2 in inert gases" (Ref. 2). A value of 5 for the critical Hall parameter has been used in some previous studies (Ref. 8 and 9); however, since Hall parameter decreases with increasing pressure, it remained low for all of the high-pressure studies reported herein and never exceeded a value of 2. The Hall parameter limit was not invoked in these studies.

B.1.2.2.3 *Finite Segmentation Model*

For Faraday devices with finite segmentation of the electrodes, it is necessary to include the effect of segmentation on performance. The effect of finite segmentation is to lower the apparent electrical conductivity and apparent Hall Parameter of the plasma. Electrical conductivity and Hall Parameter are adjusted for finite segmentation by the following amount [Ref. 2, Equation (4.14)]:

$$\frac{\sigma(apparent)}{\sigma(real)} = \frac{\beta(apparent)}{\beta(real)} = \frac{1}{1 + \frac{s}{h}(\beta - 0.44)} \qquad \text{(B.1-33)}$$

where "h" is the height of the channel and "s" is the electrode pitch or spacing (combined length of the insulator and electrode), as illustrated in Figure B.1-2 [Adapted from Ref. 2, Figure (4.7)].

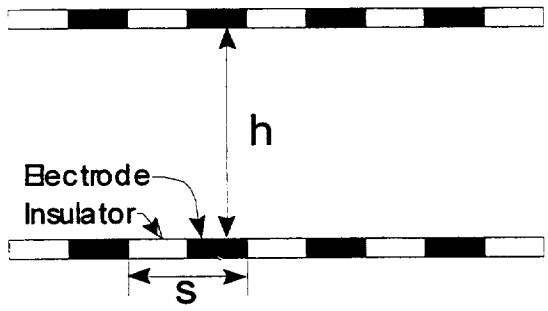

Figure B.1-2. Segmented Faraday channel.

B.1.2.2.4 *Electrode Voltage Drop Model*

When a voltage is applied between two electrodes and a current is established through an electrically conductive gas, a significant drop in the voltage occurs in the region very near the electrode surfaces. This region is the electrode sheath in which a concentration of electric charge accumulates and produces an intense electric field (the large voltage drops that are often referred to as the cathode and anode falls). In addition to creating the voltage drops, the phenomena occurring in the sheath layers increases the heat flux to the electrode surfaces.

If a voltage is applied externally to an accelerator channel, the voltage must be reduced by the magnitude of the voltage drops to determine the electric field applied to the plasma for the purposes of acceleration. Conversely, if the electric field in the plasma of an accelerator is determined during a channel design study and integrated over the height of the channel to give the voltage applied to the plasma, the voltage drops must be added to this to determine the voltage to be applied by the external power supplies. The actual magnitude of the electrode voltage drops are of no real consequence in the present MHD accelerator performance studies

since a design of the external power supplies are beyond the scope of this study. Therefore, the performance of the accelerators can be determined without regard to the power supply voltages. However, the effect of the sheath voltage drops on the electrode heat transfer rates is of interest in determining performance since this impacts the efficiency of the devices.

An approximate model for the electrode voltage drop has been implemented in the ACCEL code, primarily for the estimation of the increase in heat transfer to the electrode walls.[1] The results of the code validation study (Section B.1.3) appear to justify its inclusion. This voltage drop model is based on research into the characteristics of normal electric arcs by Nottingham (Ref. 10). The limitations of the model are described by Nottingham's requirements for a normal arc, "the arc must be free from external electrical, magnetic, atmospheric, and physical disturbances." Since all these disturbances are present in an MHD accelerator, it should be emphasized that the electrode voltage drop model is only an approximation of the effect normal arcing has on MHD accelerator performance.

The general form of the equation for the electrode voltage drop suggested by Nottingham is (Ref.10, Equation 12):

$$V_{electrode} = \left(C_1 + \frac{C_2}{i^n} \right) \tag{B.1-34}$$

where C_1, C_2, and n are constants depending on the electrode material and the medium through which the discharge occurs. C_1 and C_2 are also dependent on whether the electrode is acting as an anode or a cathode. Nottingham also shows the voltage drop is dependent on the arc length and given by the following equations (Ref. 10, Equation 19):

Anode:

$$V_{anode} = \left(C_1 + \frac{C_2}{i^n} \right) \left[1 - \exp\left\{ \left(-\alpha_1 - \frac{\alpha_2}{i^n} \right) L \right\} \right] \tag{B.1-35}$$

Cathode:

$$V_{cathode} = \left(D_1 + \frac{D_2}{i^n} \right) \left[1 - \exp\left(-\alpha_3 L \right) \right] \tag{B.1-36}$$

---

[1] This model was suggested by Rittenhouse et al. (Ref. 5) and used in the AEDC LoRho accelerator study for the same purpose.

where, α_1, α_2, and α_3 are dependent on the electrode material and the gaseous medium and L is the length of the arc. The Nottingham anode and cathode voltage drop equations with the constants evaluated for copper electrodes in air were given by Rittenhouse et al. (Ref. 5, Equations 38 and 39) as:

$$V_{an} = \left(15.5 + \frac{27}{I^{0.67}}\right)\left\{1 - \exp\left[\left(-0.235 - \frac{0.138}{I^{0.67}}\right) h\right]\right\} \qquad \text{(B.1- 37)}$$

$$V_{ca} = \left(14.5 + \frac{13.5}{I^{0.67}}\right)\left[1 - \exp\left(-6h\right)\right] \qquad \text{(B.1- 38)}$$

where "h" is the electrode separation (channel height) in millimeters (mm) (See Figure B.1- 2). Note the exponential term becomes very small for large electrode spacings. According to Nottingham, the exponential term becomes significant for electrode spacings of less than 1 mm, and the exponential term is negligible for electrode spacings greater than 15 mm (Ref. 10). Since the channel height will always be greater than 15 mm for the channels of interest in this study, the exponential terms were not implemented in the ACCEL code.

The heat transfer model for the effects of the electrode sheaths was discussed above. The electrode voltage drops, V_{an} and V_{ca}, were used in Equations (B.1- 17) and (B.1- 18).

B.1.2.2.5 *Boundary Layer Voltage Drop Model*

Boundary layer growth along the walls of an MHD accelerator channel results in velocity and temperature nonuniformities that cause nonuniformities in electrical conductivity and electric field. The velocity boundary layer results in a variation of velocity from a high value at the centerline of the channel to zero at the wall. Temperature nonuniformity resulting from cooling at the channel wall causes a variation from the core value to the wall temperature through the thermal boundary layer. Since electrical conductivity is a strong function of the gas temperature, the electrical conductivity near the channel walls is significantly reduced, and in some cases, it is reduced by several orders of magnitude.

The equation for the transverse electric field is given by equation (B.1- 29) and is dependent on the electrical conductivity and velocity of the gas. This dependency is apparent when Ohm's Law is integrated to calculate the transverse voltage V_y:

$$V_y = \int_0^h E_y \, dy \qquad \text{(B.1- 39)}$$

By substituting Ohm's Law into Equation (B.1- 39), the following expression is obtained for transverse electric field:

$$V_y = \int_0^h \left(\frac{j_y}{\sigma} + u B_z \right) d y \qquad \text{(B.1- 40)}$$

Since the electrical conductivity drops to a very low value near the cold wall of an accelerator, the first term in this integral can grow to a very large value. For the sake of illustration, assume the velocity and temperature in the core flow of an MHD duct are uniform and the variation in these values is confined to the boundary layer regions near the wall as illustrated in Figure B.1- 3a and 3b.

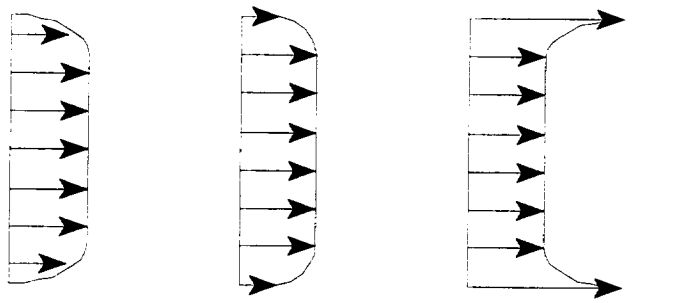

Figure B.1- 3. MHD channel velocity, temperature, and electric field profiles.

From Ohm's Law, the electric field in the core will be constant:

$$E_{yc} = \frac{j_y}{\sigma_c} + u_C B_Z \qquad \text{(B.1- 41)}$$

because the velocity and temperature are constant; however, the electric field in the boundary layer will vary with distance from the wall due to the velocity variation and the dependence of electrical conductivity on temperature:

$$E_{ybl}(y) = \left(\frac{j_y}{\sigma(y)} + u(y) B_z \right)_{bl} \qquad \text{(B.1- 42)}$$

Since the total current to an electrode is constant, an assumption of uniform current leads to a constant value of j_y, thus, j_y does not vary in the transverse direction. The integral in Equation (B.1- 40) can then be separated into a term for the uniform core region and an integral for the variation in the boundary layer:

$$V_y = E_{yc}\left(h - 2\delta\right) + 2\int_0^{\delta} E_{ybl}\, dy \qquad \text{(B.1- 43)}$$

As can be seen in Figure B.1- 3c, the variation of electrical conductivity and velocity causes the electric field to increase due to large values near the wall. Integration of Equation (B.1- 43) results in the voltage distribution shown in Figure B.1- 4.

A 1-D model, such as that described herein, does not model the detailed variation of parameters in the boundary layers. Instead, a uniform flow field from wall to wall is assumed. A uniform electric field at the core value would result in a calculated voltage that is given by:

$$V_{yc} = E_{yc}\, h \qquad \text{(B.1- 44)}$$

This value, as represented by the dotted line in Figure B.1- 4, will be less than the actual applied voltage due to the voltage drops in the boundary layer and the difference will be twice the voltage drop of one boundary layer. Thus,

$$V_{y-applied} = V_{yc} + 2V_{ybl} \qquad \text{(B.1- 45)}$$

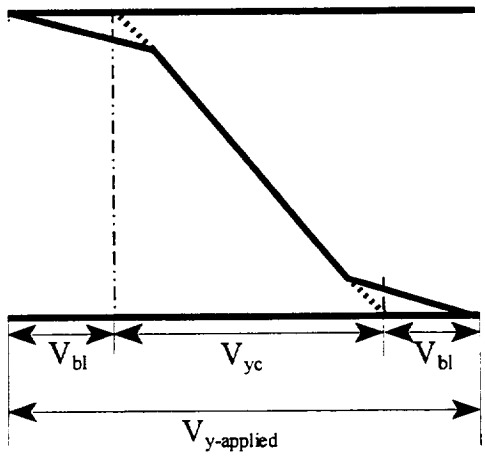

Figure B.1- 4. Voltage distribution across an MHD accelerator channel.

It should be noted that V_{yc} is not a "core" value of V_y but is the voltage imposed across the electrodes if a uniform electric field, $E_{yc,}$ extended to the walls. Since the electric field is uniform in the core region and varies in the boundary layer, the integration above can be restricted to the boundary layer region, as noted above in Equation (B.1- 43):

$$V_{y-applied} = E_{yc}\left(h - 2\delta\right) + 2\int_0^{\delta} E_{ybl}\, dy \qquad \text{(B.1- 46)}$$

and this can be rewritten as:

$$V_{y-applied} = E_{yc}\, h + 2\int_0^{\delta} E_{ybl}\, dy - 2E_{yc}\delta = E_{yc}h + 2\int_0^{\delta}\left(E_{ybl} - E_{yc}\right) dy \qquad \text{(B.1- 47)}$$

By comparing this with Equation (B.1- 45), the boundary layer voltage drop (total for the two boundary layers) is seen to be:

$$Boundary\ Layer\ Voltage\ Drop = 2V_{ybl} = 2\int_0^{\delta}\left(E_{ybl} - E_{yc}\right) d\, y \qquad \text{(B.1- 48)}$$

where the electric field in the electrode boundary layer, E_{ybl}, varies with distance from the wall as noted above:

$$E_{ybl}(y) = \left(\frac{j_y}{\sigma(y)} + u(y) B_z\right)_{bl} \qquad \text{(B.1- 49)}$$

Since the boundary layers are not modeled in the 1-D code, a boundary layer voltage drop estimate factor (*BndryVff*) has been included in this code to estimate the effect of these voltage drops.

Three choices for calculating the boundary layer voltage drop are provided in the ACCEL code:

1.) No boundary layer voltage drop:

$$Boundary\ Layer\ Voltage\ Drop = 0 \qquad \text{(B.1- 50)}$$

2.) Boundary layer voltage drop calculated based on the induced electric field, (u×B):

$$BoundaryLayerVoltageDrop = \left(BndryVff\right)\left(uB_z\right) \qquad \text{(B.1- 51)}$$

3.) Boundary layer voltage drop calculated based on both the applied and induced field, (E_y - uB_z):

$$Boundary\ Layer\ Voltage\ Drop = \left(BndryVff\right)\left(Ey - uB_z\right) \qquad \text{(B.1- 52)}$$

B.1.2.2.6 *Electrical Constraint Models*

The electrical model includes a constraint on the magnitude of the electric field vector. To prevent strong arc formation resulting in the reduction of the performance of the accelerator and causing rapid electrode erosion, the field is constrained to a value equal to or below a user specified maximum value:

$$E = \sqrt{E_y^2 + E_x^2} \le E_{\max} \qquad \text{(B.1- 53)}$$

The transverse current density, j_y is adjusted (when necessary) to keep the electric field magnitude within the specified constraint. Otherwise, the current density is maintained at the user-specified maximum value, $j_y(max)$.

Alternatively, the user can specify an axial distribution of one of the electrical parameters, and the electrical solution will be calculated at each axial position based on the value at that location. Axial distribution of transverse current density, $[j_y(x)]$, transverse electric field, $[E_y(x)]$, transverse voltage; $[V_y(x)]$, or Faraday load factor, $[E_y/uB_z]$, can be specified. When an axial distribution is specified, the current density and electric field maximum values are ignored.

B.1.2.2.7 *Total Electrical Power Required*

The total applied power is given by the power density integrated over the channel volume. Thus:

$$P_e = \int_0^V j \cdot E\, dV = \int_0^L j_y\, E_y\, A\, dx \qquad \text{(B.1- 54)}$$

where V is the channel volume and L is the channel length.

B.1.2.3 Nonequilibrium Ionization Model

The present model has the capability to evaluate either seeded or unseeded MHD flow. Seeded nonequilibrium flow is analyzed using the model discussed in the following paragraphs. Unseeded air in ionizational nonequilibrium uses the same model but assumes nitric oxide (NO) to be a surrogate seed species as discussed below. In this model, equilibrium chemistry with

nonequilibrium ionization is assumed for either seeded or unseeded MHD channel designs, requiring a table of equilibrium thermodynamic and transport properties be provided.

In the absence of an artificial seed species, the naturally occurring species having the lowest ionization potential is assumed to ionize through energy coupling of its valence electrons with the higher energy-free electrons accelerated in the electric field. In dry air at expected accelerator operating temperature (typically 3,000 K or less), the primary species present are monatomic and diatomic nitrogen (N_2), monatomic and diatomic oxygen (O_2), and NO. The ionization potential of NO can be seen from the data in Table B.1- 2 to be the lowest of the air species.

Table B.1- 2. Ionization potential of species occurring in air.

Species	Ionization Potential (eV)
N_2	15.6
N	14.53
O_2	12.05
O	13.61
NO	9.26

The plasma is assumed to be in chemical equilibrium at the fluid dynamic temperature and pressure. For the accelerator expected operating conditions, the equilibrium concentration of NO is sufficient to provide the necessary electrical conductivity from ionization. The equilibrium concentration can be seen in Figure B.1- 5 to be greater than 2 molar (M) percent at a temperature of 2,500 K and approximately 4% at 3,000 K.

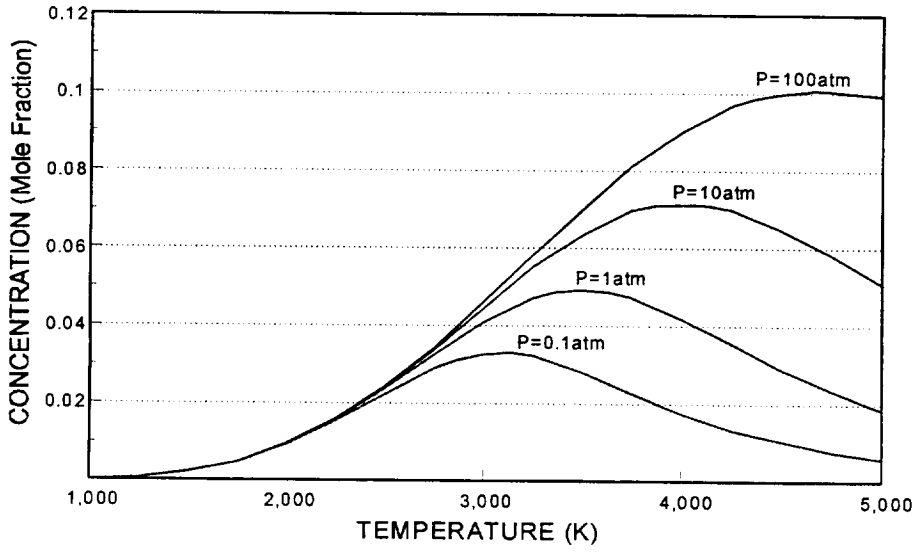

Figure B.1- 5. Equilibrium concentration of NO in air.

Because the level of ionization of NO is assumed to reach an equilibrium characterized by the electron temperature rather than the heavy gas temperature, the electron number density is determined by the Saha equation evaluated at the electron temperature. For a neutral plasma (i.e., $n_e = n_i$), the Saha equation as given by Rosa (Ref. 2) can be rearranged to solve for the electron concentration:

$$n_e = f(T_e)\frac{\left[\sqrt{1 + 4n_s / f(T_e)} - 1\right]}{2} \tag{B.1- 55}$$

where

$$f(T_e) = \frac{(2\pi m_e k T_e)^{3/2}}{h^3}\frac{2g_i}{g_0}\exp\left[-\frac{e \in_i}{kT_e}\right] \tag{B.1- 56}$$

The plasma electrical conductivity is then calculated from Reference 2, Equations 2.11 and 2.12:

$$\sigma = \frac{n_e e^2}{m_e c_e}\left\{\frac{1}{\sum_k n_k Q_k + 3.9 n_i\left[\frac{e^2}{8\pi \in_0 k T_e}\right]^2 \ln\Lambda}\right\} \tag{B.1- 57}$$

where

$$\Lambda = \frac{12\pi}{\sqrt{n_e}}\left[\frac{\in_0 k T}{e^2}\right]^{3/2} \tag{B.1- 58}$$

The Hall parameter is calculated from Reference 2, Equation 2.8:

$$\beta = \omega\tau = \frac{eB_z}{m_e n Q c_e} \tag{B.1- 59}$$

The mean random thermal velocity of the electrons is given by Reference 2, page 23:

$$c_e = \sqrt{\frac{8\,k\,T_e}{\pi\,m_e}} \qquad \text{(B.1- 60)}$$

The electron temperature, T_e, used in the above equations can be determined by considering the mechanisms by which energy is transferred to the plasma. Charged particles (electrons and ions) in the plasma are accelerated in the presence of the imposed electric field, therefore increasing their velocity and kinetic energy. However, ion acceleration and ion currents are neglected since they are very small when compared to electron acceleration and currents (due to the large mass of the ions). Energy is then transferred to the heavy particles of the working fluid through electron collisions with the neutral and ionic species (atoms and molecules) in the gas.

When electrons collide with heavy particles, they lose a fraction of their excess kinetic energy to the other particle with each collision. The energy transferred from the electron per collision is given by:

$$W = \delta \frac{3}{2} k\left(T_e - T_g\right) \qquad \text{(B.1- 61)}$$

where δ is the mean fractional energy loss per collision:

$$\delta = \delta' \left[\frac{2\,m_e}{m_g}\right] \qquad \text{(B.1- 62)}$$

and δ' is the energy loss factor for inelastic collisions.

For elastic collisions (where energy is transferred only to translation in the heavy particle), the energy loss factor, $\delta' = 1$, and the fraction of the excess kinetic energy transferred during each collision is twice the mass ratio of the particles. However, collisions involving diatomic and polyatomic molecules are inelastic due to the excitation of vibration and rotation, resulting in large energy loss factors.

Through many collisions, the electron temperature is lowered, the heavy particle gas temperature is raised, and directed kinetic energy is added to the plasma. This energy exchange is the mechanism by which the electron temperature would equilibrate with the bulk gas temperature if no external power were added. If an elevated electron temperature is to be maintained relative to the bulk gas temperature, power must be added continuously to make up for the electron kinetic energy lost through collisions.

Assuming validity of the two-temperature model described above, the power input required to maintain this temperature difference can be calculated by using an electron energy equation. As determined by Rosa (Ref. 2), the required power input is:

$$P_{reqd} = n_g n_e Q c_e \delta' \left[\frac{2m_e}{m_g}\right] \frac{3}{2} k\left(T_e - T_g\right) \qquad \text{(B.1- 63)}$$

The energy loss factor for air, δ', from Craggs and Massey *Handbuck der Physik* (Ref. 11), is given in Figure B.1- 6. Particular values of δ' over the range of electron temperature of interest to the present study are presented in Table B.1- 3, taken from Rosa (Ref. 2, Table 5.2).

Rosa, referring to Equation (B.1- 63), says, "The validity of this equation and of the assumption of ionization equilibrium at the temperature T_e has been largely verified by Kerrebrock and Hoffman (Ref. 12), and by others (Refs. 13 and 14) by studying the characteristics of discharges in seeded gases."

The electrical power density applied to the accelerator plasma is:

$$Power\ density = j_y E_y = \frac{j_y^{\,2}}{\sigma} + j_y u B_z \qquad \text{(B.1- 64)}$$

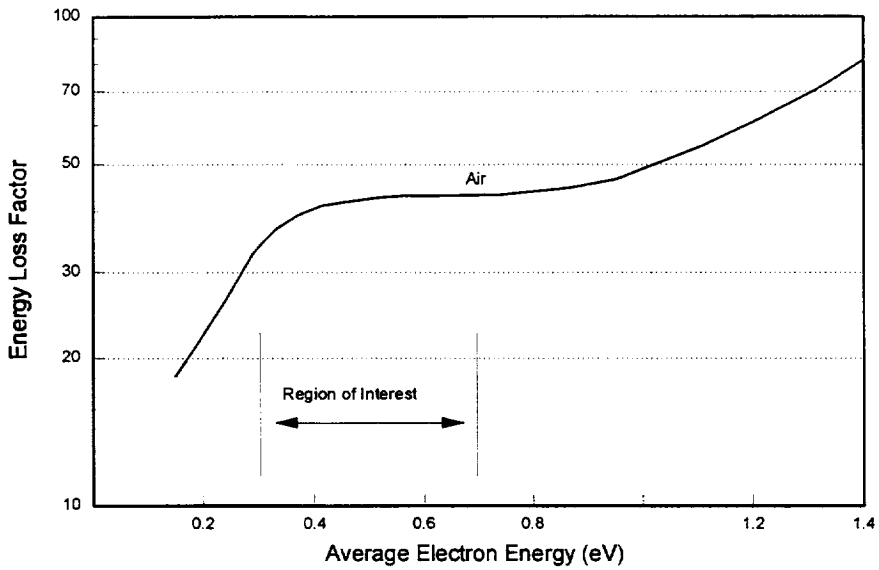

Figure B.1- 6. δ', energy loss factor for air (Ref. 11).

Table B.1- 3. Electron energy loss factor (Ref. 2.)	
Electron Temperature (K)	δ' for Air
3,000	40
4,000	43
5,000	44
6,000	44
8,000	51
$2m_e/m_0$ (air)	3.87×10^{-5}

The second term on the right hand side, $j_y u B_z$, is the "push work" term and is responsible for increasing the momentum of the flow through the MHD body force. The first term on the right hand side, j_y^2/σ, is the Joule heating term. This represents the energy added to the electrons through acceleration in the transverse electric field and is ultimately responsible for heating the gas through electron collisions with heavy particles.

Equating the Joule heating term [power applied to the electrons, Equation (B.1- 64)] to the power needed to maintain the elevated electron temperature, Equation (B.1- 63), gives the equality from which the electron temperature can be determined:

$$\frac{j_y^2}{\sigma} = n_g n_e Q C_e \delta' \left[\frac{2m_e}{m_g}\right] \frac{3}{2} k\left(T_e - T_g\right) \qquad \text{(B.1- 65)}$$

Electron temperature values higher than those that would be sustained in this manner may be possible through external augmentation using microwave, laser, or electron beams (e-beams) in the MHD channel.

B.1.2.4 Summary

A segmented Faraday, MHD accelerator computer code used in the MARIAH Project design and parametric studies is described. Multiple design models are available for studying different design constraints. The ACCEL computer program will model seeded and unseeded plasma working fluids with equilibrium chemistry and either equilibrium or two-temperature nonequilibrium ionization. The model includes approximations for electrode voltage drops, boundary layer voltage drops, finite segmentation effects, and critical Hall parameter limitations.

B.1.3 Verification and Validation

NOMENCLATURE

A - Cross-sectional area, (m^2)
B_z - Magnetic field strength, (T)
h - Static enthalpy, (J/kg)
H_t - Total enthalpy, (J/kg)
$\dot{m}$ - Mass flow rate, (kg/s)
p - Static pressure, (Pa)
p_t - Total pressure, (Pa)
p_t' - Impact pressure behind a normal shock, (Pa)
R - Gas constant, (J/kg K)
T - Static temperature, (K)
u - Flow velocity, (m/s)
γ - Ratio of specific heats
ρ - Mass density, (kg/m^3)

B.1.3.1 Overview

Verification and validation of the MSE 1-D MHD ACCEL code was completed prior to using it for the MARIAH Project analysis discussed in this report. The purpose of verification, a process that is performed continuously during the development and modification of the accelerator code, is to verify the code logic executes as designed and the calculations are correctly performed. Validation is accomplished to verify the computational model approximates the physics of MHD acceleration in an experimental device to the degree required. Verification ensures the model is being correctly computed, and validation verifies the results approximate the real-world device. MHD accelerators were tested at a number of locations in the United States and Russia during the 1960s. Documentation from many of these test programs was reviewed to locate suitable experimental data for validation of the ACCEL code. Validation of the ACCEL code was very time consuming, and time constraints did not permit validation against multiple experimental programs. Therefore, the available documentation was reviewed to locate one experimental program, which provided sufficient data to validate the model over a wide range of operating conditions. Of the experiments reviewed, one met the requirements.

A series of experiments known as LoRho (an acronym for low density) were conducted at the U.S. Air Force's Arnold Engineering Development Center (AEDC) in Tennessee during the 1960s (Ref. 5). These were continuous flow experiments with ample instrumentation to provide all the necessary data for validation of the 1-D code. Data was presented for operation of the LoRho channel at power levels from zero to 400 kW, providing sufficient information to validate the code over a range of desirable operating conditions. Furthermore, data was provided for the arc-heater flow through the unpowered accelerator channel, allowing calibration of the heat transfer and wall friction models in the code. The documentation for this series of experiments sufficiently met the needs for validation of the ACCEL code.

An overview of the AEDC LoRho experimental program is included in the next section. Much of the essential data from the LoRho documentation used for the validation has been reproduced in figures in that section. A thorough discussion of the validation analysis is presented in Section B.1.3.3. Further information on the MHD accelerator model in the ACCEL code is presented in Section B.1.2.

B.1.3.2 AEDC LoRho Facility and Data Profile

Experimental investigations into the feasibility of extending the velocity and altitude capabilities of gas dynamic testing facilities were conducted in the AEDC LoRho series of experiments. This program used a continuous flow arc heater as the plasma generator for a linear, segmented, Faraday MHD accelerator and conducted experiments at the proof-of-concept (POC) scale to assess the feasibility of MHD acceleration with high power input at near-atmospheric pressure levels. These experiments provided valuable performance data for MHD acceleration of potassium (K)-seeded nitrogen (N_2)over a wide range of operating conditions.

Three MHD accelerator channels were tested in the LoRho program. A small design verification channel known as Accelerator A, consisting of 20 electrode pairs, was first tested to verify the channel design and establish operational procedures for the LoRho program. This was followed by a more extensive testing program using two 117-electrode-pair channels known as Accelerators B and B_1. A sketch of the 117-electrode-pair channel is shown in Figure B.1- 7. All of the LoRho experiments were conducted using seeded N_2 as the working gas. Accelerator A used potassium carbonate (K_2CO_3) dissolved in water for seeding while Accelerators B and B_1 predominately used dry, powdered potassium carbonate. Seeding with a eutectic solution of potassium and sodium (NaK) was attempted; however, condensation of this seed material on the cold accelerator walls electrically shorted the channel, and the expected performance could not be achieved. Also, a limited amount of data was obtained using calcium oxide (CaO) seed.

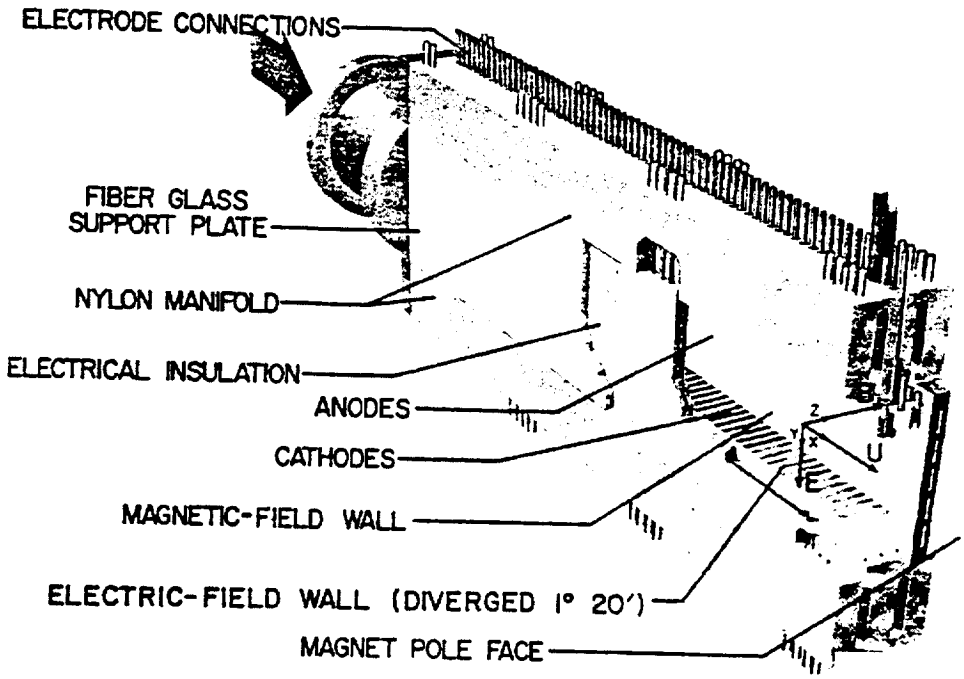

Figure B.1- 7. Sketch of the AEDC LoRho 117-electrode-pair MHD Accelerator (Ref. 5)

A direct current (dc), gas-stabilized plasma generator (arc-heater) was operated at a power input of approximately 1.2 megawatts (MW) to heat the N_2 working gas for the LoRho experiments. For accelerators A and B, seed was injected into the high temperature N_2 in a stilling chamber following the plasma generator. The plasma then entered a supersonic nozzle, which expanded the flow to the desired MHD channel entrance velocity. A detailed assembly drawing of the plasma generator and Accelerator B are shown in Figure B.1- 8. The seed injection ring and the nozzle extension shown were removed for Accelerator B_1, and the seed was injected into the nozzle. All components, including the plasma generator, stilling chamber, nozzle, and accelerator walls were water-cooled.

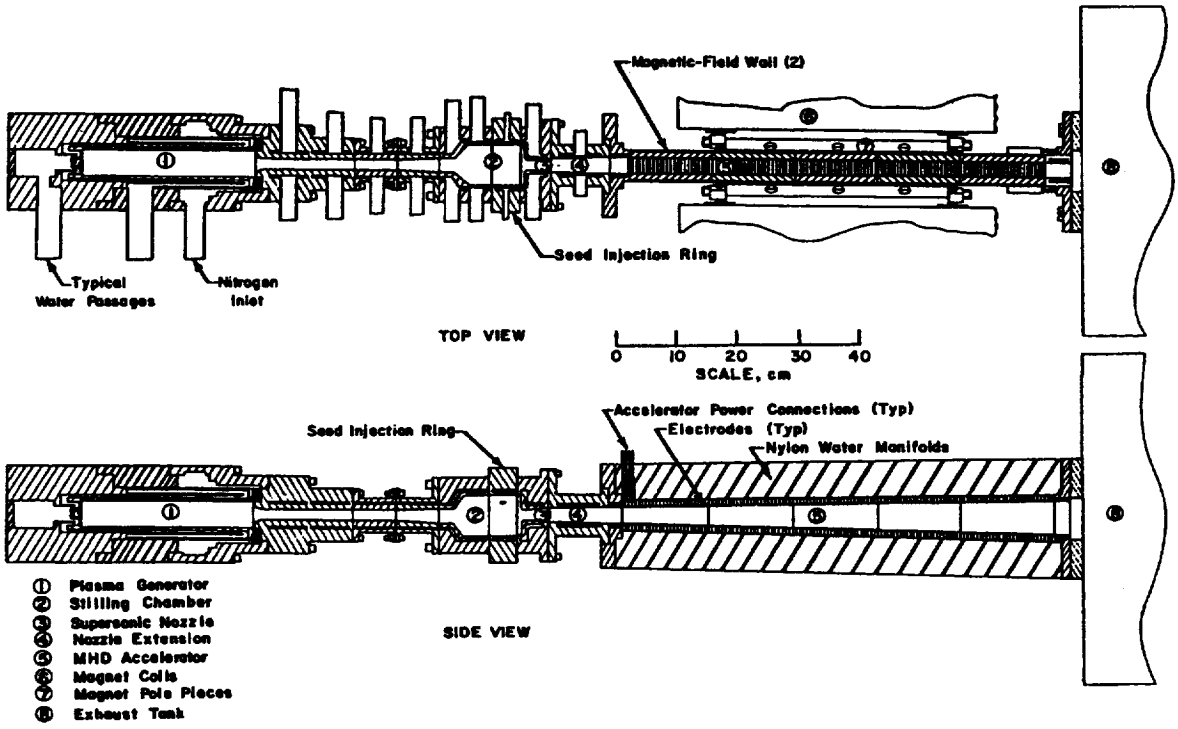

Figure B.1- 8. AEDC LoRho plasma generator and accelerator B components (Ref. 5, Fig. 5).

Accelerators B and B_1 were 77 centimeters (cm) long and geometrically identical. Both the electrode walls and magnetic field walls were segmented in the axial direction to prevent axial shorting and reduce axial eddy current loses due to the Hall electric field.[2] All electrodes and the magnetic field wall components were water cooled by copper modules that were plasma sprayed

[2] The Hall field is an axial electric field that is induced in an MHD device when operated in the Faraday mode. If an internal or external axial shorting path exists, the Hall field will result in a Hall current that will reduce the performance of the MHD device.

with beryllium oxide (BeO) or coated with aluminum oxide (Al_2O_3) to provide electrical insulation between the components. Accelerator B used BeO for all the wall components, whereas Accelerator B_1 used BeO on the cathode wall and Al_2O_3 on all other walls. The electrode surfaces exposed to the plasma were left uncoated to allow electrical discharge to the plasma; however, the magnetic field walls were completely encapsulated with the insulating material to provide the required electrical resistance. Accelerators B and B_1 entrance dimensions were 2.54 cm (1.00 in.) between the magnetic field walls and 2.98 cm (1.97 in.) between electrode walls. The magnetic field walls were parallel; however, the electrode walls diverged to provide exit dimensions of 2.54 cm (1.00 in.) by 6.22 cm (2.45 in.). The electrode spacing was 0.658 cm (0.259 in.).

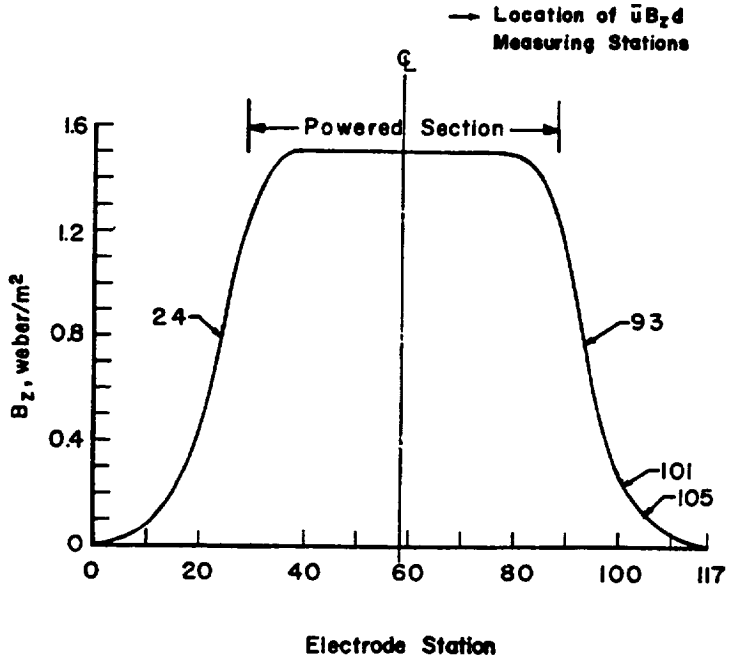

Figure B.1- 9. Magnetic field distribution for AEDC LoRho accelerator B testing (Ref. 5, Fig. 10)

An iron-core electromagnet provided a 1.51-Tesla (T) peak magnetic field for the LoRho accelerator tests. This magnet had rectangular pole faces measuring 7.6 (2.99 in.) by 38.1 cm (15.0) and a pole gap of 6 cm and produced the field distribution shown in Figure B.1- 9. LoRho accelerator channels were powered by 1,700 12-volt (V) automotive batteries configured to provide 60 electrically isolated circuits. Only the 60 center electrodes were powered in Accelerators B and B_1 (all 20 electrodes were powered in Accelerator A). Other unpowered electrodes (indicated in Figure B.1- 9) were used to measure the induced voltage (uB_zh), and from this, calculate the average velocity.

Exit static pressure data at applied power levels from zero to 400 kW, obtained in LoRho tests, is given in Figure B.1- 10; average velocity at the channel exit is presented in Figure B.1- 11; average velocity variation in the channel is shown in Figure B.1- 12; and heat transfer data is shown in Figure B.1- 13. Data from Accelerator B experiments were used to validate the MSE MHD Accelerator Code (ACCEL), as discussed in the next section.

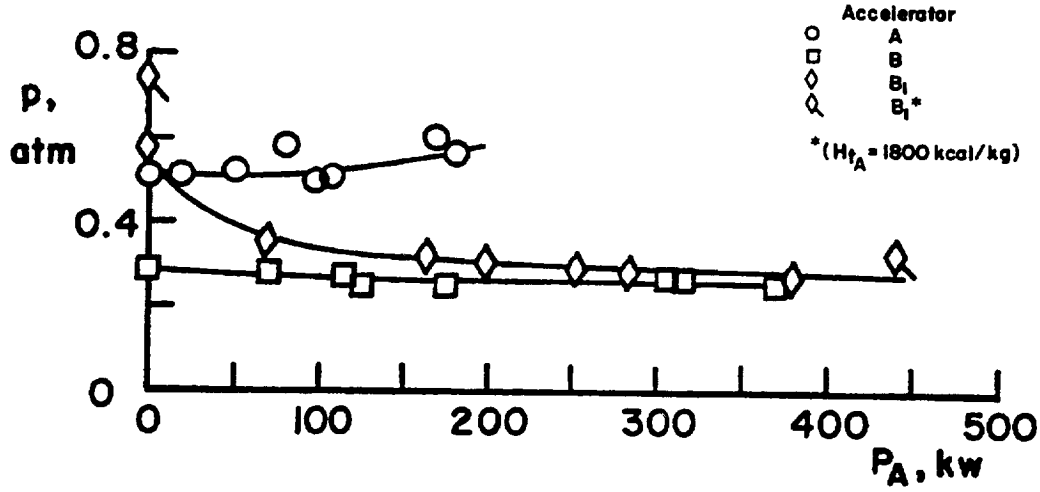

Figure B.1- 10. Exit static pressure for LoRho channels (Ref. 1, Fig. 20b).

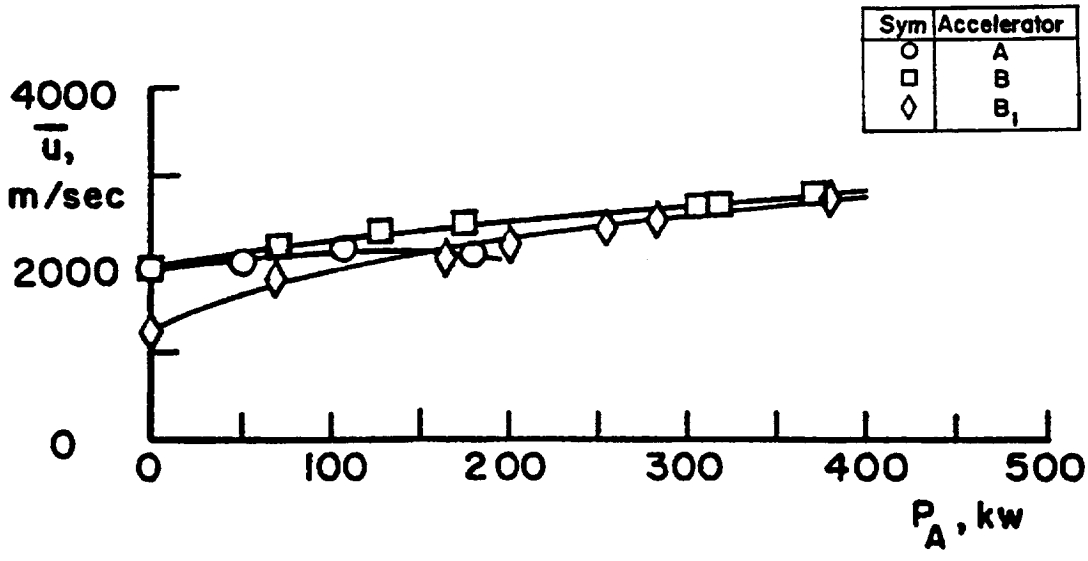

Figure B.1- 11. Average velocity at LoRho channel exit (Ref. 5, Fig. 23c)

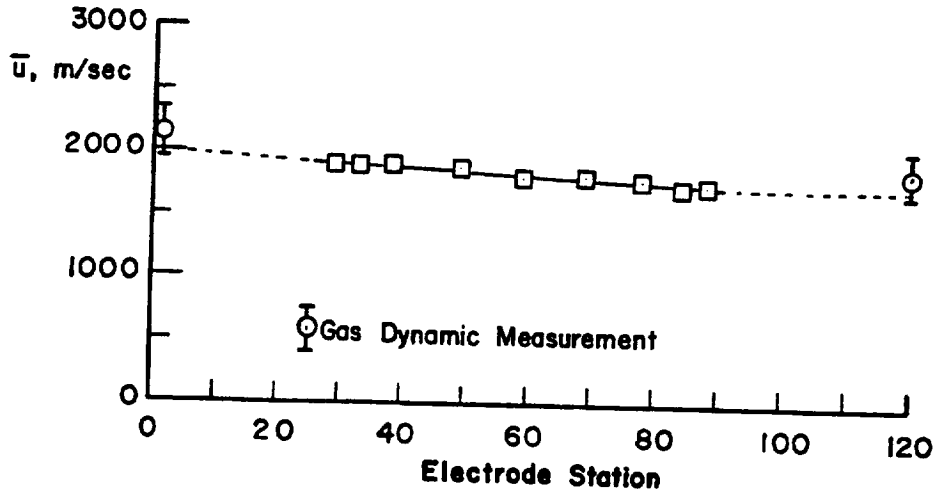

Figure B.1- 12. LoRho Accelerator B velocity distribution (Ref. 1, Fig. 38a).

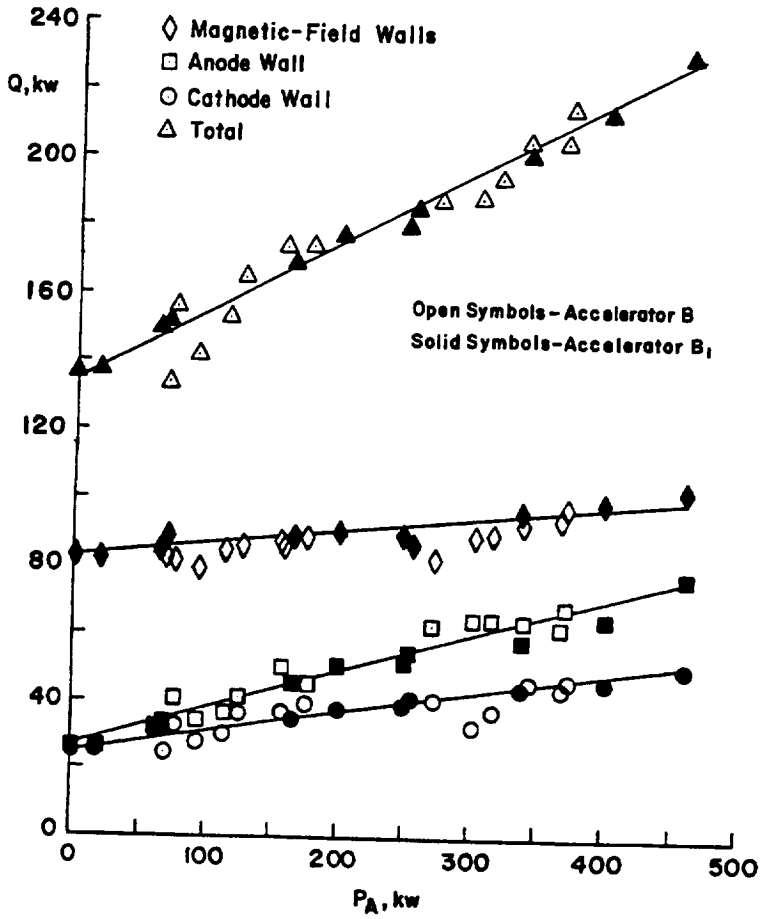

Figure B.1- 13. Heat transfer for LoRho Accelerators B and B_1 (Ref. 5, Fig. 52)

B.1.3.3 Model Validation Analysis

An analysis was conducted to validate the 1-D MHD accelerator model by comparing the predictions of the ACCEL computer code with experimental data from the AEDC LoRho experiments. Test conditions from the LoRho program (Ref. 5) were used to establish entrance conditions, channel geometry, and unknown parameters that must be approximated. Since the ACCEL MHD accelerator code is a 1-D model with approximations for boundary layer effects, a calibration was required to set parameter values used in the wall friction and convective heat transfer models. These parameters included an equivalent sand grain roughness height for the wall roughness value used in both models and the wall surface temperature used in the heat transfer model.

All of the analyses used in the validation study were performed with the segmented Faraday electrical configuration. Equilibrium chemistry, ionization, and thermodynamic properties were assumed for all analyses. The model included convective heat transfer, with contributions due to the electrode sheath, and wall friction based on an equivalent sand grain roughness (see Section B.1.2). Anode and cathode voltage drops were calculated with an adaptation of the Nottingham model (Ref. 10) described in Section B.1.2. All analyses used a table of thermodynamic and transport properties for N_2 seeded with 1.5 % K, by weight, from K_2CO_3. A properties table was created using the NASA Chemical Equilibrium with Applications Computer Code (CEA) (Refs. 15, 16, and 17).

Experimental investigations were conducted during the LoRho program using three accelerator configurations (A, B, and B_1) as discussed in the previous section. Accelerator B was chosen for the validation analysis since Accelerator A was used in the LoRho program for only design verification and development of operational procedures and Accelerator B_1 would be difficult to model accurately with a 1-D code due to flow separation that occurred during unpowered operation. Furthermore, there was very little data available for Accelerator A and only minor differences in the geometry and operating conditions of Accelerators B and B_1. Therefore, Accelerator B was chosen since an abundance of data was available, and the flow quality was suitable for modeling with a 1-D code.

A suitable validation would not have been possible without the extensive and thorough documentation of the LoRho tests reported in Reference 5. Some errors and inconsistencies were noted, but fortunately, there was sufficient data available to resolve these problems. Entrance and exit conditions for Accelerator B (taken from Tables I and II of Ref. 5) are listed in Table B.1- 4 below. However, these entrance conditions, as listed, are not consistent. Only three of the six flow parameter values are needed to define the flow conditions at the accelerator entrance; the others should be calculated from the chosen three independent variables and the known entrance area. For example, calculation of the density from the pressure and temperature values listed produces the exact value provided in the table; consequently, these values are consistent. However, calculation of mass flow from the density and velocity listed and an entrance area of 7.569×10^{-4} gives a value of 0.087 kilograms per second (kg/s), which is 11% less than the 0.098 kg/s given in the table. Since all of these values would be subject to experimental measurement error, the correct values to use for the validation study were not easily determined.

Table B.1- 4. Entrance and exit conditions for LoRho accelerator B (from Tables I and II of Ref. 5).

Location	Mass Flow (kg/s)	Seed Fraction (%)	Mach Number	Velocity (m/s)	Pressure (atm)	Temperature (K)	Density (kg/m^3)
Entrance	0.098	1.5	1.8	2,100	0.59	3,650	0.055
Exit			1.75	1,900	0.28	3,000	0.032

The methods used for measuring or calculating each of the parameters in Table B.1- 4 were considered in an attempt to determine which values were the most likely to be correct. A brief summary of the LoRho flow parameter measurements and calculations follows.

Mass flow was measured using a calibrated orifice flow meter, and static pressure was directly measured with a pressure transducer in a wall orifice. Estimates of the measurement accuracy were not given in the report:

$$\bar{H}_t = \bar{h} + \frac{\bar{u}^2}{2} = \bar{h} + \frac{(\overline{\rho u})^2 R^2 T^2}{2 p^2}$$

where

$$\bar{h} = \bar{h}(p, \bar{T})$$

$$\overline{\rho u} = \frac{\dot{m}}{A} \qquad \text{(B.1 66)}$$

Accelerator entrance flow properties (including the average entrance velocity) were determined by four different methods, which reportedly agreed within 10%. The four methods, repeated here from Reference 5, were:

1. Isentropic expansion on an N_2 Mollier diagram from the point determined by the total enthalpy and total pressure in the stilling chamber of the plasma generator to the point determined by the accelerator entrance static pressure.

2. Solution of the 1-D energy equation for the average temperature and then using the continuity equation, equation of state, and Mach number definition to obtain the remaining flow properties.

3. Normal shock calculations using the measured impact pressure, average total enthalpy, and entrance static pressure. These solutions were obtained with the aid of N_2 real-gas normal shock curves prepared at AEDC.

4. Ideal gas calculations using a value for the ratio of specific heats (γ) representative of the average thermodynamic conditions present in the nozzle. In this calculation, the entrance conditions were determined separately from the measured pressure ratios p/p_t, p_t'/p_t, and p_t'/p.

The velocity value presented in Table B.1- 4 was calculated from the normal shock calculations using Method 3 above. Velocities in the channel, determined from the open-circuit induced voltages, were also extrapolated to the entrance to estimate entrance velocities. The value reported in Table I of Reference 5 was given as 2,000 meters per second (m/s), while a point with an error bar on Figure 38a of Reference 5 (see Fig. B.1- 12) gave this value as $2{,}150 \pm 200$ m/s. No other indications of accuracy were given for reported velocities. Entrance temperature was determined from the average total enthalpy, static pressure measurement, mass flow rate, and an N_2 Mollier diagram for the average static enthalpy using Method 2 above.

With this information, the confidence that might be given each of these parameters can be assessed. Entrance pressure and mass flow rate were measured directly as noted above. Accordingly, these measurements would be expected to be reasonably accurate compared to the indirect measurement of velocity and temperature as described. Thus, in the absence of other reasons to mistrust these values, these will be referred to as two of the three independent variables needed to define the entrance conditions.

As noted above, velocity calculation required the use of two measurements at the channel entrance (impact pressure and static pressure) and the calculated value of the average total enthalpy. The average total enthalpy was obtained from a plasma generator energy balance, which involved measurement of the arc-heater electrical power, heat loss, and mass flow rate. Nitrogen real-gas thermodynamic data was used for the shock calculations because K-seeded N_2 data was apparently not available. Since velocity determination involved at least five parameter measurements, with their associated measurement errors, and the use of N_2 data in lieu of equilibrium data for the seeded N_2 chemistry, the uncertainty in this value might be relatively large. It was noted that a reasonably good agreement was obtained between the various methods for determination of velocity; yet each of these methods involved similar measurements and approximations. However, a moderate degree of confidence in the reported values should be justified.

Temperature calculation required the use of two measured quantities (static pressure and mass flow rate) and the average total enthalpy, which was also used in the velocity calculation discussed in the preceding paragraph. This calculation also required the use of N_2 thermodynamic data due to the unavailability of seeded N_2 data. It would be difficult to choose between the given values of temperature and velocity based on this information since both velocity and temperature involve similar calculations and uncertainties.

Since the report noted that an N_2 Mollier diagram was used, it is assumed that properties for the seeded N_2 plasma were not available. This could result in a significant error in the temperature calculation and, for this reason, temperature is the most probable source of the inconsistency in the entrance data. However, solutions were run with the ACCEL code using each of the

combinations in three out of the four values. It quickly became evident that any solution using the listed value of temperature (3,650 K) would significantly overpredict heat transfer and exit velocity and that no satisfactory solution could be obtained with this temperature. However, as discussed further in the analysis below, using the given values of mass flow, velocity, and pressure produced very good agreement with experimental data. Pressure, velocity, and mass flow (from Table B.1- 4) were used for all further analyses in the validation study, and temperature, density, and Mach number were calculated from these, as reported in Table B.1- 5.

Table B.1- 5. Accelerator entrance conditions used for validation study.

Mass Flow (kg/s)	Seed Fraction (percent)	Pressure (atm)	Velocity (m/s)	Temperature (Calculated) (K)	Density (Calculated) (kg/m^3)	Mach Number (Calculated)
0.098	1.5	0.59	2,100	3,274	0.0616	1.89

Code calibration then proceeded, and values for the roughness parameter used in the wall friction and heat transfer models and a wall temperature were determined using reported values for the channel heat transfer and exit velocity in the unpowered accelerator. The wall roughness and temperature each affect both the heat transfer and exit velocity; consequently, an iterative process was used to establish their values.

Reference 5 reported estimated values for the wall surface temperature to be between 500 and 600 K; however, from the discussion, there was obviously some uncertainty to this upper limit. As a result, values of 500, 600, 700, and 800 K were tested.[3] Through a trial and error process, which involved matching both heat transfer and exit velocity while varying wall temperature and roughness, a value of 600 K was found to produce acceptable results and was adopted for the remainder of the validation study.

Finally, the equivalent sand grain roughness height was determined for two different exit velocities that were reported in Reference 5. An exit velocity of 1,900 m/s was reported in Table I of Reference 5 (see Table B.1- 4); however, graphs of the exit velocity versus applied

[3] Wall temperature was rounded to hundreds for a number of reasons. First, solutions were found to be relatively insensitive to the wall temperature in this range. Second, the values of heat transfer and exit velocity used to establish this and the roughness are not known to sufficient accuracy to warrant further refinement of the wall temperature. Finally, the actual wall temperature will vary throughout the channel and depend on whether the wall is an anode, cathode, or magnetic field wall and on axial position due to differing heat transfer phenomena and thermal conditions. Thus, the wall temperature chosen for this model represents only a rough approximation that produces an acceptable computational result, and rounding to hundreds is justified.

power (Fig. 23c of Ref. 5, reproduced in Figure B.1- 11 above) indicated a value of 1,950 m/s at zero power. Therefore, both values were explored during the validation analysis. Figure B.1- 14 shows the variation of exit velocity with the roughness height. A roughness height of 0.053 millimeter (mm) (0.00209 in.) results in an exit velocity of 1,950 m/s and a 0.088-mm (0.00396 in.) height gives a velocity of 1,900 m/s. LoRho solutions were then run with the ACCEL code using each of these values at various power levels and compared to the experimental data.

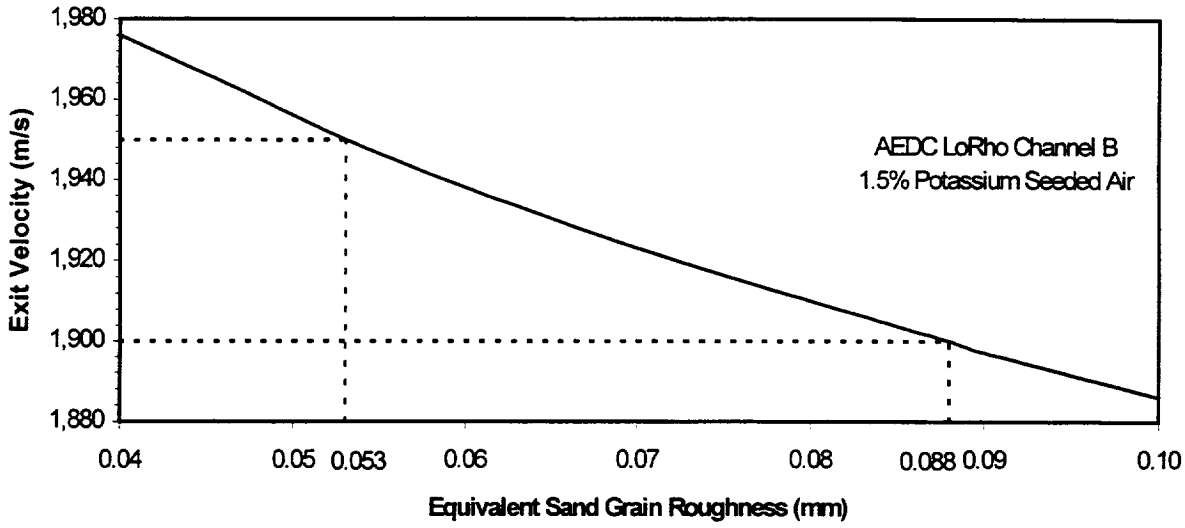

Figure B.1- 14. Variation of exit velocity with wall roughness height.

Comparison of the theoretical exit velocities at power levels from zero to 400 kW with the LoRho experimentally measured values is shown in Figure B.1- 15. Error bars are shown on the experimental data to indicate the range of uncertainty reported for exit velocities.[4] Considering the experimental uncertainties, agreement between the 1-D model predictions and experimental results is excellent.

[4] Figure 38a of Reference 5 (see Figure B.1- 12) indicated error bars for the entrance and exit velocity values with a spread of approximately ±200 m/s. This was the only indication in the report of a value for the uncertainty of measured data.

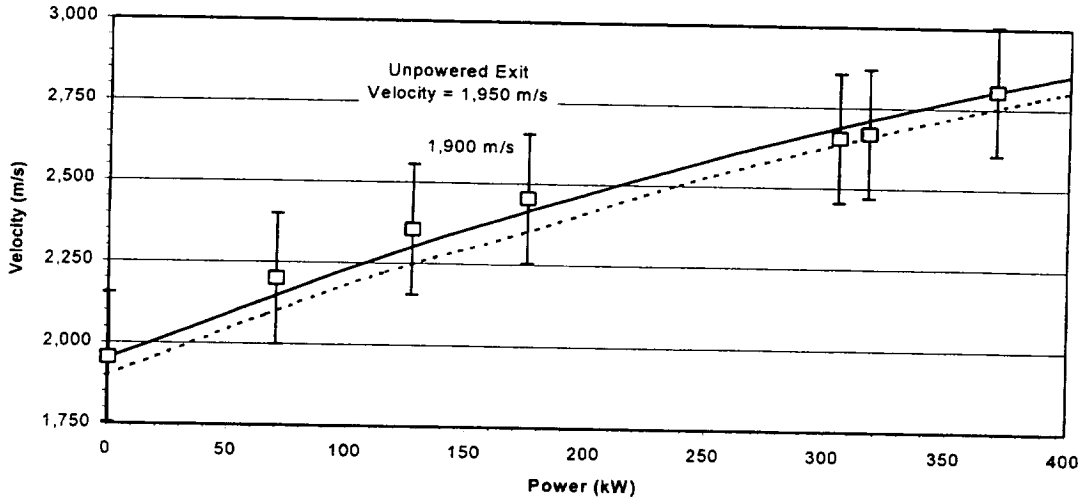

Figure B.1- 15. Comparison of exit velocity calculations with LoRho experimental data.

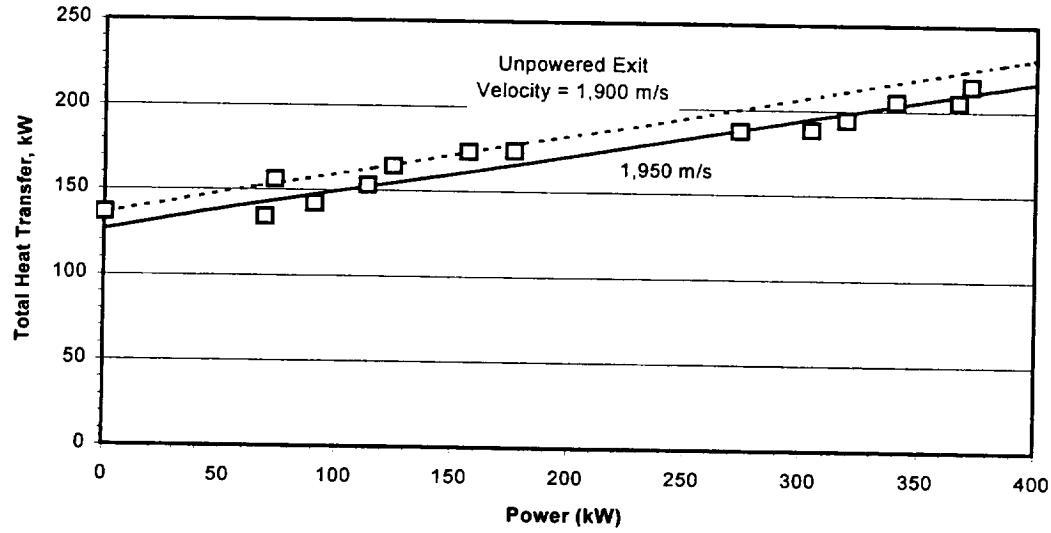

Figure B.1- 16. Comparison of heat transfer calculations with LoRho experimental data.

Excellent agreement was also obtained between the theoretical and experimental heat transfer data as shown in Figure B.1- 16. Model predictions, using the wall roughness height of 0.053 mm (0.00209 in.) (unpowered exit velocity equal to 1,950 m/s), produced the best match with experimental velocities and heat transfer, and for this reason, were adopted to complete the calibration. Calculated exit pressure for applied power levels from zero to 400 kW are compared to the LoRho experimental data in Figure B.1- 17. Exit pressures are consistently underpredicted by the 1-D model, although velocity has been shown to match. Possible causes were initially postulated to be an underprediction of electrical conductivity, an overprediction of the friction

coefficient, or the need for an adjustment to the axial area distribution to account for boundary layer displacement. A considerable effort was expended investigating these possible causes to no avail, and the exit pressure variation with applied power could not be predicted by varying these parameters within any reasonable range. However, further literature investigations lead to a plausible explanation.

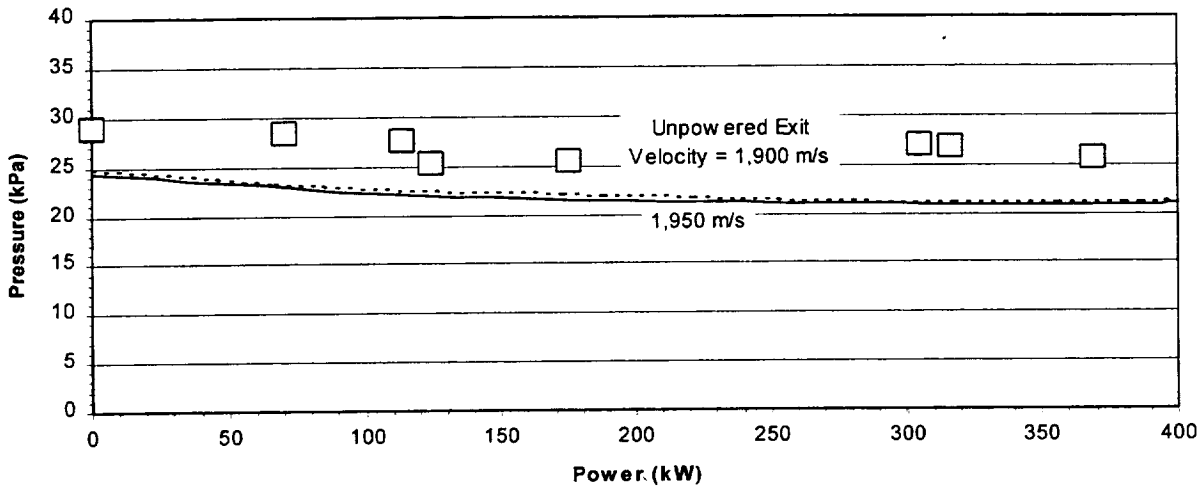

Figure B.1- 17. Comparison of exit static pressure calculation with LoRho experimental data.

Wilson (Ref. 18) conducted a thorough investigation of the gasdynamics and MHD phenomena in the AEDC Accelerator A and observed an underprediction of exit pressure similar to that noted above. He found the observed difference between theory and experiment for the unpowered accelerator duct could be explained by boundary layer effects. 1-D models that include skin friction and heat transfer incorporate these wall effects into the momentum and energy equations to predict average gasdynamic properties at any location in the channel. The friction and heat transfer act uniformly across the channel in these models, whereas in the real flow, these effects are confined to the dissipative boundary layer and do not effect the uniform core region.

Also, as shown by Wilson, nonuniformity of current density can occur in a powered accelerator and result in a higher experimental pressure than predicted by 1-D models. In these models, current is assumed to act uniformly across the surface of the electrodes; therefore, current density is taken to be uniform throughout the volume bounded by an electrode pair. However, current discharge is experimentally observed to constrict in both the axial and lateral directions in MHD devices. A series of discharge studies were conducted at AEDC using a six-electrode channel with the sidewalls removed to allow observation of current discharge in the device. This device was placed in an exhaust tank with the tank pressure adjusted to the sidewall pressure of the operating device to reduce flow disturbances to a minimum.

Photographs taken during operation showed the current discharge from the cathode arcing across the relatively cool boundary layer near the wall. Wilson reports, "At current levels on the order of several amperes, the discharge is centered laterally and at the trailing edge of the electrodes. As the current level is increased to 70 or 80 amperes, the discharge is observed to spread laterally so that eventually about 70% of the width of the electrode appears to support a discharge." Further evidence of the lateral current constriction is provided by the observed anode erosion pattern that, as Wilson states, "strongly suggests that the discharge is for the most part concentrated in a region at the center of the channel about 1 cm wide." It was also noted there was no indicated increase in the sidewall heat transfer with applied power, suggesting the discharge occurred far from the wall.

Current constrictions are probably due to the low electrical conductivity in the cool sidewall boundary layers causing current to be concentrated in the hotter, more electrically conductivity core region. Wilson showed that lateral current constriction would concentrate the MHD body force in a region around the center of the channel resulting in nonuniform acceleration of the flow. This produces nonuniform velocity, enthalpy, and total pressure distributions at the exit and a higher than predicted static pressure. Wilson developed a model to approximate the effects of the lateral constriction assuming the width of the discharge region could be specified. Although this cannot be applied in a general model, this resulted in reasonably good agreement with experimental data for the LoRho data studied.

Because, the ACCEL model obtained excellent agreement with LoRho velocity and heat transfer data at all power levels, the code is considered to be appropriately calibrated and validated for use in the MARIAH Project analyses. However, its limitation that results in underprediction of pressure should be considered in the evaluation of study results. Multidimensional codes that properly model the MHD boundary layer phenomena would eliminate the pressure inaccuracy and should be developed for future high performance MHD accelerator studies. The values for the wall roughness and temperature adopted during the calibration of the ACCEL code will be used for all studies conducted for the MARIAH Project unless other considerations dictate a change.

B.1.3.4 Summary

The ACCEL 1-D MHD accelerator code was validated against experimental data from the AEDC LoRho Program. Exit conditions for the unpowered accelerator were used to calibrate the wall friction model in the accelerator code. Theoretical results were then compared with experimental data for accelerator power levels from zero to 400 kW with excellent agreement at all power levels. Pressure was consistently underpredicted. This was due to boundary layer flow nonuniformities and lateral current constriction in the LoRho accelerator. 1-D codes are unable to properly account for these multidimensional phenomena. However, since this model achieved excellent agreement with other performance data, the usefulness of the 1-D code has been demonstrated. This model should be useful for parametric analysis and feasibility assessments of MHD accelerators as long as its limitations are properly considered.

B.1.4 MHD Accelerator Performance Analysis and Parameter Variation

NOMENCLATURE

A - Flow cross-sectional area, (m^2)
B - Magnetic field strength, (T)
E - Electric field, (V/m)
j - Current density, (A/m^2)
K - Faraday loading parameter, ($=E_y/uB$)
$\dot{m}$ - Mass flow rate, (kg/s)
q_w - Wall heat transfer, (W/m^2)
s - Entropy, (J/kg-K)
T - Gas temperature, (K)
u - Gas velocity, (m/s)
x - Axial direction
y - Transverse direction
η - Efficiency
σ - Electrical conductivity, (mho/m)
ψ - Channel perimeter, (m)

B.1.4.1 Overview

An investigation of MHD accelerator performance to support NASA requirements for hypervelocity propulsion testing has been completed. The objective of the MARIAH Project is to establish the feasibility of MHD accelerator technology to produce a clean-air, true-temperature simulation of conditions behind a bowshock wave producing a 5° deflection angle at a flight Mach number of 16.

Four independent parameters have been identified that can be controlled in the design of an MHD accelerator to affect accelerator performance. These are the applied electrical current density, channel operating temperature, MHD accelerator channel entrance conditions, and the applied magnetic field. Each of these has been varied through a range of values to establish the variation in performance with each parameter. Results from this study will be used to prepare an assessment of the feasibility of MHD for hypervelocity propulsion wind tunnel testing.

Conditions for hypersonic flight at flight dynamic pressures of 500, 1,000, and 2,000 lbf/ft^2, as well as flight Mach numbers from 6 to 22 are indicated on the Mollier diagram of Figure B.1- 18. Conditions behind a 5° deflection bow are also indicated. The NASA requirement for the MARIAH Study is shown at a flight condition of Mach 16 on the 2,000-lbf/ft^2-bowshock curve. Performance limits for advanced arc heaters at operating pressures up to 200 atm are also included. These are the maximum performance entrance conditions to be used for this arc heater-augmented MHD accelerator study. The arc-heater performance limit lines and the combustor inlet line were taken from Ref. 19.

A nominal parameter set was taken as a baseline for the parameter variations in this study. This baseline channel used a magnetic field strength of 8 T, an applied current density of 50 amps per square centimeter (A/cm^2), and a maximum channel gas temperature of 3,500 K. The entrance condition for the baseline channel is the condition labeled as "Arc Heater #1" in Figure B.1- 18. A 1% molar fraction of cesium (Cs) was used for seeding in all cases.

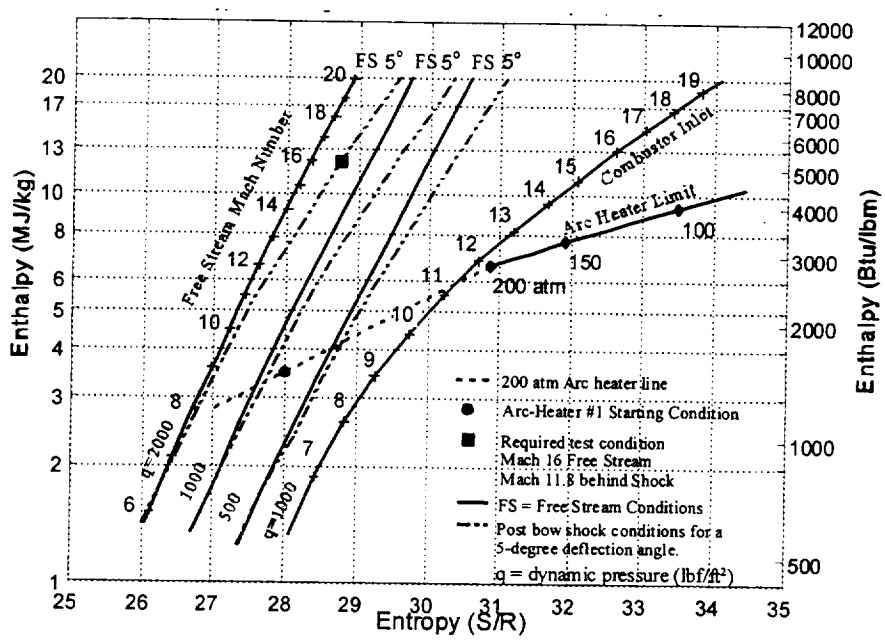

Figure B.1- 18. Hypersonic flight conditions and arc facility capability.

Several measures of channel performance have been investigated during this study. Many devices, including arc heaters, can produce the enthalpy level required for hypervelocity testing; however, they suffer from high values of entropy. In arc-heated flows, the main parameter determining entropy is the reservoir pressure, and it is limited by design considerations. Present generation arc heaters are limited to reservoir conditions of 150 atmospheres (atm) with projected, near-term arc heaters being capable of perhaps 200-atm pressures.

Since MHD generally operates best at lower pressures, it also suffers from the high entropy problem, i.e., the low entropy conditions are much more difficult to produce than the high entropy conditions. With one exception, all of the MHD analyses in this study achieved an exit enthalpy equal to the required NASA test condition. However, at the required enthalpy level, some of the MHD analyses resulted in lower entropy. The primary measure of channel performance was the exit value of entropy. For local performance, at a particular axial location within a channel, the rate of change of stagnation enthalpy with respect to entropy, dS/dx, can be used as a measure of performance. This parameter has the dimensions of temperature and may be regarded as the effective temperature at which energy is added to the gas (Ref. 20).

Exploratory investigations indicated the best MHD channel performance is obtained when the flow in the channel is maintained at approximately Mach 1. This was determined by evaluating the local rate change of stagnation enthalpy with respect to entropy at the channel entrance and the exit entropy values for overall channel performance as described above. For this reason, entrance conditions for all channels considered in this study were taken to be at Mach numbers

between 1.1 and 1.2, which provided the highest temperature entrance condition for supersonic operation. Since electrical conductivity in seeded air is a strong function of temperature in the temperature range considered practical for MHD accelerator operation, this results in the highest obtainable channel entrance equilibrium conductivity.

During variation of a selected parameter, the baseline values for the other three parameters are used, with one exception, evaluation of the Arc Heater #2 condition required operation at a channel temperature greater than the baseline channel maximum temperature be increased to lower the channel entrance Mach number. Gas temperatures throughout the MHD channel are always maintained at or below the baseline temperature except in the cases where the effects of channel exit temperature were being investigated and in the Arc Heater #2 evaluation. For evaluation of channel exit temperature effects, the gas temperature is maintained at or below the selected exit temperature. MHD channel entrance conditions for the Arc Heater #2 analysis were greater than the baseline temperature; therefore, the gas temperature was maintained constant at the entrance value for this specific case.

As indicated above, channel performance is maximized when the Mach number is closest to unity. For this reason, the temperature in the channel was allowed to rise from the entrance value to the maximum channel temperature using a variation that maintains nearly constant Mach number. Channel temperature was then held constant for the remainder of the channel length.

All analyses presented in this study were conducted using the MSE ACCEL 1-D MHD code (Ref. 1) using a segmented Faraday model. This code includes the effects of wall heat transfer, wall friction, and estimated boundary layer voltage drops. The ACCEL code is discussed further in Sections B.1.2 and B.1.3. Thermodynamic and transport data for these analyses were prepared using the NASA CEA Chemical Equilibrium Computer code (Refs. 15, 16, 17). Another MSE code, referred to as HSR, was used to calculate the enthalpy and entropy data for free-stream and bow-shock conditions at the given flight dynamic pressure values.

B.1.4.2 Results

B.1.4.2.1 *Arc Heater Variations*

Since MHD requires a high level of electrical conductivity for efficient and effective operation, an entrance temperature sufficient to significantly ionize the seed material is required. MHD is never used alone but is always used to augment heater devices such as arc heaters, which can provide appropriate entrance conditions. Three arc-heater exit conditions have been evaluated as MHD entrance conditions in this study. These are indicated in Figure B.1- 19 along the 200-atm arc heater performance limit. Baseline values of current density (50 A/cm^2), magnetic field (8 T), and maximum channel gas temperature (3,500 K) were maintained throughout the arc-heater variation study except for use of a higher temperature in the Arc-Heater #2 channel analysis as discussed below. For this series of computations, the length of the accelerator was determined by allowing the program to march down the accelerator axis until a specified total enthalpy had been attained.

Results of the MHD accelerator performance calculations are also shown in Figure B.1- 19. Arc-Heater #1 is the baseline arc heater condition for this study. This baseline arc heater was compared with Arc-Heater #2, which provided higher MHD entrance values of both enthalpy and entropy, as well as with Arc-Heater #3 which provided lower values of enthalpy and entropy. Table B.1- 6 lists the entrance conditions, and Table B.1- 7 gives the exit conditions and performance data for the MHD channel using these three arc-heater conditions.

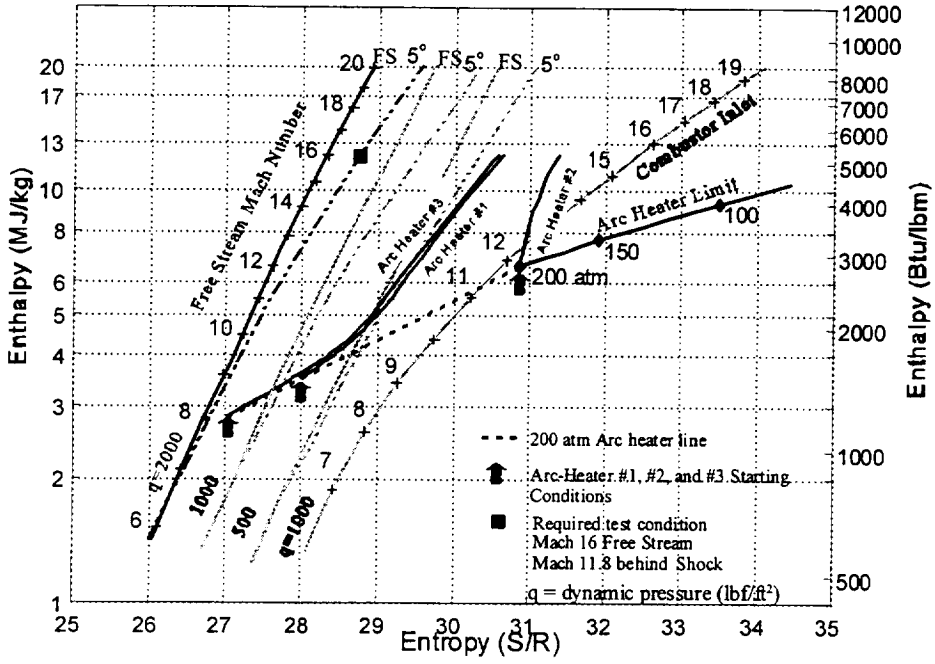

Figure B.1- 19. Comparison of MHD performance for various arc-heater exit conditions.

Table B.1- 6. MHD entrance conditions for arc-heater variations.

	Accelerator Entrance Conditions				
Arc Heater Number	**Temperature (K)**	**Pressure (atm)**	**Mach Number**	**Electrical Conductivity (Mho/m)**	**Hall Parameter (1/T)**
1	2,700	41.9	1.17	11.7	0.220
2	4,100	39.7	1.13	219.7	0.183
3	2,300	51.0	1.12	1.27	0.178

The entrance Mach number for all three channels was comparable; therefore, Arc-Heater #3 (the lowest entrance enthalpy) has the lowest temperature as well as a very low entrance electrical conductivity. With an electrical conductivity of only 1.27, most of the energy deposited in the entrance region of this channel is dissipated through Joule heating. Thus, this channel operates essentially as an arc heater until the gas is heated sufficiently to gain significant electrical conductivity through thermal ionization of the Cs seed. These phenomena can be readily seen in Figure B.1- 19, noting the MHD channel performance curve follows the arc-heater curve for a significant fraction of its total enthalpy increase. The disadvantage of this is the Joule heating increases entropy, as can be seen by the low slope of the enthalpy-entropy curve in that region. Once this solution progresses to a comparable condition to that of the Arc-Heater #1 entrance condition, it parallels that solution.

Table B.1- 7. MHD exit conditions and performance data for arc-heater variations.

	Accelerator Exit Conditions			Performance Data		
Arc Heater Number	**Temperature (K)**	**Pressure (atm)**	**Mach Number**	**Channel Length (m)**	**Electrical Power Req'd.† (MW)**	**Wall Heat Loss (MW)**
1	3,500	16.2	3.63	6.52	8,133	1,040
2	4,100	27.3	2.97	4.27	5,573	940
3	3,500	16.5	3.63	6.9	8,756	1,102

† Does not include the electrical power into the arc heaters.

MHD performance in the entrance region of the Arc-Heater #1 solution is also low as evidenced by the low slope of the curve in that region. However, since this channel starts at a significantly higher temperature compared to the channel for Arc-Heater #3, it is able to transition into a higher performance MHD operation much more quickly. The result is a shorter channel [6.2 m (244 in.) compared to 6.9 m (272 in.)] with less power required (8.7 gigawatt (GW) compared to 8.8 GW). Arc-Heater #3 results in only slightly lower exit entropy compared to Arc-Heater #1

Arc-Heater #2 is the best cost-performer (short channel and low power cost); however, it results in significantly higher exit entropy. Entrance temperature and conductivity for this configuration are much higher than the others (4,100 K and 220 mho/m), resulting in far less Joule heating and thus, a much steeper overall slope to the enthalpy-entropy curve in the entrance region. At 4.27 m (168 in.) in length, this channel is much shorter than the others and results in less wall heat transfer, even with the higher gas temperature. Power use is also significantly less for this channel (5.6 GW). However, the exit condition is far to the right of the desired target point, indicating a much lower pressure flight condition.

B.1.4.2.2 *Magnetic Field Variation*

Magnetic field strength was held constant throughout the MHD channel for these studies. Values of 6, 12, 24 and 30 T were investigated. The nominal 8-T case was used for the baseline since 8-T superconducting magnets can be fabricated using presently available technology; 12-T magnets could also be fabricated for near-term applications. In the 10- to 20-year timeframe, 18- and 24-T magnets should be available for construction of a national hypervelocity wind tunnel, and 30-T magnets may be possible with a successful research program in the 20-year time frame.

Channel entrance conditions provided by Arc-Heater #1 are used for all these analyses. Baseline values of current density (50 A/cm^2) and maximum channel gas temperature (3,500 K) were also fixed for the calculations.

Figure B.1- 20 shows a clear trend toward higher performance (lower entropy) for the higher magnetic fields. As indicated in this table, with increased magnetic field, exit pressure increases, entropy decreases, and channel length decreases. This trend should continue to higher magnetic fields as long as the Hall parameter remains low. The axial electric field is proportional to the Hall parameter and can cause shorting between electrodes and arc instabilities when it grows too large. The Hall parameter is the electron mobility multiplied by the magnetic field. Since electron mobility is inversely proportional to density, the high channel pressure (high density) keeps the Hall parameter low, even at these high magnetic field strength values.

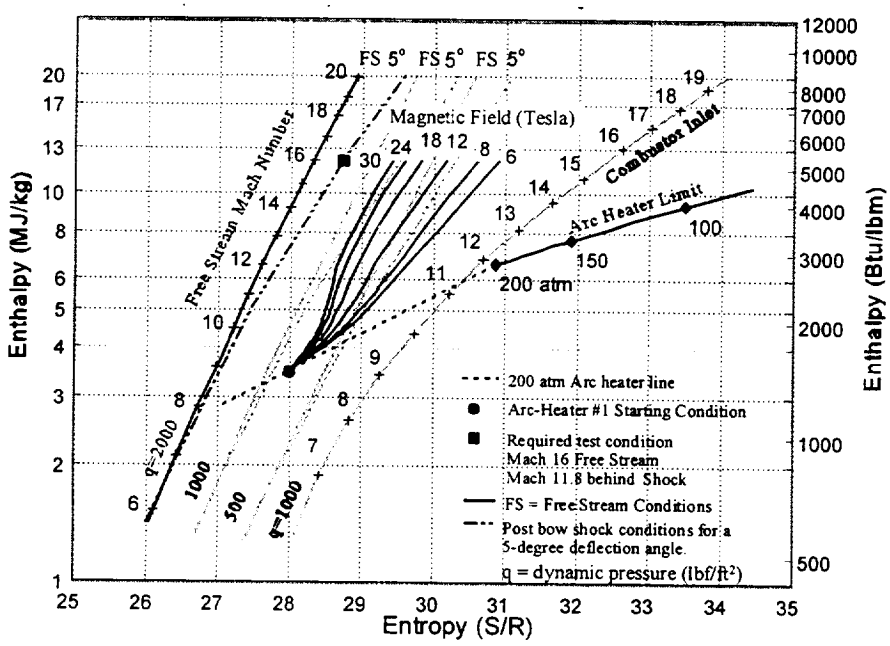

Figure B.1- 20. Comparison of MHD performance for various magnetic field values.

MHD channel entrance conditions are those of Arc-Heater #1 in Table B.1- 6. Exit conditions for the various magnetic field values used are listed in Table B.1- 8. As indicated in this table, exit pressure increases, entropy decreases, and channel length decreases with increased magnetic field. Electrical power requirements, wall heat loss, and exit Mach number are all comparable for these runs. Clearly, the highest magnetic field obtainable is beneficial for channel performance and is the best choice for this application.

Table B.1- 8. MHD exit conditions and performance data for magnetic field variations.

	Accelerator Exit Conditions			**Performance Data**		
Magnetic Field (T)	**Temperature (K)**	**Pressure (atm)**	**Mach Number**	**Channel Length (m)**	**Electrical Power Req'd.† (MW)**	**Wall Heat Loss (MW)**
6	3,500	12.5	3.61	6.94	8,091	998
8	3,500	16.2	3.63	6.52	8,133	1,040
12	3,500	22.7	3.64	6.01	8,250	1,111
18	3,500	31.3	3.65	5.35	8,250	1,146
24	3,500	38.6	3.66	4.83	8,245	1,145
30	3,500	44.9	3.66	4.38	8,217	1,120

† Does not include the electrical power into the arc heaters.

B.1.4.2.3 *Maximum Channel Temperature Variation*

As discussed above, gas temperature in the channel is allowed to rise as quickly as possible while holding the Mach number supersonic and close to unity. Temperature thus rises from the entrance value to the specified maximum value and is then held constant for the remaining channel length. A parametric variation of maximum channel temperature has been performed. Results for maximum channel temperature values of 2,700, 3,000, 3,500, 4,000, and 4,500 K are shown in Figure B.1- 21. The case for a maximum temperature of 2,700 K represents a constant temperature channel since this is also the entrance temperature. Entrance conditions for these analyses are given in the Arc-Heater #1 entry of Table B.1- 6. Baseline values of current density (50 A/cm^2) and magnetic field (8 T), as well as the entrance conditions for Arc-Heater #1 were used throughout the channel temperature variation study.

Higher temperature channels can be seen in Figure B.1- 21 to result in lower entropy values for the same stagnation enthalpy. There are two reasons this occurs. First, the electrical conductivity in the channel will be higher due to the higher temperature. Thus, the Joule heating

term (j^2/σ), which is an entropy production term, will be less, resulting in less entropy production. Secondly, the wall heat transfer rate from the gas in the channel will be higher due to the higher gas temperature, and this increased heat transfer out of the gas will lower entropy.

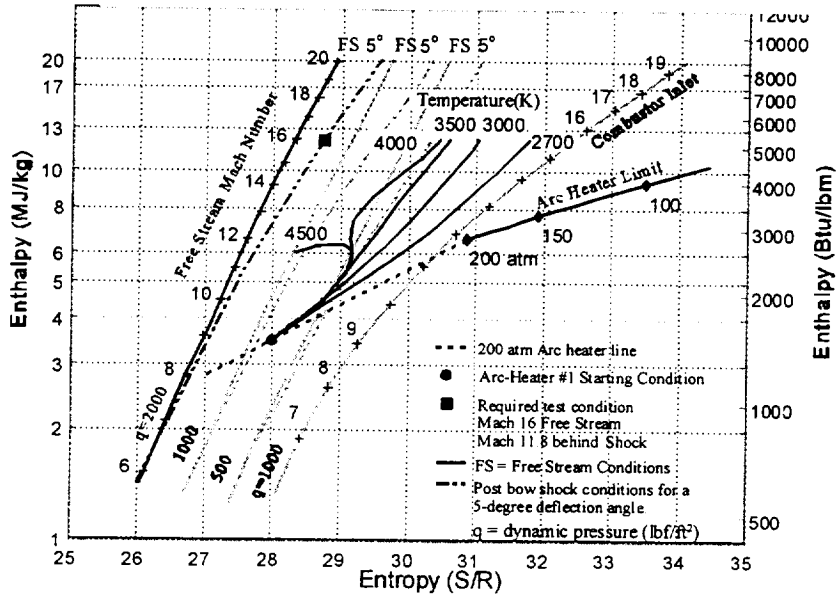

Figure B.1- 21. Comparison of MHD performance for various exit temperatures.

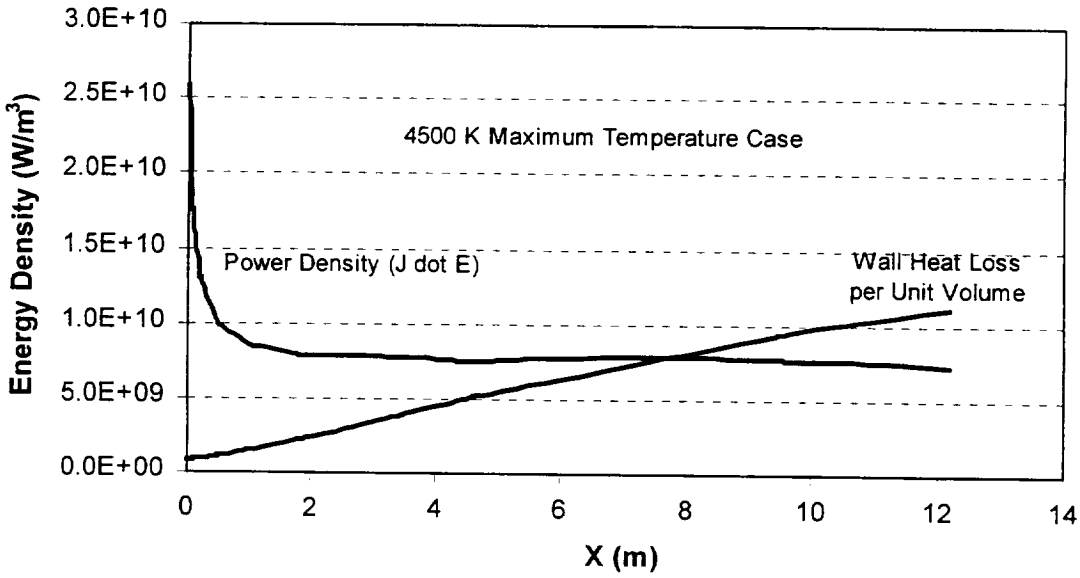

Figure B.1- 22. Comparison of power density and heat transfer.

The cases for maximum temperatures of 4,000 K and 4,500 K can be seen to diverge at a stagnation enthalpy value slightly over 6 megajoule per kilogram (MJ/kg). This is the point in the MHD channel where the temperature is equal to 4,000 K. From this point on, the temperature is constant at 4,000 K in that case but continues to increase in the 4,500 K case. At this point in the 4,500 K solution, as can be seen in Figure B.1- 22, the applied power density is continuing to decrease (due to the increase in conductivity and the consequent reduction in the Joule heating), and the wall heat transfer per unit volume is increasing. At a point just short of 8 m into the channel, the heat transfer out of the gas exceeds the electrical power deposited in the gas, and the stagnation enthalpy begins to drop as seen in Figure B.1- 23. Entropy reduces rapidly after this point due to the heat loss from the gas. However, since the stagnation enthalpy is no longer increasing, this configuration cannot reach the target enthalpy, and the analysis was terminated.

Entropy can be seen to drop slightly in the 4,000 K maximum temperature case in Figure B.1- 21 through the region of increasing temperature and for a short distance thereafter. Following this small dip, the entropy once again begins to increase. Consideration of this phenomenon raises an interesting question. Is there an increasing temperature distribution that can be tailored between the 4,000 K and the 4,500 K cases that will result in a continual increase in enthalpy with no increase in entropy? Theoretically, this would correspond to a case in which the entropy production by the Joule heating and wall friction is exactly balanced by the entropy reduction due to wall heat transfer. The net gain in enthalpy would then result purely from the "push work," i.e., the work due to the MHD body force (juB).

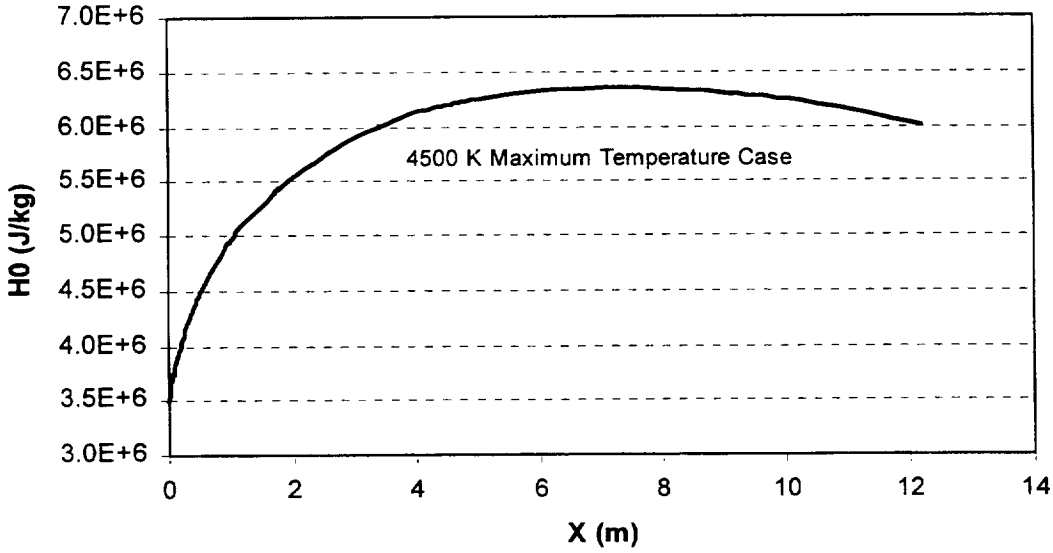

Figure B.1- 23. Axial variation of stagnation enthalpy.

The possibility of creating such a thermodynamic scenario can be demonstrated by appealing to the equation governing entropy production. In a quasi-1-D MHD channel this takes the form (Ref. 20):

$$T\frac{dS}{dx} = -\left[\frac{q_w \psi(x)}{\dot{m}}\right] + \frac{A(x)}{\dot{m}}(1-\eta)\langle j \cdot E\rangle \qquad \text{(B.1- 67)}$$

If dS/dx is set to zero and the resulting expression is solved for the critical efficiency, η_{cr}, we obtain:

$$\eta_{cr} = 1 - \frac{q_w \psi}{A(x)\langle j \cdot E\rangle} \qquad \text{(B.1- 68)}$$

Recall, for a Faraday-connected MHD channel, the load factor is inversely related to the efficiency: $\eta = 1/K$. Thus, the previous two equations demonstrate it is possible, in principle, to assign a load factor at each electrode pair that will yield a zero rate of entropy increase. For such a channel, the curves of total enthalpy vs. entropy would be vertical lines. Several attempts were made to create this solution; however, the solution was found to be extremely sensitive to small changes in the temperature distribution. Whether this sensitivity is real or just a numerical artifact is presently unknown. Because of limitations in time and resources, it was not possible to investigate this operating scenario in greater depth. Note, however, the family of operating curves shown in Figure B.1- 21 suggest this type of isentropic operation or something close to it might be achievable.

A channel configured to use this technique may be possible but would most likely be impractical for several reasons. First, the instability described above may be a physical phenomenon rather than a numerical artifact. This would mean that small fluctuations in the channel temperature would cause the solution to jump to either a high entropy case, as in the 4,000 K case, or a loss of enthalpy, as in the 4,500 K case. Second, much of the applied electrical power will be converted to heat and transferred out through the walls, resulting in very long and expensive channels and low system efficiency. Some of the numerical solutions attempted resulted in channels of up to 100 m in length. This technique was not pursued further.

Channels with higher maximum temperatures required longer lengths to reach the target enthalpy values as shown in Figure B.1- 24. Viewing this figure, the solution that may lie between the 4,000 K and the 4,500 K solutions can be imagined to be very long.

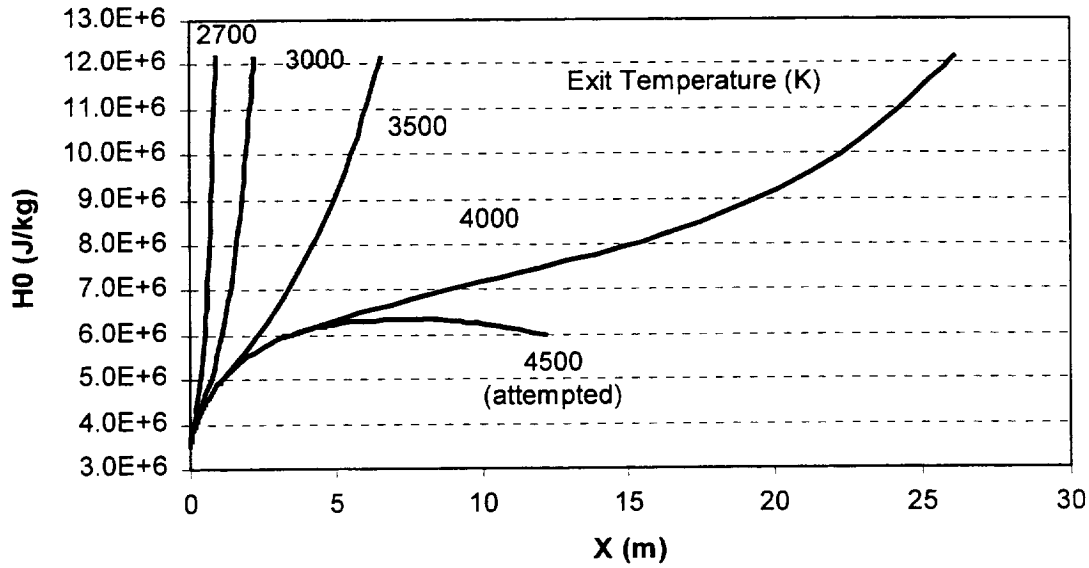

Figure B.1- 24. Axial variation of stagnation enthalpy.

The exit conditions and performance data for the exit temperature variations are presented in Table B.1- 6. This table dramatically shows the effect of increasing channel temperature. For a maximum temperature of 2,700 K, 8.5 GW of power was required; however, the wall heat loss was only 74.6 MW, and the channel length was less than 1 m. This is seen to be the highest entropy case in Figure B.1- 21, with a dimensionless entropy approaching 32. The high entropy is due to low conductivity that produces entropy through high Joule heating and low heat loss. Compare this with the 4,000 K temperature case that required a channel length in excess of 26 m, consumed 13.6 GW of electrical power, and transferred over 6 GW of heat out of the gas to the walls. Yet, due to the high electrical conductivity resulting in low Joule heating and the high heat transfer to the walls, this case had the lowest entropy of the four temperatures successfully evaluated.

The relative merits of the various temperature distributions examined in this section are not clear. Low temperature produces less stress on channel materials and less dissociation of air species. This also results in a small, compact channel and magnet. The low temperature configuration also makes the most efficient use of the applied electrical power, yet this produces high values of entropy that are far from the desired operating conditions for this application. High temperature cases approach much closer to the desired entropy but result in very long and inefficient channel and magnet systems that transfer nearly half of the applied power out of the channel as heat. Variations of channel temperature can only be optimized in the larger context of a system optimization study.

Table B.1- 9. MHD exit conditions and performance data for variations of maximum channel gas temperature.

	Accelerator Exit Conditions			Performance Data		
Maximum Temperature (K)	**Temperature (K)**	**Pressure (atm)**	**Mach Number**	**Channel Length (m)**	**Electrical Power Req'd.† (MW)**	**Wall Heat Loss (MW)**
2,700	2,700	0.97	4.50	0.868	8,467	74.6
3,000	3,000	3.80	4.15	2.20	8,324	251
3,500	3,500	16.2	3.63	6.52	8,133	1,040
4,000	4,000	45.4	3.14	26.1	13,570	6,063
4,500	Solution terminated due to decreasing stagnation enthalpy					

† Does not include the electrical power into the arc heaters.

B.1.4.2.4. *Current Density Variations*

Electrode current density values of 25, 30, 50, and 100 A/cm^2 were evaluated. In many ways, the characteristics of the solutions with various current densities paralleled those of the channel temperature solutions. Enthalpy-entropy curves for these solutions are seen in Figure B.1- 25 (25 A/cm^2 not shown). The highest value of current density results in the highest entropy. Again, this is due to the Joule dissipation (j^2/σ). For the low temperature solution discussed in the previous section, low values of electrical conductivity caused this term and the entropy production to be high. For the high current density solution, it is the high current that causes the large Joule heating term and high rate of entropy production.

Low values of current density result in solutions that are similar to the high temperature solutions. High temperature caused the heat transfer to increase until the energy loss exceeded the energy input to the channel. On the other hand, low current density causes the energy input to drop until it drops below the heat loss rate, producing a similar result.

Channel performance data for these solutions is given in Table B.1- 10. Again, the 25-A/cm^2 solution results in low entropy; however, it requires a 57-m long channel and nearly 17 GW of applied power with more than half of this lost through heat transfer. Thus, it approaches nearest to the NASA desired operating condition but is the least efficient and probably the least practical of the considered solutions. With 100 A/cm^2 applied to the electrodes, the desired stagnation enthalpy is reached in only 1.5 m. Less than half as much power is required compared to the 25 A/cm^2 case and only 250 MW is lost to heat transfer; however, this is the least desirable solution, having a large exit entropy placing it far from the desired condition. Current density optimization can only be considered in the larger context of system optimization, as was the case for channel temperature.

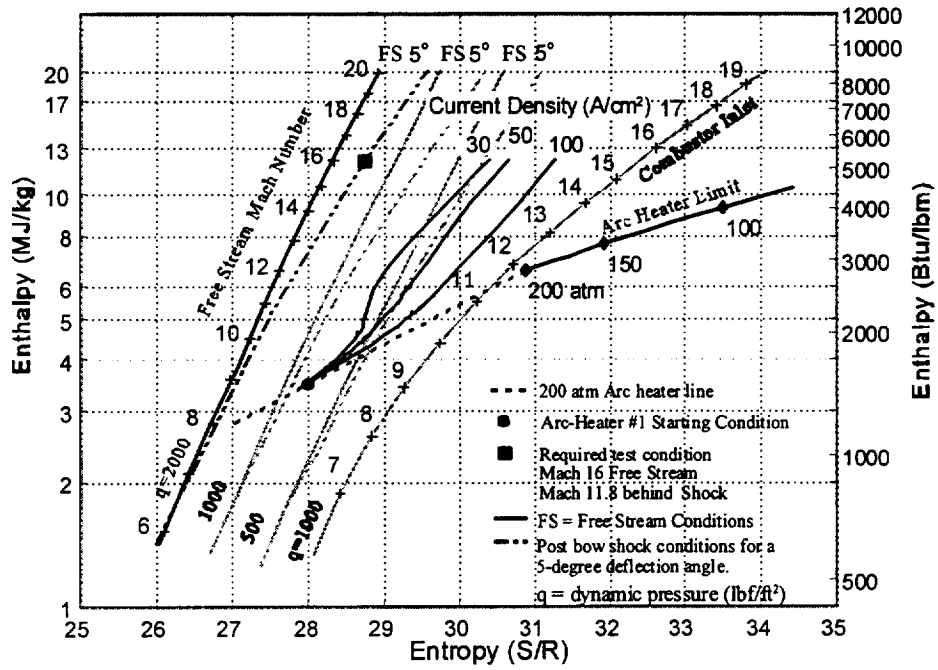

Figure B.1- 25. Comparison of MHD performance for various current density values.

Table B.1- 10. MHD exit conditions and performance data for current density variations.						
	Accelerator Exit Conditions			**Performance Data**		
Current Density (A/cm^2)	**Temperature (K)**	**Pressure (atm)**	**Mach Number**	**Channel Length (m)**	**Electrical Power Req'd.† (MW)**	**Wall Heat Loss (MW)**
25	3,500	19.2	3.73	57	16,950	8,885
30	3,500	19.2	3.64	21.1	11,060	3,383
50	3,500	16.2	3.63	6.52	8,133	1,040
100	3,500	9.3	3.59	1.53	8,020	250

† Does not include the electrical power into the arc heaters.

B.1.5 MHD Accelerator Optimization Analysis

The partial optimization of the performance of MHD accelerators to support NASA's hypervelocity propulsion wind tunnel testing requirements has been performed and is reported in this section. These analyses extend the single parameter variation analysis reported in Section B.1.4 by choosing the best combination of parameter values in an attempt to produce the highest performance accelerator design relative to the NASA target requirements discussed in Section 3.0.

Three design analyses have been completed in this study distinguishable by the level of technology advancement required for the development of a facility. Throughout all of the analyses in Section B.1.4 and in this section, one parameter (the magnetic field strength) stands out as the single most important factor in determining the limits on the performance of advanced MHD accelerator facilities. High strength magnets up to at least 30 T could be used to improve the performance of the high-pressure accelerators considered in this study without the detrimental effects associated with the high Hall parameter that would occur in lower pressure systems. Values of the magnetic field strength of 15, 24, and 30 T have been used in this analysis.

Based on extrapolation of current technology in superconducting magnets, it is estimated that magnets with a 15-T field strength could be developed for near-term applications (10 year); therefore, the accelerator designs based on these magnets are considered to be in a moderate risk category. The 24-T magnets may be available in the 20-year time frame, which is believed to be the minimum time required for development of a full-scale seeded-air ore-heater-driven MHD accelerator test facility. Thus, this value has been used for a higher risk, 20-year technology design. Further technology advancement to a 30-T magnet is considered to be high risk at present, and the future availability of these cannot yet be estimated. Although technically possible, these are not expected to come to fruition in the foreseeable future. However, if technology breakthroughs occur in the current research programs or if research and develop programs are initiated to obtain this technology, these could be available in the 20-year time frame. An analysis based on the 30-T magnet is included in this study for comparison.

B.1.5.1 Optimization Analysis

The operation of high-pressure MHD accelerators at high magnetic field strength clearly produces better performance relative to the specified NASA target test condition, as indicated in the parametric analysis of Section B.1.4. Operation of the channel at higher temperature and lower electrical current density was also shown to produce better performance. In this section, optimum values of these three parameters are sought. Since some combinations of these parameters produce very long channel lengths that would be impractical when the cost of magnet fabrication is considered, a practical limit is placed on channel length for the final optimization analysis. Variation of channel temperature and current density at high magnetic field strength is first examined, followed by an optimization of the channel temperature and current density for a practical channel length at each of the three selected magnetic field strength values. All analyses

in this study were initially constrained to an MHD accelerator channel exit stagnation enthalpy of 12.15 MJ/kg corresponding to the NASA-specified test condition. The final analyses were extended to higher enthalpy levels to identify other test conditions that can be produced with MHD technology. These analyses were performed with the MSE 1-D MHD accelerator code, ACCEL, discussed in Section B.1.2. Accelerator entrance conditions for all analyses are listed in Table B.1- 11. All analyses used the 2,700 K entrance condition except for one analysis each at the entrance temperatures 2,200, 2,300, and 2,500 K.

Table B.1- 11. Entrance conditions for all channel design analysis.

Specifications	**Accelerator Entrance Conditions**				
Exit Temperature (K)	**Entrance Temperature (K)**	**Pressure (atm)**	**Mach Number**	**Velocity (m/s)**	**Electrical Conductivity (Mho/m)**
2,200	2,200	15.1	1.85	1,624	2.2
2,300	2,300	18.7	1.72	1,540	3.4
2,500	2,500	28.4	1.45	1,353	7.0
2,700 – 3,500	2,700	41.9	1.17	1,125	11.7

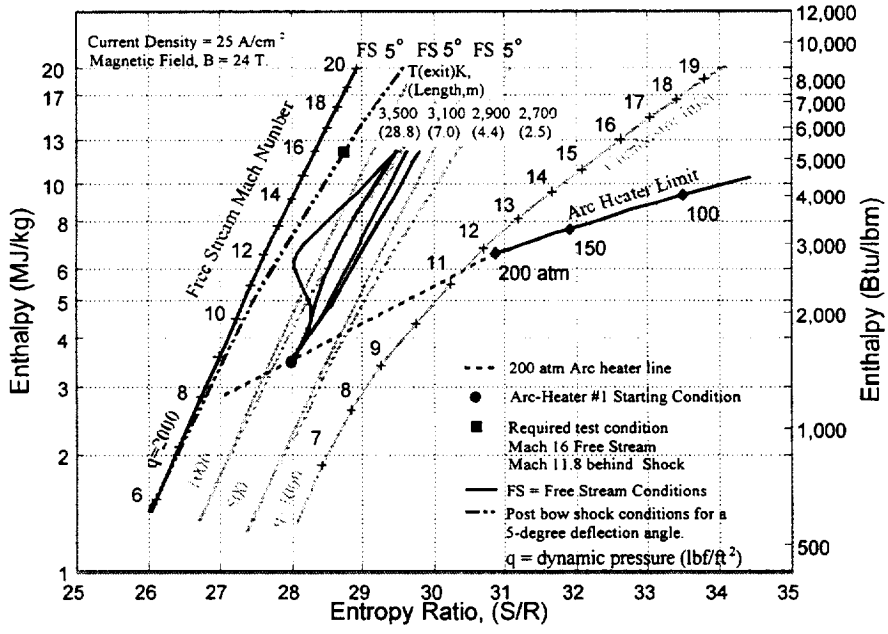

Figure B.1- 26. MHD accelerator performance with various exit temperature values.

Figure B.1- 26 shows the variation of MHD accelerator performance with temperature for a 24-T magnetic field strength and 25-A/cm^2 current density. Accelerator channel exit conditions for these analyses are listed in Table B.1- 12. As found in Section B.1.4 and shown in Figure B.1-26, operation with a high temperature working gas produces better performance but also results in long channels due to the higher wall heat transfer rate. Since heat transferred from the gas must be replaced by the electrical power added through the electrodes, the higher heat transfer rate results in longer channel lengths, as required for the energy addition to reach the final stagnation enthalpy level. The peculiar shape of the 3,500 K curve is also due to heat loss in this high temperature case. A short axial distance into the channel, the heat loss has increased to the point the entropy reduction (due to heat transfer from the gas) dominates over the entropy production (due to Joule heating and friction), thus, the entropy decreases as the flow energy increases. However, further into the channel, the friction losses begin to dominate, and once again, the entropy increases.

As indicated in Figure B.1- 26, channel length was calculated to be 28.8 m (94.5 ft.) for the 3,500 K gas temperature case. A high-strength, large-bore, superconducting magnet will cost a significant fraction of the total facility cost for even a short length magnet; an extremely long magnet could be prohibitively expensive. A full engineering and cost analysis for a facility would determine practical limits to the length of the channel and magnet, limits that are not presently known. For the purposes of this study, it is assumed the channels and their associated magnets (5 to 10 m in length) would be practical. Thus, the 7-m-long channel for the 3,100 K working temperature is assumed to be practical; however, the 28.8-m (94.5-ft.) long channel for the 3,500 K temperature is not considered practical.

Table B.1- 12. Exit conditions for channel temperature variations.[†]

Specifications	**Accelerator Exit Conditions**				**Performance Data**		
Exit Temperature (K)	**Pressure (atm)**	**Entropy Ratio S/R**	**Mach Number**	**Velocity (m/s)**	**Channel Length (m)**	**Electrical Power Req'd.**[††] **(MW)**	**Wall Heat Loss (MW)**
2,700	6.8	29.80	4.48	4,301	2.50	7,411	316
2,900	12.7	29.57	4.26	4,228	4.35	7,741	651
3,100	20.3	29.49	4.05	4,148	7.04	8,299	1,218
3,500	42.6	29.50	3.66	3,932	28.84	13,650	6,557

[†] Magnetic field strength was 24 T and current density was 25 A/cm^2 for these analyses.
[††] Does not include the electrical power into the arc heater.

Table B.1- 13. Exit conditions for current density variations.

Specifications	Accelerator Exit Conditions				Performance Data		
Current Density (A/cm^2)	Entropy Ratio S/R	Pressure (atm)	Mach Number	Velocity (m/s)	Channel Length (m)	Electrical Power Req'd.[††] (MW)	Wall Heat Loss (MW)
10	29.49	9.2	4.48	4,302	10.75	8,367	1,275
15	29.55	8.7	4.48	4,302	5.71	7,801	710
20	29.66	7.7	4.48	4,300	3.61	7,541	455
25	29.80	6.8	4.48	4,301	2.50	7,411	316

[†] Magnetic field strength was 24 T and channel temperature was a constant value of 2,700 K for these analyses.
[††] Does not include the electrical power into the arc heater.

The effect of current density on MHD accelerator performance can be seen in Figure B.1- 27; channel exit conditions are given in Table B.1- 13. Channels with a constant working gas temperature of 2,700 K and a 24-T magnetic field strength were evaluated at current densities from 10 to 25 A/cm^2. Channels with lower current densities could not reach the desired specific enthalpy since the heat losses from the channel were greater than the power added at these low currents. The channel design for 10 A/cm^2 is probably impractical due to its long length (as stated above) and its low efficiency due to its wall heat loss. The channels using 15- to 20- A/cm^2 current densities would be the most practical for this set of conditions (2,700 K and 24-T magnet). Current densities greater than 25 A/cm^2 produced increasingly shorter channels but were also further to the right (higher entropy) on the Mollier diagram. Consequently, the lower current densities are able to produce test conditions much closer to the NASA specification; however, when they are too low, they produce unacceptably long accelerator channel designs.

All of the channel designs considered produced higher entropy than desired for the NASA test condition. In fact, the low entropy level of the NASA specification is extremely difficult to reach due to the high pressure required. As Figure B.1- 26 indicates, the channels that operated at the highest temperature produced the lowest entropy test conditions. This is due in part to the heat transfer out of the working gas, which lowers entropy to the higher electrical conductivity, thereby reducing the entropy production from Joule heating (j^2/σ). Again, the higher temperature resulted in longer channels. In Figure B.1- 27, low current density produces the lower entropy solutions and also results in long channel lengths. Once again, the low entropy is due to heat transfer out of the gas and lower Joule heating, this time due to the lower current.

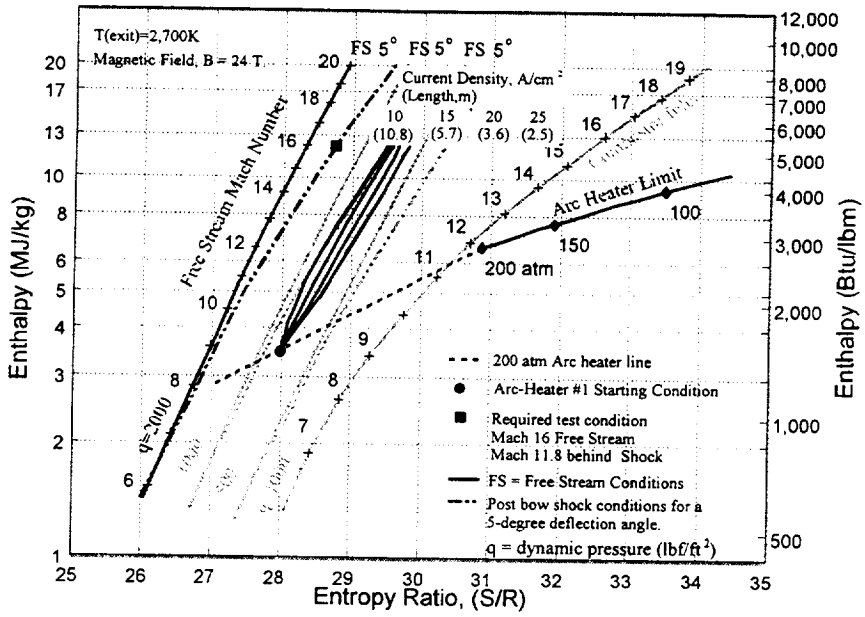

Figure B.1- 27. MHD accelerator performance with various values of current density.

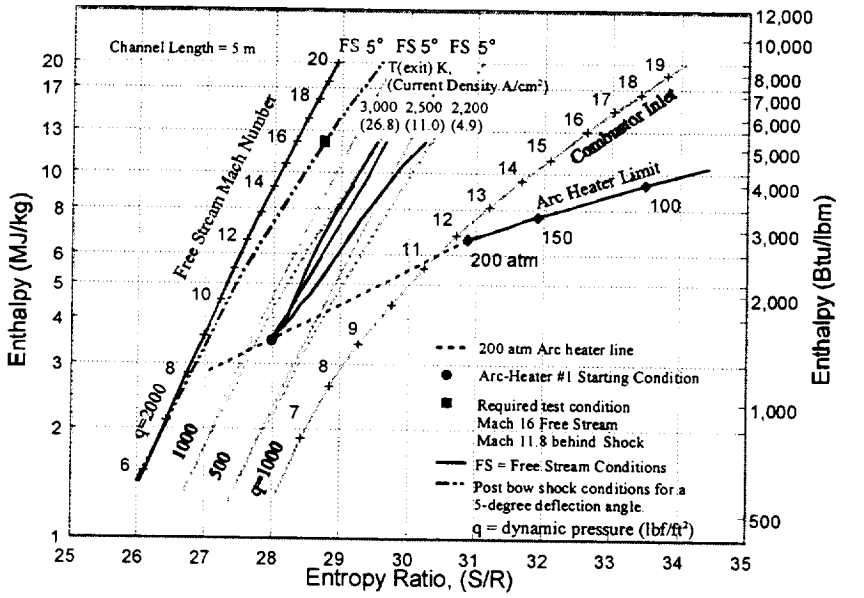

Figure B.1- 28. MHD accelerator performance for 5-m channel length.

As these figures show, lower entropy appears to correlate with longer channel lengths (within limits); however, long channels are impractical. For this reason, solutions with a 5-m channel length (assumed to be practical for this application) were explored, and the results are presented in Figure B.1- 28. Channel operating temperatures from 2,200 to 3,500 K were evaluated as indicated in Table B.1- 14. For the 5-m, fixed-length designs, low temperature channels achieved the required energy level with low current densities (4.9 A/cm^2 at 2,200 K compared to 49.3 A/cm^2 at 3,500 K). However, as Figure B.1- 29 shows, entropy at the channel exit was a minimum at a temperature of 3,000 K, and the current density of 26.8 A/cm^2 is very reasonable.

Table B.1- 14. Exit conditions for 5-m channel length analyses.[†]

Specifications		**Accelerator Exit Conditions**				**Performance Data**	
Exit Temperature (K)	**Current Density (A/cm^2)**	**Entropy Ratio, S/R**	**Pressure (atm)**	**Mach Number**	**Velocity (m/s)**	**Electrical Power Req'd.**[††] **(MW)**	**Wall Heat Loss (MW)**
2,200	4.9	30.24	1.5	5.09	4,464	7,441	346
2,300	6.7	29.92	2.6	4.96	4,434	7,500	404
2,500	11.0	29.65	5.2	4.71	4,371	7,612	516
2,700	16.3	29.58	8.4	4.48	4,304	7,725	625
2,900	23.0	29.54	13.0	4.26	4,228	7,834	745
3,000	26.8	29.53	16.0	4.16	4,194	7,912	812
3,100	30.6	29.54	19.3	4.05	4,150	7,967	877
3,200	34.8	29.55	23.2	3.95	4,110	8,042	948
3,400	44.0	29.59	32.9	3.76	4.024	8,192	1,101
3,500	49.3	29.60	38.9	3.66	3,978	8,278	1,184

[†] Magnetic field strength was 24 T for these analyses.
[††] Does not include the electrical power into the arc heater.

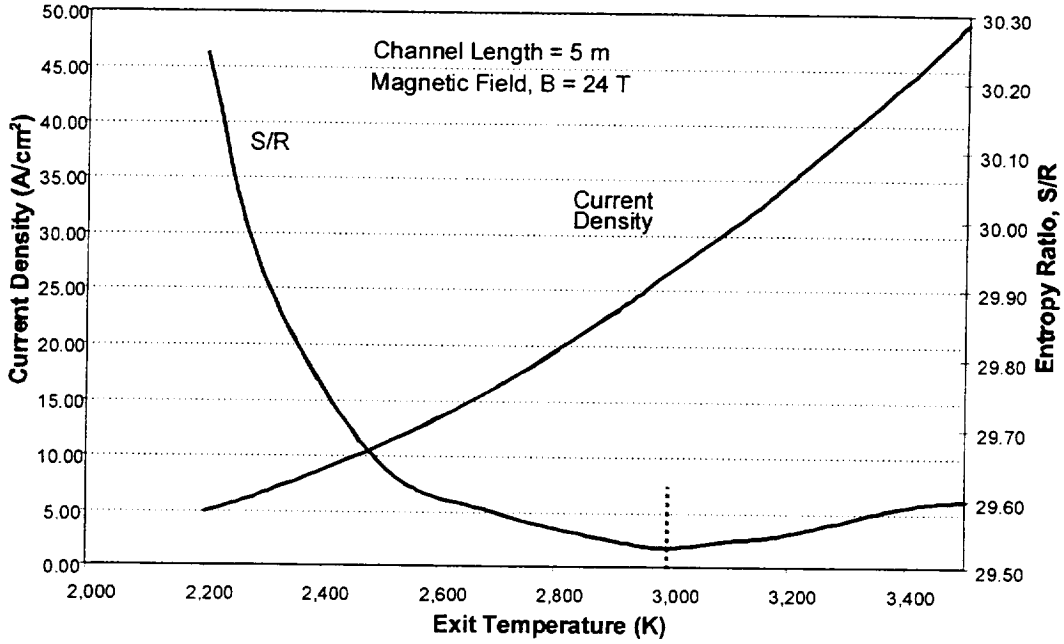

Figure B.1- 29. Variation of exit entropy and current density with maximum channel temperature.

Entropy will increase sharply at the lower temperatures but rises slowly at the higher temperatures. However, as Figure B.1- 29 also demonstrates, current density nearly doubles from 3,000 K to 3,500 K. With all issues considered, it would be best to operate with the lowest temperature and lowest current density that is practical. Higher temperatures result in higher heat transfer rates, lower efficiency, more severe material degradation for exposed surfaces, higher levels of dissociation and nitric oxide (NO) formation, and higher current density (required to overcome heat losses), which may result in faster electrode erosion. For these reasons, the minimum entropy design at 3,000 K is chosen as the recommended channel for this application. A similar analysis was performed for magnetic field strengths of 15 and 30 T, respectively. Minimum entropy results also occurred at 3,000 K for these field strengths; therefore, this temperature was selected for all recommended designs.

The results of performance calculations for the three magnetic fields are shown in Figure B.1- 30. Each of the channels is 5 m long at the indicated 12.15 MJ/kg exit point. This figure also shows the effect of extending these channels to a higher final stagnation enthalpy of 20 MJ/kg. To achieve higher enthalpy, the channels are extended to lengths ranging from 6.65 to 6.9 m (262 to 272 ft.). Table B.1- 15 lists the accelerator channel exit conditions for the 12.15 MJ/kg and 20.0 MJ/kg exits. Figure B.1- 30 indicates the high dynamic pressure test condition specified by NASA cannot be achieved by the seeded-air, arc-heater-driven, MHD accelerator designs considered in this study. These designs are unable to reach the required entropy level for the dynamic pressure of 2,000 lbf/ft^2 specified by NASA but do provide test conditions at the

same Mach number at lower dynamic pressure, which would correspond to flight at a higher altitude. Table B.1- 16 lists the flight dynamic pressure and altitude for Mach 16, post-bowshock test conditions that can be tested using these MHD accelerator designs. As can be seen, these range from a flight dynamic pressure of 710 lbf/ft^2 at an altitude of 42.8-km (140.4 kft) for the 15-T design to 1,200 lbf/ft^2 at an altitude of 38.95 km (127.8 kft) for the 30-T design.

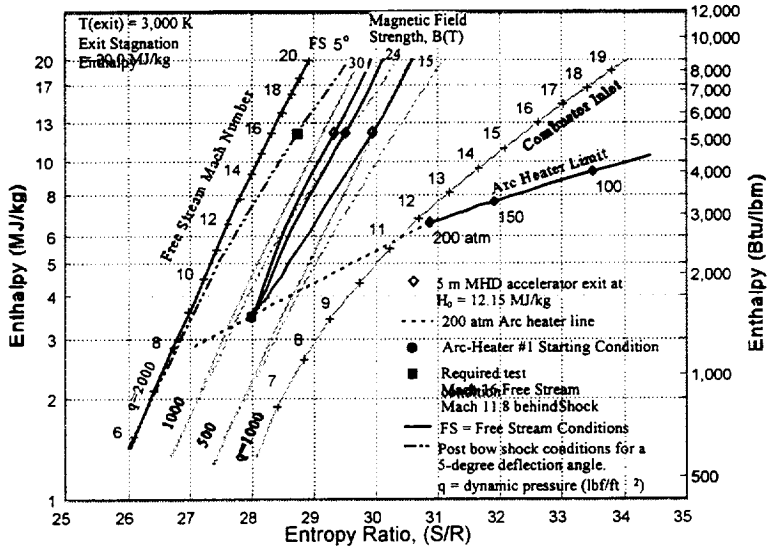

Figure B.1- 30. MHD accelerator performance for selected accelerator designs.

Table B.1- 15. Exit conditions for selected channel designs.[†]

Specifications		Accelerator Exit Conditions				Performance Data			
Magnetic Field Strength (T)	**Exit Stagnation Enthalpy (MJ/kg)**	**Entropy Ratio, S/R**	**Pressure (atm)**	**Mach Number**	**Velocity (m/s)**	**Channel Length (m)**	**Current Density (A/cm^2)**	**Electrical Power Req'd.**[††] **(MW)**	**Wall Heat Loss (MW)**
15	12.15	29.96	10.6	4.16	4,187	5.0	29.7	7,789	691
24	12.15	29.53	16.0	4.16	4,194	5.0	26.8	7,912	812
30	12.15	29.35	19.1	4.16	4,193	5.0	25.1	7,963	872
15	20.0	30.60	5.8	5.73	5,760	6.65	29.7	14,710	1,160
24	20.0	30.12	9.1	5.73	5,766	6.83	26.8	14,980	1,436
30	20.0	29.92	10.9	5.72	5,764	6.90	25.1	15,100	1,570
30	30.0	30.23	8.2	7.25	7,294	8.62	25.1	24,370	2,631

[†] Channel exit temperature was 3,000 K for these analyses.
[††] Does not include the electrical power into the arc heater.

Table B.1- 16. Test conditions achieved for a flight Mach number of 16.

Magnetic Field Strength (T)	Flight Mach Number	Flight Altitude		Flight Dynamic Pressure (lbf/ft^2)	Stagnation Enthalpy (MJ/kg)	Entropy Ratio S/R
		(km)	(kft)			
15	16	42.8	140.4	710	13.20	30.07
24	16	40.1	131.6	1,023	12.86	29.60
30	16	38.95	127.8	1,200	12.72	29.40

Table B.1- 17. Test conditions achieved for a flight dynamic pressure of 2,000 lbf/ft^2.

Magnetic Field Strength (T)	Flight Mach Number	Flight Altitude		Flight Dynamic Pressure (lbf/ft^2)	Stagnation Enthalpy (MJ/kg)	Entropy Ratio S/R
		(km)	(kft)			
30	23.4	40.8	133.7	2,000	27.91	30.14

Finally, Table B.1- 15 also lists the channel exit conditions for an extension of the channel to a 30.0-MJ/kg exit. These design exit conditions exceed the 2,000 lbf/ft^2 dynamic pressure post-bowshock conditions at a stagnation enthalpy level higher than the NASA specification. Interpolation of the data to the point where the accelerator performance matches the 2,000 lbf/ft^2 condition indicates an accelerator with a 30-T magnet can produce test conditions equivalent to the 2,000 lbf/ft^2 dynamic pressure, post-bowshock condition at a flight Mach number of 23.4 and an altitude of 40.8 km (133.7 kft). The stagnation enthalpy at this test condition is 27.91 MJ/kg. The data for this condition is listed in Table B.1- 17.

Ionization instability as a result of high Hall parameter values is always a concern when operating at high values of the magnetic field strength. As Rosa (Ref. 2) indicates, nonequilibrium ionization instability can occur in a plasma when the Hall parameter is large. He also states that, in atomic gases, observed data "show a wide departure from ideal behavior" when the Hall parameter is greater than 2. However, it is believed molecular gases can maintain stability over a much larger range of Hall parameter values; yet the limits are presently unknown. Klepeis and Louis (Refs. 21 and 22) were able to maintain nonequilibrium ionization in a molecular N_2 plasma using a disk MHD generator with Hall parameter values in excess of 3. Additionally, Rosa indicates that Hall parameter values as high as 5 might be acceptable in molecular gases such as air.[5]

[5] Personal communication, Dr. Richard J. Rosa with Gloyd A. Simmons, MSE, Inc.

Table B.1- 18. Electrical data for seven selected MHD accelerator designs.

Magnetic Field Strength (T)	Exit Stagnation Enthalpy (MJ/kg)	Hall Parameter	Maximum Electrical Fields (kV/m)	
			Transverse, Ey	Axial, Ex
15	12.15	1.39	67.2	6.1
24	12.15	1.54	105.6	7.5
30	12.15	1.65	130.8	8.3
15	20.0	2.35	89.8	8.0
24	20.0	2.54	142.1	9.4
30	20.0	2.70	176.7	10.2
30	27.91	3.20	211.5	11.1

Fortunately for this application, high static pressure in the channel helps to maintain the Hall parameter values at reasonably low values. Table B.1- 18 lists electrical data for the seven selected designs discussed above. The first three entries in this table are for the 5-m channel designs, providing an exit stagnation enthalpy of 12.15 MJ/kg, which is equivalent to the NASA target test condition. The maximum value of the Hall parameter for these analyses occurs in the 30-T case and is a moderate value of 1.65. The maximum transverse electric field (E_y) of 130.8 kV/m also occurs in the 30-T case. These values are very reasonable and should not cause any operational problems in this accelerator channel.

The next three entries in Table B.1- 18 are for the 20.0 MJ/kg exit stagnation enthalpy cases. Hall parameters are somewhat higher for these cases due to the higher Mach numbers that produce lower static pressure at the exit compared to the lower energy cases previously discussed. Hall parameter values are moderately high and vary from 2.35 for the 15-T case to 2.70 for the 30-T case. Finally, the last entry is for the 27.91-MJ/kg case discussed above. A maximum Hall parameter value of 3.2 occurs at the exit. It should be noted this value is only slightly higher than the value for which stability was maintained in the N_2 plasma during the Klepeis and Louis experiments discussed above.

B.1.5.2 Summary

Accelerator designs evaluated in Appendix Section B.1.5 indicate that seeded MHD accelerators augmenting high-pressure arc heaters cannot produce the test conditions required in the MARIAH Project specifications (see Section 3.0). However, these show that flight simulations corresponding to high flight Mach number, post-bowshock conditions at lower dynamic pressures are obtainable. Several technologies that are beyond the current state-of-the-art are implied by the design values used in these analyses; however, in most cases, these technologies should be available in the 15- to 20-year time frame for development of a major new test facility. However, the prospect of large-bore, high field strength magnets being available in the 15- to 20-year time frame is presently unknown. Today, 6-T superconducting magnets are available, and 8-T magnets could probably be developed using present technology. Magnets having 10- to 12-T fields are projected for near-term development, and 15-T magnets may be available in the 15- to 20-year time frame. At present, 24- to 30-T magnet development cannot be projected in the foreseeable future. Analyses at these field values have been included to provide a basis for recommendations on future technology development.

Higher temperature materials than available today would help to ensure the performance and reliability of these high performance accelerators; however, these devices could be fabricated with today's technology if new materials are not available. Finally, advances in arc-heater technology would be necessary before large, 200-atm arc heaters could be designed for this application. However, other higher pressure driver technologies are presently being studied for replacing arc heaters in the MHD accelerator applications, and these show excellent promise. Furthermore, use of the 150-atm arc heaters that are available today would result in some performance degradation but would still allow simulation of flight conditions close to those described herein.

B.1.6 Summary

The NASA-specified target operating conditions are (as expected) very difficult to achieve. The single variable parametric variation used in this study has provided valuable information on the performance effects of each of the individual variables. These effects have been characterized by variation about a baseline parameter set. None of these variations produced a solution that closely approached the NASA- specified condition except at the very high values of magnetic fields. However, these solutions provide insight into ways in which an MHD-augmented driver can produce higher enthalpy and lower entropy test conditions and may improve performance that leads to test conditions nearer those specified by NASA.

Performance analyses of the three arc-heater conditions were very enlightening. All arc-heater characteristics used in this study were of a 200-atm class but operated at various enthalpy levels. Arc-Heater #2 was to the far right of the 200-atm performance envelope on the Mollier diagram. This arc heater provided the MHD channel with a high enthalpy flow, but unfortunately, this was also at a high value of entropy. The MHD channel performed well in this environment; however, the entropy was too high to allow the desired condition to be reached. The Arc-Heater #3

condition was far to the left with a low value of entropy, but the enthalpy was too low to achieve adequate electrical conductivity for effective MHD operation. The MHD system heated the flow as an arc heater would and followed the arc-heater curve.

If a high-pressure driver flow (low entropy) could be heated by other means to an enthalpy value sufficient to achieve the required electrical conductivity, then MHD could perform as in the Arc-Heater #2 case but at a lower entropy as in the Arc-Heater #3 case. These higher pressure drivers will be investigated in another study.

Multiple variable optimization and axially variable parameters also offer potential for improving the performance over that predicted by this single variable parameterization. For instance, these variations indicated that high channel temperature and low current density individually lead to lower entropy solutions. These combinations might further improve the performance if used together and varied axially through the channel to locally optimize the solution.

Increases in magnetic field strength offers the most benefits observed during this study. High strength magnetic fields present no problems for the high-pressure plasma of this application. Higher magnetic fields result in shorter channels and higher operating pressures. If technology permits, high strength magnets can increase MHD performance and produce test conditions near the NASA specifications.

B.1.7 References

1. Simmons, G.A., "Final Report on the Block I Code Modifications, MHD Accelerator Code -- ACCEL," MSE Technology Applications, Inc., Butte, MT, Report MSE-20, July 1996.

2. Rosa, R.J., *Magnetohydrodynamic Energy Conversion*, McGraw-Hill, New York, 1968 or revised printing, Hemisphere Publishing Corp, Washington, D.C., 1987.

3. White, F.M., *Viscous Fluid Flow*, McGraw-Hill, New York, NY, 1974.

4. Kays, W.M. and Crawford, M.E., *Convective Heat and Mass Transfer*, 2nd ed., 1980, McGraw-Hill, New York, NY.

5. Rittenhouse, L.E.; Pigott, J.C.; Whoric, J.M.; and Wilson, D.R., "Theoretical and Experimental Results with a Linear Magnetohydrodynamic Accelerator Operated in the Hall Current Neutralized Mode," AEDC-TR-67-150, Arnold Engineering Development Center (AEDC), Nov. 1967.

6. Weast, R.C., (Ed.), *CRC Handbook of Chemistry and Physics*, 58th ed., CRC Press, Cleveland, OH, 1977-78, p. E-81.

7. Press, W.H.; Flannery, B.P.; Teukolsky, S.A.; and Vetterling, W.T., *Numerical Recipes*, Cambridge University Press, Cambridge, U.K., 1986.

8. Simmons, G.; Nelson, G.; Hiers, R.; and Western. A., "An Unseeded Air MHD Accelerator Concept for High Mach Number Hypersonic Propulsion Testing," AIAA Paper 89-2535, 1989.

9. Simmons, G.A.; Nelson, G.L.; and Lee, Y.M., "Analysis of An Unseeded, Nonequilibrium MHD Accelerator Concept for Hypersonic Propulsion Ground Testing Applications," AIAA Paper 92-3994, 1992.

10. Nottingham, W.B., "A New Equation for the Static Characteristic of the Normal Electric Arc," *Journal of AIEE,* Jan. 1923, pp. 12-19; and Simmons, G.; Nelson, G.; Hiers, R.; and Western, A., "An Unseeded Air MHD Accelerator," *Transactions of AIEE*, Feb. 1923, pp. 302-310.

11. "Atoms III - Molecules I: The Collisions of Electrons with Molecules," *Handbuck der Physik* (*Encyclopedia of Physics*) Springer-Verlag, Berlin, S. Flügge (ed.), Vol. 37 No. 1, by Craggs, J. D. and Massey, H. S. W., Sect. 15, "Experimental Results," 1959, pp. 350-353.

12. Kerrebrock, J. L. and Hoffman, M. A., "Nonequilibrium Ionization Due to Electron Heating: II Experiments," *AIAA Journal*, Vol. 2, 1964, pp. 1080-1087.

13. Cool, T. A. and Zukoski, E. E., "Recombination, Ionization and Non-equilibrium Electrical Conductivity in Seeded Plasmas," *Phys. Fluids*, Vol. 9, Apr. 1966, pp. 780-796.

14. Ben Daniel, D. J., "Theory of Nonthermal Ionization in Cesium Discharges," *Phys. Fluids*, Vol. 5, pp. 500-501, Apr. 1962.

15. *NASA Lewis Research Center Chemical Equilibrium Program with Applications (CEA)*, December 1995, Beta-test Version.

16. Gordon, S. and McBride, B.J., "Computer Program for Calculation of Complex Chemical Equilibrium Compositions and Applications, I. Analysis," NASA RP-1311, Oct. 1994.

17. McBride, B.J. and Gordon, S., *Computer Program for Calculation of Complex Chemical Equilibrium Compositions and Applications, II. User's Manual and Program Description*, NASA RP-1311, June 1996.

18. Wilson, D.R., "Gasdynamic Analysis of a Steady-Flow, High-Density MHD Accelerator," Master's Thesis, University of Tennessee, June 1965.

19. Whitehead, G.L.; MacDermott, W.N.; Siler, L.G.; and Roepke, R.G., "Assessment of MHD Applications to Hypersonic Propulsion Testing Facilities," AEDC-TMR-87-V54, Arnold Engineering Development Center (AEDC), Dec. 1987.

20. Macheret, S.; Miles, R.B.; and Nelson, G., "Feasibility Study of a Hybrid MHD/Radiatively Driven Facility for Hypersonic Ground Testing," AIAA Paper 97-2429, June 1997.

21. Klepeis, J.E. and Louis, J.F., "High Hall Coefficient Studies in a Disk Generator Driven by Molecular Gases," *Proceedings of the Tenth Symposium on Engineering Aspects of Magnetohydrodynamics*, Massachusetts Institute of Technology, Cambridge, MA, Mar. 1969, pp. 202-204.

22. Klepeis, J.E. and Louis, J.F., "Studies with a Disk Generator Driven by Molecular Gases," *Proceedings of the Eleventh Symposium on Engineering Aspects of Magnetohydrodynamics*, California Institute of Technology, Pasadena, CA, Mar. 1970, pp. 62-63.

APPENDIX B, SECTION B.2

B.2 OHIO STATE UNIVERSITY ONE-DIMENSIONAL MHD NONEQUILIBRIUM CODE

Many analytical studies have been conducted to develop computer-driven design and analysis tools for investigating the performance of MHD accelerators. This study is unique in that the flow model incorporates several novel features such as a Boltzmann equation solver for computing the electron energy distribution function, the simulation of added e-beam energy directed into the MHD channel, the simulation of chemical kinetics and vibrational nonequilibrium, and the ability to account for the ionization processes. MHD terms have been incorporated into the model through the inclusion of the Lorentz body force term in the momentum equation and a term for the work done by the MHD body force in the energy balance equation.

NOMENCLATURE

B - Magnetic Field, T
B_i - Rotational Constant of the Diatomic Species, eV
c_f - Skin Friction Coefficient
c_h - Heat Transfer Coefficient
c_p^f - Frozen Specific Heat at Constant Pressure, J/kg/K
D - electron beam load, eV/mol/s
E - electric field, V/m
DE_{beam} - absorbed electron beam power, W
$E_{vib,i}(T)$ - equilibrium vibrational energy of the species, J/kg
$E_{vib,i}(x)$ - nonequilibrium vibrational energy of the species, J/kg
e - electron charge, C
F - channel cross-section, m^2
$f_i(v)=n_i(v)/n_i$ - relative population of vibrational level v of i^{th} species (vibrational distribution function)
G - mass flowrate, kg/s
G_i^0 - Gibbs free energy of the species at standard pressure, J/kg
g_i - g-factors, efficiencies of electron beam initiated processes, mol/eV
h_i - specific enthalpy of the species, J/kg
h - enthalpy of the mixture, J/kg
$H=h+u^2/2$ - total enthalpy, J/kg
j - current density, A/m^2
j_{beam} - electron beam current density, A/m^2
l - electron beam penetration length, m
L - MHD channel length, m
k - Boltzmann constant, J/K
k_{ion} - rate of ionization, cm^3/s
k_{rec} - rate of electron recombination, cm^3/s
k_{att} - rate of electron attachment, cm^3/s
$k_{ij}(v6w)$ - vibration-translation rates, cm^3/s
$k_{ij}(v,v=6w,w=)$ - vibration-vibration rates, cm^3/s
$k_{ej}(v6w)$ - electron-vibration (e-V) rates, m^3/s
$k(v6,T)$, $k(6v,T)$ - state-specific chemical reaction rates, cm^3/s
M_f - frozen Mach number
dM_f - correction to the frozen Mach number due to vibrational specific heat
m_e - electron mass, kg
m_p - proton mass, kg
$n_i(v)$ - absolute population of vibrational level v of i^{th} species, mol/m^3
n_i - number density of the species, mol/m^3
N - total number density, mol/m^3
P - pressure, Pa
P_0 - standard pressure (1 atm)
Pr - Prandtl number
$Q_{tr,i}$ - electron transport cross-section for i^{th} species, m^2
$Q_{rot,i}$ - rotational excitation cross-section, m^2
$Q_{vib,i}$ - vibrational excitation cross-section, m^2
$Q_{el,i}$ - electronic excitation cross-section, m^2
$Q_{ion,i}$ - ionization cross-section, m^2
R_0 - universal gas constant, J/kmol/K
r - channel half-width, m
Re_d - Reynolds number based on the channel width
Re_x - Reynolds number based on the axial coordinate
S - entropy, J/kg/K

T	-	heavy species translational temperature, K
$T_{v,i}$	-	species vibrational temperatures, K
T_e	-	electron temperature, K
T_{ref}=300 K	-	reference temperature
u	-	gas velocity, m/s
$x_{e,i}$	-	anharmonicity of i^{th} diatomic species
x	-	axial coordinate, m
y	-	transverse coordinate, m
z	-	magnetic field direction
b	-	Hall parameter
$g=c_p^f/c_v^f$	-	frozen specific heat ratio
d	-	boundary layer thickness, m
e	-	plasma (secondary) electron energy, eV
e_{beam}	-	beam electron energy, eV
m_i	-	species molecular weight, kg/kmol
m	-	mixture molecular weight, kg/kmol
$n_0=(e/m_e)B$	-	plasma frequency, s^{-1}
$+n$,	-	electron-heavy species collision frequency, s^{-1}
r	-	gas density, kg/m^3
s	-	electric conductivity, mhos/m
$f_i=(n_i/n)$	-	species mole fractions
f_e	-	ionization fraction
$x_i=(n_i/n).(m_i/m)$	-	species mass fractions
$w_{e,i}$	-	vibrational quantum of diatomic species, K
W	-	instability increment, s^{-1}

B.2.1 Overview

In this section we report on an analysis of MHD accelerators that was conducted as a part of the MARIAH Program for the purpose of investigating the performance limits of such devices. This analysis is based on a 1-D simulation of the entire flow train, starting at the plenum, passing through the nozzle and MHD accelerator, and continuing through the secondary expansion duct up to the inlet of the test section. Several issues have been investigated using this model, such as: a) the question of pressures needed in the heater or plenum region, b) whether e-beam addition can be utilized in an unseeded flow to enhance conductivity in the MHD duct, c) the question of seeded vs. unseeded flows, and d) issues relating to basic thermodynamic limits of such drivers. These issues are discussed and reported on in some depth in the following sections.

There are several basic requirements that have been used to define the testing scenario and the performance objectives of this study. These have been discussed in the literature (Refs. 1, 2, 3). Since they largely define the operating scenario for the MHD flow train, these requirements are summarized below:

1. The test facility should be a test and evaluation facility in the sense that test durations of the order of tens of seconds to minutes can be obtained.
2. The facility should be capable of testing advanced engine modules at near full scale. An area cross section for the test section of 80 square feet (ft^2) has been adopted as a working number.
3. The facility should be capable of simulating true total enthalpy and thermodynamic conditions. For engine testing, this implies that the Mach numbers, total enthalpies, and entropies should match those seen behind the bowshock of the hypervelocity aircraft. The facility should be capable of matching post-bowshock conditions corresponding to the 2,000-lbf/ft^2 free-stream dynamic pressures trajectory.

4. The facility should provide an airstream chemistry corresponding approximately to the post-bowshock regime of the aircraft, i.e., having minimal dissociation, vibrational nonequilibrium, and contaminants.
5. The facility should be a true test and evaluation facility. This implies high testing throughput, high reliability and lifetimes for critical components, and versatility of the MHD accelerator across a wide range of pressures and Mach numbers.

Analytical studies similar to the present one have been conducted in the past by several researchers (Refs. 4, 5, 6). The present study is unique in that the flow model incorporates several novel features, namely a) the inclusion of a Boltzmann equation solver for the electron distribution function, b) the ability to simulate the addition of e-beam energy directed into the MHD channel, c) the ability to simulate both chemical kinetics and vibrational nonequilibrium, and d) the ability to correctly account for all important ionization processes. These capabilities permitted us to systematically explore both the nonequilibrium and the equilibrium flow regimes across a wide spectrum of control parameters. Details of the kinetic model are given in Section B.2.2.

The computer code developed on the basis of the kinetic model was run across a rather large set of control parameters, including variation of seed fraction and type, e-beam energy, plenum pressures and temperatures, and nozzle geometry (see Section B.2.3). The overall objective of the study was to demonstrate whether or not it was possible to place points on the total enthalpy versus entropy diagram corresponding to the post-bowshock, 2,000-lbf/ft^2 flight trajectory. This has been adopted as the limiting operating envelope for the hypothetical test facility. The major conclusions are given in Section B.2.4.

B.2.2 Kinetic Modeling

B.2.2.1 Kinetic Equations

To simulate the gas dynamics and kinetics of both alkali-seeded and unseeded airflows in supersonic nozzles and MHD channels, we have used quasi-1-D nonequilibrium flow kinetic modeling. The model incorporates the following equation groups:

1. The equations of 1-D magnetogasdynamics for nonequilibrium reacting ionized real gases (Refs. 7, 8):

$$\frac{dT}{dx} = \frac{u^2}{c_p^f [1 - M_f^2 (1 - \delta M_f)]} \left\{ \frac{1}{F}\frac{dF}{dx} + \frac{1}{\mu}\frac{d\mu}{dx} - \frac{\gamma M_f{}^2 - 1}{u^2}\frac{dQ}{dx} + \frac{\gamma M_f{}^2}{u^2}\left[\frac{j_y B_z}{\rho} - \frac{c_f u^2}{r} \right] \right\} \qquad \text{(B.2- 1)}$$

$$\frac{du}{dx}=\frac{1}{u}\left\{\left[\sum_j \xi_j \frac{dE_{vib.j}(T)}{dT}-c_p^f\right]\frac{dT}{dx}+\frac{d\Phi}{dx}\right\} \tag{B.2- 2}$$

$$\rho u F = G \tag{B.2- 3}$$

$$\frac{P}{\rho}=\frac{R_0 T}{\mu}, \tag{B.2- 4}$$

where

$$M_f^2=\frac{u^2\mu}{\gamma_f R_0 T},\quad \delta M_f=\frac{\gamma M_f^2-1}{c_p^f M_f^2}\sum_j \xi_j \frac{dE_{vib,j}(T)}{dT} \tag{B.2- 5}$$

$$E_{vib,j}=\frac{R_0}{\mu_j}\sum_v f_j(v)\left\{\omega_{e,j} v[1x_{e,j}(v+1)]\right\} \tag{B.2- 6}$$

$$\frac{d\Phi}{dx}=\frac{j_x E_x + j_y E_y}{\rho u}+\frac{eDN}{\rho u}-\frac{2c_h\sum_i \xi_i h_i}{r}-\frac{j_y\left(\frac{k}{e}\sum_{\substack{electrons\\ions}}\frac{\xi_i h_i}{c_{pi}}+\Delta U_e\right)}{\rho u r}-\frac{d\Phi_{chem,vib}}{dx} \tag{B.2- 7}$$

In Equation (B.2- 1), the terms in the right-hand side describe gas temperature variation due to nozzle cross-section change, change of molecular weight of the mixture, translational mode energy addition $d\Phi/dx$, push force and wall friction work. Equation (B.2- 6) gives the energy stored in vibrational mode of diatomic species such as N_2, O_2, and NO. The terms in the right-hand side of Equation (B.2- 7) describe electric field and e-beam power input (D is the e-beam load per molecule in eV/mol/s); wall heat losses due to heat transfer; enthalpy transfer by the current; and electrode voltage drop, ΔU_e, and enthalpy storage in chemical reaction products; and vibrational energy mode. The last term in Equation (B.2- 7) can be written in the following form:

$$\frac{d\Phi_{chem,vib}}{dx} = \sum_i h_i(T)\frac{d\xi_i}{dx} + \sum_j \left\{ \left[E_{vib,j}(x) - E_{vib,j}(T) \right] \frac{d\xi_i}{dx} + \xi_j \frac{dE_{vib,j}(x)}{dx} \right\} \quad \text{(B.2- 8)}$$

Note that Equation (B.2- 8) requires knowledge of both equilibrium and nonequilibrium values of diatomic species vibrational energy, $E_{vib,j}(T)$ and $E_{vib,j}(x)$, respectively. Both of these energies are calculated using Equation (B.2- 6) where the equilibrium vibrational distribution function, $f_j(v,T)$, is the Boltzmann distribution with temperature, T, and the nonequilibrium vibrational level populations, $f_j(v,x)$, are given by the master equation (see below). In Equations (B.2- 2), (B.2- 5), and (B.2- 7), (B.2- 8), the sum over index i or j is evaluated for all reacting species, and the sum over index, j, is taken only for three diatomic species, N_2, O_2, and NO.

2. Chemical and ionization kinetics equations for a number of reacting species (including electrons, ions, and electronically excited metastable species):

$$\frac{d\xi_i}{dx} = \frac{\rho}{u}\mu_i \sum_j (b_{ij} - a_{ij}) W_j \quad \text{(B.2- 9)}$$

where the sum is taken for all chemical reactions, a_{ij} and b_{ij} are stoichiometric coefficients of i^{th} species in j^{th} chemical reaction:

$$\sum_i a_{ij} A_i \Leftrightarrow \sum_i b_{ij} A_i \quad \text{(B.2- 10)}$$

and W_j is the rate of j^{th} chemical reaction per unit stoichiometric coefficient:

$$W_j = \rho^{\sum_i a_{ij} - 2} \left\{ \vec{k}_j \cdot \prod_i \left(\frac{\xi_i}{\mu_i} \right)^{a_{ij}} - \left(\frac{P\mu}{P_o} \right)^{\sum_i (b_{ij} - a_{ij})} \vec{k}_j \cdot \prod_i \left(\frac{\xi_i}{\mu_i} \right)^{b_{ij}} \right. \quad \text{(B.2- 11)}$$

In Equations (B.2- 10) and (B.2- 11), the sums and the products are taken for all reacting species. In Equation (B.2- 11), P_0=1 atm is a standard pressure. For bimolecular reaction $A_1+A_2 \rightleftharpoons A_3+A_4$, the expression for W_j is particularly simple:

$$W_j = \vec{k}_j \cdot \frac{\xi_1}{\mu_1}\frac{\xi_2}{\mu_2} \vec{k}_j \cdot \frac{\xi_3}{\mu_3}\frac{\xi_4}{\mu_4} \quad \text{(B.2- 12)}$$

For chemical reactions at vibrational equilibrium, the reverse reaction rates in Equations (B.2- 11) and (B.2- 12) are determined from thermochemical equilibrium:

$$\vec{k}_j(T) = \vec{k}_j(T) \cdot exp\left(-\frac{\sum_{products} b_{ij} G_i^0(T) - \sum_{reactants} a_{ij} G_i^0(T)}{R_0 T} \right) \qquad \text{(B.2- 13)}$$

where $G_i^0(T)$ are the molar Gibbs free energies of species evaluated at a standard pressure, P_0=1 atm.

For vibrationally stimulated reactions, such as nonequilibrium dissociation of diatomic molecules:

$$AB(v) + M \Leftrightarrow A + B + M \qquad \text{(B.2- 14)}$$

and bimolecular exchange reactions:

$$AB(v) + C \Leftrightarrow A + BC \qquad \text{(B.2- 15)}$$

the forward rates at vibrational disequilibrium are determined as follows:

$$\vec{k} = \sum_v k(v \rightarrow, T) f(v), \qquad \text{(B.2- 16)}$$

where $k(v\rightarrow\ ,T)$ are state-resolved reaction rates (see Section B.2.2.2) and $f(v)$ is the nonequilibrium relative population of vibrationally excited diatomic species, given by the master equation. In Equations (B.2- 14) and (B.2- 15), *AB* stands for diatomic molecule, *C* for atom, *M* for an collision partner, and v is a vibrational quantum number.

For nonequilibrium plasma electron impact processes (ionization, attachment, electronic excitation) the kinetic rates are determined by integration of the cross sections over the electron energy distribution function (EEDF). For example, for ionization:

$$k_{ion} = \frac{2e}{m_e} \int_{E_{ion}}^{\infty} Q_{ion}(\varepsilon) \varepsilon^{1/2} f(\varepsilon) d\varepsilon \qquad \text{(B.2- 17)}$$

where $f(\varepsilon)$ is the EEDF as a function of electron energy, determined by the Boltzmann equation (see below), Q_{ion} is the cross section of ionization, and E_{ion} is the ionization potential.

For the high-energy e-beam-initiated reactions, the reaction rates are as follows:

$$W_{j,beam} = \frac{g_j D}{\rho} \frac{\xi_i}{\mu_i} \tag{B.2- 18}$$

where D is the e-beam load, and g_j (g-factors) are the beam reaction efficiencies in mol/eV.

3. Master equation for populations of vibrational levels of three diatomic species N_2, O_2, and NO (Ref. 9):

$$\begin{aligned}\frac{df_i(v)}{dx} = {} & \frac{\rho}{\mu u}\sum_j\left\{\phi_i\sum_w\left[k_{ij}(w\to v)f_i(w) - k_{ij}(v\to w)f_i(v)\right]\right\} \\ & + \frac{\rho}{\mu u}\sum_j\left\{\phi_i\sum_{v',w,w'}\left[k_{ij}(w,w'\to v,v')f_i(w)f_j(w') - k_{ij}(v,v'\to w,w')f_i(v)f_j(v')\right]\right\} \\ & + \frac{\rho}{\mu u}\phi_{ei}\sum_w\left[k_{ej}(w\to v)f_i(w) - k_{ej}(v\to w)f_i(v)\right] + \left(\frac{df_i(v)}{dx}\right)_{chem}\end{aligned} \tag{B.2- 19}$$

In Equation (B.2- 19), the terms in the right-hand-side describe the change of vibrational distribution function $f_i(v)$ of a diatomic species due to vibration-translation (V-T), vibration-vibration (V-V), and electron-vibration (e-V) energy transfer processes and chemical reactions, respectively. Note that Equation (B.2- 19) also takes into account multiquantum vibrational energy transfer processes. The chemical reaction term in Equation (B.2- 19) can be written as follows:

$$\begin{aligned}\left(\frac{df_{AB}(v)}{dx}\right)_{chem} = {} & \frac{\rho}{u}\left[\frac{P\mu}{P_0}\cdot k(\to v,T)\frac{\xi_A}{\mu_A}\frac{\xi_B}{\mu_B}\frac{\xi_M}{\mu_M}\frac{\mu_{AB}}{\xi_{AB}} - k(v\to,T)\frac{\xi_M}{\mu_M}f_{AB}(v)\right] \\ & + \frac{\rho}{u}\left[k(\to v,T)\frac{\xi_A}{\mu_A}\frac{\xi_{BC}}{\mu_{BC}}\frac{\mu_{AB}}{\xi_{AB}} - k(v\to,T)\frac{\xi_C}{\mu_C}f_{AB}(v)\right] - \frac{f_i(v)}{\xi_i}\frac{d\xi_i}{dx}\end{aligned} \tag{B.2- 20}$$

where the first two terms in the right-hand side describe vibrationally stimulated dissociation and exchange reactions of Equations (B.2- 14) and (B.2- 15), respectively. The direct and the reverse state-resolved rates in Equation (B.2- 18) are related by the detailed balance equation:

$$\frac{k(v\to,T)\,f_{AB}(v,T)}{k(\to v,T)} = \frac{\bar{k}(T)}{\bar{k}(T)} \tag{B.2- 21}$$

where the relation between the overall direct and reverse thermal rates is given by Equation (B.2- 13). Note that in Equation (B.2- 21), $f_{AB}(v,T)$ is the equilibrium relative population of vibrational level v of molecule AB.

The vibrational "temperatures" of the diatomic species are determined as follows:

$$T_{v,i} = \frac{\omega_{e,i}(1 - 2x_{e,i})}{\ln\left[f_i(0) / f_i(1)\right]} \tag{B.2- 22}$$

4. Boltzmann equation for symmetric part of electron energy distribution function $f(\varepsilon)$ (EEDF) in crossed electric and magnetic fields (Refs. 10, 11):

$$\begin{aligned}
&\frac{1}{3}\frac{E_x^2 + (E_y - uB_z)^2}{N^2} N \frac{d}{d\varepsilon}\left(\frac{\nu(\varepsilon)^2}{\nu(\varepsilon)^2 + \nu_0^2}\frac{\varepsilon}{Q_{tr}(\varepsilon)}\frac{df(\varepsilon)}{d\varepsilon}\right) \\
&+ N\frac{d}{d\varepsilon}\left\{\left[f(\varepsilon) + \frac{kT}{e}\frac{df(\varepsilon)}{d\varepsilon}\right]\sum_i \phi_i\left[\frac{m_p}{m_p\mu_i}\varepsilon^2 Q_{tr,i}(\varepsilon) + B_i\varepsilon Q_{rot,i}(\varepsilon)\right]\right\} \\
&+ N\phi_{N_2}\sum_{0\le v,w\le 8} f_{N_2}(v)\left[Q_{vib,N_2}^{v\to w}(\varepsilon + \Delta E_{v,w})(\varepsilon + \Delta E_{v,w})f(\varepsilon + \Delta E_{v,w}) - Q_{vib,N_2}^{v\to w}(\varepsilon)\varepsilon f(\varepsilon)\right] \\
&+ N\phi_{O_2}\sum_{0\le w\le 3} f_{O_2}(0)\left[Q_{vib,O_2}^{0\to w}(\varepsilon + \Delta E_{0,w})(\varepsilon + \Delta E_{0,w})f(\varepsilon + \Delta E_{0,w}) - Q_{vib,O_2}^{0\to w}(\varepsilon)\varepsilon f(\varepsilon)\right] \\
&+ N\sum_{i,k}\phi_i\left\{Q_{i,k}^{el}(\varepsilon + \Delta E_{i,k})(\varepsilon + \Delta E_{i,k})f(\varepsilon + \Delta E_{i,k}) - Q_{i,k}^{el}(\varepsilon)\varepsilon f(\varepsilon)\right\} \\
&+ \frac{2\pi}{3} n_e \frac{q^4}{e^2}\ln\Lambda\left[I_1(\varepsilon)\frac{df(\varepsilon)}{d\varepsilon} + I_2(\varepsilon)f(\varepsilon)\right] + S(\varepsilon) = 0
\end{aligned} \tag{B.2- 23}$$

In Equation (B.2- 23), the separate terms describe the EEDF change due to applied fields, momentum transfer and rotational excitation, vibrational excitation, electronic excitation (excitation of the k^{th} electronic level of the i^{th} species), electron-electron collisions, and ionization by the e-beam electrons. Also in Equation (B.2- 23):

$$\nu(\varepsilon) = N \cdot \left(\frac{2e}{m_e}\right)^{1/2} \varepsilon^{1/2} Q_{tr}(\varepsilon) \tag{B.2- 24}$$

is the momentum transfer frequency:

$$\nu_0 = \frac{e}{m_e} B, \tag{B.2- 25}$$

$$\Lambda = \frac{r_d}{r_0} = \left(\frac{kT_e}{4\pi n_e e^2}\right)^{1/2} \frac{3kT_e}{2q^2} \qquad \text{(B.2- 26)}$$

is the ratio of the Debye length to the classical closest approach distance, and:

$$I_1(\varepsilon) = \int_0^{\varepsilon} x^{3/2} f(x)dx + 2\varepsilon^{3/2} \int_0^{\varepsilon} f(x)dx$$
$$I_2(\varepsilon) = 3\int_0^{\varepsilon} x^{1/2} f(x)dx \qquad \text{(B.2- 27)}$$

In the present study, we are interested only in the low-energy part of the EEDF (ε<20-30 eV), which is independent of the e-beam energy if ε_{beam}>>E_{ion} (Refs. 12, 13). Therefore, Equation (B.2- 23) does not incorporate the detailed model of ionization by an e-beam that uses the double differential cross section of ionization, $Q_{ion}(\varepsilon_p,\varepsilon)$ as a function of primary and secondary electron energies (Refs. 12, 13). Instead, a simplified approach is used, with the source term $S(\varepsilon)$ in Equation (B.2- 23) expressed in terms of the g-factor for the beam ionization g_{ion} (ionization efficiency) and the secondary electron energy ε:

$$S(\varepsilon) = \frac{const}{(\varepsilon + E_{ion})^{3/2}}, \qquad \int S(\varepsilon)d\varepsilon = g_{ion} D \qquad \text{(B.2- 28)}$$

The g-factors are also known to be independent of the beam energy if ε_{beam}>>E_{ion} (Ref. 13):

$$T_e = -\left.\frac{f(\varepsilon)}{df(\varepsilon)/d\varepsilon}\right|_{\varepsilon=0} \qquad \text{(B.2- 29)}$$

Note that Equation (B.2- 23) also takes into account superelastic processes (electron heating in collisions with vibrationally excited N_2 molecules):

$$N_2(v) + e(\varepsilon) \rightarrow N_2(w < v) + e(\varepsilon + \Delta E_{v,w}) \qquad \text{(B.2- 30)}$$

where $\Delta E_{v,w}$ is the vibrational energy defect. These processes are well known to strongly affect the electron temperature in gas flows at strong vibrational disequilibrium (Refs. 14,15).

5. Generalized Ohm's Law (Ref. 8):

$$j_x = \frac{\sigma}{1+\beta^2}\left[E_x - \beta(E_y - uB_z)\right]$$
$$j_y = \frac{\sigma}{1+\beta^2}\left[(E_y - uB_z) + \beta E_x\right] \qquad \text{(B.2- 31)}$$

where

$$\sigma = \frac{e^2 n_e}{m_e \langle \nu \rangle} \qquad \text{(B.2- 32)}$$

is the plasma electric conductivity and

$$\beta = \frac{\nu_0}{\langle \nu \rangle} = \frac{eB}{m_e \langle \nu \rangle} \qquad \text{(B.2- 33)}$$

is the Hall parameter. In Equations (B.2- 32) and (B.2- 33):

$$\langle \nu \rangle = N\left(\frac{2e}{m_e}\right)^{1/2} \int_0^\infty Q_{tr}(\varepsilon)\varepsilon^{1/2} f(\varepsilon) d\varepsilon \qquad \text{(B.2- 34)}$$

is the electron-heavy species collision frequency (Ref. 10).

As one can see, the effects of vibrational relaxation and chemical reactions are accounted for in the energy and motion equations (B.2- 1) and (B.2- 2). The chemistry-vibration coupling terms are incorporated into both the chemical kinetics equations (B.2- 9) and the master equation (B.2- 19). Rates of electron impact processes used in kinetic equations (B.2- 9) and (B.2- 19) (vibrational and electronic excitation, ionization, attachment etc.), as well as electric conductivity are calculated based on the EEDF calculated by the Boltzmann equation (B.2- 23). The latter takes into account superelastic processes, which couple vibrational and electron mode energies. Therefore, the system of equations solved is self-consistent.

In this quasi-1-D approach, the applied electric and magnetic fields are given as functions of the axial coordinate: $E_x(x)$, $E_y(x)$, and $B_z(x)$. Time and space derivatives in the Boltzmann equation are omitted since they become important only in extremely fast oscillating fields and in sheath

areas; consequently, the Boltzmann equation becomes a simple second-order differential equation with electron energy as an independent variable, solved by standard iteration method (Ref. 11). The rest of the differential equations are first-order equations solved by a widely used stiff ordinary differential equation system solver LSODE (Ref. 16).

B.2.2.2 Rates and Cross-Sections

The list of the neutral species chemical reactions (32 reactions for 12 species N, N_2, O, O_2, NO, O_3, NO_2, N_2O, NO_3, N_2O_4, N_2O_5, N_3), as well as the reaction rates at thermal equilibrium are taken from the Russian AVOGADRO database (Ref. 17), where the most reliable available data has been recommended in a wide temperature range. The vibration-chemistry coupling is modeled using the Macheret-Fridman-Rich nonequilibrium rate model (Refs. 18, 19), and the state-specific reaction rates $k(v\rightarrow,T)$ for the reactions:

$$\begin{aligned} N_2(v) + M &\leftrightarrows N + N + M \\ O_2(v) + M &\leftrightarrows O + O + M \\ NO(v) + M &\leftrightarrows N + O + M \\ N_2(v) + O &\leftrightarrows NO + N \\ NO(v) + O &\leftrightarrows O_2 + N \end{aligned} \qquad \text{(B.2- 35)}$$

used in chemical and vibrational kinetics equations (B.2- 9) and (B.2- 19) are the same as in our previous paper (Ref. 20).

The list of ion-molecular reactions, including ionization, recombination, ion conversion, attachment and detachment processes (more than 300 reactions for 13 species e^-, N^+, N_2^+, O^+, O_2^+, NO^+, O^-, O_2^-, N_2O^+, NO_2^-, Na^+, K^+, Cs^+), as well as most of the reaction rates were taken from the review (Ref. 21, 22, 23, 24, 25). The rates of electron impact ionization and electron attachment to the species N_2, O_2, NO, Na, K, Cs are calculated by the Boltzmann equation solver using the experimental cross sections of these processes as functions of electron energy (Refs. 26, 27, 28, 29). The latter group of processes describes kinetics of nonequilibrium ionization and attachment of the plasma electrons in the presence of external electric and magnetic fields.

Note that thermochemical data for both neutral and charged species are incorporated into the code; therefore, the rates of reverse processes are evaluated from detailed balance, e.g., see Equation (B.2- 13). Therefore, the kinetic model correctly predicts the chemical composition of alkali-seeded air, including electron and ion concentrations, in thermodynamic equilibrium (with no fields applied). Thermochemical parameters such as enthalpies, entropies, and specific heats of the species in the temperature range 300-6,000 K are taken from References 30 and 31.

The rates of electronic excitation and dissociation of N_2 and O_2 by the plasma electrons, with the

production of metastable species $N_2(A^3\Sigma_u^+)$, $N(^2D)$, $N(^2P)$, $O_2(a^1\Delta_g)$, $O_2(b^1\Sigma_g^+)$, $O(^1D)$, $O(^1S)$ are also calculated by the Boltzmann solver using the experimental cross sections (Refs. 26, 27). Metastable species collisional quenching and chemical reaction rates are taken from the review (Ref. 21).

The rates of vibrational excitation of N_2 ad O_2 by plasma electrons are evaluated by the Boltzmann solver using the experimental cross sections $Q_{vib}^{0\to v}$ (Refs. 26, 27). The detailed cross-section matrix for N_2, $Q_{vib}^{v\to w}$, $0\le v,w\le 8$, needed for modeling of superelastic processes (Ref. 27), is calculated using the semi-empirical method (Ref. 32). The rates of V-T and V-V rates for N_2 and O_2, including multiquantum processes, are taken the same as in Reference 20 where they have been evaluated using the forced harmonic oscillator (FHO) rate model (Ref. 33). These rates show good agreement with the recent experiments and state-of-the-art close-coupled calculations in a wide temperature range (Ref. 33). The V-T rates for N_2-Na, N_2-K, and N_2-Cs are taken from Reference 34. As shown in Reference 35, these rates are consistent with the Na-seeded N_2 vibrational relaxation measurements behind shock waves.

The experimental electron transport cross sections for N_2, O_2, NO, Na, K, and Cs necessary for the plasma electric conductivity calculations are taken from References 26 through 28 and 36.

In these calculations, we considered the use of a high-energy e-beam as a possible efficient way to sustain nonequilibrium ionization in the supersonic flow. It is well known that up to 50% of the relativistic e-beam power goes into electron impact ionization (Ref. 21). This external ionization method has been previously extensively used to sustain a discharge in supersonic flows in gas dynamic lasers (Ref. 37). The e-beam power fractions going into ionization, dissociation, and electronic excitation of N_2 and O_2 in air (g-factors) are taken from the review (Ref. 21). The experimental secondary electron energy distribution in N_2 and O_2 for the beam energies 50-2,000 eV are taken from References 26 and 27 and extrapolated toward the higher energies (Ref. 12). Note that in the present study, we do not address the high-power e-beam engineering issues (beam entering the high-pressure flow, focusing, X-ray radiation etc.). Our primary interest is the e-beam-initiated kinetics.

Wall heat transfer coefficient, c_h, and skin friction coefficient c_f, as well as the boundary layer thickness, δ, are estimated based on the results of turbulent compressible boundary layer theory (Ref. 38):

$$c_f \cong \frac{0.059}{\mathrm{Re}_x^{0.2}} \frac{1}{1+\mathrm{Pr}^{1/3}(\gamma-1)M_f^2/2}, \quad 5\cdot 10^5 \le \mathrm{Re} \le 10^7 \qquad \text{(B.2- 36)}$$

$$c_h = \frac{1}{2} c_f / \mathrm{Pr}^{2/3}, \quad 5\cdot 10^5 \le \mathrm{Re} \le 10^7 \qquad \text{(B.2- 37)}$$

$$\frac{\delta(x)}{r} = \frac{0.37}{\mathrm{Re}_x^{0.2}} \frac{x}{r}, \quad 5 \cdot 10^5 \le \mathrm{Re} \tag{B.2- 38}$$

Heat fluxes to the electrode surfaces [see Equation (B.2- 7)] are estimated based upon the experimental heat transfer measurements in MHD accelerators (Ref. 39) (see Section B.2.2.3).

B.2.2.3 Code Validation

Various parts of the kinetic model used in the present paper have been previously validated in modeling calculations. First, V-T and V-V rates, neutral species chemical kinetic rates, and vibration-chemistry coupling in high temperature air were validated in modeling of NO production in N_2-O_2 mixtures behind shock waves that showed good agreement with time-resolved shock tube measurements (Ref. 20). Second, electron swarm parameters (drift velocity, magnetic drift velocity, diffusion coefficient, ionization, and attachment coefficients) for N_2, O_2, and air, predicted by the Boltzmann equation solver are in very good agreement with available experimental data (Refs. 10, 40).

We have also carried out two series of validation calculations for the entire model. The results of the first series was compared with the experimental data (somewhat scarce), which were obtained on the GE unseeded air MHD accelerator (Refs. 41, 42). In these experiments, air was heated to T_0=9,500 K at a pressure P_0=550 atm behind the reflected shock and expanded through a supersonic MHD channel (channel length L=30 cm, area ratio F_2/F_1=2.0, magnetic field B=4.2 T). The experimentally determined test area impact pressure in the MHD-augmented flow was approximately 1.5-2 times higher than in the isentropic flow in the same channel. Figure B.2- 1 shows calculated axial profiles of the gas temperature and velocity in the channel for both MHD-augmented and isentropic flow, as well as the velocity profile obtained from the GE group 1-D equilibrium flow model (Ref. 41). The close agreement between these two models, both predicting approximately 15% velocity increase, is due to the fact that at the high temperature, T≅6,800 K, and pressure, P=10-30 atm, the flow in the channel is very close to the local thermodynamic equilibrium. The effective reduced electric field that determines the electron energy in crossed electric and magnetic fields was also quite low:

$$\left(\frac{E}{N}\right)_{eff} = \frac{1}{N}\left[\frac{E_x^2 + (E_y - uB_z)^2}{1+\beta^2}\right]^{1/2} \le 10^{-17} V \cdot cm^2 \tag{B.2- 39}$$

therefore, the electron temperature was very close to the gas temperature throughout the channel. The electric conductivity calculated by the present model is also in good agreement with the value

measured in the channel, σ=110 mhos/m. Figure B.2- 2 shows the axial pressure profile as well as distributions of NO and atom mole fractions and ionization fraction. One can see that the flow quality in the test area is poor, i.e., the atom fractions remain frozen and reach 10% for N atoms and 30% for O atoms. In other words, O_2 is almost completely dissociated. Another disadvantage of this reflected shock tunnel MHD accelerator is an extremely short test time (approximately 1 millisecond (ms) in these experiments). The calculated total flow power increase for these experiments is approximately 25%, from 20 to approximately 25 MW, which corresponds to a total enthalpy increase from 24 to 30 MJ/kg.

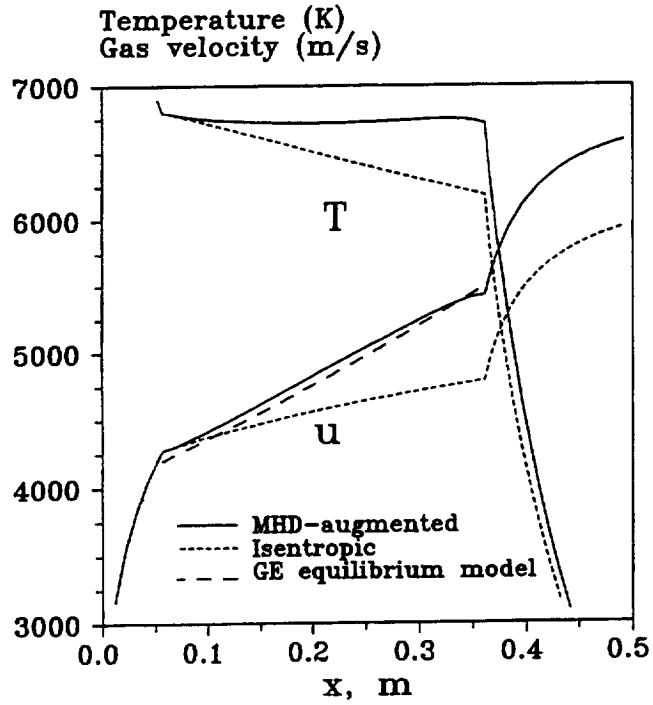

Figure B.2- 1. Axial temperature and velocity profiles for the GE reflected shock unseeded air accelerator.

The second series of calculations was made for the AEDC continuous-mode MHD accelerator running on K-seeded (at 1.5%) N_2 (Accelerator B of Ref. 39). In these experiments, N_2 was heated by an arc heater up to a temperature of about T_0=6,000 K at a pressure P_0=3.3 atm and expanded through an MHD channel (channel length L=77 cm, area ratio F_2/F_1=2.1, magnetic field B=1.5 T). Figure B.2- 3 shows the temperature and the flow velocity distributions along the channel. Figure B.2- 4 presents gas temperature and velocity at the channel exit as functions of the accelerator power. One can see that experimental and calculated data are in good agreement, temperature and pressure in the MHD-augmented flow being up to 30-50% higher than in the isentropic flow.

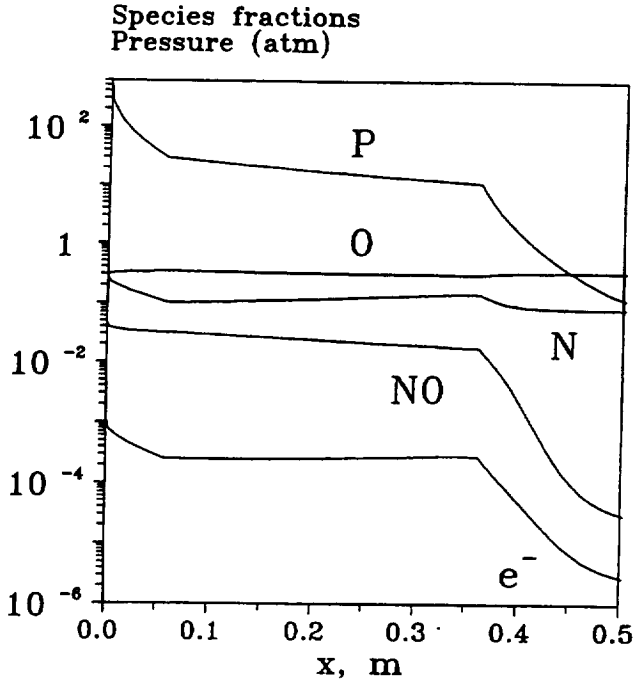

Figure B.2- 2. Axial profiles of pressure and species mole fractions for the GE accelerator.

Nonequilibrium effects in the channel (N_2 vibrational disequilibrium) and chemical dissociation are both insignificant. The gas temperature in the channel, T~3,000-4,000 K, is not high enough to stimulate substantial thermal dissociation of N_2, while fast N_2 V-T relaxation on K atoms and quite slow expansion prevented freezing of N_2 vibrations. Again, the effective reduced electric field was low, $(E/N)_{eff} \cong 10^{-17}$ V×cm^2, so that $T_e \cong T$ in the channel. The experiments also show that the boundary layers in the channel overlap (Ref. 39) so one has a fully developed channel flow. Indeed, the estimate of Equations (B.2- 34) gives the ratio of the boundary layer thickness to the channel half-width, $\delta/r \cong 1$, already at x/L=0.5 ($Re_x=6\times10^5$). This results in significant power loss due to heat transfer and wall friction. Experiments (Ref. 39) and present calculations show that in the fully powered accelerator (at maximum power loading of 375 kW) as much as 30% of the initial flow power of 640 kW is lost in heat transfer. Both measured and calculated total enthalpy increase for the fully powered accelerator is approximately 25%, from 7.6 to 9.5 MJ/kg.

In both series of calculations, the agreement with the experiments is quite good. However, we note that additional model validation is desirable, specifically for MHD flows where the flow is far from thermal and ionization equilibrium.

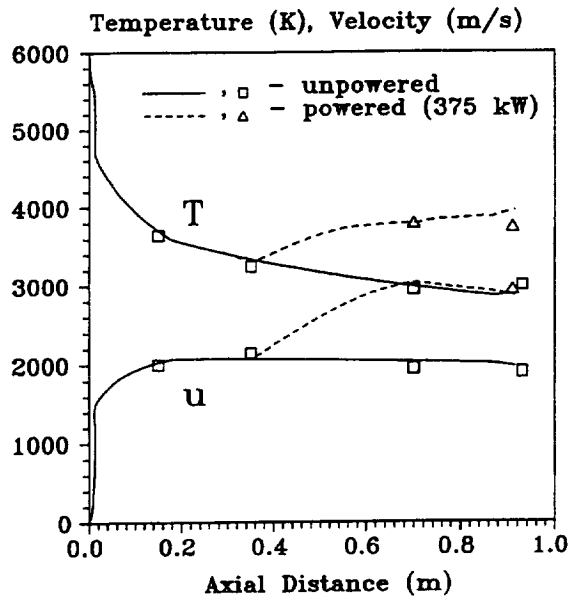

Figure B.2- 3. Experimental and calculated temperature and velocity axial profiles for the AEDC K-seeded accelerator.

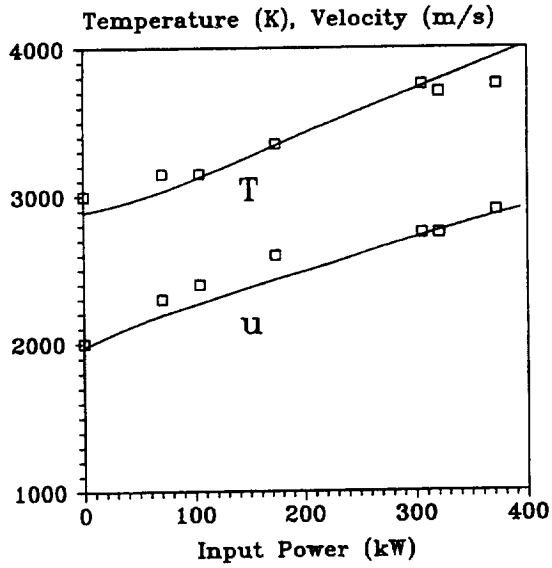

Figure B.2- 4. Experimental and calculated exit temperature and velocity for the AEDC K-seeded accelerator.

B.2.3 Results and Discussion

We applied the kinetic model described and validated in Section B.2.2 for modeling of both alkali-seeded and unseeded airflows in MHD accelerators in a wide range of plenum conditions and for various nozzle geometries. The main objective was to determine the feasibility and efficiency of using the MHD technology for the high Mach number energy addition wind tunnel. All subsequent calculations are made for the nozzle throat cross-section area F_{throat}=4 cm^2 and ideal Faraday accelerator [$E_x=\beta(E_y-uB_z)$, $j_x=0$ throughout the channel] with the magnetic field in the channel B_z=10 T. The secondary expansion duct was assumed to be 2 m long with the exit area of 9 m^2.

B.2.3.1 Unseeded Flows

The first series of runs was made for the N_2:O_2=78:22 air for the plenum temperatures T_0=3,000-6,000 K and plenum pressures P_0=10-1,000 atm. The MHD channel length was L=30 cm, with the entrance cross-section area F_1=8 cm^2, and the area ratio F_2/F_1=2 (geometry similar to the MHD channel used in References 41 and 42. In all calculated cases, the Mach number at the MHD channel entrance was M=2, and the channel entrance pressure was approximately 10% of the plenum pressure (1, 10, and 100 atm, respectively). Constant loading parameter $K=E_y/uB_z$=2 was assumed. Ionization in the MHD channel was sustained by a relativistic e-beam. The e-beam loading per molecule D was in the range 0.0-1.0 keV/mol/s and was assumed to be constant.

Figures B.2- 5 and B.2- 6 summarize the obtained results. Figures B.2- 5 shows the total enthalpy of the flow, H, as a function of the flow entropy, S, for the beam load D=1.0 keV/mol/s. The exceptions are Runs #6 and #3 for which the beam load was taken to be D=0.3 and 0.1 keV/mol/s, respectively, to avoid thermal instability. One can see that the total enthalpy increase is very small unless the plenum pressure is low. Note that all runs with D=0 did not show any enthalpy increase since the thermal ionization of air at these plenum temperatures is too small. Figure B.2- 6 gives the ratio of the total enthalpy increase, ΔH, to the initial enthalpy, H_0, and also the ratio of the absorbed e-beam power to the enthalpy increase $\Delta E_{beam}/\Delta H$ (beam efficiency) for T_0=3,000 K. As one can see, only for the plenum pressure of P_0=10 atm (channel pressure $\leq$ 1 atm), does the nonequilibrium ionization sustained by the e-beam provide substantial flow power increase at reasonable efficiency ($\Delta H/H_0$=0.5-2 and $\Delta E_{beam}/\Delta H$=0.03-0.05). At higher plenum pressures, the power increase does not exceed 10-20% of the initial flow power ($\Delta H/H_0<0.2$), and it is mainly due to the e-beam stimulated gas heating in recombination processes ($\Delta E_{beam}/\Delta H$=0.6-1.0). The reason is that at the high number densities, the recombination and electron attachment rates are so fast that the ionization fraction sustained by the beam in the MHD channel becomes far too low to produce a noticeable Lorentz force. For example, for the same beam load of 0.3 keV/mol/s, the ionization fraction in the channel is ~10^{-5} at the channel pressure of 1 atm, ~10^{-6} at 10 atm, and ~10^{-7} at 100 atm. Since the total power addition in the full-scale high-pressure

wind tunnel facility has to be $\Delta H \sim 1$ GW and at the high channel pressure conditions, $\Delta E_{beam}/\Delta H \sim 1$, this would require the use of about a 1-GW e-beam (in a very inefficient way). Let us emphasize that the low efficiency of this method at high pressures is primarily due to the high rate of electron loss (recombination and attachment), which is independent of the particular method of nonequilibrium ionization. Since the high-energy e-beam is one of the most efficient ionization sources available (see Section B.2.2.2), the use of any other method of external ionization in the high-pressure MHD channels (P>1 atm) is also not feasible.

The only conceivable way of efficient use of e-beams (or any other ionization source) in high plenum pressure flows appears to be expanding the flow down to the low pressures prior to creating nonequilibrium ionization. We considered the feasibility of this mode of operation in the second series of calculations made for T_0=3,000-6,000 K, P_0= 1,000 atm, and the beam load D=1 keV/mol/s. The MHD channel length was again L=30 cm, with the entrance cross-section area F_1=170 cm^2, the area ratio F_2/F_1=2.35 and K=2=const. The channel entrance Mach number now was M=5, and the channel pressure was approximately 1 atm. The results shown in Figure B.2- 7 demonstrate a considerable total enthalpy rise (up to 70%) and reasonable beam efficiency (5-10%) for the high plenum and channel temperatures. Higher temperature in the channel leads to (a) partial compensation of electron attachment by thermal detachment from the negative ions, and (b) slower recombination rates at the lower number density.

It is easy to see that the slope of the H(S) curves on the Mollier charts (Figs. B.2- 4 and B.2- 6) is

$$\tan\theta = \frac{dH}{dS} = \frac{dQ_{total}}{dQ_{thermal}}T = \frac{j \cdot E}{j \cdot E - u \cdot (j \times B)}T = \frac{\sigma K(K-1)u^2 B_z^2}{\sigma(K-1)^2 u^2 B_z^2}T = \frac{K}{K-1}T \qquad \text{(B.2- 40)}$$

the steepest slope dH/dS corresponding to the highest value of T_{avg}. Reducing the loading parameter would not increase tan (Θ) since it would reduce the total power added to the flow proportional to K (K-1) [see Equation (B.2- 40)] and inhibit the Joule heating, which would result in further reduction of T_{avg}.

The third series of calculations for the full-scale accelerator was made for T_0=5,000 K, P_0= 1,000 atm, mass flow rate G=17.4 kg/s, and beam loads 0.0-2.0 keV/mol/s. The MHD channel length now was L=140 cm, with the entrance cross-section area F_1=200 cm^2, and the area ratio F_2/F_1=1.65 (channel entrance Mach number M=5, channel pressure P=1-2 atm). To prevent the large-scale thermal instability (see Section B.2.3.3) leading to excessive gas heating in the channel and increasing chemical dissociation, the loading parameter at high temperatures was reduced:

$$\begin{aligned} &K = 1.5, T < 2{,}500K \\ &K = 1.0 + 0.5 \cdot (T/2{,}500), T \geq 2{,}500K \end{aligned} \qquad \text{(B.2- 41)}$$

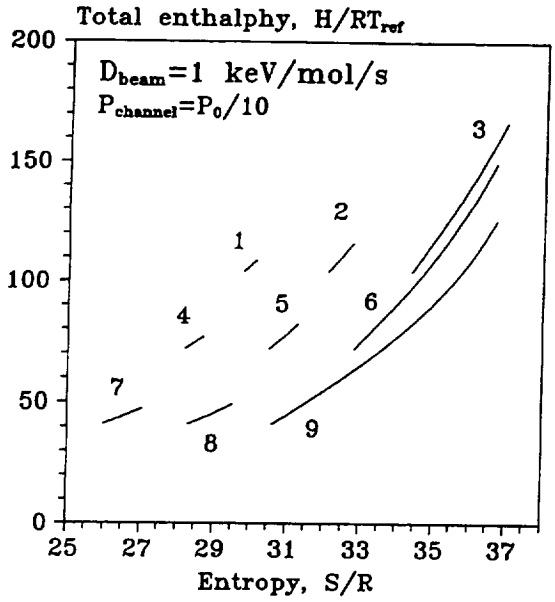

1- T_0=6000 K, P_0=1000 atm;
2- T_0=6000 K, P_0=100 atm;
3- T_0=6000 K, P_0=10 atm;
4- T_0=4,500 K, P_0=1,000 atm;
5- T_0=4,500 K, P_0=100 atm;
6- T_0=4,500 K, P_0=10 atm, D_{beam}=0.3;
7- T_0=3,000 K, P_0=1,000 atm;
8- T_0=3,000 K, P_0=100 atm;
9- T_0=3,000 K, P_0=10 atm, D_{beam}=0.

Figure B.2- 5. Total enthalpy vs. entropy diagram for the MHD-augmented unseeded air flows, ionized by a high-energy e-beam (D_{beam}=1 keV/mol/s):

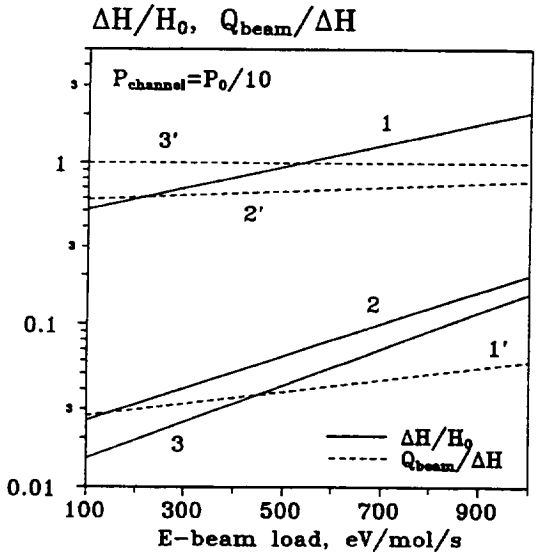

Figure B.2- 6. Total enthalpy increase $\Delta H/H_0$ and beam efficiency $\Delta E_{beam}/\Delta H$ for the MHD-augmented unseeded air flows at T_0=3,000 K: 1,1'- P_0=10 atm, 2,2'- P_0=100 atm, 3,3'- P_0=1,000 atm.

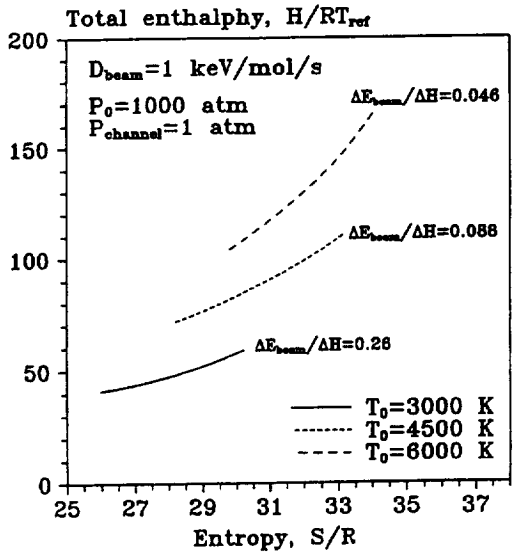

Figure B.2- 7. Total enthalpy vs. entropy diagram for the high plenum pressure (P_0=1,000 atm) MHD-augmented unseeded airflows, ionized by a high-energy e-beam (D_{beam}=1 keV/mol/s). The flow is expanded to P~1 atm before entering the MHD channel.

The results of calculations are shown in Figures B.2- 8 through B.2- 11. Figure B.2- 8 presents the obtained H(S) curves, plotted together with the target values for transatmospheric vehicle (TAV) trajectory ("flight envelope"). One can see that although the total enthalpy of the flow increases 1.5-2.5 times, the flow entropy is considerably larger than the target values. The main reason for that, as discussed above, is the low MHD channel entrance temperature [see Figure B.2- 9 and Equation (B.2- 40)]. Therefore, while the calculated Mach numbers in the MHD-augmented flow are close to the target values and conditions, the flow pressure is more than an order of magnitude lower than the pressure behind the bowshock (see Table B.2- 1).

Table B.2- 1. Unseeded air MHD accelerator performance.

Left and central sub-columns-target values for P_{dyn}=2,000 and 1,000 lbf/ft^2, respectively, right subcolumn – present calculations.

Case	H, MJ/kg			S/R			U, km/s			M		
1	7.2	7.0	6.9	27.9	28.6	28.9	3.76	3.64	3.60	9.4	9.0	8.9
2	11.6	11.0	11.4	28.7	29.3	32.1	4.78	4.58	4.60	10.9	10.4	10.4
3	13.6	14.6	14.5	29.0	29.9	33.5	5.16	5.31	5.15	11.4	11.3	10.9
4	15.8	16.9	17.2	29.3	30.2	34.8	5.58	5.71	5.49	11.8	11.8	10.9

Case	P,mbar			y_O,%	y_{NO},%	$T_V(N_2)$	D_{beam}, keV/mol/s	ΔE_{beam}, MW	ΔH, MW
1	41.1	21.4	12.8	0.4	7.0	1,574	0.0	0.0	0
2	35.7	18.5	2.0	1.5	6.2	2,776	0.3	6.5	77
3	34.4	17.2	1.3	5.6	6.2	2,857	1.0	21	130
4	33.1	16.1	1.3	14.7	6.2	2,455	2.0	41	176

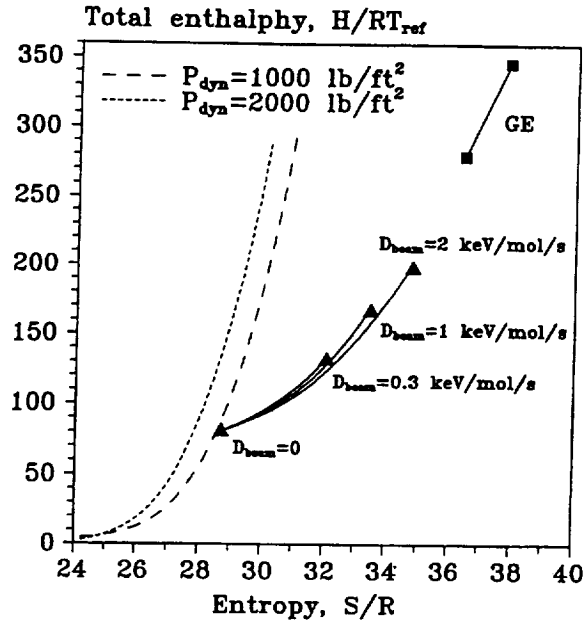

Figure B.2- 8. Total enthalpy vs. entropy diagram for the full-scale unseeded air MHD accelerator with external ionization by an e-beam. P_0=1,000 atm, T_0=5,000 K, L=140 cm, F_2/F_1=1.65. Dashed lines - TAV flight envelope. Also shown H(S) for the GE reflected shock unseeded air accelerator.

Note that raising the beam load increases recombination losses (the ratio $\Delta E_{beam}/\Delta H$, see Table B.2- 1). In particular, this makes greater the average loading parameter, K_{avg}, defined as the ratio of the total power going into internal degrees of freedom to the total power into kinetic energy. For this reason, the slope dH/dS actually decreases with the beam load despite the fact the T_{avg} becomes higher (see Figures B.2- 8 and B.2- 9).

The calculated transverse current density in the channel did not exceed j_y=10 A/cm^2. Both Joule heating and e-beam electron impact induce chemical reactions in the channel, such as dissociation of O_2, which raises the O atom fraction in the test section (see Figure B.2- 10). Note that at the same time the exit NO concentration changes very weakly (see Figure B.2- 10, Table B.2- 1). This type of behavior simply reflects the dependence of equilibrium concentration of these species on temperature at P≅1 atm at the channel exit that was verified by comparing the results with the equilibrium chemical composition data. Higher-than-equilibrium O and NO exit fractions at D_{beam}=0 (see Table B.2- 1) are due to their considerable initial concentrations in high temperature plenum. Figure B.2- 11 also shows that the flow becomes close to the vibrational equilibrium toward the end of the channel. However, one can see from Table B.2- 1 and Figures B.2- 10 and B.2- 11, the flow in the test section is far from being at equilibrium, both molecular vibrations and chemical composition being frozen in the rapid expansion that occurs at low

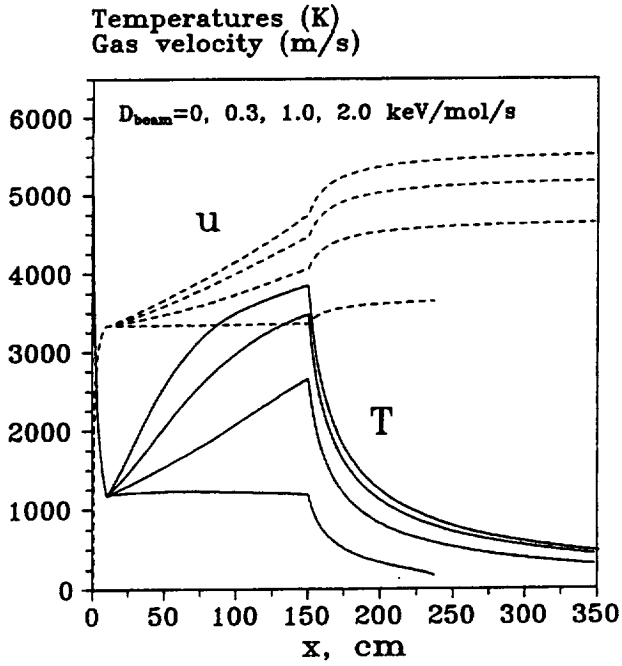

Figure B.2- 9. Axial temperature and velocity profiles for the accelerator of Fig. B.2- 8 for different beam loads.

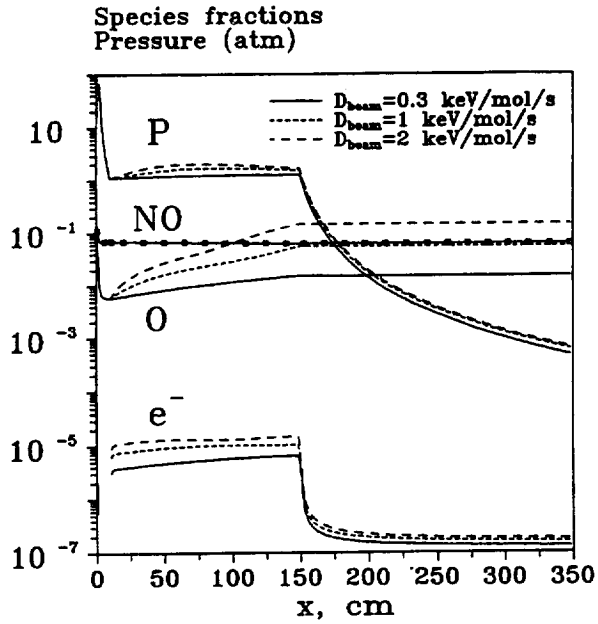

Figure B.2- 10. Axial profiles of pressure and species mole fractions for the accelerator of Fig. B.2- 8 for different beam loads.

pressure and temperature. This effect can be somewhat reduced a) if the energy is added at the high pressure (which in this case is not feasible) so the relaxation in the secondary expansion becomes faster or b) slower expansion is used.

Finally, Table B.2- 1 shows that one would need a tens of MW ionization source to operate the full-scale facility at the channel pressure of about 1 atm. The beam efficiency can be improved by further reducing the channel pressure; however, this would lead to an even greater flow entropy rise because of the lower channel entrance temperature, according to Equation (B.2- 40). The e-beam load, D, can be simply related to the beam current density, j_{beam}, and the energy of the beam electrons, ε_{beam}, that determines the penetration length:

$$l \approx 0.5 \cdot \frac{(\varepsilon_{beam}/300)^{1.35}}{(\rho/1.2)} \qquad \text{(B.2- 42)}$$

where l is in m, ε_{beam} is in keV, and ρ is in kg/m^3 (Ref. 21). For the conditions of Table B.2- 1, keeping in mind that $l \cong 2r \cong 0.2$ m and the absorbed beam power $\Delta E_{beam} = eDN \times (Ll^2) \cong j_{beam}\, \varepsilon_{beam} \times (Ll)$, one has $\varepsilon_{beam} \sim 30$ keV and for D=1 keV/mol/s:

$$j_{beam} \cong \frac{eDNl}{\varepsilon_{beam}} \cong 0.3 A/cm^2 \qquad \text{(B.2- 43)}$$

B.2.3.2 Seeded Flows

The first series of runs was made for K-seeded (at 1%) air for the plenum temperatures T_0=3,000-6,000 K and pressures P_0=10-1,000 atm. The MHD channel length was L=30 cm, with the entrance cross-section area F_1=8 cm^2, and the area ratio F_2/F_1=2-25. Again, in all calculated cases, the channel entrance Mach number was M=2, and the channel entrance pressure was about 10% of the plenum pressure. Some of the results are shown in Figure B.2- 12. All runs for T_0=3,000 K did not show any flow acceleration due to MHD augmentation since the thermal electric conductivity of the mixture was too low (see Figure B.2- 12). Calculations for T_0=4,500 K demonstrated noticeable total enthalpy rise, ΔH, only for the plenum pressures of P_0=100 atm and lower (see Figure B.2- 12). One can see that ΔH also increases with the channel area ratio that results in the lower channel pressure. This is understandable since the term describing the flow acceleration in the motion equation is inversely proportional to the gas density [see Equations (B.2- 1) and (B.2- 2)]:

$$\frac{du}{dt} \sim \frac{j_y B_z}{\rho} \sim \frac{\sigma(T) u B_z^2 (K-1)}{\rho} \qquad \text{(B.2- 44)}$$

where $\sigma(T)$ is proportional to the ionization fraction $\phi_e=n_e/N$ [see Equations (B.2- 32) and (B.2- 34)]. Thus, to produce the same acceleration at the higher pressure, higher ionization fraction (and therefore higher plenum temperature) is needed. Finally, substantial acceleration for P_0=1,000 atm was obtained only at the highest plenum temperature considered, (T_0=6,000 K), also for the large area ratio F_2/F_1=9-25 (see Figure B.2- 12). One can see that the seeded MHD accelerator for the wind tunnel, which requires plenum pressures of the order of 1,000 atm (see Table B.2- 1) should also operate at high plenum temperatures of T_0~6,000 K. This limit can be somewhat lowered if a seed with lower ionization potential, (e.g. Cs) is used. Large operating area ratios F_2/F_1~25 are also preferable.

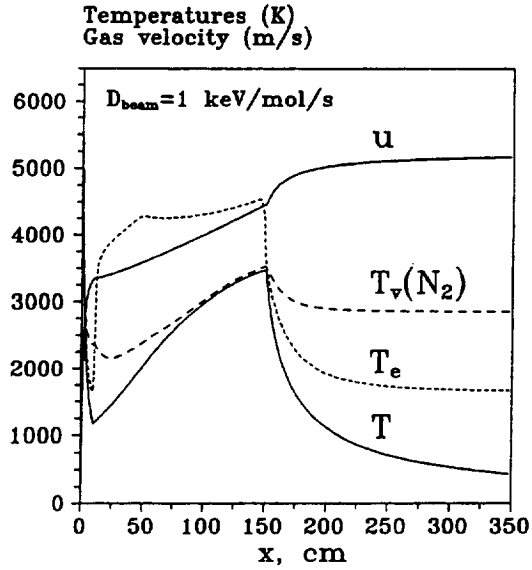

Figure B.2- 11. Axial profiles of the translational temperature, vibrational temperature of N_2, and electron temperature for the accelerator of Fig. B.2- 8 for D_{beam}=1 keV/mol/s.

The second series of runs was carried out for the full-scale Cs-seeded (at 0.5%) air accelerator for plenum conditions T_0=5,000 K and P_0= 1,000 atm (mass flow rate G=17.4 kg/s). The MHD channel length was L=140 cm with the entrance cross-section area F_1=8 cm^2, and the area ratio F_2/F_1=36 (channel entrance Mach number M=2, entrance pressure P=120 atm). The loading parameter was again limited to prevent the developing of the thermal instability (see Section B.2.3.3) and the current density becoming too high:

$$K = 1.0 + \frac{j_{y\max}}{\sigma u B_z} \qquad \text{(B.2- 45)}$$

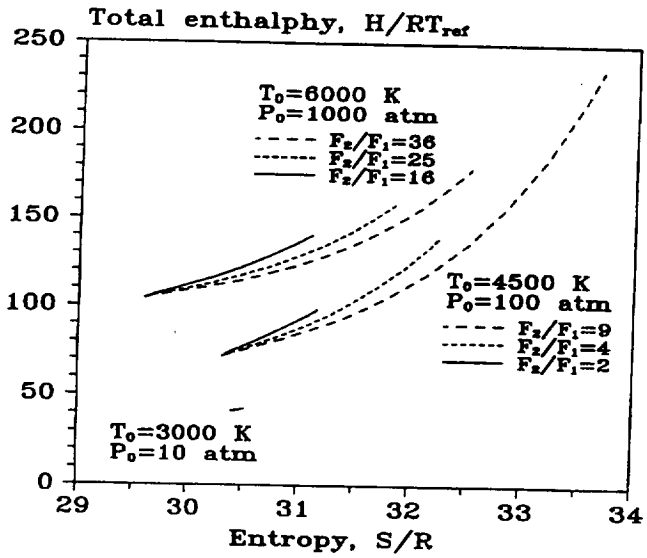

Figure B.2- 12. Total enthalpy vs. entropy diagram for the MHD-augmented K-seeded (at 1%) air flows.

The calculated H(S) curves are shown in Figure B.2- 13 for different values of j_{ymax}, plotted together with the target TAV trajectory data. One can see that at these conditions the total enthalpy can be increased up to 5 times if the maximum current density does not exceed j_{ymax}=100 A/cm^2, while the flow entropy rise is considerably less than for the unseeded flows discussed in Section B.2.3.1 (see Figure B.2- 8). Although the flow entropy is still somewhat greater than the target value (see Figure B.2- 13), the seeded accelerator performance is clearly much better. NO and O fractions in the test section are much less than in the unseeded accelerator at comparable total enthalpy (Table B.2- 1, Table B.2- 2). Also, the calculated flow pressure is now only 1.5-4 times less than the pressure behind the bowshock (see Table B.2- 2).

Table B.2- 2. Cs-seeded air MHD accelerator performance.

Left and central subcolumns – target values for p_{dyn}=2,000 and 1,000 lbf/ft^2, respectively, right subcolumn – present calculations.

Case	H, MJ/kg			S/R			u,km/s			M		
1	7.2	7.0	6.7	27.9	28.6	28.3	3.76	3.64	3.53	9.4	9.0	9.1
2	13.6	14.6	14.1	29.0	29.9	30.8	5.16	5.31	5.14	11.4	11.3	11.5
3	18.4	19.4	19.7	29.6	30.4	31.4	6.02	6.14	6.07	12.3	12.2	12.3
4	24.8	25.7	25.2	30.2	31.0	31.9	6.99	7.07	6.88	13.1	13.0	13.1
5	33.2	33.8	33.9	30.9	31.6	32.5	8.08	8.12	7.98	13.9	13.8	13.7

Case	P, mbar			y_{cs},%	y_o,%	y_{NO},%	$T_v(N_2)$	J_{ymax},A/cm^2
1	41.1	21.4	14.5	0.5	0.01	4.5	1,992	0
2	34.4	17.2	3.9	0.5	0.6	4.3	2,630	30
3	32.1	16.1	5.4	0.5	1.6	4.1	2,829	50
4	30.4	15.3	6.3	0.5	2.9	4.2	2,944	70
5	29.1	14.7	9.6	0.5	5.1	4.9	3,078	100

The latter result is in agreement with the criterion of Equation (B.2- 40). First, the average channel temperature in the seeded MHD accelerator is generally higher than in the e-beam controlled channel, even though it is being controlled to reduce chemical dissociation (see Figures B.2- 8 and B.2- 15). Second, the average loading parameter in these runs is considerably lower ($K_{avg}\cong$1.1-1.3 vs. $K_{avg}\cong$1.6-1.8 for the unseeded runs); therefore, the greater part of the input power goes directly into the flow kinetic energy and does not contribute to the entropy rise. One can see from Figure B.2- 14 that the efficiency of the first half of the channel is less than that of the second (du/dx is lower) due to the higher gas density near the channel entrance [see Equation (B.2- 44)]. The flow in the channel is very close to the thermochemical equilibrium, (e.g., see Figure B.2- 16), which is also confirmed by the equilibrium chemical composition calculations. However, freezing of molecular vibrations (despite the fast V-T relaxation of N_2 on Cs and O_2 atoms) and of chemical composition of the mixture in the test area is still well pronounced (see Figures B.2- 15 and B.2- 16).

The boundary layer growth in the channel is quite significant. The estimate of Equation (B.2- 38) gives $\delta/r\sim0.25$ at $x/L=1$ ($Re_x=10^7$). The calculated heat transfer losses, although quite large, did not exceed 15% of the initial flow power. However, the calculated local wall heat fluxes in the channel reach 10-20kW/cm^2 for j_{ymax}=100 A/cm^2, which may severely limit the operation time.

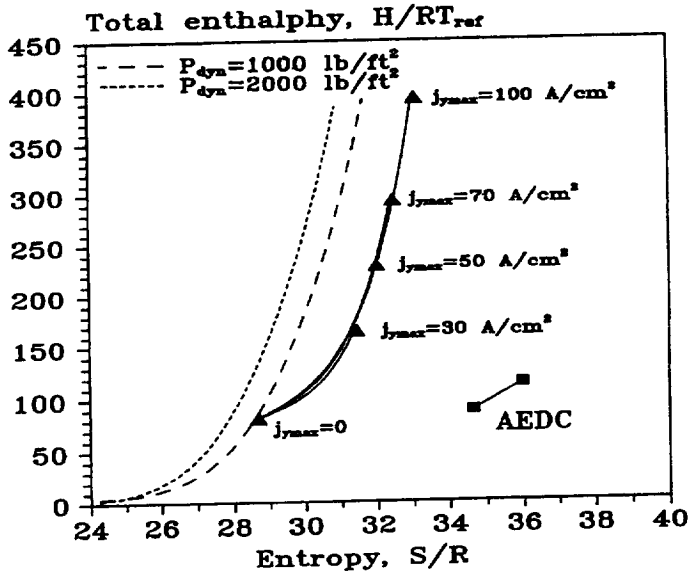

Figure B.2- 13. Total enthalpy vs. entropy diagram for the full-scale Cs-seeded (at 0.5%) air MHD. P_0=1,000 atm, T_0=5,000 K, L=140 cm, F_2/F_1=1.65. Dashed lines - TAV flight envelope. Also shown H(S) for the AEDC K-seeded (at 1.5%) accelerator.

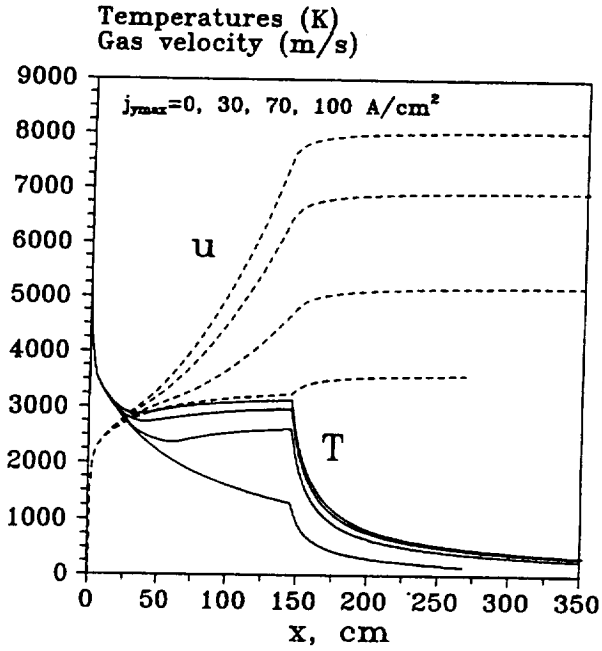

Figure B.2- 14. Axial temperature and velocity profiles for the accelerator of Fig. B.2- 13 for different maximum current densities.

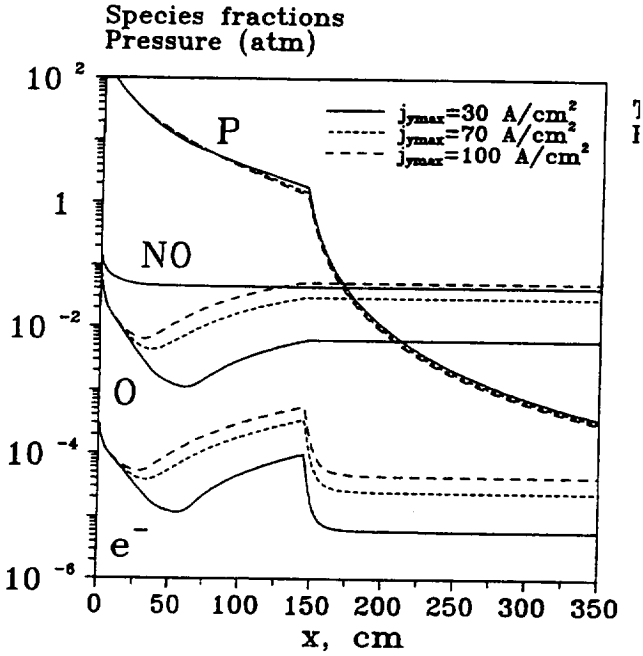

Figure B.2- 15. Axial profiles of pressure and species mole fractions for the accelerator of Fig. B.2- 13 for different maximum current densities.

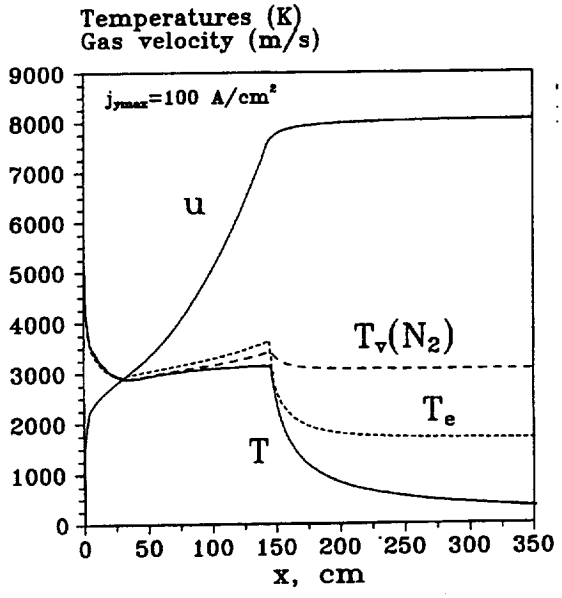

Figure B.2- 16. Axial profiles of the translational temperature, vibrational temperature of N_2, and electron temperature for the accelerator of Fig. B.2- 13 for j_{ymax}=100 A/cm².

B.2.3.3 Flow Stability

Calculated effective reduced electric field values [see Equation (B.2- 39)] are quite low for all calculated regimes, typically $(E/N)_{eff} \leq 0.5\times10^{-16}$ V×cm² for unseeded flows and $(E/N)_{eff} \leq 1.0\times10^{-17}$ V×cm² for the alkali-seeded flows. Analysis of the results shows that in both cases nonequilibrium ionization by the slow plasma electrons is negligibly small. For this reason, thermal instability (Ref. 37) and breakdown due to the field-stimulated nonequilibrium ionization in the core flow are extremely unlikely. However, thermal instability due to the Joule heating might still develop. Using the linear stability analysis (Ref. 37), one can obtain expression for the large-scale instability increment:

$$\Omega = \frac{K-1}{K}\frac{\gamma-1}{\gamma}\frac{j_y E_y}{P}\left(\frac{\delta \ln n_e}{\delta \ln T}+\frac{1}{2}\right)-\frac{2u}{L} \qquad \text{(B.2- 46)}$$

The last term in Equation (B.2- 46) is the reciprocal characteristic time of gas cooling. In high-pressure flows where the convective cooling is dominant, it is simply proportional to the channel residence time L/u. Combining Equation (B.2- 46) with the expression for the quasi-steady-state electron density:

$$S_{beam} = k_{rec} n_e^2 + k_{att} n_e N^2 \qquad \text{(B.2- 47)}$$

for the e-beam-sustained discharge (note that S_{beam} (1/cm^3/s)~N and k_{rec}~$T^{-0.5}$); or with the Saha equation:

$$n_e = const \cdot n_{seed}^{1/2} \cdot T^{3/4} \exp\left(-E_{ion}/2T\right) \qquad \text{(B.2- 48)}$$

for the thermal ionization, one obtains the thresholds of the large-scale thermal instability. For the MHD channel with external ionization by an e-beam one has:

$$j_y \le a \frac{K}{K-1} \frac{\gamma}{\gamma-1} \frac{P}{E_y} \frac{u}{L} \qquad \text{(B.2- 49)}$$

where a=8 and a=4/3 for the recombination and attachment controlled discharges, respectively. The first regime is realized only at high ionization fractions ϕ_e~10^{-4} and higher, when $k_{rec}n_e >> k_{att}N^2$ in Equation (B.2- 47) (in air, k_{rec}~10^{-8} cm^3/s, k_{att}~10^{-30} cm^6/s^2), or high temperatures T≥3,000 K when thermal detachment from the negative ions compensate electron attachment. For the channel with equilibrium ionization one has:

$$j_y \le \frac{1}{\frac{3}{8} + \frac{E_{ion}}{4T}} \frac{K}{K-1} \frac{\gamma}{\gamma-1} \frac{P}{E_y} \frac{u}{L} \qquad \text{(B.2- 50)}$$

The equilibrium flow is less stable than the flow controlled by the external ionization: for E_{ion}/T~10-15, typical for the seeded MHD flows, one has $(3/8+E_{ion}/4T)^{-1}$≅0.2-0.4. The criteria of Equations (B.2- 49) and (B.2- 50) applied to the full-scale accelerators simulated in Sections 3.1 (K≅1.6-1.8) and 3.2 (K≅1.1-1.3), predict stable flow at j_y≤8-10 A/cm^2 and j_y≤40-100 A/cm^2, respectively, depending on the loading parameter K. One can see that in both cases the channels operate on the verge of stability that was actually observed in the calculations. This was the primary reason for the limiting of the loading parameter for both accelerators [see Equations (B.2- 41) and (B.2- 45)]. The criteria (Refs. 49, 50) used for the estimate of the flow stability in experimental MHD accelerators (Refs. 39, 41) predict stable core flow at j_y≤120 A/cm^2 for the unseeded GE accelerator and at j_y≤15 A/cm^2 for the K-seeded AEDC accelerator. In these experiments, where the stable core flow was indeed observed, the current densities did not exceed 20 A/cm^2 and 15 A/cm^2, respectively.

Note that this 1-D core flow stability analysis cannot be applied to the boundary layer, and it also does not account for the spoke instability that occurs in the nonuniform flows with large Hall parameters (Ref. 43).

The possibility of arcing in the boundary layer appears to be very high for two reasons. First, electric field in the sheath regions near the electrodes is much higher than in the core flow due to

the voltage drop across the sheath (Ref. 37), which leads to the electron heating by the field and may result in a breakdown and arc formation between the adjacent electrodes. Second, core flow Faraday mode conditions $E_x=\beta(E_y-uB_z)$, $j_x=0$, assumed in these calculations, will no longer hold in the boundary layer, which would result in the Hall current, j_x, flowing between the adjacent electrodes. This current can be very large because of the high recovery temperature in the boundary layer and high scalar electric conductivity σ (in fact, the seed could be completely ionized). Both these effects would short-circuit the segmented electrodes along each wall; therefore, in the worst possible case in which the accelerator would run in a continuous electrode mode $E_x=0$, $\sigma_{eff}=\sigma/(1+\beta^2)$ (see Equation 31). The effective electric conductivity in the full-scale accelerator calculations, where $\beta_{max}\sim$5-10, would therefore be reduced by 1-2 orders of magnitude, making the accelerator performance much worse. These simple arguments are consistent with the experimental observations made on the GE unseeded MHD accelerator (Ref. 41) where the diffuse discharge in the core flow and arcing between each pair of electrodes on the same wall was observed in the high-pressure MHD channel at P=10-30 atm and $(E/N)_{eff}$ $\sim 10^{-17}$ V×cm^2. Severe electrode erosion due to arcing was also found.

The spoke instability results from increasingly small flow nonuniformities at the higher values of the Hall parameter, β, (the threshold nonuniformity scale is $\Delta\sigma/\sigma\sim 1/\beta^2$), for example near the segmented electrodes. It can be analyzed using a 2-D linear stability model that must incorporate electric field perturbations and Maxwell equations (Ref. 43).

The quasi-1-D approach used in the present study, where the electric and magnetic field axial profiles are assumed given (see Section B.2.2.1), does not allow determining whether these distributions are consistent with the boundary layer effects or whether they can be operated at the stable conditions. At the same time, we believe these issues are of utmost importance for MHD channel performance. A time-dependent 2-D model, where the coupled flow equations, chemical kinetics equations, Maxwell equations for the fields distributions, and Boltzmann equation are solved, is required to address this problem, which is beyond the scope of this study.

B.2.3.4 Comparison with the Thermal Energy Addition Methods

If all the energy added to the flow goes into internal degrees of freedom by pure heating, Equation (B.2- 40) simplifies:

$$\tan\theta = \frac{dH}{dS} = T \qquad \text{(B.2- 51)}$$

We estimate the average energy addition temperature for this pure heating, assuming the initial and the final flow conditions are the same as in Case #5 of Table B.2- 2 (ΔH=27.2 MJ/kg, ΔS=1.18 kJ/kg/K, see Table B.2- 2). Equation (B.2- 51) gives $T_{avg}\cong$23,000 K, while the average temperature for the MHD energy addition process is just about 3,000 K (see Figure B.2- 14).

This remarkable difference is due to the fact that most of the field power in the MHD channel goes directly into the flow kinetic energy ($K_{avg}\cong 1.2$ for Case #5). Let us also estimate T_{avg} for pure heating from plenum conditions T_0=2,000 K and P_0=10,000 atm to the conditions of Case #5, assuming that caloric equation of state (Refs. 30, 31) is still valid at these pressures. One obtains ΔH=31.9 MJ/kg and ΔS=3.15 kJ/kg/K, giving $T_{avg}\cong$10,000 K ($T_{ond}\cong$8,000 K for T_0=1,000 K). For the more modest conditions of Case #2, $T_{avg}\cong$4,500 and 3,800 K and for T_0=2,000 and 1,000 K, respectively. Note the gas temperature prior to energy addition is considerably lower than T_{avg}. This means that any attempt of reaching the test section Mach number higher than M~11-12 by means of thermal energy addition to the high-pressure air flow would require heating the gas to prohibitively high temperatures, thereby inducing considerable chemical contamination of the flow.

B.2.4 Summary

The results of the modeling calculations based on the quasi-1-D kinetic model described and validated in Section B.2.2 allow making the following conclusions:

1. The use of high-energy e-beams (or any other external ionization source) to sustain nonequilibrium ionization in high-pressure MHD channels is not feasible due to the fast electron loss in recombination and attachment processes. In the high plenum pressure (P_0~1000 atm) flows, e-beams can be efficiently applied to create nonequilibrium ionization only after the flow is expanded to the low pressures P≤1 atm.
2. In the latter mode of operation, nonequilibrium ionization sustained by an e-beam allows considerable increase of the total enthalpy of the flow (1.5-2.5 times, M~11 in the test section) due to MHD augmentation. However, in this case the static pressures in the test section are more than an order of magnitude lower than required by the TAV flight envelope.
3. The test section flow quality is rather poor and gets steadily worse with the increase of the total enthalpy due to both e-beam-initiated dissociation and thermal chemical reactions.
4. The high plenum pressure (P_0~1,000 atm) alkali-seeded flows, which also require high plenum temperatures ($T_0\geq$5,000-6,000 K), look more promising for the wind tunnel application. Calculations for Cs-seeded flows predict up to 5 times total enthalpy increase (test section Mach number M~14). Predicted test section static pressures are also closer to the reference values (although they are still 1.5-4 times lower). The calculated O_2 atom and NO concentrations in the test section are considerably lower than for the unseeded flows.
5. These predicted test section flow parameters can be obtained in a flow stable with respect to large-scale thermal instability.

6. Simple thermodynamic analysis shows the advantage of adding energy to the flow by means of a body force over the purely thermal energy addition.

A 2-D time-dependent kinetic model including Maxwell equations is necessary to study the sheath and boundary layer effects as well as to get a better insight into the flow stability.

B.2.5 References

1. Simmons, G.; Nelson, G.L.; Hiers, R; and Western, A., "An Unseeded Air MHD Accelerator Concept for High Mach Number Hypersonic Propulsion," AIAA Paper 89-2535, 25th Joint Propulsion Conference, Monterey, CA, July 1989.

2. Nelson, G.L. and Simmons, G., "Augmentation of Hypersonic Propulsion facilities Using MHD," AIAA Paper 95-1937, 26th Plasmadynamics and Lasers Conference, San Diego, CA, June 1995.

3. Simmons, G.A.; Nelson, G.L.; and Lee, Y.M. Lee, "Feasibility Study of a Nonequilibrium MHD Accelerator Concept for Hypersonic Propulsion Ground Testing," AIAA Paper 95-2720, 31st Joint Propulsion Conference and Exhibit, San Diego, CA, July 1995.

4. Lineberry, J. and Chapman, J., "MHD Accelerators for Hypersonic Applications," AIAA Paper 91-0384, 29th AIAA Aerospace Sciences Meeting, Reno, NV, Jan. 1995.

5. Crawford, R.A.; Chapman, J.N.; and Rhodes, R.P., "Potential Application of Magnetohydrodynamic Acceleration for Hypersonic Environment Testing," Report AEDC-TR-90-6, Aug. 1990.

6. Simmons, G.A.; Nelson, G.L.; and Lee, Y.M., "Analysis of an Unseeded, Nonequilibrium MHD Accelerator Concept for Hypersonic Propulsion Ground Testing Applications," AIAA Paper 92-3994, 17th AIAA Aerospace Ground Testing Conference, Nashville, TN, July 1992.

7. Clark, J.F. and McChesney, *Dynamics of Real Gases*, London, Boston, Butterworths, 1976.

8. Sutton, G.W. and Sherman, A., *Engineering Magnetohydrodynamics*, New York, McGraw-Hill, 1965.

9. Gordiets, B.F. and Zhdanok, S., *Analytical Theory of Vibrational Kinetics of Anharmonic Oscillators, Nonequilibrium Vibrational Kinetics*, Capitelli, M. (ed.), M. Berlin, Springer, 1986, pp. 47-83.

10. Huxley, L.G.H. and Crompton, R.W., *The Diffusion and Drift of Electrons in Gases*, New York, Wiley, 1974.

11. Dyatko, N.A.; Kochetov, I.V.; and Napartovich, A.P., *J. Phys. D.: Appl. Phys.*, Vol. 26, 1993, p. 418.

12. Suhre, D.R. and Verdeyen, J.T., *J. Appl. Phys.*, Vol. 47, 1976, p. 4484.

13. Konovalov, V.P. and Son, E.E., *Sov. Physics: Technical Physics*, Vol. 50, 1980, p. 300.

14. Aleksandrov, N.L.; Konchakov, A.M.; and Son, E.E., *Sov. J. Plasma Phys.*, Vol. 4, 1978, p. 663.

15. Aleksandrov, N.L.; Konchakov, A.M.; and Son, E.E., *Sov. Physics: Technical Physics*, Vol. 49, 1979, p.1200.

16. http://www.netlib.org/odepack/index.html.

17. Krivonosova, O.E.; Losev, S.A.; Nalivaiko, V.P.; Mukoseev, Yu.K.; and Shatalov, O.P., "Recommended Data on Rates of Chemical Reactions Between Molecules Consisting of N and O Atoms," *Khimiya Plazmy (Plasma Chemistry)*, Smirnov, B.M. (ed.), Vol. 14, Moscow, Nauka, 1987, pp. 3-31.

18. Macheret, S.O.; Fridman, A.A.; and Elkin, A.A., *Sov. Chem. Phys.*, Vol. 9, 1990, p. 174.

19. Macheret, S.O. and Rich, J.W., *Chem. Phys.*, Vol. 174, 1993, p. 25.

20. Treanor, C.E.; Adamovich, I.V.; Williams, M.J.; and Rich, J.W., *Thermophys. Heat Trans.*, Vol. 10, 1996, p. 193.

21. Matzing, H., "Chemical Kinetics of Flue Gas Cleaning by Irradiation with Electrons," *Adv. in Chem. Phys.*, Vol. 80, pp. 315-403.

22. Cool, T.A. and Zukoski, E.E., *Phys. Fluids*, Vol.9, 1966, p. 780.

23. Ashton, A.F. and Heyhurst, A.N., *Combustion and Flame*, Vol. 21, 1973, p. 69.

24. Olson, R.E., *J. Chem. Phys.*, Vol. 56, 1972, p. 2979.

25. Torr, D.G., "The Photochemistry of Upper Atmosphere," *The Photochemistry of Atmospheres*, J.S. Levine (ed.), New York, Academic Press, Chap.5, 1985.

26. Itikawa, Y.; Hayashi, M.; Ichimura, A. et al., *J. Phys. Chem. Ref. Data*, Vol. 16, p. 985, 1986.

27. Itikawa, Y.; Hayashi, M.; Ichimura, A. et al., *J. Phys. Chem. Ref. Data*, Vol.18, p. 23, 1989.

28. Mojarrabi, B.; Gulley, R.J.; Middleton, A.G. et al., *J. Phys. B: At. Mol. Opt. Physics*, Vol. 28, p. 487 and references therein, 1995.

29. Lennon, M.A.; Bell, K.L.; Gilbody, H.B. et al., *J. Phys. Chem. Ref. Data*, Vol.17, 1988, p. 1988.

30. Glushko, V.P., (ed.), *Thermodynamic Properties of Individual Substances*, Moscow, Nauka, 1976.

31. "JANAF Thermochemical Tables," J. *Phys. Chem. Ref. Data*, Vol. 14, Suppl.1, 1985.

32. Chen, J.C.Y., *J. Chem. Phys.*, Vol. 40, 1964, p. 3507.

33. Adamovich, I.V.; Macheret, S.O.; Rich, J.W.; and Treanor, C.E, AIAA Paper 95-2060.

34. Fisher, E. and Smith, G., *Chem. Phys. Letters*, Vol. 13, 1972, p. 448.

35. Eremin, A.V.; Kulikovsky, A.A.; and Naboko, I.M., *Chem. Phys. Letters*, Vol. 45, 1976, p. 351.

36. Perel, J.; Englander, P.; and Bederson, B., *Phys. Rev.*, Vol. 128, 1962, p.1148.

37. Raizer, Yu. P., *Gas Discharge Physics*, Berlin, Springer, Chap.14, 1991.

38. Schlichting, H., *Boundary Layer Theory*, New York, McGraw-Hill, Chap.21, 1960.

39. Rittenhouse, L.E.; Pigott, J.C.; Whoric, J.M.; and Wilson, D.R., "Theoretical and Experimental Results with a Linear Magnetohydrodynamic Accelerator Operated in the Hall Current Neutralized Mode," AEDC-TR-67-150, Nov. 1967.

40. Gallagher, J.W.; Beaty, E.C.; Dutton, J.; and Pirchford, L.C., *J. Phys.Chem. Ref. Data*, Vol. 12, 1983, p. 109.

41. Warren, W.R., Harris, C.J. et al.,"Feasibility Study of a High Density Shock Tunnel Augmented by a Magnetohydrodynamic Accelerator," AEDC-TR-65-225, Oct. 1965.

42. Haris, C.J.; Marston, C.H.; and Warren, W.R., *AIAA Journal*, Vol. 13, p. 229, 1975.

43. Rosa, R.J., *Magnetohydrodynamic Energy Conversion*, New York, McGraw-Hill, 1968.

APPENDIX B, SECTION B.3

B.3 OHIO STATE UNIVERSITY TWO-DIMENSIONAL MHD CODE

An accelerator code previously developed at OSU was modified to develop a computational tool that might be used to compare MHD shock tube experimental data taken at NASA Ames on a small diameter tube. The hardware experiments are reported in Appendix A, and the code development and comparison is reported in the following section of this appendix.

B.3.1 Overview

Reacting plasma flows occur in a wide variety of discharges. The characteristics of such discharges vary widely depending on operating conditions, geometry, and the characteristics of the gaseous medium. The experiments conducted by the NASA Ames researchers underscore the need for a simulation model that enables theoretical investigation of gaseous discharges in high-speed flows. A detailed simulation model allows the relative importance of various phenomena to be assessed for a given discharge configuration. It has the added quality of predicting parameters of interest that cannot be obtained experimentally. The research described below was conducted by the OSU computational plasma physics group and was primarily directed toward developing high-performance simulation tools to understand the physics of gaseous discharges occurring in high-speed reacting plasma flows. This research, including the code validation efforts, is further described in Sections B.3.2 through B.3.4

The OSU 2-D reacting plasma flow code has been developed over a period of several years by the computational plasma physics group at OSU. This code solves the unsteady, compressible, Navier-Stokes equations coupled with an energy equation and a set of species equations describing the chemical kinetics. The unsteady equations describing flow, chemical kinetics, and electromagnetics are solved in a fully coupled manner. This enables transient as well as steady-state solutions to be obtained for a wide variety of flows, both subsonic and supersonic. The experiments conducted at NASA Ames involve unsteady, supersonic MHD flows with considerable air plasma chemistry. The OSU code was selected for simulating the Ames experiments because it has excellent capabilities in terms of being able to capture both the high-speed gas dynamics and the chemical kinetics in time-dependent multidimensional flows. Prior to the MSE subcontract, the numerical algorithm and code had undergone several validation exercises, as explained in Section B.3.3.1 through B.3.3.3. The 2-D code developed at OSU was an ideal choice to model the complex interactions between electromagnetics, flow, and chemical reactions taking place in the shock tube experiments conducted at NASA Ames. Finally, the time-dependent capability of the code lends itself naturally to the simulation of the highly unsteady flows characteristic of impulse facilities. For these reasons, it was selected over other candidate codes as a starting point for the developmental efforts described below.

The OSU computational plasma physics group, under subcontract to MSE, conducted the research described in this section. The primary tasks defined in the subcontract are described below.

1. Generalize and extend the OSU 2-D unsteady reacting flow code to study the chemical kinetics of air and 'pseudo-air' plasmas in high-speed flows. This required the chemical rate database be upgraded to include rate data for the $N_2O + N_2$ reaction products ("simulated air") used in the NASA Ames test program.
2. Modify modules of the code to study the interaction of applied electric and magnetic fields with the charged species. This task required the modification of the Poisson solver developed earlier to accommodate the effects of an applied magnetic field as well as the tensorial constitutive relationship between current density and electric field (Generalized Ohm's Law). The derivation of the governing partial differential equation for the electric potential is given in Section B.3.2 below.
3. Modify the existing geometry to permit computations in rectangular ducts. The original code was restricted to axisymmetric geometries.
4. Upgrade the numerical algorithms. This involved the use of efficient block-tridiagonal matrix solvers for all of the high-level solution algorithms.
5. Validate the code against experimental data, especially data taken from the NASA Ames test program discussed in Section A.2.

The ultimate objectives of this work were to apply the upgraded code to simulate the NASA Ames testing scenario, to use the code as an investigative tool to aid in the interpretation of the test data, and to apply this validated code to realistic MHD accelerator problems.

As discussed in subsequent sections, Tasks 1 through 4 were fully accomplished. Task 5 was partially accomplished. A thorough analysis of the NASA Ames data was accomplished through the use of both the OSU 2-D code and the OSU 1-D nonequilibrium code described in Section B.2. However, in using the 2-D code, it was found that grid resolution and computer run time became significant problems largely due to the fact that very strong shocks were present in the NASA Ames experiments. The shock Mach numbers were as high as 10 - 12 in some cases, and the pressure ratios across the shock were as high as 350. Resolving the shock region adequately required the use of an extremely fine grid, which greatly increased the computing time. It should be noted that in its present form, the OSU code requires a uniform grid; therefore, if one refines the grid to accommodate a shock layer, the grid must be refined to the same level everywhere else.

Lack of knowledge of conditions upstream of the shock presented another source of difficulty in conducting the 2-D simulations. The computation appeared to be quite sensitive to the precise values of the input parameters (pressure, temperature, velocity) specified at the inlet to the skimmer tube. Incorrect specification of such parameters led to numerical difficulties or erroneous results. To resolve these issues, attempts were made to model the propagating shock in N_2 without chemical reactions. The conditions in these simulations were specified to be the same as in the NASA Ames experiments. This was performed as a test case solely for the purpose of investigating the fundamental convergence problems. In this mode it was possible to

reduce computing time and circumvent numerical problems arising due to stiffness of chemical reactions. Several simulations were conducted to study the effects of different inlet boundary conditions on numerical stability and the results of the simulations. The experience gained in implementing and running the modified code under the NASA Ames test conditions, as well as a discussion of the numerical results, is described in Section B. 3. 4. The evaluation of the NASA Ames experiments, including both the 1-D and 2-D modeling efforts, is described in Section B. 3.4.4. and Section B.3.4.5.

B.3.2 Model Description

B.3.2.1 Overview of the OSU 2-D Time-Dependent Nonequilibrium Code

For present purposes, a continuum description is assumed to hold. This allows the plasma to be treated as a conducting fluid. This approximation is valid in the reacting plasma flows studied in this work since the mean-free paths are much less than any length scale of interest. The governing equations are essentially the compressible Navier-Stokes equations supplemented by species continuity equations and Maxwell's equations. A complete description of these flowing plasmas requires a coupling between the flow, chemical kinetics, and electromagnetics. The resulting set of governing equations describes the close interaction between several physical and chemical processes. In addition to the governing equations, appropriate initial and boundary conditions, transport properties, and rate coefficients are needed to complete the theoretical formulation of the problem. Solving this set of equations is a computationally intensive task that challenges the best numerical algorithms and available hardware. Variable properties, presence of $\vec{j}x\vec{B}$ body forces, ohmic heating, species diffusion, and chemical reactions with ionization/ recombination processes render this system of equations extremely nonlinear and stiff, which makes them difficult to solve.

As noted in Section B.3.1, an objective of the present research was to enhance the existing 2-D unsteady, gas dynamics code to enable accurate computer simulations of the experiments conducted at NASA Ames. Therefore, several upgrades were developed and implemented in the code, as directed in the MSE/OSU statement of work (SOW).

Task 1 required additional rate data be added to simulate the working gas used by the NASA Ames researchers. The gas consists of a mixture of N_2O and N_2 in molar ratios that will yield N_2-to- O_2 ratios equivalent to that of air when the N_2O dissociates. Rate data for N_2O and associated reaction products were added to the chemical kinetics database in the code.

In Task 2, two independent electromagnetic routines to evaluate the electric potential both with and without the presence of an applied magnetic field were developed. This approach proved useful in simulating the NASA Ames experiments in which there was no magnetic field. Use of a special, potential solving algorithm for the case of zero magnetic field accelerated the solution

process significantly by eliminating calls to subroutines, which would return a value of zero in any case.

In Task 3, the axisymmetric code was modified to solve the governing equations in Cartesian coordinates (Ref. 1).

Task 4 involved the implementation of high-level block tridiagonal solvers for the solution algorithms. This is further described in Section B.3.2.3.

Task 5 specified the modified 2-D code be used to analyze the results of the NASA Ames tests. These tests are described in great detail in Section A.2. Because of certain convergence difficulties associated with the fact that very strong shocks were present in the NASA Ames experiments, the application of this code to interpret these tests was supplemented by the use of the OSU 1-D nonequilibrium code. The results of the investigations are described in Section B.3.4.

In implementing these code upgrades, the algorithm computing the vibrational kinetics was developed separately from the algorithm computing the chemical reactions for the air (or simulated air) species. This approach allowed evaluation of the computing time required for incorporating vibrational nonequilibrium in a molecular discharge. This development strategy also permits independent testing of the codes and thus enhances code reliability. The two separate modules can be combined to obtain a code capable of simultaneously studying vibrational nonequilibrium and chemical reactions in air plasmas. These modifications have thus laid the foundation to study chemical reactions and internal mode disequilibrium (vibrational modes) in high-speed air plasmas in some detail.

B.3.2.2 Governing Equations

The governing equations consist of the unsteady equations describing overall conservation of mass, two components of momentum, energy, and individual species. These equations are solved in conjunction with the electric potential equation (derived below from Maxwell's Equations). Constitutive equations (such as the generalized Ohm's Law, the equation relating pressure, temperature, and density, and the kinetic rate data) are also required. The species conservation equations given in this section include effects of chemical kinetics only.[1] Since the gaseous medium in the NASA Ames experiment consists of a mixture of N_2O and N_2 (to reproduce the same composition as air for the postshock conditions), the following species are modeled because they are the most important. The relative importance of the various neutral and ionic species was obtained by equilibrium calculations performed at the operating conditions of temperature and pressure in the NASA Ames experiment. On the basis of these calculations, the

[1] Internal mode disequilibrium was not included in this model used to validate NASA Ames experiments.

following species are included in this work for detailed study: N_2, O_2, N, O, NO, NO^+, N_2O, NO_2 and electrons.

$$
\begin{aligned}
N_2 + M &\Leftrightarrow N + M \\
O_2 + M &\Leftrightarrow O + O + M \\
NO + M &\Leftrightarrow N + O + M \\
N_2 + O &\Leftrightarrow NO + O \\
O_2 + N &\Leftrightarrow NO + O \\
NO_2 + M &\Leftrightarrow NO + O + M \\
N_2O + M &\Leftrightarrow N_2 + O + M \\
N + O &\Leftrightarrow NO^+ + e^-
\end{aligned}
$$

In the above reactions, M denotes any of the possible heavy particle species, hence, 48 chemical reactions are being modeled in the set of governing equations.

The set of governing partial differential equations is given below. The continuity equation is given by:

$$\frac{\partial \rho}{\partial t} + \frac{\partial}{\partial x}(\rho u) + \frac{\partial}{\partial y}(\rho v) = 0 \qquad \text{(B.3- 1)}$$

Conservation of momentum in the x – direction (streamwise direction) is:

$$\frac{\partial}{\partial t}(\rho u) + \frac{\partial}{\partial y}(\rho uv) + \frac{\partial}{\partial x}\left(\rho u^2\right) = -\frac{\partial p}{\partial x} + \frac{\partial}{\partial x}\left[2\eta\frac{\partial u}{\partial x} - \frac{2}{3}\eta\nabla.\vec{u}\right] + \frac{\partial}{\partial y}\left[\eta\left(\frac{\partial v}{\partial x} + \frac{\partial u}{\partial y}\right)\right] + J_y B \qquad \text{(B.3- 2)}$$

Conservation of momentum in the y – direction (transverse direction) is:

$$\frac{\partial}{\partial t}(\rho v) + \frac{\partial}{\partial y}\left(\rho v^2\right) + \frac{\partial}{\partial x}(\rho uv) = -\frac{\partial p}{\partial y} + \frac{\partial}{\partial r}\left[2\eta\frac{\partial v}{\partial y} - \frac{2}{3}\eta\nabla.\vec{u}\right] + \frac{\partial}{\partial x}\left[\eta\left(\frac{\partial v}{\partial x} + \frac{\partial u}{\partial y}\right)\right] \qquad \text{(B.3- 3)}$$

Conservation of energy for the total internal energy per unit volume:

$$\frac{\partial e_T}{\partial t} + \frac{\partial}{\partial x}\left[e_T + p\right]u) + \frac{\partial}{\partial y}\left[e_T + p\right]v) = \frac{\partial}{\partial x}\left(k\frac{\partial T}{\partial x}\right) + \frac{\partial}{\partial y}\left(k\frac{\partial T}{\partial y}\right) + \eta\Phi + \vec{j}\cdot\vec{E} \qquad \text{(B.3- 4)}$$

where $e_T = e + \rho\left(u^2 + v^2\right)/2$ is the total internal energy per unit volume:

$$e = \frac{3}{2}n_T kT + \sum_{i=1}^{i=N_d} f_i n_i \frac{kT}{2} + \Delta\varepsilon$$

and f_I is the number of degrees of freedom in rotation for a molecule.

The species continuity equations are:

Atomic N_2:

$$\frac{\partial n_N}{\partial t} + \frac{\partial}{\partial x}(n_N u) + \frac{\partial}{\partial y}(n_N v) + \frac{\partial}{\partial x}\left(-\frac{D_N}{k_B T}\frac{\partial}{\partial x}(n_N k_B T)\right) + \frac{\partial}{\partial y}\left(-\frac{D_N}{k_B T}\frac{\partial}{\partial y}(n_N k_B T)\right) = \dot{n}_N \qquad \text{(B.3- 5)}$$

Molecular N_2:

$$\frac{\partial n_{N_2}}{\partial t} + \frac{\partial}{\partial x}(n_{N_2} u) + \frac{\partial}{\partial y}(n_{N_2} v) + \frac{\partial}{\partial x}\left(-\frac{D_{N_2}}{k_B T}\frac{\partial}{\partial x}(n_{N_2} k_B T)\right) + \frac{\partial}{\partial y}\left(-\frac{D_{N_2}}{k_B T}\frac{\partial}{\partial y}(n_{N_2} k_B T)\right) = \dot{n}_{N_2} \qquad \text{(B.3- 6)}$$

Atomic O_2:

$$\frac{\partial n_O}{\partial t} + \frac{\partial}{\partial x}(n_O u) + \frac{\partial}{\partial y}(n_O v) + \frac{\partial}{\partial x}\left(-\frac{D_O}{k_B T}\frac{\partial}{\partial x}(n_O k_B T)\right) + \frac{\partial}{\partial y}\left(-\frac{D_O}{k_B T}\frac{\partial}{\partial y}(n_O k_B T)\right) = \dot{n}_O \tag{B.3- 7}$$

Molecular O_2:

$$\frac{\partial n_{O_2}}{\partial t} + \frac{\partial}{\partial x}(n_{O_2} u) + \frac{\partial}{\partial y}(n_{O_2} v) + \frac{\partial}{\partial x}\left(-\frac{D_{O_2}}{k_B T}\frac{\partial}{\partial x}(n_{O_2} k_B T)\right) + \frac{\partial}{\partial y}\left(-\frac{D_{O_2}}{k_B T}\frac{\partial}{\partial y}(n_{O_2} k_B T)\right) = \dot{n}_{O_2} \tag{B.3- 8}$$

Nitric NO:

$$\frac{\partial n_{NO}}{\partial t} + \frac{\partial}{\partial x}(n_{NO} u) + \frac{\partial}{\partial y}(n_{NO} v) + \frac{\partial}{\partial x}\left(-\frac{D_{NO}}{k_B T}\frac{\partial}{\partial x}(n_{NO} k_B T)\right) + \frac{\partial}{\partial y}\left(-\frac{D_{NO}}{k_B T}\frac{\partial}{\partial y}(n_{NO} k_B T)\right) = \dot{n}_{NO} \tag{B.3- 9}$$

NO_2:

$$\frac{\partial n_{NO_2}}{\partial t} + \frac{\partial}{\partial x}(n_{NO_2} u) + \frac{\partial}{\partial y}(n_{NO_2} v) + \frac{\partial}{\partial x}\left(-\frac{D_{NO_2}}{k_B T}\frac{\partial}{\partial x}(n_{NO_2} k_B T)\right) + \frac{\partial}{\partial y}\left(-\frac{D_{NO_2}}{k_B T}\frac{\partial}{\partial y}(n_{NO_2} k_B T)\right) = \dot{n}_{NO_2} \tag{B.3- 10}$$

Electrons:

$$\frac{\partial n_e}{\partial t} + \frac{\partial}{\partial x}(n_e u) + \frac{\partial}{\partial y}(n_e v) + \frac{\partial}{\partial x}\left(-n_e \mu_e E_x' - \frac{D_e}{k_B T}\frac{\partial}{\partial x}(n_e k_B T)\right) + \frac{\partial}{\partial y}\left(-n_e \mu_e E_y' - \frac{D_e}{k_B T}\frac{\partial}{\partial y}(n_e k_B T)\right) = \dot{n}_e \tag{B.3- 11}$$

In each of the above species conservation equations, the right-hand side represents the rate of change in concentration due to chemical reactions. Quasi-neutrality is assumed and consequently, the electron concentration is set equal to the concentration of NO^+. The concentration of nitrous oxide (N_2O) is then obtained from the equation relating mass density to the individual species concentrations. The right sides of the various species conservation equations are as follows:

$$\begin{aligned}\dot{n}_N &= 2\,[k_{f_1} n_{N_2} n_M - k_{r_1} n_{N_2} n_M] + k_{f_3} n_{NO} n_M \\ &\quad - k_{r_3} n_O n_N n_M + k_{f_4} n_{N_2} n_O - k_{r_4} n_{NO} n_N \\ &\quad - k_{f_5} n_{O_2} n_N + k_{r_5} n_N n_O - k_{r_8} n_N n_O + k_{r_8} n_e^2\end{aligned}$$

$$\begin{aligned}\dot{n}_O &= 2\,[k_{f_2} n_{O_2} n_M - k_{r_2} n_{O_2} n_M] + k_{f_3} n_{NO} n_M \\ &\quad - k_{r_3} n_O n_N n_M - k_{f_4} n_{N_2} n_O + K_{r_4} n_{NO} n_N \\ &\quad + k_{f_5} n_{O_2} n_N - k_{r_5} n_{NO} n_O + k_{f_6} n_{NO_2} n_M \\ &\quad - k_{r_6} n_{NO} n_O n_M + k_{f_7} n_{N_2O} n_M - k_{r_7} n_{N_2} n_O n_M \\ &\quad - k_{f_8} n_N n_O + k_{r_8} n_e^2\end{aligned}$$

$$\begin{aligned}\dot{n}_{N_2} &= -k_{f_1} n_{N_2} n_M + k_{r_1} n_{N_2} n_M - k_{f_4} n_{N_2} n_O \\ &\quad + k_{r_4} n_{NO} n_N + k_{f_7} n_{N_2 0} n_M - k_{r_7} n_{N_2} n_O n_M\end{aligned}$$

$$\begin{aligned}\dot{n}_{O_2} &= -k_{f_2} n_{O_2} n_M + k_{r_2} n_{O_2} n_M - k_{f_5} n_{O_2} n_N \\ &\quad + k_{r_5} n_{NO} n_O\end{aligned}$$

$$\begin{aligned}\dot{n}_{NO} &= -k_{f_3} n_{NO} n_M + k_{r_3} n_O n_N n_M + k_{f_4} n_{N_2} n_O \\ &\quad - k_{r_4} n_{NO} n_N + k_{f_5} n_{O_2} n_N - k_{r_5} n_{NO} n_O \\ &\quad + k_{f_6} n_{NO_2} n_M - k_{r_6} n_{NO} n_O n_M\end{aligned}$$

$$\dot{n}_{NO_2} = -k_{f6} n_{NO_2} n_M - k_{r_6} n_{NO} n_O n_M$$

$$\dot{n}_e = k_{f8}\ n_N n_O - k_{r_8} n_e^2$$

A detailed description of the rates used in the above equations is given in Section B.3.4.

Having described the equations describing the flow gas and the chemical kinetics of the various species in the gas, an equation to solve for the electric potential in the region between the electrodes is given next.

The computation for the electric potential, ϕ, proceeds on the assumption that at any stage in the computation, the electrical conductivity, σ, Hall Parameter, β, fluid velocity, $\vec{U}$, and the applied magnetic induction, $\vec{B}$, can be computed locally. Two other simplifying assumptions have been made, the first being the local charge density, $e(n_i - n_e)$, is assumed to be negligible everywhere. This is the standard charge neutrality approximation commonly made in MHD problems. The approximation is likely to be invalid in the near-electrode sheath regions. For example, very close to the anode surface, electrons will be strongly drawn to the anode, whereas positive ions will be repelled. The presence of the electrode prevents the ions repelled from the sheath region to be readily replenished by diffusion processes as they are in the outer regions, i.e., there are few, if any, ions flowing from the anode into the gas. The net effect is a polarization of electric charge is created, leading to a nonneutral charge density distribution in this thin layer. The problem is further complicated by the fact that properties of the electrode material (such as the work function) will influence the diffusion of electrons and ions across the sheath region. Thermionic emission or field-enhanced thermionic emission may also be important, implying the wall heat transfer will be strongly coupled to electron emission. In view of the complexity of the problem and the limits on available resources, it was determined only the core flow electric fields would be computed. These would be adequately simulated by the charge neutrality assumption.

The second simplifying assumption made is the magnetic Reynold's number is much less than 1. This assumption is tantamount to assuming the currents induced in the plasma will not significantly alter the internal magnetic field. Thus, the local magnetic field is everywhere equal to the applied magnetic field. For purposes of simulating MHD accelerator problems, this approximation is generally valid.

Using the above assumptions, the governing equations for the electric potential are the Maxwell equation for electric field and the current conservation equation. These equations take the form:

$$\vec{\nabla} \times \vec{E} = 0$$

$$\frac{\partial \rho_c}{\partial t} + \vec{\nabla} \cdot \vec{J} = 0$$

In these equations, $\vec{E}$ is the local electric field, ρ_c the charge density, and $\vec{J}$ the current density. The first equation can be formally satisfied by the relation, $\vec{E} = -\vec{\nabla}\phi$, where φ is the electrostatic potential function. Under the assumption of charge neutrality, the second equation above reduces to:

$$\vec{\nabla} \cdot \vec{J} = 0$$

The current density, $\vec{J}$, and the electric field, $\vec{E}$, are related through a constitutive relation, namely the generalized Ohm's Law:

$$\vec{J} = \sigma(\vec{E} + \vec{U} \times \vec{B}) - \mu \vec{J} \times \vec{B}$$

The last three equations can be combined into a single partial differential equation for the potential by first solving the generalized Ohm's Law for $\vec{J}$ as a function of $\vec{E}$ and $\vec{U} \times \vec{B}$, followed by substitution into the current conservation equation. The algebra is straightforward but somewhat lengthy. The final result for the case of a magnetic field aligned along the z direction ($\vec{B} = B\hat{e}_z$) is:

$$\nabla^2 \phi + \vec{A} \cdot \vec{\nabla} \phi = \delta^{-1} \frac{\partial}{\partial x}[\delta \beta U B] - \delta^{-1} \frac{\partial}{\partial y}[\delta U B] \qquad \text{(B.3- 12)}$$

where $\delta = \sigma / \left(1 + \beta^2\right)$, *and* $\vec{A} = (A_x, A_y)$.

The components of the vector A are:

$$A_x = \delta^{-1} \frac{\partial \delta}{\partial x} + \beta \delta^{-1} \frac{\partial \delta}{\partial y} + \frac{\partial \beta}{\partial x}$$

$$A_y = \delta^{-1} \frac{\partial \delta}{\partial y} - \beta \delta^{-1} \frac{\partial \delta}{\partial x} - \frac{\partial \beta}{\partial x}$$

In the above equations, $\beta = \mu B$ is the Hall parameter, μ is the plasma mobility, and σ is the electrical conductivity. Equation (B.3- 12) is a partial differential equation for the electric potential, ϕ, and is a generalization of the standard Poisson equation encountered in elementary electrostatic field theory. The right-hand side may be regarded as a charge density function induced by the magnetic field. Note that if $B = 0$, the right-hand side vanishes. The first term in each of the expressions for the components of A is due to the presence of gradients in the effective electrical conductivity. The last two terms in the expressions for A_x and A_y have no analog in standard treatments of the potential field. These terms arise because of the tensorial character of the Ohm's Law relationship between J and E. Assuming the local gradients in conductivity, the Hall parameter, velocity, and magnetic field can be computed, Equation (B.3-12), with appropriate boundary conditions, can be solved to obtain the potential. For the important case $B = 0$, $\beta = 0$, the right side of Equation (B.3- 12) is identical to zero, and the A vector reduces to:

$$\vec{A} = \vec{\nabla} \ln(\sigma)$$

For the sake of completeness, the full matrix equation for the case of an applied magnetic field in an arbitrary direction is given below.

$$\nabla \cdot \left[\sigma \beta^{-1} (\nabla \phi)\right] = \nabla \cdot \left[\sigma \beta^{-1} \left(\vec{U} \times \vec{B}\right)\right]$$

here β^{-1} is the matrix given by:

$$\frac{1}{\Delta} \begin{bmatrix} (1+\beta_x^2) & -(\beta_z - \beta_x \beta_y) & (\beta_y - \beta_x \beta_z) \\ (\beta_z - \beta_x \beta_y) & (1+\beta_y^2) & -(\beta_x - \beta_y \beta_z) \\ -(\beta_y - \beta_x \beta_z) & (\beta_x - \beta_y \beta_z) & (1+\beta_z^2) \end{bmatrix}$$

In the above equation, $\Delta = 1 + \beta_x^2 + \beta_y^2 + \beta_z^2$, where $\beta_x = \mu B_x$, $\beta_y = \mu B_y$, and $\beta_z = \mu B_z$.

The above sets of governing equations describe flow, chemical kinetics, and electromagnetics. These equations are time-marched in a fully coupled manner to obtain spatial and temporal variations of parameters of interests such as mass density, velocities, temperature, species concentrations, and electric potential.

B.3.2.3 Method of Solution

The governing equations given in the previous section describe the interaction between several complex physical and chemical processes. This makes the system of equations very stiff; therefore, it is necessary to time-march the system of equations using implicit methods. However, implementation of implicit methods requires an intensive programming effort in contrast with explicit methods. Implicit methods aimed at solving a coupled system of equations are known as block implicit methods developed originally by Lindemuth and Killeen, McDonald and Briley, Beam and Warming, and Briley and McDonald for solving the unsteady, compressible, Euler and Navier-Stokes equations (Ref. 2). In the present study, the linearized block implicit (LBI) method of Briley and McDonald is used to time march the unsteady set of governing equations in an implicit, fully coupled manner (Ref. 3). Implicit methods allow stable time marching of the system of equations with larger time steps (as compared to explicit method), which makes it possible to obtain solutions within reasonable amounts of time. The

LBI method essentially consists of an implicit scheme in which the solution is linearized by a Taylor expansion about the value at the previous time level. This produces a set of coupled, linear, difference equations that are valid for a given time step. The implementation of this method to reacting and plasma flows is explained in greater detail in Reference 4 and will be briefly described here.

The system of governing equations is transformed from the physical domain to the computational domain. The transformed equations are then linearized and discretized. In each coordinate direction, the time derivatives are discretized using the Crank-Nicholson method, whereas spatial derivatives are discretized using central differencing. The Douglas-Gunn alternating direction implicit (ADI) method is used to split the 2-D operator self-consistently into two 1-D operators. This procedure gives rise to block tridiagonal matrices in each coordinate direction. Such matrices can be solved quite efficiently using LU decomposition methods (Ref. 5). A uniform, nonstaggered grid is used, and the dependent variables are treated implicitly in all the governing equations. Transport properties and rate equations (which depend on temperature and species concentrations) are treated explicitly. Explicit treatment of these quantities enables different models of transport properties to be used without extensive code modifications.

The governing equations are written in conservation-law form, and hence shocks and discontinuities are obtained as a part of the solution, requiring no special treatment. The shock is smeared over a few grid points; however, the simplicity of the approach greatly outweighs the slight compromise in results obtained using shock-capturing methods.

B.3.3 Verification and Validation

The complexity of the governing equations describing plasma flows makes it imperative to test the model and the code at every stage to ensure accurate results. The algorithm used to study reacting plasma flows is amenable to extension from quasi-1-D to 2-D and 3-D situations. Our efforts to develop a modular high-performance reacting flow code have progressed in stages of increasing complexity. Quasi-1-D cold flow simulations were performed on different geometries. The results of these simulations were compared with analytical solutions for isentropic flow. This was followed by 2-D axisymmetric cold flow calculations. Next, the electromagnetics were included to simulate the presence of an arc in the 2-D axisymmetric formulation. These simulations were then applied to a variety of cases. Internal flow simulations in arcjet thrusters with hydrogen as the propellant were studied for two different geometries corresponding to two different power levels - 30 kW (Ref. 6) and 1 kW (Ref. 7). These simulations included simple reactions in hydrogen but disregarded internal mode disequilibrium. No analytical solutions exist for these flows. To verify the accuracy of the results of our simulations, detailed comparisons have been made with available experiments for the 1-kW arcjet geometry (Ref. 7). This model has also been used to study internal and external flows in welding plasmas to explore completely different plasma densities. The results of these simulations have also been compared with available experimental data.

In this section, results for three case studies involving quasi-1-D flows are presented and compared with analytical solutions. The geometries used in these simulations have an exit-to-throat area ratio of 10, 100 and 225 (1-kW arcjet geometry). These three case studies bring to fore the ability of the numerical scheme to handle widely varying geometries and serve to identify the limits of the model's applicability. The area-ratio 10 and 100 configurations were each studied with two different grid sizes (150 and 1,500 grid-points) for two different values of γ (ratio of specific heats): 1.4 (diatomic gases) and 1.67 (for monatomic gases). Flow in the 1-kW arcjet geometry (see Figure B.3- 4) was studied for two different grid sizes (150 and 1,500) for γ=1.4. The variation of Mach number in the streamwise direction obtained from these simulations was compared with analytical solutions for isentropic, quasi-1-D flows. These are presented in the next section for each of the three cases.

B.3.3.1 Results for Quasi-1-D, Isentropic Flow

Figures B.3- 1 - B.3- 3 show comparisons between quasi-1-D code predictions and analytical relationships for the Mach number in an isentropic flow, for exit-to-throat area ratios of 10, 100 and 225 respectively. The figures show the effects of different grid-sizes and γ. As can be seen, the calculated values match analytical solutions closely. The difference between the predicted values and theoretical values is largest in the supersonic region near the exit plane (approximately 10% in the case of the coarse grid), yet, with finer grid spacing, this discrepancy is reduced. Also, as area ratios increase, the discrepancy increases. For a given area ratio, the error is greater for γ = 1.67 than for γ = 1.4, because larger gradients occur in the flow in the diverging section for monatomic gases compared to diatomic gases.

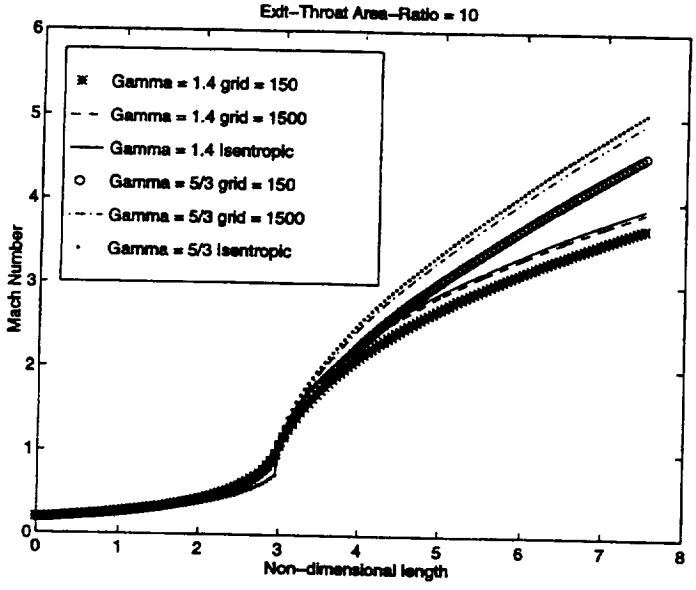

Figure B.3- 1. Comparison of analytical and computed results (Area-Ratio = 10).

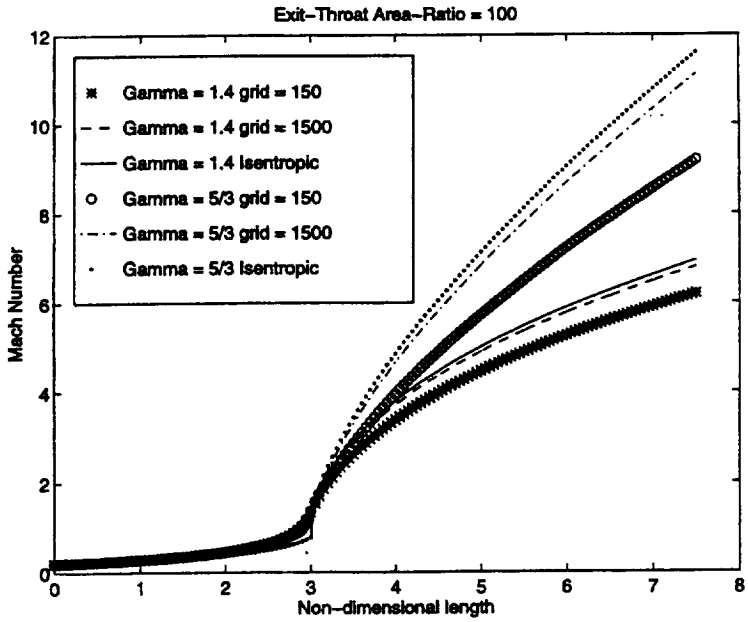

Figure B.3- 2. Comparison of analytical and computed results (Area-Ratio = 100).

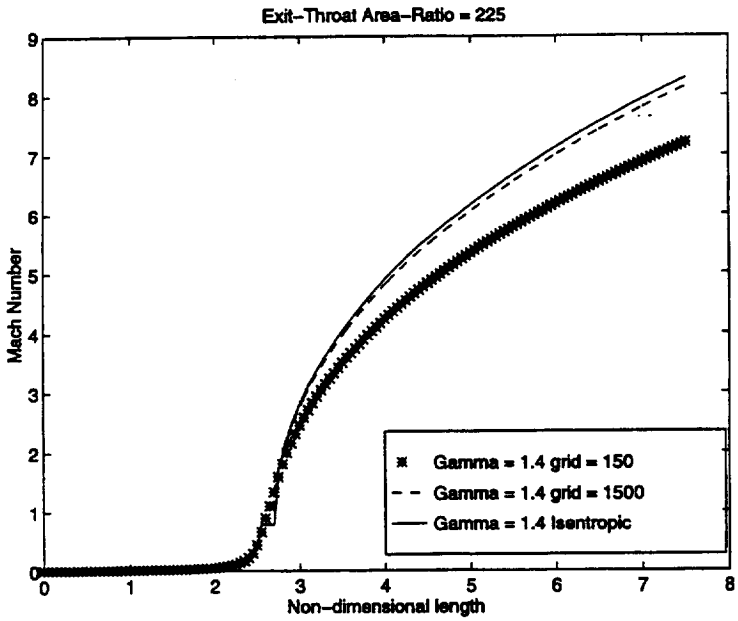

Figure B.3- 3. Comparison of analytical and computed results (Area-Ratio = 225).

As Figures B.3- 1 - B.3- 3 show, the agreement between analytical results and the computations is quite good. The maximum discrepancy is about 10% for the case of coarse grids. This discrepancy is due to the effect of artificial dissipation (Ref. 8) and truncation errors. The artificial dissipation term used in here is in the form $\varepsilon_x \partial^2\psi/\partial x^2$, where ε_x is given by $0.5\rho w dx$ with dx being the mesh spacing, and ψ is any dependent variable. As expected (in all the case studies), the effect of numerical dissipation is larger for the coarser grids. It must be mentioned the analytical results for isentropic flow do not take into consideration the effects of friction. However, the LBI scheme requires the addition of artificial dissipation for stability of the time-marching procedure. Addition of artificial dissipation introduces effects similar to viscous effects. It is well known that friction decelerates supersonic flows. Temperatures obtained from quasi-1-D computations are higher when compared to the analytical solutions. Axial velocities in the quasi-1-D simulations are lower than those values given by the analytical solution; therefore, the Mach numbers computed from the quasi-1-D simulations are lower than those predicted by analytical solutions. The influence of artificial dissipation is highest in regions close to the exit plane, where the discrepancy is largest. Reducing ε_x by a factor of 10 in the supersonic regions of the flow alone reduced the discrepancy to less than 1% for the nozzle geometry with an exit-to-throat area ratio of 10.

There is no unique way to prescribe the optimum amount of artificial dissipation at each point in the computational domain to maintain positivity, and consequently, stability. This is a drawback of the numerical scheme used, though the results of the simulation are not affected a great deal. Increasing the number of grid points for a given area ratio tends to improve the accuracy of the results, largely due to the fact that increasing the number of grid points reduces the effects of numerical dissipation, which scales directly with the grid spacing dx. The effects of artificial dissipation are expected to be less pronounced in the solution of real viscous flows since dissipation is naturally present. However, the present code has the capability to provide results for quasi-1-D flow problems that converge to the twelfth decimal place within a few seconds or a few minutes of central processing unit (CPU) time on a Silicon Graphics Indigo Workstation. The CPU time depends on the initial guess and number of grid points. It is this highly efficient feature of the LBI algorithm that makes it attractive for computations involving multidimensions and large coupled sets of governing equations.

B.3.3.2 Validation for 2-D Flows: Low-Pressure Discharges (Hydrogen Arcjet)

Arcjet thrusters have primarily been targeted as low-power, high-specific-impulse ($I_{sp} \sim 1{,}000$ s) space propulsion devices. These thrusters are currently used for North-South Station Keeping (NSSK) of communication satellites in geosynchronous orbits. Arcjet thrusters impart directed kinetic energy to a propellant stream by ohmically heating it and subsequently expanding to supersonic speeds. In addition to aerospace applications, the thrusters also have terrestrial applications in the area of materials processing. Arcjets are used commercially in the growth of freestanding diamond films and coatings.

Essentially, the device is comprised of an inlet plenum, a converging section, a straight portion called the constrictor, followed by a diverging section or supersonic nozzle. The propellant enters the inlet plenum relatively cold and unionized at subsonic speeds. The flow entering the plenum is randomly injected with swirl, which some believe stabilizes the arc. This cold, unionized gas is rapidly heated by an arc discharged between the cathode and the anode as a result of an electric field applied between the two electrodes. The heated gas reaches near-sonic speeds by the end of the constrictor and rapidly expands in the diverging section to supersonic speeds. The propellant in this study was molecular hydrogen (H_2).

The governing equations describing arcjet flow are similar to the conservation equations described in the section on model description. They are adapted to the case of H_2 arcjets and solved to obtain the velocity, temperature, and species concentrations. In this study, the following reactive processes are considered:

$$H_2 + H_2 \Leftrightarrow H + H + H_2$$
$$e^- + H \Leftrightarrow H^+ + e^- + e^-$$
$$H_2 + e^- \Leftrightarrow H + H + e^-$$
$$H + H_2 \Leftrightarrow H + H + H$$

The plasma in the H_2 arcjet is assumed to be composed of H_2, atomic hydrogen (H), electrons (e^-), and singly ionized hydrogen atoms (H^+). H_2 is the only diatomic species. No vibrational states of molecular H_2 are considered here, and a single temperature is used to describe the heavy particles and the electrons. Quasi-neutrality is assumed, which allows us to set the number density of e^- equal to that of H^+. Therefore, in this case study, the species conservation equations are written for H and electrons. The concentration of molecular H_2 is then evaluated using the algebraic relationship between mass density and the species concentrations.

Flow through two different arcjet thrusters have been modeled, specifically a 30-kW arcjet thruster (Ref. 6) and a 1-kW (Ref. 7) arcjet thruster, with hydrogen as the propellant. Unfortunately, no detailed experimental results for the 30-kW arcjet geometry exist. However, experimental measurements have been performed on 1-kW arcjet thrusters (see Figure B.3- 4) with H_2 as the propellant by groups at the U.S. Air Force's Phillips Laboratory (Edwards Air Force Base (Ref. 9) and at Stanford University (Refs. 10, 11). The operating conditions for these experiments were a power level ~1.4 kW, current = 10 A and a mass flow rate of ~13 mg/s. Simulations for these experimental conditions (geometry, propellant, and operating conditions) were performed to compare directly with experimental measurements. In this subsection, results from numerical simulations are compared with experimental data.

Figures B.3- 5 through B.3- 8 show comparisons between the results of our simulation with experimental measurements from along the exit plane of the 1-kW H_2 arcjet thruster (Refs. 9, 10, 11). Figure B.3- 5 shows a comparison of the predicted H_2 atom concentration at the exit plane with experimental data. The circles denote H-atom concentrations measured by LIF

measurements on H-atoms from Reference 9, while the solid line represents the results of our simulations. As can be seen, the H-atom number density across the exit plane predicted by our simulations matches the experimental data quite well.

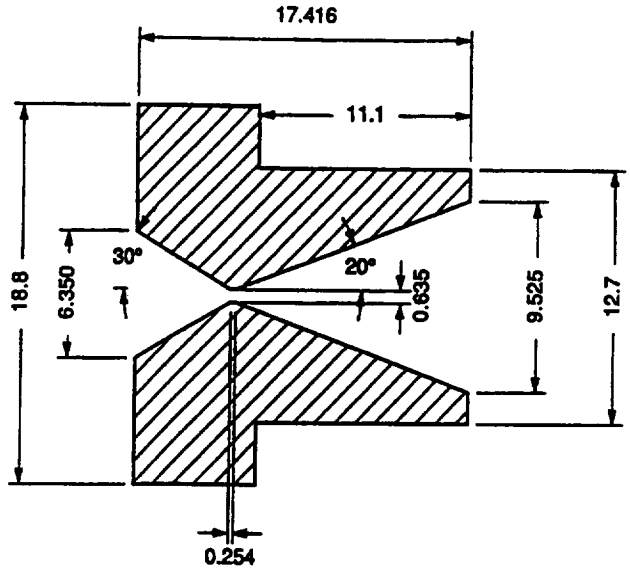

Figure B.3- 4. Schematic of the 1-kW arcjet geometry (all dimensions in mm).

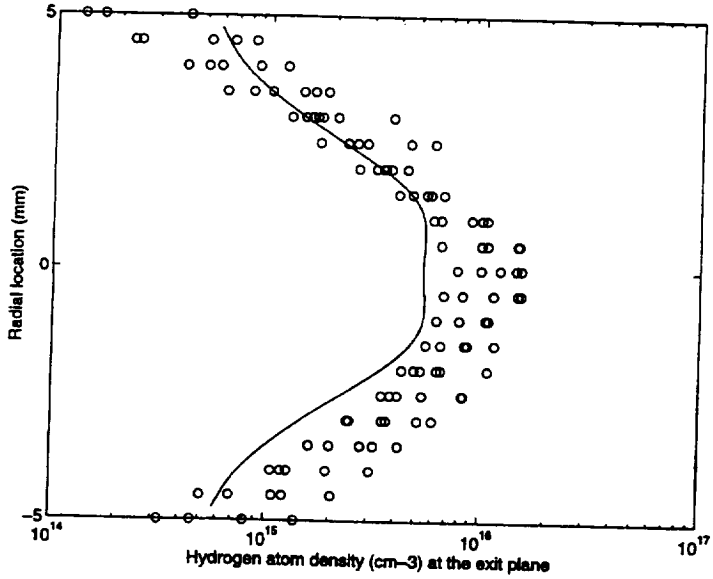

Figure B.3- 5. Comparison of predicted H-atom concentration at the exit plane with experimental data. The circles denote H-atom concentrations measured by LIF measurements on H-atoms from Reference 9, while the solid line represents the results of the simulations.

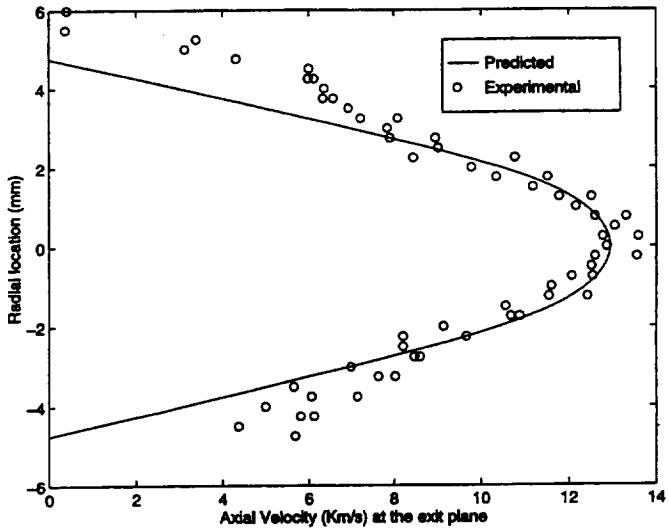

Figure B.3- 6. Comparison of the stream-wise velocity at the exit-plane with experimental data. The circles denote experimental measurements from Reference 9, while the solid line represents the results of the simulation.

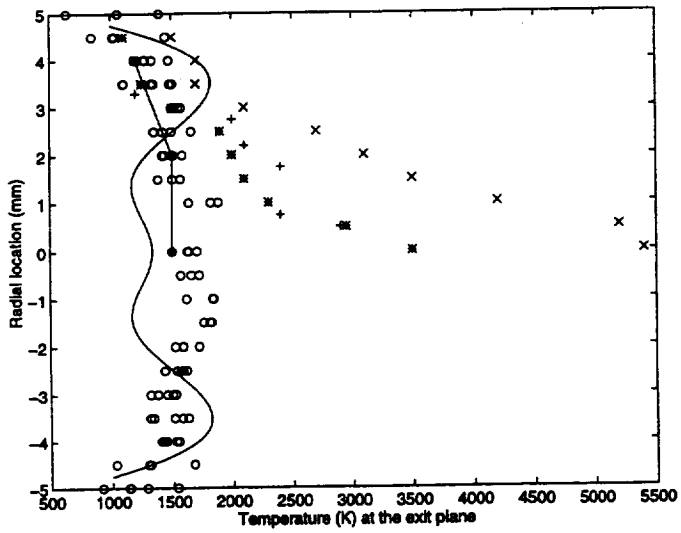

Figure B.3- 7. Comparison of calculated radial distribution of temperature at the exit plane with experimental data. The solid curve represents the results of simulations; "o" denotes experimental data based on LIF measurements on H-atoms from Ref. 9; "x" denotes measured temperatures based on uncorrected H-atom LIF data from Ref. 10; "" denotes measured temperatures based on Stark corrected H-atom LIF data from Ref. 10; "+" denotes measured temperatures from H-atom emission data from Ref. 10; and the circle with "+" connected by lines denotes measured temperatures obtained from H_2 Raman spectroscopy data from Ref. 10.*

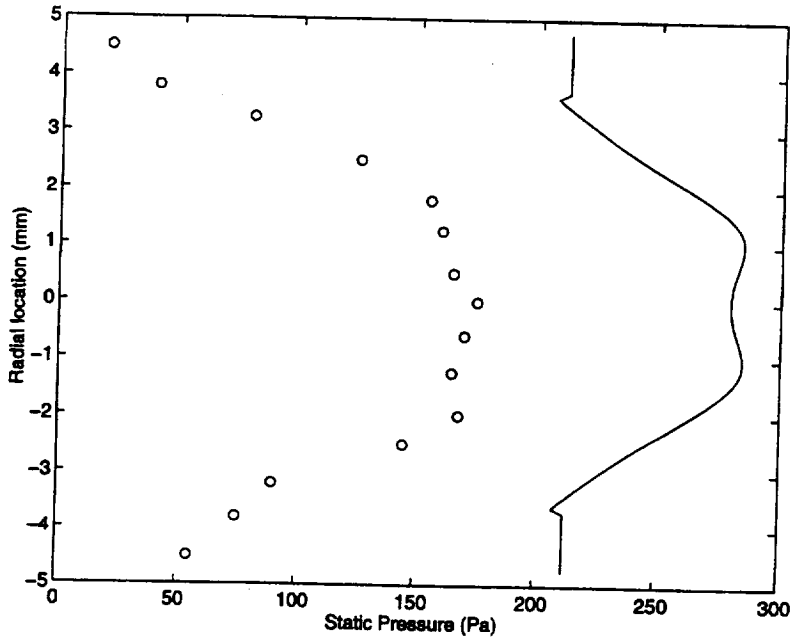

Figure B.3- 8. Comparison of radial distribution of static pressure at the exit plane with experimental data.

Figure B.3- 6 shows a comparison of the stream-wise velocity along the exit-plane predicted by our simulations against experimental data from Reference 9. The agreement is very good. The simulation underpredicts the experimentally observed values along the centerline by approximately 10%. It must be mentioned that other single temperature models published in the literature also underpredict velocities at the exit plane in a similar manner (Refs. 12, 13).

Figure B.3- 7 shows the radial temperature profile at the exit plane along with experimental results (Ref. 9, 10, 11). The noticeable bulge in the temperature profiles is reminiscent of hypersonic thermal boundary layers near cooled surfaces (Ref. 14). The existence of the local maximum in the radial temperature profile is due to the opposing effects of viscous dissipation heating the flow and the relatively colder wall trying to cool it. The scatter in the experimental data makes it difficult to ascertain the presence or absence of bulges in temperature. It should be noted that the temperature measurements made by Storm et al (Ref. 10) differ considerably from those reported by Wysong et al (Ref. 9), although the measurements have been reportedly made for two arcjets operating under identical conditions. Temperatures inferred from Raman spectroscopy on H_2 differs from temperature measurements made by LIF on H-atoms from the same group (Ref. 10). The reason for the difference in the LIF temperature measurements reported by References 9 and 10 could be due to different arc attachments in the two experiments. The differences in exit-plane temperatures between LIF and H_2 Raman spectroscopy measurements as reported by References 10 and 11 could be due to nonequilibrium effects.

Direct Simulation Monte Carlo (DSMC) calculations by Boyd (Ref. 12) show a considerable disequilibrium exists between the internal and external (translational) modes of H_2 molecules at the exit plane. These calculations show centerline vibrational temperatures at the exit plane close to 3,000 K, centerline rotational temperatures near 2,000 K, and the centerline translational temperatures at about 1,000 K. The differences between the internal modes and external mode temperatures may be explained by disequilibrium between the internal and external modes of H_2. Due to the high velocities and low densities at the exit plane, the finite rates for V-V, V-R, and V-T transfer could lead to disequilibrium between internal and external modes of the different constituents. Furthermore, V-T rates will increase with the vibrational quantum number; therefore, the translational temperatures obtained in the experiments using LIF on the H-atom may be inferring the vibrational temperatures of excited H_2 molecules via:

$$H_2(v) + H \rightarrow H_2(v\text{-}n) + H^*$$

where H^* is translationally hot. Thus V-T relaxation of higher vibrational levels of H_2 by H could result in the translational temperatures of H-atoms being higher than that of H_2.

Figure B.3- 8 shows a comparison between the predicted pressures along the exit plane and experimental data from Reference 15. The pressure profile predicted by our simulation agrees qualitatively with the experimental data. In regions close to the centerline, the variation in static pressure is negligible, both in the experiment and the present study. However, the pressure begins to drop off steeply after this initial flat portion near the centerline. Also, static pressure along the exit plane is not constant in the supersonic region, and the bell-shaped profile is due to the combined effects of increasing total number density (n_T) and decreasing temperature, with increasing radius. It is also possible the region near the centerline represents a core flow with a constant static pressure, whereas the pressure drops in regions near the wall due to viscous boundary layer effects. It is interesting to note that static pressure values computed by Butler et al (Ref. 13) overpredict the experimental results as well.

B.3.3.3 Validation for Two-Dimensional Flows: Atmospheric Pressure Discharge – Plasma Welding Arcs (Internal and External Flows)

Electric arcs are widely used in applications ranging from industrial-scale arc furnaces and switchgears to materials synthesis and processing. Plasma torches form an important class of electric arcs. Plasma torches are used as clean and efficient sources of intense heat in many industrial applications. Two notable examples are plasma spray coating and welding. Welding is one of the basic industrial processes widely used in the manufacturing and fabrication of parts and components; therefore, studies of techniques to produce joints of high quality and strength are of great importance. Consequently, a great deal of effort has been expended in recent years to determine the characteristics of electric arcs. This second case study involves just such a welding arc.

Electric arc-welding processes consist of an electrode and a workpiece of opposite polarities. An arc is struck by applying an electric field between two electrodes, causing current flow through the partially ionized gas column (established between the electrodes). The heat generated in the arc produces the high temperatures needed to sustain the gas in its ionized state. The thermal energy is transferred to the workpiece primarily due to particle fluxes (Ref. 16) causing it to melt. The subsequent solidification of this molten region, the "weld pool", forms the weld or actual joint. Gas-tungsten arc welding (GTAW), gas-metal arc welding (GMAW) and variable polarity plasma arc (VPPA) welding are some of the popular methods of welding. In many cases, a discharge is initially struck between an electrode and another auxiliary electrode using high frequency ac excitation. Then, the main arc is struck between the electrode and workpiece by transferring the discharge. Such an arc is called a transferred arc.

In the plasma arc welding process, a metallic nozzle and the cathode centerbody constrict the plasma gas flow. The VPPA torch assembly essentially consists of a central electrode concentric with two enclosing outer surfaces, which confine the main plasma gas and shield gas flows called the constricting nozzle and the shield gas nozzle, respectively. The constricting nozzle confines the plasma gas and also acts as the anode for supporting a pilot-arc (nontransferred arc). The shielding gas flows through the annulus between the constricting nozzle and the shielding gas nozzle. Both the plasma and shield gases are inert. Typically, argon is used as the plasma gas, while the shield gas is either argon (Ar) or helium (He). An inert shielding gas is used to reduce oxidation of the work piece due to entrainment of ambient O_2. The main plasma gas enters the torch cold and at low velocities and is rapidly accelerated near the exit plane by ohmic heating within the arc. The resulting high-velocity plasma jet then impinges on the workpiece (transferred arc) and provides enough penetration to produce a deep weld and/or a keyhole.

A systematic study of the design and operating conditions of the torch and the plasma jet is required to obtain a better understanding of the operating characteristics of the torch. Such a study provides a more rational basis for improving existing designs. With this objective in mind, the present study endeavored to study the flow in these torches as well as the external jet impinging on the work-piece.

As explained in the previous section on arcjet thrusters the conservation equations for mass, momentum, energy, and species continuity are solved in conjunction with the magnetic transport equation. A plasma-welding arc using Ar as both the plasma and shield gas was studied. A single reaction modeling electron impact ionization of Ar, and its reverse (three-body recombination) was modeled. The Ar plasma was assumed to consist of Ar atoms, singly ionized Ar atoms (Ar^+) and electrons (e^-). A single equation describing the conservation of electrons is solved with the governing equations describing the flow and electromagnetics. Concentration of Ar^+ is equal to the electron concentration since quasi-neutrality is assumed. Concentration of Ar atoms is obtained from the overall mass density and electron concentration.

The plasma welding process was modeled in two separate stages, namely plasma flow within the torch body (internal flow) and the plasma jet impinging on the work-piece (external flow). The

governing equations describing these two situations are the same; however, the boundary conditions for the internal and external flows are different. A simple and inexpensive diagnostic technique is used in the present work for model validation. A radial pressure profile was measured on a water-cooled copper plate while the plasma jet impinged on it.[2] This measured radial pressure distribution was compared with calculated pressure profiles. Model predictions were compared with experimental results at three different current levels. As in the case study on arcjets, the total stagnation pressure, total current, and power level were made to match experimental conditions to enable direct comparisons. Details of the geometry, boundary, and initial conditions are given in Reference 4.

The results of simulations are compared with experiment for conditions listed in Table B.1- 1.

Table B.1- 1. Operating conditions for plasma welding torch.	
Polarity	Straight
Plasma Gas	Ar
Shield Gas	Ar
Plasma Gas Flow Rate (CFH)	13
Shield Gas Flow Rate (CFH)	35
Current (Amps)	100 and 150
Stand-Off Distance (in.)	3/8
Power (kW)	2.2

Spatial variations of temperature, velocity, and ionization fraction (in both the internal and external flows) are discussed in detail in Reference 4. Figures B.3- 9 and B.3- 10 show a comparison between the predicted radial distribution of static pressure along the surface of the cooled workpiece and experimental data for a total current of 100 A and 150 A, respectively (Ref. 17). The experimental data in both these figures shows the plasma jet tends to remain collimated. The arc pressure (gauge) drops sharply to values close to zero within a distance of about three times the nozzle radius from the centerline. The simulations predict a broader pressure profile as compared to the experiment because of the combined effects of the simple heat-transfer model used in the work to simulate the cooling of the copper plate and effects of numerical dissipation. Nevertheless, the results of the simulations agree with experiment.

[2] These experiments were conducted in the Department of Industrial, Systems, and Welding Engineering, at The OSU (see Ref.17 for details).

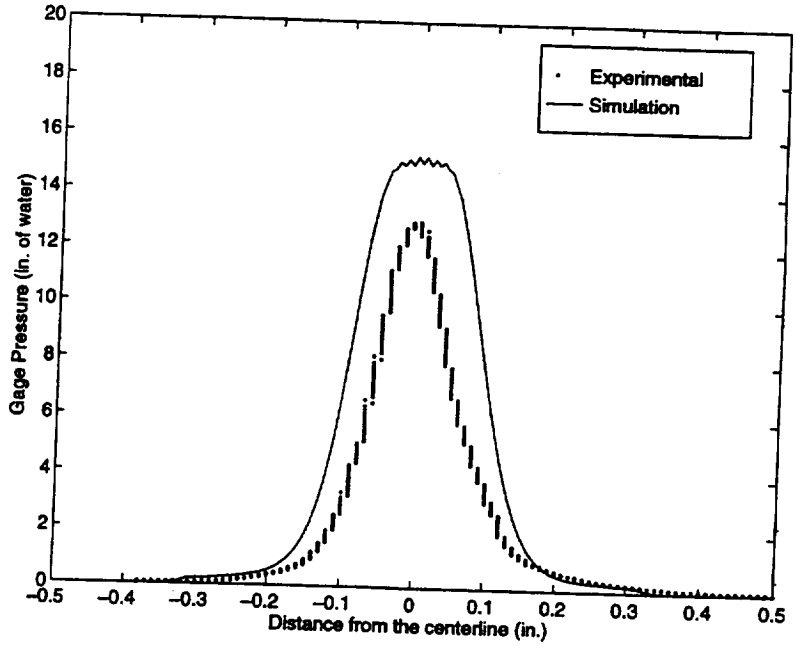

Figure B.3- 9. Comparison of the radial distribution of static pressure along the surface of the workpiece with experimental data from Reference 17 (I = 100 A)

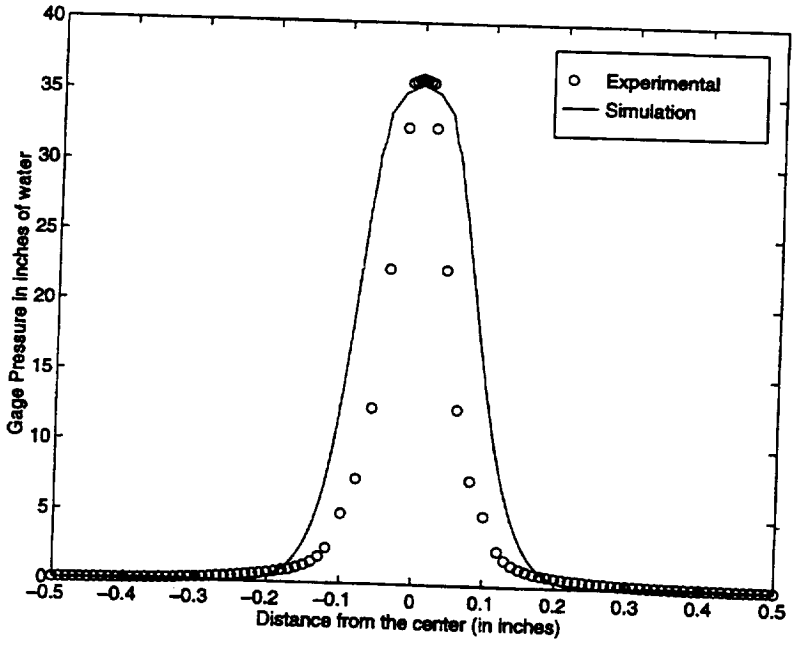

Figure B.3- 10. Comparison of the radial distribution of static pressure along the surface of the workpiece with experimental data from Reference 17 (I = 150 A)

B.3.4 Analysis of the NASA Ames Experiments

B.3.4.1 One-Dimensional Calculations

The interpretation of the shock tube ionization data measurements at NASA Ames requires analysis of coupled vibrational relaxation, molecular dissociation, and ionization behind the shock. First consider nonequilibrium ionization behind shock waves in air. The kinetic mechanism of this process is well established. In particular, the principal mechanism of ionization for shock velocities of u_s<7 km/s is associative ionization in collisions of N and O atoms (Ref. 18):

$$N + O \rightarrow NO^+ + e \tag{1}$$

This process cannot begin until after the atoms are produced in nonequilibrium chemical reactions:

$$N_2(v) + M \rightarrow N + N + M \tag{2}$$

$$O_2(v) + M \rightarrow O + O + M \tag{3}$$

$$NO(v) + M \rightarrow N + O + M \tag{4}$$

$$N_2(v) + O \rightarrow NO + N \tag{5}$$

$$O_2(v) + N \rightarrow NO + O \tag{6}$$

The symbol (v) behind a species indicates vibrational excitation of this particular species enhances the reaction rate. This requires modeling of chemical kinetics coupled with the V-T relaxation of N_2, O_2, and NO:

$$AB(v) + M \rightarrow AB(v + \Delta v) + M \tag{7}$$

In Reaction (7), AB stands for diatomic molecule, v is the vibrational quantum number, and Δv is its change in a collision (note that Δv is not necessarily equal to 1). In addition, V-V energy exchange between the two most abundant air species is also of great importance:

$$N_2(v) + O_2(w) \rightarrow N_2(v + \Delta v) + O_2(w - \Delta w) \tag{8}$$

Reaction (3) is the "bottleneck" for the entire ionization process because O_2 has lower dissociation energy and shorter relaxation time than N_2. As soon as atomic oxygen appears in the flow, NO and N atom production begins in the chain reactions (5) and (6). The net rate of this chain process is strongly dependent on the vibrational temperature of N_2, which makes vibrational relaxation of N_2 another "bottleneck". Note that other associative ionization processes such as:

$$N+N \rightarrow N_2^+ + e \text{ and } O+O \rightarrow O_2^+ + e \tag{9}$$

as well as charge transfer processes such as:

$$NO^+ + N_2 \rightarrow NO + N_2^+ \text{ and } NO^+ + O_2 \rightarrow NO + O_2^+ \tag{10}$$

are not important at shock velocities less than about 7 km/s because of the much greater ionization potentials of N_2 and O_2.

The kinetic processes discussed above have been extensively studied in the past. Both the experimental rates of reactions (1) through (8) and theoretical models of coupled vibrational relaxation, dissociation, and ionization are available in the literature (see Ref. 19). For the present study, a 1-D normal shock/nonequilibrium flow code developed at OSU for the MARIAH Project was used (Refs. 20, 21). It is based on the most reliable set of experimentally measured rates for processes [Reactions (1)- (8)] and on a state-of-the-art analytic model of coupled vibrational relaxation and dissociation (Refs. 22, 23, 24, 25). The code has been previously validated by comparing its predictions with the NO nonequilibrium infrared radiation history behind a shock measured for the shock velocities of 3 to 4 km/s (Ref. 20). Briefly, the code solves master equations for the populations of each vibrational level of N_2, O_2, and NO, which is fully coupled with the set of chemical kinetics equations for a number of neutral and charged species including N, N_2, O, O_2, NO, N_2O, NO_2, NO^+, and e^-; Boltzmann equation for the electron energy distribution function; and 1-D gas dynamics equations (see Refs. 20, 21 for details).

Calculations using this code show that ionization behind the shock proceeds in accordance with the well-known qualitative scenario discussed above. Figures B.3- 11 and B.3- 12 show translational and vibrational temperatures, as well as species mole fractions behind the 4-km/s shock in air as functions of P_1t (i.e., the product of the static pressure ahead of the shock and the laboratory time). Figure B.3- 13 compares the calculated ionization rise time, τ, (time to reach the equilibrium electron concentration behind the shock) with the available experimental data (Refs. 26, 27, 28, 29) showing satisfactory agreement. One can see that $P_1\tau$ does not exceed 1 Torr·μs for the shock velocities u_s>4 km/s. In other words, for the conditions of the NASA Ames experiments (u_s=4.5-5.0 km/s, P_1=5-35 Torr, P_2=2-13 atm), the ionization rise time should not exceed 0.1 μs. However, the measurements report ionization rise times of tens of microseconds (see Figure B.3- 14).

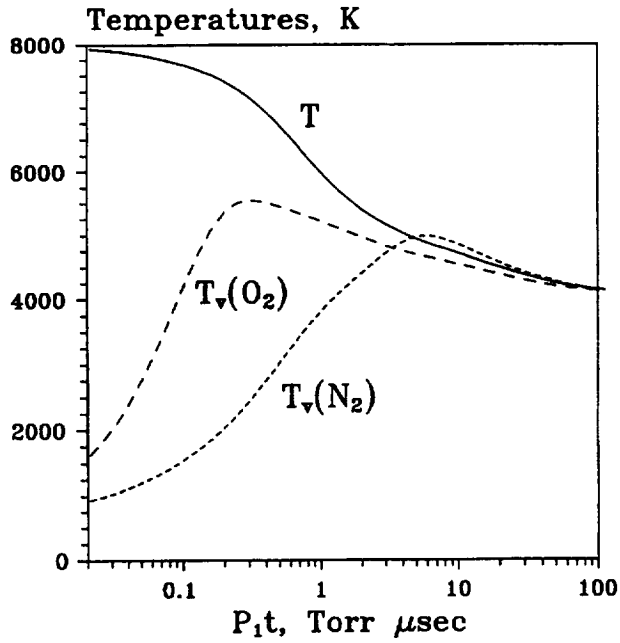

Figure B.3- 11. Translational and vibrational temperature distributions behind the normal shock wave in air. Shock velocity u_s=4 km/s.

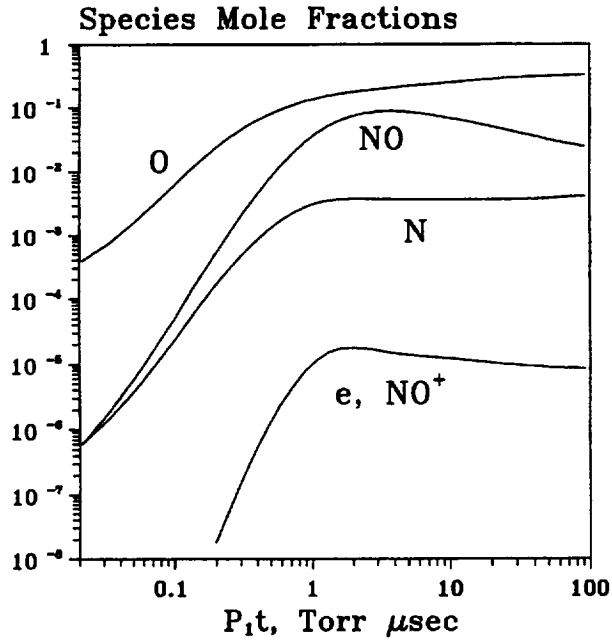

Figure B.3- 12. Species mole fraction distributions behind the normal shock wave in air. Shock velocity u_s=4 km/s.

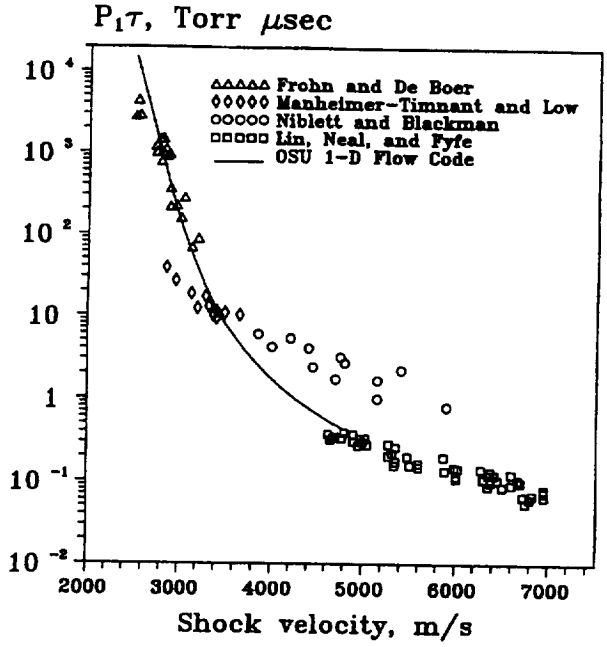

Figure B.3- 13. Ionization rise time behind the shock wave in air.

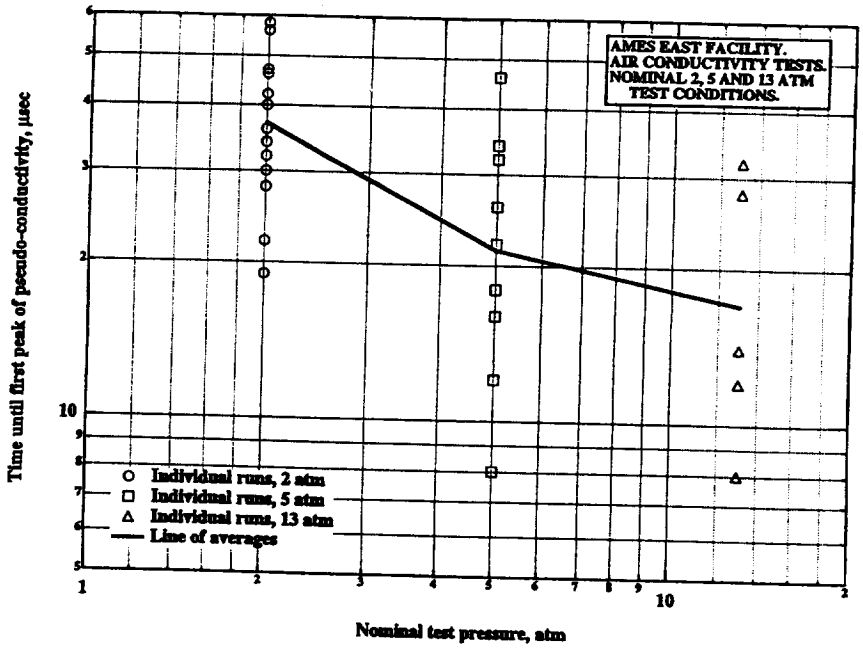

Figure B.3- 14. Ionization rise time at the NASA Ames shock tube experiments.

The fact that the NASA Ames ionization measurements have been made not in air but in N_2O-N_2=53.2:46.8 mixture to increase the available test time may considerably change the ionization kinetics. Can the presence of N_2O result in the increase of the ionization time up to tens of microseconds? We cannot directly model the process of N_2O vibrational relaxation and dissociation behind such strong shocks. The translational temperature overshoot immediately behind a 4.5-km/s shock wave in such a mixture exceeds T=10,000 K (the equilibrium temperature is T_{eq}=5,500 - 6,000 K), while the vibrational relaxation data for N_2O (to the best of our knowledge) is available only up to T=2,000 - 2,500 K. However, the relatively low temperature N_2O relaxation data shows its vibrational relaxation time, τ_{vib}, is much shorter than that of both N_2 and O_2, which is demonstrated in Figures B.3- 15 and B.3- 16. One can see, for example, that T=2,000 K $\tau_{vib}(N_2O)$ is approximately 5,000 times shorter than $\tau_{vib}(N_2)$ and 25 times shorter than $\tau_{vib}(O_2)$. In addition, the experimentally measured $\tau_{vib}(N_2O)$ is the relaxation time of the asymmetric stretch mode ν_3 (Ref. 30) (the energy of the 00^01 level is 2,223.5 cm^{-1}) and longer than the relaxation time of the symmetric stretch and bending modes ν_1 and ν_2 (the energies of the 10^00 and 01^10 levels are 1,285.0 and 588.8 cm^{-1}, respectively). For this reason, it can be assumed that N_2O behind the shock reaches equilibrium with the translational temperature instantaneously, as compared to N_2 and O_2 (let us call this assumption "case A"). On the other hand, the energy spacing between the N_2O level 00^01 and first vibrational level of N_2 is fairly small (107 cm^{-1}), which facilitates rather fast vibration/vibration energy exchange between these two modes. The rate of this process is induced by the dipole-quadruple interaction at T=2,000 K is $k_{vv}\sim10^{-11}$ cm^3/s (Ref. 30). Therefore, one can also make a somewhat opposed limiting assumption that the ν_3 mode temperature is equal to the vibrational temperature of N_2, while the other two modes are still in equilibrium with the translational temperature ("case B"). In this case the simplest phenomenological approach, widely used for modeling of nonequilibrium dissociation of diatomic molecules (Ref. 19), is to evaluate the N_2O dissociation rate using the "effective" temperature $T^* = [T \cdot T_v(N_2)]^{1/2}$. Note the dissociation energy of N_2O in Reaction (11)

$$N_2O + M \rightarrow N_2 + O + M \qquad (11)$$

is much lower than that of N_2 (32,000 K as opposed to 113,000 K), and N_2O is expected to dissociate behind the shock much faster than N_2.

It is not clear which of the two processes would dominate at the high temperatures of T = 6,000-10,000 K: V-T self-relaxation of N_2O or V-V exchange $N_2O(\nu_3)$-N_2. However, the two opposite assumptions (cases A and B) permit estimates of the lower and upper limits for the ionization rise time in the N_2O-N_2 mixtures, respectively. Figure B.3- 17 compares the ionization fraction behind the 3.5-km/s shock in air and in N_2O-N_2=53:47 mixture, cases A and B. One can see that in both cases, the presence of the rapidly relaxing and dissociating N_2O results in a faster production of atomic species, which substantially accelerates ionization.

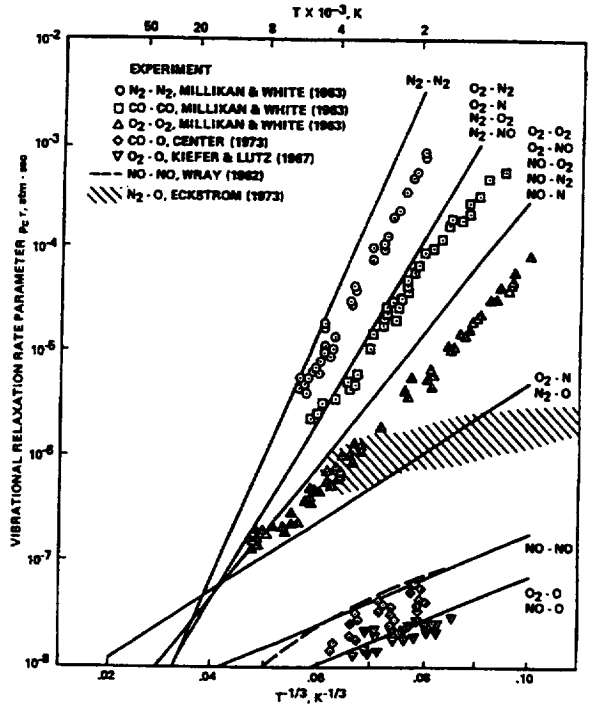

Figure B.3- 15. Vibrational relaxation time data for N_2 and O_2 (from Reference 19).

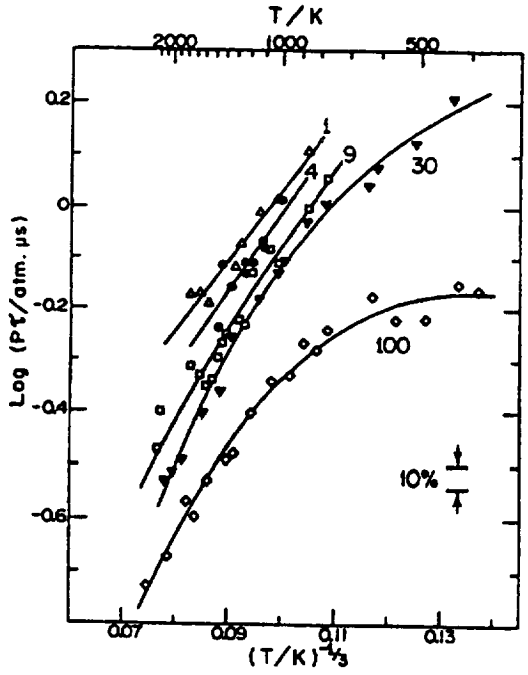

Figure B.3- 16. Vibrational relaxation time data for N_2O (Reference 31).

Note the higher steady-state value of ionization fraction in the N_2O-N_2 mixture, as opposed to that in air at the same shock velocity (see Figure B.3- 17), is simply due to the higher initial enthalpy of the flow containing N_2O (nitrous oxide has rather high enthalpy of formation, about 72 MJ/kmol).

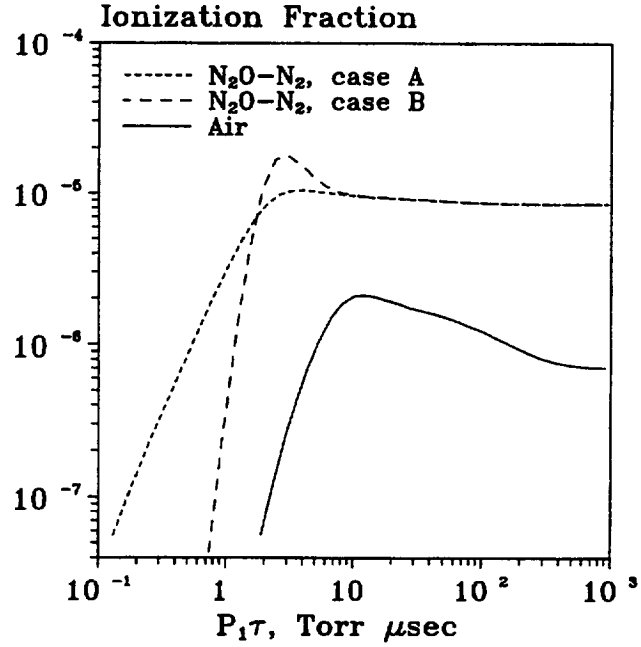

Figure B.3- 17. Ionization fraction distribution behind the shock in air and in an N_2O-N_2=53:47 mixture.

For the shock velocities u_s=2-4 km/s, the calculated ionization rise times in the N_2O-N_2 mixture are always much shorter than in air. Therefore, we must conclude that the long ionization rise times observed in the NASA Ames experiments cannot be due to the relaxation processes in the flow behind the shock. The observed ionization time, up to few tens of microseconds, must be pertinent to a particular method of conductivity measurements that involve strong perturbation of the flow by the applied electric field and the induced current.

Another observation made in the calculations was that, at these conditions, the flow reaches almost complete thermodynamic equilibrium at the temperature T_{eq} soon after the shock arrival (less than 1 μs), which is expected at these high temperatures and pressures.

In addition to calculation of vibrational distribution functions of the diatomic air species and species concentrations, the OSU 1-D nonequilibrium flow code also allows calculation of the electron swarm parameters of the high-enthalpy gas flows, including its electric conductivity. The conductivity is evaluated using the EEDF calculated by the Boltzmann solver and the

experimental values of the electron transport cross-sections for N_2, O_2, NO, N, and O as functions of electron energy. The comparison of the equilibrium electric conductivity of air calculated by the code with available experimental data and other theoretical calculations shows good agreement. In addition to showing it reaches the equilibrium value behind the shock extremely fast, the results of the 1-D conductivity calculations for the NASA Ames experiment conditions also show that the ionization level is unlikely to be enhanced by the applied fairly low electric field.

The estimated reduced electric field in the core flow (outside the sheath and the boundary layer) did not exceed $E/N \sim 0.5 \cdot 10^{-16}$ V·cm^2, which is more than an order of magnitude lower than the breakdown threshold. Even for the applied voltage of V=400 V, the electron temperature exceeds the gas temperature (T~5,500-6,000 K) by only about 500 K. The resultant field-induced (electron impact) ionization rate in the core flow is minute compared to the thermal ionization rate in process (by 15 orders of magnitude) (Ref. 32). However, due to the large current drawn (current density up to j=100 A/cm^2), the ohmic heating of the flow may be substantial (also reaching a few hundred degrees K), which may result in a noticeable conductivity increase. Figures B.3- 18 and B.3- 19 compare the calculated flow conductivity with the experimentally measured "pseudo-conductivity," defined as:

$$\sigma = \frac{jd}{U} \qquad \text{(B.3- 13)}$$

where j is the current density, U is the applied voltage, and d=3.1 cm is the interelectrode distance. First, at P_2=2 atm and U=400 V, which is close to the maximum quasi-steady-state voltage applied in the experiment, the ohmic heating results in about 15 - 25% conductivity increase. As expected, at P_2=13 atm the effect is much smaller since the ohmic heating term is proportional to the factor $\sigma E^2/\rho u$, where ρ is the gas flow density. Second, one can observe that at the small-applied voltage, the measured pseudo-conductivity is much smaller than the theoretical value, approaching and sometimes exceeding it as the voltage increases.

One can easily show the NASA Ames data demonstrates the presence of the field-induced ionization in the test section between the electrodes. Let us take as an example a run at P_2=2 atm, u_s=4.5 km/s T_{eq}=5575 K, $n_e/N=0.88 \cdot 10^{-4}$ (see Figure B.3- 20). The flux of electrons entering the test section with the flow is $Q=n_e d^2(u_s-u_2) \cong 8.7 \cdot 10^{20}$ 1/s, where $u_2 \cong 0.6$ km/s is the velocity of the compressed gas with respect to the shock velocity. If all of the electrons are removed from the flow by the applied field, the current would reach maximum. The maximum current that can be obtained without additional ionization produced in the test section is $I_s=eQ$=140 A.

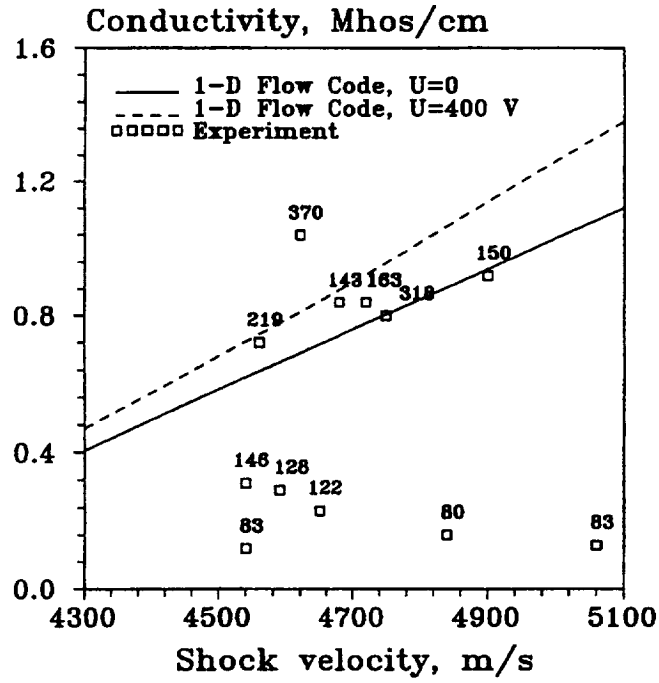

Figure B.3- 18. Calculated and experimental flow conductivity in an N_2O-N_2=53:47 mixture. P_2=2 atm.

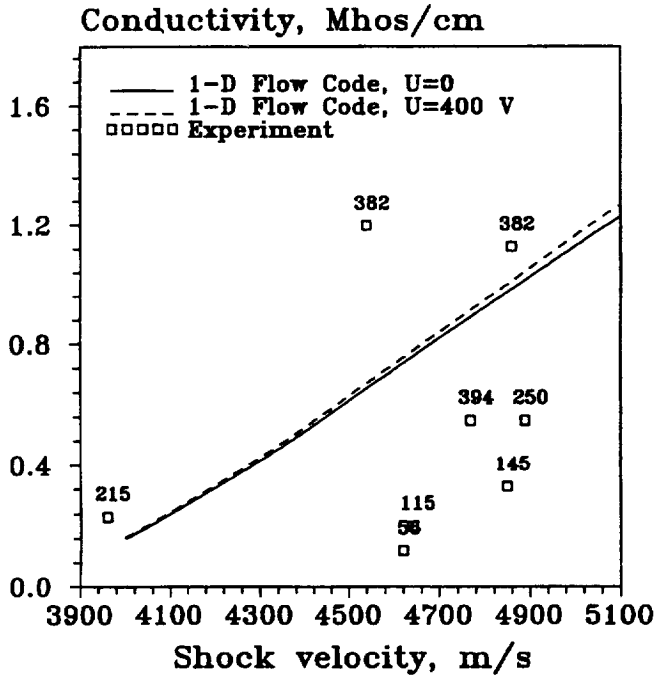

Figure B.3- 19. Calculated and experimental flow conductivity in an N_2O-N_2=53:47 mixture. P_2=13 atm.

Most strikingly, this value of the current (which corresponds to the saturation current of the nonself-sustained Thomson discharge) (Ref. 32), can be obtained only at enormously high-applied voltage (Ref. 33),

$$U_s = \frac{1}{2}\left(\frac{eQd}{\mu_+ \varepsilon_0}\right)^{1/2} \cong 10^7 \text{ V} \qquad \text{(B.3- 14)}$$

In Equation (B.3- 14), $\mu_+ \sim 10^{-3}$ m^2/V/s is the ion mobility. The fact the currents measured by the NASA Ames group at P_2=2 atm exceeded 1,000 A at voltages of 300-400 V (see Figure B.3- 21) unambiguously shows that some additional ionization definitely occurs in the interelectrode region. Since we have already shown the core flow reduced electric field is far too low to produce any electron impact ionization, the boundary layer/sheath region is left as the only place where this ionization may occur. Thus, the electric discharge in the test section is clearly an intermediate case between a completely nonself-sustained Thomson-type discharge and a completely self-sustained discharge (such as a regular glow discharge). It is sustained both by the external ionization source (electrons arriving with the flow) in the core flow and by the electron production in the near-electrode regions where the breakdown certainly must occur.

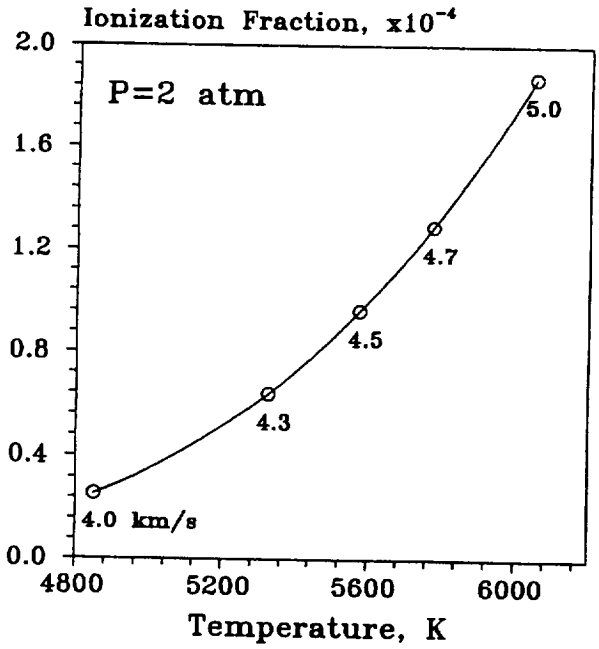

Figure B.3- 20. Equilibrium ionization fraction as a function of temperature and the shock velocity in an N_2O-N_2=53:47 mixture. P_2=2 atm.

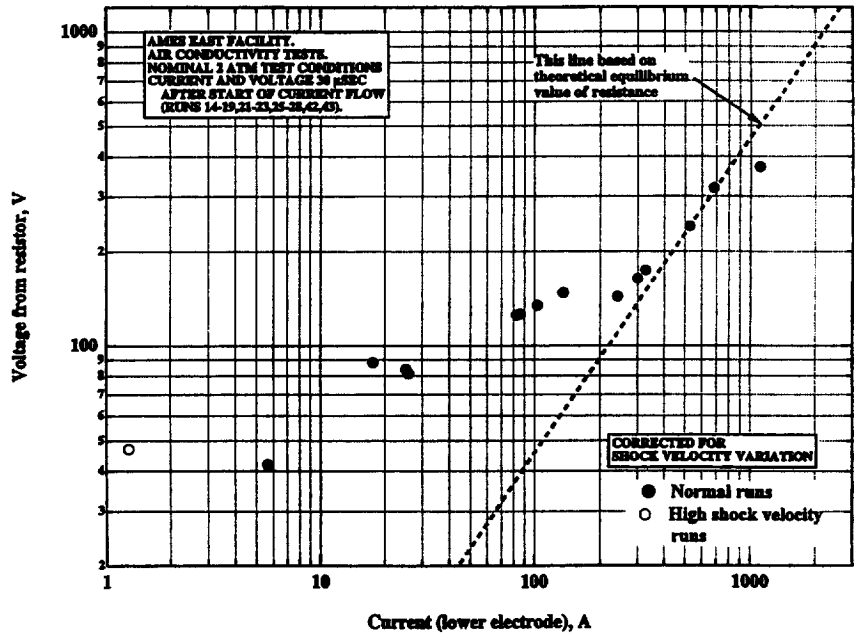

Figure B.3- 21. Applied voltage as a function of the induced current in the NASA Ames experiment. P=2 atm.

Based on these elementary arguments, we can conclude that the core flow, like any discharge sustained by external ionization (e.g., by UV radiation or by e-beam), should be fairly stable with respect to the ionization instabilities since there is no direct feedback between the electric field and the ionization rate for the core flow. The ohmic heating of the core flow, potentially leading to the greater thermal ionization, might be controlled by the supersonic flow expansion. On the contrary, the sheath region (where ionization is sustained by the strong electric field) may be unstable. In addition, ohmic heating of the slow flowing boundary layer is much more difficult to control. The core flow, where the electric field is far too weak to sustain the electron production, serves as a stabilizing factor so that an arc filament, even if developed in the sheath, cannot propagate across the channel. This, as well as a quite short flow residence time in the test section (<10 μs), may explain why breakdown was not observed in the NASA Ames experiments. The situation may be quite different if the electrodes are sectioned and not only transverse but also axial electric fields are applied (to reduce the Hall current). This will generate strong axial field regions (between the edges of the closely spaced adjacent electrodes) located in potentially unstable high electric field sheath regions. For this reason the "axial" arcing between sectioned electrodes located on the same wall appears to be much more probable than the "transverse" arcing which was not observed by NASA Ames.

The qualitative interpretation of the NASA Ames pseudo-conductivity measurements appears to be quite straightforward and is mostly consistent with the conclusions suggested by the NASA Ames group. At low applied voltage, most of the voltage drop must occur in the sheath to

sustain higher electric field and ionization. In this regime, space charge in the sheath is shielding the core flow so the electric field might be actually very low and much lower than the U/d ratio. This reason is why the conductivity determined from Equation (B.3- 13) is much lower than the theoretical value for the core flow (see Figures B.3- 18 and B.3- 19) where the applied voltage is indicated beside the pseudo-conductivity value. As the voltage increases, the sheath voltage drop becomes an increasingly smaller fraction of the applied voltage, and the pseudo-conductivity value should be approaching the theoretical value. Since it is clear from Figures B.3- 18 and B.3- 19 the ohmic heating of the flow cannot explain the higher-than-equilibrium values of the pseudo-conductivity, especially at high pressure, and the electron concentration in the core flow is at its equilibrium value, the effect of the current propagating along the hot sidewall boundary layers might be a likely explanation.

The anomalously long ionization rise times (see Figure B.3- 14) are at least partially due to the finite size of the electrodes. It takes the shock about 7 μs to pass the electrodes, and this time might be somewhat increased due to the edge effects. However, the rise time tends to decrease as the pressure goes up (see Figure B.3- 14). The two main reasons for this long rise time are the thermal boundary layer buildup behind the shock (as has been pointed out by the NASA Ames group) and also sheath formation, which is controlled by the drift of electrons and ions in strong fields near electrodes and the nonequilibrium ionization. The latter process also controls the electric field value in the core flow.

B.3.4.2 Two-Dimensional Calculations

To analyze the effects of the boundary layer, we have also attempted 2-D simulation of a propagating shock wave using the Navier-Stokes flow code developed at OSU (Ref. 34). Complete understanding of the ionization kinetics in the near-electrode regions of the test section of the NASA Ames experiments needs analysis of coupled boundary layer and sheath effects, which requires solution of chemical kinetics equations and the Poisson equation for the electric field. For example, it is not clear what the electron concentration near the cathode would be. It might be affected by the boundary layer temperature as well as the strong repulsion from the cathode in a strong electric field. However, the effects of chemical reactions and electromagnetics were not included in the present simulations of very strong shocks. The purpose of this study was to determine the appropriate formulation (consistent set of initial and boundary conditions) that would allow a further numerical modeling of strong propagating shocks. This is a crucial first step following which effects of chemical reactions and electromagnetics can be included with confidence. Prescribing appropriate boundary conditions at the inlet of the skimmer tube is perhaps the most important issue in the formulation.

Shock propagation through a tube of length 45 cm (corresponding to the length of the skimmer tube and the electrode region in the NASA Ames experiment) containing N_2 was investigated. One of the main objectives was to reproduce the energy loading to the driver gas to match the shock velocity and static pressure (obtained experimentally) at the inlet of the skimmer tube,

which is accomplished by the prescription of a stagnation pressure and stagnation temperature. In these simulations, it is assumed the diaphragm is at the inlet of the skimmer tube. These stagnation conditions would be related to temperature and pressure at the inlet of the skimmer tube using the following relationships:

1. The inlet velocity is obtained by setting $dw/dx = 0$ at the inlet, where w is the axial component of the flow velocity
2. $T_0 = T_{inlet} + w_{inlet}^2/2c_p$
3. $P_0/P_{inlet} = (T_0/T_{inlet})^{\gamma/\gamma-1}$

The first derivative of all dependent variables in the radial direction is set to zero along the wall and the centerline. The second derivative of all dependent variables in the axial direction is set to zero at the exit of the tube. Prior to the rupture of the diaphragm (initial conditions), the N_2 gas in the driven section is assumed to be stationary and at room temperature. This set of boundary and initial conditions allows a realistic study of a shock wave propagating into the driven tube after the rupture of the diaphragm. Since the inlet boundary conditions are not held constant, the time-marching procedure allows one to study the relaxation of temperature, velocity, and pressure behind the shock with the passage of time. Prescribing the experimental conditions at the inlet plane as boundary conditions is incorrect, as the relaxation phenomena cannot be studied.

The computational domain extends from the centerline to the inner wall of the skimmer tube (and electrodes) in the radial direction and from the inlet of the skimmer tube to the about 3-cm beyond the electrodes. A 300×18 grid was used in these computations. Since the pressure ratio between the driver section and the driven section is about 350, a large number of grid points are necessary to adequately resolve the gradients encountered at the shock front. The problem of studying a propagating shock wave is it requires an adaptive grid technique, wherein clustering of grids in regions of high gradients (i.e., along the shock front) can be achieved (Ref. 16). However, this greatly complicates the transformed governing equations. Additionally, the Courant condition would necessitate the use of extremely small time-steps for such highly nonuniform grids, thus greatly increasing the computational time. In this simulation, a uniform, nonstaggered, and fixed grid was used. Oscillations are typical of solutions obtained using fixed grid methods; however, the solutions obtained using fixed grids compare very well with solutions obtained using adaptive grids (Ref. 34). Simulation of shocks with steep pressure ratios requires a considerable amount of parametric studies to access the influence of grid size and artificial dissipation on the quality of the solution.

The results for the case of the driver tube were 2 atm and the driven tube being 5.2. Centerline profiles of pressure, temperature, and gas velocity are shown in Figures B.3- 22 through B.3- 24. Each of the figures shows profiles at three instants of time as the shock propagates through the tube. The pressure profile shows the drooping characteristics expected following the rupture of the diaphragm (Ref. 35). The velocity profiles follow the pressure profile; therefore, the pressure

drop allows the acceleration of the gas behind the shock. The velocity profile also shows the relaxation of the gas velocity far downstream of the shock. The oscillations seen along the shock front are due to the simulations being carried out on a fixed grid and use of central differencing of the spatial derivatives.

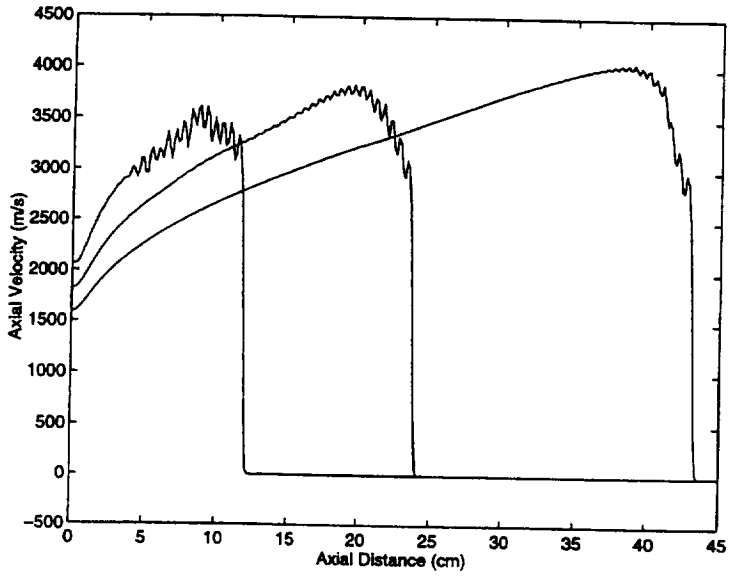

Figure B.3- 22. Variation of gas velocity along the centerline at three different instants of time.

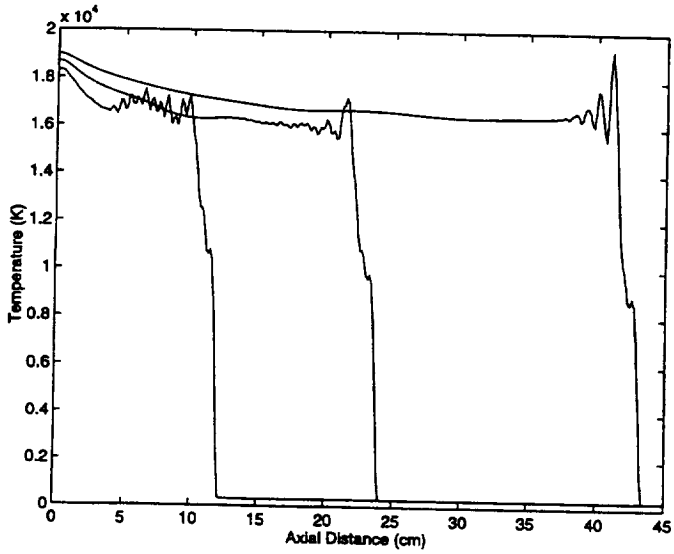

Figure B.3- 23. Variation of temperature along the centerline at three different instants of time.

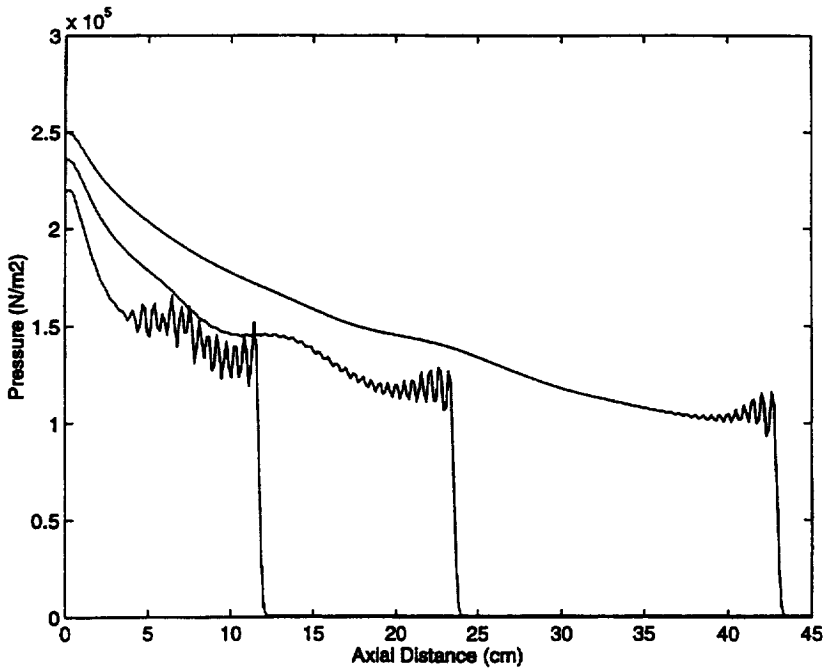

Figure B.3- 24. Variation of pressure along the centerline at three different instants of time.

The pressure ratio along the shock front predicted by the simulations is about 1.3 atm as against the pressure of about 2.2 atm reported in the experiments. The reasons for this are as follows:

1. In the experiment, the diaphragm is ruptured far from the inlet of the skimmer tube, whereas in the simulations, the diaphragm is assumed to be at the inlet of the skimmer tube. This was done because simulating the entire region from the diaphragm to the electrode section would require an enormous amount of computational time. The drop in pressure is steepest close to the location of the diaphragm; however, as the shock establishes itself, the pressure remains fairly constant at a pressure lower than the driver tube pressure. The simulations predict this behavior well.

2. The exact energy loading of the gas following the rupture of the diaphragm could be much higher in the experiment. This would also lead to the simulations predicting a lower pressure ratio along the shock front.

3. Artificial dissipation, though at a bare minimum in this simulation, could affect the results. It is difficult to evaluate the effect of dissipation in such simulations. However, a detailed parametric study on the effects of various levels of dissipation was conducted. The lowest possible level of dissipation, which allowed stable time marching without strong oscillations, was used in this study. Past experience has

shown that even minimum levels of artificial dissipation can affect the accuracy of the solution by about 5 or 10%.

Finally, Figures B.3- 25 and B.3- 26 show contour plots of the axial velocity and the translational temperature near the test section. Unlike in steady-state supersonic flows, the boundary layer behind the shock is initially cold since the shock front does not penetrate into the viscous layer. It takes quite a long time for the thermal boundary layer to heat up. For example, the flow in the test section at the pressure of 1.3 atm does not reach the steady state for at least 40 μs after the shock arrival (see Figures B.3- 25 and B.3- 26). This confirms the explanation for the long ionization rise time we suggested in the previous section. Further development of the OSU Navier-Stokes code, which will extend its ability to model high-pressure discharges in reacting flows behind strong ionizing shocks, is currently underway. It is expected to provide new insight into the problem of stability and efficient control of such environments.

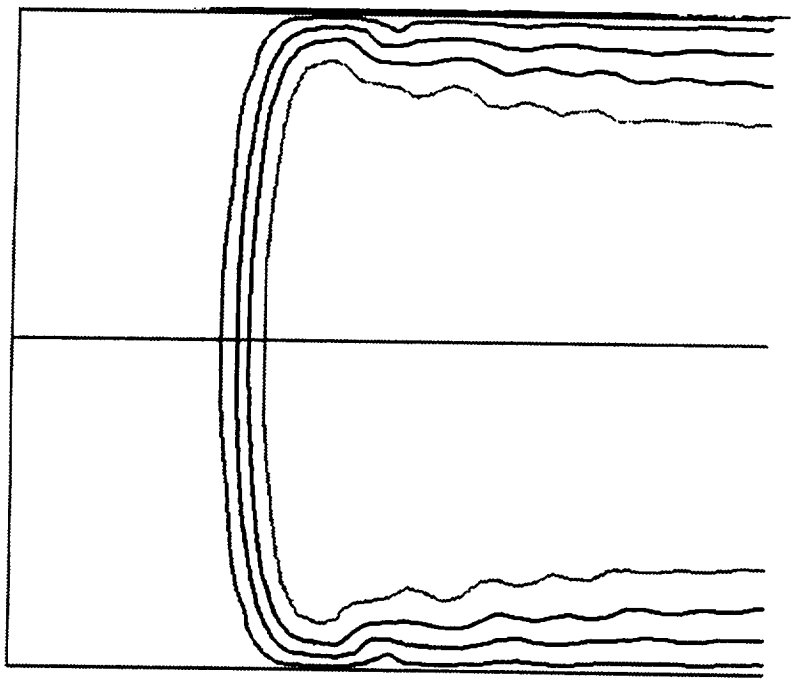

Figure B.3- 25. Contour plot of the axial component of gas velocity near the test section. Outermost contour represents a velocity of 314 m/s; innermost contour represents a velocity of 2,519 m/s; the increment is 725 m/s. The region shown in the figure is 7.75 cm long.

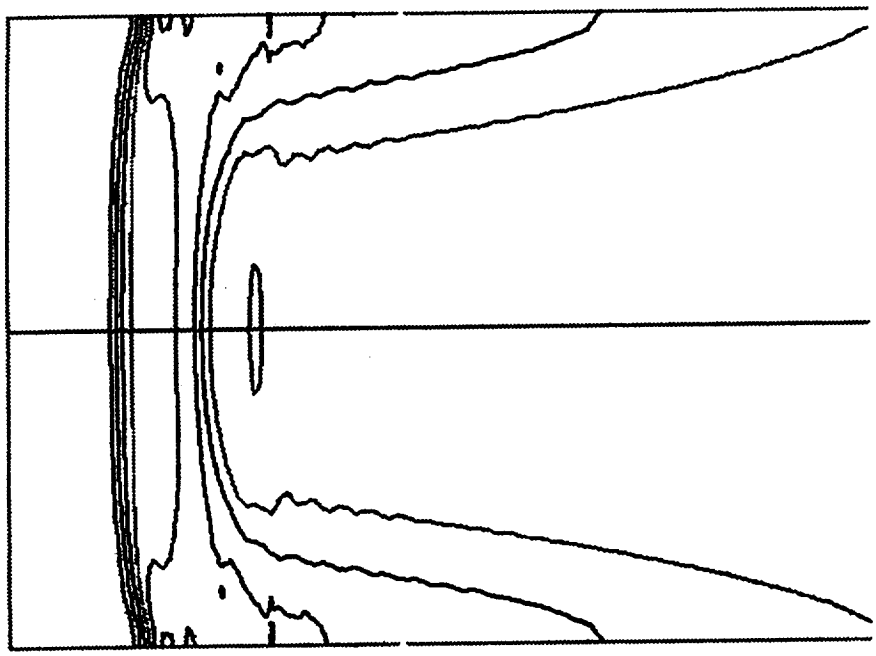

Figure B.3- 26. Contour plot of the gas temperature near the test section. Outermost contour represents a temperature of 2,000 K; innermost contour represents a temperature of 16,000 K; the increment is 2,000 K. The region shown in the figure is 15.15 cm long.

B.3.4.3 Conclusions

1-D and 2-D analysis of kinetics of vibrational relaxation, chemical reactions, and ionization behind the normal shock waves in air and in the N_2O-N_2 mixture showed:

1. In the shock tube ionization experiments performed at NASA Ames, the core flow reached vibrational, chemical, and ionization equilibrium extremely fast (over a period of less than 1 μs). The observed long ionization rise time cannot be explained by the relaxation phenomena. 2-D modeling suggests this anomalously long delay of ionization is due to the slow heating of the boundary layer behind the shock.
2. The estimated reduced electric field in the core flow is very low ($E/N \leq 0.5 \cdot 10^{-16}$ $V \cdot cm^2$) even at the lowest pressure of P_2=2 atm and cannot result in any nonequilibrium ionization.
3. The measured current-voltage characteristic of the discharge in the flow indicates the presence of electron impact ionization in the sheath regions.
4. The core flow, where ionization is not self-sustained, is a stabilizing factor. The sheath regions, operating in a postbreakdown regime, are inherently unstable. The

most likely instability scenario appears to be the arcing between the adjacent same-wall electrodes due to axial component of the electric field.

5. The measured pseudo-conductivity is lower than the theoretical core-flow value at the low voltage (due to the voltage drop in the sheath) but exceeds the theoretical equilibrium limit (most likely due to the hot sidewall boundary layer currents after the steady-state temperature distribution is reached)

B.3.5 Summary

OSU's model and numerical technique have been tested extensively to simulate a wide variety of discharges. The arcjet thruster and the plasma torch differ in geometries, operating pressures, and gas compositions. Nevertheless, the model and the numerical scheme have been able to successfully simulate these discharges with reasonable accuracy. It is important to mention that there are no adjustable constants in OSU's formulation; therefore, it is a truly predictive tool. Comparison with experiments for both cases studied show excellent agreement. The generality, stability, and accuracy of the numerical method/model make it a valuable tool to study reacting and plasma flows.

B.3.6 References

1. Rosa, R.J., *Magnetohydrodynamic Energy Conversion*, McGraw-Hill, New York, NY, 1968.

2. Oran, E.S. and Boris, J. P., *Numerical Simulation of Reactive Flow*, Elsevier, 1987.

3. Briley, W.R. and McDonald, H. *Journal of Computational Physics*, Vol. 24, 1977, p. 372-397.

4. Aithal, S.M., "Numerical Simulation of Plasma and Reacting Flows," doctoral dissertation, Ohio State University, Columbus, OH, March 1997.

5. Isaacson, E. and Keller, H.B., *Analysis of Numerical Methods*, Wiley, New York, 1966.

6. Babu, V.; Aithal, S.M.; and Subramaniam, V.V., "Numerical Simulation of a Hydrogen Arcjet," *J. Propulsion & Power*, Vol. 12, No. 6, Nov.-Dec. 1996.

7. Aithal, S.M.; Subramaniam, V.V.; and Babu, V., "Effects of Arc Attachment on Arcjet Flows," AIAA Paper 96-3295, the 32nd AIAA/ASME/SAE/ASEE Joint Propulsion Conference, July 1-3, 1996, Lake Buena Vista, FL.

8. Roache, P.J., *Computational Fluid Dynamics*, Hermosa, Albuquerque, NM, 1972.

9. Pobst, J.A.; Wysong, I.J.; and Spores, R.A., "Laser-Induced Fluorescence of Ground State Hydrogen Atoms in an Arcjet Plume," IEPC Paper 95-28, the 24th International Electric Propulsion Conference, Sept. 19-23, 1995.

10. Storm, P. V. and Cappelli, M. A., "High Spectral Resolution Emission Study of a Low Power Hydrogen Arcjet Plume," AIAA Paper 95-1960, the 26th AIAA Plasmadynamics and Lasers Conference, June 19-22, 1995, San Diego, CA.

11. Storm, P.V. and Cappelli, M.A., "Fluorescence Velocity Measurements in the Interior of Hydrogen Arcjet Nozzle." *AIAA Journal,* Vol. 34, Mar. 1996, p. 853-855.

12. Boyd, I., "Monte Carlo Simulation of Non-Equilibrium Flow in Low Power Hydrogen Arcjets," AIAA Paper 96-2022, the 27th AIAA Fluid Dynamics Conference, June 17-20, 1996, New Orleans, LA.

13. Butler, G.W.; Boyd, I.D.; and Cappelli, M.A. "Non-Equilibrium Flow Phenomena in Low Power Hydrogen Arcjets," AIAA Paper 95-2819, the 31st AIAA/ASME/SAE/ASEE Joint Propulsion Conference and Exhibit, July 10-12, 1995, San Diego, CA.

14. Hayes, W.D. and Probstein, R. R., *Hypersonic Flow Theory*, Academic Press, New York, NY, 2nd edition, 1966.

15. Hargus, Jr., W.A. and Cappelli, M.A., "Mass Flux Measurements in the Plume of a Low Power Arcjet Nozzle," AIAA Paper 96-3190, the 32nd AIAA/ASME/SAE/ASEE, Joint Propulsion Conference, July 1-3, 1996, Lake Buena Vista, FL.

16. Dowden, J.; Kapadia, P.; and Fenn, B., "Space Charge in Plasma Arc Welding and Cutting" *J. Phys. D: Applied Phys.* Vol. 26, 1993.

17. Pagan, J. M., doctoral dissertation, Ohio State University, Columbus, OH, June 1996.

18. Lin, S.C. and Tear, J.D., *Physics of Fluids*, Vol. 6, 1963, p. 355.

19. Park, C., *Nonequilibrium Hypersonic Aerodynamics*, Wiley, New York, NY, 1990.

20. Treanor, C.E.; Adamovich, I.V.; Williams, M.J.; and Rich, J.W., *Journal of Thermophysics and Heat Transfer,* Vol. 10, 1996, p. 193.

21. Adamovich, I.V.; Rich, J.W.; and Nelson, G.L., AIAA Paper 96-2347, June 1996.

22. Adamovich, I.V.; Macheret, S.O.; Rich, J.W.; and Treanor, C.E., *AIAA Journal*, Vol. 33, 1995, p. 1064.

23. Adamovich, I.V.; Macheret, S.O.; Rich, J.W.; and Treanor, C.E., *AIAA Journal*, Vol. 33, 1995, p. 1070.

24. Macheret, S.O. and Rich, J.W., *Chemical Physics*, Vol. 174, 1993, p. 25.

25. Macheret, S.O.; Fridman, A.A.; Adamovich, I.V.; Rich, J.W.; and Treanor, C.E., AIAA Paper 94-1994, June 1994.

26. Frohn, A. and De Boer, P.C.T., *Physics of Fluids Supplement I*, 1969, p. I54.

27. Manheimer-Timnant, Y. and Low, W., *Journal of Fluid Mechanics*, Vol. 6, 1959, p. 449.

28. Niblett, B. and Blackman, V.H., *Journal of Fluid Mechanics*, Vol. 4, 1958, p. 191.

29. S.C. Lin; R.A. Neal; and W.I. Fyfe, *Physics of Fluids*, Vol. 5, 1962, p. 1633.

30. Biryukov, A.S.; Yu, A.; Volkov, Demin; A.I., Kudryavtsev; E.M., Kulagin; Sobolev, N.N.; and Shelepin, L.A., *Soviet Physics – JETP*, Vol. 41, 1975, p. 834.

31. Baalbaki, Z.; Teitelbaum, H.; Dove, J.E.; and Nips, W.S. *Chemical Physics*, Vol. 104, 1986, p.107.

32. Thomson, J.J. and Thomson, G.P., *Conduction of Electricity Through Gases*, Vol. 1, University Press, Cambridge, MA, 1928.

33. Adamovich, I.; Hiltner, J.; Macheret, S.; and Rich, J.W., AIAA Paper 92-3028, June 1992.

34. Babu, V.; Aithal, S.M.; and Subramaniam, V.V., *AIAA Journal*, Vol. 12, 1996, p. 1114.

35. Anderson, D. A.; Tannehill, J. C.; and Pletcher, R. H., *Computational Fluid Mechanics and Heat Transfer*, Taylor & Francis, 1984.

APPENDIX C

CONTENTS

SECTION C.2

TABLES

SECTION C.3

FIGURES

TABLES

SECTION C.4

FIGURES

TABLES

APPENDIX C. SEED STUDIES

In magnetohydrodynamic (MHD) accelerators, a seed material is normally required to increase the ionization potential of the plasma, so as to increase its electrical conductivity to provide a source of electrons through ionization and enhance the electrical conductivity. This appendix addresses two types of seeding materials, fullerenes and alkali metals. Fullerenes are a class of high molecular weight carbon molecules that have been investigated as propellants for ion thrusters as noted in Section C.1. The more traditional MHD seed material, alkali metal, has been used in MHD accelerator and power generation experiments since high temperature MHD research began. The cost and availability of the various alkali metal seed materials is discussed in Section C.2. Unseeded MHD accelerators have been proposed for wind tunnel applications to avoid the contamination of the flow with the alkali metal material. The effects of the seed material on combustion in propulsion testing experiments must be considered if the propulsion experiments are to simulate actual flight performance, which is the subject of Section C.3. Finally, in Section C.4, the issue of electron attachment to oxygen and other species in cesium seeded air for MHD operating conditions is addressed. Under some conditions, electrons can attach to atomic and molecular species to form negative ions resulting in the loss of free electrons and the reduction of electrical conductivity.

APPENDIX C, SECTION C.1

C.1 CARBON-60 AND OTHER FULLERENES

MSE has investigated the use of fullerenes as a seed to enhance the ionization characteristics of an MHD accelerator. The properties of fullerenes, including their high mass, low ionization potential, and extreme resilience, suggested that these molecules could be an excellent source of ions for ion thrusters (Refs. 1, 2, 3, 4). Fullerenes were proposed as a possible seed material by MSE since seed materials for MHD accelerators require some of the same characteristics as those reported for fullerenes in the ion thruster application. However, this study found that fullerenes would decompose and combust in the high-temperature air-operating environment of MHD accelerators.

Although fullerenes may be promising for other MHD applications with a less harsh environment, they are not practical for the high performance air accelerators needed for hypersonic propulsion testing applications. However, designer molecules being developed from fullerenes may have characteristics that allow them to be used in the MHD accelerator environment. Thus, future studies may need to revisit fullerenes to assess their viability in other applications. The MSE study on the use of fullerenes for this application is further reported in *The Properties, Behavior and Applications of Fullerene Molecules* (Ref. 5).

C.1.1 Overview

Fullerenes are a recently discovered class of carbon molecules that have high molecular weight, a high degree of structural symmetry, remarkable impact resilience, an even number of carbon atoms, and unusual chemical properties (Refs. 6, 7, 8, 9). Fullerenes are the third form of pure carbon; the other two pure forms are diamond and graphite. The best known and most prevalent representative of this class is an isomer of carbon 60 called Buckminster Fullerene. This molecule possesses a symmetry similar to a geodesic sphere and is named for the architect and scientist, Richard Buckminster Fuller (1895-1983), who first described the geodesic dome structure. Typically, fullerene structures have 12 pentagons, with differing numbers of hexagons and an even number of carbon atoms. The pentagons allow the curvature and eventual closure of the surface upon itself. The second most prevalent fullerene is the C_{70}. The lighter C_{20} is widely accepted as the smallest fullerene; quantum mechanical calculations project fullerenes as large as C_{600}. Bucky tubes (hollow carbon tube-like fullerenes) and bucky-onions (concentric spherical shells of carbon) have also been observed.

Aside from its chemical novelty, C_{60} occurs naturally in a coal-like mineral called shungite and a glassy rock called fulgurite and has been noted in frozen gas matrices of diffuse interstellar material. Buckminster fullerene is of interest to the astrophysics community because it appears it may be created in the interior of stars during supernova explosions. It is of interest to the aerospace community due to its relatively low ionization potential and high molecular weight, making it an interesting candidate as a propellant for ion propulsion engines. These properties also suggested that it might have some application to MHD accelerators and generators.

C.1.2 Properties of Carbon-60 Fullerenes

C.1.2.1 General

C_{60} is a solid brown-black powder at room temperature but is yellow when presented as a thin film. Fullerite, C_{60} crystals, are primarily a face-centered cubic structure; however, approximately 20% of the solid is also hexagonal-close-packed that easily converts to face-centered cubic with thermal annealing in vacuum (Ref. 1).

Careful storage and treatment of C_{60} is necessary to ensure its purity since it reacts readily with O_2, is decomposed by ultraviolet (UV) rays, adsorbs gases, and tenaciously holds solvents. There is no reaction between fullerenes and stainless steel, molybdenum, alumina, boron nitride, aluminum nitride, and quartz. One characteristic to note is the superconductive behavior of an alkali metal-doped C_{60} with a transition temperature of 42.5 K for ($Rb_{2.7}$ $Tl_{2.2}$ C_{60}).

All 60 carbon atoms in the fullerene are equivalent as proven by nuclear magnetic resonance measurements. C_{60} arranges atoms so symmetrically that the strain of closure is equally distributed. It is the most symmetric molecule possible in 3-dimensional Euclidean space, i.e., the roundest molecule. Edgeless, chargeless, and unbound, the molecule spins freely more than 100 million times per second. When deposited on a crystalline surface, they pack as regularly as billiard balls. C_{60} crystallizes in a face-centered cubic lattice in which the crystals are as soft as graphite. When squeezed to less than 70% of their initial volume, calculations predict they become even harder than diamond. However, when the pressure is relieved, they are observed to spring back to their normal volume. Thrown against steel surfaces at speeds somewhat greater than 17,000 miles per hour (about the orbital speed of the U.S. Space Shuttle), they are incredibly resilient since they simply bounce back (Ref. 9). There is no experimental evidence of impact-induced fragmentation, even at impact energies exceeding 200 electron volts (eV).

C_{60} readily forms both positive and negative ions and long-lived multiple ions up to C_{60}^{6+}. Due to their aromatic design, the multiply charged species do not succumb to coulomb explosion and are strong enough to form free-standing films due to strong van der Waals forces within the solid.

C.1.2.2 Ionization Potential

The most consistently reported first ionization potential for C_{60} is 7.61 eV, however, it has been reported in experiments as high as 7.8 eV with a second ionization potential of 16.4 eV (Ref. 1). As experimental work continues, these values may be refined.

C.1.2.3 Cross Section

The peak ionization cross-section of C_{60} is estimated to be 59.8×10^{-16} cm^2, occurring at 52 eV, which is significantly lower than estimated by both the additivity rule and the polarizability correlation (Ref. 1). The cross section for single ionization is possibly lower because fragmentation processes are present even at 45 eV electron energies, and the additivity rule breaks down when a large number of collisions lead to excitation rather than ionization of the fullerene. Consequently, this cross section is the best estimate and possibly will be refined in future studies. Inelastic collision cross section has not been reported.

C.1.2.4 Electron Attachment

C_{60} has a large cross section for negative ion formation even at electron energies as high as 14 eV. Due to the large cross section for anion formation, electron attachment can dominate over positive ion formation allowing C_{60} to behave as an electron scavenger.

C.1.2.5 Sublimation

Fullerenes will evaporate or sublime easily by comparison to particles of diamond or graphite. The fullerene, or derivatives of fullerene, exist as molecules that are relatively volatile in comparison with other forms of carbon (Ref. 10). However, C_{60} sublimates at a relatively low temperature of 800 K with a vapor pressure of 2 millitorr and a heat of sublimation of 7.9 kilojoules per mole (kJ/mol) indicating the likelihood of the existence of a C_{60} liquid phase is minimal (Ref. 1). C_{60} will sublimate kJ without fragmentation (Ref. 2).

C.1.2.6 Combustibility

In the absence of O_2 and at low pressure, C_{60} degrades, as shown by spectroscopic data, by successively fragmenting into smaller fullerenes with even numbers of carbon atoms. Over time, at temperatures above 1,073 K, C_{60} will decompose through the reaction sequence (Ref. 1).

$$C_{60} \rightarrow C_{58} + C_2$$ (At low pressure and in the absence of O_2, the cage successively closes.)

$$C_{58} \rightarrow C_{56} + C_2$$

$$C_{56} \rightarrow C_{54} + C_2$$

The reaction mechanism for fullerenes in the presence of O_2 is quite different than without O_2. In O_2, the fullerene cage does not close when decomposition and combustion begin at approximately 573 K.[1] In this case, the mechanism in which the fullerene fragments is unpredictable. The O_2

1. Personal Communication, Stephanie Leifer, Ph.D., California Institute of Technology, Pasadena, CA.

molecules readily attach to any open carbon bonds, possibly preventing the closure of the cage, and the dome structure basically crumbles.

The reactivity of C_{60} with O_2 is temperature dependent. It will not noticeably react in ambient air. Noticeable reaction will occur at temperatures beyond approximately 573 K, and reactivity increases and becomes appreciable as the temperature rises.[2]

C.1.2.7 Critical Decomposition Temperature

Due to solid-state unimolecular decay, fullerenes in a vapor phase degrade between 1,073 and 1,173 K with an activation energy of 266± 9 kJ/mol in vacuum, which is comparable with previously published energies (complete degradation within this range is implied but not specifically stated). Simulations predict rate constants with a much higher activation energy than the experimental data reveals, suggesting the possibility of a second, low-barrier decay channel of one or more ring rearrangement isomerization reactions prior to a C_2 fragmentation. The maximum vapor pressure that can be achieved in the feed system is dictated by an upper bound temperature (a point just prior to degradation) i.e., at 1,073 K the vapor pressure of C_{60} is approximately 1 torr (Ref. 1). Experimental work using higher pressures was not available through literature searches or discussions with researchers.

C.1.3 Availability and Cost

C.1.3.1 Producibility

Generation of graphitic soot comprising of C_{60} and C_{70} fullerenes may be easily accomplished. The process consists of evaporating an electrically conductive carbon rod in an electric arc plasma in a tubular evaporator. The plasma is sustained between the carbon rod and a second electrically conductive carbon rod. Each of the carbon rods are aligned coaxially in the evaporator with at least one of the rods being moveable. An inert gas flows coaxially over the carbon rods at an inlet flow rate of at least about 0.02 cubic meters per hour (m^3/hr). The graphitic soot may then be collected from internal surfaces of the evaporator. By adjusting the vaporization conditions in the apparatus, the concentration of C_{60} may be changed by as much as 40% (See Footnote 2 on page 4). The fullerene compound can then be extracted with toluene or almost any nonpolar (aromatic) solvent (this compound is insoluble in polar solvents, moderately soluble in benzenes and haloalkanes, and highly soluble in naphthalenes since solubility increases with the increase in the number of carbon atoms within the solvent molecule) (Refs. 1, 9). To further purify, boiling and reflux will develop a fairly pure C_{60} precipitate since the C_{70} will stay in solution.

---

2. Personal Communication, Mark Anderson, NASA Jet Propulsion Laboratory, Analytical Chemist, Pasadena, Ca.

C.1.3.2 Cost

The current cost of C_{60} is exorbitant for most applications with 25 milligrams (mg) of C_{60} costing $75 and 100 mg of C_{60} costing $280 (Ref. 11). When the first large-scale applications of fullerenes are found, the manufacturing cost of C_{60} will probably fall close to that of aluminum, a few dollars per pound (Ref. 9).

C.1.4 Application of Carbon-60 for MHD Accelerators

For some applications, C_{60} could be an excellent seed material candidate due to its reasonably low ionization potential, resilience, and possible versatility due to doping. Thermal ionization of the plasma could occur within the temperature range of an MHD accelerator by introducing C_{60} to lower the plasma ionization potential. A fullerene with Cs or potassium (K) to further adapt the molecule to an MHD application might possibly be doped (addition of impurity elements to achieve a desired characteristic).

To be useful as a seed material in the MARIAH study MHD accelerators, C_{60} must remain stable for approximately 1 to 2 milliseconds (ms) within the MHD channel between 2,500 and 3,500 K and up to 100 atmospheres (atm) in an air-working fluid. However, the lack of high temperature thermal stability of fullerenes precludes their use in this environment. To avoid significant C_{60} degradation, the operating temperature within the apparatus must remain below 1,073 K, and the maximum vapor pressure should be at or below 1.0 torr. However, at 1 atm in the main working fluid (air), 1 torr would represent a seed fraction of only 0.1%, which is probably less than necessary for sufficient electrical conductivity. MHD accelerator applications presently under study may require pressures of 10 to 100 atm; however, current fullerene research appears to be focused on experimental systems of less than 1 torr. Consequently, information on systems using higher pressures, such as needed in this MHD application, is not currently available.

The ionization potential of C_{60} (7.6 eV), although reasonably low compared to species in high temperature air, is almost double that for Cs. This means that Cs at 3.894 eV would be more effective in lowering the plasma's thermal ionization potential in this application. Another disadvantage to fullerene use in MHD is its propensity for electron attachment. Negative fullerene ion production rates exceed those of positive ion production at electron energies below approximately 10 eV. High energy electrons need to be produced; however, the electron population can be depleted by fullerene anion formation. Due to the very large electron attachment cross section of C_{60} for electron energies up to 14 eV, an electron temperature of 10 eV or greater would be necessary for positive fullerene ion production rates to exceed that of negative ion production rates.

C.1.5 Summary

At this time, the available research results cited above indicate that the use of C_{60} as a seed material for this MHD application is not viable. Due to the decomposition of fullerene molecules at high temperature and the likely decomposition and combustion in high-pressure air, C_{60} would seem to be an unacceptable alternative for seeding in the typical MHD accelerator applications. Fullerenes degrade at temperatures below that necessary for MHD application, then readily react with O_2. Since the decomposition process proceeds by freeing C_2 molecules at very low pressures, it seems very probable that combustion would readily occur in typical air accelerator applications. Furthermore, high pressures are necessary for this application; however, adequate research has not been completed to pinpoint possible pit falls at pressures of 10 to 100 atm. The electron affinity of fullerenes is another reason why fullerenes are poor candidates for MHD seeding.

C_{60} could be considered for other MHD applications in which the conditions are more suitable for fullerene use. Also, the physical attributes of fullerenes may hold promise if the thermal degradation problem is circumvented, experimental work is completed on fullerenes at high pressures, advantageous MHD-related characteristics are developed from doping, and combustion characteristics are determined. The lower ionization potential, possibility of designer molecules, and stability of the molecule in suitable environments offer incentives for further investigation into other MHD applications.

C.1.6 References

1. Leifer, S., "Characterization of Fullerenes for Electrostatic Propulsion Associations," doctoral dissertation, California Institute of Technology, Pasadena, CA.

2. Takegahara, H. and Nakayama, Y., "C_{60} Feasibility Study on Application to Ion Thruster," AIAA Paper 95-2665, *31st AIAA/ASME/SAE/ASEE Joint Propulsion Conference and Exhibit*, July 10-12, 1995.

3. Leifer, S.D. and Rapp, D., "Assessment of C_{60} as a Propellant Material for Ion Thrusters," *NASA Tech Brief*, Vol. 19, No. 5, Item #59, June 1995.

4. Anderson, J.R.; Fitzgerald, D.; Leifer, S; and Mueller, J., "Design and Testing of a Fullerene FR Ion Engine," *31st AIAA/ASME/SAE/ASEE Joint Propulsion Conference and Exhibit,* July 10-12, 1995, San Diego, CA.

5. Wagner, K., "Properties, Behavior, and Applications of Fullerene Molecules," MSE Technology Applications, Inc., Technical Report MSE-18, Apr. 1996.

6. Bunshah, R.F.; Jou, S.; Prakash, S.; and Doerr, H.J., "Production of Fullerenes by Electron Beam Evaporation," Patent Number 5,316,636, May 31, 1994.

7. Smith, R.L., *Fullerenes*, New York, McGraw Hill Book Company, 1993, pp 312-314.

8. Goran, S.M., "Method of Making Metal Fulleride," Patent Number 5,324,495, June 28, 1994.

9. Curl, R.F. and Smalley, R.E., "Fullerenes," *Scientific American,* Vol. 60, pp. 57, 60, Oct 1991.

10. Stephens, W.D., "Fullerene Rocket Fuels," Patent Number 5,341,639, Aug. 30, 1994.

11. Aldrich Chemical Company C60 Price List.

APPENDIX C, SECTION C.2

C.2 CESIUM, RUBIDIUM, AND POTASSIUM SEEDING MATERIALS

Potassium carbonate (K_2CO_3) has been the most commonly used seed for gas-phase MHD accelerators and generators. However, Cs and rubidium (Rb) both exhibit a lower ionization potential than K, resulting in higher performance for most applications. A study was completed for the MARIAH Project to evaluate the cost and availability of Cs for application to large-scale wind tunnels (Ref. 1). This study summarized the cost, availability, and safety data of three alkali seed materials (Cs, Rb, and K). The following paragraphs provide an overview of the properties, cost and availability, safety, and performance aspects of these seed materials that will lead to a recommended seed material choice. More information can be obtained in the noted report.

C.2.1 Physical Properties

C.2.1.1 Cesium Materials

Cesium metal is a silver-white, ductile metal with a hexagonal fracture. It is the most electropositive and most alkaline element. Cesium, gallium (Ga), and mercury (Hg) are the only three metals that are liquid at room temperature. Cesium reacts explosively with cold water and reacts with ice at temperatures above 116 °C. Cesium hydroxide, the strongest base known, attacks glass. Because of its great affinity for O_2, the metal is used as a getter in radio tubes. Theoretically, burning a pound of Cs in outer space will propel a vehicle 140 times as far as burning the same amount of any known liquid or solid materials. Synonyms for cesium carbonate (Cs_2CO_3) are dicesium salt and dicesium carbonate. It is a white powder that is quite deliquesce (to become liquid by absorbing moisture from the air). Cesium carbonate is hygroscopic (absorbing or attracting moisture from the air) and is extremely soluble in water, alcohol, and ether. Its mass composition is C 3.69%, Cs 81.58%, and O 14.73%.

Cesium oxide appears as green, yellow, and orange marbled chunks. The physical properties of cesium materials are tabulated in Table C.2- 1.

C.2.1.2 Rubidium Materials

Rubidium metal tarnishes rapidly on exposure to air, can spontaneously ignite in air, and reacts vigorously with halogens. Its chemical properties closely resemble K. The metal forms a series of solid solutions with K, Cs, and sodium (Na) and combines vigorously with Hg.

Rubidium is considered to be the sixteenth most abundant element in the earth's crust. Rubidium can be liquid at room temperature. It is a soft, silvery white metallic element of the alkali group

Table C.2- 1. Properties of Cs materials.

Property	Cesium Ingot	Cesium Carbonate	Cesium Oxide
Ionization Potential	3.894 eV		
Formula Weight	132.91 g/mol	325.83 g/mol	281.81 g/mol
Density	1.873 g/cm^3 at 20 °C		4.25 g/cm^3 at 20 °C
Melting Point	28.5 °C (Liquid at room temp.)	Dissociates at 610 °C	Dissociates in O_2 at 400 °C m.p. at 490 °C in N_2
Boiling Point	705 °C		
Thermal Conductivity	0.359 W cm^{-1} K^{-1}		
Electrical Resistivity	19 :S/cm at 0 °C 36.6 :S/cm at 30 °C		
Vapor Pressure	1 mm 279 °C		
Specific Heat	0.06 cal/g at 28.5 °C		
Violent in	Air, water		Water
Toxicity	Burns skin, Low toxicity, Analog of K	Possible mutagen, Skin irritation	Inhalation may be fatal
Machining	Ductile metal or in mesh form	Deliquesce crystal Powder only)	6-mm pieces and smaller chunks

and is the second most electropositive and alkaline element. It ignites spontaneously in air and reacts violently in water, setting fire to the liberated hydrogen (H). As with other alkali metals, it forms amalgams with Hg, and it alloys with gold (Au), Cs, Na, and K. It must be kept under a dry mineral oil, in a vacuum, or in an inert atmosphere. Seventeen isotopes of Rb are currently known. Naturally occurring Rb is made of two isotopes Rb^{85} and Rb^{87}. Rubidium-87 is present to the extent of 27.85% in natural Rb and is a beta emitter with a half-life of 6×10^{10} years. Ordinary Rb is sufficiently radioactive to expose a photographic film in about 30 to 60 days. Because Rb can be easily ionized, it is being considered for use in ion engines for space vehicles. Rubidium, like K, has a weak radioactivity with the emission of beta particles. The beta emission is about one-thousandth that of an equal weight of uranium (U). There is no real Rb ore;

however, this element is disseminated in small quantities over the earth. As a necessary element in plant and animal life, it is found in everyday plants such as tea, coffee, and tobacco.

Rubidium double salts are not hygroscopic and usually insoluble in water. Rubidium can alloy with other alkaline earth metals and other alkali metals. Cabot Performance Materials produces Rb metal in purities ranging from 99.5% to 99.999%, as well as a full range of Rb compounds.

The synonyms for rubidium carbonate are dirubidium carbonate, dirubidium monocarbonate, and rubidium carbonate. It is a white deliquesce powder that is strongly alkaline. Rubidium carbonate is soluble in water and insoluble in alcohol. Containers must be kept tightly closed since it is hygroscopic. Rubidium oxide appears as green, yellow, and orange marbled chunks.

C.2.1.3 Potassium Materials

Potassium metal is a soft, silvery white metal, which has a body-centered cubic structure, tarnishes to gray upon exposure to air, and becomes brittle at low temperatures. It is soluble in liquid ammonia, ethylenediamine, aniline, and in several metals-forming alloys. The metal reacts vigorously with O_2, water, and acids. Potassium metal also reacts vigorously with halogens, igniting with bromine and iodine. The molten metal reacts with sulfur and hydrogen sulfide, and will react slowly with hydrogen at 200 °C and rapidly at 350 – 400 °C.

Potassium is the seventh most abundant metal and makes up about 2.4% by weight of the earth's crust. Most K minerals are insoluble. It is one of the most reactive and electropositive of metals. Potassium is soft, easily cut with a knife, and silvery in appearance immediately after a fresh surface is exposed. It rapidly oxidizes in air and must be preserved in a mineral oil or kerosene. As with other metals of the alkali group, K reacts violently with water in an exothermic reaction that releases H. The heat released in this reaction is often sufficient to cause spontaneous combustion of the H when it is released to an O_2 atmosphere. Ordinary K is composed of 0.0119% K^{40}, a radioactive isotope with a half-life of 1.4×10^9 years. The radioactivity is only about 1/1,000 that of U, and therefore, presents no appreciable hazard.

The synonyms for K_2CO_3 are dipotassium salt, kaliumcarbonate, K-gran, pearl ash, and potash. It is hygroscopic and has small odorless granular crystals. Potassium carbonate is soluble in 1 part cold, 0.7 part boiling water and practically insoluble in alcohol. Its aqueous solution is strongly alkaline with a pH of 11.6. Containers of dry K_2CO_3 must be kept tightly closed. The mass composition of K_2CO_3 is C 8.69%, K 56.58%, O 34.73%. The physical properties of K materials are tabulated in Table C.2- 2.

Table C.2- 2. Properties of K materials.		
Property	**Potassium**	**Potassium Carbonate**
Ionization Potential	4.341 eV	
Formula Weight	39.102 g/mol	138.21 g/mol
Density	0.862 g/cm^3 at 20 °C	2.428 g/cm^3 at 20 °C
Melting Point	63.65 °C	891 °C
Boiling Point	774 °C	Dissociates before boiling
Thermal Conductivity	1.025 W cm^{-1} K^{-1} at 25 °C	
Electrical Resistivity	6.1 : S/cm at 0 °C	
Vapor Pressure	0.09 mm 260 °C	
Heat Capacity	0.18 cal/g	
Violent in	Air, water	
Toxicity	Burns tissue	Severe Irritation
Machining	Ductile metal or in mesh form	White Powder (Powder only)

C.2.2 Cost and Availability

C.2.2.1 Cesium Materials

Canada is the major source of the raw Cs material. The Cs market is very small; therefore, there is no active trading in the metal and no official market price. Prices are relatively stable. Data on mine production of Cs is not available. However, Cabot Performance Materials stated there would not be an availability limitation for the Cs ore.

In 1993, Cabot Corporation™ obtained full ownership of Tantalum Mining Corporation of Canada (Tanco) in Lac du Bonnet, Manitoba, which is the source of 70% of the world's known high-grade pollucite reserves. Currently, the ore from Tanco Mine is shipped to Cabot's processing factory in Revere, Pennsylvania. However, Cabot Performance Materials, a division

of Cabot Corporation, is building a new Cs production facility at Tantalum Mining Corporation of Canada (Tanco), a wholly owned subsidiary of Cabot Corporation. The Tanco facility will provide oilfield quantities of cesium formate, a nontoxic, biodegradable, water-soluble chemical whose primary application is as a high-density specialty drilling and completion fluid for use in deep well applications resists formation pressures and maintains well integrity. The current world demand for Cs chemicals is approximately 500,000 pounds a year; however, demand is expected to increase ten-fold due to new applications in the chemical and oil industries using Cs chemicals. The pilot plant is to begin production early in 1997 with a capacity of over 5 million pounds per year. The new plant will be used to produce large quantities of materials; whereas, the Revere plant will produce the smaller quantities of chemicals. With minimal additional capital investment, the plant has the flexibility to double its volume.

Table C.2- 4 through Table C.2- 6 make a cost comparison of 50 grams of each material. The materials are listed in categories by chemical composition with the highest purity first. As the metals, oxides, and carbonates (except K_2CO_3) are available in smaller quantities, quotes for 50 grams are compared. However, K_2CO_3 is produced and supplied in larger quantities (1 kg or more), so pricing for 50 grams is not reasonable.

Table C.2- 3. Properties of Rb materials.

Property	Rubidium	Rubidium Carbonate	Rubidium Oxide
Ionization Potential	4.177 eV		
Formula Weight	85.87 g/mol	230.95 g/mol	186.94 g/mol
Density	1.532 g/cm^3 at 20 °C (solid) 1.475 g/cm^3 at 39 °C (liquid)		3.72 g/cm^3 at 20 °C
Melting Point	38.89 °C	837 °C	Dissociates at 477 °C
Boiling Point	688 °C	Dissociates at 900 °C	N/A
Thermal Conductivity	0.582 W cm^{-1} K^{-1} at 25 °C		
Electrical Resistivity	11 :S/cm at 0 °C		
Specific Heat	0.0802 cal/g		
Violent in	Air, water		Water
Toxicity	Burns skin, Analog of K	Irritating	Inhalation may be fatal
Machining	Ductile metal or in mesh form	Deliquesce Powder	6-mm pieces and smaller chunks

Table C.2- 4. Comparative pricing and availability for Cs materials.				
Purity (%)	**Quan.**	**Cost ($)**	**Availability**	**Source**
Cesium Metal (ingot)				
99.998	50 g	325.00	50 grams maximum	CERAC
99.995	50 g	157.50	Annual production is 22.7	Cabot
99.98	50 g	115.00	Annual production is 22.7	Cabot
99.95	50 g	1,122.50	N/A	Aldrich
99.5	50 g	1,581.50	N/A	Aldrich
99.99	50 g	600.00	10 kg/month maximum	CM Chemical
99.5	50 g	105.00	Annual production is 22.7	Cabot
Cesium Carbonate				
99.996	50 g	110.00	No supply problems	CERAC
99.995	50 g	140.00	No supply problems	Aldrich
99.9	50 g	3.30	No supply problems	Cabot
99.9	50 g	39.00	No supply problems	CERAC
99.9	50 g	47.35	No supply problems	Aldrich
99.8	50 g	60.00	No supply problems	CM Chemical
99.3	50 g	2.86	No supply problems	Cabot
Cesium Oxide				
99.0	50 g	176.00	1 kg maximum	CERAC
99.0	50 g	46.30	22.7 kg/year maximum	Cabot

C.2.2.2 Rubidium Materials

Canada is the major source of the raw material. The Rb market is very small; therefore, there is no active trading in the metal and no official market price. Prices are relatively stable. Data on mine production of Rb is not available.

Table C.2- 5. Comparative pricing and availability for Rb materials.				
Purity (%)	**Quan.**	**Cost ($)**	**Availability**	**Source**
Rubidium Metal (ingot)				
99.8	50 g	142.50	22.7 kg/year Maximum	Cabot
99.8	50 g	338.00	1 kg maximum	CERAC
99.6	50 g	966.00	Data not available	Aldrich
99.5	50 g	130.00	22.7 kg/year Maximum	Cabot
98+	50 g	704.00	Data not available	Aldrich
Rubidium Carbonate				
99.9	50 g	66.00	No supply problems	CERAC
99.8	50 g	19.28	No supply problems	Cabot
99.8	50 g	114.30	No supply problems	Aldrich
99.0	50 g	13.17	No supply problems	Cabot
99	50 g	67.43	No supply problems	Aldrich
Rubidium Oxide				
99.0	50 g	65.20	22.7 kg/year maximum	Cabot
99.0	50 g	206.00	1 kg maximum	CERAC

C.2.2.3 Potassium Materials

In 1993, the potash industry was in a state of overcapacity in the U.S.; consequently, to support prices, the domestic potash production declined 12% to 1.5 million metric tons. Many producers in the United States and Canada have attempted to operate at partial capacity to maintain prices; however, in 1994, the world's potash producers still remained in a state of overcapacity. In addition, a mine in Michigan will start up before the year 2000 due to the use of mining technology that is relatively low in cost; the mine is located near the world's largest potash-consuming area. The excess production allows for the pricing of K products to remain relatively stable in an increasingly expensive economy.

Table C.2- 6. Comparative pricing and availability for K materials.				
Purity (%)	**Quan.**	**Cost ($)**	**Availability**	**Source**
Potassium				
99.95	50 g	308.00	Maximum of a few kg supplied	CERAC
99.95	50 g	566.00	Data not available	Aldrich
Potassium Carbonate				
99.99	50 g	55.90	No supply problems	Aldrich
99.9	1 kg	29.00	No supply problems	CERAC
99+	100 g	20.35	No supply problems	Aldrich
99	1 kg	19.30	No supply problems	Aldrich
99.0	100 lb (bulk)	39.00	By truckload	Chemical Marketing Reporter

C.2.3 Hazards and Safety Issues

MSE has developed a very comprehensive profile on the hazards and safety issues relating to the various seed materials discussed in this appendix (Ref. 1). In essence, it is found that these materials are generally and characteristically flammable, corrosive, highly reactive, toxic, highly damaging to animal tissue, and liberate extremely flammable gases when reacting with water.

First aid measures to be made available at the site where these materials are being used or handled are water washing capability for all skin areas and eyes. Be prepared to remove clothing and shoes and discard, and have O_2 available for breathing assistance and artificial respiration. Provide a contact for medical personnel (physician).

Fire fighting equipment should include class D extinguishers or dry sand, self-contained breathing apparatus, and protective clothing. Other fire fighting media include carbon dioxide, foam, and dry chemical powder for particular applications. Fire fighters should also be prepared for explosive hazards.

In the event of accidental release of these materials, shut off all ignition sources; evacuate the area effected; use protective clothing and self-contained breathing apparatus; ventilate the area and wash the spill site; use dry lime, sand, or soda ash for sweep up; and place in covered containers.

Personnel protection during storage should include National Institute of Occupational Safety and Health (NIOSH) and Mine Safety and Health Administration (MSHA) approved respirator, chemical-resistant gloves, safety goggles, and other protective clothing. Safety shower and eye baths are necessary. Do not breathe dust and fumes in the storage area.

These materials are incompatible with oxidizing agents, halogens, alcohol, chlorinated solvents, water, acids, Teflon, and phosphorus.

Acute toxicological effects will occur if swallowed, inhaled, or absorbed through skin contact. They can cause severe burns and destruction of mucus membranes in the upper respiratory tract, eyes, and skin and can be lethal because of spasm, inflammation, and edema of the larynx and bronchi.

Specific disposal procedures are required for the particular seed material considered.

C.2.4 References

1. Wagner, K., "Summary of Cost, Availability and Safety Data on Selected Seed Materials for MHD Accelerators," MSE Technology Applications, Inc., May 1996.

APPENDIX C, SECTION C.3

C.3 EFFECTS OF SEEDING ON COMBUSTION

The objective of a hypervelocity ground test facility is to conduct combustion testing on air-breathing engines to determine their in-flight performance characteristics. Therefore, it is critical that the facility does not introduce deviations between the test environment and the in-flight operating environment that are not well understood. The critical issues that arise in this context are: a) the alteration of ignition times caused by alkali metals, b) the delay time effect on the turbulent mixing, and c) the effect of seed on the airflow mixing rate. The first issue was addressed as part of the MARIAH Project. The other two issues were beyond the scope of the MARIAH Project, and in fact, can only be addressed in the context of a specific combustor geometry.

C.3.1 Overview

Efficient and effective operation of an MHD accelerator requires a high electrical conductivity that can only be achieved in a plasma with significant ionization of the working fluid. A small amount of an alkali metal seed material is typically added to the working fluid in MHD accelerators to enhance the level of ionization and achieve a sufficient electrical conductivity. In equilibrium air accelerators, the alkali metal seed allows the desired ionization to be achieved at a temperature much lower than would be required in the air alone. However, for some applications, such as propulsion wind tunnels, the alkali metal can be an undesirable contaminate that may adversely affect the results of experiments. Thus, the use of a seed material must be carefully considered to ensure the accuracy of results.

Since the objective of the proposed ground test facility is to conduct combustion testing on air-breathing engine modules to assess their expected in-flight performance, it is critical that the test facility not introduce differences between the ground test simulation and in-flight operation that are not well understood. High supersonic velocities in the combustor section of scramjets, coupled with engine size and weight limitations for flight vehicles, results in short residence time in these engines. Thus, the performance of scramjets will likely be limited by either the time required for mixing of the fuel with the incoming air or by the reaction rates of the fuel and air mixture. However, neither the supersonic combustion of a fuel nor the mixing process is well understood. For this reason, it is critical that such tests closely reproduce the chemistry and fluid dynamic environment that a full-scale engine would see in flight.

Three important questions arise in this context:

1. Is it likely that small amounts of alkali metal seed will change the ignition delay times by changing either the reaction rates or the set of important reactions?
2. If addition of the seed does appear to increase the ignition delay times, will the delay times approach or exceed the turbulent mixing times?
3. Does the presence of a small amount of seed affect the mixing rate in the turbulent, supersonic airflow?

A study that was conducted to address the first issue is reported in this section. Presently, combustion in full-scale, operational scramjets is thought to be mixing limited.[1] Thus, if the combustion in scramjets is indeed mixing limited, small changes to the reaction kinetics would not affect performance. However, if large effects were identified, an analysis combining the physics of mixing and reaction would be necessary. Although this study does not address the second and third issues, some preliminary conclusions about the significance of this work in the context of supersonic combustion are presented in Section C.3.3 below.

To simplify the problem, an assumption was made that the presence of seed in small amounts has no affect on the mixing times. This was done because the available computational tools cannot calculate turbulent mixing times from first principles, and in fact, cannot correctly model the two-way interactions between turbulent mixing and the chemistry. The problem was further simplified by assuming that the primary variable of interest is the ignition delay time, which was to be determined as a function of the mole fraction of alkali metal in the flow. A general set of reactions and reaction rates that adequately describe combustion in the presence (or absence) of an alkali metal seed material was determined based on research reported in the literature, and computations were done for a series of seed mole fractions ranging from zero to 5 mole percent. Further details about the kinetics model are described below. In addition to characterizing the effect of an alkali seed, the effect on ignition times of varying amounts of atomic O_2 and nitric oxide was also computed.

C.3.2 Analysis

This section presents results of ignition delay time calculations in a stoichiometric mixture of H_2 and air (or O_2) with admixtures of other species such as O, NO, K, and Na. All calculations are for an adiabatic combustion process at a constant pressure of 1 atm. The ignition time is determined as the time required for the temperature to increase to 100 K above the initial value (other delay time definitions resulted in similar results).

The kinetic mechanism of H_2 ignition in O_2 or in air (without the admixtures specified above) is well known (Refs. 1, 2). The kinetic model used includes 19 species (see Table C.3- 1) and about 80 chemical reactions (see Table C.3- 2) (for each, both forward and reverse reaction were considered). The model is based upon the well-known Warnatz mechanism of H_2-O_2 combustion combined with the well-known Zel'dovich mechanism of N_2 oxidation and reactions of $H_xN_yO_z$ species (Ref. 3). In spite of the large number of reactions considered, only a few of them are critical for H_2 combustion [this had been previously confirmed on the basis of a sensitivity analysis (Ref. 2)]. For example, in an H_2-O_2 mixture with no radicals present (such as O, H, and OH), the most important initiation reaction is:

$$H_2 + O_2 \quad \rightleftharpoons \quad HO_2 + H \qquad (1)$$

[1] Personal communication, Mr. Gordon Nelson, MSE with Dr. Phil Drummond, NASA Langley Research Center, April 1996.

This reaction has quite large activation energy (that is why H_2-O_2 mixtures do not ignite spontaneously at low temperatures). This reaction produces H atoms that initiate the chain reaction mechanism (very much like Zel'dovich mechanism reactions for NO production):

$$O_2 + H \rightleftharpoons OH + O \quad (2)$$

$$H_2 + O \rightleftharpoons OH + H \quad (3)$$

A small amount of H or O atoms present in the gas mixture starts the self-accelerating chain reaction (Reactions 2, 3), while the initial reaction (Reaction 1) is a bottleneck for the entire chain process. For comparison, in a nitrogen (N_2) oxidation process in air, the similar bottleneck reaction is thermal or electron impact dissociation of O_2:

$$O_2 + M \rightleftharpoons O + O + M \quad (4)$$

$$O_2 + e \rightleftharpoons O + O + e \quad (5)$$

Finally, water is produced in Reactions 6 and 7:

$$H_2 + OH \rightleftharpoons H_2O + H \quad (6)$$

$$O_2 + H + M \rightleftharpoons H_2O + M \quad (7)$$

The last reaction releases a large amount of energy, thereby heating the mixture and accelerating the combustion process. This is a classical, well-established mechanism.

Table C.3- 1. Reaction species used in the H_2 – Air – K ignition delay study.				
Air – H_2 Combustion Species				
H	H_2O_2	NH	NNH	O
H_2	HO_2	NH_2	NO	O_2
HNO	N	NH_3	NO_2	OH
H_2O	N_2	N_2H_2	N_2O	
Potassium and Sodium Species				
K	KOH	Na	NaOH	

The addition of N_2 does not qualitatively change this scenario in spite of the addition of many chemical reactions. In this case, however, the ignition time is always greater than for the H_2-O_2 mixture (see Figure C.3- 1) because a) N_2 provides a thermal inertia, and b) some thermal

energy released in the H_2-O_2 reactions sustains nitric oxide (NO) formation in Zel'dovich mechanism reactions:

$$N_2 + O \rightleftharpoons NO + N \quad (8)$$

$$O_2 + N \rightleftharpoons NO + O \quad (9)$$

This NO formation mechanism is globally endothermic. Quite obviously, the ignition time steeply decreases with temperature in the temperature range 1,000-2,000 K but increases again above 2,000 K (see Figure C.3- 1). This happens because of the reverse radical reactions that become important at the high temperatures and decrease the overall water production and energy release rates.

This analysis shows that the presence of NO in the mixture, even in considerable concentrations (a few percent) does not substantially affect the O, H, and OH radical concentrations in the mixture, and therefore, does not appreciably change the ignition delay time within the entire temperature range considered (see Figure C.3- 1). Atomic O_2, however, results in a well-pronounced effect. In the presence of O atoms, the initial reaction (Reaction 1) is no longer a bottleneck, and the chain mechanism (Reactions 2, 3) starts instantaneously. This is especially important at temperatures less than 2,500 K when there are no other fast processes of O atom formation. Therefore, in this temperature range, the ignition time is reduced by about an order of magnitude if the atomic O_2 concentration is 0.1-1.0% (see Figure C.3-2).

Of course, these are unrealistically high concentrations for an airflow expanding from a high temperature plenum (the typical O atom concentrations at the nozzle exit are several orders of magnitude lower due to fast recombination in the subsonic section of the flow). However, if nonequilibrium ionization is sustained in the supersonic section of the nozzle (by an e-beam or by seeding the gas), then related chemical processes can increase the amount of O atoms up to a few percent (Ref. 4). Note that O atoms produced in the supersonic flow recombine quite slowly because of the low pressure in the secondary expansion section. Therefore, the presence of atomic O_2 can substantially accelerate the ignition in energy addition flows at temperatures less than 2,500 K. In other words, an air mixture contaminated with O atoms would have a shorter ignition delay in a wind tunnel experiment than would occur in a real flight where there are almost no O atoms present in the flow (photoionization of O_2 which substantially alters the chemical composition of air only at the altitudes above ~90 km can be disregarded).

The catalytic effect of O atoms becomes much weaker, however, at temperatures greater than 2,500 K (see Figure C.3-2). This is due to the faster rate of H atom production in Reaction 1, which becomes comparable with the rate of radical productions in Reactions 2 and 3, initially catalyzed by O atoms present in the flow.

Table C.3- 2. Reactions for H_2 combustion in air with alkali metal additive.					
Reactions		A	N	Ea	Third Body Species
$H + O_2 + M$	$\rightleftharpoons HO_2 + M$	3.61×10^{17}	-0.72	0.0	H_2O/18.6/, H_2/2.86/, N_2/1.3
$H + H + M$	$\rightleftharpoons H_2 + M$	1.0×10^{18}	-1.0	0.0	
$H + H + H_2$	$\rightleftharpoons H_2 + H_2$	9.2×10^{16}	-0.6	0.0	
$H + H + H_2O$	$\rightleftharpoons H_2 + H_2O$	6.0×10^{19}	-1.25	0.0	
$H + OH + M$	$\rightleftharpoons H_2O + M$	1.6×10^{22}	-2.0	0.0	H_2O/5/
$H + O + M$	$\rightleftharpoons OH + M$	6.2×10^{16}	-0.6	0.0	H_2O/5/
$H_2O_2 + M$	$\rightleftharpoons OH + OH + M$	1.3×10^{17}	0.0	45,500.	
$H_2 + O_2$	$\rightleftharpoons 2OH$	1.7×10^{13}	0.0	47,780.	
$OH + H_2$	$\rightleftharpoons H_2O + H$	1.17×10^{9}	1.3	3,626.	
$O + OH$	$\rightleftharpoons O2 + H$	3.61×10^{14}	-0.5	0.0	
$O + H_2$	$\rightleftharpoons OH + H$	5.06×10^{4}	2.67	6,290.	
$OH + HO_2$	$\rightleftharpoons H_2O + O_2$	7.5×10^{12}	0.0	0.0	
$H + HO_2$	$\rightleftharpoons 2OH$	1.4×10^{14}	0.0	1,073.	
$O + HO_2$	$\rightleftharpoons O_2 + OH$	1.4×10^{13}	0.0	1,073.	
$2OH$	$\rightleftharpoons O + H_2O$	$6.0\times10^{+8}$	1.3	0.0	
$H + HO_2$	$\rightleftharpoons H_2 + O_2$	1.25×10^{13}	0.0	0.0	
$HO_2 + HO_2$	$\rightleftharpoons H_2O_2 + O_2$	2.0×10^{12}	0.0	0.0	
$H_2O_2 + H$	$\rightleftharpoons HO_2 + H_2$	1.6×10^{12}	0.0	3,800.	
$H_2O_2 + OH$	$\rightleftharpoons H_2O + HO_2$	1.0×10^{13}	0.0	1,800.	
$N_2 + M$	$\rightleftharpoons N + N + M$	1.92×10^{17}	-0.5	224,900.	N_2/2.5/, N/0/
$O_2 + M$	$\rightleftharpoons O + O + M$	3.62×10^{18}	-1.0	118,000.	N_2/2/, O_2/9/, O/25/
$NO + M$	$\rightleftharpoons N + O + M$	4.0×10^{20}	-1.5	150,000.	NO/20/, O/20/, N/20/
$N_2 + O$	$\rightleftharpoons NO + N$	7.0×10^{13}	0.0	75,000.	
$O_2 + N$	$\rightleftharpoons NO + O$	1.34×10^{10}	1.0	7,080.	
$N_2 + O_2$	$\rightleftharpoons NO + NO$	9.1×10^{24}	-2.5	128,500.	
$N_2 + N$	$\rightleftharpoons N + N + N$	4.1×10^{22}	-1.5	224,900.	
$HO_2 + NO$	$\rightleftharpoons NO_2 + OH$	2.11×10^{12}	0.0	-479.	
$NO_2 + H$	$\rightleftharpoons NO + OH$	3.5×10^{14}	0.0	1,500.	
$NO_2 + O$	$\rightleftharpoons NO + O_2$	1.0×10^{13}	0.0	600.	
$NO_2 + M$	$\rightleftharpoons NO + O + M$	1.1×10^{16}	0.0	66,000.	
$NH + O_2$	$\rightleftharpoons HNO + O$	1.00×10^{13}	0.0	12,000.	
$NH + O_2$	$\rightleftharpoons NO + OH$	7.60×10^{10}	0.0	1,530.	
$NH + NO$	$\rightleftharpoons N_2O + H$	2.40×10^{15}	-0.8	0.0	

Table C.3-2 Cont'd.					
Reactions		A	N	Ea	Third Body Species
$N_2O + OH$	$\rightleftharpoons N_2 + HO_2$	2.00×10^{12}	0.0	10,000.	
$N_2O + H$	$\rightleftharpoons N_2 + OH$	7.60×10^{13}	0.0	15,200.	
$N_2O + M$	$\rightleftharpoons N_2 + O + M$	1.60×10^{14}	0.0	51,600.	
$N_2O + O$	$\rightleftharpoons N_2 + O_2$	1.00×10^{14}	0.0	28,200.	
$N_2O + O$	$\rightleftharpoons 2NO$	1.00×10^{14}	0.0	28,200.	
$NH + OH$	$\rightleftharpoons HNO + H$	2.00×10^{13}	0.0	0.0	
$NH + OH$	$\rightleftharpoons N + H_2O$	5.00×10^{11}	0.5	2,000.	
$NH + N$	$\rightleftharpoons N_2 + H$	3.00×10^{13}	0.0	0.0	
$NH + H$	$\rightleftharpoons N + H_2$	1.00×10^{14}	0.0	0.0	
$NH + O$	$\rightleftharpoons NO + H$	2.00×10^{13}	0.0	0.0	
$NH_2 + O$	$\rightleftharpoons HNO + H$	6.63×10^{14}	-0.5	0.0	
$NH_2 + O$	$\rightleftharpoons NH + OH$	6.75×10^{12}	0.0	0.0	
$NH_2 + OH$	$\rightleftharpoons NH + H_2O$	4.00×10^{6}	2.	1,000.	
$NH_2 + H$	$\rightleftharpoons NH + H_2$	6.92×10^{13}	0.0	3,650.	
$NH_2 + NO$	$\rightleftharpoons NNH + OH$	6.40×10^{15}	-1.25	0.0	
$NH_2 + NO$	$\rightleftharpoons N_2 + H_2O$	6.20×10^{15}	-1.25	0.0	
$NH_3 + OH$	$\rightleftharpoons NH_2 + H_2O$	2.04×10^{6}	2.04	566.	
$NH_3 + H$	$\rightleftharpoons NH_2 + H_2$	6.32×10^{5}	2.39	10,171.	
$NH_3 + O$	$\rightleftharpoons NH_2 + OH$	2.10×10^{13}	0.0	9,000.	
NNH	$\rightleftharpoons N_2 + H$	1.00×10^{4}	0.0	0.0	
$NNH + NO$	$\rightleftharpoons N_2 + H + NO$	6.00×10^{13}	0.0	0.0	
$NNH + H$	$\rightleftharpoons N_2 + H_2$	1.00×10^{14}	0.0	0.0	
$NNH + OH$	$\rightleftharpoons N_2 + H_2O$	5.00×10^{13}	0.0	0.0	
$NNH + NH_2$	$\rightleftharpoons N_2 + NH_3$	5.00×10^{13}	0.0	0.0	
$NNH + NH$	$\rightleftharpoons N_2 + NH_2$	5.00×10^{13}	0.0	0.0	
$NNH + O$	$\rightleftharpoons N_2O + H$	1.00×10^{14}	0.0	0.0	
$HNO + M$	$\rightleftharpoons H + NO + M$	1.50×10^{16}	0.0	48,680.	$H_2O/10/$, $O_2/2/$, $N_2/2/$, $H_2/2/$
$HNO + OH$	$\rightleftharpoons NO + H_2O$	3.60×10^{13}	0.0	0.0	
$HNO + H$	$\rightleftharpoons H_2 + NO$	5.00×10^{12}	0.0	0.0	
$HNO + NH_2$	$\rightleftharpoons NH_3 + NO$	2.00×10^{13}	0.0	0.0	
$N + OH$	$\rightleftharpoons NO + H$	3.80×10^{13}	0.0	0.0	
$2HNO$	$\rightleftharpoons N_2O + H_2O$	3.95×10^{12}	0.0	5,000.	
$HNO + NO$	$\rightleftharpoons N_2O + OH$	2.00×10^{12}	0.0	26,000.	
$NH_2 + NH$	$\rightleftharpoons N_2H_2 + H$	5.00×10^{13}	0.0	0.0	

Table C.3-2 – Cont'd.					
Reactions			A	N	Ea	Third Body Species
2NH	⇌	$N_2 + 2H$	2.54×10^{13}	0.0	0.0	
$NH_2 + N$	⇌	$N_2 + 2H$	7.20×10^{13}	0.0	0.0	
$N_2H_2 + M$	⇌	$NNH + H + M$	5.00×10^{16}	0.0	50,000.	$H_2O/15/$, $O_2/2/$, $N_2/2/$, $H_2/2/$
$N_2H_2 + H$	⇌	$NNH + H_2$	5.00×10^{13}	0.0	0.0	
$N_2H_2 + O$	⇌	$NH_2 + NO$	1.00×10^{13}	0.0	0.0	
$N_2H_2 + O$	⇌	$NNH + OH$	2.00×10^{13}	0.0	1,000.	
$N_2H_2 + OH$	⇌	$NNH + H_2O$	1.00×10^{13}	0.0	1,000.	
$N_2H_2 + NO$	⇌	$N_2O + NH_2$	3.00×10^{12}	0.0	0.0	
$N_2H_2 + NH$	⇌	$NNH + NH_2$	1.00×10^{13}	0.0	1,000.	
$N_2H_2 + NH2$	⇌	$NH_3 + NNH$	1.00×10^{13}	0.0	1,000.	
$2NH_2$	⇌	$N_2H_2 + H_2$	5.00×10^{11}	0.0	0.0	
$NH_2 + O_2$	⇌	$HNO + OH$	4.50×10^{12}	0.0	25,000.	
$KOH + H$	⇌	$K + H_2O$	1.08×10^{13}	0.0	1,987.	
$K + OH + M$	⇌	$KOH + M$	5.40×10^{20}	-1.0	0.0	
$NaOH + H$	⇌	$Na + H_2O$	1.08×10^{13}	0.0	1,987.	
$Na + OH + M$	⇌	$NaOH + M$	1.80×10^{21}	-1.0	0.0	
Forward Reaction Rate Equation $k = A\cdot T^n e^{-Ea/T}$						

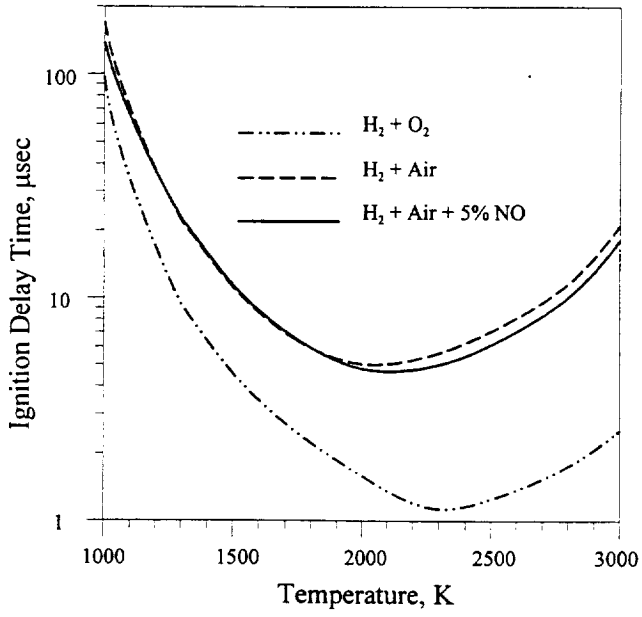

Figure C.3- 1. Effect of NO on ignition delay in H_2 - air mixture.

The effect of the alkali atoms on H_2 ignition appears to be quite straightforward. The global kinetic mechanism of K and Na reactions in H_2-O_2 flames by Jensen (Refs. 5, 6) (Reactions 10a and 11a for K; 11a and 11b for Na) is sustained by the later studies of Na and K kinetics in flames (Refs. 7, 8), although with some corrections. Slack et al. (Ref. 8) refines this two-reaction mechanism by replacing it by a five-reaction scheme (See Table C.3- 3) that produces quite similar results. The most serious correction by Slack et al. is a recommendation to reduce the rate of Reaction 11b for Na by a factor of 3 to get better agreement with experiments, making the rates for reactions 10 and 11 for K and Na very nearly equal. It remains uncertain, however, what the reaction rates are for temperatures greater than 2,500 K since the available experimental data have been obtained in flames. In these calculations, the global Jensen mechanism for both K and Na is assumed.

$$K + OH + M \rightleftharpoons KOH + M \qquad (10a)$$

$$Na + OH + M \rightleftharpoons NaOH + M \qquad (10b)$$

$$KOH + H \rightleftharpoons K + H_2O \qquad (11a)$$

$$NaOH + H \rightleftharpoons Na + H_2O \qquad (11b)$$

One can see that the Reactions 10 and 11 can be written as an overall process:

$$K + H + OH \rightleftharpoons K + H_2O \qquad (12a)$$

$$Na + H + OH \rightleftharpoons Na + H2O \qquad (12b)$$

Table C.3- 3. Slack et al. K reaction set (Ref. 9)

Reactions	A	N	Ea	Third Body Species
$K + O_2 + M \rightleftharpoons KO_2 + M$	6.80×10^{25}	-2.68	596.0	
$K + OH + M \rightleftharpoons KOH + M$	6.80×10^{22}	-2.0	0.0	
$KOH + H \rightleftharpoons K + H_2O$	2.20×10^{12}	0.5	0.0	
$KO_2 + H \rightleftharpoons KO + OH$	2.20×10^{12}	0.5	0.0	
$KO + H_2O \rightleftharpoons KOH + OH$	5.90×10^{11}	0.5	0.0	

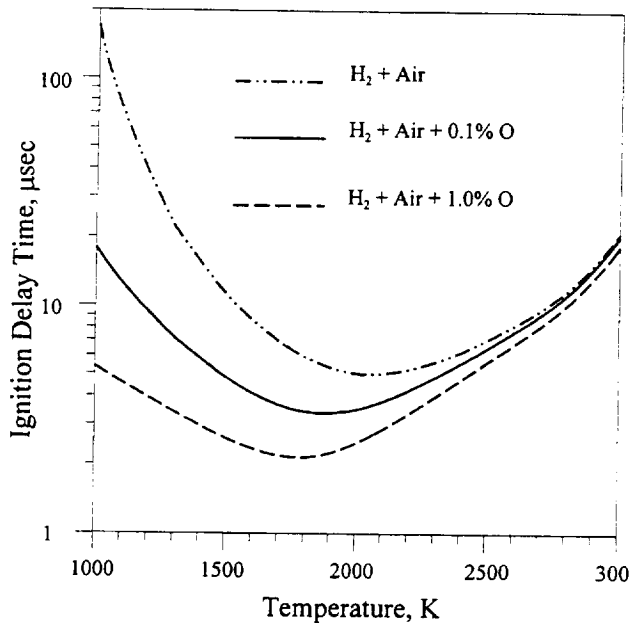

Figure C.3-2. Effect of atomic O_2 on ignition delay in H_2 - air mixture.

Depending on temperature, the effect of this process on H_2 ignition can be different. At temperatures, less than 1,500 K, when the rates of the shuffle reactions (Reactions 2, 3) are not very fast, and the radical concentrations increase quite slowly; Reactions 10 and 11 result in radical removal (H and OH) from the mixture. This tends to terminate the chain process (Reaction 2, 3) and delay the ignition (see Figure C.3-3). The energy release in Reactions 10 and 11, is exothermic and is very slow at these temperatures. In this temperature regime, alkali atoms act as inhibitors.

At the high temperatures, however, the radical production rate by the chain mechanism (Reactions 2, 3) becomes much faster, and Reactions 10 and 11 can no longer keep up with it. These reactions now act as an additional exothermic channel of water production, and both K and Na act as catalysts (see Reaction 12). One can see that the presence of K or Na at a 1% level can reduce the ignition delay time at temperatures greater than 2,000 K by about a factor of 2 (see Figure C.3-3). Note if one follows the recommendation of Slack et al. and reduces the rate of Reaction 11b for Na by a factor of 3, the effect of both metals on the ignition time is almost identical. Additionally, the results for temperatures greater than 2,500 K are obtained using the experimental data extrapolated from the lower temperatures. To the best of our knowledge, the reaction rate measurements in this regime are not available.

C.3.3 Analysis Limitations

The kinetic model used here for the ignition delay time calculations is not applicable to modeling of the entire combustion process in supersonic flows since it is not coupled with the flow. First, the assumption of adiabaticity is justified only at the initial stage of combustion (i.e., ignition), when the energy released into the flow is small. This is not so when the combustion process is well under way. Secondly, the model does not take into account the turbulent mixing of the species that in fact may control the chemical reaction rates. The latter effect critically depends on a particular combustor geometry that might be rather complicated. Unfortunately, the existing models of turbulence can not adequately simulate reacting compressible flows since they do not properly consider the coupling between fluid mechanics and chemistry (i.e., correlation between the temperature fluctuations and the species production rates, e.g., see Reference 9 and references therein). Therefore, for this case, the coupling of the kinetic model and the multidimensional turbulent flow model does not produce reliable computational results.

For these reasons, the most efficient way of using the data obtained in the present study is to compare the calculated ignition delay time for a particular gas mixture (scaled as 1/P, if necessary) with the turbulent mixing time, experimentally measured for a particular combustor as a function of temperature, pressure, and Mach number (e.g., see Reference 10). This answers the question as to what really delays ignition in particular flows, chemical processes, or turbulent mixing. Obviously, reaction kinetics, including the effect of alkali seeds is only relevant in the former case. Effects of pressure were not considered in this study, and all calculations were performed at a constant pressure of 1 atm.

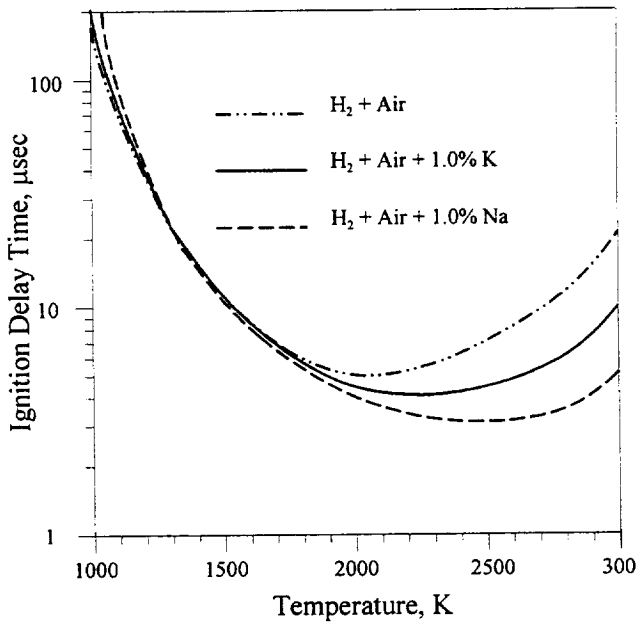

Figure C.3-3. Effect of alkali atoms on ignition delay in H_2 - air mixture.

Table C.3- 4. Ignition delay time in $H_2:O_2 = 2:1$ mixture as a function of pressure.		
P (atm)	T(K)	Ignition Delay time, μs
0.01	2,000	187.0
0.03	2,000	60.9
0.1	2,000	17.6
0.3	2,000	5.64
1	2,000	1.6
3	2,000	0.50

C.3.4 Summary

From Figures C.3- 1 through C.3-3, one can see that a) NO had very little effect on H_2 ignition in the entire temperature range considered; b) atomic O_2 strongly decreases the ignition time at the low temperatures by removing a radical production bottleneck (Reaction 1); and c) K and Na both decrease the ignition time at the high temperatures due to catalytic effects in Reactions 10 and 11. Ignition delay time scales with pressure as approximately 1/P (see Table C.3- 4). A slight deviation from the 1/P law results from the three-body reactions involved.

No attempt was made in this study to model the turbulent mixing of the fuel and air. For scramjet flow regimes that are mixing limited, the effect on scramjet performance of small additions of K seed may not be significant. However, if the flow is limited by the chemical kinetic rates rather than by mixing, the decrease of the ignition delay time due to the presence of an alkali metal seed would most likely affect the scramjet performance in the ground test simulation.

C.3.5 References

1. Maas, U. and Warnatz, J., "Detailed Numerical Modeling of H_2-O_2 Ignition by Hot Spots," *Progress in Astronautics and Aeronautics,* Vol. 131, *Dynamics of Deflagrations and Reactive Systems: Flames*, Kuhl A.L.; Leyer, J.C.; Borisov, A.A.; and Sirignano, W.A. (eds.), Washington, American Institute of Aeronautics and Astronautics, 1991, pp. 3-19.

2. Trevino, C., "Ignition Phenomena in H_2-O_2 Mixtures," *Progress in Astronautics and Aeronautics,* vol. 131, *Dynamics of Deflagrations and Reactive Systems*: *Flames*, Kuhl, A.L.; Leyer, J.C.; Borisov, A.A.; Sirignano, W.A. (eds.), Washington D.C., American Institute of Aeronautics and Astronautics, 1991 pp. 19-44.

3. Mallard, W.G., "NIST Chemical Kinetics Database," NIST Standard Reference Database 17, National Institute of Standards and Technology (NIST), Gaithersberg, MD, Nov. 1994.

4. Adamovich, I.V.; Rich, J.W.; and Nelson, G.L., "Feasibility Study of MHD Acceleration of Unseeded and Seeded Airflows," AIAA Paper 96-2347, June 1996.

5. Jensen, D.E., *J. Chem. Soc. Farad,* Trans. I, Vol. 78, 1982, p. 2835.

6. Jensen, D.E. and Jones, G.A., *J. Chem. Soc. Farad,* Trans. I, Vol. 78, 1982, p. 2843.

7. Haynes, A.J.; Steinberg, M.; and Schofield, K., *J. Chem. Phys.*, Vol. 8, 1984, p. 2585.

8. Slack, M.; Cox, J.W.; Grillo, A.; and Ryan, R., *Combust. Flame*, Vol. 77, 1989, p. 311.

9. Drummond, J.P. and Carpenter, M.H., "Mixing and Mixing Enhancement in Supersonic Reacting Flowfields," *Progress in Astronautics and Aeronautics*, Vol. 137, *High Speed Flight Propulsion Systems*, Murthy, S.N.B. and Curran, E.T. (eds.), Washington, American Institute of Aeronautics, 1991, pp. 383-456.

10. Dimotakis, P.E., "Turbulent Free Shear Layer Mixing and Combustion," *Progress in Astronautics and Aeronautics*, Vol. 137, *High Speed Flight Propulsion Systems*, Murthy, S.N.B. and Curran, E.T. (eds.), Washington, American Institute of Aeronautics and Astronautics, 1991, pp. 265-340.

APPENDIX C, SECTION C.4

C.4 OXYGEN ATTACHMENT IN SEEDED AIR

MSE conducted a study to determine if electron attachment to O_2 or other air species will significantly reduce the availability of free electrons and electrical conductivity in Cs seeded air at the expected MHD accelerator operating conditions.

NOMENCLATURE

- B - Magnetic field strength, (T)
- c_e - Mean random thermal velocity of electrons
- C_p° - Constant pressure specific heat (reference state), (J/kmol-K)
- e - Electron charge, (1.60203×10^{-19} coulomb)
- E - Electric field, (V/m)
- h - Static enthalpy, (J/kg)
- H - Stagnation enthalpy, (J/kg)
- H° - Enthalpy (reference state), (J/kmol)
- j - Current density, (A/m^2)
- k - Boltzmann's constant, (1.38047×10^{-23} J/K)
- m_e - Electron mass, ($9.110\text{x}10^{-31}$ kg)
- n - Number density, ($\#/m^3$)
- N - Molar quantity, (moles)
- p - Pressure, (Pa)
- Q - Momentum transfer cross section, (m^2)
- R - Universal gas constant, (8314.34 J/kmol-K)
- S° - Entropy (reference state), (J/kmol-K)
- T - Temperature, (K)
- u - Velocity, (m/s)
- x - Distance in axial direction, (m)
- ϵ_0 - Permittivity of free space, (8.85525×10^{-12} farad/m)
- η - MHD conversion efficiency
- Λ - Ratio of Debye length to average impact parameter
- ρ - Mass density, (kg/m^3)
- σ - Electrical conductivity, (mho/m)
- ϕ - Seed fraction (molar), (moles of seed atom per total moles)

Subscripts

- e - Electron
- I - Ion
- k - k^{th} species
- n - Neutral species
- s - Seed species
- x - Axial coordinate direction
- y - Transverse coordinate direction
- z - Coordinate direction perpendicular to axial and transverse direction

C.4.1 Overview

A study was conducted to determine if electron attachment to O_2 or other air species will significantly reduce the availability of free electrons and electrical conductivity in Cs seeded air at expected MHD operating conditions. During the course of this study, differences were discovered in the predictions of free electron concentrations as calculated by three leading equilibrium chemistry codes, and this study was extended to compare the results and evaluate the performance of the three codes.

The first objective of this study was to evaluate the effect of electron attachment of O_2 and other air species on the total free electron concentration. MHD accelerator performance depends on achieving a sufficient concentration of free electrons, through ionization of the working fluid, to provide good electrical conductivity. For equilibrium air accelerators, ionization is achieved through the addition of a seed that is easily ionized and a static temperature that is sufficient for a high degree of seed ionization. However, this will not ensure a sufficient electrical conductivity if the highly mobile electrons, produced from the seed ionization, are then attached by other species in the working fluid, producing the much less mobile negative ions.

This study examines the variation of free electron concentration and the attachment of free electrons to form negative ions over a wide range of temperature, pressure, and Cs seed concentration in air. These results, reported in Section C.4.2, can then be used in guiding the design of MHD accelerator applications by providing the information necessary to pick optimum operating regimes.

A second objective of this study became necessary when the results from three popular chemical equilibrium codes were compared and found to disagree in their predictions of electron concentration. The most recently released code is a beta-test version of the NASA Chemical Equilibrium Code, CEA (Chemical Equilibrium with Application) (Refs. 1, 2, 3). This code is compared with an older version of the NASA code CET89 (Refs. 4, 5, 6, 7), that has been used extensively at MSE, as well as a commercial code available for PC computers called HSC (Ref. 8). Source code is available for the CEA and CET89 codes and has been modified by MSE to add electrical conductivity calculations. Source code is not available for the HSC code. This code has been used at MSE for lower temperature, environmental engineering applications; however, this application represents the first time that it has been used at MSE for the higher temperature MHD applications. Since all three codes produced significantly different results in this analysis, an evaluation was necessary to determine which was most likely to be correct. This study is reported in Section C.4.3.

C.4.2 Evaluation of Electron Attachment for MHD Operating Conditions

When free electrons in an ionized gas attach to neutral atoms and molecules in the gas, negative ions are formed that reduce the overall mobility of the charge carriers and the electrical conductivity. Free electrons in a gas are highly mobile because their low mass results in very high velocity in their random thermal motion and allows them to be directionally accelerated in an electric field to effectively transport electrical energy in the gas. Singly charged ions, having

the same magnitude of charge as an electron, will experience the same force as an electron in an electric field; however, their acceleration will be far less due to much greater mass as compared to the electron mass. Furthermore, their random thermal velocity will be far less than that of the electrons at the same temperature, thus ions are much less mobile and far less effective as transporters of electrical energy than the light mass electrons. The electrical conductivity contribution of ions will be nearly insignificant compared to an equal concentration of free electrons in a gas.

To achieve good MHD performance, a seed material with a low ionization potential (such as an alkali metal) is often added to the MHD working gas as a source of free electrons. If the temperature is sufficiently high, a significant fraction of the seed material can ionize to provide the free electrons and the necessary electrical conductivity. However, if atoms or molecules in the working gas have a strong propensity for electron attachment, these can form negative ions that reduce the number of free electrons, the electrical conductivity, and overall MHD performance.

Section C.4.2.1 addresses the mechanisms by which electron attachment affects the performance of MHD accelerators. Section C.4.2.2 discusses the chemical equilibrium calculations used to obtain the results presented in Sections C.4.2.3 and C.4.2.4. Additionally, Section C.4.2.3 shows the effects of temperature, pressure, and seed fraction on the ionization fraction of Cs seed in air, the electron attachment to air species, and the electrical conductivity of the plasma. Finally, the effect of temperature, pressure, and seed fraction on the electrical conductivity of Cs-seeded air is mapped in Section C.4.2.4 to show the most effective regimes for MHD accelerator operation.

C.4.2.1 Effect of Electron Attachment on MHD Performance

The predominate effect of electron attachment is the resulting reduction of the electrical conductivity of the plasma. High values of electrical conductivity are essential to achieving good performance from an MHD accelerator, and electron attachment can substantially reduce the electrical conductivity. Consider the simple 1-D energy equation for MHD, without heat transfer, as given by Rosa (Ref. 9):

$$\rho u \frac{d}{dx}\left(\frac{u^2}{2} + h\right) = \vec{j} \cdot \vec{E} \qquad \text{(C.4-1)}$$

The term on the right-hand side is the electrical power density (the electrical power added to the flow per unit volume), and the left-hand side represents the increase of flow stagnation enthalpy. For a segmented Faraday MHD accelerator, the only component of current is the transverse or Faraday current, j_y. Thus, the energy equation can be rewritten as:

$$\rho u \frac{dH}{dx} = j_y E_y \qquad \text{(C.4-2)}$$

From Ohm's Law for a segmented Faraday device:

$$E_y = \frac{j_y}{\sigma} + u B_z \tag{C.4-3}$$

Substitution of this into the energy equation then gives:

$$\rho u \frac{dH}{dx} = \frac{j_y^2}{\sigma} + j_y u B_z \tag{C.4-4}$$

The first term on the right-hand side is the Joule heating term and is due to the thermal dissipation of electrical energy in an electrically resistive medium. This is the mechanism by which the energy is increased in any medium by electrical resistance heating. For instance, arc heaters for aerodynamic testing achieve high enthalpy conditions by heating of the working gas through Joule dissipation in an electric arc. However, heating in this manner also increases the entropy of the working gas, which prevents all conventional heating devices from reaching the high enthalpy, low entropy conditions needed for hypervelocity propulsion testing.

Body force acceleration is the unique capability that allows MHD accelerators to outperform conventional heating devices in this application. From the 1-D momentum equation for a Faraday MHD accelerator:

$$\rho u \frac{du}{dx} + \frac{dp}{dx} = \vec{j} x \vec{B} = j_y B_z \tag{C.4-5}$$

The $j_y B_z$ term on the right-hand side is a body force per unit volume and is responsible for the increase in momentum in an MHD accelerator. When this force is applied to a flowing plasma, the result is an increase in the flow energy through the "push work" as represented by the second term on the right-hand side of the energy equation [Eq. (C.4-4)], i.e.,

$$push\ work = j_y u B_z \tag{C.4-6}$$

For optimum MHD performance relative to conventional heater devices, this push-work term should be maximized. That is, the more energy that is added by the push-work term compared to the Joule-heating term, the more MHD will outperform other heaters in this application. Macheret, Miles, and Nelson (Ref. 10; see also Appendix E of this report) defined an MHD conversion efficiency, η, as:

$$\eta = \frac{< j_y u B_z >}{< j_y E_y + j_x E_x >} \tag{C.4-7}$$

where the brackets < > denote an average across the duct. For a 1-D, uniform flow approximation, the brackets can be removed. This can then be rewritten for a Faraday accelerator ($j_x = 0$) using the Ohm's Law relationship [Eq. (C.4-3)] as:

$$\eta = \frac{j_y u B_z}{\left(\frac{j_y^2}{\sigma} + j_y u B_z \right)} \tag{C.4-8}$$

From this, the importance of the push-work term is evident -- a large push-work term (compared to the Joule-heating term) results in a large MHD conversion efficiency. Now multiply the numerator and denominator of this equation by the electrical conductivity, σ:

$$\eta = \frac{\sigma j_y u B_z}{j_y^2 + \sigma j_y u B_z} = \frac{\sigma u B_z}{j_y + \sigma u B_z} \tag{C.4-9}$$

For large values of σ, the term resulting from the push-work (σuB) will dominate, and the conversion efficiency can approach unity. For low values of σ, the current density (resulting from the Joule-heating term) will dominate, and the conversion efficiency will be low. Therefore, large values of electrical conductivity are clearly desirable since these will allow better MHD performance while low values will constrain the device to perform little better than conventional arc heaters.

Rosa (Ref. 9) presents an elementary derivation of electrical conductivity in an ionized gas for electrical conduction by electrons and shows this to be proportional to the number density of electrons in the gas:

$$\sigma_e = \frac{n_e e^2}{m_e n Q c_e} \tag{C.4-10}$$

A partially ionized gas will consist of electrons, ions, and neutral particles, each having different electron collision cross sections (effective cross section for collision of electrons with the particle). Thus, the product of number density and the momentum-transfer cross section can be written as a summation to account for the contributions of each species. This gives:

$$nQ = \sum_k n_k Q_k = \sum_n n_n Q_n + \sum_i n_i Q_i \tag{C.4-11}$$

where the subscript 'n' indicates a summation over all neutral species in the flow and "I" indicates a summation over all ions. Electron-electron collisions can generally be neglected when the electron fraction in the plasma is small, as it is for MHD accelerators in the applications discussed in this report. If the ionization occurs predominantly from a single ion as

would be expected when an alkali metal seed is added to the flow, the ion term in the summation of Equation (C.4-11) can be given by [see Rosa, Ref. 9, Eq. 2.11]:

$$n_i Q_i = 3.9 n_i \left(\frac{e^2}{8\pi \varepsilon_0 kT} \right)^2 \ln \Lambda \qquad \text{(C.4-12)}$$

where

$$\Lambda = \frac{12\pi}{\sqrt{n_e}} \left(\frac{\varepsilon_0 kT}{e^2} \right)^{3/2} \qquad \text{(C.4-13)}$$

is given by Sutton and Sherman (Ref. 11, Eq. 5.110) as the ratio of the Debye length to the average impact parameter. Thus, considering electron-ion collisions, the electrical conductivity can be written:

$$\sigma = \frac{n_e e^2}{m_e c_e} \left[\frac{1}{\sum_n n_n Q_n + 3.9 n_i \left(\frac{e^2}{8\pi \varepsilon_0 kT} \right)^2 \ln \Lambda} \right] \qquad \text{(C.4-14)}$$

where the summation in the denominator is over all neutral species, and the last term is due to electron-ion collisions.

Electron attachment to atomic and molecular species in the flow reduces the number of free electrons and increases the number of ions. Thus, it can be seen from Equation (C.4-14) that the electrical conductivity could be reduced significantly by electron attachment in a plasma, and it is this mechanism by which MHD performance would be reduced by electron attachment.

C.4.2.2 Equilibrium Chemistry Calculations for Evaluating Electron Attachment in Air

Chemical equilibrium concentrations for electrons and ions presented in Sections C.4.2.3 and C.4.2.4 were calculated using the NASA Lewis Research Center (NASA-LeRC) CEA Chemical Equilibrium Code (Refs. 1, 2, 3). Electrical conductivities presented in these sections were calculated using an algorithm developed by MSE and added to the CEA code based on a method described by Demetriades and Argyropoulos (Ref. 12). All seed fractions used for these analyses were based on a molar fraction of the seed material in the parent gas at ambient conditions.

Thus, if the total number of moles of the parent gas is given by:

$$\textit{Parent Moles} = \sum_k N_k \qquad \text{(C.4-15)}$$

then the number of seed moles is calculated as:

$$N_s = \frac{\phi}{1 - \phi} \sum_k N_k \qquad \text{(C.4-16)}$$

For all air calculations in these sections, air is simulated as a mixture of 78.85% N_2 and 21.15% O_2 on a molar basis. Cesium metal is used as the seed material for all seeded air and N_2 calculations. The CEA reactant data for these calculations is given in Table C.4- 1.

Table C.4- 1. CEA reactant data for electron attachment analysis.

Species	Relative Moles for 1% Seed Fraction	Relative Moles for 0.01% Seed Fraction
N_2	78.85	78.85
O_2	21.15	21.15
Cs	1.0101	0.0101

C.4.2.3 Evaluation of Electron Attachment in Air

Ionization of the Cs seed provides the free electrons necessary for electrical current conduction in the plasma. As seen in Figure C.4- 1, the ionization fraction is a strong function of temperature, pressure, and seed fraction. For a seed fraction of 0.01%, Cs is ionized to only a few percent at temperatures up to 2,200 K but exceeds 95% at a temperature of approximately 3,750 K for the 1-atm plasma. However, for a 100-atm plasma at this same temperature, the ionization fraction is only about 43%, indicating a strong pressure effect.

Ionization fractions are much lower for the 1% seeded air -- approximately 35% for 1 atm and only 5% for 100 atm at the same temperature of 3,750 K used in the example above. Although ionization fractions are lower, the addition of 1% Cs seed significantly increases the concentration of Cs ions compared to the 0.01% seed as illustrated in the inset of Figure C.4- 1. This results in increased electrical conductivity, even with electron attachment as will be discussed below.

Electron attachment is most prominent at the lowest temperatures as seen in Figure C.4- 2, which shows the concentrations for the most significant ions in 1% Cs-seeded air at 1-atm pressure. At 1,400 K, the mole fraction concentration of the nitrous oxide negative ion (NO_2^-) is seen to be only very slightly less than the Cs positive ion (Cs^+) concentration indicating that almost all of the available electrons are attached to the NO_2 molecules at this condition. The mole fraction concentration of all other ions is more than two orders of magnitude less than Cs^+. However, the strong electron attachment at this condition is not particularly significant since the ionization fraction of the Cs is actually very low at this temperature as seen in Figure C.4- 1 (this value is

actually approximately 3×10^{-5} as taken from the data set used for this figure). Thus, at this condition, the concentration of the Cs^+ is insignificant so the electron attachment is inconsequential.

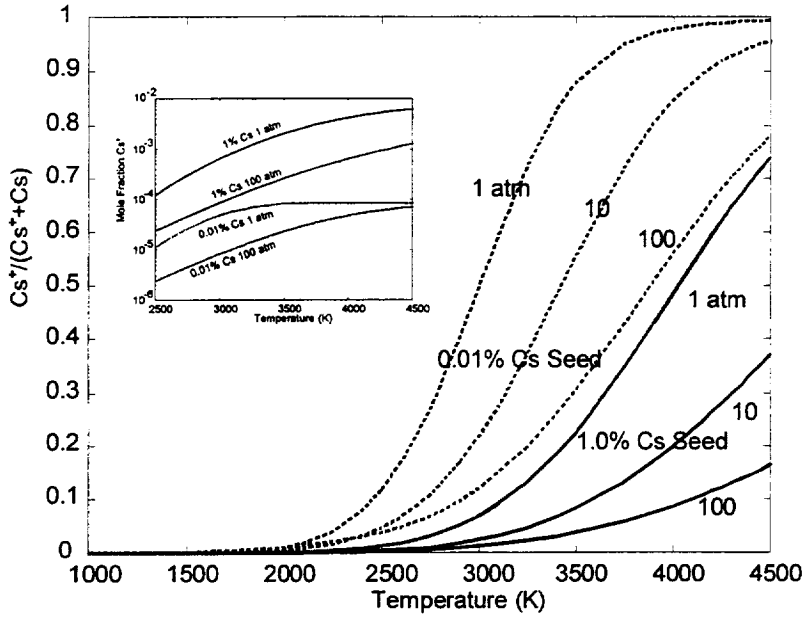

Figure C.4- 1. Ionization fractions for Cs-seeded air.

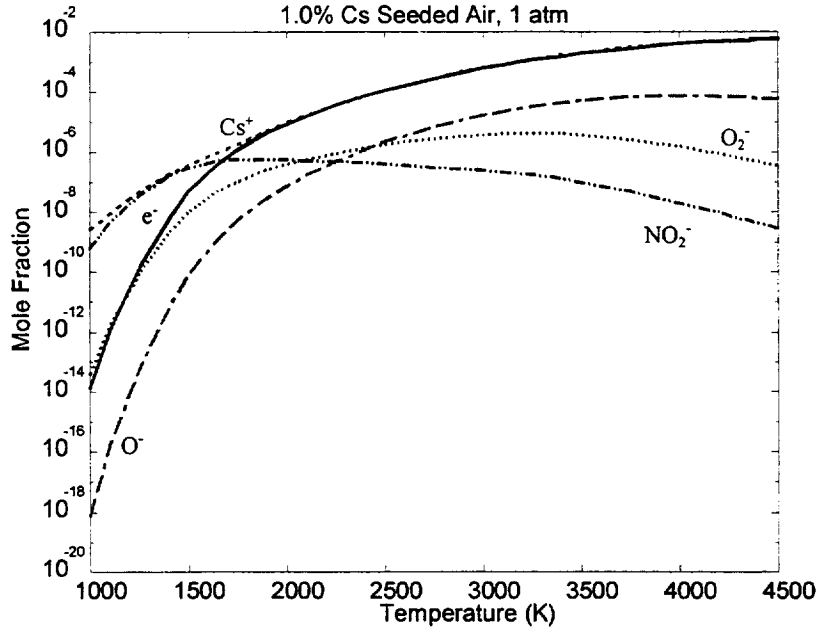

Figure C.4- 2. Concentrations of the dominant charged species for 1% Cs-seeded air at 1 atm.

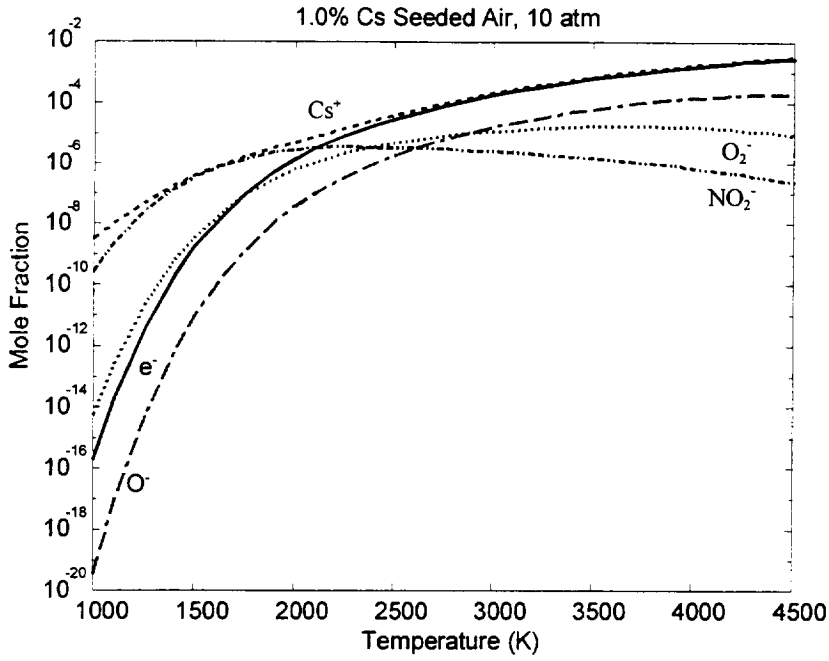

Figure C.4- 3. Concentrations of the dominant charged species for 1% seeded air at 10 atm.

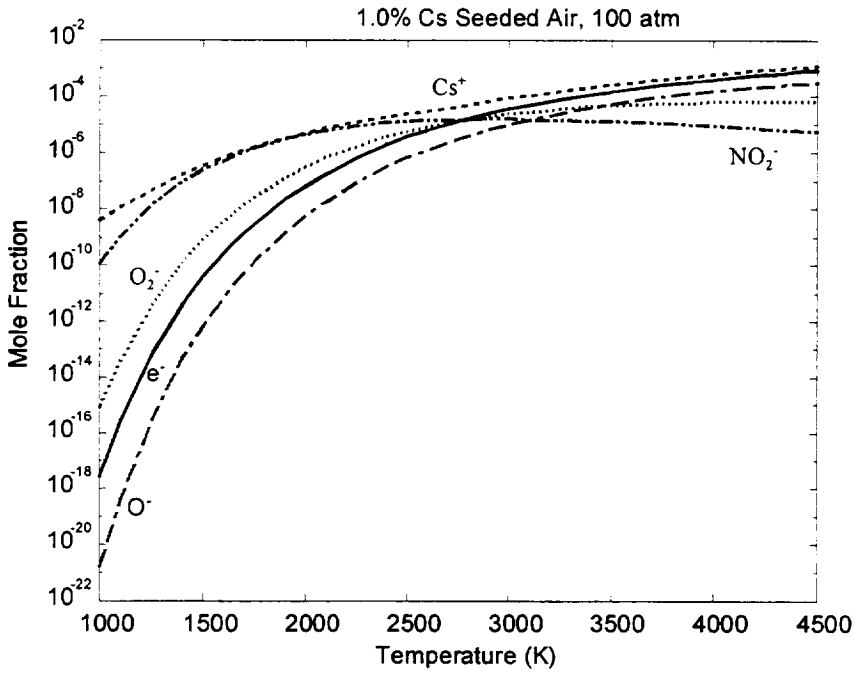

Figure C.4- 4. Concentrations of the dominant charged species for 1% seeded air at 100 atm.

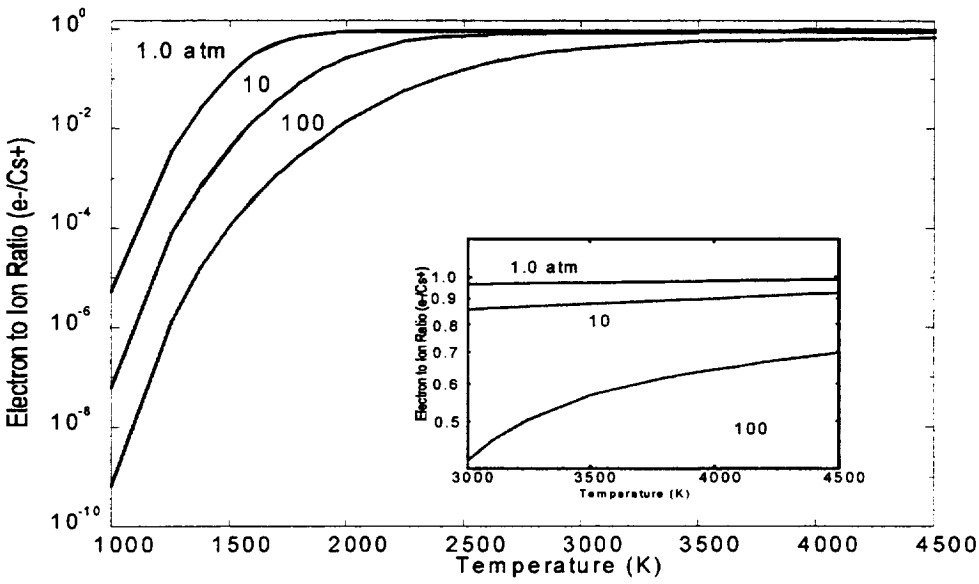

Figure C.4- 5. Electron-to-Cs ion fraction for Cs-seeded air.

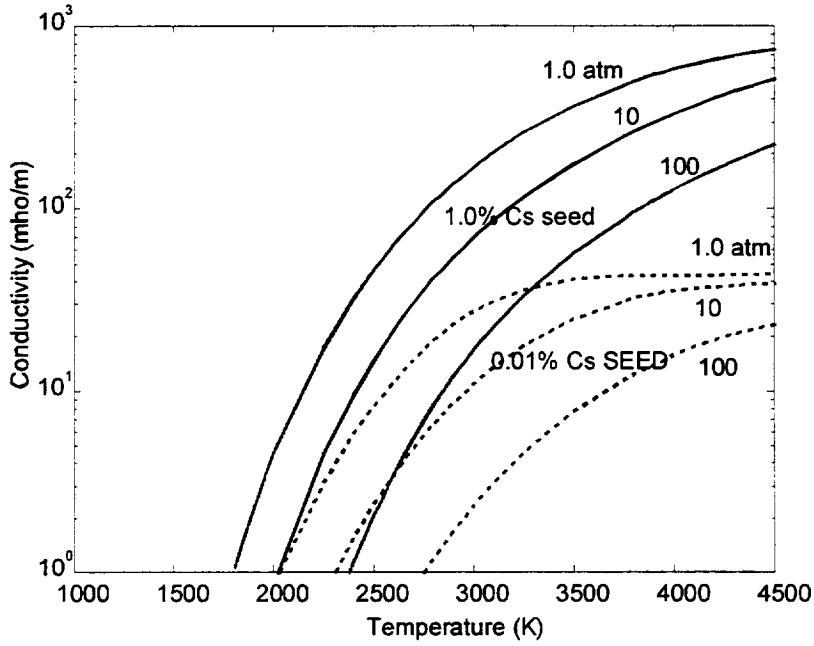

Figure C.4- 6. Electrical conductivity for Cs-seeded air.

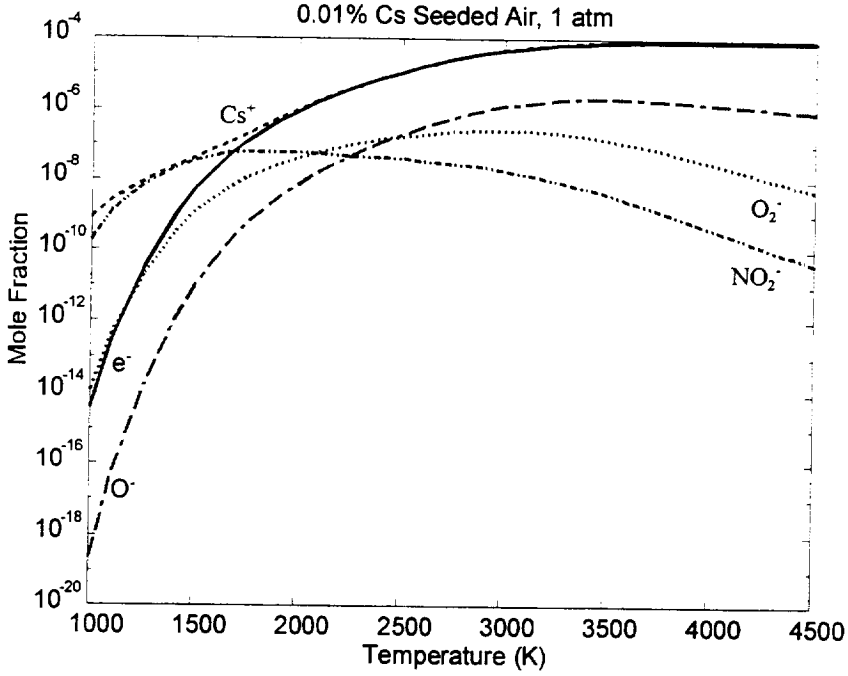

Figure C.4- 7. Concentrations of the dominant charged species for 0.01% Cs-seeded air at 1 atm.

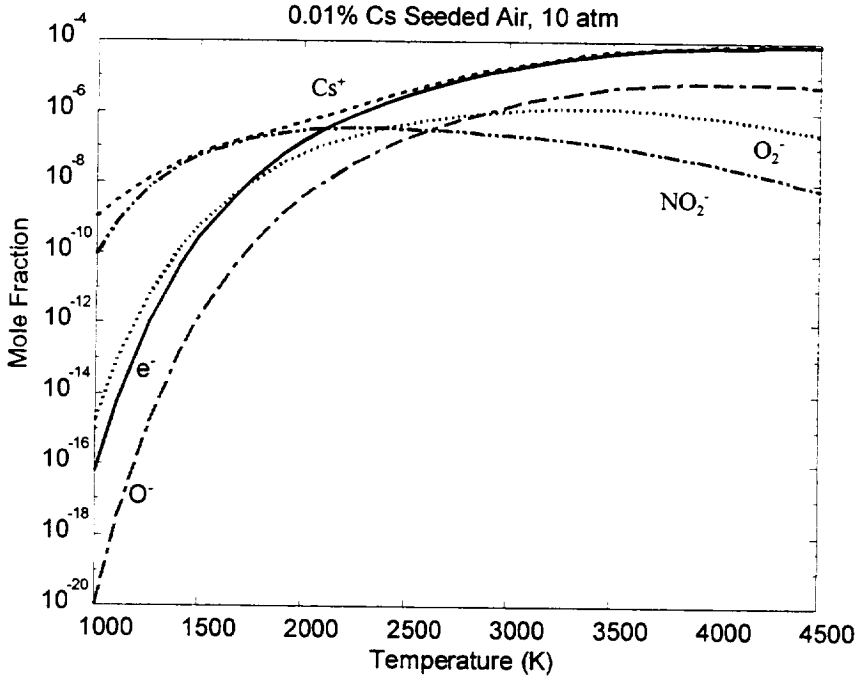

Figure C.4- 8. Concentrations of the dominant charged species for 0.01% Cs-seeded air at 10 atm.

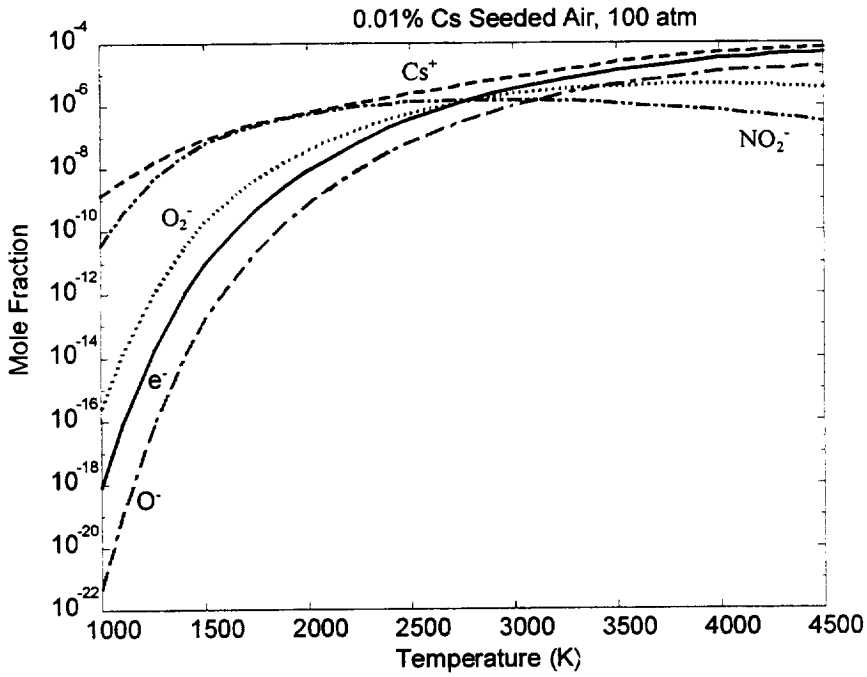

Figure C.4- 9. Concentrations of the dominant charged species for 0.01% Cs-seeded air at 100 atm.

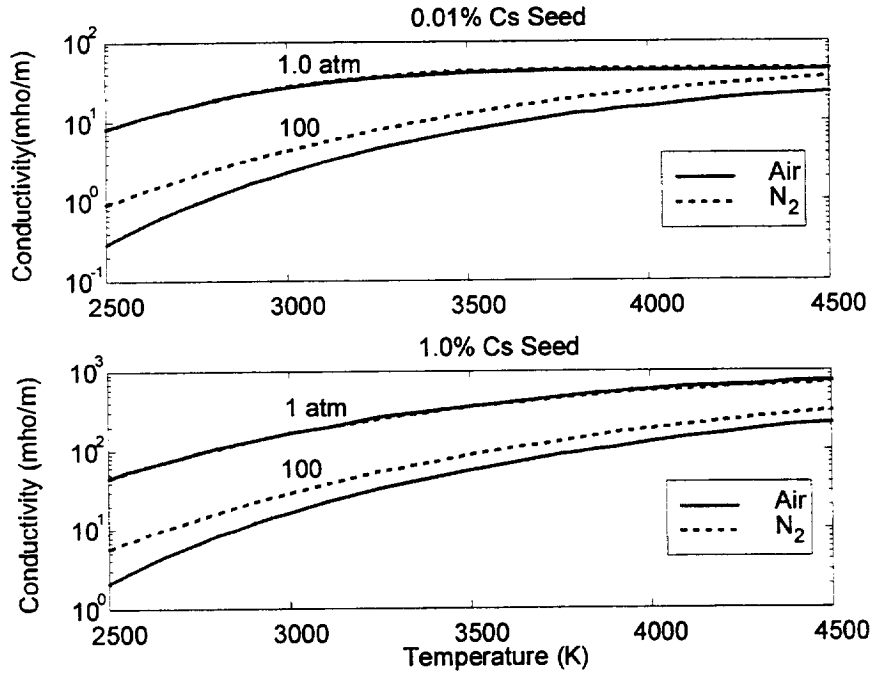

Figure C.4- 10. Comparison of electrical conductivity for Cs-seeded N_2 and Cs-seeded air.

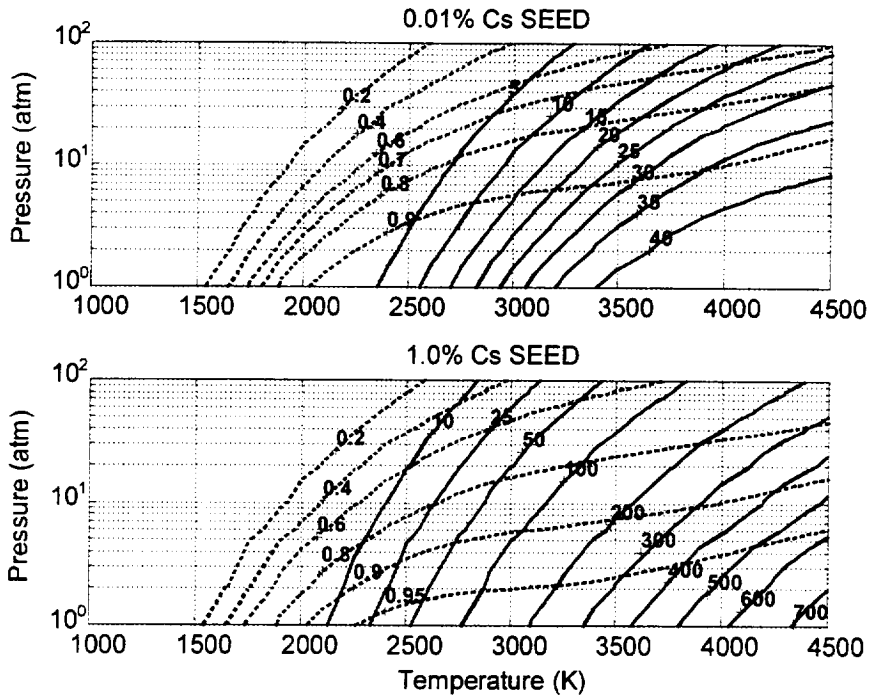

Figure C.4- 11. Electrical conductivity map for Cs-seeded air.

Referring again to Figure C.4- 2, the concentration of NO_2^- decreases rapidly above a temperature of 1,500 K, and the electron concentration rises to approach very close to the Cs^+ concentration, indicating that electron attachment is insignificant in the 1% seeded, 1-atm air plasma. These same trends are observed for a 10-atm air plasma in Figure C.4- 3 and a 100-atm plasma in Figure C.4- 4. However, by comparing these three figures, concentrations of Cs are seen to decrease, and those of the negative ions increase with increasing pressure. Thus, the effects of electron attachment become more significant with increasing pressure in the 1% seeded plasma.

This can more readily be seen in Figure C.4- 5 showing the electron-to-Cs ion ratio (e^-/Cs^+) for the 1-% Cs-seeded air. This is the fraction of available electrons that are still free in the plasma. As noted previously in Figure C.4- 2, the electron concentration for the 1-atm plasma approaches that of Cs^+ at a relatively low temperature. From Figure C.4- 5, the ratio of these concentrations can be seen to approach a value of 1 at temperatures above 2,000 K, indicating that most of the electrons are not attached to other air species.

At 3,000 K (see the inset in Figure C.4- 5), approximately 97% of the available electrons are seen to be free in a 1-atm plasma, while this drops to 85% at 10 atm and 42% at 100 atm. Thus, the percentages of electrons that are attached in negative ions are 3%, 15%, and 58% for these three pressures. Figure C.4- 1 shows that the ionization fraction at this temperature is still low but significant (less than 10% for 1 atm and less than 2% for 10 atm). Since electrical conductivity is proportional to the number of free electrons [see Eq. (C.4-14)], the 1-atm plasma would be expected to have a reasonably high conductivity with an ionization fraction

approaching 10% and very few electrons lost to negative ion formation. However, at the 100-atm pressure, the ionization fraction is on the order of only 1%, and 58% of the electrons are lost to attachment, thus the conductivity would be expected to be low. These speculations can be seen to be true in Figure C.4- 6 where the 1-atm plasma has an electrical conductivity of approximately 165, and the 100-atm plasma conductivity is only 17.

The electron attachment trends are very similar at a seed fraction of 0.01% to those discussed above for the 1% seed fraction as can be seen in Figure C.4- 7 for the 1-atm plasma, Figure C.4-8 for the 10-atm plasma, and Figure C.4-9 for 100 atm. However, the mole fractions for the electrons and all ions are considerably lower due to the smaller amount of seed available.

Comparing these figures to Figures C.4- 2, C.4- 3, and C.4- 4 for 1% seeding, it is seen that the NO_2^- approaches very close to the Cs^+ concentration in the temperature range from 1,400 to 1,800 K as in the more heavily seeded case. Again, the electron concentration is almost identical to the Cs^+ concentration in the 0.01% case at high temperature but deviates more at the higher pressure due to the dominance of the O^- ion. In fact, when Figure C.4- 5 was created showing the electron-to-Cs ion ratio (e^-/Cs^+), data for both 1% and 0.01% seed was plotted; however, the lines for the two cases could not be distinguished at this scale. Therefore, the seed fraction, at least in the range of 0.01-1.0%, has no significant effect on the electron ion ratio. Since the fraction of available electrons that are attached in negative ions is equal to one minus this ratio, this is equivalent to saying that the seed fraction has no significant effect on electron attachment. Electrical conductivities for the 0.01% seed fraction are compared to the 1% seed fraction in Figure C.4- 6. As would be expected, the electrical conductivities are lower for the lower seed fraction at 3,000 K and 1 atm; the 0.01% seed plasma has an electrical conductivity of approximately 28 compared to 165 noted earlier for the 1.0% seed case. As discussed above, the electrical conductivity is proportional to electron concentration [Eq. (C.4-14)]. The Cs fraction is greater by a factor of 100 for the high seed case; however, the electron fraction is increased by a much smaller factor since the ionization fraction for the high seed case is much smaller (see Figure C.4- 1). Thus, the electrical conductivities for the low seed case are not reduced as much as might be expected since the available seed is used more effectively at the lower level of seeding.

The effect of electron attachment on electrical conductivity can be estimated by comparing the Cs-seeded air conductivities with values for Cs-seeded N_2 since significant negative ion formation does not occur in the N_2. Electrical conductivities for seeded N_2 and air plasmas are compared for two pressures and two seed fractions in Figure C.4- 10. As expected, electrical conductivities for seeded N_2 are higher than those for air, especially at high pressure and high temperature where electron attachment was shown to be most dominant in the discussions above. At low pressure, the electrical conductivities in N_2 and air are almost identical. However, at high pressure, the electrical conductivity of the seeded N_2 is significantly higher than that of the seeded air. Comparison of electrical conductivities at low, moderate, and high temperatures are presented in Table C.4- 2.

Table C.4- 2. Comparison of seeded air and N_2 electrical conductivities at 100-atm pressure.

Temperature (K)	1.0% Cesium			0.01% Cesium		
	Electrical Conductivity (mho/m)		Percent Decrease in Air	Electrical Conductivity (mho/m)		Percent Decrease in Air
	Air	N_2		Air	N_2	
4,500	225.1	318.5	29%	23.2	35.7	35%
3,500	56.9	88.0	35%	7.7	12.8	39%
2,500	2.1	5.8	63%	0.3	0.9	68%

As seen in Table C.4- 2 and Figure C.4- 10, the electrical conductivity of seeded air can be depressed significantly by electron attachment in some temperature and pressure regimes. The large depression of the conductivities at the lowest temperature are inconsequential since the magnitude of the electrical conductivities at this high pressure, low temperature condition are so low that MHD using equilibrium ionization would not be considered in this regime. At the highest temperature and with 1% Cs seeding, the conductivity is depressed less than 30%.

C.4.2.4 Mapping of Electrical Conductivity for Cs-Seeded Air MHD

Maps of the electrical conductivity of 0.01% and 1.0% Cs-seeded air are shown in Figure C.4- 11. With 1% seeding as shown in the lower diagram, reasonably high values of electrical conductivity (on the order of 100-300 mho/m) can be obtained at operating temperatures of 3,000 to 3,500 K for pressures below 10 atm. Conductivities decrease with increasing pressure; however, as can be seen, values in excess of 50 can still be obtained at a 100-atm pressure in this temperature range. Much higher temperatures would be required to achieve high values of electrical conductivity (100 mho/m or more) at this pressure.

C.4.3 Comparison and Evaluation of Chemical Equilibrium Codes

C.4.3.1 1% Cesium, 100 Atm

Figures C.4- 12 through C.4- 14 present the dominant charge transport species concentrations for a 1% Cs-seeded, diatomic (no CO_2, H_2O, or Ar), air plasma at 100 atm, with temperature variations from 1,500 to 3,500 K.

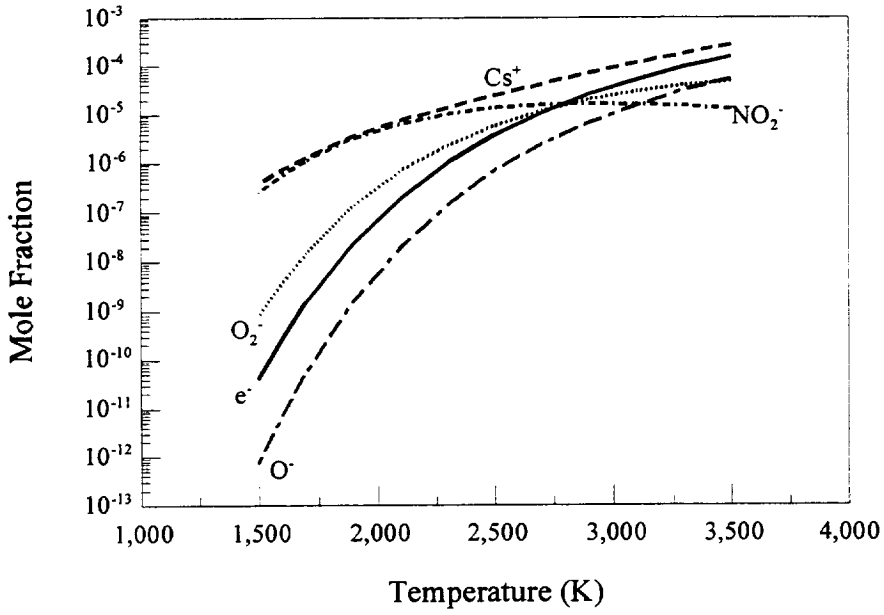

Figure C.4- 12. Dominant charge transport species, CEA Code, 1% Cs in air at 100 atm.

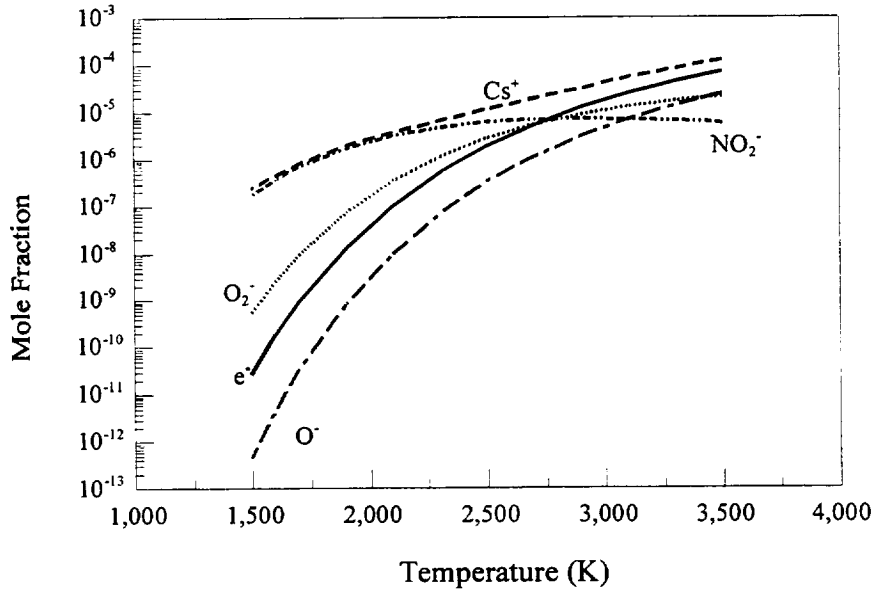

Figure C.4- 13. Dominant charge transport species CET89 Code, 1% Cs in air at 100 atm.

Data obtained from the CEA code is presented in Figure C.4- 12. Prior experience with combustion plasmas would indicate that Cs^+ ions should be the only source of free electrons and that the large majority of electrons should be free. Thus, the free electron (e^-) curve in Figure C.4- 12 should have nearly coincided with the Cs^+ curve but did not. Figure C.4- 12 indicates that at low temperatures most of the electrons were attached by the NO_2^- ion. At the high end of the temperature range most of the electrons were free, although the O^- ion was gaining in importance as an electron attacher as the temperature increased.

Figure C.4- 13 presents concentrations for the same plasma state range as calculated by the CET89 code. Note that exactly the same trends are shown as for Figure C.4- 12, except the values were offset somewhat. This offset will be examined later.

Figure C.4- 14 presents the HSC calculation for the same parameter variation. Note that here, however, the free electron concentration was depressed even further, with O_2^- attaching more electrons than remain free across the entire temperature range. This is of major significance for MHD performance. If HSC were right, equilibrium MHD performance would be poor because of a lack of free electrons to carry enough current to achieve an adequate Faraday force. However, if CEA (Figure C.4- 12) is right, equilibrium MHD performance will be much better.

Free electron concentrations calculated by all three codes for the same parametric variation are compared in Figure C.4- 15. Note that CEA consistently predicts the highest free electron concentration, while HSC consistently predicts the lowest. This is consistent with the observations from Figures C.4- 12 through C.4- 14 that HSC predicted more electron attachment by the negative ions.
The next section examines the same conditions at a reduced pressure of 10 atm. Less electron attachment would be expected for that condition since it is nearer to previous experience obtained with MHD generators operating in the 1-atm neighborhood where little attachment was observed.

C.4.3.2 1% Cesium, 10 Atm

Figures C.4- 16 through C.4- 18 display the concentration profiles predicted by CEA, CECTRN, and HSC, at 10 atm.

Comparing Figure C.4- 12 to Figure C.4- 16, the basic relationship of the various species concentrations is seen to be similar, but NO_2^- dominated the free electrons at temperatures below 2,000 K. Negative O_2 ions were present at the higher temperatures but at an order of magnitude lower concentration than the free electrons.

The CET89 results for the same conditions, shown in Figure C.4- 17, are similar to CEA in Figure C.4- 16 except that the concentrations of negative ions are somewhat lower. Figure C.4- 18 shows the same conditions as calculated by HSC. As was the case with Figure C.4- 14, HSC calculated that negative ions dominated free electrons at all temperatures. The free electron concentrations for the three codes are compared in Figure C.4- 19. Note that differences between the three codes are a little larger than for the 100-atm case in Figure C.4- 15.

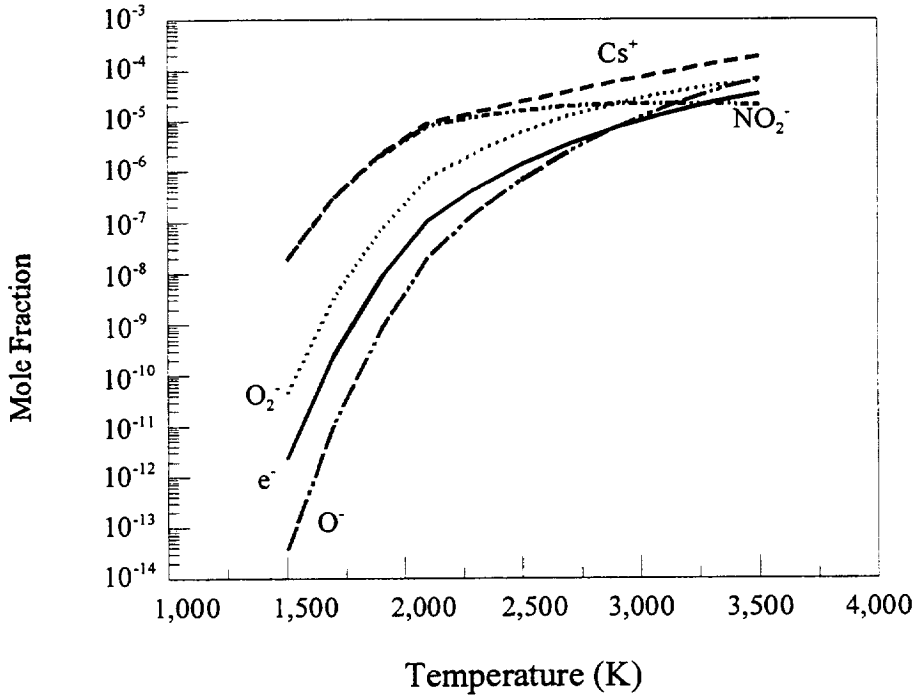

Figure C.4- 14. Dominant charge transport species, HSC 1% Cs in air, 100 atm.

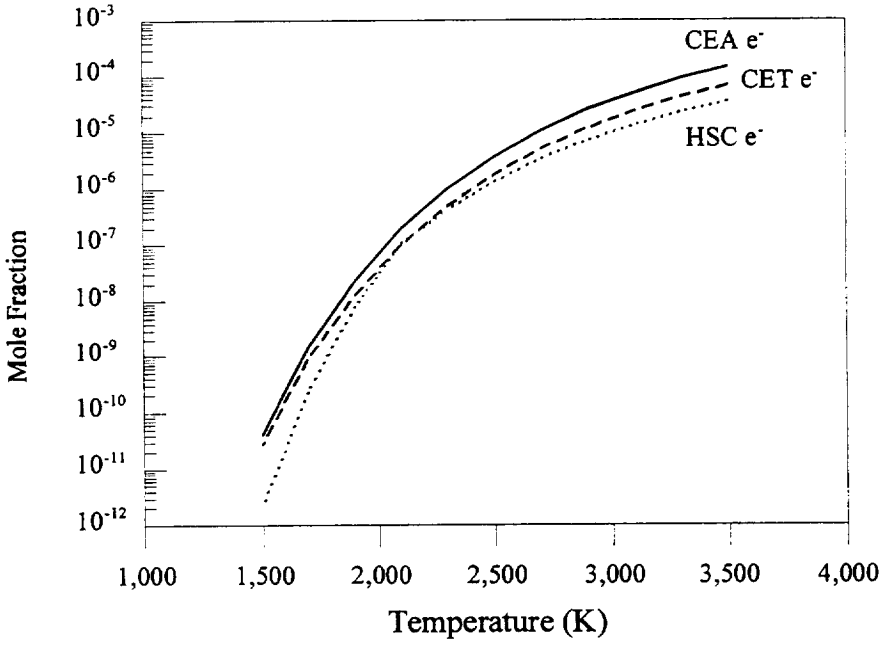

Figure C.4- 15. Free electron concentration comparison, 1% Cs in air, 100 atm.

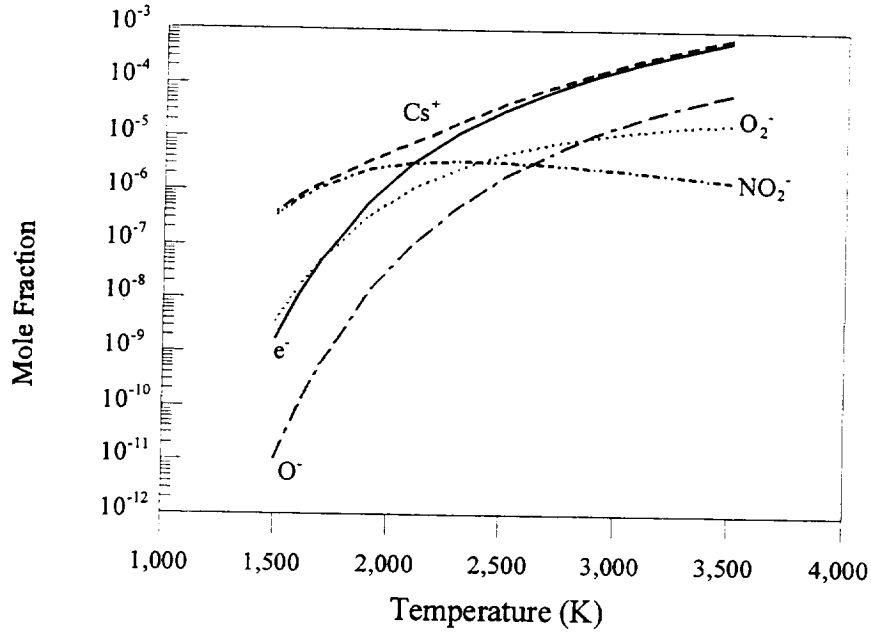

Figure C.4- 16. Dominant charge transport species CEA, 1% Cs in air, 10 atm.

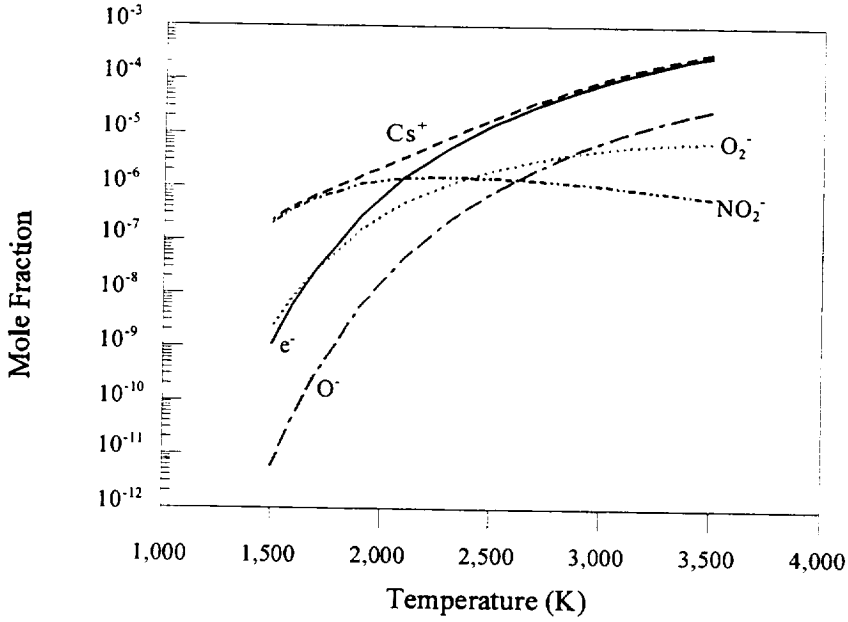

Figure C.4- 17. Dominant charge transport species CET89 Code, 1% Cs in air, 10 atm.

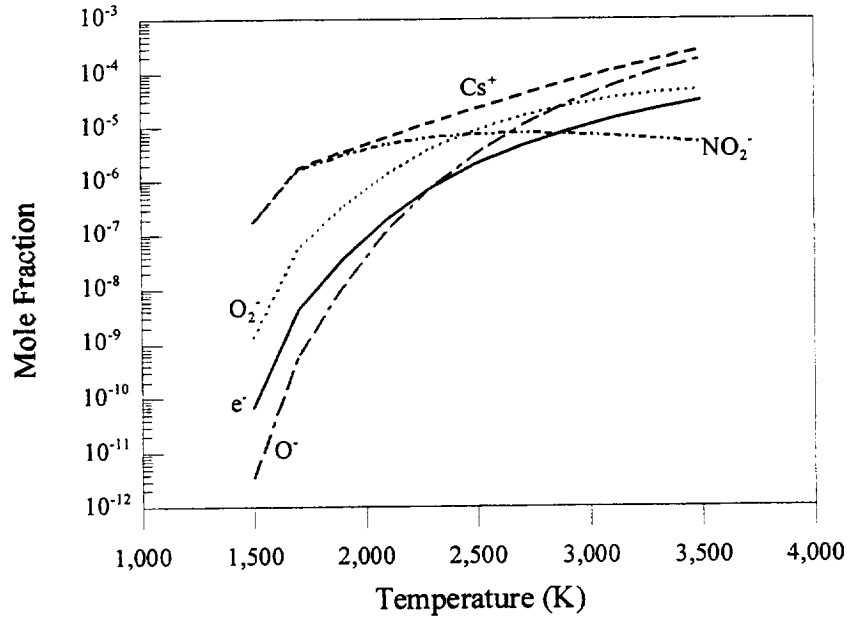

Figure C.4- 18. Dominant charge transport species HSC, 1% Cs in air, 10 atm.

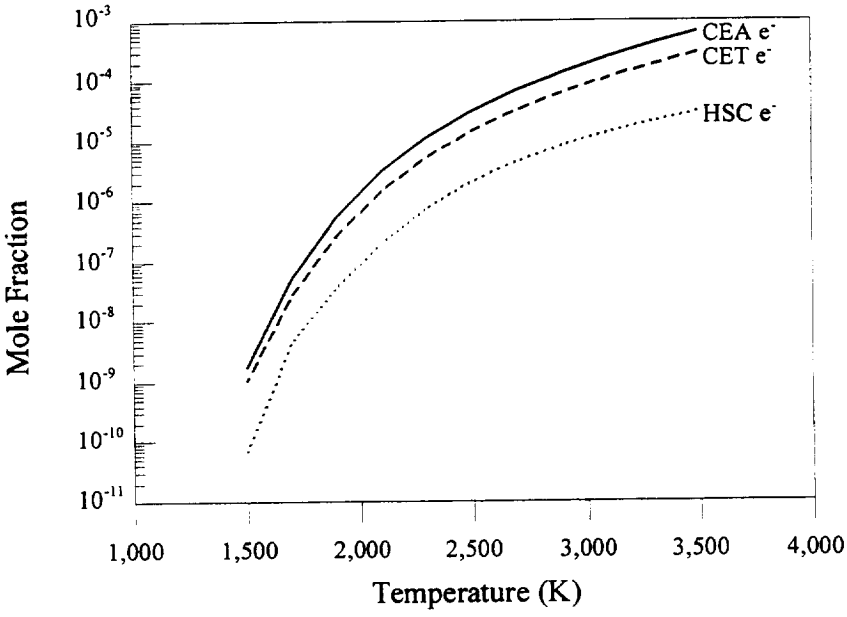

Figure C.4- 19. Free electron concentration comparison, 1% Cs in air, 10 atm.

C.4.3.3 0.01% Cesium, 100 Atm

The previous two cases considered (Figures C.4- 12 through C.4- 19) are for 1-% Cs seed. While this yielded fairly high electrical conductivity, and thus could be good for equilibrium performance, it could also lead to instabilities. Therefore, Cs seed levels of 0.01% have been considered at the same two pressures. Figures C.4- 20 through C.4- 22 present the results from CEA, CET89, and HSC for 0.01% Cs seed in air at 100 atm.

The CEA solution in Figure C.4- 20 looks very similar to the equivalent 100-atm CEA solution of Figure C.4- 12 except that the free electron concentration is approximately an order of magnitude lower. Figure C.4- 21, the CET89 equivalent to Figure C.4- 13, shows no obvious differences. HSC calculations in Figure C.4- 22 over the same range shows a similar pattern to Figure C.4- 14 where both O_2^- and NO_2^- are greater than the free electrons for almost the entire temperature range.

Figure C.4- 23 compares the free electron concentration calculated by CEA, CET89, and HSC in Figures C.4- 20 through C.4- 22. Note that this figure looks very much like Figure C.4- 15 that displayed the same plasma conditions but with 100 times the Cs content. The fact the comparison curves closely resemble each other suggests the differences in the codes are not related to the Cs data. This result is considered more closely in the next section for a low Cs seed ratio and 10-atm pressure.

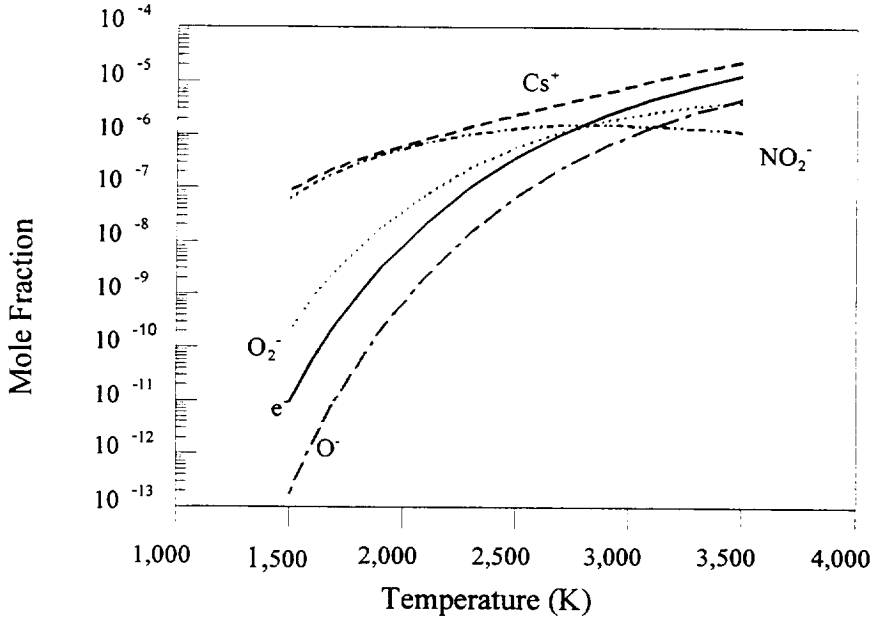

Figure C.4- 20. Dominant charge transport species CEA, 0.01% Cs in air, 100 atm.

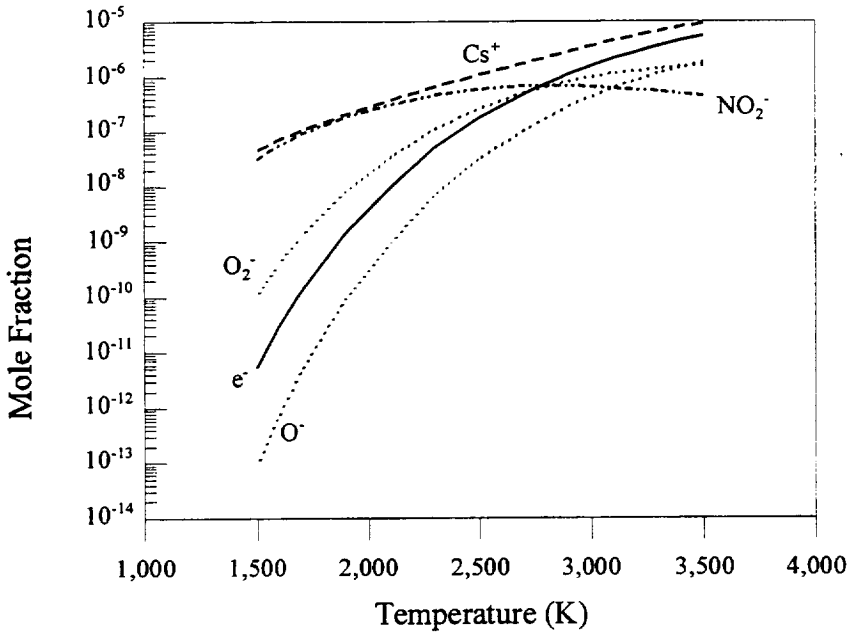

Figure C.4- 21. Dominant charge transport species CEC, 0.01% Cs in air, 100 atm.

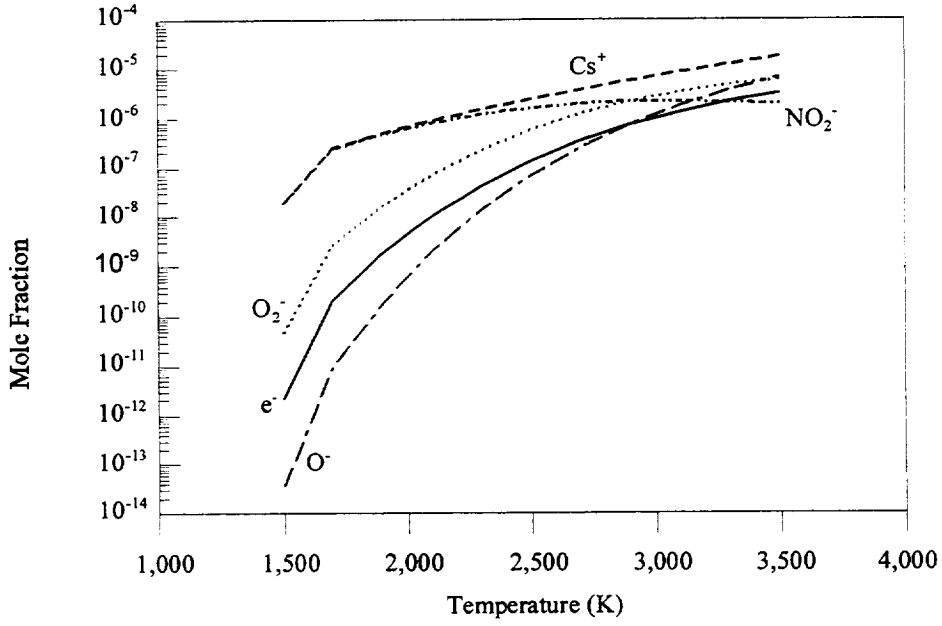

Figure C.4- 22. Dominant charge transport species HSC, 0.01% Cs in air, 100 atm.

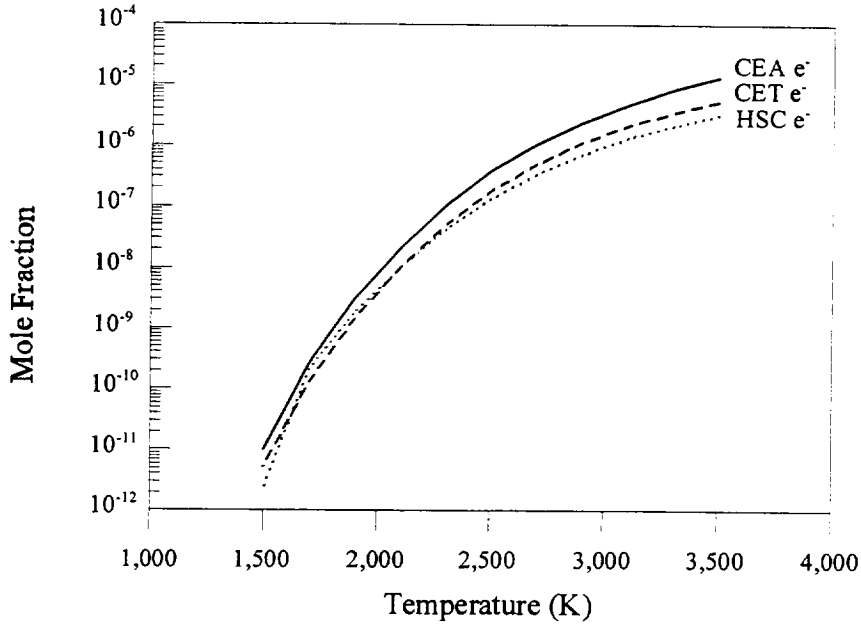

Figure C.4- 23. Free electron concentration comparison, 0.01%Cs in air, 100 atm.

C.4.3.4 <u>0.01% Cesium, 10 Atm</u>

Figures C.4- 24 through C.4- 26 present the species concentrations for this condition as calculated by CEA, CET89, and HSC. Figure C.4- 24 was consistent with Figures C.4- 12, C.4- 16, and C.4- 20 in that at low temperatures negative ions dominate but at intermediate and higher temperatures, free electrons dominate the charge transport. Figure C.4- 25, from CET89, indicates a similar trend.

HSC calculations presented in Figure C.4- 26 are consistent with Figures C.4- 14, C.4- 18, and C.4- 22, indicating that various negative ions capture the free electrons at all temperatures. Again, this would not be good for MHD accelerators if HSC is correct.

Finally, Figure C.4- 27 compares free electron concentration as calculated from all three codes for the 0.01% Cs, 10-atm case. This confirms that CEA and CET89 are fairly close, with HSC showing considerably lower electron concentration. It is interesting that the free electron deficit is fairly constant over the temperature range. This suggests the difference is not associated with the electronegativity of only one species, unless it is O_2^- whose influence is spread over the entire temperature range. The next section further addresses the differences between the three codes in an attempt to determine the cause.

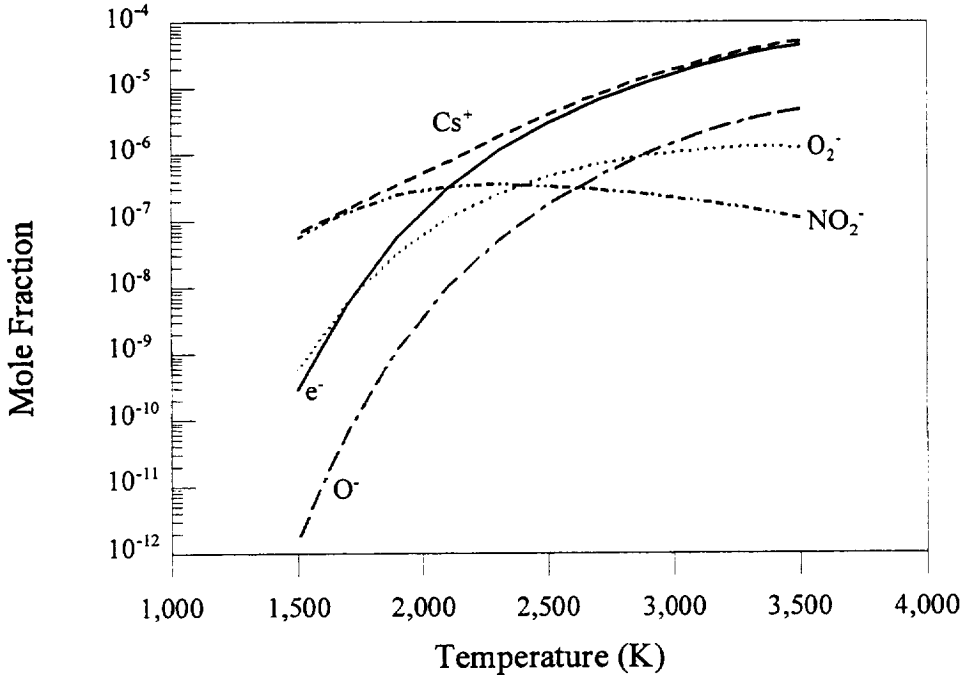

Figure C.4- 24. Dominant charge transport species CEA, 0.01% Cs in air, 10 atm.

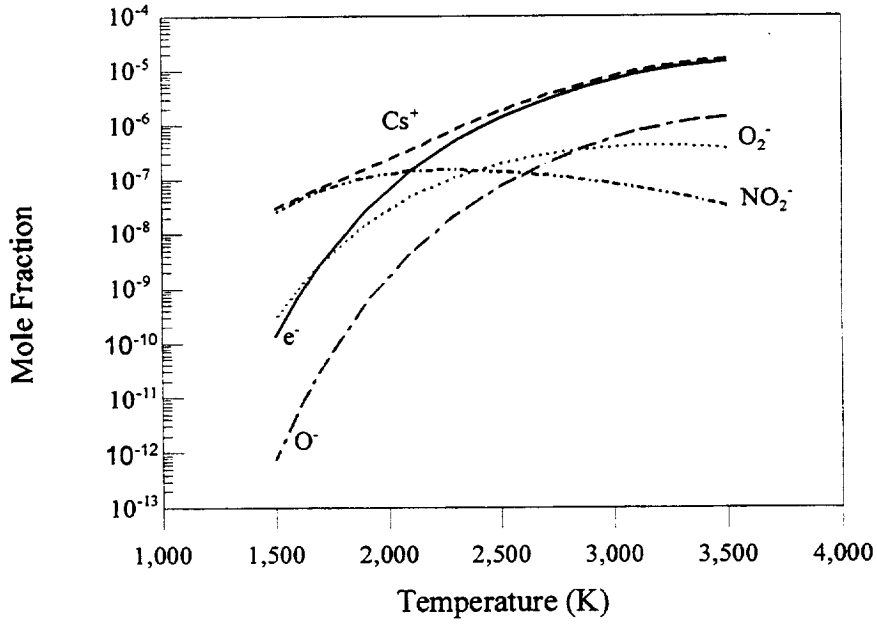

Figure C.4- 25. Dominant charge transport species CEC, 0.01% Cs in air, 10 atm.

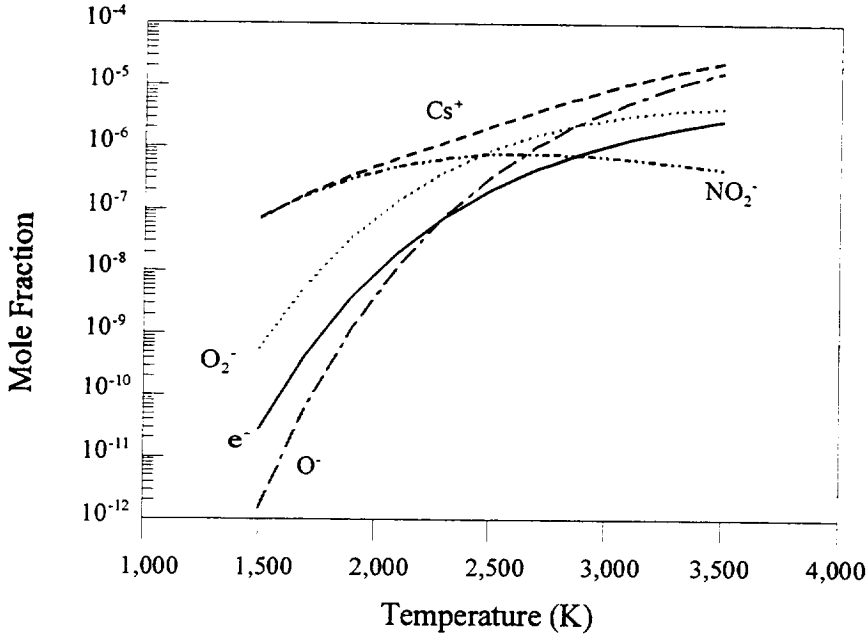

Figure C.4- 26. Dominant charge transport species HSC, 0.01% Cs in air, 10 atm.

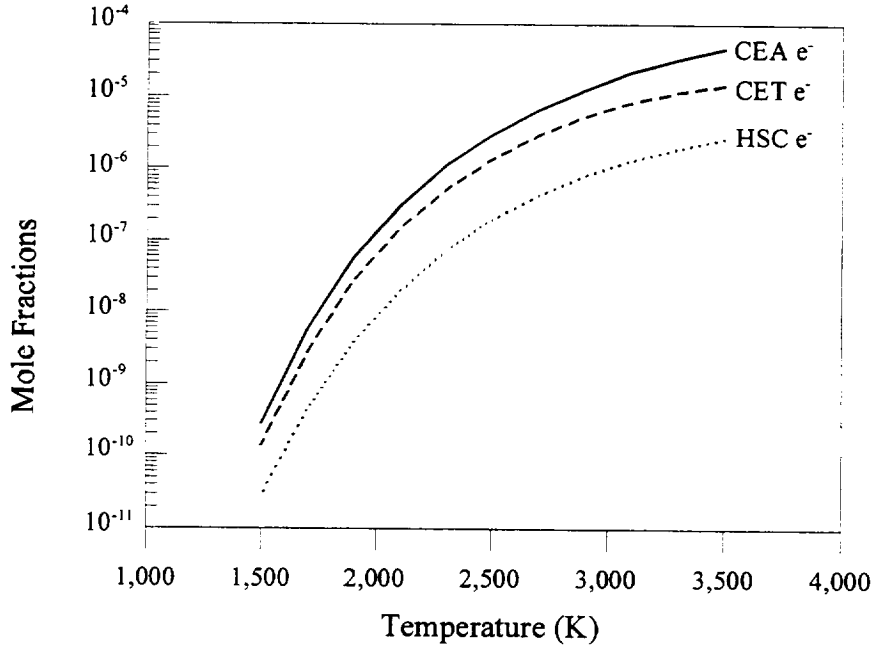

Figure C.4- 27. Free electron concentration comparison, 0.01% Cs in air, 10 atm.

C.4.3.5 Other Species

One of the first possibilities explored was that the differences of Figures C.4- 15, C.4- 19, C.4- 23, and C.4- 27, which compare free electron concentrations for the three codes at each condition, might be due to differences in the predicted concentrations of Cs^+ ions. This seemed plausible since Cs ionization was the source of almost all of the electrons.

Comparing these predictions for the conditions of the last section in Figure C.4- 28 yields an interesting result. HSC agrees with CEA at low temperatures but drifts over to agree with CET89 at high temperatures. This suggests HSC uses Cs ion data close to that of CEA, which was evaluated at low temperature. Since all the codes extrapolate this data to higher pressures where it was not measured (see next section for data comparisons), it may be that HSC uses the same extrapolation technique as CET89 but from data similar to CEA.

Next, Figure C.4- 29 compares the NO_2^- predictions from all three codes. At high temperatures the differences do not matter since there is not much NO_2^- at high temperature. At low temperature, CEA and HSC are in good agreement. This again suggests they may share the more modern data but a different extrapolation.

Figure C.4- 30 compares O^- concentration profiles for the three codes. Again the pattern emerges with CEA and HSC in agreement at low temperatures and diverging as temperatures increase. No divergence is evident between CEA and CET89, although they are different at all temperatures. Finally, Figure C.4- 31 compares O_2^- concentrations. Again, CEA and HSC agree at low temperature but diverge as temperature increases.

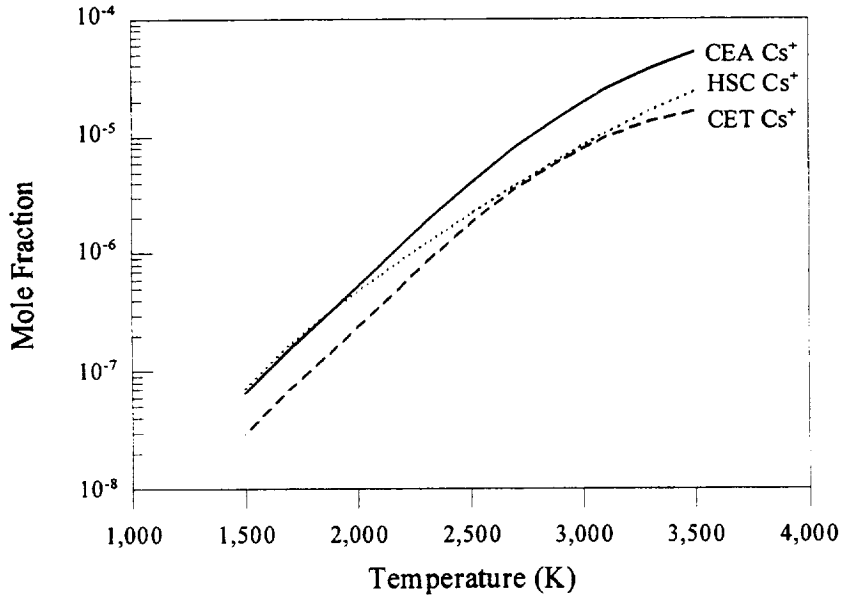

Figure C.4- 28. Cs^+ concentration comparison, 0.01% Cs in air, 10 atm.

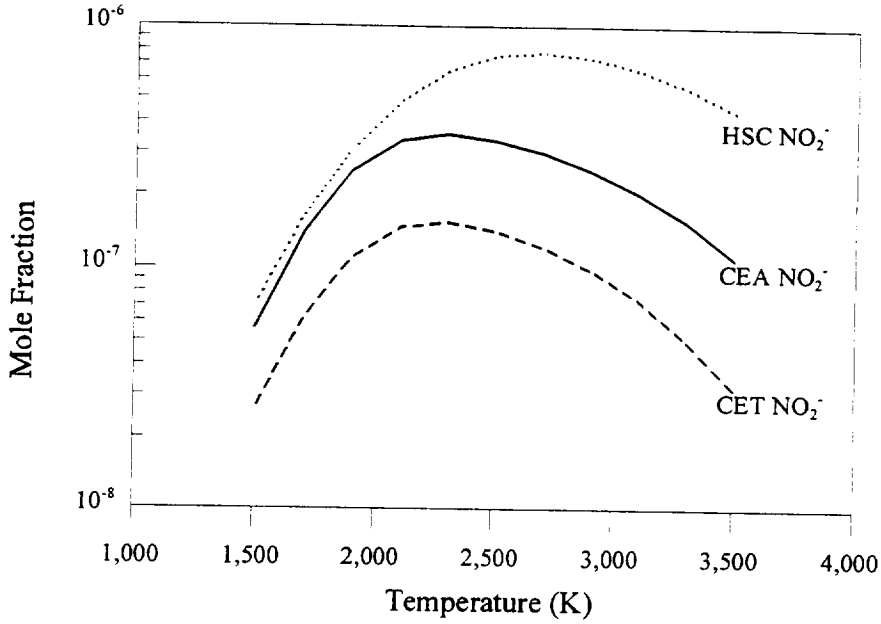

Figure C.4- 29. NO_2^- ion concentration comparison, 0.01% Cs in air, 10 atm.

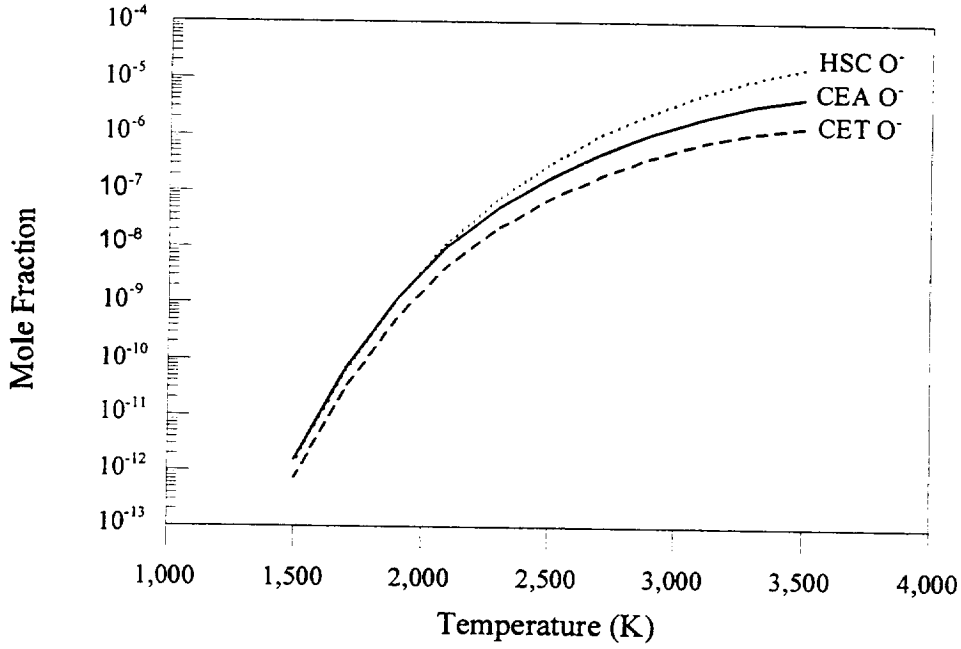

Figure C.4- 30. O^- ion concentration comparison 0.01% Cs in air, 10 atm.

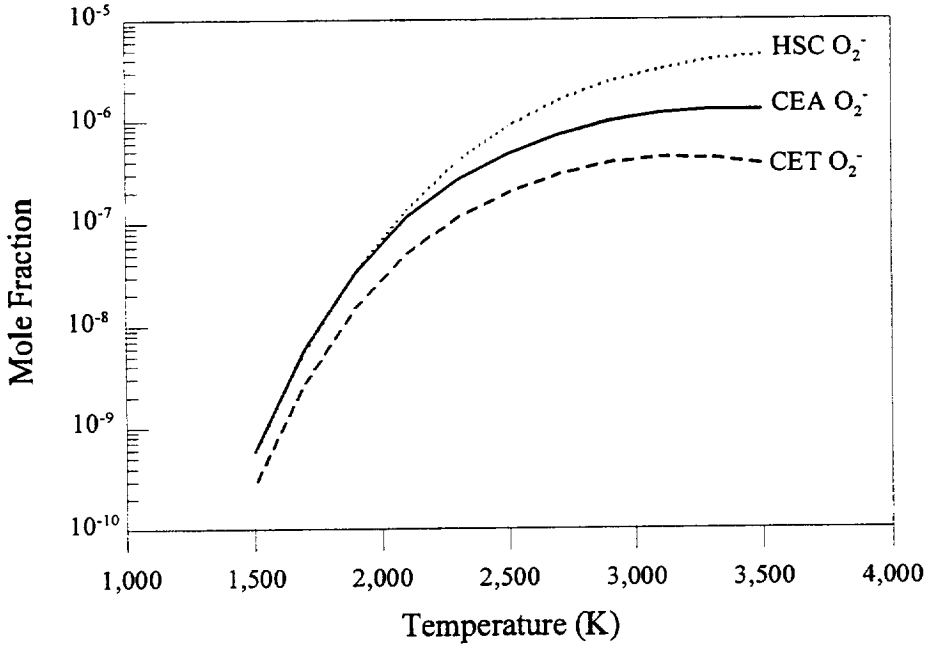

Figure C.4- 31. O_2^- ion concentration comparison 0.01% Cs in air, 10 atm.

The foregoing examination of various other concentration profiles for the 0.01% Cs, 10-atm case suggests that the key to the differences may be in the extrapolation method for negative ions from low temperature data. The next section examines this data and extrapolations to the extent they are known.

C.4.3.6 Thermodynamic Data for CEA, CET89, and HSC Codes

Thermodynamic data for each of the three codes evaluated in this study is presented in this section. Previous sections have described the differences in the electron concentrations calculated by the three codes. The thermodynamic data is then used in the next section to investigate these differences in an attempt to select the most accurate code and database for the Cs-seeded MHD accelerator analysis.

Data for the most recent version of CEA is maintained in a library of thermodynamic data that is read by the code for each equilibrium problem evaluated. Thermodynamic data for each species is formatted as indicated in Table C.4- 1. Each species requires a minimum of five lines or records for tabulating the data for the thermodynamic curve-fits.

Table C.4- 3. Thermodynamic data format for CEA Chemical Equilibrium Code (See Ref. 13).			
Record	Contents	Format	Columns
1	Species name or formula	A24	1-24
	Comments (data source)	A56	25-50
2	Number of temperature intervals	I2	2
	Optional identification code	A6	4-9
	Chemical formulas, symbols, and numbers	5(A2,F6.2)	11-50
	Zero for gas and nonzero for condensed phases	I1	52
	Molecular weight	F13.5	53-65
	Heat of formation at 298.15 K, J/mol	F13.5	66-80
3	Temperature range	2F10.3	2-21
	Number of coefficients for C_p°	I1	23
	T exponents in empirical equation for C_p°	8F5.1	24-63
	{H°(298.15)-H°(0)}, J/mol	F15.3	66-80
4	First five coefficients for C_p°	5D16.8	1-80
5	Last three coefficients for C_p°	3D16.8	1-48
	Integration constants b_1 and b_2	2D16.8	49-80
	Repeat 3, 4, and 5 for each interval	---------	-------

Dimensionless thermodynamic properties are calculated using the curve-fit coefficients from the following equations.

Heat capacity:

$$\frac{C_p^\circ}{R} = a_1 T^{-2} + a_2 T^{-1} + a_3 + a_4 T + a_5 T^2 + a_6 T^3 + a_7 T^4 \qquad \text{(C.4- 17}$$

Enthalpy:

$$\frac{H^\circ(T)}{RT} = -a_1 T^{-2} + a_2 T^{-1} \ln T + a_3 + a_4 \frac{T}{2} + a_5 \frac{T^2}{3} + a_6 \frac{T^3}{4} + a_7 \frac{T^4}{5} + \frac{b_1}{T} \qquad \text{(C.4- 18)}$$

Entropy:

$$\frac{S^\circ(T)}{R} = -a_1 \frac{T^{-2}}{2} - a_2 T^{-1} + a_3 \ln T + a_4 T + a_5 \frac{T^2}{2} + a_6 \frac{T^3}{3} + a_7 \frac{T^4}{4} + b_2 \qquad \text{(C.4- 19)}$$

CEA data for selected species used in this analysis are taken from the CEA thermodynamic database and presented in Table C.4- 2. This data is well documented (Refs. 13, 14); however, details of how this data is extended or extrapolated are not discussed. Diatomic O_2 and N_2 (neutral) data is presented in the form of nine-coefficient least-squares curve fits over a 200 to 20,000 K temperature range, with break points at 1,000 and 6,000 K. Nitrogen data in the database was taken from Gurvich (Ref. 15) and is referred to as TPIS78. Oxygen data, referred to as TPIS89, is from Gurvich (Ref. 16).

Data for the positive Cs ion, Cs^+, has been curve-fitted in two ranges, from 298 to 1,000 K and 1,000 to 6,000 K. Since the curve fit for this data extends beyond the range of temperature investigated in this analysis, the concerns expressed in the previous section about extrapolation of the data are probably not warranted for the CEA code. Data for the negative ions presented in Table C.4- 1 were also curve-fitted over the ranges 298 to 1,000 K and 1,000 to 6,000 K. The CEA data is used as the standard of comparison for the other data discussed below.

Dimensionless thermodynamic properties are calculated for the CET89 code using the curve-fit coefficients from the following equations.

Heat capacity:

$$\frac{C_p^\circ}{R} = a_1 + a_2 T + a_3 T^2 + a_4 T^3 + a_5 T^4 \qquad \text{(C.4- 20)}$$

Enthalpy:

$$\frac{H^\circ(T)}{RT} = a_1 + \frac{a_2}{2} T + \frac{a_3}{3} T^2 + \frac{a_4}{4} T^3 + \frac{a_5}{5} T^4 + \frac{a_6}{T} \qquad \text{(C.4- 21)}$$

Entropy:

$$\frac{S^\circ(T)}{R} = a_1 \ln T + a_2 T + \frac{a_3}{2} T^2 + \frac{a_4}{3} T^3 + \frac{a_5}{4} T^4 + a_7 \qquad \text{(C.4- 22)}$$

CET89 data for the same selected species discussed above is taken from the CET89 thermodynamic database and presented in Table C.4-6. The format for this data is obviously different from that of CEA, and the data can be seen to be substantially older. Data for these five species was curve-fitted over the range from 300 to 5,000 K, which is somewhat more restrictive than the CEA curve fits but sufficient for this analysis. Extrapolation of the data as discussed in the previous section was of no more concern in this data than it was for the CEA data.

Thermodynamic data for the HSC code is available in a database manager for the windows program. Species data for this analysis was taken from the HSC database manager and is listed in Table C.4-7.

Table C.4- 4. Thermodynamic data from CEA computer code.

O_2	Oxygen. Gurvich et al. v.1, pt. 2, p.9, 1989										
3 tpis89	O	2.00	0.00	0.00	0.00	0.00	0	31.99880	0.000		
200.000	1000.000	7	-2.0	-1.0	0.0	1.0	2.0	.3.0	4.0	0.0	8680.104
-3.42556269D+04		4.84699986D+02		1.11901159D+00		4.29388743DD-03		-6.83627313D-07			
-2.02337478D-09		1.03904064D-12		0.00000000D+00		-3.39145434D+03		1.84969912D+01			
1000.000	6000.000	7	-2.0	-1.0	0.0	1.0	2.0	3.0	4.0	0.0	8680.104
-1.03793994D+06		2.34483275D+03		1.81972949D+00		1.26784887D-03		-2.18807142D-07			
2.05372411D-11		-8.19349062D-16		0.00000000D+00		-1.68901253D+04		1.73871835D+01			
6000.000	20000.000	7	-2.0	-1.0	0.0	1.0	2.0	3.0	4.0	0.0	8680.104
4.97515261D+08		-2.86602339D+05		6.69015464D+01		-6.16971869D-03		3.01623757D-07			
-7.42087888D-12		7.27744063D-17		0.00000000D+00		2.29348755D+06		-5.53044968D+02			
CS^+											
2J12/83	CS	1.00E	-1.00	0.00	0.00	0.00	0	132.90488	458402.000		
298.150	1000.000	5	0.0	1.0	2.0	3.0	4.0	5.0	0.0	0.0	
2.50000000D+00		0.00000000D+00		0.00000000D+00		0.00000000D+00		0.00000000D+00			
0.00000000D+00		0.00000000D+00		0.00000000D+00		5.43873989D+04		6.18275756D+00			
1000.000	6000.000	5	0.0	1.0	2.0	3.0	4.0	5.0	0.0	0.0	
2.50000000D+00		0.00000000D+00		0.00000000D+00		0.00000000D+00		0.00000000D+00			
0.00000000D+00		0.00000000D+00		0.00000000D+00		5.43873989D+04		6.18275756D+00			
O_2^-	Cons and Hf0: TPIS, v.1, pt.1, p.100, 1989.										
214/89	O	2.00E	1.00	0.00	0.00	0.00	0	31.99935	-48027.921		
298.150	1000.000	7	-2.0	-1.0	0.0	1.0	2.0	3.0	4.0	0.0	9349.611
1.88394450D+04		1.14946026D+02		1.51892644D+00		8.01596940D-03		-9.85034935D-06			
6.04401914D-09		-1.48638364D-12		0.00000000D+00		-7.10149439D+03		1.50118282D+01			
1000.000	6000.000	7	-2.0	-1.0	0.0	1.0	2.0	3.0	4.0	0.0	9349.611
-5.65835514D+04		-2.36693979D+02		4.67573915D+00		-2.19216582D-05		1.71007607D-08			
-1.75562971D-12		8.23710369D-17		0.00000000D+00		-5.96074102D+03		-2.43620517D+00			
O^-	EA and levels: TPIS, 1989, v.1, pt.1, p.93.										
2tpis89	O	1.00E	1.00	0.00	0.00	0.00	0	15.99995	101663.792		
298.150	1000.000	7	-2.0	-1.0	0.0	1.0	2.0	3.0	4.0	0.0	6570.792
-5.69561025D+03		1.09925919D+02		2.18473253D+00		5.32605772D-04		-5.29849371D-07			
2.86996365D-10		-6.52402341D-14		0.00000000D+00		1.09109515D+04		6.72979000D+00			
1000.000	6000.000	7	-2.0	-1.0	0.0	1.0	2.0	3.0	4.0	0.0	6570.792
9.76966374D+03		7.15884132D+00		2.49496248D+00		1.96787226D-06		-4.30322612D-10			
4.91085933D-14		-2.27097780D-18		0.00000000D+00		1.14736118D+04		4.83703095D+00			
NO_2-	Cons & HfO: Tpis, v.1, pt. 1, 1989,p.334.										
2tpis89	N	1.00O	2.00E	1.00	0.00	0.00	0	46.00609	-200035.575		
298.150	1000.000	7	-2.0	-1.0	0.0	1.0	2.0	3.0	4.0	0.0	10177.009
-1.28180466D+04		6.98982172D+02		-2.81244411D+00		2.41285688D-02		-2.83155730D-05			
1.67047604D-08		-3.98324031D-12		0.00000000D+00		-2.80989972D+04		4.06345105D+01			
1000.000	6000.000	7	-2.0	-1.0	0.0	1.0	2.0	3.0	4.0	0.0	10177.009
1.32536966D+05		-1.55694090D+03		8.12662861D+00		-2.72816023D-04		-4.70874841D-08			
2.82688437D-11		-2.35406432D-15		0.00000000D+00		-1.71585409D+04		-2.22824214D+01			

Table C.4-5. Thermodynamic data format for CET89 Chemical Equilibrium Code

Record	Contents	Format	Columns
1	Species name	3A4	1 to 12
	Date	2A3	19 to 24
	Atomic symbols and formula	4(A2,F3.0)	25 to 44
	Phase of species (S, L, or G for solid, liquid, or gas, respectively)	A1	45
	Temperature range	2F10.3	46 to 65
	Integer 1	I15	80
2	Coefficients a_i (i=1 to 5) (for upper temperature interval)	5(E15.8)	1 to 75
	Integer 2	I5	80
3	Coefficients (a_6, a_7, for upper temperature interval, and a_1, a_2, and a_3 for lower)	5(E15.8)	1 to 75
	Integer 3	I5	80
4	Coefficients (a_4, a_5, a_6, a_7 for lower temperature interval)	4(E15.8)	1 to 60
	Integer 4	I20	80
	Repeat cards numbered 1 to 4 for each species		

Table C.4-6. Thermodynamic data from CET89 computer code.

O_2	GLU78	O	2	0	0	0G 300.000	5000.000 1
3.66449339E+00		6.48086726E-04		-1.34938164E-07		1.87386952E-11	-1.11692523E-15 2
-1.21716909E+03		3.39586346E+00		3.78247909E+00		-2.99622655E-03	9.84388004E-06 3
-9.67773050E-09		3.24286164E-12		-1.06394930E+03		3.65691304E+00	4
Cs^+	J12/70CS	1E	-10	00	0g	300.000 5000.000	1
0.25038682E+01		-0.75238859E-05		0.47346482E-08		-0.11801810E-11	0.10117554E-15 2
0.54405152E+05		0.61482962E+01		0.25050509E+01		-0.35642646E-04	0.88202967E-07 3
-0.91546770E-10		0.33935528E-13		0.54406031E+05		0.61481749E+01	4
O_2^-	J12/66O	2E	100	000	0G	300.000 5000.000	1
0.38147234E01		0.77444546E-03		-0.30677649E-06		0.56618118E-10	-0.38229492E-14 2
-0.69910087E04		0.29587995E01		0.31440525E01		0.12127972E-02	0.23812161E-05 3
-0.40614092E-08		0.16885304E-11		-0.67369752E04		0.67688687E01	4
O^-	J3/77O	1E	1	0	0G	300.000 5000.000	1
.25494971+01		-.56262531-04		.24902683-07		-.48702865-11	.35042005-15 2
.11493119+05		.44820553+01		.29002546+01		-16354106-02	.28202166-05 3
-.22688058-08		.69736252-12		.11426745+05		.28209917+01	4
NO_2-	J6/72N	1O	2E	1	0G	300.000 5000.000	1
0.50160903E+01		-.0.21884463E-02		-0.94586144E-06		0.17939789E09	-0.12052428E-13 2
-0.26200160E+05		-0.12861447E+01		0.29818036E+01		0.49398681E-02	0.28557293E-05 3
-0.78905297E-08		0.35391483E-11		-0.25501540E+05		0.99161680E+01	4

Table C.4-7. Thermodynamic data from HSC computer code.

O_2(g)	Oxygen						31.999 g/mol	
	Enthalpy	Entropy	Heat Capacity				Temperature Range	
	H	S	A	B	C	D	T1	T2
	KJ/mol	J/(mol*K)	J/(mol*K)				K	K
G	0.000	205.147	31.323	3.894	-3.105	-0.335	298.150	5000.000
1.429	G/cm³	Barin	1993					

Cs(+g)	Cesium						132.905 g/mol	
	Enthalpy	Entropy	Heat Capacity				Temperature Range	
	H	S	A	B	C	D	T1	T2
G	KJ/mol	J/(mol*K)	J/(mol*K)				K	K
	458.402	169.836	20.790	0.000	1.000	0.000	298.150	6000.000
	g/cm³	JANAF	1985					

O_2(-g)	Oxygen						31.999 g/mol	
	Enthalpy	Entropy	Heat Capacity				Temperature Range	
	H	S	A	B	C	D	T1	T2
	KJ/mol	J/(mol*K)	J/(mol*K)				K	K
G	-48.593	209.591	25.000	19.930	0.220	-7.500	298.150	600.000
G	0.000	0.000	37.200	0.530	-11.800	0.000	600.000	6000.000
0.000	g/cm³	JANAF	1985					
0.000	g/cm³	JANAF	1985					

O(-g)	Oxygen						16.000 g/mol	
	Enthalpy	Entropy	Heat Capacity				Temperature Range	
	H	S	A	B	C	D	T1	T2
	KJ/mol	J/(mol*K)	J/(mol*K)				K	K
G	101.846	157.790	25.310	-18.030	-0.100	20.850	298.150	400.000
G	0.000	0.000	20.790	0.000	0.950	0.000	400.000	6000.000
0.000	g/cm³	JANAF	1985					
0.000	g/cm³	JANAF	1985					

NO_2(-g)	Nitrogen Peroxide						46.006 g/mol	
	Enthalpy	Entropy	Heat Capacity				Temperature Range	
	H	S	A	B	C	D	T1	T2
	KJ/mol	J/(mol*K)	J/(mol*K)				K	K
G	-202.720	236.598	27.680	27.090	0.270	17.880	298.150	400.000
G	0.000	0.000	33.940	33.580	-5.930	-13.430	400.000	1100.000
G	0.000	0.000	60.490	-1.760	-58.450	0.340	1100.000	6000.000
0.000	g/cm³	JANAF	1985					
0.000	g/cm³	JANAF	1985					
0.000	g/cm³	JANAF	1985					

Heat Capacity Formula: C=A+B*10^-3*T+C*10^5*T^-2+D*10^-6*T^2

Table C.4-8. Comparison of Cs data for three computer codes.

HSC DATA

Cs(g)	Cesium						132.905 g/mol				
	Enthalpy	Entropy	Heat Capacity				Temperature Range				
	H	S	A	B	C	D	T1	T2			
	KJ/mol	J/(mol*K)	J/(mol*K)				K	K			
G	76.500	175.598	20.786	0.000	0.000	0.000	298.150	952.000			
G	0.000	0.000	20.786	0.000	0.000	0.000	952.000	1100.000			
G	0.000	0.000	17.807	1.556	15.627	0.000	1100.000	2000.000			
0.000	G/cm^3	BKK	1977								
0.000	G/cm^3	BKK	1977								
0.000	G/cm^3	BKK	1977								
Cs	11 3/93	Cs	1.00	0.00	0.00	0.00	0.00	0	132.90543	76500.000	
200.000	1000.000	5	0.0	1.0	2.0	3.0	4.0	5.0	0.0	0.0	
2.50004554D+00		-4.66833356D-07		1.68005061D-09		-2.48218029D-12		1.27712190D-15			
0.00000000D+00		0.00000000D+00		0.00000000+00		8.45540436D+03		6.87573539D+00			
1000.000	6000.000	5	0.0	1.0	2.0	3.0	4.0	5.0	0.0	0.0	
2.82023315D+00		-3.34840327D-04		-9.82915709D-08		1.27564369D-10		-1.46119271D-14			
0.00000000D+00		0.00000000D+00		0.00000000+00		8.30639354D+03		5.00894042D+00			
CEA Data											
Cs	J 6/68CS	10	00	00	0G	300.000	5000.000			1	
0.18710101E01		0.14068071E-02		-0.10636222E-05		0.30583738E-09		-0.19977219E-13		2	
1.86814554E04		0.10235611E02		0.24999466E01		0.10382792E-05		-0.38771191E-08		3	
0.49283910E-11		-0.19810542E14		0.84737829E04		0.68627707E01				4	

A complete description of the format of the data in the HSC database can be located in the HSC User's Manual (Ref. 8). Generally, the first line of coefficients in a species data set contains the heat of formation (*H*), a standard state entropy (*S*), curve-fit coefficients for the heat capacity (A, B, C, and D), and the temperature range of validity for the curve fit (T^1 and T^2). Subsequent rows of data in the set provide curve-fit coefficients for other temperature ranges.

Heat capacity is calculated from the following equation using the HSC curve fit coefficients listed in this data:

$$C_p^\circ = A + Bx10^{-3}\ T + Cx10^{5}\ T^{-2} + Dx10^{-6}\ T^{2} \qquad \text{(C.4-23)}$$

Note in Table C.4-7 that except for neutral O_2, which was only fitted for a temperature range up to 5,000 K, all the other dominant ions were fitted up to 6,000 K. Thus, the behavior of Figures C.4-17 through C.4-20 that suggests differing methods of extrapolation is not easily attributed to the five species indicated here.

However, the ion concentrations may have been affected by accumulating errors resulting from closely related neutral species that were not curve-fitted to high temperature. Reviewing the data for other species in the three databases, it appears the worst of these is HSC data for Cs. Data for gaseous Cs from each of the three codes is provided in Table C.4-8 for comparison. The HSC curve fit for neutral Cs covers only the range from 298 to 2,000 K. Thus, the calculations in this study, carried out up to 3,500 K, involve extrapolation of the data in the HSC code.

Data for the neutral Cs from the CEA database was curve-fitted for a range up to 6,000 K, and data for the CET89 code extends to 5,000 K, thus no extrapolation was required in these codes. This does not mean that extrapolation was not used in generating the data. The data was prepared with the PAC91 code (Ref. 17) for the CEA database and an earlier version of this code for CET89. It is presumed this would use a more physical rationale for extrapolations than would occur in the HSC Chemical Equilibrium Code.

C.4.3.7 Code Comparison Summary

CEA and CET89 yielded significantly different results, with CEA yielding higher free electron concentrations for all conditions studied. This difference was attributed to the fact that CEA used more recent thermodynamic data. HSC predicted much higher negative ion concentrations, and hence lower free electron concentrations, than either CEA or CET89. This was attributed to the fact HSC did not uniformly use data that was curve fitted to temperatures above 3,500 K. Specifically, the neutral Cs vapor curve fit only extended to 2,000 K. Thus, even though the dominant ions were all fitted to 5,000 K, the Cs neutral atom concentration deviated from the predictions of the other codes as the temperature increased due to the data extrapolation. This effected all of the ion concentrations, although probably not to the extent that was exhibited in the solution profiles.

The Cs neutral data is suspected of being a significant contributor to this difference but is probably not the only one. Curve-fitted thermodynamic data for each of the species considered in this study may differ between the three databases. The species data was not compared since this would have involved a much more in-depth study to determine which data was correct, and this task would have required considerable effort that was not justified for the study.

The primary objective of this task was to determine which code is most reliable for studies of MHD accelerator applications involving Cs-seeded airflows. HSC should not be used since its database is incomplete at the temperatures desired for MHD accelerator operation. CEA is preferred over CET89 since its database contained the most recent data, including negative ion data that almost certainly has been influenced by recent beam neutralization work. However, equilibrium results should always be viewed with a reasonable degree of skepticism. CEA is a beta-test version, and its code or database could contain errors. However, in its favor, CEA has evolved over a 30-year period from the early chemical equilibrium rocket codes developed at NASA-LeRC. Two of its predecessors are the popular and very reliable CEC76 (Ref. 2) and the CET89, which were also evaluated in this study. Each generation of the code has brought new and improved performance, corrections, and improvements to the database.

For the reasons discussed above, CEA has been chosen for Cs-seeded MHD accelerator studies. However, this should be used cautiously, and its predictions should be compared with experimental data whenever this data becomes available.

C.4.4 References

1. "NASA Lewis Research Center Chemical Equilibrium Program with Applications (CEA)," Beta-Test Version, Dec. 1995.

2. Gordon, S. and McBride, B.J., "Computer Program for Calculation of Complex Chemical Equilibrium Compositions and Applications, I. Analysis," NASA RP-1311, 1994.

3. McBride, B.J. and Gordon, S., "Computer Program for Calculation of Complex Chemical Equilibrium Compositions and Applications, II. Users Manual and Program Description," NASA RP-1311, 1996.

4. Gordon, S. and McBride, B.J., "Computer Program for Calculation of Complex Chemical Equilibrium Compositions, Rocket Performance, Incident and Reflected Shocks, and Chapman-Jouguet Detonations," NASA SP-273, NASA Lewis Research Center, 1971.

5. Gordon, S. and McBride, B.J., "Computer Program for Calculation of Complex Chemical Equilibrium Compositions, Rocket Performance, Incident and Reflected Shocks, and Chapman-Jouguet Detonations," NASA SP-273, NASA Lewis Research Center, Interim Revision, Mar. 1976.

6. Gordon, S.; McBride, B.J.; and Zeleznik, F.J., "Computer Program for Calculation of Complex Chemical Equilibrium Compositions and Applications, Supplement I – Transport Properties," NASA TM-86885, 1984.

7. Gordon, S. and McBride, B.J., "Finite Area Combustor Theoretical Ricket Performance," NASA TM-100785, 1988.

8. Roine, A. and Outokumpu, A., "HSC Chemistry for Windows: Chemical Reaction and Equilibrium Software with Extensive Thermochemical Database – User's Guide," Vers. 2.03, 94027-ORC-T, Outokumpu Research Oy, Finland.

9. Rosa, R.J., *Magnetohydrodynamic Energy Conversion*, New York, McGraw-Hill, 1968.

10. Macheret, S.O.; Miles, R.B.; and Nelson, G.L., "Feasibility Study of a Hybrid MHD/Radiatively Driven Facility for Hypersonic Testing," AIAA Paper 97-2429, *28th Plasmadynamics and Lasers Conference*, June 1997.

11. Sutton, G.W. and S.A., *Engineering Magnetohydrodynamics*, New York, McGraw-Hill, 1965.

12. Demetriades, S.T. and Argyropoulos, G.S., "Ohm's Law in Multicomponent Nonisothermal Plasmas with Temperature and Pressure Gradients," *The Physics of Fluids,* Vol. 9, No. 11, Nov. 1966, pp. 2136-2149.

13. McBride, B.J. and Gordon, S., "Coefficients for Calculating Thermodynamic and Transport Properties of Individual Species," NASA TM-4513, Oct. 1993.

14. McBride, Bonnie J.; Gordon, Sanford; and Reno, Martin A., *Thermodynamic Data for Fifty Reference Elements,* NASA Technical Paper 3287, Jan. 1993.

15. Gurvich, L.V. et al., *Thermodynamic Properties of Individual Substances*, Vol. 1, Pts. 1 & 2, Nauka, Moscow, USSR, 1978.

16. Gurvich, L.V.; Veyts, I.V.; and Alcock, C.B., *Thermodynamic Properties of Individual Substances*, Fourth Ed., Vol. 1, Pts. 1 &2, New York, Hemisphere Publishing Corp., 1989.

17. McBride, B.J. and Gordon, S., "Computer Program for Calculating and Fitting Thermodynamic Functions," NASA Reference Publication 1271, Nov. 1992.

APPENDIX D

CONTENTS

SECTION D.1

TABLES

SECTION D.2

FIGURES

TABLES

APPENDIX D. APPLICABLE SYSTEMS ISSUES

In the development of magnetohydrodynamic (MHD)-augmented hypervelocity wind tunnel technology, a number of issues become evident as problems that will require further investigation as they impact the overall design and development process. The MHD Accelerator Research Into Advanced Hypersonics (MARIAH) Project identified two such areas that are addressed in this appendix. These include thermal management of MHD accelerators (Section D.1) and performance enhancement through improved ionization technologies (Sections D.2 and D.3).

APPENDIX D, SECTION D.1

D.1 THERMAL MANAGEMENT OF MHD HYPERVELOCITY ACCELERATORS

MHD accelerators for hypervelocity propulsion ground test facilities will operate in a very challenging thermal environment due to the required high stagnation pressures and temperatures. Thus, a thermal management assessment is essential to identify the requirements for the MHD accelerator walls, as well as the methods and materials that can be applied to alleviate the associated thermal problems. A preliminary study was conducted under the MARIAH Project (Ref. 1), and the results are summarized in this appendix.

D.1.1 Overview

The primary objective of this work was a preliminary investigation of thermal management issues for MHD hypervelocity accelerators. Initial literature review and relevant analyses suggest the MHD-induced hypervelocity flow may produce recovery temperatures in the boundary layer that approach 10,000 K. The objective includes the following: a) define the thermal environment; b) identify possible materials that can be used in that environment, with or without active cooling; and c) identify innovative methods of cooling (passive or active) that can improve the thermal management for future, high performance MHD accelerator systems.

D.1.2 MHD Accelerator Hypervelocity Flow High-Temperature Environment

Aerodynamic heating in an MHD accelerator is produced from radiative and convective heat transfer resulting from the high-velocity, high temperature ionized plasma. Although the magnitude of the heating is primarily dependent on the plasma flow velocity, density, and temperature; it can also depend on the channel geometry, the electrode, insulator, and sidewall materials, as well as the wall cooling method used. The degree of ionization of the plasma and the presence of metal ions and/or particles in the flow can also have a substantial effect on the rate of radiative heat transfer to the walls. In a hypervelocity flow, the high-velocity gas contains a large amount of kinetic energy that when converted to thermal energy in the boundary layers, results in very high recover temperatures (approaching 10,000 K) that occur very close to the wall surface. Also, electrical energy dissipation in the boundary layer and the electron and ion dynamics in the electrode sheath layers can considerably increase the electrode heat rate. Thus, the walls, electrodes, and insulators exposed to the hypervelocity flow in MHD accelerators can experience an extremely harsh thermal environment, and the performance and reliability of these devices depend on the development of methods and materials to protect the exposed surfaces.

MHD accelerator research aimed at developing drivers for various aerospace testing applications was very active in the 1960s (see MHD Accelerator Technology Background, Section 2). Two otherwise similar programs, one in the United States and one in Russia, used very different approaches to thermal management. During the 1960s, an arc-heater driven MHD accelerator experimental program known as LoRho (for low density) was conducted at the U.S. Air Force (USAF) Arnold Engineering Development Center (AEDC) in Tennessee [(Ref. 2), also see

Appendix Section B.1.3]. As discussed below, active cooling was used for the walls of this MHD accelerator. During this same period, Russian researchers at the Central Aerohydrodynamics Institute (TsAGI) developed an arc-heater driven MHD accelerator of similar scale as LoRho; however, the device used passive cooling (heat sink) for thermal control (Ref. 3).

Three small proof-of-concept (POC) accelerator channels were tested during the LoRho program with a potassium (K)-seeded nitrogen (N_2) plasma at power levels up to 400 kilowatts (kW) and power densities approximately 1 megawatt per cubic meter (MW/m^3). The accelerator channel known as LoRho Accelerator B was 0.77 m long with entrance dimensions of 2.54 centimeters (cm) by 2.98 cm and exit dimensions of 2.54 cm by 6.22 cm. The accelerator had 117 electrode pairs, but only the center 60 electrode pairs were powered. At the high power level, centerline gas temperature exceeded 5,000 K; and the total heat transfer exceeded 200 kW, or approximately 50% of the applied power. Average heat flux to the walls was approximately 2 MW/m^2. Typically, the centerline Mach number for these tests was approximately 2. Electrodes were water-cooled, uncoated copper, and the sidewalls were water-cooled copper coated with a plasma-sprayed, beryllium oxide (BeO). Maximum current densities on the LoRho accelerator electrodes approached 20 amps per centimeters squared ($A/cm^{2)}$ for the high power tests. The LoRho BeO insulation and copper electrodes reportedly survived very well in this environment, and no appreciable damage was noted after minutes of run time for normal operation.

Several MHD accelerators have been built and tested at TsAGI. The TsAGI accelerators have been actively used for aerospace testing applications from the 1960s through the present. Typical accelerators were 55 - 70 cm in length with 40 - 45 electrodes. These accelerators operate with centerline Mach numbers from 2 to 4 and centerline gas temperatures from 4,000 to 5,000 K. No active cooling is provided for these channels; they operate in a heat sink mode for run times on the order of 10 seconds or less with high heat fluxes of 10-50 MW/m^2. Channels are commonly operated at maximum currents of 55 A and Faraday voltages in the range 200-400 volts (V), with total input power to the accelerator in the range 0.5 to 1.0 MW.

Typical electrode-insulator lifetimes are in the range of 5 to 10 seconds. The most common failure mode is erosion of the interelectrode insulators along the anode wall.

These are small and low power accelerators compared to the devices needed for the next generation of full-scale, hypervelocity propulsion wind tunnel facilities. Preliminary analyses discussed in Appendix Section B.1 of this report indicate that seeded MHD accelerator designs for full-scale, hypervelocity propulsion test facilities would have dimensions of ½- to 1-meter-square crosssection and be 2 to 7 meters long. Applied electrical power for these accelerators may be on the order of 1 to 10 gigawatts (GW), with wall heat losses of 0.5 to 1 GW. The thermal management problems for these accelerators will be immense compared to the MHD accelerators of the 1960s. New materials for electrodes, insulators, and sidewalls, as well as sophisticated new methods for active cooling and thermal recycling (effective use of the thermal energy removed from the device) will need to be developed to enable these devices to perform at the required level.

D.1.3 Thermal Protection Systems

Some general methods for protecting the electrodes and walls of MHD accelerator channels from the harsh thermal environment will be briefly discussed in this section. There are two broad types of thermal protection systems: systems based on heat dissipation (active and radiative cooling) and systems based on heat absorption (passive cooling or heat sink).

D.1.3.1 Systems Based on Heat Dissipation

Active cooling systems used in many MHD accelerator and generator devices since the 1960s are one of the best examples of heat dissipation systems. In these systems, water or another cooling fluid is circulated through passages to transfer heat by convection from the hot exposed surfaces in the MHD device. The cooling fluid then transfers the heat to a low temperature system away from the MHD accelerator. These systems are generally effective but have disadvantages in their complexity and the loss of efficiency of the device being cooled. Since the objective of MHD acceleration is to increase the stagnation enthalpy of the working fluid, cooling the fluid is counter productive but necessary to protect the device.

Another form of heat dissipation is radiation from the surfaces to be cooled. Although this is effectively used in many applications, it may not be possible in the MHD accelerator environment. Since the amount of heat that can be dissipated depends on the surface temperature, it is limited by the capacity of the surface material to absorb heat without melting or vaporizing (in the case of sublimative material). The amount of heat rejection by radiation is proportional to the fourth power of the surface temperature. Therefore, selecting a material that can withstand very high temperatures will allow a large amount of heat to be radiated. Since the rate of radiation from a surface is also proportional to its emissivity, the effectiveness of the radiation can also be improved by increasing the surface emissivity through surface treatment. However, in the MHD environment, increasing the surface emissivity may not be advantageous since this will also increase the surface absorptivity. Some materials are known to effectively absorb radiant energy at one wavelength and reradiate it at another. If such a material could be used in the MHD environment, the energy could be "reflected" back into the flow without a significant loss of efficiency.

D.1.3.2 Systems Based on Heat Absorption

Heat absorption methods can be either intrinsic or extrinsic. Intrinsic methods use the material exposed to the high temperature environment (walls, electrodes, nozzle, etc.) to absorb the heat and store the energy (heat sink) or remove the heat by ablation. Extrinsic methods transfer the heat to another medium and include such methods as transpiration and film cooling.

Heat sink methods can be used when the exposure times are short and the thermal capacity of the heat sink material is sufficient to prevent an excessive rise in the material temperature that would cause the material to melt, vaporize, react chemically with its environment, or loose its structural integrity. This method is frequently utilized in hypersonic research facilities where short run times are adequate and sufficient time can be provided between tests to allow for ambient cooling. This may not be practical for test and evaluation (T&E) facilities where long run times will be necessary and high facility productivity is desirable. For these applications, heat sink methods should only be considered if their use, in conjunction with other cooling methods, provides a practical benefit in the facility design.

Ablative systems have been successfully used in the thermal protection of reentry ballistic systems and are promising in that application. Heat is absorbed by a rise in temperature, chemical reaction, melting, and vaporization of the surface material. The thermal energy and waste products of these processes are then discharged in the boundary layer.

Historically, various forms of sacrificial electrodes have been considered for MHD applications. This method can theoretically provide a solution to both the electrode heat transfer problem and electrode arc erosion; however, practical problems and disadvantages must be overcome. First and foremost is the problem of replenishment of the lost material. Systems designed for one-time use (such as reentry vehicles and MHD power systems for weapons) can be designed with sufficient material to complete the mission; however, continuous use systems must have a simple, cost effective method for continuously replacing the ablated material. Electrode wire feeders and liquid electrode concepts have been proposed, but no working system for a high power system such as the MARIAH MHD accelerators has been demonstrated.

Another disadvantage of ablative systems for this application is the contamination of the working fluid in the channel. However, this may not be a problem if the vaporized material does not degrade the testing environment or if it can be confined to the boundary layer and removed prior to entering the test section. Ablation may have some limited use in hypervelocity MHD accelerator systems; however, the majority of the heat transfer solutions must come from other means for these devices.

Transpiration cooling methods remove heat by vaporization of a coolant at the surface to be protected. Liquid coolant is pumped through porous surfaces into the slow moving flow along the wall where it is heated and vaporized while absorbing the heat from the flow before the heat reaches the wall surface. Coolant vapor is convected from the surface in the boundary layer flow. Film cooling is a closely related method in which a liquid film is introduced and allowed to flow over the area being protected. Introducing a liquid coolant in the laminar sublayer next to the wall surface creates the film and vaporization of the liquid and prevents the surface from excessive heating.

Transpiration and film cooling methods may be suitable for MHD accelerator applications if an appropriate cooling fluid is used. For example, if liquid N_2 were used, the flow entering the accelerator channel could be oxygen (O_2) rich so the flow at the exit of the channel would have

the correct ratio of N_2 to O_2 for simulating air. A liquid alkali metal material might also be used in which the vapor might increase the electrical conductivity of the boundary layer flow, thereby solving the problems of low conductivity that results from the cold electrodes in accelerator devices.

Transpiration cooling has been successfully applied in liquid propellant rocket nozzles and may be the only available method in applications with extremely high heat flux and where ablation is not acceptable. Difficulties of this method include the distribution of the cooling fluid to the surfaces, proper control of the coolant flow through the porous surfaces, and clogging of the pores. Obviously, the efficiency of transpiration and film cooling systems is limited by the thermal capacity of the cooling fluid.

D.1.4 Search for a Suitable Material

One of the more demanding tasks in the development of an advanced, a high-performance, hypervelocity MHD accelerator will be finding suitable materials and cooling methods, or a combination of both, to manage the extremely harsh thermal environment of these devices. The availability of suitable materials and cooling methods will be a significant factor in the feasibility of MHD accelerators for this application. The extreme thermal environment demands the exploration of state-of-the-art materials and methods. One candidate material for possible use in MHD accelerator sidewalls (if coupled with an appropriate cooling system) is discussed below. Other materials requiring further investigation for this application are also identified.

Hypervelocity vehicles and reentering vehicles experience boundary layer temperatures in nearly the same range as expected for the proposed MHD accelerator. These vehicles undergo a large range of heating conditions during the excursion through the atmosphere. Thorough research has been conducted for the design of reusable thermal protection systems (TPS) for these vehicles. A typical TPS is composed of a combination of high temperature reusable materials and ablative materials and can also involve active cooling systems.

D.1.4.1 Space Shuttle Material

The Space Shuttle is an example of a successful application of a reusable TPS. Anderson reports that when the Space Shuttle reenters the earth's atmosphere at Mach 25, it experiences a boundary layer temperature behind the shock wave of about 8,000 K (Ref. 4). Thus, Space Shuttle tiles (especially at the nose region) experience very high boundary layer temperature yet are reused without much damage and replacement. This is due in part to the reradiation of energy from the tile surface to the cooler environment beyond the shuttle hypersonic flow. In fact, the Space Shuttle tiles release most of the heat they receive from the boundary layer back to the atmosphere by reflection and reradiation, thereby keeping the surface temperature to a value of approximately 2,000 K.

Although the boundary layer temperature of Space Shuttles at reentry and the boundary layer temperature of the proposed MHD accelerator are expected to be in approximately the same range, the two surfaces may experience two very different heat transfer mechanisms. In the case of MHD channels, reradiation of energy from the surface might occur but would require much higher surface temperature since the core flow will have a temperature in excess of 3,000 K. However, Shuttle tile material or its derivatives may be useful in MHD accelerators if these can be supplemented with other forms of cooling. For this reason, a brief overview of the Shuttle tile material, its fabrication, and its thermal and mechanical properties follows.

Space Shuttle tiles are made from a material called carbon-carbon composite, also known as reinforced carbon-carbon (RCC) material. Since the mid-1960s, RCC began replacing fine-grained graphite as nose tips in rockets because they represented significant improvement in thermoshock and erosion behaviors. The RCC structure is composed of a carbonaceous or graphitic matrix that is reinforced by carbon and graphite. This material has the most desirable properties of monolithic graphite. Additionally, it has the high strength and versatility of a composite material and has some unusual combination of properties, including high temperature resistance, low thermal stress due to low thermal expansion, retention of properties at elevated temperature, high strength, high stiffness, and chemical inertness. These properties are of special interest for specialized high temperature applications such as in the aeronautical, space, missile, propulsion, chemical, and nuclear fields and may be of interest for MHD applications.

Carbon-carbon composite is a generic term referring to a class of materials composed of carbon (or graphite) fibers with carbon (or graphite) matrix. The early research conducted on this material in the United States was government funded, and a large portion of the work, including its detailed manufacturing techniques, is classified. Originally, carbon-carbon materials were produced using two-dimensional (2-D) reinforcement of low modulus rayon precursor carbon and graphite fibers. In this application, 2-D signifies the reinforcement is two-directional. Until now, 2-D composites have satisfied the requirements of most applications; however, both 3-D and multidirectional composites are becoming increasingly available (although still very expensive to manufacture) (Ref. 5). Graphite is used because it is an attractive material for applications in high temperature and ablative environments and has a high sublimation temperature of 3,870 K. Additionally, it shows improved strength with increasing temperature and has high thermal stress resistance, low density, and chemical inertness.

Although the manufacturing details of carbon-carbon composites are still classified and/or proprietary, a general outline of this process is known. First, carbon fibers are impregnated by a suitable matrix precursor and fixed by winding in definite directions. The matrix is derived from pitch or pyrolyzed high char yield thermosetting resins such as phenolic. A pressing and/or curing cycle is followed by carbonization between 1,070 and 1,470 K in an inert atmosphere. Further heat treatment at temperatures greater than 2,770 K leads to graphitization. The resultant product is a porous carbon-carbon composite with approximately 30% porosity. This porosity is eventually reduced to approximately 5% through densification cycles consisting of impregnation, followed by recarbonization or impregnation, recarbonization, and then regraphitization.

Occasionally, chemical vapor impregnation (CVI) of paralytic carbon into the porous skeleton is performed (instead of densification via liquid precursors) to fill the interior void spaces.

The properties of the carbon-carbon composites span a wide range. The mechanical, thermal, and electrical properties of the material are dependent on the fiber type, fiber volume fraction, fiber architecture, precursor, and processing cycle. For example, use of more re-densification cycles decreases the porosity and increases density, flexural strength, and stiffness. Physical properties, such as electrical resistivity and thermal conductivity, are influenced by the final heat treatment temperature (HTT). Carbon-carbon composites have anisotropic properties, which are due to the presence of carbon fibers, and carbon fibers are anisotropic due to the presence of a graphite crystal lattice. Typical electrical resistivity and thermal conductivity values for different HTT along directions parallel and perpendicular to a fiber axis are shown in Table D.1- 1. Along the fiber axis, the electrical and thermal conductivities have high values, whereas along the direction perpendicular to the fiber axis, the values are low. In 2-D carbon-carbon materials, the ratio of anisotropy is approximately between 5:1 and 10:1.

The high-temperature strength capability of carbon-carbon composites is of interest for MHD applications. Most materials lose their strength at elevated temperature, conversely, carbon-carbon materials keep their mechanical properties up to 2,270 K or higher.

Table D.1- 1. Electrical resistivity and thermal conductivity parallel and perpendicular to the axis of the fiber of 2-D carbon-carbon composites.

Heat Treatment Temperature		Electrical Resistivity μΩ·m		Thermal Conductivity W/m K	
K	°F	Parallel	Perpendicular	Parallel	Perpendicular
473	390	33 - 37	98 - 114	36 - 43	4 - 7
1,073	1,470	8 - 12	68 - 81	127 – 134	39 - 46

The manufacturing history is an important factor to determine the final properties of this composite material. As shown in Table D.1- 1, graphitization temperature increases the thermal and electrical conductivities. These properties are more pronounced if pitch-based carbon or pyrolitic graphite is used as the graphitization matrix. As mentioned earlier, the properties of the carbon-carbon composites vary considerably in directions parallel and perpendicular to the axis of the fiber. This quality makes this material attractive for certain MHD applications. For example, the material can be used as a good conductor of heat and electricity if it is placed such that conduction is in a direction parallel to the axis of the fibers. On the other hand, the same material can be used as an insulator when placed such that the conduction is in a direction perpendicular to the fiber axis. In an MHD accelerator, an electrode material should be a good conductor of both electrical current and heat. An added advantage would be that this material has the capability to withstand high temperature and retain its properties.
However, there are drawbacks to carbon-carbon composites. For example, the oxidation

resistance of this material is low without the use of oxidation protection coatings. Schmidt (Ref. 6) has discussed the general advantage and limitations of this composite material, and his findings are summarized in Table D.1- 2

Table D.1- 2. Advantages and limitations of carbon-carbon composites.

ADVANTAGES	LIMITATIONS
High Temperature Shape Stability	**Materials**
High Sublimation Temperature	Low Off-Axis Mechanical Properties
Low Ablation Recession	Low Strain-to-Failure
High Strength and Stiffness at Parallel to Reinforcement Direction	High Void Content
	Nonuniform Pore Distribution
	Low Fiber/Martix Bond Strength
Retention of Strength and Stiffness at Elevated Temperatures	High Thermal Conductivity [Advantages for MHD Applications]
Thermal Stress Resistant	Low Oxidation Resistance [Can be Improved by Proper Coatings]
Thermal Shock Resistant	
Pseudo-Plastic Mechanical Behavior	Low Particle Erosion Resistance
	High Costs
Crack Propagation Resistant	**Processing**
Nonbrittle Fracture	Long Fabrication and Processing Times
Impulse Attenuating	Reproducibility
Chemical Inertness	**Design**
Lightweight	Limited Design and Engineering Properties
Radiation Resistance	Failure Criteria Lacking
Tailorable Properties	Complex Design Methodology
Nonstrategic Materials	Complex Response to Environment
Fabricable	Anisotropic Behavior (Advantage in MHD Applications)
Machinable	
	Nondestructive Inspection (Not Well Developed)
	Limited Applications Experience
	Attachments and Joints

Carbon-carbon composites, when used in Space Shuttles, experience a severe thermal environment where oxidation is a major problem. However, the material is saved from degradation and attains its durability from a diffusion coating of silicon carbide and a glass sealant. In addition, a sealer called Tetraethyl-Ortho Silicate (TEOS) is added on top of the silicon carbide coating. At elevated temperatures during reentry, O_2 reacts with silicon carbide to form a thin layer of glass. This layer is a few microns in thickness and is primarily a sodium silicate glass with very low diffusion coefficient for O_2. The glass layer flows over the surface and protects the carbon-carbon material from oxidation. However, under extreme flight conditions, viscous drag can shear the glass sealant from the surface, thereby exposing the surface to oxidation damage and degradation. It is speculated that this is the main reason the Space Shuttle tiles show small pinholes at the leading edges after many missions.

It should be noted the silicon carbide coating has high total hemispherical emittance at an operating temperature of about 1,800 K. This high emittance enhances the radiative heat rejection from the surface. However, at more severe operating conditions, the emittance of silicon carbide decreases as the surface temperature increases. The surface temperature is dependent on the amount of heat transfer from the surface while the rate of heat transfer is directly proportional to the surface emittance. A detailed knowledge of the total hemispherical emittance at different operating conditions is essential for an accurate thermal analysis. Surface emittance of carbon-carbon composites at various conditions has been documented. Studies of mass loss of carbon-carbon composites at various operation conditions can be found in Stroud and Rummler (Ref. 7).

D.1.4.2 Other Possible Materials

Explorations for materials other than carbon-carbon composites were concentrated into several broad areas. These materials were chosen because the available references indicate their applicability at elevated temperature. The summary of these materials is shown in Table D.1- 3.

Another prospective material, not included in Table D.1- 3, is the ceramic-matrix composite. This material may not be a good candidate for electrodes; however, it potentially may be used as an MHD channel side wall. This material is still in the development stage, but one French company has successfully produced ceramic-matrix composites in large complex shapes for use in oxidation-resistant turbine wheels, liquid rocket engine nozzles, leading edges for multiple reentry vehicles, and spacecraft thermo-mechanical protection shingles.

Table D.1- 3. Summary of other suggested materials.
Silicon-Based Reusable Materials
FRCI-12 (Silica 78%, Aluminum Borsilicate fiber 22%)
LI-2200 (Silica)
Cerachrome-8, Previously known as Dynaflex (Al_2O_3 42.5%, SiO_2 55%, Cr_2O_3 2.5%)
Mink-K-1301 (Composition unknown)
HTP-6, (Silica fiber 78%, Alumina fiber 22%)
Reusable Metals
Columbium, C-103 (Composition unknown)
Platinum, melting point = 2,046 K (3,224 °F)
Tungsten, melting point = 3,683 K (6,170 °F)
Oxide Materials
Hafnium Dioxide, melting point = 3,004 K (5,020 °F)
Zirconium Dioxide, melting point = 2,950 K (4,850 °F)

D.1.4.3 Organizations Involved in Materials Development and Manufacturing

A number of organizations were identified that are involved in materials development and manufacturing in the United States. The following list of organizations is included to facilitate future research in high-temperature materials for MHD accelerator applications:

1. SAIC, Santa Ana, CA
2. Textron Specialty Materials, Lowell, MA
3. Rohr Industries, San Diego, CA
4. Aerospace Corporation, Los Angeles, CA
5. HITCO, Glendale, CA
6. Atlantic Research, Falls Church, VA
7. Fiber Materials Inc., Biddeford, ME
8. CCAT, Forth Worth, TX
9. MER Corp., Phoenix, AZ
10. Kaiser Aerotech, Sacramento, CA
11. Loral Vought, Dallas, TX [manufacturer of space shuttle tiles]
12. NASA Lewis Research Center, Cleveland, OH
13. Johnson Space Center, Houston, TX

D.1.5 Cooling Techniques

The following are research options that might lead to solutions for the thermal management of MHD systems:

1. Identify or develop new materials that can survive in an air environment with surface temperatures approaching 10,000 K. (Not likely to be a near-term solution. To date, no such material exists.)
2. Identify or develop new materials that can survive in an air environment with surface temperatures in the range of 2,000 to 3,000 K with the aid of an active cooling system.
3. Use of high temperature materials available in the near term--supplement with active cooling systems.
4. Ablating (sacrificial) electrodes--these could contaminate the air in the test section, and some means for replenishing the electrode material would be necessary.
5. Porous or slotted electrodes (transpiration or film cooling)--pump cooling fluid through the electrode opening(s), allowing the fluid to vaporize on the surface. Cooling liquid could be N_2, argon (Ar), or an alkali metal. Each has advantages and disadvantages.
6. Cool electrodes by pumping a liquid metal through passages inside the body of the electrode itself--in this case, using liquid metal as coolant may also allow it to be used as a conductor for the electrical current to the electrode.

A few points warrant some discussion. In those options discussed above that involve pumping a cooling fluid through the electrode surface into the flow, there are a few choices of an appropriate fluid, each with its own merits and demerits. For example, Ar and N_2 can be used very effectively as coolants. These materials have very low boiling temperatures (63 K for N_2, 84 K for Ar) and relatively high specific heats (523 J/kg K for Ar and 1,070 J/kg K for N_2). However, Ar and N_2 have high ionization potentials [approximately 15 electron volts (eV)], which in turn, requires higher temperature for ionization. On the other hand, cesium (Cs) and K have ionization potentials of 3.89 eV and 4.34 eV, respectively. Consequently, these materials ionize at a lower temperature than Ar and N_2. However, a disadvantage of using Cs and K is they have boiling points a few hundred degrees higher than Ar and N_2 (302 K for Cs, 337 K for K). These materials will not be in liquid form at room temperature. In addition, Cs and K have undesirable reactions when they come in contact with air and water. Potassium and Cs compounds could also be considered.

Mercury (Hg) or liquid sodium (Na) could be used as a circulating cooling fluid. Mercury has an advantage in that its melting point is well below the melting point of liquid Na. On the other hand, liquid Na has very high specific heat (1,240 J/kg K) as compared to Hg (140 J/kg K). Also, liquid Na has low electrical resistivity (4.2 $\mu\Omega$·cm) compared to Hg (98.4 $\mu\Omega$·cm). Because of the high specific heat, liquid Na is often used to transfer thermal energy in nuclear reactors. In recent years, Russian scientists have successfully used a eutectic mixture of liquid Na and K as a seed material in MHD accelerators; this mixture is in liquid form at room temperature.

D.1.6 Summary

A preliminary review of thermal management methods and materials that may be applied to MHD accelerators for producing hypervelocity flow conditions was performed as a task in the MARIAH Project. The heat exchange mechanism was explored, as well as possibilities of implementing different thermal protection systems for surfaces exposed to very high temperature were investigated. It is concluded that to withstand the severe thermal environment in an MHD channel, the electrodes and the channel walls must use state-of-the-art materials coupled with a suitable cooling method. Several cooling methods in this regard were discussed. In search of a suitable material, important information about a state-of-the-art material used as the heat shield on Space Shuttles was discussed in detail. Guidelines and information on other possible materials are also given in this report.

Space Shuttle tile material was explored in some detail because of its unique physical and mechanical properties. This material has anisotropic properties and can withstand considerably high temperatures without losing its structural integrity. It has high thermal and electrical conductivities in one direction of the fibers and low values of the conductivities in the other direction. Oxidation of this material can be avoided at elevated temperatures with an appropriate and already known coating. However, due to the possibility of a higher surface temperature of the MHD channel walls than the surface temperature of a Space Shuttle, additional cooling mechanisms will definitely be needed to keep the temperature at an acceptable level.

Development of a thermal management system to be used in the harsh environment of an MHD accelerator, including selection of appropriate materials for the walls and electrodes, is a very challenging problem. Numerical modeling can help define the thermal environment and the response of advanced materials and cooling systems when used in this application.
The assistance and contributions of the following individuals through personal communications during this review is acknowledged and appreciated: Dr. Howard Maahs, NASA Langley Research Center; Dr. John Mandell, Montana State University; and Dr. Doug Cairns, Montana State University.

D.1.7 References

1. Amin, M.R. "Thermal Management of Magnetohydrodynamics (MHD) Hypersonic Accelerators - Final Report," MSE, Technology Applications, Inc., Report No. MSE-23, Oct. 1996. Prepared under contract No. DE-AC22-88ID12735.

2. Rittenhouse, L.E.; Pigott, J.C.; Whoric, J.M.; and Wilson, D.R., "Theoretical and Experimental Results with a Linear Magnetohydrodynamic Accelerator Operated in the Hall Current Neutralized Mode," AEDC-TR-67-150, Arnold Engineering Development Center (AEDC), Nov. 1967.

3. "A Program of Experiments for Investigating Into Performance of MHD Accelerator with Increased Pressure in Its Channel by Using the TsAGI SMGDU Facility," Final Report on work completed under subcontract to MSE in support of the NASA MARIAH Project, ENGO, Moscow, Russia, June 1996.

4. Anderson, J.D., *Hypersonic and High Temperature Gas Dynamics*, McGraw-Hill, 1989.

5. McAllister, L.E. and Lachman, W.L., *Multidirectional Carbon-Carbon Composites*, Handbook of Composites, Kelly, A. and Rabotnov, Yu N. (eds.), Vol. 4, Elsevier Science Publishers, The Netherlands, 1983, pp. 111-175.

6. Schmidt, D.L., "Carbon/Carbon Composites," *SAMPE Journal*, Vol. 8, No. 3, 1972, pp. 9-19.

7. Stroud, C.W. and Rummler, D.R., "Mass Loss of a TEOS-Coated, Reinforced Carbon-Carbon Composite Subjected to a Simulated Shuttle Entry Environment," NASA TM-81799, 1980.

APPENDIX D, SECTION D.2

D.2 IONIZATION TECHNOLOGIES FOR ENHANCING MHD ACCLERATOR PERFORMANCE

As part of the overall MARIAH Project, MSE Technology Applications, Inc. (MSE) has undertaken to characterize and evaluate several technologies that may have the potential to enhance the electrical conductivity within an MHD accelerator or to improve the channel efficiency. The purpose of this report is to provide a synopsis of a number of candidate technologies that have been or are being evaluated for possible application to MHD. Such technologies include electron beams (e-beams), microwave sources, heavy charged particle beams, neutral particle beams, x-rays, gamma radiation, laser irradiation, microwaves, and radio frequency (rf) sources. Each has its own unique characteristics and operating regime. Likewise, each has its own advantages, disadvantages, and technology issues. These are addressed in greater depth in the following sections.

D.2.1 Problem Statement

The purpose of the MHD accelerator is to augment the total enthalpy of the flow by accelerating an incoming airstream to high velocities. To accomplish this, it is necessary to substantially increase the total enthalpy through the addition of work or heat while at the same time minimizing the entropy generation through the system. Figure D.2- 1 shows the target flow regime for a "good" hypervelocity propulsion test facility. This graph represents the conditions that would be seen behind the bowshock of a hypothetical vehicle moving along trajectories of constant dynamic pressure. As a point of reference, it should be noted, according to these plots, a total enthalpy of 98 MJ/kg is required to simulate post-bowshock conditions corresponding to an altitude of 50 km along the 2,000-lbf/ft^2 corridor.

Chemistry issues are quite important in this context. It is known from past studies (Refs. 1, 2) that the flow through the secondary expansion duct downstream of an MHD accelerator tends to remain frozen. Reference 2 describes a detailed analytical treatment of the problem using a 1-D fluid dynamics model that incorporates kinetic rate equations for the nonequilibrium chemistry. The chemistry aspects of the model have been validated by comparing the code predictions of nitric oxide (NO) production and radiation in N_2-O_2 mixtures behind normal shocks. The predictions agreed well with time-resolved shock tube measurements of the infrared radiation from the NO molecules (Ref. 3). When applied to typical MHD scenarios for accelerators operating near thermodynamic equilibrium, this code predicts levels of NO of 3 to 8 mole percent in the exit region as well as monatomic mole percentages of a few percent for both N_2 and O_2. Thus, production of such alien species appears to be a problem characteristic of most MHD systems. These same calculations show the chemistry can be improved by tuning some of the operating parameters. For example, if the transverse current densities in the channel are maintained below approximately 40 A/cm^2 and the channel pressure is kept above 1 atmosphere (atm), then monatomic oxygen levels in the exit duct can be kept below about 0.6%, although NO levels will still be several percent.

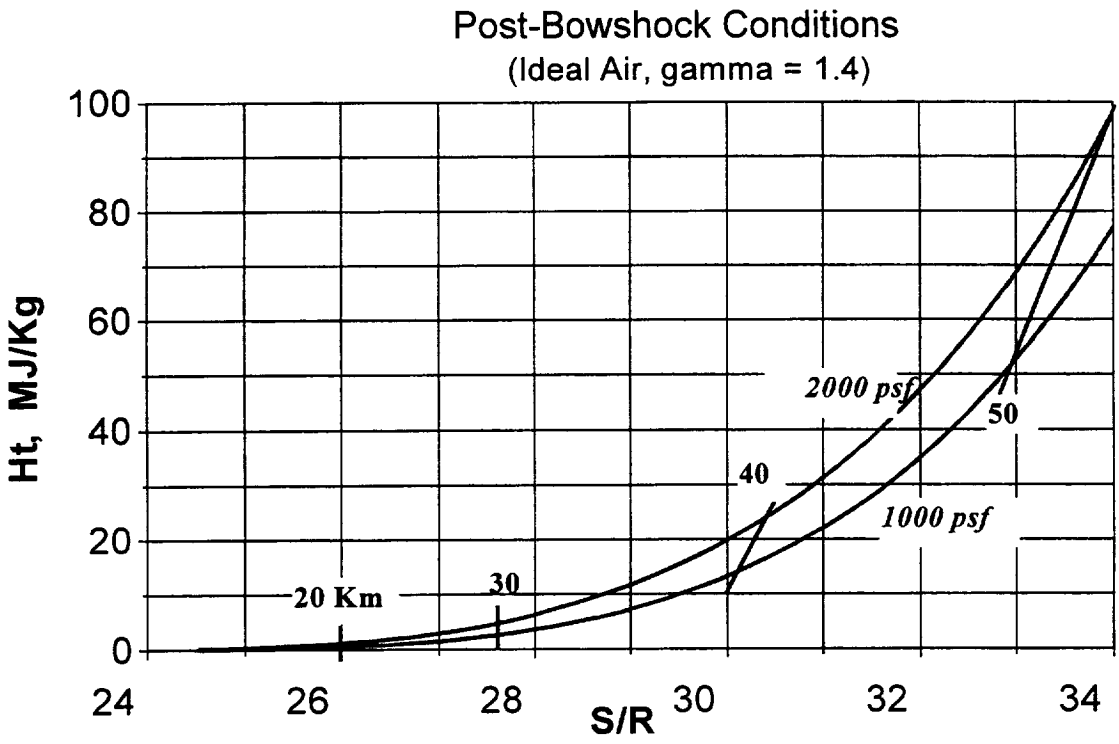

Figure D.2- 1. Total enthalpy vs. entropy at selected dynamic pressures.

One of the primary issues with respect to MHD acceleration is the question of whether it is possible to maintain a diffuse discharge at the accelerator electrodes. Arc discharges will generally create additional amounts of NO and dissociated species and may also cause rapid erosion of electrode faces. This in turn may confound the air chemistry by introducing metal into the flow. Experimental work at the NASA Ames Electric Arc Shock Tunnel (NASA Ames EAST) facility and the University of Texas, Arlington (UTA) was conducted as part of the MARIAH Project to develop an envelope of operating parameters (i.e., pressures, temperatures, and velocities behind a detonation wave or a shock wave) within which electrode discharges will remain diffuse. This experimental work is discussed in appendix sections A.1 and A.2.

The issue of the effects of seed is also important. In the context of the diffusive burning scramjet combustion processes, a major question is: To what degree does the presence of 1-2 mole percent of an alkali metal affect the ignition delay times in the supersonic combustion regime? Other modes of combustion, such as the premixed detonation concept, raise similar questions with regard to seed. The first question has been addressed by Drummond, who performed preliminary computations using finite rate kinetics models and who also summarized the work of others.[1] His results indicated the ignition delay times were somewhat affected by the presence of Na up to a few mole percent. For example, at an initial temperature of 2,500 K and a pressure of 1 atm in a mixture of stoichiometric hydrogen (H_2) and O_2, the ignition delay time went from

[1] Dr. Phil Drummond, private communication with Gordon Nelson.

about 1.4 microseconds to 0.9 microseconds as the mole percent of Na increased from 0 to 5%. A Mach number of 4 was assumed in the combustor, implying ignition delay lengths of a few hundredths of an inch. Since the critical length scale for supersonic combustion is the mixing length, which may be of the order of several feet or more, these changes in delay times as a function of seed fraction will not be significant.

As noted, the calculations just cited were preliminary and based on the use of Na. Additional analysis needs to be done to characterize other seed candidates such as K and Cs and to investigate a wider range of conditions. Since the results of any kinetics computation are sensitive to the set of selected chemical equations as well as the associated rate constants, additional computations were done using enhanced equation sets and the best available rates. The results of their more recent computations are discussed in Section D.3.

To summarize the chemistry issues, a good hypervelocity propulsion testing environment will require a final flow stream that has minimal amounts of alien species such as NO and monatomic O_2 and N_2. MHD appears to have some potential for being able to control this problem. Questions of the effects of seed on the combustion process have not yet been definitively answered.

A further consideration is the question of the efficiency of the MHD process. The conversion efficiency , η , is equal to the ratio of the push-work done on the gas by the MHD forces to the input electrical power. For an ideal Faraday-connected MHD channel, η is given by the formula

$$\eta = \frac{1}{0.5 + \sqrt{0.25 + \frac{P_{mhd}}{\sigma U^2 B^2}}}$$

where σ is the conductivity, U is the flow velocity, B is the magnetic field, and P_{mhd} is the input power density (Watt/meter^2) to the MHD accelerator. Note parenthetically that (1 - η) is the fraction of the input power that is converted to entropy through Joule dissipation. An MHD accelerator operating with a conversion efficiency of zero is functionally equivalent to an electric heater. In this limit, the use of a magnetic field is irrelevant. The additional system complexity associated with adding a magnet to a heating device can only be justified if substantial gains in efficiency can be realized. For maximum efficiency and minimal entropy generation, the dimensionless parameter $\varepsilon = P_{mhd}/(\sigma U^2 B^2)$ must be minimized. On the other hand, to achieve the required total enthalpy addition, it is necessary to add large amounts of power to the flow within a reasonable length of duct, implying large values of ε. Since there are practical limits on conductivity, magnetic fields, and flow velocity, the goal of high efficiency must usually be compromised to some degree to achieve a workable accelerator design. In practical accelerators, the parameter ε will typically take values in the range 0.3 to 2.

MHD accelerators designed for continuous operation have typically been run in the past with arc heaters on the upstream end to heat the gas (Ref. 4). Here again, entropy generation is an important consideration. Since the entropy of the gas in the plenum is inversely related to the logarithm of its stagnation pressure, it is imperative that the heater be run at as high a pressure as possible to ensure high efficiency. Arc heaters such as those under development at the AEDC are presently running at approximately 150 atm and 5,000 K stagnation temperature.[2] Substantially higher stagnation pressures will be necessary to reach the end point thermodynamic conditions depicted in Figure D.2- 1. Total pressures of the order of thousands of atmospheres are characteristic of the hypervelocity flight regime.

D.2.2 Technology Evaluation

D.2.2.1 E-Beams

MSE has been evaluating e-beams as a means of enhancing the ionization of air within the MHD accelerator. E-beams have been employed successfully in gas lasers where they have been used to create a population inversion in the vibrational modes of gases such as carbon dioxide (Refs. 5, 6). That application represents a much more benign environment from the standpoint of creating ion-electron pairs because in all of the laser applications the working pressures are subatmospheric, usually of the order of a few torr, whereas in typical MHD accelerators, the pressures may be several atmospheres or more. The static pressure is a critical parameter in any ionization scheme that relies on impact ionization. The high-pressure requirement also impacts the hardware requirements. These issues are briefly discussed below.

In a general sense, there are three essential issues with respect to the propagation of e-beams in air: a) What kinetic energies are necessary to ensure that the beam penetrates the gas to a sufficient depth? b) How much ionization occurs per unit path length assuming the beam can propagate? and c) What is the availability and capability of e-beam sources?

The first question can be answered quite completely based on the formulas for particle ranges as a function of kinetic energy, originally derived by Hans Bethe. These formulas include the relativistic effects that come into play at high beam energies and are valid under the assumption that the beam scattering is due to Coulomb forces. The formulas are summarized in the book by Turner (Ref. 7). Evaluation of the range parameter involves evaluation of an integral over the energy spectrum from the lower limit zero up to the specified incident beam energy. Details of the computational method may be found in Reference 7. Some results from the numerical integrations are shown in Table D.2- 1.

[2] Dennis Horn, private communication.

Table D.2- 1. Range of electrons in air.					
CASE	Pressure (atm)	Temp (K)	β	Kin. Energy (MeV)	Range (cm)
A.	1	300	0.506	0.0816	10
			0.800	0.342	100
B.	10	3,000	0.506	0.0816	10
			0.800	0.342	100
C.	100	3,000	0.800	0.338	10
			0.981	2.12	100

The parameter β is the ratio of the incident beam velocity to the speed of light in a vacuum. The pressures and temperatures for case A represent air at standard temperature and pressure (STP). Cases B and C represent conditions typical of an MHD accelerator. Strictly speaking, the range of a beam of particles is not identical with the penetration depth. The range is defined as the distance traveled along the path of the most energetic particle from the point of incidence to the point where the particle is brought to rest. The penetration depth is a parameter that is measured normal to the plane of incidence. Therefore, one would expect that the range is always somewhat greater than the penetration depth. Turner shows detailed statistical comparisons of the maximum penetration depths vs. the particle ranges for electrons in water. The conclusion is (to quote Turner), "Additional calculations reveal that the average maximum depth of penetration for electrons is approximately one-half their range for energies up to the maximum of 1.25 MeV used in the computations."

Note the last two rows correspond to β values of 0.8 or higher. The main point made by the above table (and by Figures D.2- 2 and D.2- 4 below) is that to penetrate such high-pressure, high-density gases to depths of a few centimeters or more, it will be necessary to use relativistic electrons. If lower energy electrons are used, all the energy will be deposited in a thin region near the window, resulting in little more than heating of the boundary layer. Note the range calculations represented in the table do not take the radiative stopping power into account. The radiative effects will become equal to the Coulomb collisional effects at roughly 100 MeV, depending somewhat on the medium and other parameters.

More detailed computations of the particle ranges have recently been completed. These were undertaken for the purpose of identifying possible temperature-pressure regimes where particle beams could be used to advantage. Three cases were run corresponding to: a) air at standard temperature and pressure; b) high-pressure, high-temperature MHD channel operation; and c) low-pressure, room temperature air. The results of this analysis are shown in Figures D.2- 2 through D.2- 4.

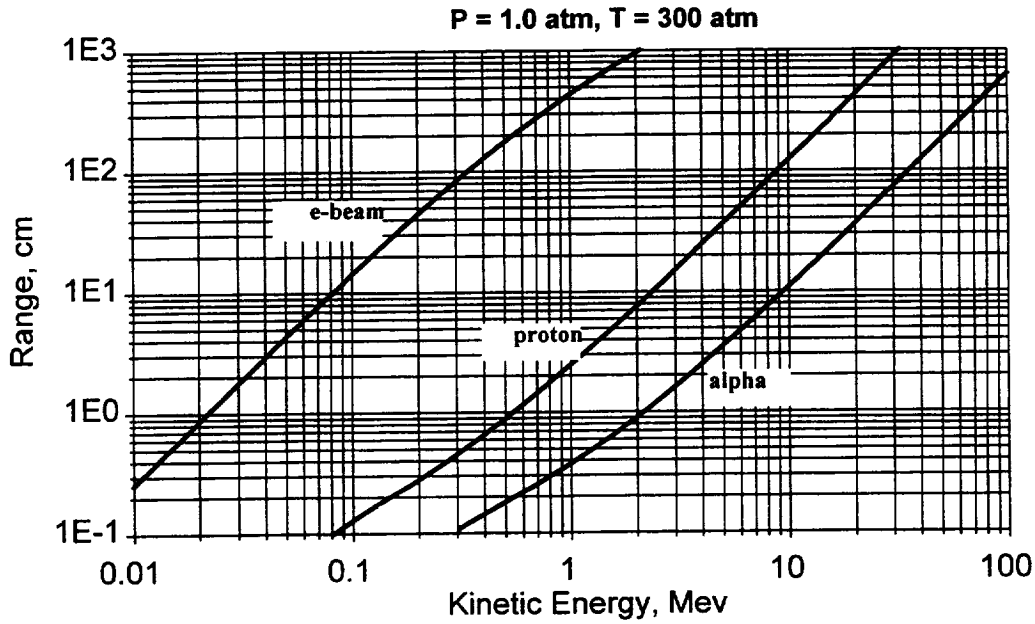

Figure D.2- 2. Range of charged particles in air at atmospheric pressure.

One of the more important conclusions of these graphs is that for any of the three selected thermodynamic conditions, the heavy particles have significantly lower penetrating power than do electrons at the same kinetic energy. However, it would be premature to dismiss the possible use of heavy particles since at this point nothing has been said about their ability to create ion-electron pairs through impact ionization. To conduct an analysis of the pair creation process will require additional cross section data for a spectrum of kinetic energies. MSE is continuing to research this question. As discussed below, the ionization cross section date of Rapp is useful for characterizing electron-ion pair creation for electrons impacting N_2 and O_2 molecules. Cross section data for protons and alpha particles impacting the same molecules has been difficult to find. A more complete answer must wait until heavy particle ionization cross sections have been collected.

Another important inference that can be drawn from Figures D.2- 2 through D.2- 4 is, for electrons, beam energies in the range 0.2 to 4 MeV will be necessary to penetrate the gas to depths of a few centimeters up to about a meter. Since the rest mass energy of an electron is 0.512 MeV, the electrons will be quite relativistic in the energy range of interest. Since the range is by definition the farthest distance traveled by any of the incident particles, a multiplier of 0.5 was applied to the range numbers taken off the graph. This ensures that some significant fraction of the particles will reach the depth specified. For 1-MeV electrons, for example, the range for electrons is 43 cm, implying that a significant fraction (roughly one-half) of the particles will penetrate to a depth of 22 cm.

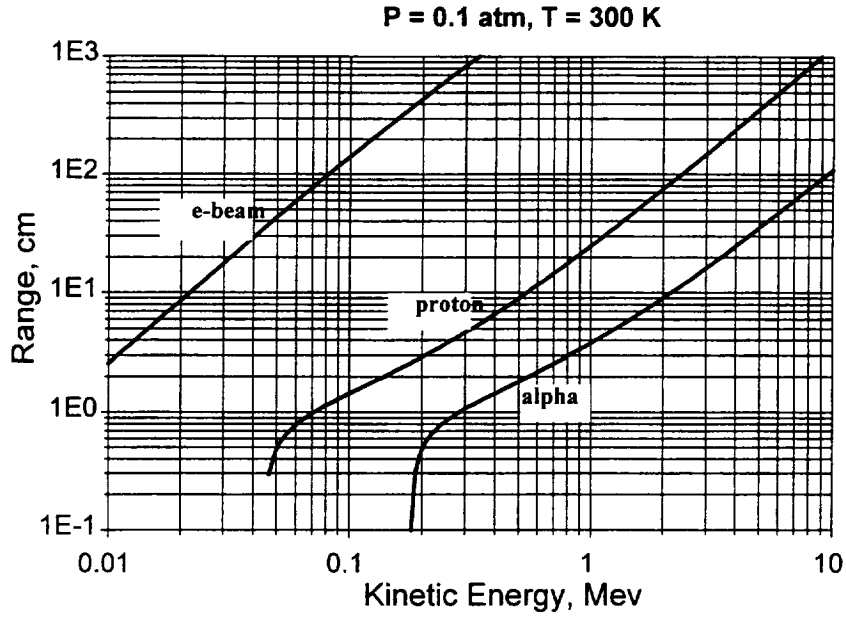

Figure D.2- 3. Range of charged particles in air at low pressure.

The second question, regarding the number of ion-electron pairs created per unit of path length, can be answered by appealing to the notion of an ionization mean-free path. The mean-free path is a simple function of the ionization cross section. This parameter was measured for electron impact ionization in N_2, NO, and O_2 by Rapp in the 1960s up to energies of roughly 1 keV (Ref. 7). Although Rapp's data is for the low energy limit, it can serve to illustrate the general approach to the problem. The results for NO are shown in Figure D.2- 3.

The data for N_2 and O_2 are quite similar. In all cases, the measured cross section data have been converted into mean-free path numbers using the formula:

$$l = \frac{1}{n\Sigma}$$

where l is the mean-free path (in cm) for impact ionization, n is the number of target molecules (NO in this case) per cubic cm, and Σ is the measured ionization cross section.

Analysis shows that an ionization fraction of about 10^{-4} is required to achieve reasonable conductivities in the MHD accelerator. For the pressure and temperature corresponding to Figure D.2- 3, this implies an electron number density of about 10^{16} cm^{-3}. From D.2- 5, it is found that the mean-free path for the high-energy limit (>1,000 eV) conditions is about 1.0 cm. If a channel width of 20 cm were envisioned, one could expect about 20 ionization events per cm, then one can also estimate the number of electron pairs created per second by the beam. Such data can also be used for modeling purposes to provide a computational basis for

simulating the beam-plasma interactions. This illustrates the utility of the concept of an ionization mean-free path. For the high-pressure high temperature example discussed above, it is clear that e-beams having kinetic energies up to several MeV will be required. Ionization cross section data in this energy range is quite scant. MSE is presently attempting to locate ionization cross section data for the high-energy regime. This would be useful for future computations on MHD plasmas.

The problem of computing the steady-state conductivity in a gas irradiated by an e-beam of known intensity can be formulated using a set of rate equations into which empirically known rate coefficients are introduced. This technique was used in Reference 8 to analyze a "hybrid" flow train consisting of an ultrahigh-pressure gas piston driver, followed by an expansion region into which beamed energy was directed. Downstream of the beamed energy region the flow entered an MHD accelerator. Electrical conductivity in the accelerator was assumed to be sustained by an e-beam having a beam current density j_b.

In Reference 8, the authors analyzed the e-beam interaction for the case of low pressures and moderate temperatures through the accelerator (p~0.1 atm, T<1,500 K). A set of five chemical kinetics equations was developed that describe the interaction of electrons with the air molecules. The flow was assumed to be unseeded. The reader is referred to Appendix F for further details of the kinetics model. Appendix F contains a review and summary of Reference 13. The important result is equation (D.2- 1) of Reference 8:

$$\sigma = \frac{e^2\left(M/m\right)}{\rho K_{en}}\sqrt{\frac{j_b \rho y}{e W_i K_{dr}}} \qquad \text{(D.2- 1)}$$

where M is the average mass of an air molecule; m is the electron mass; y is the mass stopping power of air; j is the electrical conductivity; ρ is the mass density; e is the electron charge; K_{en} is the electron – neutral collision rate, and K_{dr} is the rate of dissociative recombination reactions. To illustrate the ability of an e-beam to augment the conductivity of air, an eV beam propagating through air at a pressure of 1 atm and a temperature of 1,500 K was considered.

E	=	30 keV
T	=	1,500 K
P	=	1 atm
j_b	=	1.0 A/cm^2
W_i	=	9.26 eV (ionization energy for NO)
ρ	=	0.232 kg/m^3
dE/dx	=	$\rho Y = 1.97 \times 10^{-3}$MeV/cm (Ref. 7)
M/m	=	5.29×10^4 (assuming the molecular weight of air is 28.8)
K_{en}	=	5.8×10^{-9}cm^3/s
K_{dr}	=	1.5×10^{-7} cm^3/s

Substituting these values into the above formula for σ yields:

$$\sigma \quad = \quad 95 \text{ mho/m}$$

Thus, the calculations show that reasonable conductivity levels can be achieved through the use of e-beams. It should be emphasized that the above computation for j is valid only in the vicinity of the beam. Outside the beam, j_b is zero, and σ will rapidly decrease due to electron-ion recombination. To maintain acceptable levels of conductivity through the MHD accelerator will require that the heavy particle number density be kept low to suppress recombination. This appears to be a key technical issue with respect to the use of e-beams for the purpose of enhancing ionization. The other technical issues with respect to e-beams are the questions of foil materials, foil cooling, and the feasibility of operating a pulsed mode. These issues are addressed in some detail below.

In Reference 2, the e-beam problem was addressed in a somewhat different way. The conclusions of that paper are that e-beams are useful for MHD only in the low-pressure limit, i.e., only for channel pressures below approximately 1 atm. For high-pressure operation in the range of 50 -100 atm, the authors concluded that recombination would be so rapid as to render the process useless. However, if the MHD duct could be run at subatmospheric pressures, the recombination rates drop dramatically, and the electron beam ionization process would become attractive. Another conclusion that can be drawn from Reference 2 is that, for good MHD performance, one needs an ionization fraction (i.e., the fraction of all molecules in the flow that are ionized) of about 10^{-5}-10^{-4}. For channel pressures above 10 atm, the steady-state ionization fractions in the unseeded, e-beam-irradiated flows were less than 10^{-6}.

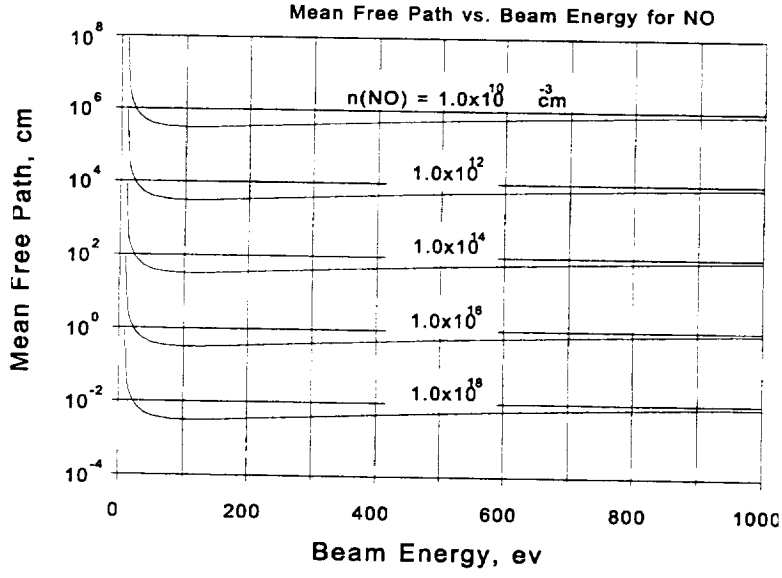

Figure D.2- 4. Mean-free path vs. beam energy for nitrogen oxide.

A more practical issue in the use of e-beams is the question of window design. Based on knowledge gained to date, it appears there are two major problems with regard to design of the foil windows that are used to isolate the working gas from the incoming e-beam. First, the window material may be subjected to high current densities, and this often implies a very rapid temperature rise. The equation relating the rate of temperature rise to e-beam parameters may be derived from a simple heat transfer analysis.

$$\frac{dT}{dt} = \frac{j_b}{e\rho C_p}\frac{dE}{dx}$$

In the above equation, T is the temperature in degrees K, t is the time, j_b is the e-beam current, e is the electron charge, ρ is the mass density, C_p is the specific heat of the window material, and dE/dx is the stopping power of the window material, measured in eV per cm. The last parameter has been tabulated for many materials (Ref. 7). Typical values for dE/dx are in the range 1-4 MeV/cm. The following representative numbers illustrate the magnitude of the problem. For a current density of 48 A/cm^2, mass density of 1 gram/cm^3, dE/dx = 1.86 MeV/cm, and a heat capacity of 1 calorie per gram, the predicted temperature rise is 21.3 million degrees per second. Judicious choices of foil materials along with various schemes for actively cooling the foil can alleviate the problem to some extent; however, in general it is not possible to operate in a continuous mode at very high current densities, irrespective of the foil material. The heating problem is the primary consideration that dictates a pulsed mode of e-beam operation when high current densities are required.

The second major problem relating to window design is the pressure standoff problem. Because the foils must be very thin to avoid absorbing significant numbers of electrons, they are unable to withstand any large pressure differential. In practice, this restricts most e-beam windows to a pressure difference of 1-2 atm, and in many cases substantially less.

The remaining question with respect to e-beams is: "What is available in terms of hardware?" There are several such questions; a) is it possible to buy off-the-shelf beam sources capable of delivering a continuous beam with kinetic energies in the range 0.5-5 MeV? b) what kinds of current densities can be delivered? and c) is the window problem more difficult or less difficult in the MeV range than for the low energy regime?

Discussions with Dr. Lou Rosocha at Los Alamos National Laboratory have provided some answers to the above questions. According to Dr. Rososcha, there is off-the-shelf hardware available capable of delivering electrons at the beam energies required for MHD (0.5-5 MeV). One class of such devices is Linear Accelerators (LINACCS), which are used widely in the medical imaging field. They have typical ratings of 1 kW of beam power and can deliver particles with kinetic energies up to 10 MeV. Dr. Rososcha indicated a used LINACC suitable for our use would cost in the neighborhood of $1 million. He also said that because of the large pressure and temperature differences across the duct walls, the biggest problem will be window design.

Dr. Rosocha stated that titanium has been used to construct foil windows with apertures of up to 1 m by 2 m. It is able to withstand high temperatures; however, he had doubts about whether it would be capable of withstanding anything like 100 atm. He also stated there is a new technique called fusion bonding in which titanium is bonded to the wall material, giving a composite that has greater strength than the foil alone. Aerodynamic windows have been used only for small apertures (about ¼-in. dia.). Diamond has also been used as a window material for windows up to approximately 1½-in. in diameter.

Dr. Rosocha cited Textron Defense Systems of Everett, Massachusetts, and the Boeing North American Rocketdyne Division as two companies that have built cooled windows for laser weapons applications. Finally, he mentioned that graphite fiber has been used for e-beam windows. This material can take high stress but not high temperature.

Dr. Ron Gielgenbach at the University of Michigan has also been consulted on the same topic, and he suggested talking to a company called AECL in Canada, Ontario. AECL has built high power, continuous wave e-beams that operate at up to 13 MeV for materials deposition processes. Dr. Gielgenbach mentioned there is an ongoing effort by the people who do flue gas processing to utilize e-beams for ionizing particulates so they can be removed in electrostatic precipitators. Reference 9 describes this concept in some depth. He also cited the "Nike" project at the Naval Research Laboratory as having utilized high-energy e-beams in a pulsed mode. The pulse widths were about 100 nanoseconds (ns). Dr. Gielgenbach indicated he was uncertain whether pulse repetition at high repetition rates would be feasible.

D.2.2.2 Microwaves

Microwave beams have been suggested as a means of achieving enhanced ionization. From experimental work done in the post-war years, it is known that microwaves can be used to ionize gases. The work of MacDonald and his colleagues is noteworthy (Ref. 4). They measured the breakdown fields of microwaves in low temperature air, H_2, N_2, and O_2 as a function of pressure, with pressures ranging from about 0.1 to 100 millimeters (mm) Hg. Plots of the breakdown field amplitude vs. cavity pressure typically exhibit a minimum at a critical pressure in the range 1-40 mm Hg. This critical pressure is dependent on the frequency and the gas type; however, the dependence generally appears to be weak for both of these parameters. Data for high pressures (1 atm and above) seems to be quite scant.

Based on the work of MacDonald and others, it is well established that the predominant ionization mechanism in most gases of interest is electron impact. Electron impact may involve several mechanisms.

The collision frequency, ν_c, of an electron with neutral particles is a fundamental parameter. To achieve ionization by microwaves, the collision frequency must be substantially higher than the beam frequency:

$$\nu_c >> \nu_b$$

If this condition does not hold, the electrons will typically undergo many periods of oscillation before colliding with a neutral, and therefore, on the average, will gain no net energy from the electric field. Conversely, the electrons will gain net energy if the ac field does not change appreciably over one collision time. If the collision time is long enough (but still smaller than the beam period), sufficient kinetic energy will be imparted to the electrons to ionize a neutral particle upon impact. This is the basic mechanism of microwave ionization.

Pressure and temperature dependence is a significant issue. For MHD applications, the pressures in an accelerator duct may range from 0.01 atm to 100 atm or higher, depending on the inlet conditions and the applied fields. The local static pressure affects the probability of ionization by changing the mean-free path.

As a means of characterizing the microwave absorption, computations have been run for three different cases, as shown in Table D.2- 2 below. For each case, three different electron energies (0.03, 0.3, and 3.0 eV) were analyzed. This permitted an examination of whether or not nonthermal electrons would affect the beam absorption length. For each case, Table D.2- 2 shows the equilibrium electron energy (labeled by an "*") in eV.

Table D.2- 2. Summary of system parameters for microwave beam case study

	Pgas (atm)	Tgas (K)	Eel (eV)	N (cm^{-3})	n_e (cm^{-3})	ν_p (Hz)	ν_c (M-Hz)
D	0.01	1,000	0.13*	7.34(16)	7.34(11)	7.70(9)	5.465
			1.3	7.34(16)	7.34(11)	7.70(9)	17.28
			3.0	7.34(16)	7.34(11)	7.70(9)	26.25
E	1.0	3,000	0.39*	2.45(18)	2.45(13)	4.44(10)	315.5
			3.0	2.45(18)	2.45(13)	4.44(10)	875.0
			10.0	2.45(18)	2.45(13)	4.44(10)	1,597.0
F	100	3,000	0.26*	2.45(20)	2.45(15)	4.44(11)	25,800
			1.0	2.45(20)	2.45(15)	4.44(11)	50,520
			5.0	2.45(20)	2.45(15)	4.44(11)	113,000

The wave propagation vector k of a microwave is given by:

$$k = \beta + i\alpha$$

and the real quantities α and β are the attenuation and phase constants, respectively. Both have the units of inverse length. The skin depth (or absorption length) is then defined as the inverse of α. The absorption length is a fundamental parameter that characterizes the distance to which microwave energy can penetrate a material or a gas.

As shown in Mitchner and Kruger (Ref. 10), the relation that gives α as a function of the frequency (omega) and other parameters of the problem is:

$$\frac{\alpha c}{\omega} = \sqrt{\frac{-B + \sqrt{B^2 + C^2}}{2}}$$

with ω being the beam frequency in radians/s (assumed given), and B and C being defined by:

$$B = 1 - \frac{(\omega_p/\omega)^2}{1 + (\nu_c/\omega)^2}$$

and

$$C = \frac{(\omega_p/\omega)^2(\nu_c/\omega)}{1+(\nu_c/\omega)^2}$$

The quantities ν_c and ω_p are the collision frequency (collisions/s) and the plasma frequency (rad/s), respectively, the latter being given by:

$$\omega_p = \sqrt{\frac{n_e e^2}{\varepsilon_0 m_e}}$$

For conditions corresponding to MHD accelerator operation, the free electron densities for adequate electrical conductivity should be in the range of 10^{-5} to 10^{-4} of the heavy particle density. This is the scenario depicted in Figures D.2- 6 through D.2- 7. Other plasma and gas dynamic parameters of interest are summarized in Table D.2- 2.

As in the case of e-beams, it is desirable the absorption length be roughly matched to the dimensions of the hardware. This would imply depths of roughly 1 cm to 2 m. For Case E, it appears from Figure D.2- 7 this cannot be achieved within the microwave frequency band (up to roughly 300 GHz). As was the case with e-beams, the problem is fundamentally the high pressures. If the MHD channel could be operated at somewhat lower pressures (lower particle densities), microwave propagation would become much more feasible.

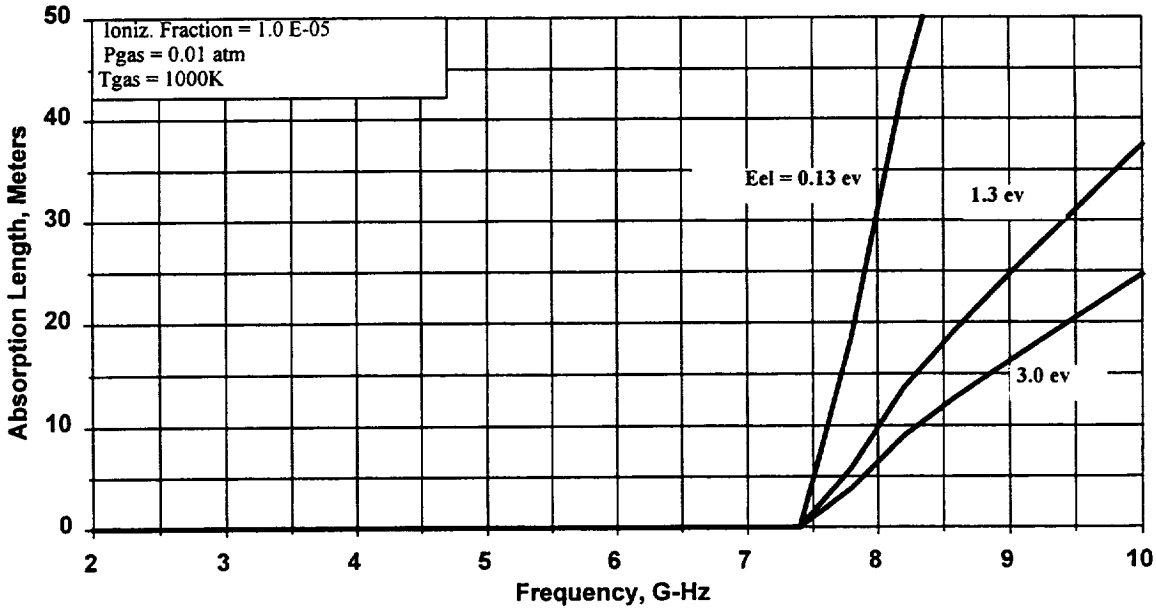

Figure D.2- 5. Microwave absorption length vs. beam frequency.

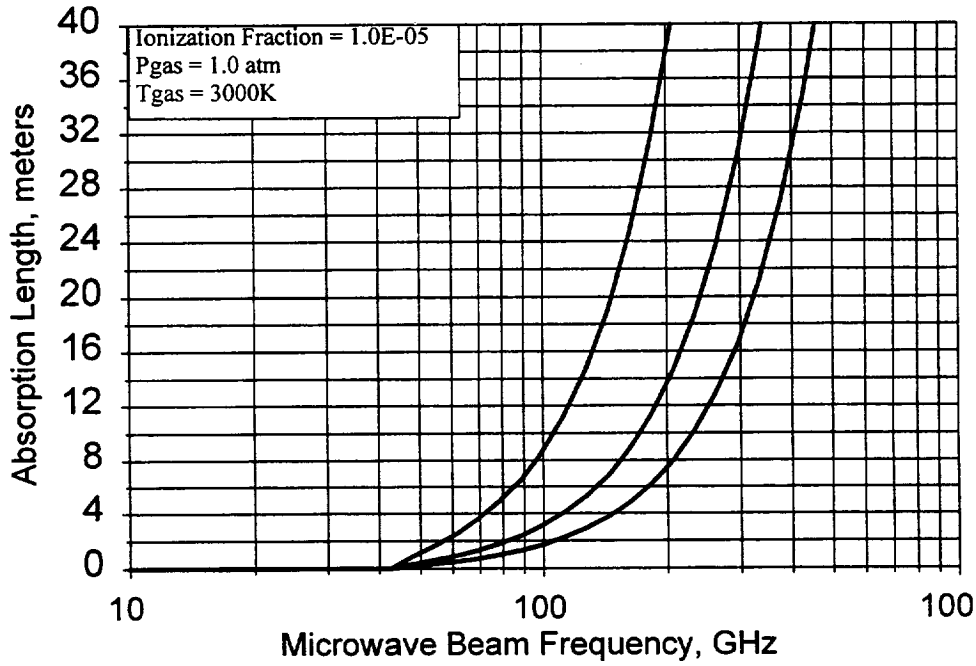

Figure D.2- 6. Microwave absorption length vs. beam frequently.

This statement is confirmed by Figures D.2- 6 and D.2- 7. It should be noted the conclusions regarding absorption depth are based on a highly simplified model of the gas-microwave interaction. The electron density in this model is a specified parameter, whereas in an experimental sense, it is determined by the impact kinetics of electrons being accelerated and then colliding with and ionizing neutral molecules. Further simulations needing to be performed ought to be done taking into account the kinetics and the gas-wave interactions before ruling out microwaves as a potentially applicable technology.

Micci (Ref. 11) has demonstrated microwave heating and plasma creation in several gases, including He and N_2, at pressures up to 3 atm using a 2.2-kW microwave thruster operating at 2.45-gigahertz (GHz). His device was a resonant cavity into which gas was introduced after a standing wave had been set up in the cavity. He further describes laser-induced fluorescence equipment that has been used to measure exit flow velocities from the exit of the microwave thruster. This technology appears to be reliable and practical for the lower pressures at which Micci has worked.

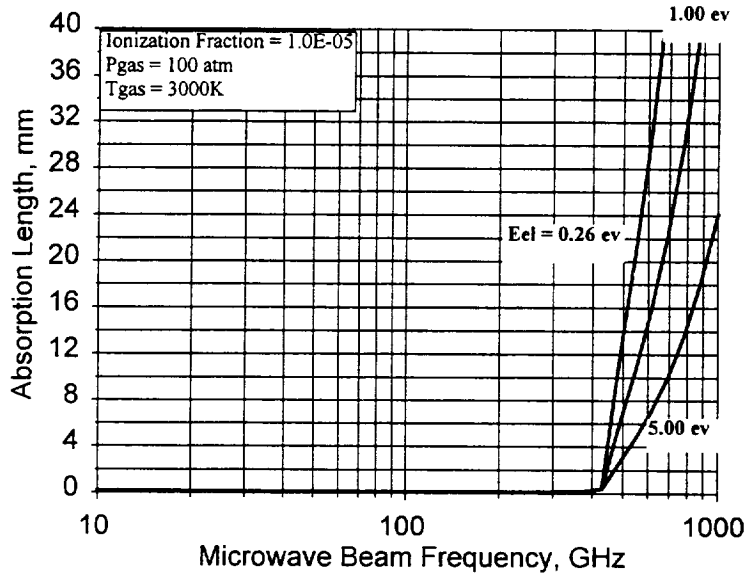

Figure D.2- 7. Microwave absorption length vs. beam frequency.

D.2.2.3 Heavy Particle Beams

Heavy particle beams include alpha particles, proton beams, neutrons, and more exotic species such as pions. To date, we have only examined the first two in a preliminary manner. Figures D.2- 2 and D.2- 4 show the range calculations for air at selected temperature and pressures. As noted previously, the ranges for these two particle types are consistently lower than for electrons. Further study is required to determine whether the total number of ion-electron pairs created per unit length by a beam of alpha particles, for example, can be comparable to that of an electron beam. Additional ionization cross section data will be required to make such a determination.

D.2.3 References

1. Crawford, R.A.; Chapman, J. N.; and Rhodes, R.P., "Potential Applications of MHD Acceleration for Hypersonic Environment Testing," Report AEDC-TR-90-6, Aug. 1990.

2. Adamovich, I.V.; Rich, J.W.; and Nelson, G.L., "Feasibility Study of MHD Acceleration of Unseeded and Seeded Air Flows," AIAA Paper 96-2347, June 1996.

3. Treanor, C.E.; Adamovich, I.V.; Williams, M.J.; and Rich, J.W., "Kinetics of Nitric Oxide Formation Behind Shock Waves," *Journal of Thermophysics and Heat Transfer*, Vol. 10, No. 2, Apr.-June 1996, pp. 193-199.

4. Rittenhouse, L.E.; Pigott, J.C.; Whoric, J.M.; and Wilson, D.R., "Theoretical and Experimental Results with a Linear Magnetohydrodynamic Accelerator operated in the Hall Current Neutralized Mode," AEDC-TR-67-150, Nov. 1967.

5. Webb, C.E., "The Fundamental Discharge Physics of Atomic Gas Lasers," presented at the Conference on High Power Gas Lasers, 1975, pp 1-28. Published by the Institute of Physics, Conference Series number 29. Lectures given at a summer school organized by the International College of Applied Physics, Capri, Italy, Sept. 23 – Oct. 4, 1975.

6. Judd, O., "The Fundamental Discharge Physics of Atomic Gas Lasers," presented at the Conference on High Power Gas Lasers, 1975, pp. 29-43. Published by the Institute of Physics, Conference Series number 29. Lectures given at a summer school organized by the International College of Applied Physics, Capri, Italy, Sept. 23 – Oct. 4, 1975.

7. Turner, J., *Atoms, Radiation, and Radiation Protection*, John Wiley, 1995.

8. Macheret, S.; Miles R.; and Nelson, G., "Feasibility Study of a Hybrid MHD/Radiatively Driven Facility for Hypersonic Ground Testing" AIAA Paper 97-2429, June 1997.

9. Matzing, H., "Chemical Kinetics of Flue Gas Cleaning by Irradiation with Electrons," *Advances in Chemical Physics*, Vol. 80, pp. 315-403.

10. Mitchner, M. and Kruger, C.H., *Partially Ionized Gases*, Wiley-Interscience Publication, reprinted in 1992.

11. Sullivan, D.J. and Micci, M. M., "Performance Testing and Exhaust Plume Characterization of the Microwave Arcjet Thruster," presented at the AIAA/ASME/SAE Joint Propulsion Conference, Indianapolis, IN, June 1994.

APPENDIX D, SECTION D.3

D.3 PULSATRON STUDY ON IONIZATION METHODS FOR MHD ACCELERATORS

Pulsatron Technology Limited (Pulsatron) is a research organization with main offices in the United States but with a staff of Russian scientists residing in Moscow. Pulsatron has a past investigatory history in the area of gas discharge phenomena, application of corona discharges to the problem of pollutant removal from gas streams, and high-voltage discharges in long air gaps. The research Pulsatron performed for the MARIAH Project had the primary objective of investigating various schemes for creating a favorable conductivity regime within the MHD accelerator. The activity was limited to computational modeling and analysis. The Pulsatron study describes analytical work in these three areas: a) conventional equilibrium MHD acceleration using alkali metal seed materials; b) the use of e-beams to sustain nonequilibrium electrical conductivity through the MHD channel; and c) the application of the "plasma snowplow" concept to accelerate successive slugs of air to high speeds. All three of these schemes relied on MHD body force as the accelerating agency.

D.3.1 Overview

As part of the work scope, a target flight regime was established for the purpose of focusing the research. For simplicity, a free-stream condition corresponding to an altitude of 31 km and 2,000-lbf/ft^2 dynamic pressure was adopted as a target simulation point. The temperature, Mach number, static pressure, and total enthalpy (shown at the bottom of page 5 of the report) correspond to this free-stream condition. MSE determined that Pulsatron's research would be evaluated by their ability to produce these test conditions through specific ionization methods.

In preliminary discussions with Pulsatron, MSE emphasized that one of the gasdynamic regimes of interest to NASA was the high-pressure regime, characterized by MHD channel static pressures of 100 atm or higher. This is the basis for Pulsatron's selection of a very high-pressure reservoir with a stagnation pressure of 1,000 atm. If one specifies a pressure of 100 atm at the inlet of the MHD accelerator channel and a minimum Mach number of 2, then the required reservoir pressures must be at least 800 atm to satisfy the isentropic expansion relations. While reservoir pressures in the range 800-1,000 atm are far beyond present arc-heater capabilities, it is not completely unreasonable to assume that a 100-atm static pressure condition with temperatures of at least 2,500 K could be achieved at the accelerator inlet. Methods for realizing such high-pressure inlet conditions are one facet of the MARIAH II hybrid concept discussed in Section F.

The approach adopted by Pulsatron consisted of investigating three different MHD acceleration schemes:

1. An MHD accelerator that operates in the local thermodynamic equilibrium regime and for which alkali metal seed is required. The required electrical conductivity is achieved through thermal ionization of the seed material. Pulsatron selected Cs as the seed material.

2. Nonequilibrium gas ionization by means of e-beams. This technique has been proposed in the past and was studied analytically by Macheret et al. (Ref. 1) as well as experimentally by Shair and Sherman (Ref. 2). The Pulsatron analysis assumes a beam energy of 40 keV, which according to the curves shown in Figure D.2-2 of Section D.2 should be adequate to penetrate air to a distance of several cm.

3. Plasma acceleration by means of the so-called "snow plow" technique. This method relies on creating a highly localized sheet of very high conductivity plasma and utilizing the MHD process to accelerate the sheet. The supposed advantage of this scheme over conventional MHD processes is that the plasma is produced through a series of arc filaments, within which the current density and the conductivities are extremely high, leading to very high J_yB body forces. This scheme is not without both theoretical and practical difficulties. Difficulties include electrode erosion due to the high current densities impinging on the electrodes; the problem of generating many such sheets at a high pulse repetion rate so as to accelerate the gas more or less continuously; and the problem of controlling the instabilities that are characteristic of this type of localized plasma.

   It should be noted that the snow plow technique did not originate with Pulsatron. The scheme has been often referred to in the literature as the T-layer concept. A number of researchers in Russia and the United States have investigated the T-layer scheme in the context of MHD power generation. An excellent analysis and description of the process has been given in the Ph.D. dissertation of Lin (Ref. 3), which also contains numerous references to recent research in this area.

MSE has also written a section entitled "MSE Summary and Evaluation of the Pulsatron Work," Section D.3.3. This section is intended to summarize the major points of the study as well as provide an evaluation of the Pulsatron work in the context of how it addresses some of the basic issues of the MARIAH Project.

D.3.2 Final Report on Achieving Enhanced Ionization in MHD Accelerators

(presented in pp. D.3-3 through D.3-26)

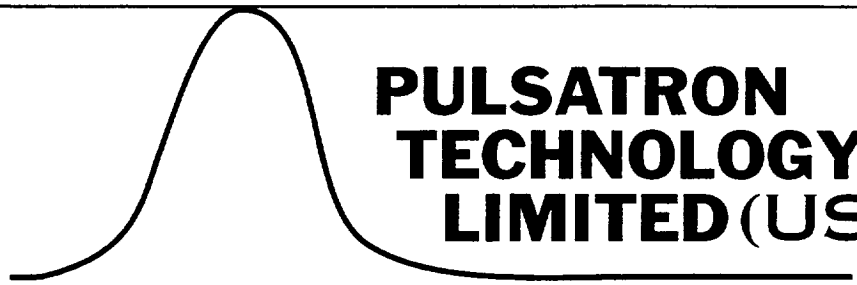

PULSATRON TECHNOLOGY LIMITED (USA)

FINAL REPORT
on

ACHIEVING ENHANCED IONIZATION IN MHD ACCELERATORS

for

MSE APPLICATIONS
PO BOX 4078
BUTTE, MONTANA 59802

under
PURCHASE ORDER
NO. 7J009
CONTRACT NO. DE-AC22-96EW96405

April 14, 1997

[Corrected and Reprinted May 21, 1997]

TABLE OF CONTENTS

ABSTRACT

This report proposes three different approaches to the problem of creating hypersonic wind tunnels with electrodynamic gas acceleration. The findings from the theoretical research done are supported by technical data. Basic data for creating a feasible set of experiments are also presented.

INTRODUCTION

It was clear by the early 1960's that further progress in aviation and aeronautics would depend on the development of hypersonic wind tunnels with gas flows of Mach 10 and higher to design aircraft capable of flying in the upper atmosphere. Although more than three decades have passed, the problem of creating such a wind tunnel remains unsolved. One of the promising approaches to finding a solution, however, seems to be the use of electrodynamic gas acceleration methods.

To look at the question of electrodynamic gas acceleration in depth, Pulsatron Technology Ltd. (PTL) organized a team of highly experienced Russian specialists in the field of electrophysics and thermophysics. The team was comprised of three Ph.Ds and three graduate engineers led by Dr. Aleksandr Z. Ponizovsky, Director of the Pulsatech™ Manufacturing Division, and Lazar Z. Ponizovsky, Director of the Pulsatech™ Research Division.

The work was performed under a contract between MSE and PTL and pursuant to a revised Statement of Work dated December 18, 1996. As the work proceeded, additional correspondence and exchanges clarified elements of the Statement of Work and responded to specific questions. Copies of these materials can be found in Appendix A.

Under the revised Statement of Work, the device to be proposed had to ensure a gas flow at the wind tunnel test section with the following parameters:

Mass flow rate Q	**40 kg/s**
Temperature T_{ts}	**298 K**
Density ρ_{ts}	**$1.54*10^{-2}$ kg/m3**
Pressure p_{ts}	**10^{-2} atm**
Mach number M_{ts}	**11.65**
Gas flow velocity V_{ts}	**$3.45*10^{3}$ m/s**
Entropy S_{ts}/R	**27.6**
Total enthalpy H_{ts}	**$6.44*10^{6}$ Joule/kg**

[NOTE: Not all the parameters presented are independent, but given in the interest of completeness.]

In deciding on possible directions for the study to take, the current state of the problem was examined with reference to the aerodynamic parameters presented. The essential results of this examination are reviewed briefly below.

To begin with, the use of ordinary wind tunnels with isentropic gas flow does not allow the stated objectives to be attained. Indeed, the process is graphically displayed on the Mollier diagram as a vertical straight-line segment originating at the abscissa axis of point S_{ts}/R and terminating at enthalpy value Hts. When applied to air with $H_{ts} = 6.44*10^6$ Joule/kg and $S_{ts}/R = 27.6$, gas pressure within a heater is noticeably higher than 1000 atm with a temperature of about 4600 K, whereas these two parameters need to be restricted to 1000 atm and 3500 K, respectively (see Appendix A.) As a result, there is no way other than increasing total enthalpy downstream of the flow to achieve the desired result.

In accordance with the Statement of Work, an enthalpy gain must be accomplished through ionization enhancement and, hence, by electrodynamic acceleration. It follows from the literature in this area that all presently known methods of electrodynamic acceleration of ionized gases can be subdivided into two types: MHD acceleration [1] and the "snow plow" technique [2,3]. In both cases, however, an ionized gas is accelerated through the action of crossed electric and magnetic fields so that such a bi-polar classification is arbitrary.

In principle, MHD acceleration allows two ways of creating sufficiently high enough electric conductivity within an MHD channel:

A. ***Thermal ionization.*** Starting with pure air from $P_h \leq 1000$ atm), $T_h \leq 3500$ K), and S_h/R (<27.6) within a heater, and using calculations [3] of equilibrium air electric conductivity, the latter turns out too low for ensuring the required increase in enthalpy at magnetic fields B ≤6T and reasonable channel lengths. Only if seeded with an admixture of lower ionization potential, can air exhibit enough conductivity. Preliminary estimates show that the wanted total enthalpy and corresponding aerodynamic parameters at the test section could be attained at a seed level of approximately 10^{-2} per cent, which is much less than the amount usually employed. Although use of seeds do not immediately conform to the Statement of Work, consideration of MHD gas acceleration under extremely low admixture levels was permitted after an exchange of correspondence between MSE and PTL.

B. ***Nonequilibrium gas ionization by external ionization sources.*** An analysis of the literature shows that existing microwave radiation sources do not permit a necessary electric conductivity to be obtained at the required pressures. To a large extent this is attributable to the possibility of laser-induced ionization enhancement; to our knowledge, though, there are no lasers of the required power operating continuously. As for X-ray sources, we excluded them from our consideration for medical reasons. As a result, only high energy electron sources would be of practical usefulness, although their technical realization involves certain difficulties. High energy electrons may be produced either with electron guns or by what is called a hollow cathode technique.

In plasma acceleration by the "snow plow" technique, gas ionization occurs in an arc discharge. Worldwide experience shows that it is technically feasible to design such an accelerator with the required gas flow parameters. This device by its very nature, though, involves periodic actions. Large scale pulsations of the gas flow parameters on a target would not be desirable. (See Appendix A.) To resolve this problem, we propose a plasma ejector using the "snow plow" technique to accelerate the ejected plasma. Because an ejected plasma mass flow rate is small compared to the bulk of gas, the resulting flow

is estimated to display relatively small oscillations on a target.

To assess different approaches from the standpoint of their technical feasibility, computer codes in one-dimensional approximations have been developed. Given some additional assumptions, preliminary numerical simulations were performed. As a result, some possible ways of increasing total gas enthalpy in hypersonic wind tunnels are proposed. They are as follows:

* MHD acceleration regimes with the use of a negligibly small seed of alkaline metal.

* MHD acceleration regimes with the ionization of air by a high energy source of electrons.

* Plasma acceleration by "snow plow" technique.

Each of these proposals is discussed in more detail below.

MHD ACCELERATION REGIMES FOR INCREASING TOTAL GAS ENTHALPY

The theory of MHD flows and related plasma physics topics have received a great deal of attention in the literature and need not be reviewed here. Our emphasis has been on finding the conditions that can be realized experimentally for obtaining gas flow parameters on a target approaching those required by the Statement of Work. For convenience, however, our results are briefly preceded by a review of the necessary mathematics.

Basic Statements

MHD flows are completely described by the conservation equations for mass, momentum, and energy supplemented with the equation of state. The relationship between electric current density, J, and applied electric field, **E**, generally in a tensor form, must also be stated. For purposes of the present study, the conservation equations can be taken in a quasi-one-dimensional approximation and the equation of state in a form like that of an ideal gas. Because the electric field, **E**, and the degrees of ionization to be considered are rather small, no account is taken of perturbing thermodynamic gas parameters as compared to those under full thermodynamic equilibrium. We further assume a Faraday channel with segmented electrodes so that **J** and **E** are directed in parallel. Then, taking the Cartesian frame of reference with **E** = (0,E,0), magnetic field **B** = (0,0,B), and gas velocity **U** = (u,0,0), we arrived at the following set of equations:

$$\rho u A(x) = Q \quad (1)$$

$$\rho u \, (du/dx) + d\rho/dx = jB \quad (2)$$

$$\rho u \, (C_p dT/dx + u du/dx) = jE \quad (3)$$

$$p = R\rho T \quad (4)$$

$$j = \sigma \, (E - uB) \quad (5)$$

Here p, ρ, and T are the gas pressure, mass density and temperature, respectively. A(x) is the channel cross-section normal to x-axis; C_p is specific heat at constant pressure per unit mass depending in general on p and T. Scalar electrical conductivity, σ, needs to be considered in greater detail.

Electrical conductivity, σ, is determined by the frequency of electron momentum transfer, $\nu_m(\varepsilon)$, depending on electron energy, ε, and the electron energy distribution function, $f(\varepsilon)$. At low reduced electric fields, E/N (N, a gas particle density) can be written in the following form:

$$\sigma = e^2 n_e / m \langle \nu_m \rangle, \quad \langle \nu_m \rangle^{-1} = \int_0^\infty [\varepsilon^{3/2} / \nu_m(\varepsilon)] \, (df(\varepsilon)/d\varepsilon) \, d\varepsilon \quad (6)$$

where e and m are the electron charge and mass, respectively and n_e is the electron particle density. To find $f(\varepsilon)$, the electron kinetic Boltzmann equation can be generally solved taking into account both elastic and inelastic electron scattering. In case of heated gases, allowance should also be made for super elastic electron collisions with vibrationally and electronically excited gas particles, even though the degree of ionization is not high.

Given the accuracy of the calculations needed, a simpler procedure for determining σ turns out workable. Indeed, it is well known that there is a link between averaged frequency, $\langle \nu_m \rangle$, and "electron temperature," $T_e = 2\langle \varepsilon \rangle / 3$, where $\langle \varepsilon \rangle$ is the mean electron energy. For our purposes, a good approximation is to take $\langle \nu_m \rangle = \nu_m(T_e)$. In the presence of an external electric field, gas temperature T and T_e differ so that the electron energy balance equation has to be generally solved for determining T_e. In practice, however, simpler considerations often allow T_e to be found with an appropriate tolerance. As far as the determination of electron concentration n_e is concerned, this issue will be analyzed as applied to concrete physical situations considered below.

Acceleration Regime with Ionization of Seed

Electrical Conductivity Determination. In seeded air, ionization enhancement is attained through thermal ionization of an alkaline metal admixture. The admixture is further assumed to be Cs with the lowest ionization potential. Preliminary analysis shows, however, that electron concentrations n_e, as calculated by the Saha equation with gas temperature T, turns out to be insufficient for ensuring an appreciable rise in gas enthalpy under reasonable cesium concentrations, N_{cs}, and MHD channel lengths. Additional gas heating has to be accomplished because of an external electric field.

In a gas at ambient temperatures, T_e obeys the well-known energy balance equation:

$$e^2 E^2 / m \nu_m(T_e) = (3/2) \delta_{eff} \nu_m(T_e) n_e \, (T_e - T) \quad (7)$$

and can immediately be found if E and n_e are known. Parameter δ_{eff} accounts efficiently for electron energy losses owing to their elastic scattering by heavier particles and the rotational excitation of molecules. In heated gases with essentially excited vibrational degrees of freedom at temperatures T comparable to vibrational quantums $h\omega_v$, typical for the conditions in question, no simple relationship like Equation (7) hold. Here, making use of the electron energy balance method would ultimately be the equivalent of finding electron energy and vibrational energy distributions.

With this in mind, it has been proposed to determine Te as

$$T_e = T \, [1 + \xi(E/N)] \quad (8)$$

where function $\xi(E/N)$ is taken in accord with data on cold gas. For air, this function is given, for instance, in [1, 5]. Since $T_e > T$ is not actually higher than 0.5 eV, the disparity between rigorous calculation assessments are no more than about 10 to 20 per cent.

The degrees of ionization we deal with here are so small that only elastic electron collisions with neutral gas particles can contribute to frequency $\langle \nu_m \rangle$. At gas temperatures and pressures of interest, molecular nitrogen, as in ambient air, prevails; the data on $\nu_m(T_e)$ for cold air are used and taken as $\nu_m(T_e) \sim T_e$. Accordingly, $\langle \nu_m \rangle \sim T_e$.

The "bulk" of the electron energy distribution function may be considered as being in quasi-equilibrium with temperature T_e. Given $T_e \sim 0.5$ eV, $N_{cs} \leq 10^{15}$ cm^{-3} and cesium ionization potential 3.89 eV, this results in almost full ionization of the seed. In further calculations, it is therefore accepted that $n_e = N_{cs}$.

Numerical Simulation. A typical hypersonic wind tunnel with the MHD channel is schematically sketched in Fig. 2.2.1.

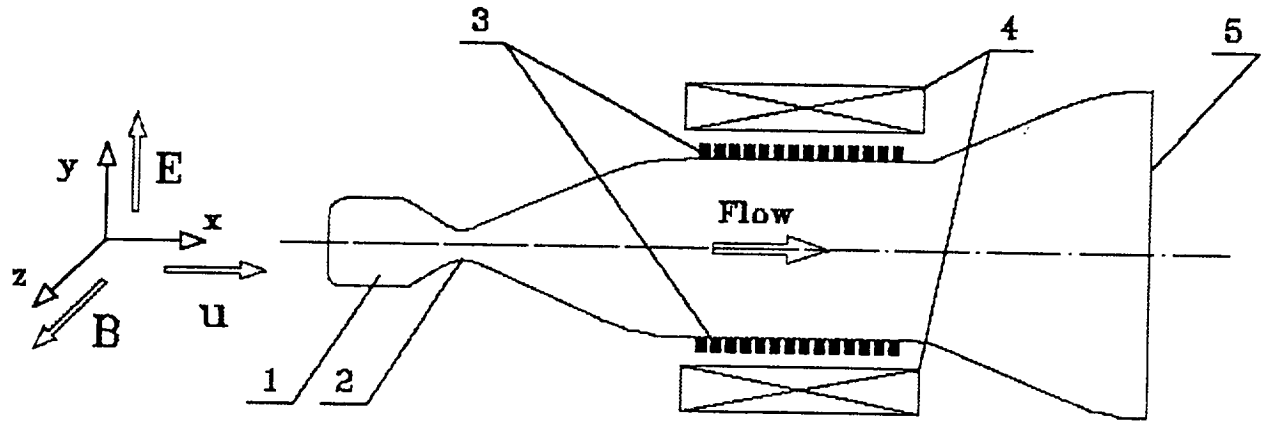

Fig 2.2.1 General view of hypersonic wind tunnel with MHD gas acceleration:
1–heater,2–throat,3–segmented electrodes,4–magnet,5–test section

Gas flow parameters upstream and downstream of the MHD channel were calculated with the well-known relationships for an isentropic flow of an ideal gas

$$T_1/T_2 = [1+ (\gamma -1)M_2^2 /2]/[1+ (\gamma-1)M_1^2/2] \quad (9)$$

$$p_1/p_2 = (T_1/T_2)\gamma/(\gamma-1) \quad (10)$$

linking thermodynamic parameters at two arbitrary cross-sections. γ is the isentropic exponent. It should be pointed out that for the relationship of real gases, Equations (9) and (10) are to be transformed into mathematically more sophisticated ones [6]. For our purposes, however, the corresponding correction is not of essential importance.

For the computer simulation, initial equations (1) through (5) were rewritten with respect to the derivatives of thermodynamic parameters sought [1]. Also, allowance has been made for the dependence of C_p and γ on p and T. To solve the equations numerically, the Runge-Kutta procedure was then used. Fig. 2.2.2a presents, as an example, relative variations in thermodynamic parameters along the MHD duct for a typical acceleration regime. [E = $3.4*10^5$V/m, B = 6 T, the MHD channel length l_c = 17cm, hydraulic diameter D = 5.2cm and mole cesium fraction 10^{-2} per cent.] The heater parameters taken were T_0 = 2800K, p_0 = 980 atm. In Fig. 2.2.3 (a-f), on page 17, these quantities are given in dimensional variables.

Fig. 2.2.2a

GAS FLOW PARAMETERS ALONG THE MHD DUCT

RELATED TO INPUT

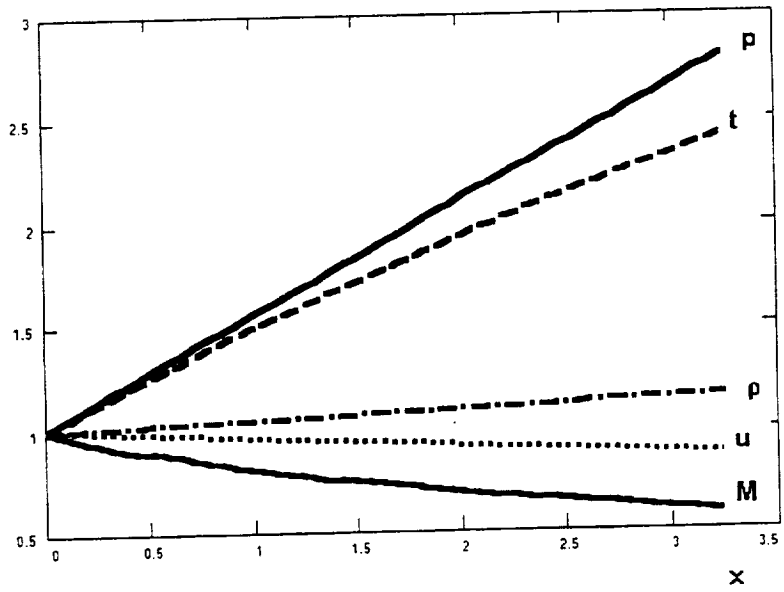

u—Velocity; p—Pressure; t—Temperature; ρ—Density; M—Mach #
x—length related to the hydraulic diameter

To explain the results obtained, use the Resler-Sears' u-M diagram [7]. Although derived in assuming C_p and γ to be constant, it nevertheless allows clear qualitative analysis of the process. The diagram classifies all possible gas flow regimes with respect to three characteristic velocities. They are as follows:

$$u_d=E/B;\ u_1 = u_d(\gamma-1)/\gamma;\ u_2 = u_1(1+\gamma M^2)/[2+(\gamma-1)M^2] \quad (11)$$

The flows with $u>u_d$ are related by definition to generator regimes; otherwise acceleration regimes are realized. For supersonic flows (M>1) with $u_2 < u < u_d$, both the gas velocity and the Mach number progressively increase along the MHD duct. If $u_1 < u < u_2$, the gas continuously accelerates while M first drops and then begins to rise. At last, under supersonic flows with $u < u_1$, both u and M decrease with distance in the direction of the flow. When studying Fig. 2.2.3, observers can find that velocity at the MHD duct entrance u_{en} = 2020 m/s, whereas $u_d = 5.67*10^4$ m/s and $u_1 = 1.62*10^4$ m/s.

Fig. 2.2.3

CHANGE OF GAS FLOW PARAMETERS ALONG THE MHD DUCT

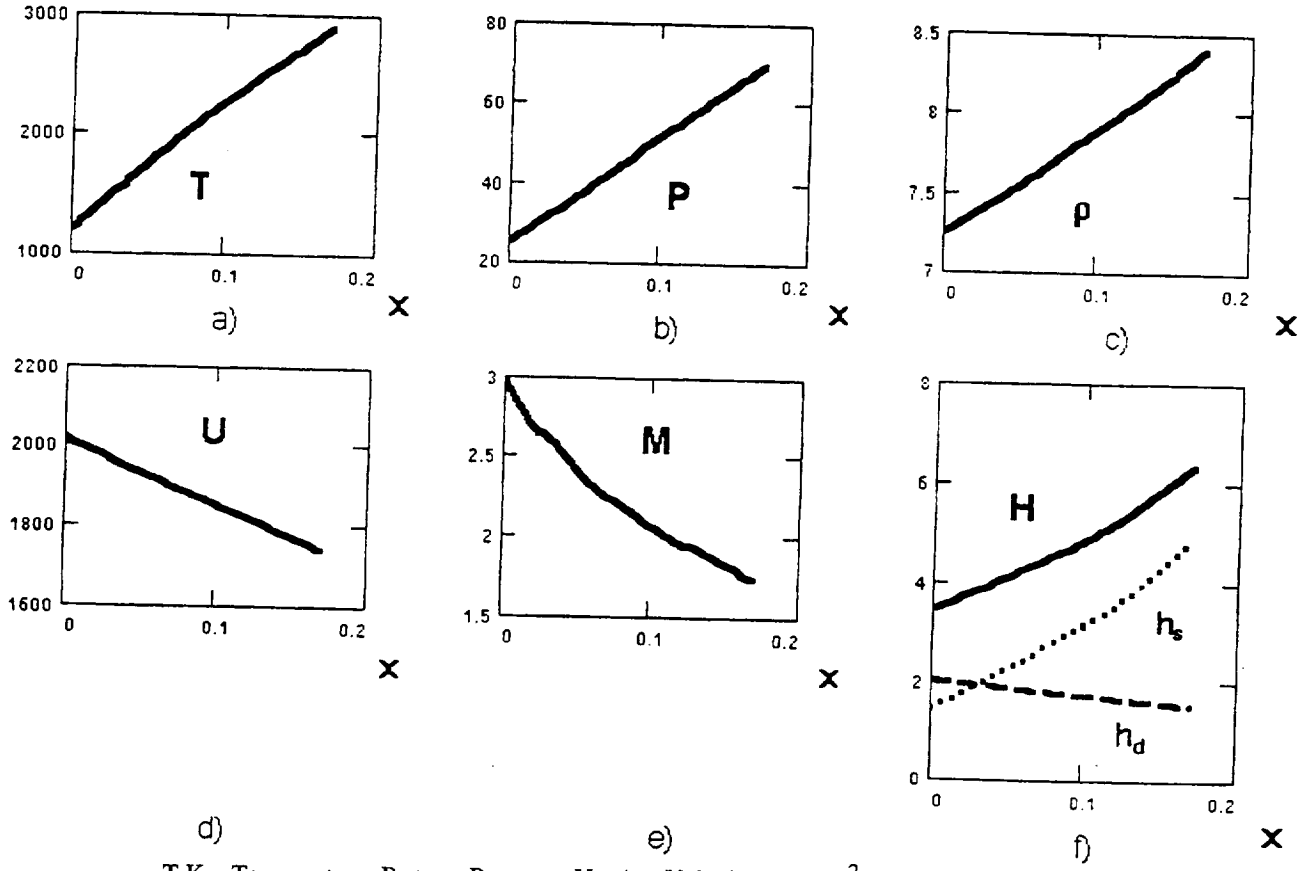

T,K—Temperature; P,atm—Pressure; U,m/s—Velocity; ρ,kg/m^3—Density; M—Mach #;
h_S—static enthalpy—h_d—dynamic enthalpy; H—total enthalpy;(all in MJoule/kg); x,m—length

It therefore becomes clear why the flow velocity and the Mach number calculated both decrease, although the regime itself is attributable to an accelerating one. A great difference between u_{en} and u_d, u_1 arises from a relatively high electric field strength E. The latter in turn is due to the necessity of having E/N ((2-3) Td for ensuring T_e, allowing full ionization of the seed.

It is interesting to note that the problem also allows an analytical solution in assuming C_p and γ to be constant. Being in a good qualitative agreement with numerical calculations, analytical solutions permit starting points for computer simulation to be determined. The principal objective of the simulation was to verify the possibility of attaining the required total gas enthalpy, H_{ts}, at entropy S_{ts}/R beyond the MHD channel exit. The calculated variations in static h_s, dynamic $h_d = u^2/2$ and total H enthalpies along the MHD duct for the considered conditions are shown in Fig. 2.2.3f. It is seen that total enthalpy of $6.44*10^6$ Joule/kg is actually attained at the MHD duct exit.

True, this exclusively results from an increase in static enthalpy rather than the gas acceleration. This peculiarity can be seen more clearly from a schematic representation of the process as a whole on the Mollier diagram Fig. 2.2.2.b.

Fig. 2.2.2b

SCHEMATIC REPRESENTATION OF THE ACCELERATION PROCESS IN THE MHD DUCT ON THE MOLLIER DIAGRAM

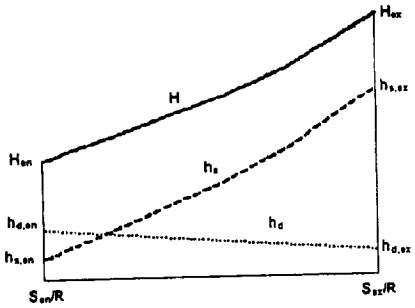

H—total enthalpy; h_S—static enthalpy—h_d—dynamic enthalpy; S/R—reduced entropy. Subscripts 'en' and 'ex' refer to entrance and exit of the MHD duct.

It also follows from data [8] and the obtained gas pressure p_{ex} and temperature T_{ex} at the MHD duct exit, that $S_{ex}/R = S_{ts}/R = 28.9$. Moving on the Mollier diagram along isentrope S_{ex}/R down from $h_{s,ex}$ (the gas expansion in the diffuser), one arrives at parameters on the post bow shock flight envelope that are only negligibly different from those required by the Statement of Work. Thus, theoretically the calculations show that no obstacles actually exist in attaining $H_{ts} = 6.44*10^6$ Joule/kg and $S_{ts}/R = 27.6$ in the MHD acceleration regimes using an air flow with extremely low N_{cs}(10^{-2} per cent) seed fraction and reasonable MHD channel geometric sizes.

Technical Feasibility. At the present time, there is worldwide experience in design and practice with MHD channels utilizing the parameters considered above. High voltage equipment of the required grade involves use of no special supply sources or insulating materials. The heater parameters are within the limits specified. A hypersonic wind tunnel has been estimated to be of common geometrical sizes. If selected, this variant would present no technical problem to being implemented.

MHD Acceleration Regime with Gas Ionization by High Energy Electrons

The general scheme of examining MHD flow remains unchanged, the basic equations (1) to (5) included. However, the fact that free electrons now make their appearance in the bulk of a gas is quite different from the environment considered above. Therefore, the question of electrical conductivity needs to be specially discussed.

Electrical Conductivity Calculation. Equations (6) have been derived from principles of general plasma physics and remain, of course valid for this project. By the same token, everything concerning quantities $\langle \nu_m \rangle$ and T_e involve well accepted principles. To calculate n_e, the following method is to be used.

> When passing through a body of air, high energy monoenergetic electrons produce electron-ion pairs. The newly created (secondary) electrons in turn are capable of ionizing the air again. Losing their energies in successive acts of excitation and ionization they "move" downstream of the energy axis giving rise to an ionization

cascade. As a result, a so-called degradation electron spectrum is ultimately established displaying two sharp maximums, one being in the vicinity of the primary electrons energy and the second in the domain of thermal energies [8]. In reality, the beam of primary electrons is not strictly monoenergetic because of electron scattering in a gas and in a foil it passes through before entering the gas, so that the first (high-energy) maximum turns out smoothed.

For a quantitative description, function D(x) is introduced and defined as a primary electron energy loss per unit of gas mass and unit path in the direction it is moving [9]. In a sense, this characteristic is similar to the optical path in optics. The magnitude of D(x) depends also on the energy of the primary electron. Function D(x) is generally calculated numerically, e.g., by the Monte-Carlo method. The results may be found in [9,10] and references cited therein. Given D(x) and high energy electrons flux density j_b(A/cm^2), the number of electron-ion pairs produced per unit volume per unit time S(x) is then determined as

$$S(x) = j_b D(x)\rho / (eE_i) \quad (12)$$

where E_i is the averaged energy spent for production of one electron-ion pair. This quantity is apparently greater than ionization potentials of components composing air. Electric field strengths (more properly E/N) typical for the problem (~ 1 Td) are low for impact ionization processes in air and are to be taken into account. Therefore S(x) is the only source of ionization in air in our conditions.

Electron production is balanced out by their losses in the bulk of air, owing to the recombination and attachment processes. At present, full clarity of the question of recombination mechanisms in air under high pressures (p> 1 atm), moderate gas temperatures (T< 1000 K) and the degrees of ionization $\chi_i < 10^{-4}$, has not yet been achieved. The commonly accepted point of view is that the dissociative recombination mechanism

$$e + M_2 \rightarrow M^- + M^* \quad (13)$$

prevails, with M^- being a molecular ion and M*, the excited atom [11]. In some cases, however, a three-body mechanism with a neutral molecule as a third particle is additionally invoked. Electron assisted three-body recombination is of no significance here because n_e is too small.

More complicated, however, is the problem of electron attachment. To begin with, one can give no consideration to a dissociative attachment process by reaction

$$e + O_2 \rightarrow O + O^- \quad (14)$$

because values E/N of present interest are too low and reaction (14) exhibits a threshold of several electronvolts [11]. Note, nevertheless, that other physical situations, e.g., air breakdown reaction (14), contributes significantly to electron disappearance [9,11]. The main electron attachment mechanism to be considered is a three-body process

$$e + O_2 + M_2 \rightarrow O_2^- + M_2 \quad (15)$$

Rate Ka of reaction (15) depends in general on E/N, the kind of neutral particle M_2 entering the air, air density, and some other factors. O_2^- can further participate in various ion-molecule reactions to form negative ions of different kinds, as a rule with higher electron binding energies. The fact is, however, that

at elevated gas temperatures, negative ions begin to decay while releasing attached electrons. Thus the totality of attachment-detachment processes should be simultaneously examined to determine the effective attachment rate K_a^{eff}.

Taking the above into account, a variation in electron concentration along the MHD duct is written in the following form

$$dn_e/dx = S(x) - \beta n_e^2 - K_a^{eff} N^2 n_e \quad (16)$$

where β is the electron-ion recombination rate.

Numerical Simulation. Under air densities and characteristic transverse channel sizes here considered, S(x) can be taken as a constant. In accord with the data [9,10], it is reasonably to accept S = 0.5 MeV*m^2/kg and E_i = 34 eV. Recombination rate (depends in general on T_e and T.) The temperature dependencies are not fully understood. The commonly accepted relationship is as follows [12,13]

$$\beta = 1.5*10^{-7}(300/Te)^{-1/2}(300/T),\ cm^3/s \quad (17)$$

To calculate air parameters upstream and downstream along the MHD duct, ordinary equations of isentropic gas flow were used. As a numerical method, the Runge-Kutta procedure was used. For modeling of the MHD flow, equations (1) to (5) have been supplemented with Equation (16) above, quantities Cp and γ being taken to vary with p and T. This set was then numerically solved as a stiff differential system [14].

As an example, in Fig. 2.3.1. changes of air velocity, pressure, temperature and the Mach number downstream of the flow are shown and calculated from the nozzle throat to the test section for j_b = 1 A/cm^2. The heater parameters taken are T_h = 1800 K, p_h = 1000 atm. High energy electrons are accepted to be of 40 KeV. To estimate the greatest possible contribution of electron attachment K_a^{eff} was taken to equal to 10^{-31} cm^6/s that corresponds to attachment of thermal electrons. For convenience, the numbered flow parameters as derived for each characteristic section of the wind tunnel are also given in Table 2.3.1 on the following page.

Fig. 2.3.1

GAS FLOW PARAMETERS ALONG THE WIND TUNNEL

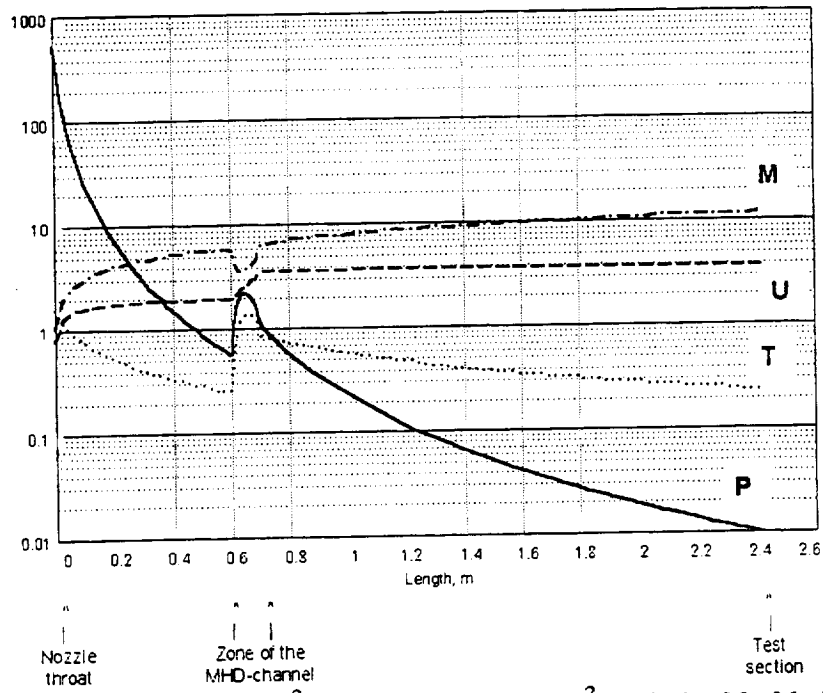

P,atm—Pressure; T,K*10^3— temperature; U,m/s*10^3—velocity; M—Mach #.
Initial gas parameters (in the heater): P=1000 atm; T=1800 K

TABLE 2.3.1
GAS FLOW PARAMETERS AT CHARACTERISTIC SECTIONS OF THE WIND TUNNEL

Section	Cross-section, cm x cm	Pressure, atm	Temp., K	Density, kg/m^3	Velocity, m/s	Mach #
Heater		1000	1800	193		
Nozzle Throat	2.1 x 2.1	536	1528	121	773	1.0
MHD Channel Entrance	16.7 x 16.7	0.54	242	0.78	1858	5.9
MHD Channel Exit	16.7 x 16.7	1.00	830	0.42	3418	6.2
Test Section	85.5 x 85.5	0.010	228	0.015	3595	11.6

Fig. 2.3.2 below illustrates relative variations in basic parameters along the MHD duct. In dimensional variables they are given in Fig. 2.3.3 (a-f) on page 17. Because flow velocity u_{en} at the MHD entrance obeys the inequality $u_1 < u_{en} < u_2$, the Mach number first drops and then rises in full accordance with the Resler-Sears' diagram. Contribution of the electron attachment process turned out to be negligibly small even with K_a^{eff} as great as 10^{-31} cm^6/s.

Fig. 2.3.2
GAS FLOW PARAMETERS ALONG THE MHD CHANNEL RELATED TO THE INPUT PARAMETERS

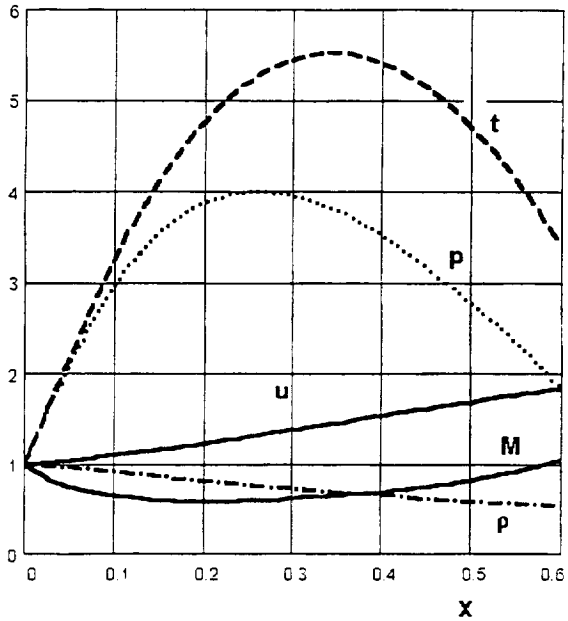

u—Velocity; p—Pressure; t—Temperature; ρ—Density; M—Mach #
x—Length related to the hydraulic diameter

Variations in enthalpies along the MHD duct are shown in Fig. 2.3.3 (f) below. By contrast to the situation of seeded air, dynamic enthalpy progressively increases with distance from the MHD duct entrance and mainly contributes to the total enthalpy gain. As this takes place, both an acceleration regime and air acceleration are simultaneously realized. What is of special importance is the fact that air entropy at the MHD duct exit, Sex/R, is approaching the amount that is required.

Fig. 2.3.3

CHANGE OF GAS FLOW PARAMETERS ALONG THE MHD DUCT

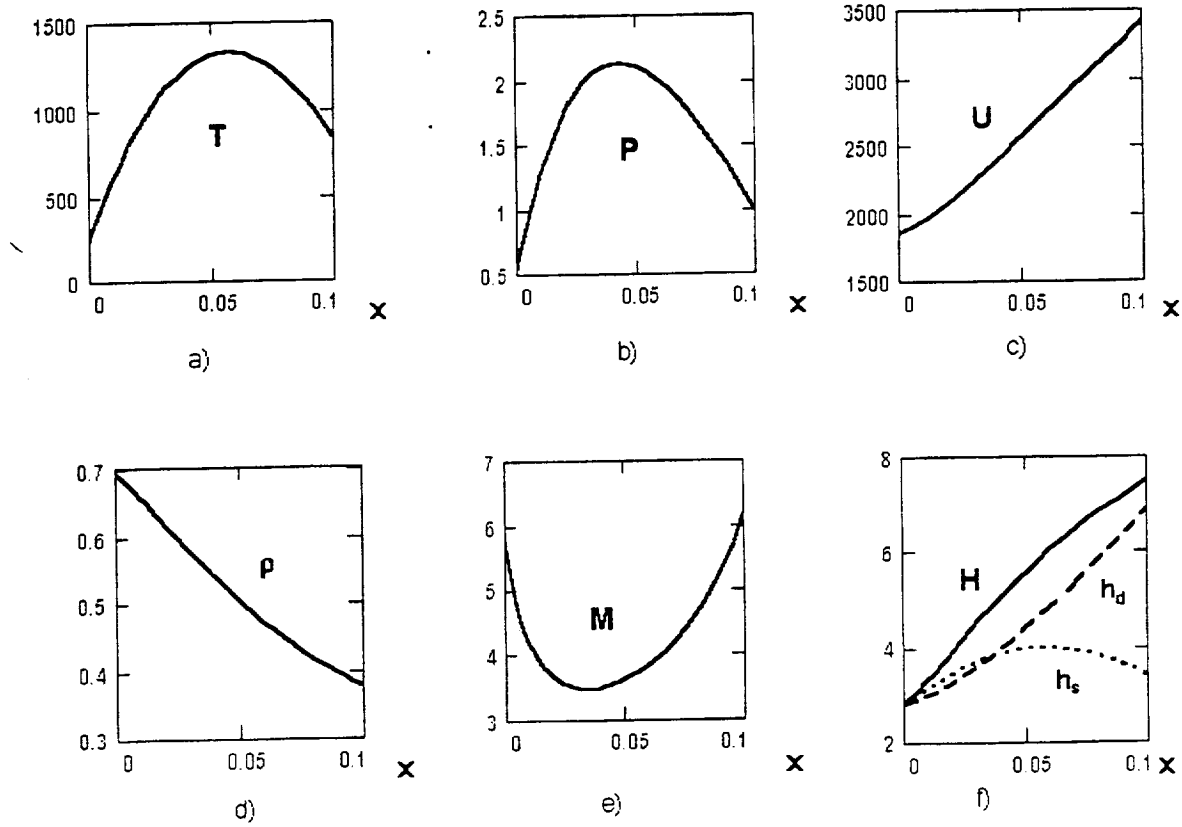

T,K—Temperature; P,atm—Pressure; U,m/s—Velocity; ρ,kg/m^3—Density; M—Mach #; h_s—static enthalpy—h_d—dynamic enthalpy; H—total enthalpy (all in MJoule/kg); x,m—length

Technical Feasibility. The general view of the MHD channel is schematically represented in Fig.2.3.4. The MHD channel is proposed to be a duct of 15 cm square and design length of about 15 cm, the working length being 10 cm. Dielectric walls (1) are fabricated from an insulating material offering a high thermal resistance up to temperatures of about 2000 K. Walls (2) aligned parallel to each other bear a system of segmented electrodes (3) permitting a high voltage of about 6.5 KV across the duct to be applied uniformly throughout the length of the channel.

The magnetic system (4)—Helmholtz coils—are placed close to the insulating walls (1). The hollow cathode electron flux sources (6) are located in the openings of the magnetic systems (4) and attached to the insulating walls (1) such that each source (6) irradiates the gas through its own window. We estimate the number of sources to be 12,, disposed bilaterally in the channel; for example, four rows, each containing three sources. The anodes of all sources in one row are maintained at potentials fitting the voltage distribution across the channel, thus avoiding a breakdown between the anodes and segmented electrodes.

Accordingly, the negative voltage applied to the cathodes varies. As a result, one needs four high voltage devices, each supplying six sources. The total power required to supply the electron flux sources is estimated to be about 6 MW, i.e., about several percentages of the total power required for supplying the MHD accelerator (more than 200 MW).

The numerical results obtained suggest that high energy electron fluxes with $j_b \sim 1$ A/cm^2 will be employed. As far as we know, generation of such fluxes by electron guns to date has been rather problematical. As a result, we propose to use electron flux sources based on the gas flow hollow cathode technique [15-17]. So far, such sources have been used for generating electron fluxes up to several hundred A/cm2 with electron energies up to 1 KeV. This restriction in voltage arises from an arc mode realized during the operation of the device. Investigations also show that the discharge is to be directed in parallel to the magnetic field applied. This fact directs that the sources should be arranged as was noted above. Of importance is also the fact that they operate at pressures of the order of 1 atm. It is our belief that we would succeed in realizing a high voltage glow discharge regime in a strong magnetic field and thus obtain electron energies at levels of (30-40) KeV.

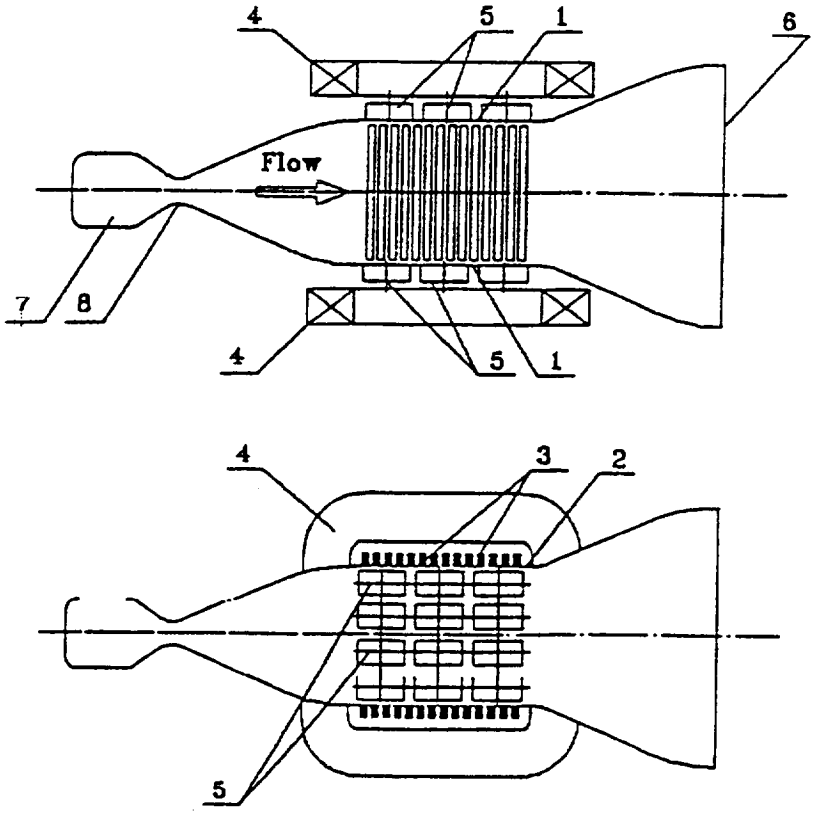

Fig.2.3.4 MHD accelerator with gas ionization by high energy electrons:

PLASMA ACCELERATION BY "SNOW PLOW" TECHNIQUE

General Principles

Plasma acceleration by the "snow plow" technique is ultimately based on the electromagnetic interaction similar to that considered above. The difference between the two methods results from the mechanism of plasma generation and some additional phenomena resulting from the propagation of high velocity plasmoids in atmospheric air. As a whole, the process can be represented as follows.

> Plasma is formed in atmospheric air by pulsed high voltage discharge between two electrodes directed in parallel. Also possible are divergent and coaxial geometries with a plasma bridging the interelectrode gap. The breakdown results in an arc discharge with a large electric current flowing along the "rails" and being completed through the plasma. A strong axial magnetic field thus produced interacts with the arc current, resulting in the Ampere's force pushing the formed plasmoid. When constantly connected to a source of energy, the plasmoid driven by the ponderomotive force compresses the air in front of it and gives ultimate rise to a shock wave formation. The effect can be enhanced by adding an external magnetic field. The process is schematically pictured in Fig. 3.1.1. Propagation of strong shock waves occur when compressed gas is heated to temperatures sufficient for this gas to become conductive. As a result, the whole volume is limited by the discharge channel and the shock wave can be thought of as a uniformly-filled plasma "piston." When the plasma piston "pushes" the air in front of it, it acts as a sort of "snow plow." In reality, however, the pattern is not so simple. First, the piston turns out to be partly permeable. Secondly, the compressed gas is often far from being conductive. All these features in one form or another can be specified in concrete calculations.

Experiments show that the "snow plow" technique allows gas temperatures up to several thousands of degrees and velocities up to 10 km/s and higher. Therefore the plasmoids expelled possess high enough total

enthalpy even though their masses are not large. Unfortunately, plasma accelerators designed on the basis of the "snow plow" technique display large scale gas flow pulsations and cannot immediately be employed in the device to be designed for this project. To circumvent this difficulty, we propose the use of railgun "snow plow" accelerators in combination with ordinary gas ejectors. The principles of operation of such a construction will be considered in greater detail below.

Numerical Simulation

Numerical simulation of the combined plasma ejector implies simultaneous calculation of the "snow plow" plasma acceleration and ejection processes. It is convenient to start with the former.

The railgun to be considered is comprised of two electrodes directed in parallel to an x-axis added to two walls made of dielectric to form a rectangular duct. With the primary aim of obtaining estimated results, a quasi-one-dimensional approximation has been developed. An initial set of equations takes the form

$$\delta\rho/\delta t+\delta(\rho u)/\delta x=q_e \quad (18)$$

$$\delta(\rho u)/\delta t + \delta(\rho u^2 + p)/\delta x = jB - f_r \quad (19)$$

$$\delta/\delta t\,(\rho\varepsilon + 1/2\rho u^2) + \delta/\delta x\,[\rho u\,(\varepsilon + 1/2u^2 + p/\rho) + q] = jE - q_r + q_e E_0 \quad (20)$$

$$\delta B/\delta t + \delta\,(uB)/\delta x = -\,\delta\,(j/\sigma)/\delta x \quad (21)$$

$$j = -(1/L')\delta B/\delta x \quad (22)$$

$$E = j/\sigma + uB \quad (23)$$

Here q_e is the source of the eroded electrode mass calculated per unit volume per unit of time; E_0 is the specific energy of erosion products; ε is the internal gas energy per unit mass; L' is the effective inductance per unit length; q_r accounts for radiation losses; q is the heat flux density; and f_r is the summary volume density of resistance forces. All other symbols are those explained earlier. With reference to the problem addressed in Equations (18) and (19), allow further simplifications.

The intensity of the erosion process can be assessed by the relation $m_e = k_e Q_e$, linking heat Q_e released at the electrodes and the eroded electrode mass m_e. By the order of magnitude, k_e is about $(1\text{-}2)*10^{-7}$ kg/Joule. The total power in our conditions as estimated below is about $2*10^8$ W. Even with all this power released at the electrodes and taking into account the acceleration process time τ_{ac} to be typically 10^{-4} s, one arrives at $m_e \sim (2\text{-}4)*10^{-3}$ kg that is much less than the "raked up" air mass. As a result, quantity q_e in Equations (18) and (20) can be neglected.

Comparing characteristic time τ_m for the molecular heat conductivity mechanism with τ_{ac}, one finds $\tau_m >> \tau_{ac}$. The intensity of the radiation assisted conductivity is proportional to T^3. Therefore, figure q in Equation (20) can also be omitted. As a first approximation, the resistance forces described mathematically by f_r are allowed to be ignored within the accuracy of our analysis.

For numerical calculations, Equations (18) to (20) were used in their integral form. When integrated over

the volume with allowance for the above assumptions, Equations (18) to (20) transform to the following

$$dM/dt = \rho_0 uA \quad (24)$$

$$d(Mu)/dt = IlB \quad (25)$$

$$d\,[\varepsilon+u^2/2)M]/dt=IU - Qr \quad (26)$$

where ρ_0 is the gas density before the shock wave; M, the "raked up" air mass; l is the interelectrode distance; U and I are the gap voltage and the arc current. Radiation losses Q_r are taken in accordance with the Stefan-Boltzmann law corrected for the deviation from the total thermal equilibrium. No account is taken of the gas remaining behind the discharge zone and the pressure and specific internal energy of the air in front of the shock wave.

The processes in the ejector—the ejecting, ejected and stirred gases are directed in parallel—can be described with the equations that follow:

$$G_1+ G_2= G_3 \quad (27)$$

$$G_1u_1+ G_2u_2 + p_1A_1 + p_2A_2 =G_3u_3 + p_3A_3 \quad (28)$$

$$G_1H_1 + G_2H_2 = G_3H_3 \quad (29)$$

where G_i, u_i, p_i, A_i, H_i are mass flow rates, flow rates, cross-section areas, static pressures, and total enthalpies, respectively, for each flow.

The calculation was carried out as follows. Starting from T_h and p_h within the heater, the ejected gas flow parameters at the ejector entrance were determined. Then going from the test section, the stirred gas parameters at the ejector exit were chosen. Given both sets of parameters, those at the railgun exit were calculated using Equations (27) to (29). With the outlet railgun parameters and the railgun operating mode, the designed parameters can finally be evaluated by Equations (24) to (26). Table 3.3.1 and Table 3.3.2 present

TABLE 3.3.1
PARAMETERS OF EJECTING, EJECTED AND STIRRED FLOWS

	Ejector Entrance		**Ejector Exit**
	Ejecting Gas	Ejected Gas	Stirred Gas
H, Joule	$1.84*10^7$	$3.44*10^6$	$6.44*10^6$
T, K	3200	1300	1400
p , atm	189	5.4	4
G, kg/s	8	32	40
A, m^2	0.01	0.013	$1.4*10^{-2}$
u, m/s	$5.26*10^3$	$1.76*10^3$	$2.97*10^3$

TABLE 3.3.2
HEATER AND RAILGUN PARAMETERS

T_h, K	p_h, atm	U, V	I, kA	Railgun length, m	Railgun cross-section, m^2
3500	90	900	170	2.8	$1.3*10^{-3}$

the results of one such calculation carried out for test section parameters given in the Statement of Work.

It should be strongly emphasized that the energetic parameters as seen from the tables are rather far from the limiting values that have already been attained in Russia and America. Moreover, an easily realizable increase in the ejecting gas parameters would allow Mach 16 and even higher to be attained.

Technical Feasibility

Use of the "snow plow" accelerator in combination with a plasma ejector that has negligibly small pulsations at the ejector exit is possible. To attain this goal, continuity in time and insignificant displacements in space of successively expelled plasmoids is required. This can be accomplished by a system of several railguns switched on with shift in time such that each plasmoid breaks away from its own railgun just at the instant the next one comes to be expelled from its own railgun. The design offered in consideration of this concept is illustrated in Fig. 3.3.1.

The ejected gas from a primary heater [1] arrives through the Laval nozzle [2] at the central region of ejector [3] whose length is based on attaining uniform distribution of all parameters over the section. The nozzle is inserted into a conducting cylinder being a common inner electrode [4] for ten circularly positioned accelerators of the railgun type. External electrodes [6] are separated by insulating partitions [5]. The inlet sections of the accelerators are capped with insulating covers. To fill up the internal cavities of accelerators with a gas between pulses, electrodes [6] are built with pores arranged uniformly throughout the length of the electrodes. The electrodes are connected to a cavity formed by pipe [8], limited by dielectric covers [7] and [9]. Electrodes [4] and [6] of the accelerators are in parallel connected to DC source [10]. In addition, each pair of electrodes [4] and [6] is connected to its own pulsed high voltage HF source [11], designed like the Pulsatech™ device in Butte. It ensures that the breakdown of the interelectrode gap and rise in electron current is up to maintaining the DC source [10]. This will provide for "raking up" of a gas in an amount sufficient for effective ejecting, source [11] being switched on with a shift in time of 0.1/f, where f is the frequency of successive pulses. This results in a quasi rotating plasma nozzle in front of the ejector with gas parameters equal to those of plasmoids, although the railguns are actually stationary.

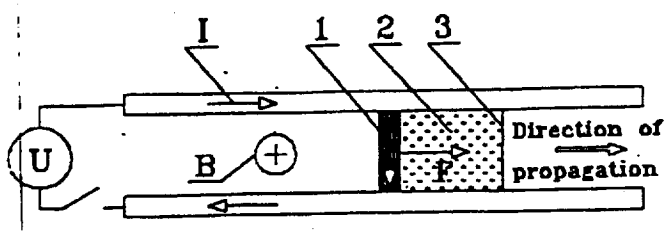

Fig.3.1.1 Gas acceleration by "snow plow" technique:
U-energy supply source, I-electric current,
B-magnetic field, F-Ampere's force,
1-discharge plasma region, 2-shock-compressed gas,
3-shock wave

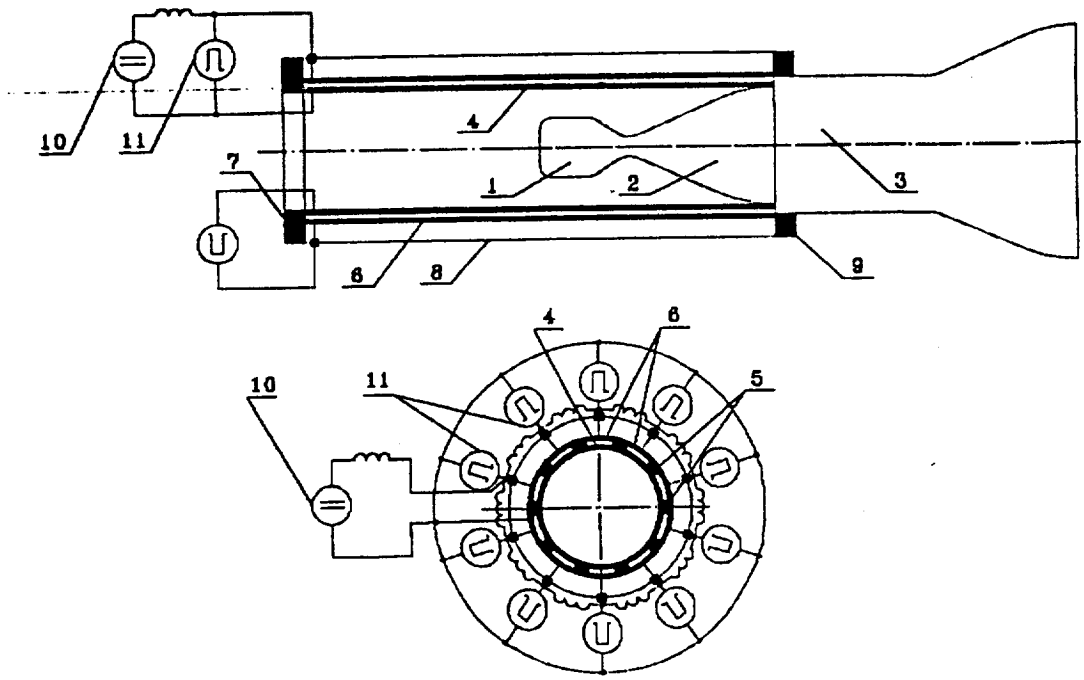

Fig3.3.1 Combined plasma ejector:
1-heater,2-Laval nozzle,3-central region of ejector,4-inner electrode,5-insulating partitions,6-external electrode,7,8-dielectric covers,10-DC supply source,11-pulsed high voltage HF source

CONCLUSION

We have examined three possible ways of increasing a total gas enthalpy by plasma acceleration. The calculations conducted in this study show that all three allow the required total enthalpy gain to be attained. Of course, some approximations and assumptions were involved. But these did not seem to be of significant importance when carrying out the preliminary estimated calculations.

In our opinion, the design for future experiments could be adopted on the basis of mutual consultations between MSE, Pulsatron Technology Ltd, and others for a given project. Once such a design were created, comprehensive numerical calculations in a two-dimensional approximation could be conducted. Then with these results in hand, equipment for an experimental installation could be produced in Russia and/or America.

REFERENCES

1. G.W. Satton, A. Sherman. Engineering Magnetohydrodynamics, N.Y., 1965
2. T.D. Butler, Phys. Fluids, V.12, No.9, p. 1904. 1969
3. J. Grosu, Beitr. Plasmaphys., H.22, No.6, p. 503. 1982
4. G. Gilmore, Equilibrium Composition and Thermodynamic Properties of Air to 24000 K; Rand. Comp. Res. Mem., 1543, Aug. 1955.
5. L.G.H. Huxley, R.W. Crompton, The Diffusion and Drift of Electrons in Gases, N.Y., 1974.
6. A.M. Schekhtman, Gasdynamic Functions of Real Gases, Energoizdat, Moscow, 1988 (in Russian).
7. E.L. Jr. Resler, W.R. Sears, J.Aeron.Sci., V.25, p.235, 1958.
8. Tables of Thermal Properties of Gases, Nat.Bureau of Standards, Circular 564, 1955.
9. Yu. Korolev, G.A. Mesyats, Principles of Pulse Breakdown in Gases, Moscow, 1991 (in Russian).
10. M.J. Berger, S.M. Seltzer, Tables of Energy Losses and Ranges of Electrons and Positrons, Washington: NASA, 1964 - (Spec. publ. No.3012).
11. H.S.W. Massey, Negative Ions, Cambridge Univ. Press, 1976.
12. M.G. Dunn, J.A. Lord, AIAA J., V.8, p.9, 1970.
13. M.A. Biondi - In: Principles on Laser Plasma/ Ed. G.Bekefi, N.Y., 1976.
14. H.H. Rosenbrock, Comput. J., V.5, p.329, 1963.
15. V.K. Rochadge, AIAA J., V.10, p.214, 1966.
16. J.E. Whitte, J.Appl.Phys., V.31, p.1709, 1960.
17. J.E. Whitte, J.Appl.Phys., V.41, p.3245, 1970.

D.3.3 MSE Summary and Evaluation

The three different ionization schemes considered by Pulsatron are discussed in separate subsections below.

D.3.3.1 Thermal Ionization Scheme

The most important conclusion of this section is the targeted free stream conditions could theoretically be obtained using very small seed fractions. The assumed molar seed fraction adopted by Pulsatron was 0.01%, or about 50-100 times smaller than is usually assumed. The report further indicates that the model for ionization relies on an elevated electron temperature. Electron temperatures of 0.5 eV, or 5,700 K, are mentioned, while Figure 2.2.2 in the report shows the heavy gas temperature to be less than 3,000 K everywhere, and at the inlet to be only 1,200 K. At the same time, the pressure is shown to be in the range 25-70 atm through the channel. Because the static pressures are quite high and the temperatures moderate, the heavy particle number densities will be substantially above that of ambient air. This would seem to preclude the possibility of substantial elevation in electron temperature unless very high electric fields were employed. This is what Pulsatron assumed in the analysis. Electric fields of 3,400 V/cm are quoted. This is to be compared to the MHD analysis done by MSE (Section B.1) in which the pressures and temperatures in the channel are comparable to those just quoted, but typical electric fields are in the range of a few hundred volt/cm.

Given past experience with segmented Faraday accelerators, the possibility of imposing such high electric fields without risking damage to the MHD channel appears to be a serious design challenge. The TsAGI MHD facility provides a useful reference point. In that facility, the applied electric fields in the channel were of the order of 200 V/cm. The proposed Pulsatron channel would therefore be run at roughly 17 times the applied electric fields of the TsAGI MHD channel. The main impediments to running at such high fields are the tendency for arcs to form in the gas, and the tendency toward interelectrode arcing and breakdown. It is possible that certain design changes, such as the use of wider insulators in the interelectrode regions, could mitigate the axial breakdown problem, but this change will also accelerate insulator erosion, which was the typical failure mode observed at TsAGI.

One major distinction between the Pulsatron "low seed" channel and the TsAGI MHD channel is that the Pulsatron device will run at high pressures. This implies very low Hall parameters so that the Hall field may be quite weak. If so, the Pulsatron concept may indeed be workable. The Pulsatron method for computing the nonequilibrium conductivity was based on a nonequilibrium parameter called 'ζ', which is the difference in electron and heavy gas temperatures. It was determined using empirical data for cold air. The details of this part of the model are somewhat sketchy. It is unclear, for example, whether the parameters properly account for recombination and electron attachment processes. It would be desirable to attempt to reproduce the Pulsatron results by using a nonequilibrium model for conductivity which includes all of the important kinetics processes, and which relies on a more "first principles" approach to the computation of electrical conductivity.

D.3.3.2 Ionization by Means of Electron Beams

The analysis of the interaction of an electron beam in a high temperature flow is formulated through a set of gasdynamic equations supplemented by a constitutive equation for pressure (ideal gas law), the Ohm's Law relation for a plasma, and a rate equation which balances free electron creation due to impact ionization against the sum of electron losses due to dissociative recombination and three body attachment to oxygen. The analysis is reasonably complete and the authors give estimates of the attachment rate and recombination rate coefficients. Based on this nonequilibrium conductivity model, the case of an MHD channel employing reservoir conditions of 1,800 K and 1,000 atm is simulated. Because it is more energetically favorable to ionize at low gas densities rather than high ones, the gas was expanded to approximately 0.6 atm at the MHD accelerator inlet. An electron beam having energy of 40 keV and current density of 1 A/cm^2 was assumed to be injected along the axis of the accelerator. Table 2.3.1 in the report illustrates the results of the computations based on the above model. At the test section the target conditions of 0.01-atm pressure and Mach number of 11.6 were met.

This simulation is important not only because it shows the possibility of enhanced MHD performance through the use of electron beams, but also because it shows the general approach to be taken in formulating the problem of electron beam interaction in high temperature air. This model should be capable of being easily generalized to two and three dimensions. The major uncertainties in the model are those due to uncertainties in the rate coefficients for electron attachment and dissociative recombination. Ultimately, one must have recourse to experiments to demonstrate the feasibility of using electron beams to achieve enhanced MHD accelerator performance.

D.3.3.3 Snowplow Method

As noted above, the snowplow method is not a novel idea, and considerable study has been devoted to it in the recent past. The work of Lin (Ref. 3), Bityurin (Ref. 4, 5) and Veefkind (Ref. 6) is noteworthy. The last two researchers have studied the problem experimentally. It is known from these studies that T-layers can be formed in a time scale of a few milliseconds, and can propagate for some distance. It is also known that a sheet of hot plasma being accelerated into a cooler region ahead of it will be subject to the Rayleigh-Taylor instability, and will have a pronounced tendency to disintegrate. Thus, a major challenge for the T-layer scheme is to demonstrate that the layer can cohere for a sufficiently long time to provide a more or less uniform acceleration to the gas in the channel.

Another problem is the question of how a localized plasma sheet can be used to provide uniform and continuous flow conditions in an aerodynamic or combustion test facility. The proposed solution is to provide multiple rail electrodes along the walls of the accelerator, which would permit multiple plasma sheets to propagate through the channel simultaneously, spaced at more or less uniform intervals from each other. It is also recommended in the report that the T-layer concept be combined with a gas ejector system, which would help to damp out the nonuniformities. This concept is interesting, but will require experimental demonstration before

it can be seriously considered as a candidate for driving an MHD accelerator for the purpose of reproducing hypervelocity flight conditions.

Finally, there is the question of entropy generation. The very high current densities inside the plasma sheet may have the effect of increasing the entropy generation to intolerable levels, resulting in exit conditions that are far to the right of the desired Ht-vs. -S trajectory. Although the Pulsatron computations indicate that this should not be the case, there are several questions concerning the model equations that were used. These are the subject of ongoing discussions between Pulsatron and MSE.

D.3.4 References

1. Macheret, S.O., Miles, R.B., and Nelson, G.L., "Feasibility Study of a Hybrid MHD/Radiatively Driven Facility for Hypersonic Ground Testing," AIAA Paper 97-2429, 1997.

2. Shair, F.H., and Sherman, A., "Electron Beam Preionization in an MHD Generator," 6th Symposium on Engineering Aspects of MHD, Apr. 1965, pp. 7-12.

3. Lin, B., "A Study of the T-Layer Generator/Accelerator Using Nonequilibrium Plasma," doctoral dissertation, University of Tennessee, Knoxville, TN, Dec. 1994.

4. Bityurin, V.A., et al., "On the Dynamics of a Nonuniform Conducting Flow in an MHD Generator," International Journal on Magnetohydrodynamics, Vol. 2, No. 2-3, 1989.

5. Butyurin, V.A., and Likhachev, A.P., "High Efficiency MHD Generator With Space and Time Dependent Current Carrying Nonuniformities," *10th Int'l Conference on MHD Electrical Power Generation,* Vol. 2, X.191, Tirchirappalli, India, Dec. 4-8, 1989.

6. "Shock Tube Experiments on Non-Uniformities in Combustion MHD Generators," 31st Symposium on Engineering Aspects of MHD, III.4.1, Whitefish, MT, June 1993.

APPENDIX E

CONTENTS

SECTION E.1

FIGURES

TABLES

SECTION E.3

FIGURES

APPENDIX E. RUSSIAN MHD FACILITY RESEARCH

This appendix describes work performed as part of separate subcontracts with the Central Aerohydrodynamics Institute (TsAGI) and a consortium called ENGO (also referred to as ENERGYGO). TsAGI is a Russian government technology organization and ENGO is a private Russian consortium comprised of researchers from a number of Russian scientific, academic and technical agencies. The Principal Investigator (PI) for both subcontracts was Dr. Vadim Alfyorov, a noted MHD researcher at TsAGI. In the 1960s, Dr. Alfyorov and his colleagues developed an MHD accelerator facility that included a small aerodynamic test section. As of this writing, the facility is still operational and has been used to characterize the hypersonic flow around various small-scale models, including models of the Russian Buran Space Shuttle vehicle. Model sizes are limited to lengths or diameters of 15 cm or less. The facility is the only hypersonic, MHD-driven aerodynamic test facility in existence. The product of these two subcontracts was a set of three reports dealing with a) MHD accelerator experiments investigating performance at increased channel pressure, b) MHD channel electrode characterization, and c) the reproduction of flight conditions in hypersonic wind tunnels. These reports were written in Russian and translated into English and appear below as Sections E.1, E.2 and E.3 in the text to follow.

Because of the potential for error in translating the Russian reports, the three reports are presented as received. MSE has written Overview and Summary sections for each report. The purpose of the Overview section is to explain the motivation for, and the scope of the research. The Summary sections represent an attempt to highlight the important findings in the report and also to embed the conclusions and the technical issues considered by the Russian scientists into the larger context of the MARIAH Project.

APPENDIX E, SECTION E.1

E.1 TsAGI REPORT ON FACILITY UPGRADES AND FACILITY CAPABILITIES

Because the TsAGI system is a small-scale, 30-year-old device, it was realized it would be difficult and expensive to upgrade the facility to anything resembling a pilot-scale (i.e., large-scale) MHD-driven aerodynamic test facility. However, the facility could potentially be utilized for the investigation of several fundamental design and performance issues if adequate diagnostic capabilities were available. Several such issues were identified:

- Flow chemistry issues, including the formation of monatomic oxygen and nitrogen oxide (NO) within the arc heater and accelerator.
- Thermal management questions, such as the demonstration of gas cooling by means of injecting helium (He) or argon (Ar) at critical points along the electrode wall. These "gas curtains" might reduce the effective wall temperature and wall heat fluxes, while providing a conductive path through the boundary layer regions. Another study that would be useful in future MHD accelerator system designs would be to characterize the wall heat fluxes as a function of power input and applied magnetic field.
- Characterization of the nature of the conduction mechanism within the electrode sheath layers. Such studies would require special diagnostics and specially constructed electrode wall sections which would permit the photographing of arc patterns and the characterization of the arc structure and current densities as a function of magnetic field, temperature, and static pressure.

These studies would require a number of upgrades to the TsAGI facility including: a) improved diagnostics, b) special MHD accelerator channels, c) special diagnostic wall sections, d) improved seed injection system, and e) a higher field strength magnet. The identification of these required facility upgrades and their costs constituted one of the primary tasks of the TsAGI subcontract.

E.1.1 Overview

The TsAGI subcontract had several objectives:

1. Summarize and document all of the operating characteristics and capabilities of the TsAGI MHD test facility and describe recent operating experience. This included an explanation of the significant facility limitations, such as electrode lifetimes, power requirements and magnet limitations.
2. Provide descriptions and cost estimates of new equipment required in upgrading the facility. The specific envisioned facility upgrades, as described above include: a) improved seed injection system, b) special MHD accelerators for diagnostics on electrode walls, and c) a 7.5-Tesla (T) superconducting magnet.
3. Investigate the electrode phenomena in the TsAGI MHD channel. This was understood to include a description of the basic modes of conduction within the sheath layers and

electrode wall boundary layers, along with experimental investigations to characterize the mode of conduction in the near-wall region (i.e., whether arc mode or diffuse mode). No new experiments were conducted for this phase of the research. Instead, data from past Russian papers, reports, and previous electrode tests was researched.

Objectives 1) and 2) were addressed in the first TsAGI report (Section E.1.2), and objective 3) was the subject of the second TsAGI report (Section E.2.2).

Subsections 1 and 2 of the TsAGI facilities report give a reasonably detailed description of the test capabilities and operating conditions of the existing facility. The MSE Summary (Section E.1.3) supplements this information, which includes photographs of the facility, in addition to a discussion of some of the salient features of the facility. TsAGI supplied the photographs at the request of MSE.

The proposed facility modifications described in the report are divided into two stages. Stage 1 addresses the issue of upgrading the seed injection system and constructing the new MHD channels, and Stage II addresses the costs for upgrading the magnet to a 7.5-T superconducting magnet. Conclusions and findings of the report are presented in the Summary, Section E.1.3.

E.1.2 TsAGI Report on the Performance of MHD Accelerator with Increased Channel Pressure (presented in pp. E.1-3 through E.1-34)

PROGRAM
OF EXPERIMENTS FOR INVESTIGATION INTO PERFORMANCE OF MHD ACCELERATOR WITH INCREASED PRESSURE IN ITS CHANNEL BY USING THE TsAGI SMGDU FACILITY

TABLE OF CONTENTS

1. Introduction

The present program envisages the efforts to be fulfilled in two stages.

At the first stage the studies are assumed to be conducted with full use of the design test capabilities of the existing SMGDU stand with no replacement in its equipment/subsystems.

At the second stage, the studies will be undertaken after replacing a part of the SMGDU stand equipment.

2. Test capabilities of SMGDU at B ≈ 3 T (as designed)

A schematic of the installation is provided in Fig. 1. The installation consists of the following units and systems:

- a source of conducting gas,
- MHD accelerator,
- secondary nozzle,
- test section and exhaust passage,
- power supply system,
- gas supply system,
- cooling system,
- adjustment system,
- control system, and
- measurement system.

2.1. General parameters of the installation

Working gas	Air + 1% (by weight) KNa eutectic seed (77% K + 23% Na)
Nozzle exit section in test section	F=(0.025x0.025 - 0.4x0.4) m
Flow Mach number	M up to 15
Flow speed	U up to 8 km/s
Test section flow density	$\rho=10^{-2}$ - 10^{-4} kg/cu.m
Effective stagnation pressure*)	$P_{0\ eff.e} > 20$ MPa $P_{0\ eff.f} > 4$ MPa
Effective total temperature*)	$T_{0eff.e} > 10000$ K $T_{0eff.f} > 24000$ K

*) The effective stagnation parameters are meant to be the stilling chamber pressures and temperatures necessary for obtaining the test section gas parameters for nozzle output: $\{P_{0eff.e}, T_{0eff.e}\}$ for equilibrium adiabatic conditions, $\{P_{0ef.f}, T_{0eff.f}\}$ for frozen state, with γ being computed on the basis of the test section gas composition.

Stilling chamber stagnation pressure	$P_0 \leq 2$ MPa
Total temperature at heater	$T_0 \leq 3700$ K
Gas mass flowrate	$\dot{m} \leq 0.2$ kg/s
Electric energy supply total power:	
rated	$N_\Sigma = 5.75$ MW
with overload	$N_\Sigma = 11.5$ MW
including:	
a) heater	
rated	$N_h = 1.2$ MW
with overload	$N_h = 2.4$ MW
b) accelerator	
rated	$N_{acc} \sim 4$ MW
with overload	$N_{acc} \sim 8$ MW
c) electromagnet	
rated	N_{mag} up to 300 kW
with overload	N_{mag} up to 460 kW
d) compressor and vacuum pumps	N_{compr} up to 150 kW
Installation "productivity" (the total number of runs per shift)	~4
Operating mode duration	
a) without operating the MHD accelerator	$\tau < 30$ s
b) with MHD accelerator engaged	$\tau < 1 - 2$ s

The possibility to change the construction and dimensions of individual components is provided; free access to all principal details is ensured.

2.2. Characteristics and parameters of installation constituents

The conducting gas source consists of an arc heater, a mixing chamber, a metering devices for feeding the easily ionizable seed, and a primary supersonic nozzle. The arc heater with a coaxial discharge gas has close stabilization of discharge and heating the gas to T_0=3700K at pressure P_0 up to 3 MPa.

The plunger-type device supplying the seed provides the liquid metal (K+Na eutectic) with rigorous metering in time, synchronously with other processes during the facility run cycle.

The source has a set of primary nozzles for M=1.5, 2, 2.5 and 3 with various nozzle exit section sizes.

The arc heater is supplied with power from a thyristor converter with the following rated parameters: strength of current, 1600 Amps; voltage, ~750 V. In the case of short-term operation (~60 s) a two-fold overload is allowed (the strength of current up to 3200 Amps).

The power supply system of the accelerator is based on three-phase transformers containing 1 - 20 mutually isolated secondary three-phase windings; each of them through a rectifier (a three-phase bridge), a ballast resistor and a filter choke is connected to the corresponding pair of electrodes. The total number of the electrically isolated circuits is 100; their characteristics are given in Table:

Nos. of circuits	V_{max} (V)	J_{max} (Amps)
1—20	600	100
21—35	750	100
36—50	750	100
51—62	900	100
63—100	900	85

Strength of current in the circuits is established and supported by a current automatic control based on direct current amplifiers. Duration of transients in the power supply circuits (i.e., attaining the stationary regime and switching-off) is about 0.05 s. Voltage pulsations on an active load do not exceed 1%.

Any of the circuits can be routed to any pair of electrodes of the accelerator. With the transformers segmented, both the maximum voltage on electrodes and strength of current in their circuits can be raised by a factor of 2 or 3 by using serial and parallel connection of neighbouring rectifier bridges.

Electromagnets are energized by a DC generator with power of 20 kW (500 Amps, 40 V). In addition, use may be made of a DC generator rated to 300 kW (up to 460 kW with overload).

The gas supply system feeds (1) the air to the conducting gas source and the ejectors and (2) inert gases (argon, nitrogen, etc.) to the metering device and the test section.

The system that supplies the air to the conducting gas source consists of gas holders (whose total volume is 9 cu.m), compressor, pipelines, and shut-off/control

fittings. The maximum pressure in gas holders is 2.5 MPa; however, it may be raised to 4.5 MPa. This system supplies the air to the conducting gas source with the flowrate of up to 0.2 kg/s without notable pressure losses. This air supply system, together with the vacuum tank ensures autonomous work of the facility. If necessary, almost any other gas can be utilized as working gas.

Inert gases into the installation are provided from standardized bottles with the corresponding system of routes and shut-off/control fittings.

The cooling system is a closed design; it consists of a 4 cu.m tank, pipelines with the necessary fittings, and a water pump with the maximum flowrate of about 5 kg/s at a maximum exit pressure of 1.8 MPa.

The multichannel measurement and data acquisition system performs in the course of a test run the measurement and registration of both the constant process parameters (necessary for establishing the installation operating mode and the test section stream characteristics) and the parameters specific to a particular experiment.

The first group of parameters includes the gas and seed mass flowrate; pressure; strength of current; heater voltage; strength of current on the electromagnet; static pressure distribution along the MHD channel and the secondary nozzle; distributions of voltage and strength of current across electrodes along the MHD channel; static pressure in the test section, etc. The second group of values includes fields of temperature in walls of structural components and a test model, as well as distribution of electric current over the electrode surface exposed to the open flame. This also includes information obtained with the help of visual methods such as discharge video registration and visualization of the flow, flow speed fields etc. To achieve this, special techniques have been developed.

Schlieren photography is performed by a specially developed equipment based on the effect of anomalous dispersion of resonant radiation (with the wavelength of 5890 Å) passing through vapour of Na present in the flow. The device ensures obtaining the schlieren photographs in high-intensity self-illuminating flow of rarefied air.

To measure the flow speed, a resonant Doppler velocimeter using resonant laser excitation of the medium and analyzing the scattered signal spectrum was installed. The device provides both the flow point speed measurement and speed field determination with an error of approximately ~ 3% at U=5÷6 km/s.

A method and a device for studying electric discharge in MHD channels in usual operational conditions have been developed. They determine current strength distribution in various electrode wall zones, including the interelectrode isolator zones.

The parameters measured are recorded by a computer. All measuring circuits are shielded; where necessary, circuits are decoupled halvanically.

The control system of the wind tunnel, its elements and units handles them remotely.

3. Stand operating modes implemented and their parameters

The installation has been completely matured to reach the operating modes with test section air flow speed up to 7.5 km/s, density of 10^{-2} - 10^{-4} kg/cu.m, **Mach number up to 15 when the secondary nozzle exit section is 200x200 mm**. The gas flowrate in this case is 7 ÷ 22.5 g/s. Under all operating modes of the setup the flow conditions at the entry of the accelerator are identical, except for static pressure which depends on both the gas flowrate and the channel entry cross-section dimensions. The flow speed U is 1800 m/s (Mach number of about 1.9); T_{st}~2800K; σ~150 mho/m; P_{st}~25 - 42 kPa; stilling chamber stagnation parameters: T_0~3500 - 3700K, P_0=150 - 300 kPa. With this, the power consumption of the conducting gas source is 200 - 260 kW (J~1000 Amps, U~200 - 260 V).

To implement the operating modes, use is made of magnet with magnetic field uniform over a 390 mm interval at induction of 2.4 T. The MHD channels were 555 mm in length, with the cross-sectional area at the entry being 15x10 mm and 15x15 mm with 60 pairs of electrodes. The electrode wall segmentation step size was 8 mm, including the electrode open-flame surface length (along the longitudinal axis) of 4.5 mm. Active (energized) pairs of electrodes (up to 45 pairs) were arranged in the uniform magnetic field zone. The maximum strength of current through electrodes did not exceed 55 Amps. With these values the MHD channel service life between repairs (dictated by gradual erosion in interelectrode isolators in the anode wall) was 5 or 6 runs with 1 - 2 s duration of power supply to electrodes. The electrode voltage range in all the regimes was 200 - 400 V. Typical distributions of electric and gasdynamic characteristics along the accelerator channel longitudinal axis is given in Fig. 2.

The MHD accelerator operated no more than 45 power supply circuits with the total power consumption of 550 kW, not exceeding 15% of the power available. In this case the conducting gas source consumes less than 20% of the nominal value.

Detailed study of electric and gasdynamic characteristics of the accelerator, temperature fields and heat transfer in channel walls, the influence of the Hall effect, and features of electric discharge near MHD channel electrode walls allow us to be sure that the flowrate ranges (thus, pressure in the MHD channel) can be significantly extended.

When developing a hypersonic wind tunnel with MHD acceleration to provide real-flight values of flow density and enthalpy in a test section, one of the challenging problems that should be settled is to protect MHD channel walls against ultrahigh heat fluxes (10 - 50 MW/sq.m). Cooling the walls by means of heat sink into the structure (which method is employed currently) provides very short run time, mainly because of thermal destruction of protective materials. Utilization of fluid heat carriers (such as water) does not mitigate the difficulty.

With this, preference should be given to the use of gas curtains (screens) with cool gas supply. Investigation into performance of gas curtains for cooling the isolator walls in the TsAGI facility is anticipated to provide data necessary to solve this essential "superproblem" in MHD accelerator development.

4. Design stand operating modes, their parameters; expedient experimental test types

When using the magnetohydrodynamic method, a particular set of test section flow characteristics can be implemented at different combinations of major parameters such as magnetic induction, channel geometry, current density/distribution, accelerator active area length, and parameters of the gas at the entry of the accelerator. Therefore, to outline the likely operational conditions, parametric analyses were carried out, taking into account accumulated test data on the MHD accelerator. These relied upon the commonly used set of simultaneous equations for thermodynamically nonequilibrium flow, the only difference being that the energy equation was written in the following form:

$$\frac{\partial}{\partial x}(\rho U \cdot H_0 \cdot F) = \frac{V \cdot I_k}{S_k} - St \cdot \pi \cdot \rho U \cdot (H_0 - H_w)$$

Potential difference for electrodes was calculated as

$$V_k = \frac{h_k \cdot I_k \cdot B}{e \cdot n_e \cdot F} \cdot \left(\frac{h_k}{\beta_\chi \cdot S_k} + 1\right) + U \cdot B \cdot h_k$$

The Stanton number St was adopted as $St=C_f/2$.

The analyses were conducted for the following versions. Conducting gas source pressure was assumed to be 2.0 MPa (the maximum possible value for the present gas supply system), and total temperature, 3700K and 4700K. The former temperature corresponds to a standardized mode, whereas the latter, to the maximum for the coaxial discharge arc heaters. The gas mass flowrate was 0.15 kg/s, and the Mach number at the primary nozzle exit was equal to 2.

In the analyses, the geometry of the MHD channel, vertex angle and segmentation parameter were in correspondence with the existing channels of the SMGDU stand and were as follows: 15x10 and 15x15 mm entry cross-sectional area, 30' - $1^0$20' vertex angle, 8 mm segmentation parameter (with the lengths of the electrode itself of 4.5 mm and the interelectrode isolator, 3.5 mm).

In the analyses, the strength of current per electrode (20, 40, and 60 Amps) and magnetic induction (3; 5; 7.5 T) were varied. The first value of B is for the currently existing magnet; other two values are obtainable when use is made of quasi-stationary magnets with short-term operation capability (t=10 - 20 s).

Typical results of prediction of gasdynamic and electrodynamic parameters along the MHD channel are presented in Figs. 3 - 8. It can be seen that the facility with the existing magnet (B~3 T, l~800 mm) is not capable to notably increase the flow speed and enthalpy. Increasing the pressure (and the mass flowrate, accordingly) implies substantial losses in output parameters as compared with those implemented by now. The velocity V=6000 m/s which is necessary to simulate conditions inherent in the combustion chamber for M=15 - 20, may be realized (while maintaining a suitable length of the MHD channel) at B $\geq$ 5 T only. The highest results may be obtained at B=7.5T.

Dependence of gasdynamic parameters of the accelerator and its length on magnetic induction B at the exit speed of approximately 6000 m/s is shown in Figs. 9 and 10. It can be seen that in a channel with B ≈ 7.5 T the static pressure is higher and temperature is less , so achieving the target speeds requires a notably shorter length.

Figures 11 through 13 compare potentialities of the existing power supply system with design values for the channel at higher pressures therein. It is seen that the existing system "as is" completely satisfies the modes obtainable with B=3 T, and partially offers the conditions corresponding to B=5 T.

To reach the induction B=7.5 T, we should modify the channel design concept and re-route some power supply circuits serially in pairs. In this case, a certain distribution of magnetic induction along the channel may provide channel exit velocities up to 10 km/s (Fig. 14).

Resorting to higher total temperatures (some 4700 K) in the conducting gas source at the same stagnation pressure does slightly reduce the MHD accelerator channel length (some 15%, depending on an operating mode), while not changing the output flow condition. However, the high temperature, as a rule, intensifies erosion of electric arc heater electrodes and spoils the air flow with evaporated copper.

It shall also be mentioned that chemical composition of gas leaving the MHD channel with the gas speed of 6000 m/sec does at all values of B differ from the real-flight composition. Here, a considerable concentration of atomic oxygen takes place (refer to Figs. 3 through 8). This can markedly influence the H_2 priming duration when reproducing gasdynamic characteristics of the scramjet combustion chamber.

The computation results and the TsAGI SMGDU stand test capabilities show that the currently available stand can be used to carry out

(1) experiments necessary for development of a gasdynamic setup with magnetohydrodynamic acceleration under greater pressure in its channel, as well as

(2) study of the impact of both the easily ionizable seed and differences in composition of gas flow (as compared to real air) on simulation of hypersonic flight conditions.

Investigations of type 1 include:

- optimization of conditions of joint work of the electric arc heater and the metering device, with the aim being to ensure the required gas flow parameters at the entry of the MHD accelerator channel;

- studies on both the electric discharge processes in the MHD channel and the methods to control these;

- analysis of temperatures in MHD channel structures; search for feasible methods to improve serviceability.

The type 2 studies include, in particular, the study of the effect of the seed on hydrogen burning process.

Although the equipment in the present stand (the electromagnet and MHD accelerator electrode power supply system) does not ensure the flow in the test section to reach the required speed (~6 km/s) at higher pressures, much of the important research can be carried out without replacing the equipment (stage I).

The very necessity of R&D work and its amount at the stage II (after replacing the equipment) must be refined upon a thorough survey of the stage I results.

Stage I program (to be implemented with the equipment available)

#	Work description	Interval (months)																		Working amount (person-months)	Costs (US $)
		1	2	3	4	5	6	7	8	9	10	11	12	13	14	15	16	17	18		
1.	1. Optimization of joint work of the electric heater, metering device, mixing chamber and primary nozzle, with the aim being to reach the required gas flow parameters at the entry of the MHD accelerator channel at $P_{0heat} \leq 2$ MPa																				
1.1.	Formulating the work programs	—																		1	3200
1.2.	Revising and aligning the equipment and subsystems	—	—																	6.5	15000
1.3.	Upgrading the heater		—	—																6	14000
1.4.	Upgrading the metering device	—	—																	1.5	5000
1.5.	Study on performance of conducting gas source (joint work of the electric heater, metering device, mixing chamber and primary nozzle)			—	—															6	14000
1.6.	Processing/analyzing the results; writing the report					—														1.5	5000
2.	Studying the installation at $B \approx 3$ T, channel length of 555 mm and $P_{0heat} \leq$ 2 MPa																				
2.1.	Revising and modifying the channel	—	—																	4	10000

#	Work description	Interval (months)																		Working amount (person-months)	Costs (US $)
		1	2	3	4	5	6	7	8	9	10	11	12	13	14	15	16	17	18		
2.2.	Revising the accelerator systems for power supply, measurement and control		—	—	—															10	20000
2.3.	Evaluating heat transfer from external flow into various channel structures																				
2.3.1.	Developing the work programs				—															1.5	5000
2.3.2.	Equipping the MHD channel with measuring components for thermal tests				—	—	—													4	8000
2.3.3.	Procedure-concerned tests						—	—						—						7	16000
2.3.4.	Testing							—						—	—					8	16000
2.3.5.	Processing and analyzing the results; writing the report								—						—					2	6500
2.4.	Studying features of electric discharge existence near electrode walls																				
2.4.1.	Developing the work programs			—																1.5	5000
2.4.2.	Equipping the MHD channel with measuring components				—															2	4000
2.4.3.	Testing					—	—													6	14000
2.4.4.	Processing and analyzing the results; writing the report						—													1.5	5000
2.5.	Studies on control of electric discharge near electrode walls with 2 to 10 pairs of electrodes																				

#	Work description	Interval (months)																		Working amount (person-months)	Costs (US $)
		1	2	3	4	5	6	7	8	9	10	11	12	13	14	15	16	17	18		
2.5.1.	Equipping the MHD channel					—	—													2.5	5000
2.5.2.	Developing and constructing the control system mockup						—	—				—	—							6	20000
2.5.3.	Adjusting the mockup							—						—	—					1.5	4500
2.5.4.	Procedure-concerned work on stand								—						—	—				6	16000
2.5.5.	Testing									—						—				8	16000
2.5.6.	Processing the results; issuing the technical documentation										—						—			3	10000
3.	Investigations for improving MHD channel reliability and a run duration																				
3.1.	Specifying the basic parameters of gas curtain (numerical study)									—	—									3	9000
3.2..	Selecting the materials for side walls; designing the accelerator section with electrode/side-wall thermal protection system										—	—								4	12000
3.3.	Manufacturing the section												—	—						5	10000
3.4.	Developing the measurement system to evaluate the gas curtain performance														—	—				1.5	5000
3.5.	Tests															—	—	—		6	15000
3.6.	Writing the report																		—	1	3000

#	Work description	Interval (months)																		Working amount (person-months)	Costs (US $)
		1	2	3	4	5	6	7	8	9	10	11	12	13	14	15	16	17	18		
4.	Study of the effects of seed (K, Na) and initial concentration of radicals (O, N and NO) on hydrogen burning in supersonic flow																				
4.1.	Computational analysis of the effect of seed on hydrogen burning kinetics under conditions close to scramjet engine operating conditions																			10	32000
4.2.	Developing the concept of model combustor							—												3	8000
4.3.	Manufacturing/adjusting the model combustor								—	—										6	12000
4.4.	Tests to evaluate H_2 burning in gas flow outgoing from the heater - with and without seed									—	—	—								12	32000
4.5.	Processing/analyzing the results; writing the report											—	—	—						5	15000
																			Total:	**157**	**400700**

Stage II program (to be implemented after partial replacement of equipment)

#	Work description	Interval (months)																		Working amount (person-months)	Costs (US $)
		1	2	3	4	5	6	7	8	9	10	11	12	13	14	15	16	17	18		
1.	Modifying the facility																				
1.1.	Mounting the electromagnet with magnetic induction up to 5 - 7 T																				
1.1.1.	Examining the possible primary structure concepts; choosing the optimum version of magnet; selecting an organization where to acquire magnet. Writing the specifications on delivery																			3	9000
1.1.2.	Developing the technical documentation on mounting the magnet, its power supply/control systems and operating equipment																			4	9000
1.1.3.	Fulfilling the activities relating to mounting/operating the magnet																			8	16000
1.1.4.	Adjustment and alignment work (in particular, evaluating the magnetic induction distribution, timing with other elements, etc.)																			4	12000

#	Work description	Interval (months)																		Working amount (person-months)	Costs (US $)
		1	2	3	4	5	6	7	8	9	10	11	12	13	14	15	16	17	18		
1.1.5.	Acquiring the magnet and equipment (for alignment and operation) and control/measurement systems																				100000 - 500000
1.1.6.	Materials																				100000
1.2.	Equipping the stand with MHD channel																				
1.2.1.	Formulating the MHD channel specifications																			3	9000
1.2.2.	Designing the MHD channel																			8	21000
1.2.3.	Manufacturing the channel																			30	60000
1.2.4.	Installing and adjusting the channel																			8	20000
1.2.5.	Preliminary testing of the channel (in particular, together with magnet)																			6	15000
1.3.	Mounting the full size systems to control the near-electrode phenomena																				
1.3.1.	Writing the specifications																			8	25000
1.3.2.	Designing																			8	21000
1.3.3.	Manufacturing, mounting and adjusting the systems																			30	60000
1.3.4.	Preliminary testing in combination with channel																			6	15000
1.4.	Formulating the recommendations on design of large scale facility																			5	15000
																			Total:	**131**	**507000-1007000**

The work package is assumed to be implemented by a team of experts in various speciality areas, including

project manager: Professor,

2 Leading Research Scientists,

5 Senior Research Scientists,

3 Research Scientists,

5 Leading Designers,

6 Staff Designers,

8 Leading Engineers,

12 Research Engineers,

8 Test Engineers and Technics, and translators and other assistants, 7 persons.

Particular participants will be listed after you will have refined amounts and schedules of efforts in the work packages.

V.P.Roukavets,
Chief Wind Tunnel
Design Division

Prof. V.I.Alfyorov,
project manager

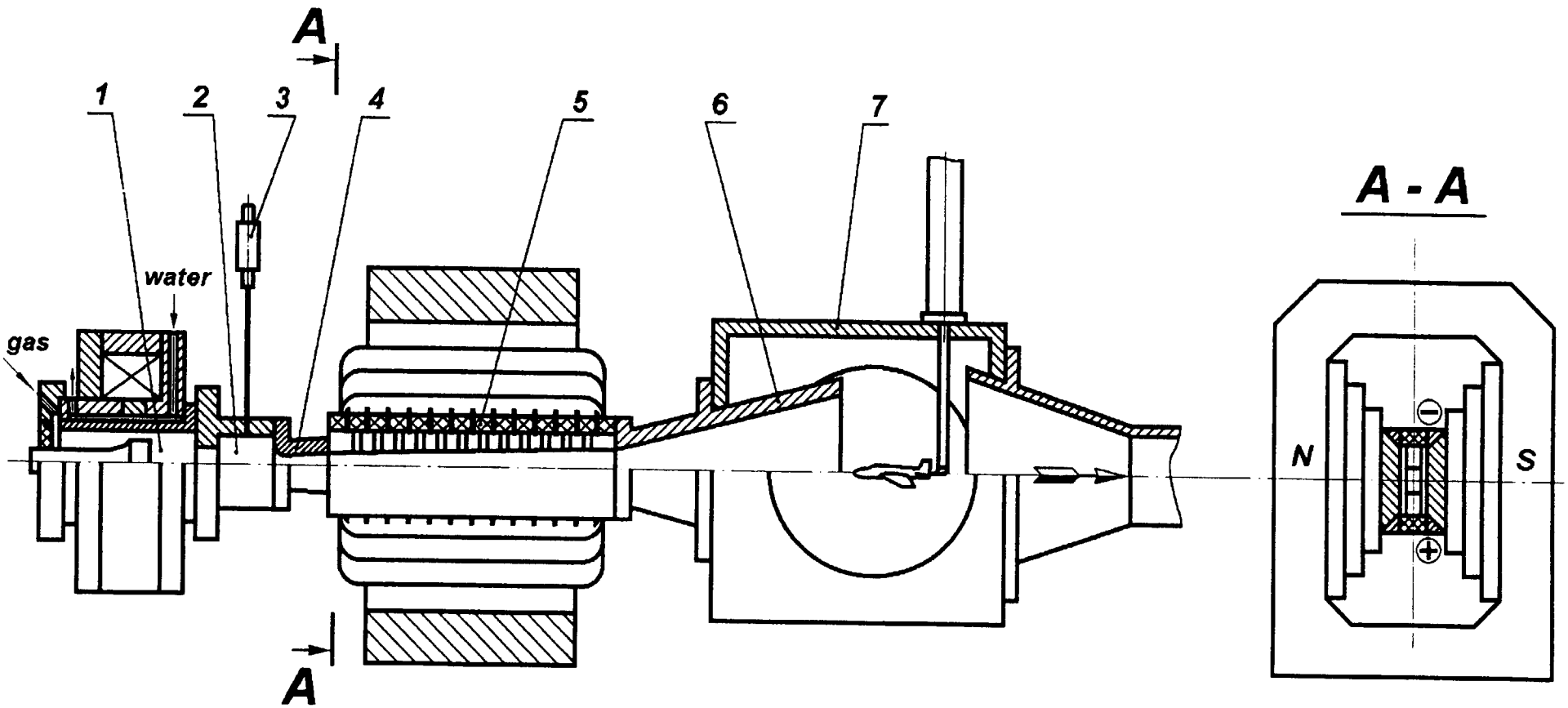

Fig. 1 Schematic of hypervelocity MHD - gas acceleration wind tunnel

1 - arc-heater
2 - mixing camber
3 - metering device
4 - primary supersonic nozzle
5 - MHD-accelerator
6 - secondary nozzle
7 - test section

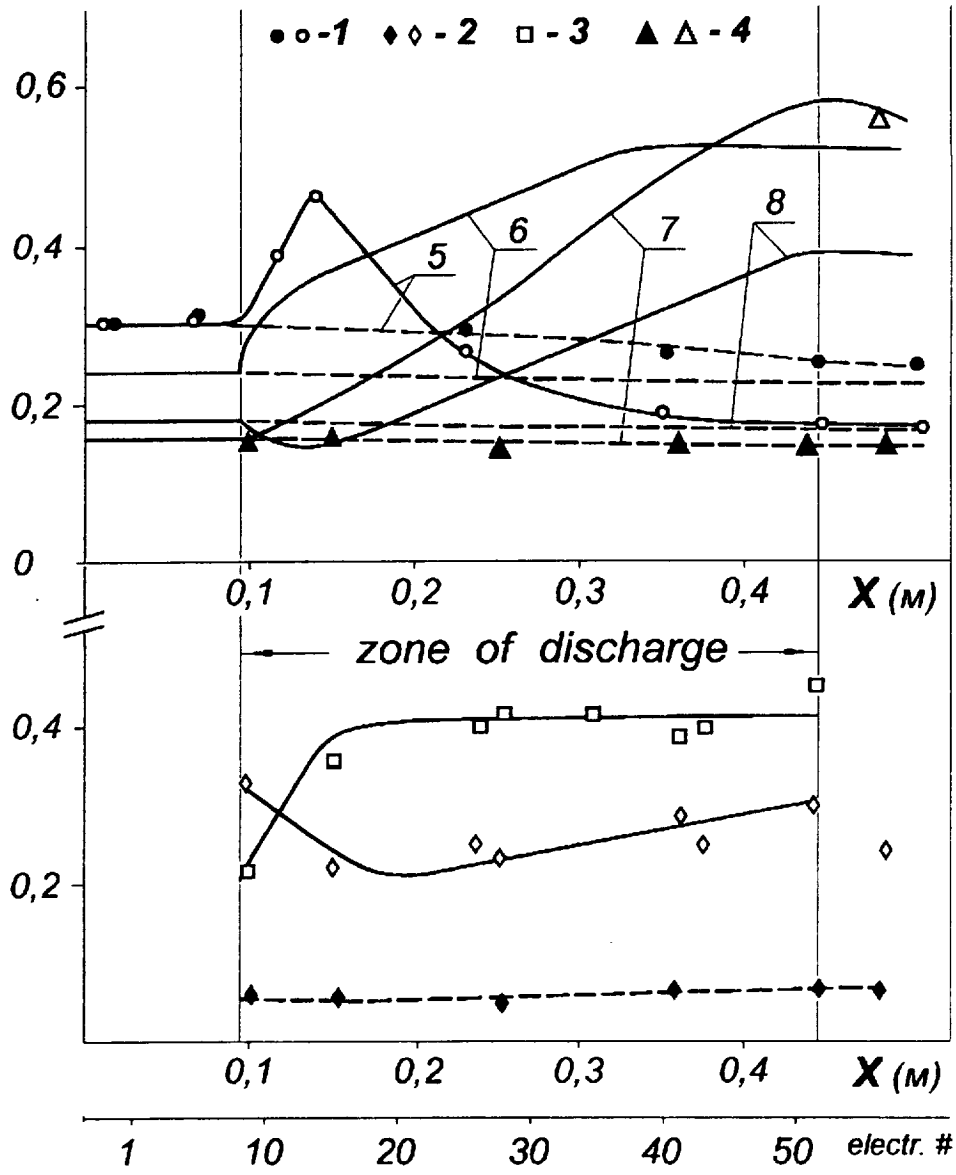

Fig. 2. Distribution of electric and gas-dynamic parameters along the accelerator channel

Test results:

1 - static pressure $P * 10^{-5}$ Pa, ***2*** - electrode voltage $V * 10^{-3}$ B,

3 - current through electrodes $J * 10^{-2}$ A, ***4*** - velocity defined by measuring the induced voltage value $U * 10^{-4}$ m/s.

Light points show the MHD-accelerator operating, dark points show the absence of MHD-acceleration

Analitic results:

5 - pressure $P * 10^{-5}$ Pa, ***6*** - temperature $T * 10^{-4}$ K,

7 - velocity $U * 10^{-4}$ m/s, ***8*** - Mach number $M * 10^{-1}$.

Solid line - the accelerator operating, dash line - without MHD-acceleration.

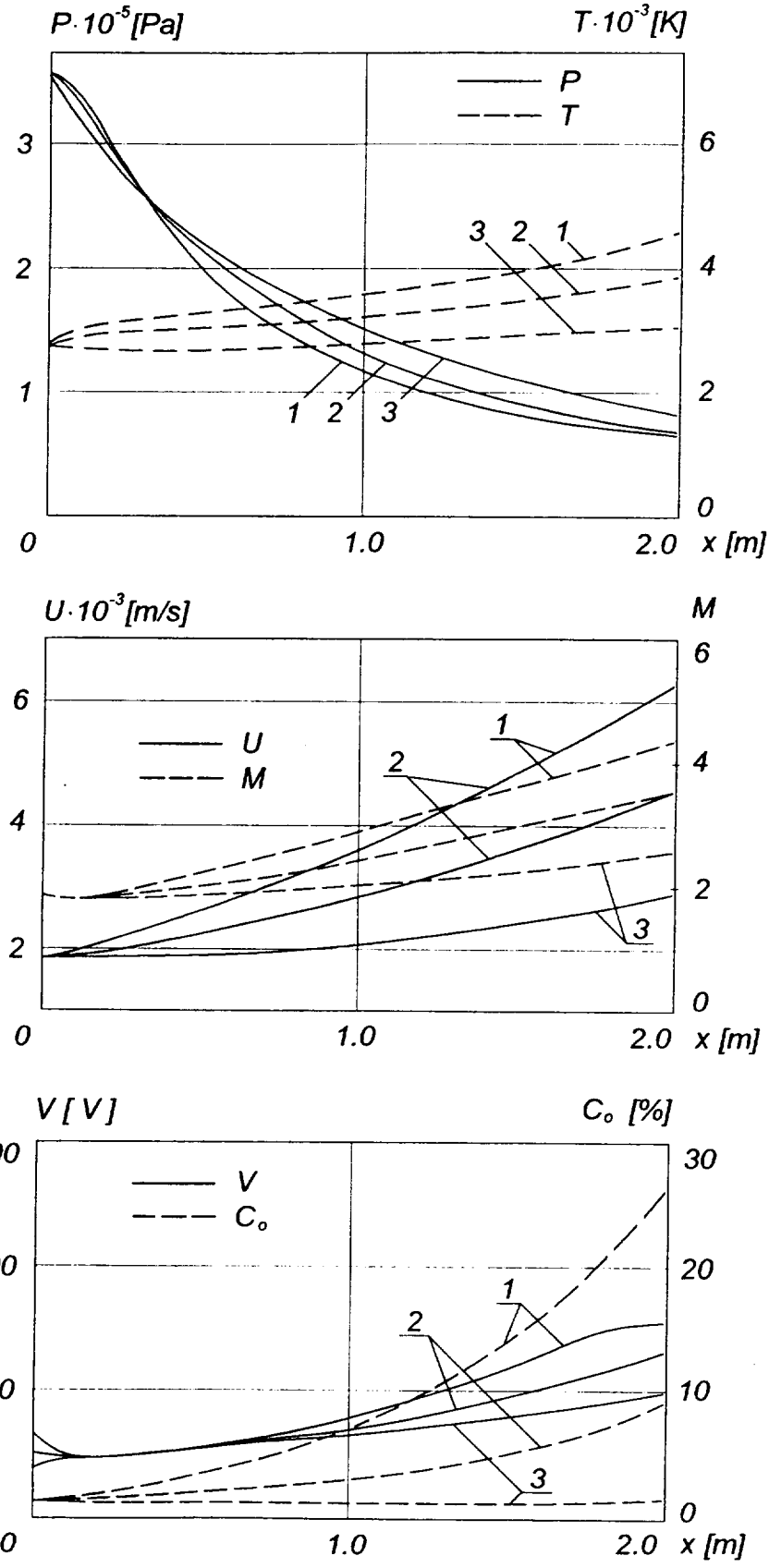

Fig. 3 $P_o = 20 \cdot 10^5 Pa$, $T_o = 3700\ K$, $B = 3\ T$
$1 - J_e = 60\ A$, $2 - J_e = 40\ A$, $3 - J_e = 20\ A$,

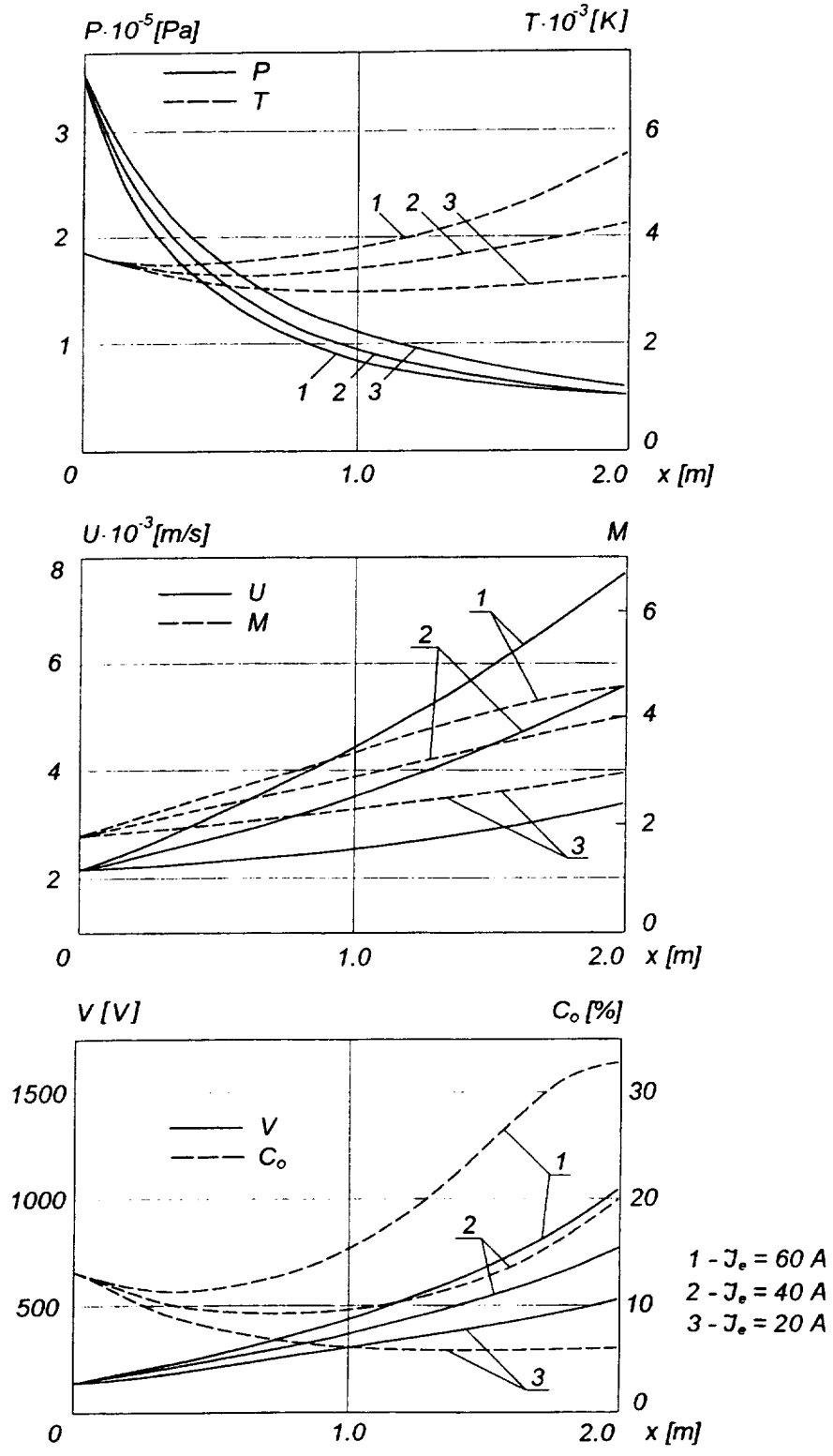

Fig. 4 $P_o = 20 \cdot 10^5$ Pa, $T_o = 4700$ K, $B = 3$ T

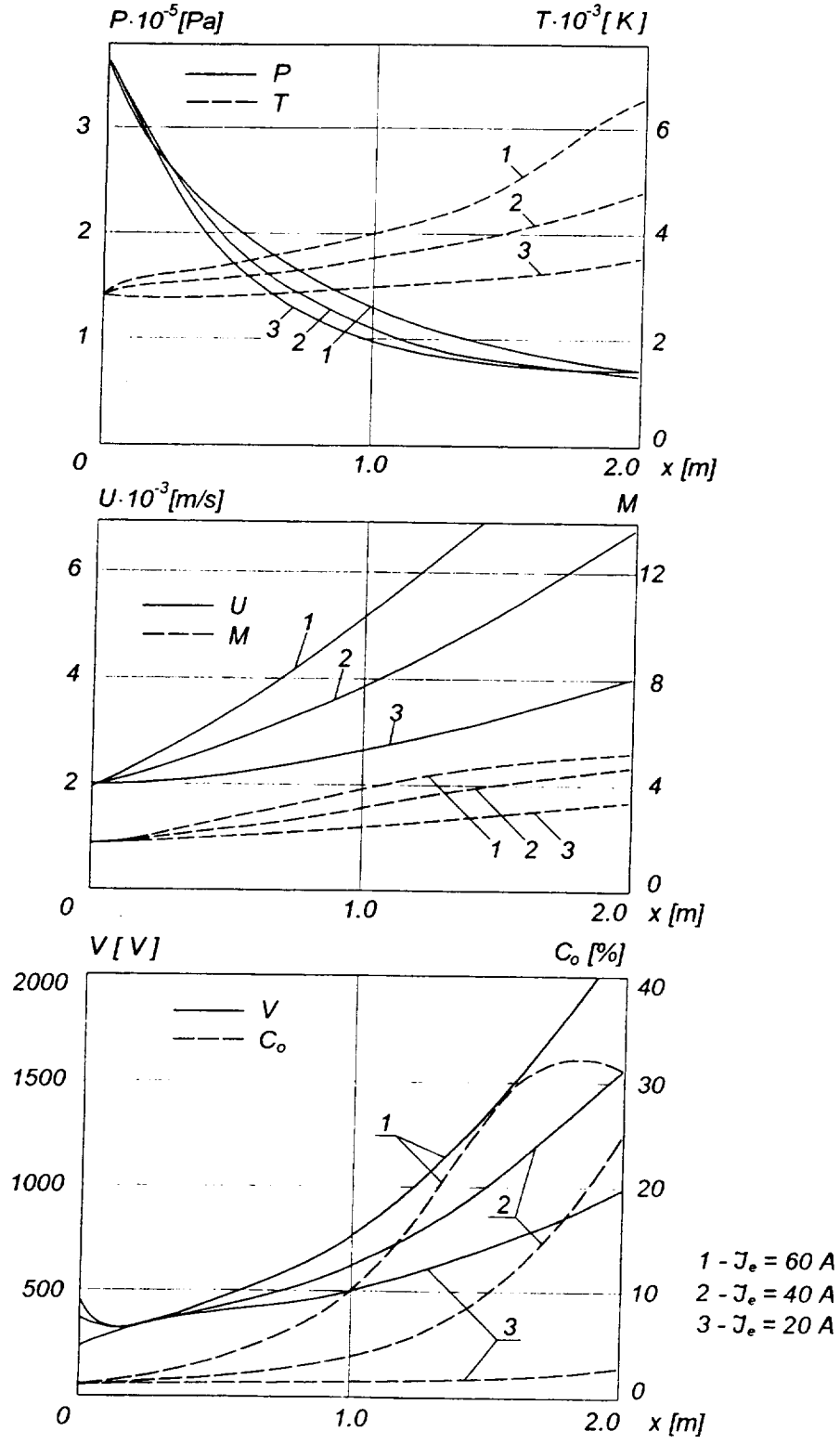

Fig. 5 $P_o = 20 \cdot 10^5$ Pa, $T_o = 3700$ K, $B = 5$ T

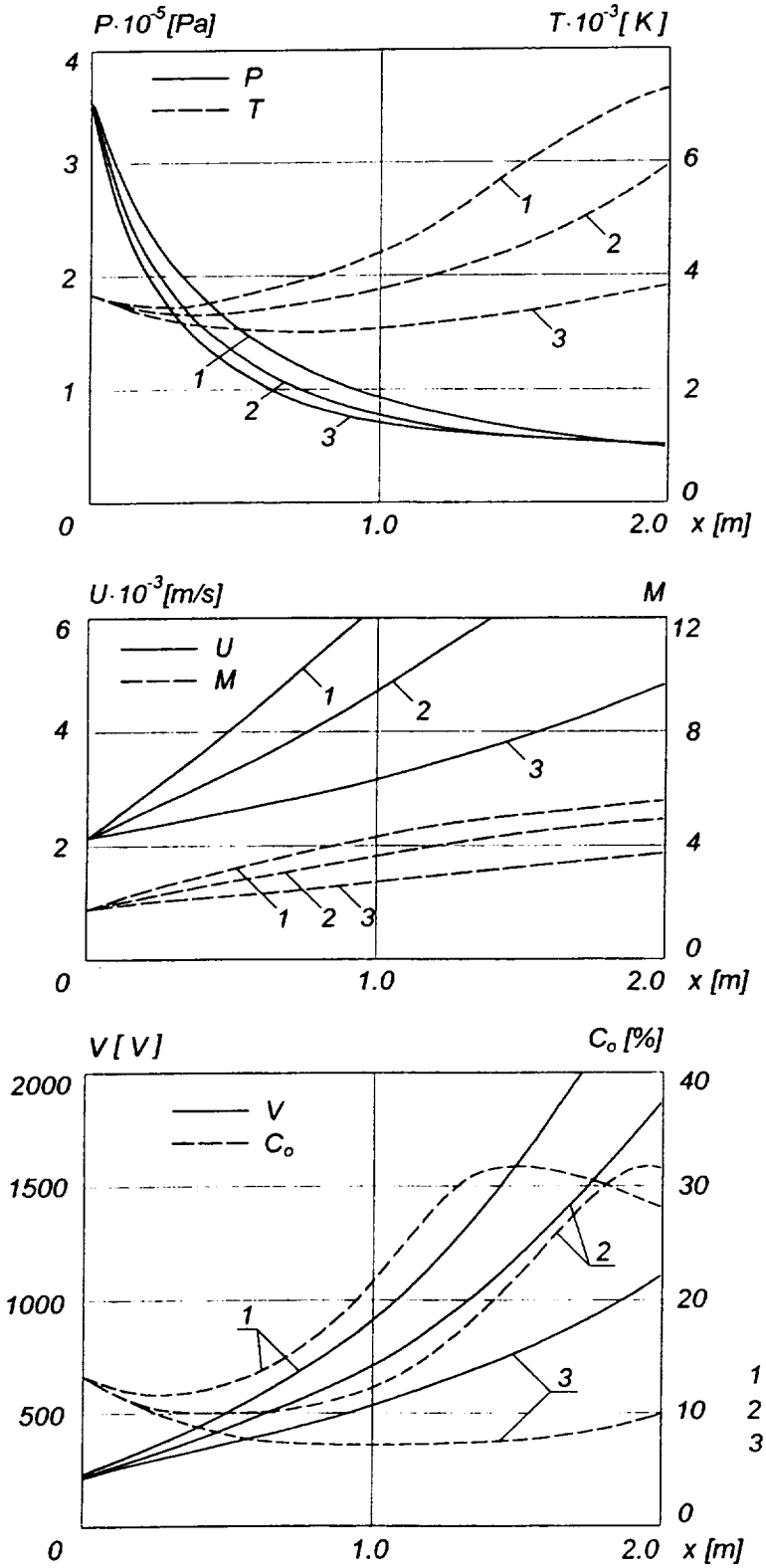

Fig. 6 $P_o = 20 \cdot 10^5$ Pa, $T_o = 4700$ K, $B = 5$ T

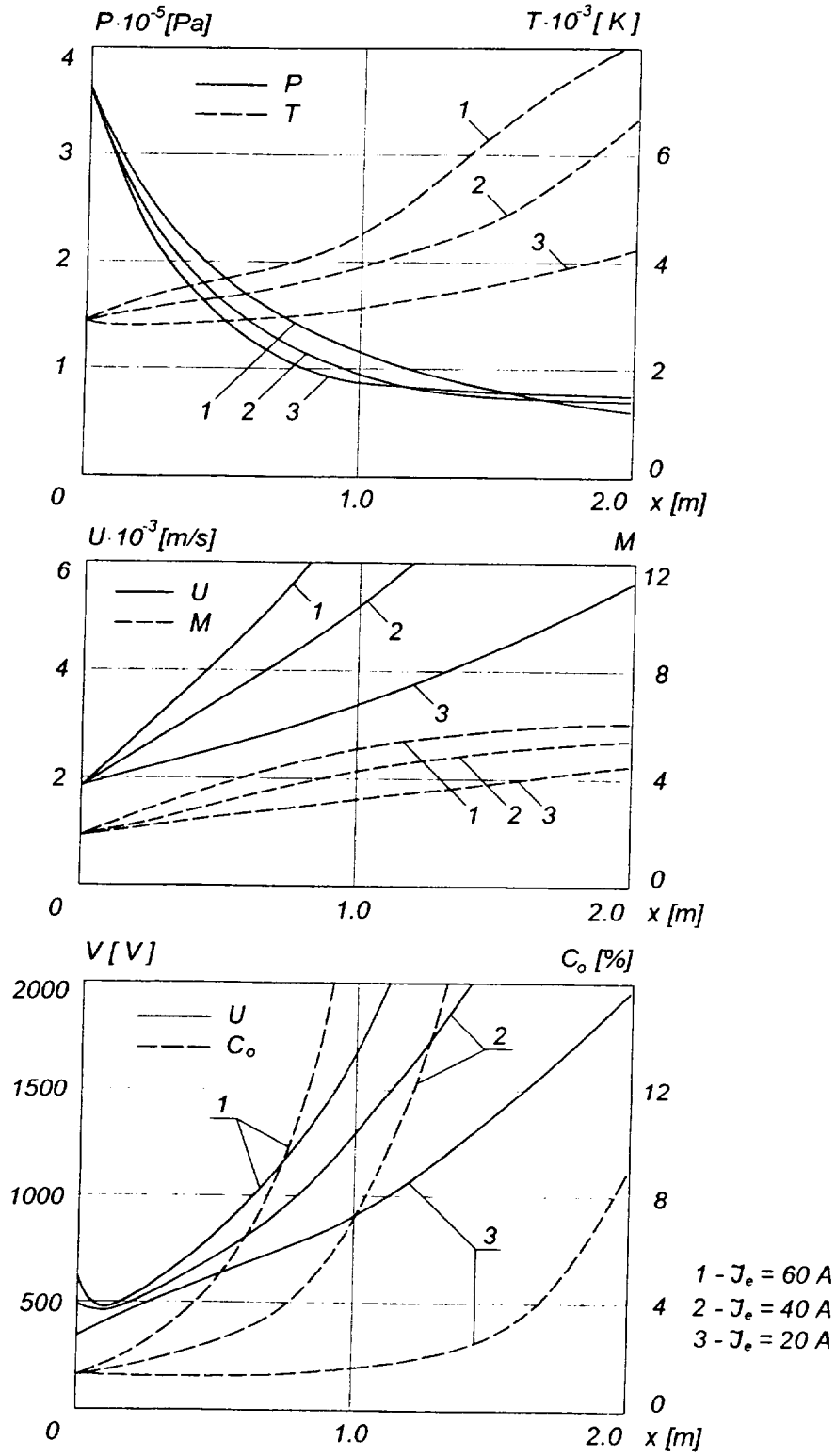

Fig. 7 $P_o = 20 \cdot 10^5 Pa$, $T_o = 3700\ K$, $B = 7.5\ T$

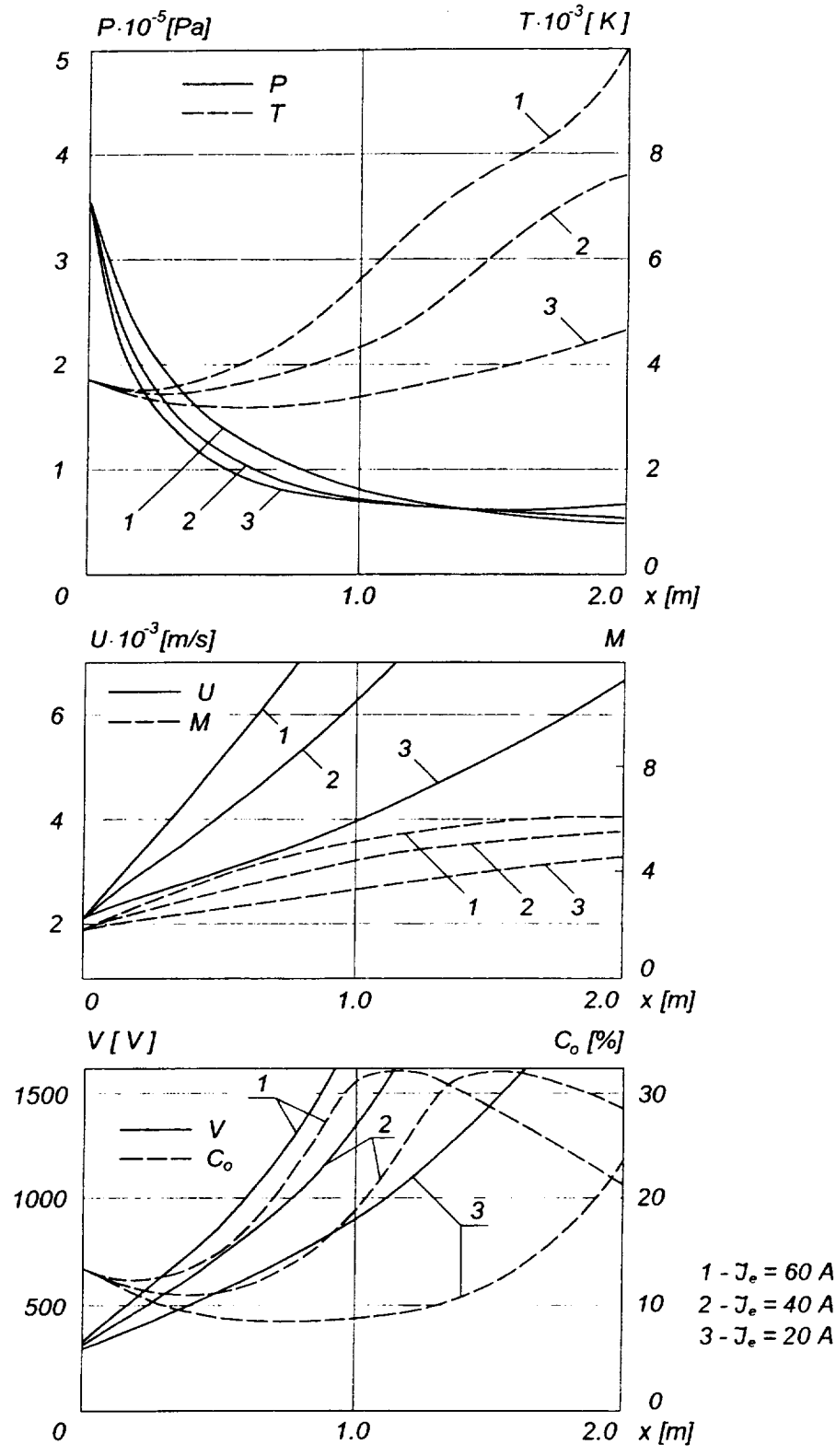

Fig. 8 $P_o = 20 \cdot 10^5 Pa$, $T_o = 4700\ K$, $B = 7.5\ T$

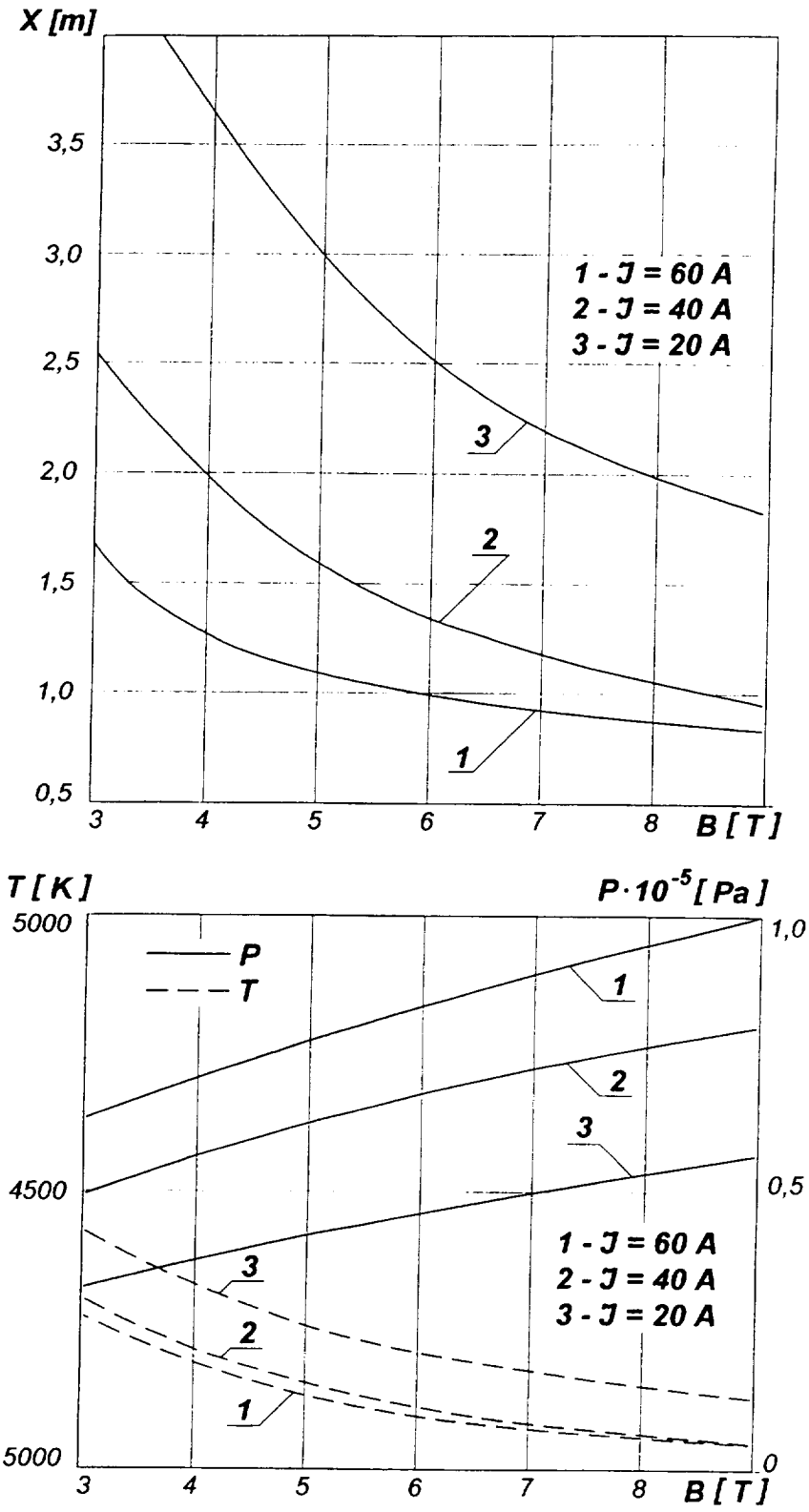

Fig. 9 $P_0 = 20 \cdot 10^5$ Pa, $T_0 = 3700$ K, $U = 6000$ m/s

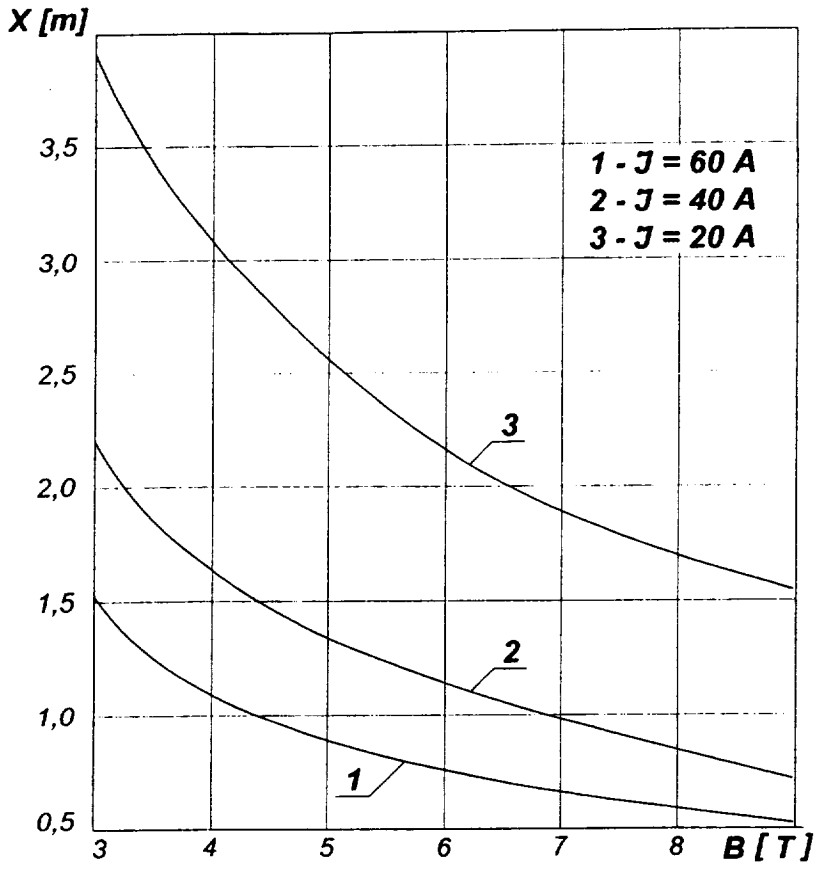

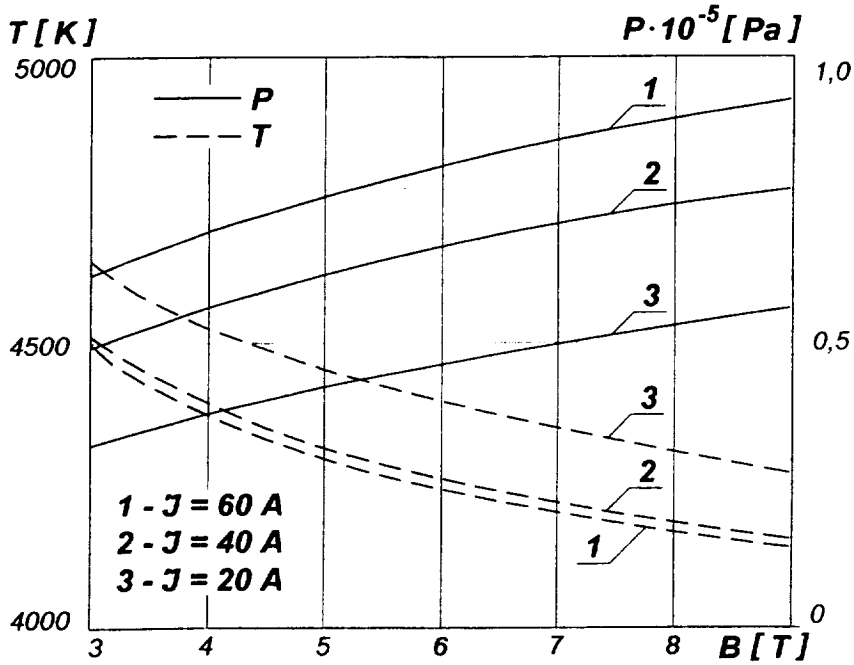

Fig. 10 $P_0 = 20 \cdot 10^5$ *Pa*, $T_0 = 4700$ *K*, $U = 6000$ *m/s*

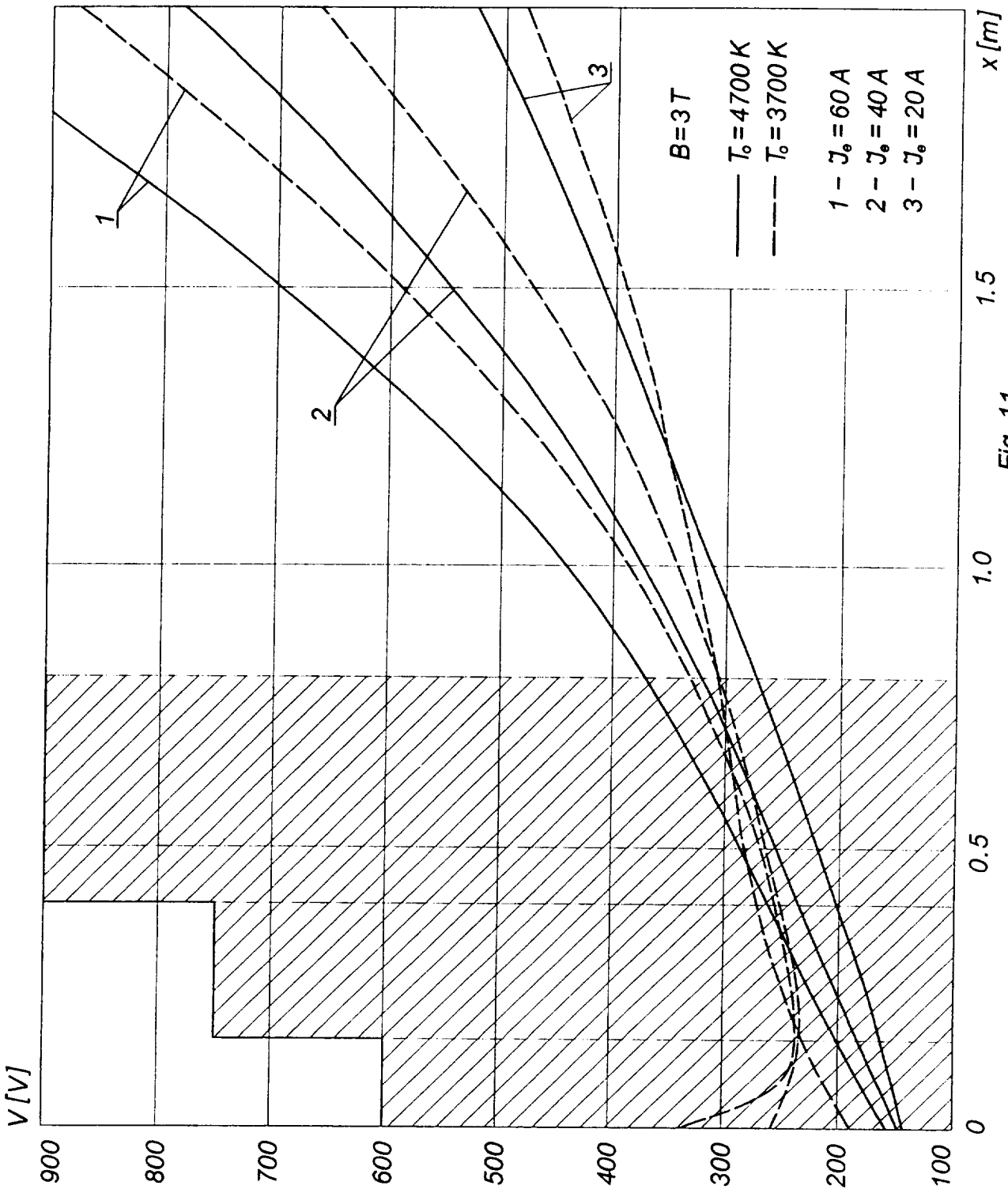
V [V]
900
800
700
600
500
400
300
200
100
0
0.5
1.0
1.5
x [m]
B=3 T
T_o=4700 K
T_o=3700 K
1 – J_e=60 A
2 – J_e=40 A
3 – J_e=20 A
1
2
3

Fig. 11

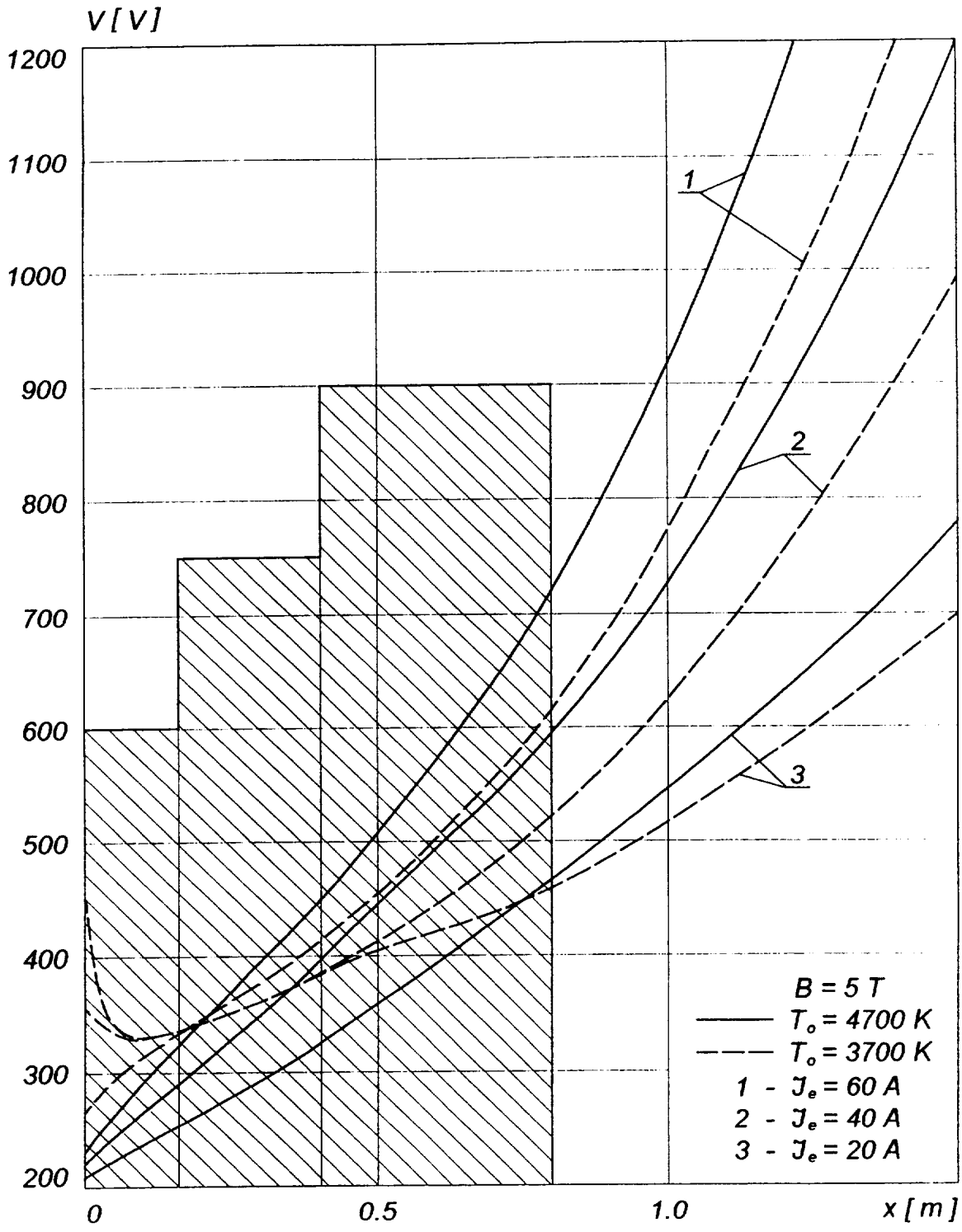
V [V]
1200
1100
1000
900
800
700
600
500
400
300
200
0
0.5
1.0
x [m]
1
2
3
B = 5 T
T_o = 4700 K
T_o = 3700 K
1 - J_e = 60 A
2 - J_e = 40 A
3 - J_e = 20 A

Fig. 12

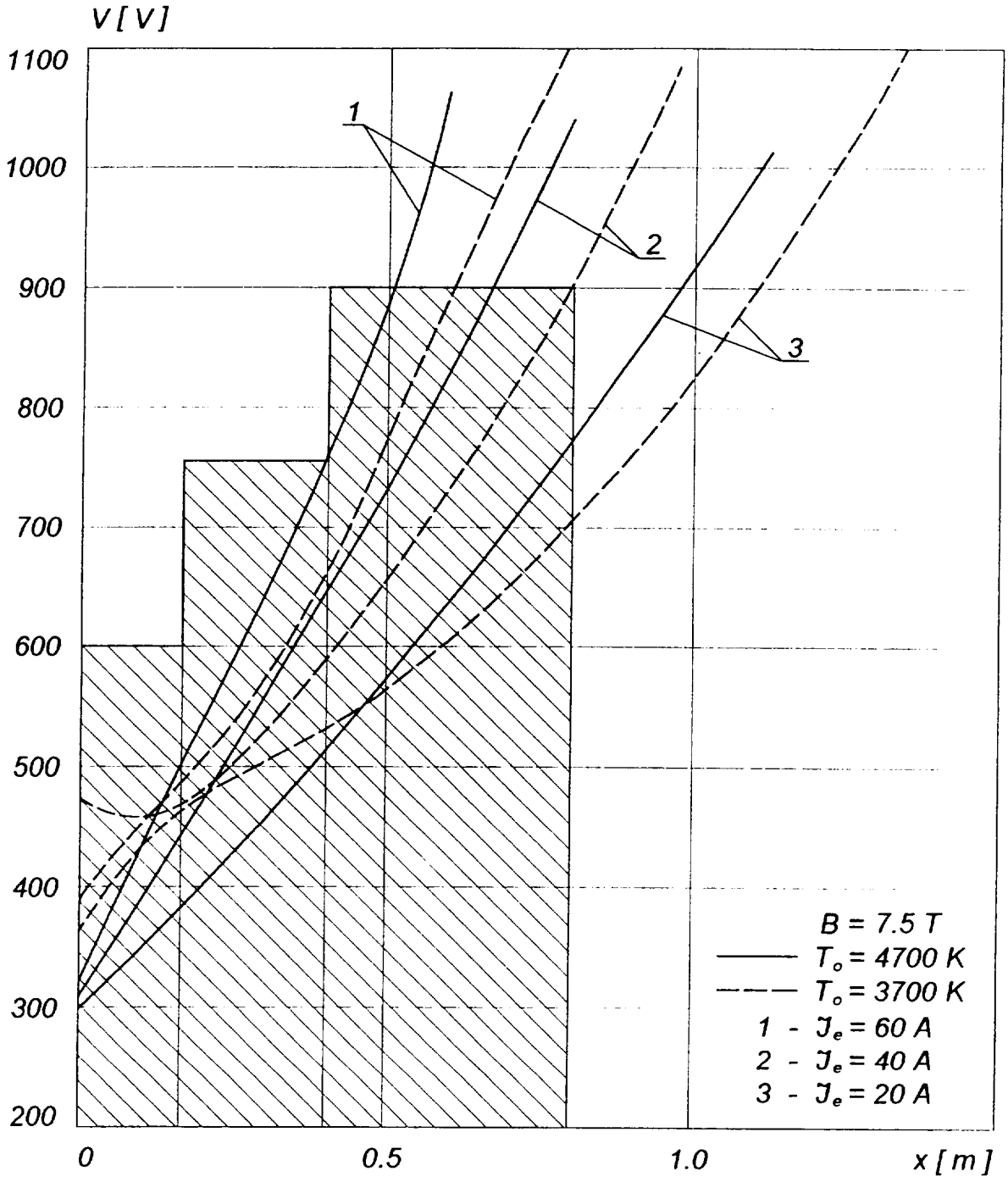
V [V]
1100
1000
900
800
700
600
500
400
300
200
0
0.5
1.0
x [m]
1
2
3
B = 7.5 T
T_o = 4700 K
T_o = 3700 K
1 - J_e = 60 A
2 - J_e = 40 A
3 - J_e = 20 A

Fig. 13

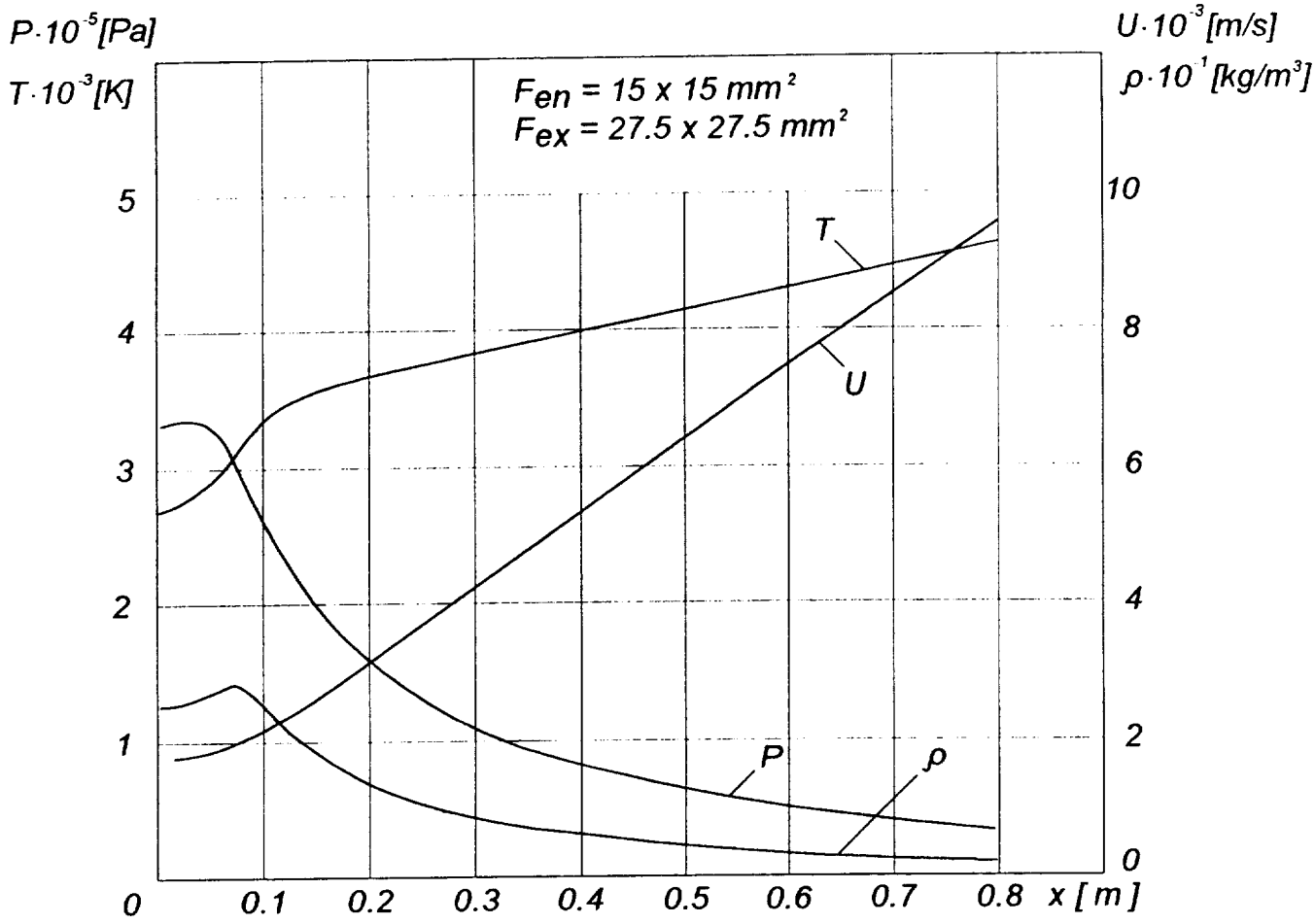

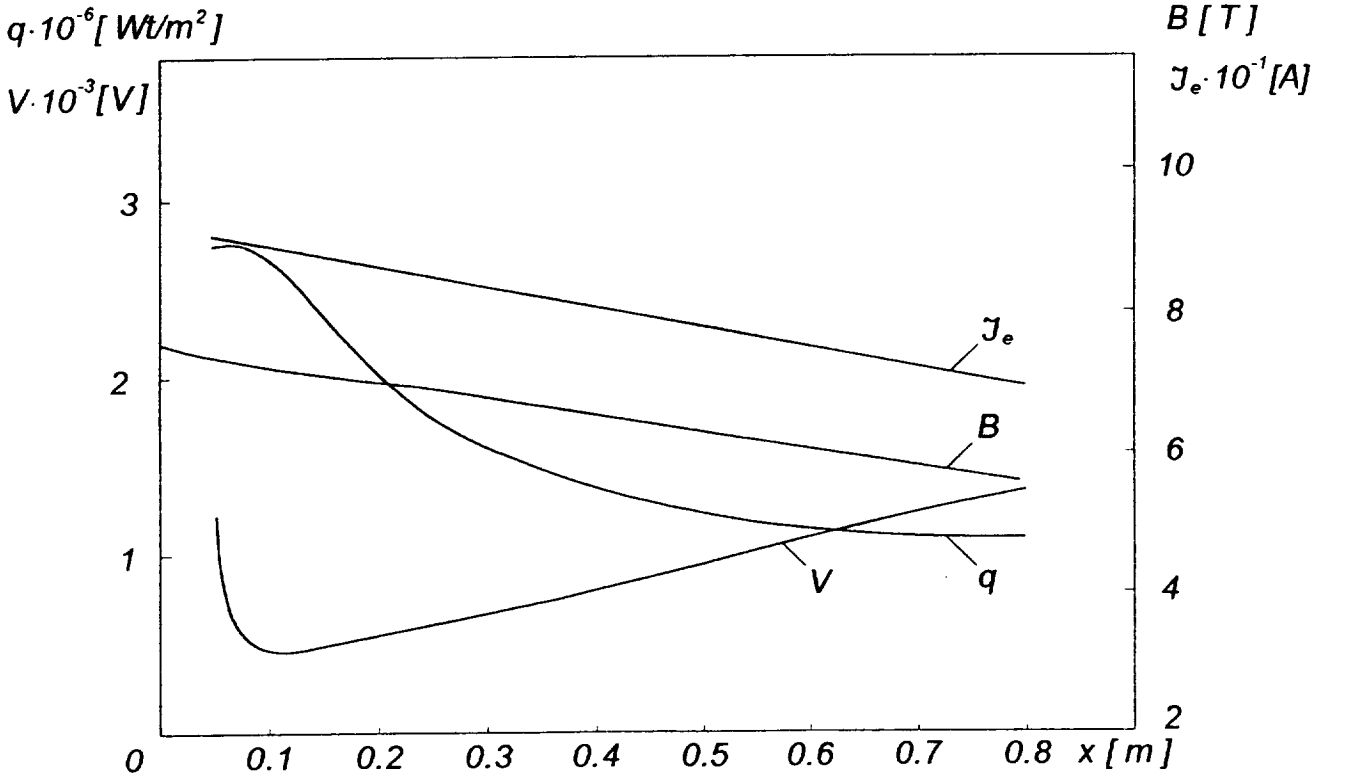

Fig. 14 $P_0 = 20$, $T_0 = 3700$

E.1.3 Summary of TsAGI Report on Facility Capabilities and Facility

Several points in the above report merit emphasis or further discussion. First, the cost of the proposed upgrades amounted to approximately $400,000 for the Stage I modifications (high-pressure facility utilizing the existing magnet), and $500,000 to $1 million for Stage II. The large uncertainty in the cost estimate for Stage II is primarily due to the uncertainty of magnet costs. The total cost for all proposed upgrades would be in the range $900,000 to $1.4 million. Because this exceeded the funds available for experimental research in the MARIAH Project, these facility upgrades were not pursued.

Some of the more important operating characteristics contained in the report are summarized below in Table E.1- 1. Supplementary material, including photographs of the facility and its components, have been included in this section (Figures E.1- 1 - E.1- 7). Also, some of the information below has also been derived from observation of the facility during a visit to the site by MSE personnel in 1995.

The photograph of the TsAGI Hypersonic MHD Facility is an end-to-end view of the entire facility. The flow direction is from right to left, away from the observer. The main components beginning at the upstream end, include: the arc heater; the MHD accelerator enclosed by one half of the magnet in place; the test cabin with the large diagnostic window clearly visible; and the ejector system that conducts the exhaust gases into a storage tank.

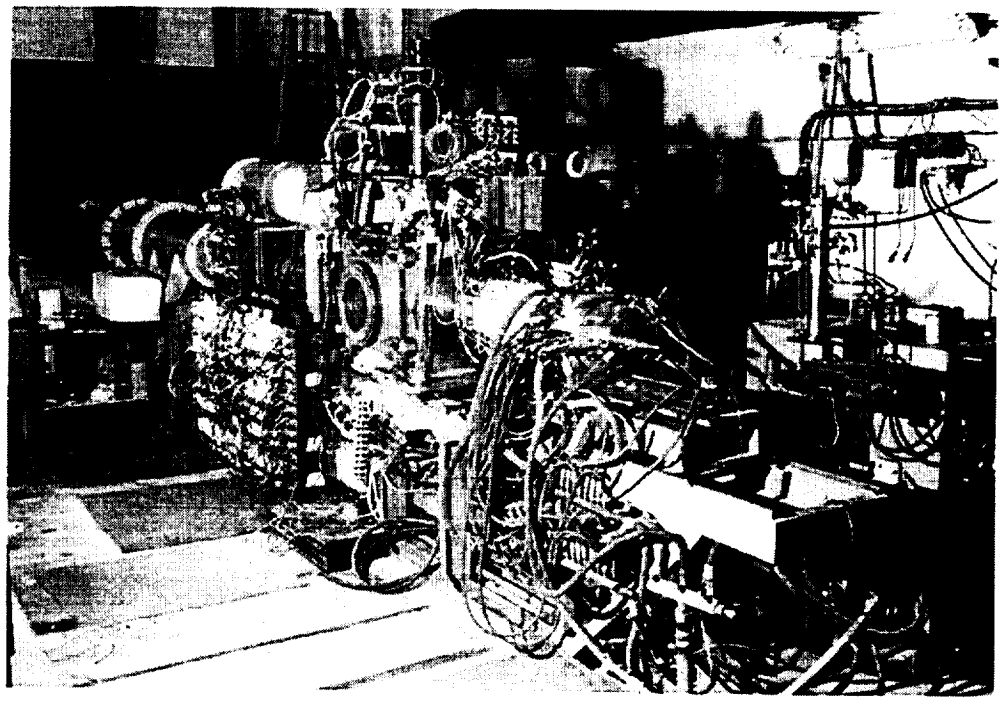

Figure E.1- 1. Photograph of the TsAGI hypersonic MHD facility.

Table E.1- 1. Summary of the TsAGI MHD facility operating parameters	
ARC HEATER	
Power Input	200-260 kw
Stilling Chamber Temperature	3,700 K
Stilling Chamber Pressure	20-30 atm
Mass Flow Rate	7.0 to 22.5 g/s
ACCELERATOR	
Inlet Dimensions	1.5×1.0 or 1.5×1.5 cm^2
Channel Length	variable, 14.5 to 72.5 cm
Inlet Flow Velocity	1,800 m/s
Inlet Mach number	1.9 (variable, depending on choice of nozzle)
Magnetic Field	2.4 T
Gas Conductivity In Stilling Chamber (Nominal)	150 mho/m
Electrode Pitch (Longitudinal)	8.0 mm
Electrode Width (In Longitudinal Direction)	4.5 mm
Number of Active Electrode Pairs	45
Maximum Current Per Electrode Pair	55 A
Applied Voltage Per Electrode Pair	200-400 V
Total Input Electric Power	0.5-1.0 MW
Heat Flux	10–50 MW/m^2
Powered Run Times	1-2 s
TEST SECTION	
Dimensions (Cross Section)	50 cm × 50 cm
Maximum Flow Velocity	7.5 km/s
Densities	10^{-4} - 10^{-2} kg/m^3
Mach Number	15 (for sec. nozzle exit area of 20×20 cm^2)

The seed material used in virtually all of the TsAGI testing has been a eutectic mixture of sodium (Na) and potassium (K), with a mixture ratio of 77/23 by mass of K/Na. This mixture is commonly referred to as NaK. The advantage of NaK over more common seed materials such as cesium (Cs) or K is it is liquid at room temperature. This permits the seed to be injected by means of a pressurized injection system, shown in the photograph of Figure E.1- 2. The quartz ampoule containing the NaK is shown near the center of the photograph. Seed flow is initiated when a mechanical plunger breaks the glass near the base of the ampoule. Pressurization of the seed is achieved by use of the gas cylinders shown in the photograph.

Liquid injection of the seed eliminates many of the problems associated with the use of powdered seed materials. It is also superior to other liquid systems, such as the potassium carbonate (K_2CO_3) - water mixture that was briefly used in the U.S. Department of Energy (DOE) MHD power generation program. The major failing of this scheme was that the introduction of water depressed the flame temperature in the combustor.

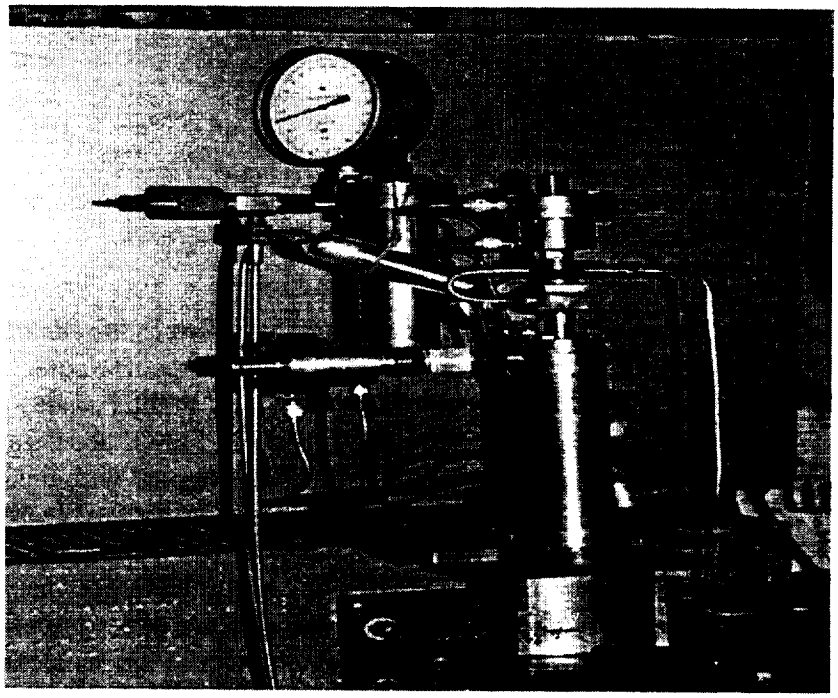

Figure E.1- 2. Seed material and seed injection system.

The arc heater is shown in the schematic of Figure E.1- 3, as well as in disassembled form in Figure E.1- 5. The arc is spin stabilized using a coaxial magnetic field. It is water-cooled and operates at a stilling chamber temperature of 3,700 Kelvin (K) and a pressure of approximately 20 atmospheres (atm). Note that Table 2.1 in the report indicates an effective stagnation pressure of 20 megapascal (MPa). This is not the operating stagnation pressure of the arc heater; but rather the effective stagnation pressure, assuming an isentropic, adiabatic stagnation process at the exit of the MHD accelerator.

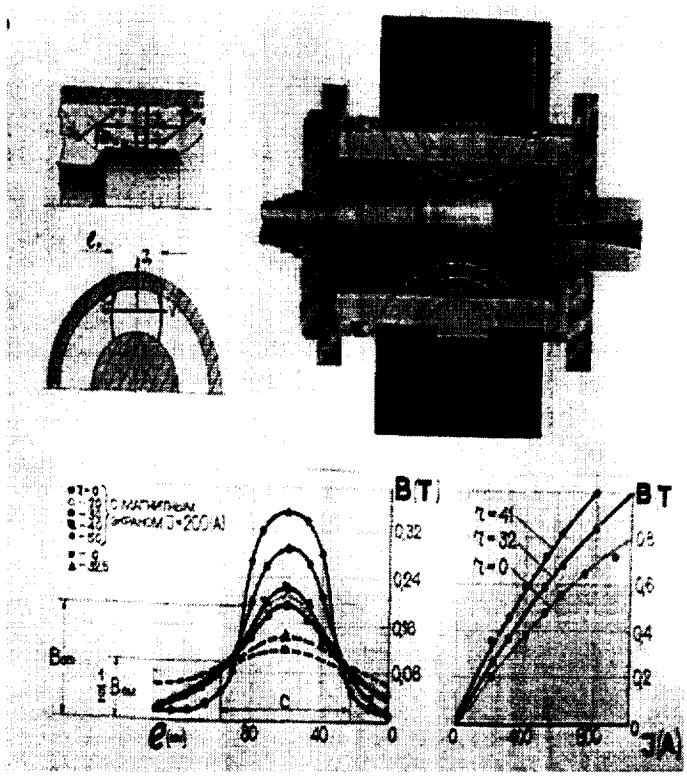

Figure E.1- 3. Cross-section of arc heater with coaxial magnetic field.

The accelerator is shown disassembled in Figure E.1- 6 and installed in the flow train in Figure E.1- 4. Several different accelerators have been built and tested in recent years. Typical accelerators are 55-70 centimeters (cm) in length, designed to run in the Faraday (two-terminal) mode, and contain 40-45 electrodes. An important feature of the TsAGI accelerators is they run in the heat sink mode (i.e., - without active cooling). This fact, coupled with the high heat fluxes [10-50 megawatts per meter (MW/m)], implies very short lifetimes for the electrodes and insulators. As noted in the report, typical electrode-insulator lifetimes are in the range of 5-10 seconds (s). The most common failure mode is erosion of the interelectrode insulators along the anode wall. Channels are commonly operated at maximum currents of 55 amperes (amps) and Faraday voltages in the range 200-400 volts (V). The input power to the accelerator is typically in the range ½ to 1 MW.

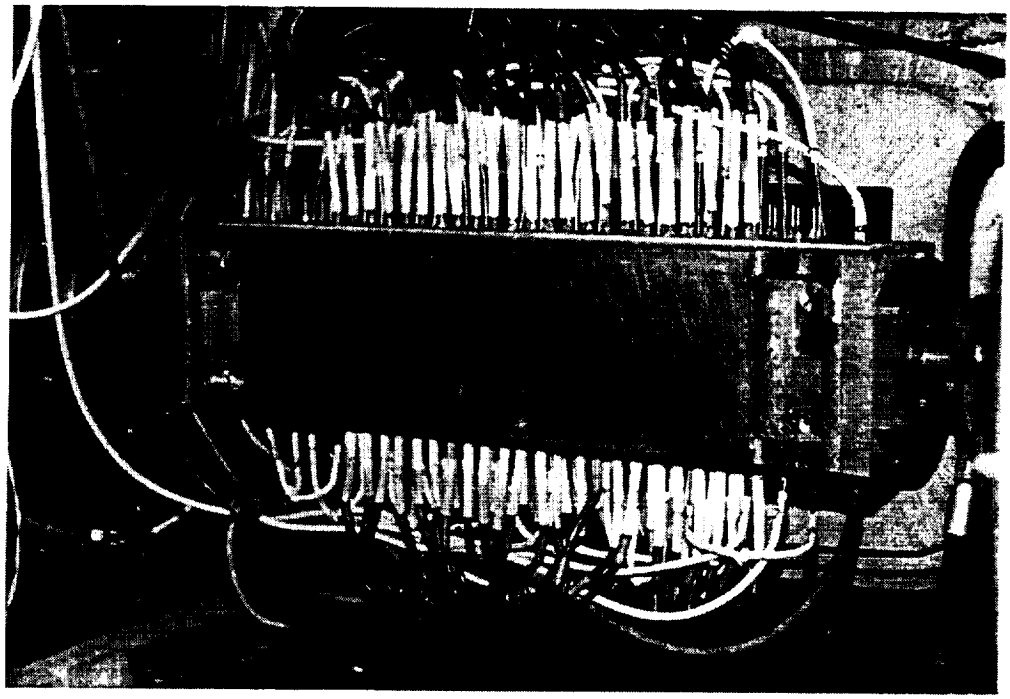

Figure E.1- 4. MHD Accelerator installed in the flow train.

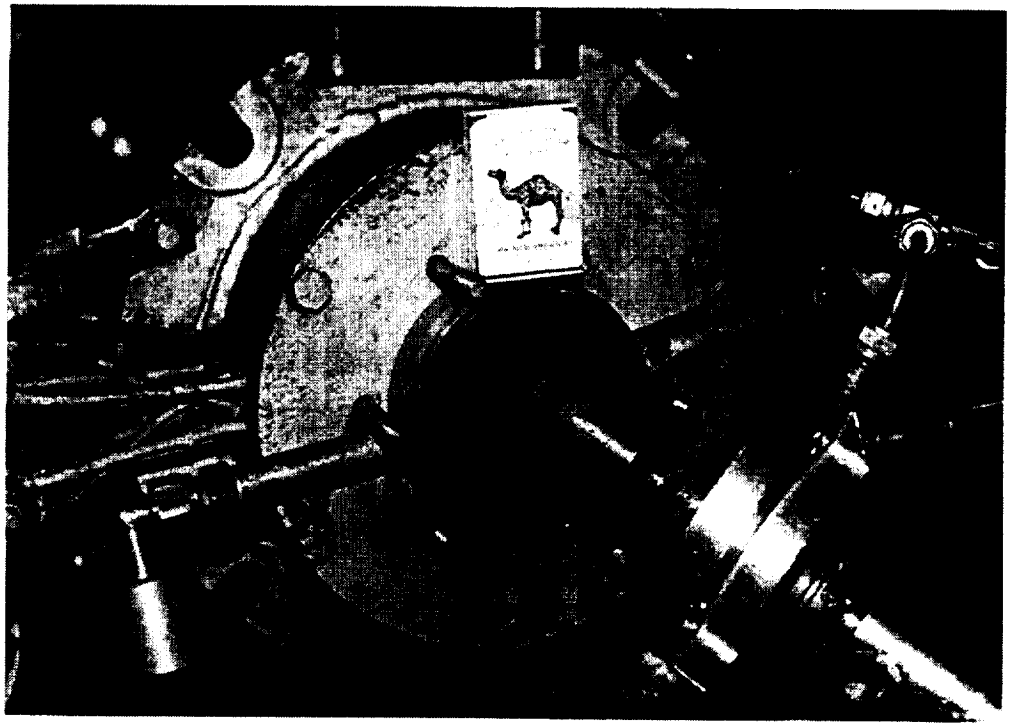

Figure E.1- 5. Disassembled arc heater.

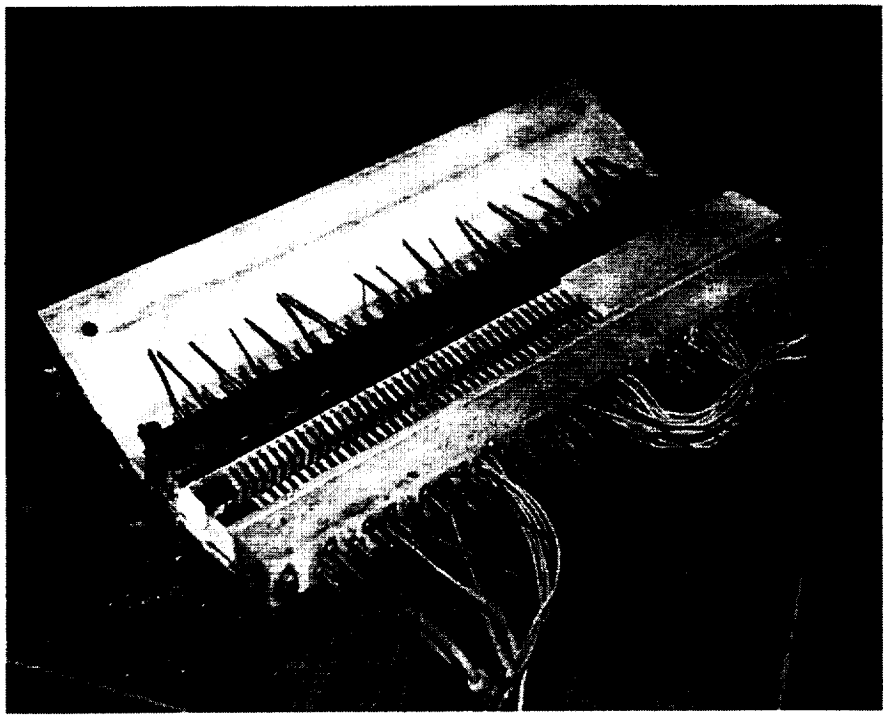

Figure E.1- 6. MHD accelerator channel with sidewall removed.

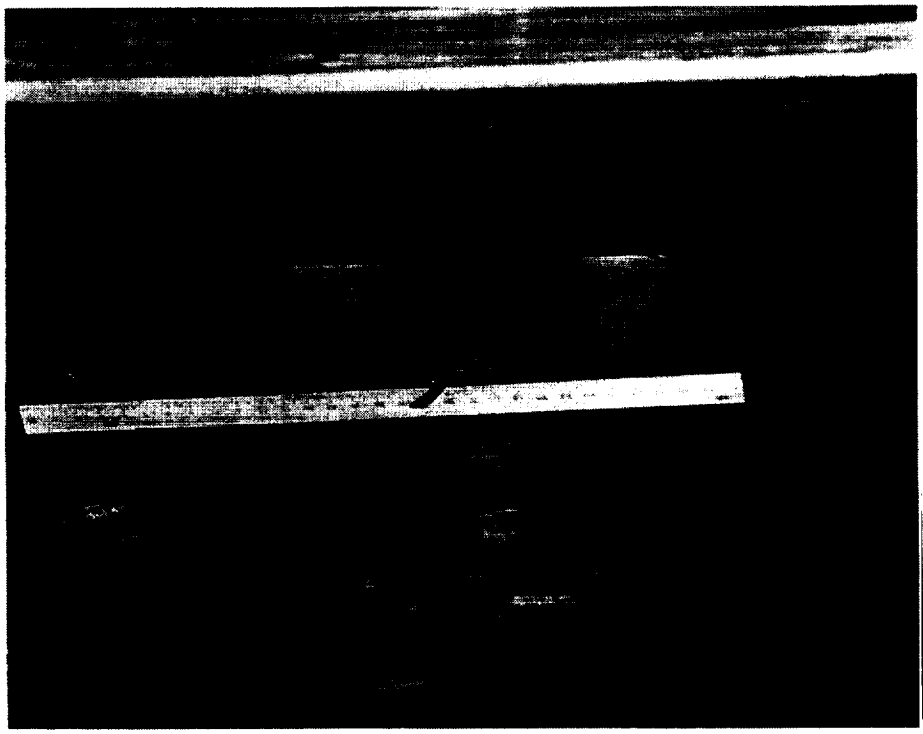

Figure E.1- 7. Secondary expansion nozzle.

Sequence of Operation

The sequence of events for a typical test is as follows:

1. Cooling water flow is initiated in the arc heater and other downstream components (excluding the accelerator).
2. Magnet power supply is activated.
3. Airflow is initiated.
4. Power to the arc heater is activated.
5. Seed flow is initiated.
6. Power to the MHD accelerator is activated. A typical powered run time is 1-2 s.
7. Measurements and diagnostics in the test section are recorded.
8. Power to the accelerator is terminated.
9. Seed flow is terminated.
10. Arc heater power is terminated.
11. Airflow is terminated.
12. Magnet power is terminated.
13. Cooling water flow is terminated.

E.1.3.1 Summary

The most important points of the TsAGI study are summarized below.

1. The most severe barrier to increasing the run times of the MHD accelerator is the extremely high wall-heat flux that is typically in the range 10-50 MW/square meters (m^2). Such high-heat-fluxes imply very short electrode wall lifetimes (typically 10-12 s). The most common failure mode that was observed in the TsAGI experimental program was the erosion of the anode wall insulators at the electrode-insulator interface. According to the report the use of active cooling instead of relying on heat sink operation will not significantly improve the problem.

2. The chemical composition of the gas leaving the MHD accelerator will generally be different from the in-flight composition. Indeed, as shown in Figure E.1- 3 of the report, the molar concentration of monatomic oxygen increases strongly with the applied MHD currents. At a reservoir pressure of 20 atm and an applied field of 3 T, the molar monatomic oxygen content was computed to be 27%. As the report notes such high concentrations of this species will almost certainly confound the combustion chemistry occurring in a scramjet test module.

3. One of the recommendations made by MSE during a visit to TsAGI in the fall of 1995 was to investigate the feasibility of modifying the facility to operate at substantially higher pressures. This would improve the overall performance of the system, permitting the test section conditions (Mach number and static pressure) be moved somewhat closer to the post-bowshock conditions. According to the report (see Section 4): "Increasing

the pressure (and the mass flow rate, accordingly) implies substantial losses in output parameters as compared with those implemented by now. The velocity V=6000 m/s is necessary to simulate conditions inherent in the combustion chamber for M=15-20, may be realized (while maintaining a suitable length of the MHD channel) at B > 5 T only. The highest results may be obtained at B=7.5 T."

The high cost associated with the design and implementation of facility modifications to support higher pressure, higher magnetic field operation of the facility was the primary reason MSE decided not to pursue these recommendations further.

APPENDIX E, SECTION E.2

E.2 TsAGI REPORT ON MHD ELECTRODE STUDY

This section describes experimental work done at TsAGI to characterize the various modes of current transport in the vicinity of the MHD accelerator electrode walls. The report is a review and compilation of research previously accomplished at TsAGI under separately funded efforts. The intent of the discussion below is to provide the background and objectives of the TsAGI experimental investigations.

E.2.1 Overview

Current flow through an MHD accelerator is a complex process for many reasons. First, even in the ideal case where the pressure, temperature, velocity, and magnetic field are everywhere uniform, the current density and electric field vectors will not be parallel to each other due to the tensorial character of the generalized Ohm's Law relationship. Nonuniformities in temperature and velocity further complicate the current flow patterns. The TsAGI report (Section E.1.2) addresses these issues in the context of three distinct zones within the flow stream in which the current flow and current nonuniformities are dominated by different mechanisms.

The Ohm's Law relations written in two dimensions for an MHD accelerator are

$$Jx = \frac{\sigma \beta E_x}{(1 + \beta^2)} - \frac{(K-1)\sigma UB}{(1 + \beta^2)} \qquad \text{(E.2- 1)}$$

$$Jy = \frac{\sigma E_x}{(1 + \beta^2)} + \frac{\beta(K-1)\sigma U B}{(1 + \beta^2)} \qquad \text{(E.2- 2)}$$

The x coordinate is taken in the streamwise direction and the y coordinate in the direction perpendicular to the electrode walls. The parameter K is the load factor, defined as Ey/UB, and β is the Hall parameter. Equations (E.2- 1) and (E.2- 2) show the root cause of several important nonuniformities. These equations must be interpreted in a pointwise sense (i.e., in the sense of a field) because quantities such as σ, β and U will in general exhibit large variations across the duct. Note that in an ideal Faraday accelerator the high degree of electrode segmentation implies that $Jx = 0$. This implies that:

$$Ex = \beta(K-1)UB \qquad \text{(E.2- 3)}$$

and

$$Jy = (K-1)\sigma UB \qquad \text{(E.2- 4)}$$

In the typical MHD accelerator the electrode wall is highly segmented in the flow direction, and the voltage across each electrode pair is applied independently. For this reason the load parameter in a Faraday accelerator may be regarded as a control variable. By imposing a prescribed voltage across each electrode pair and controlling the magnetic field, the load parameter at each station can be effectively specified. Because the accelerating force (per unit volume) is JyB, the last equation shows that to obtain positive acceleration the load factor must be greater than one. However, if K is too large, as Equations (E.2- 3) and (E.2- 4) show, the axial field (Ex) will become excessive and may result in interelectrode breakdown. Another factor that may induce axial breakdown is the Hall parameter, β. When an MHD accelerator is operated at subatmospheric pressures and high temperatures, the electron mobilities become quite high. Since β is the product of electron mobility and magnetic field, high mobilities usually imply high Hall parameters which may again cause axial breakdown.

There are at least two other types of strong nonuniformities that can lead to either high current concentrations or high local electric fields in an MHD channel. One is the classic thermal instability due to the interaction of Joule heating, electrical conductivity, and local heat transfer. A transient, localized temperature increase will cause an increase in electrical conductivity resulting in a local increase in the current density. Increased current density causes increased Joule heating which drives the temperature and the electrical conductivity even higher. Thus, a positive feedback loop is established that can result in very high concentrations of current limited only at the point where the temperature of the heated filament increases sufficiently to establish a new (steady-state) balance between Joule heating and heat transfer out of the region. Alternatively, the transient-arc filament may be extinguished by increased cooling due to turbulence or to other poorly understood mechanisms.

The Joule heating instability occurs both with and without an applied magnetic field. The presence of a magnetic field only exacerbates the onset of the instability because the magnetic field lines tend to tie up the electrons in helical orbits effectively preventing them from migrating in any direction transverse to the magnetic field. The net result is electron heat transfer is seriously inhibited in two of the three dimensions leading to an even greater tendency toward instability.

Another type of nonuniformity is a result of thermal overshoot within the boundary layer. It occurs only in high Mach number flows where the wall recovery temperatures may be substantially higher than the core flow static temperatures. In a high-speed flow the temperature of an adiabatic wall can be estimated knowing the core flow properties from the equation

$$\frac{Taw}{T} = 1 + \frac{r(\gamma - 1)}{2} M^2 \qquad \text{(E.2- 5)}$$

where T is the static temperature in the core flow and M is the core flow Mach number.

The parameter r is the recovery factor, a number which depends on the Prandtl number and is generally close to, but less than one. For a high-Mach-number flow, Equation (E.2- 5) indicates

that the adiabatic wall temperature may be significantly higher than the core flow temperature. In a real accelerator, the actual wall temperature will be lower than the adiabatic wall temperature; however, the overall result is thermal overshoots can occur in high Mach number flows due to the conversion of kinetic energy to thermal energy through the mechanism of viscous dissipation. The term "thermal overshoot" simply means that a local maximum occurs in the static temperature profile somewhere within the boundary layer.

The existence of such a thermal nonuniformity will have the effect of locally increasing the electrical conductivity, thereby causing a local increase in the current density Jy. Increased Jy will result in an increased body force, JyB on the fluid leading to an increase in the flow velocity. Therefore, in a high Mach number MHD accelerator flow, one can expect overshoots of both temperature and velocity within the boundary layer.

It should be noted that the velocity overshoot phenomenon is unique to MHD accelerators. In an MHD generator the body force acts in the upstream direction, and the current Jy is in the opposite direction from what occurs in an accelerator. The local increase in conductivity will cause the current density to be more negative, thus retarding the flow in the boundary layer more than in the core region. It is also true that Mach numbers in generators are usually somewhat lower than in accelerators; therefore, the recovery temperatures are closer to the core flow temperature. Consequently, the mechanism leading to thermal overshoots is somewhat diminished in generators; and due to the opposite direction of the current density, there is no mechanism for velocity overshoots in MHD generators.

Finally, there is the class of nonuniformities caused by velocity variation. In any duct flow the no-slip boundary condition dictates that $U = 0$ at a solid wall. This has important implications for the electrical behavior in the near-wall region. It is convenient to rewrite Equations (E.2- 3) and (E.2- 4) in terms of Ey and UB, eliminating K:

$$Ex = \beta(Ey - UB) \tag{E.2- 6}$$

$$Jy = \sigma(Ey - UB) \tag{E.2- 7}$$

As noted above, to obtain positive acceleration of the gas, the device must be operated in a condition that assures the current density Jy is positive in the core flow. The minimum applied transverse electric field is U_cB, where U_c is the velocity of the core flow. For realistic operating conditions, Ey may be two or three times this value. At the electrode or sidewall surfaces, the velocity must be zero. This implies that the axial field Ex may become quite high at a gas-wall interface. For the electrode walls, Equation (E.2- 5) indicates interelectrode breakdown may be a problem, especially for high Hall parameters (which occur typically at low pressures), and for high values of UB. The main function of sidewalls aside from structural integrity and confinement of the plasma is to stand off the applied transverse voltages. Because the sidewall is designed to carry no current, Equation (E.2- 7) implies that $Ey = UB$; that is, the entire open

circuit voltage is impressed top to bottom along the sidewalls. *Ex* may also become quite large near the sidewalls, as indicated by Equation (E.2- 6). For operation at low pressures, this issue becomes quite critical since the Hall parameter may reach values of 10 or more, even for modest magnetic field strengths. Consequently, the design of both the electrode walls and the sidewalls must take into account the possibility of very high electric fields.

The above discussion concerning the various mechanisms for current and field nonuniformities suggests the design of electrodes for MHD accelerators must take into account a number of factors. Some of these mechanisms are not well understood and can only be resolved by recourse to experiment. These considerations were the primary motivating factor for the TsAGI study on electrode phenomena.

E.2.2 TsAGI Report on Electrode Phenomena in the MHD Channel of the Hypervelocity Wind Tunnel (presented in pp. E.2-5 through E.2-14)

TSAGI CENTRAL AEROHYDRODYNAMIC INSTITUTE

Review of investigations carried out at TsAGI on electrode phenomena in the MHD-channel of the hypervelocity wind tunnel

1996

E.2-5

Introduction

The investigation of the electrode phenomena taking place in the boundary layers near the MHD-channel electrodes received much attention in developing MHD-generators. Several good reviews are devoted to this subject [1]. The present review considers the electrode phenomena in the Faraday-type MHD-accelerator. The basic differences of the phenomena in question from those in the MHD-generators are caused by change of magnetic induction sign and, accordingly, electric Hall field direction, essentially high current density $J_{acc} \sim 10-100$ A/cm^2 and, consequently, significantly high heat transfer in the electrode layers, considerably great Mach numbers M_∞ in the flow core ($M_\infty \sim 2-4$) and, as a result, by regions in the boundary layer near the electrode surface which are characterized by high temperatures (recovery temperatures) and, thus, by a substantially greater conduction than in other flow regions.

The electrode phenomena were investigated in the MHD-channel of the SMGDU stand (stand of magnetogasdynamic acceleration). The basic flow characteristics at the channel entry were as follows: $P_0 = (2-5)\times 10^5$ Pa, $T_0 = 3500-3700$K, Mach numbers are 1.6–3.0. The tests were conducted with air using a seed in the form of ~1% euthectics KNa. The flow field measured at the primary nozzle exit was uniform and the air flow in the nozzle and at its exit was in thermodynamic equilibrium. The Reynolds numbers, Re_x, based on the flow parameters and the distance from the nozzle throat were $Re_x \sim 4000$. At the above numbers Re_x and M, the boundary layer was in the transition region between the laminar and turbulent flows. The calculated and experimental values of the boundary layer thickness coincided to be of ~1.0–1.5 mm on each side of the channel. The boundary layer structure on the insulating wall differed from that on the electrode wall because of different values of T_w (wall temperatures). Some flow swirling due to the arc rotation in the arc heater exerted influence on the boundary layer flow. The flow deviation angle near the wall was ~3–5°. The imposition of electric and magnetic fields on this flow resulted in distortion of its uniformity, appearance of fields with increased temperatures, spatial charge etc.

Analysis of electrode phenomena

An important problem causing flow uniformity distortions is the plasma instability which may be thermal, ionization, acoustic one etc. The thermal instability leads, as a rule, to a local discharge ionization which affects essentially the flow uniformity. The conditions in the boundary layer are especially favorable for such instability to be caused because of sharp nonuniformity of the gas density, temperature and conduction in it. In the presence of the magnetic field, the Hall effect produces an additional strong influence on the flow pattern in the boundary layer. Hence, it is very important to investigate peculiarities of current flow in the boundary layer.

It may be suggested that the current flow through the cold sublayer of the boundary layer whose dimensions are close to those of a laminar sublayer in the turbulent boundary layer (0.3–0.5 mm) is caused by three different mechanisms [2].

1. Electric arc in the boundary layer resulting in a hot spot in the electrode surface which provides thermoionic emission.
2. Electric fields of high intensity occurring in a very thin gas layer between a high-conductive gas dynamic layer, where the temperature of a supersonic flow is equal to the recovery temperature, and the cathode surface. In this case, the current flow can be provided by self-electron emission.
3. Conduction due to drift of positively charged ions in the fields of high intensity between the electrode and the high-conductive layer.

The engineering definition of the MHD-channel design depends on a mechanism which prevails in the provision of current flow through the cold sublayer of the boundary layer.

The arc generation is generally preceded by spark breakdown of the gas gap. In this case, there must be the threshold voltage U^* and when voltage is less than U^* there is essentially no current between the electrodes. Besides, high-conduction regions in the cold sublayer must exist locally and possess a strong luminance. The latter must be clearly seen in filming.

Below are discussed the analysis results for current flow through the boundary layer on the electrode wall depending on strength of current and magnetic intensity including the following investigations:

1. Nature of current concentration on the electrodes and their erosion.
2. Visual discharge glow pattern using conventional and superhigh-speed filming. Estimation of local current concentrations in the boundary layer and in the flow core.
3. Motion of current spots and erosion, caused by them, of the electrode and interelectrode insulator surfaces.

The investigations were carried out on facilities described in the literature [2-4].

The initial investigations were devoted to the current flow pattern between plane polished electrodes of a rather great mass so as their temperature can be considered constant. The electrodes were made of copper, molybdenum, graphite. In order to exclude possible influence of current fluctuations, a storage battery was served as a source. The current fluctuations were analyzed simultaneously within three time scales: 10^{-4}—10^{-6} s, 10^{-4}—10^{-2} s, 10^{-3}—10^{-1} s with the application of three oscillographs of different types, the gas dynamic flow parameters being $P_0 = 6\times10^5$ Pa, $T_0 = 4000$K, $P_\infty = (0.05-0.3)\times10^5$ Pa, $T_\infty = 1400-3000$K, $M_\infty = 2.5-3.5$. The discharge gap was fixed by a camera at a rate of 50images/s and a SFR device at a rate of 15×10^3 image/s. Particular attention was paid to synchronization of filming the discharge gap and recording electrode current I and voltage U by oscillographs. The records were used to plot volt-ampere characteristics, and the superfilming registrator (SFR) data and records of U and I parameters were applied to estimate a characteristic fluctuation frequency and the relation of these fluctuations to the generation and disapearance of discharge on the electrodes. The analysis of the filming data revealed that the life time of a local channel was within 10^{-5}—10^{-2} s to coincide with the oscillograph measurement results within the limits of measurements. High-frequency fluctuations in the electrode circuit were caused by generation and decay of separate conduction channels. The strength of current in an individual arc was 5—10 A. The number of microarc channels increased as the strength of current rose. The investigation technique was considered in detail in [2].

For the purpose of investigating the current spot motion in the electrodes, a series of experiments were carried out using segmented electrodes. To do this, one or several pairs of electrodes, each divided into segments (4—7) were insulated from each other to have a common power supply source for each pair of electrodes. The current and voltage in each segment were fixed using an oscillograph. Fig. 1,2 presents the measurement scheme. The strength of current through a separate electrode was varied from 0 to 40 A, and the magnetic intensity from 0 to 2.4 T. In different experiment series, the segmented electrodes were placed immediately in the test channel of the accelerator or in a special section with a window through which it was possible to observe the discharge formation pattern (Fig.3). In order to evaluate erosion due to microarc discharge motion, some experiments were conducted on highly polished steel electrodes. The erosion traces were examined using optic and scanning electron microscopes. The experiments were carried out both for the cathode and the anode. As for the cathode, local microarc discharges were observed which moved at a speed of 5—10 m/s along the flow at B = 0. The life time of a separate microarc was defined as the time of its motion along the cathode $\sim10^{-2}\div10^{-3}$ s.

With the imposed magnetic field, the minimum velocity of the cathode spot motion displaces upstream in the acceleration regime (Fig.4). Some current bursts on the segments are noted over the total cathode surface but mainly on forward downstream segments [3].

The number of simultaneously existing arcs seems to depend on the plasma conduction at the cathode. For lesser conduction, more intense current concentrations are revealed with a smaller number of current spots. This problem is similar, to some extent, to the problem of geophysical prospecting by electric means for current spreading from an individual electrode near the surface, i.e., the next microarc can occur only at such a distance from the preceding one when the potential drop in the current spreading region is greater than the breakdown voltage and microarc burning voltage. In this case, the supersonic boundary layer region with a high recovery temperature can be considered as a zone of high conduction.

In regard to the anode, the current distribution on separate segments in the absence of magnetic field is rather uniform when $I < 5$ A. As the strength of current rises it becomes to concentrate at the rear downstream electrode end. At $I \sim 20$A, 50% of the current flows through the last segment. Without the magnetic field, the current occurs, as a rule, on the first downstream segment to become immediately equal to the electrode current, i.e., the total current flows through one segment, then through the second one, and so forth. The current on the last segment increases abruptly up to the discharge current value, while on the preceding one it reduces to zero. The discharge stays somewhat at the rear downstream edge and then the process repeats again.

The anode current distribution pattern changes considerably when the magnetic field is imposed. In this case, the current flows almost completely through the last segment. The speed filming data (24000 image/s) show that the region of bright gas glow near the anode begins immediately from the electrode-insulator joint to spread in the form of a bright strip up to the next electrode. This region of increased temperature is also a zone of increased conduction through which the Hall current are shunted (Fig.5). This finding is verified by current measurements on segments placed downstream. The current enters the forward edges and leaves the rear edges. The decay law is as follows:

$$I_i \sim I_i \cdot \exp(-k \cdot B^2 \cdot X_i),$$

where B is induction and X_i are segment coordinates. The facility description and the investigation results are contained in [4].

The analysis of the anode edge state at the anode-insulator joint reveals some traces of the local insulator erosion (Fig.6). Because the high-temperature near-anode layer fails to transfer the heat due to convective transfer along the electrode length even in the presence of a turbulent boundary layer it is possible to show that the layer spreading δ for the length x is as follows:

$$\delta \approx \sqrt{x \delta_T \, St}$$

where δ_T is the boundary layer thickness, St is the Stanton number. This layer, having passed over the anode surface, will form an anode current spot at the rear anode edge, i.e., the anode spots are arranged successively along the gas flow lines which is confirmed by the electrode and insulator erosion patterns (Fig.6). Thus, high-temperature layers form near the surfaces of the anodes which provide the commutation between the flow core and the electrodes. Similar pattern takes place in forming extended tails with a high conduction past the electrodes placed in a supersonic flow [5] (Fig.7).

High thermal loads experienced by the anode-insulator joint require special measures to be undertaken to diminish the insulator erosion. Below is given a system of controling the arc motion over the anode surface to prevent discharge localization near the anode-insulator joint which is described in the Russian patent [6]. The key of the system is to make the anode spot move on the copper anode surface, providing thereby the protection against the intense erosion of the electrode-insulator joint. To do this, the anode is divided into three segments of different characteristic dimensions approximately in the proportion of 1:4:2, all segments being connected to the common power supply source. The last downstream segment is connected to the power source via a coil with a great electric resistance. Another coil with a greater number of winds is mounted on this coil so that when a microarc discharge moves to the last segment with the current impulse in the primary coil a current

pulse with a higher voltage is generated in the second coil which is transferred to the first downstream segment. The presence of a high-voltage impulse favors for the formation of a microarc on the first segment, while the current from the microarc on the rear segment must flow through a great resistance in the coil which results in its extinguishing. A microarc occurring on the first segment is carried away downstream to appear on the last segment and, thus, the process repeats (Fig.8). There are also possible other ways of protecting the electrode-insulator joint. One of them is the electrode with a boundary layer separation zone used instead of an interelectrode insulator. These measures make it possible to decrease the current concentration on the electrode-insulator joint and distribute artificially the thermal load due to the current flow over the total electrode surface.

Influence of electrode phenomena on the flow

The electrode regions can be divide conventionally into three zones:

1. Narrow zone adjacent immediately to the electrode. Its size is much less than the boundary layer size. Considerable energy corresponding to the electrode potential drop is released in these zones. Almost the total energy is absorbed by the electrodes.
2. Discharge zone in the boundary layer. The gas conduction is provided either by arc channels or a high-temperature layer with a nonequilibrium conduction. The released energy is transferred to the gas and partially (through radiation and convective transfer) to the electrodes.
3. Zone of current concentration in the core immediately above the boundary layer. The released energy is transferred to the gas and, through radiation, to the electrodes.

The processes proceeding in zones 2 and 3 exert the strongest disturbing effect on the gas flow.

Intense Joule heating in zone 3 can lead to strong flow disturbances up to the appearance of shocks and, thereby, to additional dissipation in the flow and to increased friction in the channel. As shown in [7], a spatial discharge division region occurs in the shock waves with an increased conduction and, accordingly, a greater current density. The calculations of flows with due consideration of all above listed factors are not carried out so far.

In [8], some numerical investigation results for the boundary layer in the presence of some current concentration near the electrode edges are presented. The calculations are performed for a two-dimensional layer, the flow in the stream adjacent to the boundary layer being taken one-dimensional. The gas conduction is determined for a thermodynamically equilibrium electron concentration. The gas parameters in the flow core at the channel entry are as follows: $P_0 = 5$ atm, $T_0 = 3000$ K, $M = 3$, the electrode temperature being $T_w = 1500°C$. The current concentration near the rear electrode edge is represented by means of specifying current density along the electrode using the functions of the form:

$$j(x) = \exp\left(\frac{mx}{a} - 1\right)\sin^n \frac{\pi x}{a}$$

where m,n are the parameters, a is the electrode size. As may be inferred from the calculation results, the increased current concentration ($j_{max} > 500$ A/cm^2) leads to the boundary layer separation. The basic factor causing the separation is Joule heating. The layer separation takes place in the region of maximum current density j_{max}.

Conclusion

1. Discharges of microarc configurations are realized on the MHD-channel electrodes at high current densities of $j > 10$ A/cm^2. The number of microarcs existing simultaneously on the electrodes depends on the current density and on the distance from the MHD-channel entry. The number of microarcs increases as the distance rises and their intensity decreases.

2. In full compliance with the theoretical ocnsiderations, microarcs on the cathode generate mainly closer to the forward electrode edge, while on the anode they occur at the rear edge causing intense erosion of the electrode-insulator joint. The anode arcs give rise to downstream current layers which shunt the electrodes with each other. In order to decrease the anode-insulator joint erosion, a device is suggested and tested to provide microarc motion on the anode surface. Artificially formed boundary layer separation zones are also applied for this purpose.

3. According to the theoretical calculations, at $j > 500$ A/cm^2 the current concentration in the microarcs can cause the boundary layer separation and generation of weak shock waves. Significant development of the boundary layer along the MHD-channel is not noted because under the Lorentz force it accelerates more intensively than the main gas flow. These investigations were accomplished under financial support of NASA through MSE Inc. as a subcontractor.

References

1. Richard Rose, Boundary layer arc behavior, 8 International Conference MHD Electrical Power Generation, Moscow, 1983, vol.1, pp.251

2. V.I.Alfyorov, Yu.S.Ustinov, Investigation of physical pattern of the discharge between cold electrodes in a supersonic plasma flow with a seed, Izv. AN SSSR, MZhG, 1968, N2, pp.95-99 (In Russian)

3. V.I.Alfyorov, O.N.Vitkovskaja, A.P.Labazkin, A.P.Rudakova, G.I.Shcherbakov, The investigation of influence of Hall Effect on MHD Accelerator Performance, X International Congress on MHD Electrical Power Generation, Tirchi, India, vol.1, 1989

4. A.P.Labazkin, G.I.Shcherbakov, Experimental Investigation of Current Sheet in MHD Accelerator Electrode Wall Region. XI International Conference on MHD Electrical Power Generation, China, 1992

5. V.I.Alfyorov, A.S.Bushmin, B.V.Kalachev, Investigation of discharge burning process in a high-velocity gas flow, Zhurnal teoreticheskoi i eksperimentalnoi fiziki, 1966, vol. 51, N5, pp.1281-1287 (In Russian)

6. V.I.Alfyorov, V.P.Rukavets, Magnetogasdynamic device, Certificate of invention N776491, January 15, 1979

7. V.I.Alfyorov, L.M.Dmitriev, Electric discharge in a gas flow in the presence of density gradients, Teplofizika vysokikh temperatur, 1985, vol.23. N4, pp.677-682 (In Russian)

8. V.I.Alfyorov,L.M.Dmitriev, G.N.Dudin,Numerical in vestigation of the boundary layer separation in a magnetogasdynamic channel. Teplofizika vysokikh temperatur, 1973, vol.11, 677-682 (In Russian)

Department Head
V.P.Rukavets

Principal Investigator
V.I.Alfyorov

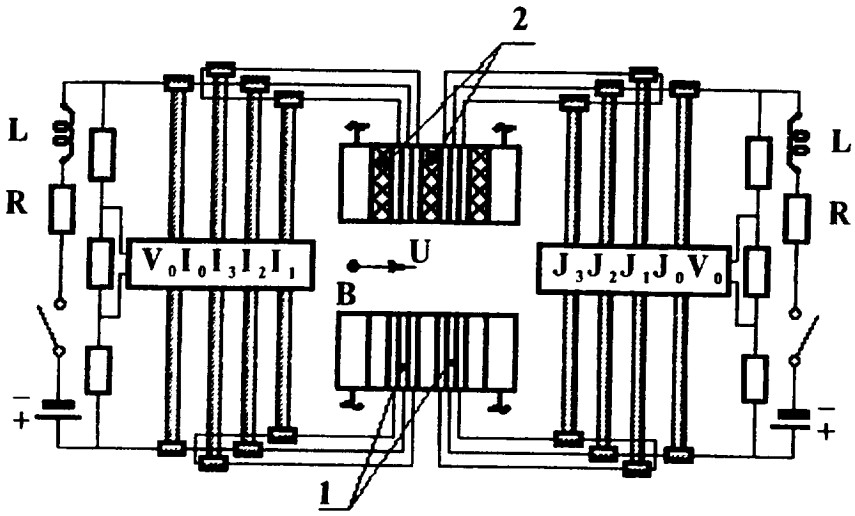

Fig.1. Measuring schema for current distribution along electrodes.
1 segmented electrodes;
2 interelectrode insulators.

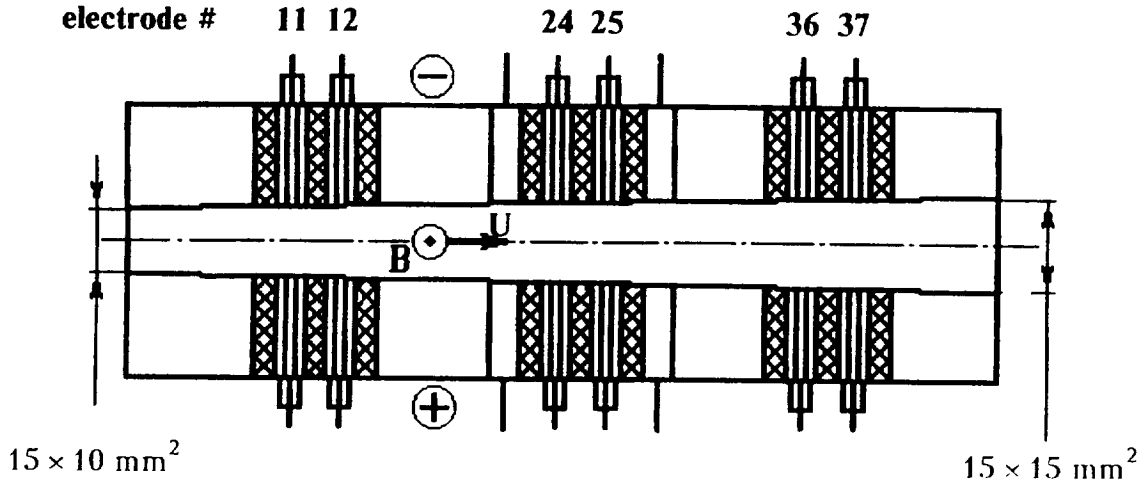

Fig.2. Arrangement of segmented electrodes.

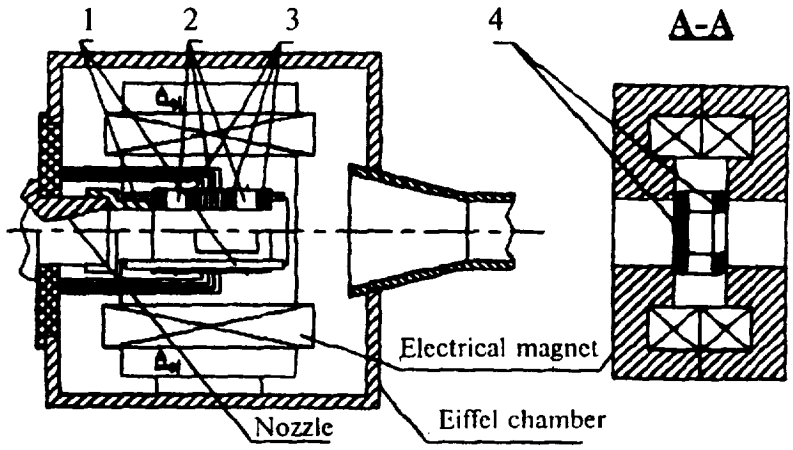

Fig.3 Facility lay-out
1 – electrical insulating panel
2 – electrodes
3 – interelectrode insulators
4 – side insulating walls

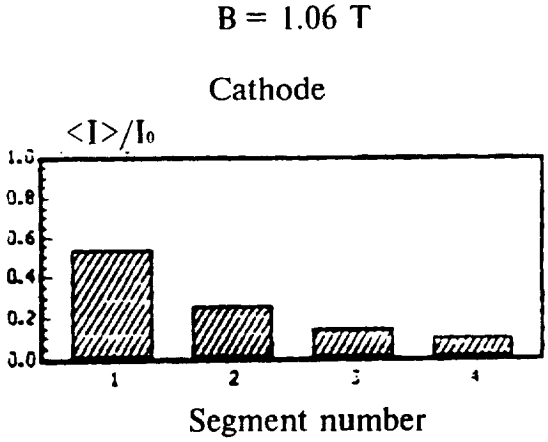

Fig.4 Current distribution along cathode segments

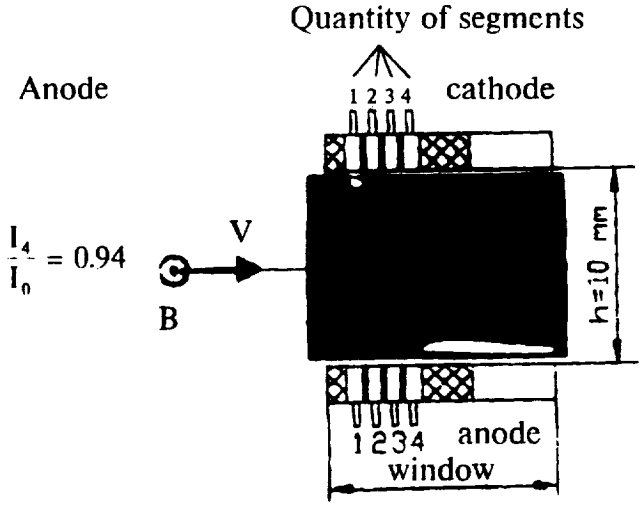

Fig.5 Visual picture of gas flow at anode-cathode joint

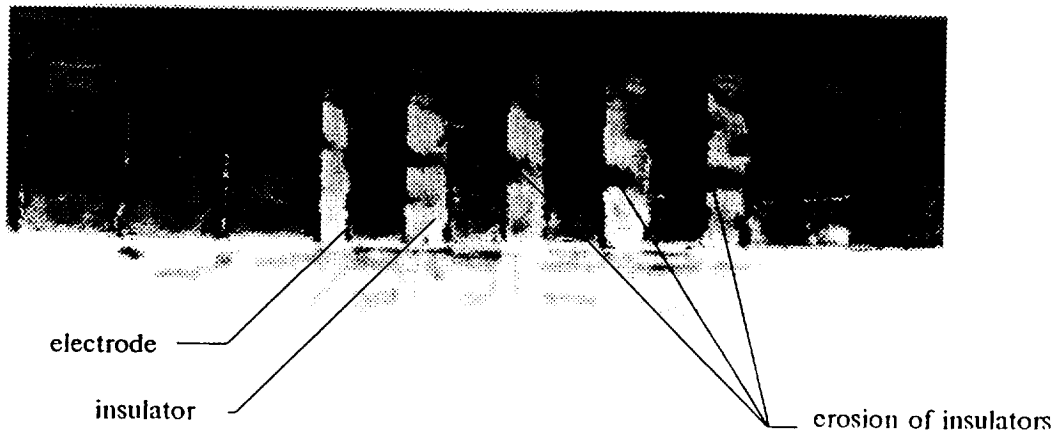

Fig.6. Local erosion of interelectrode insulators.

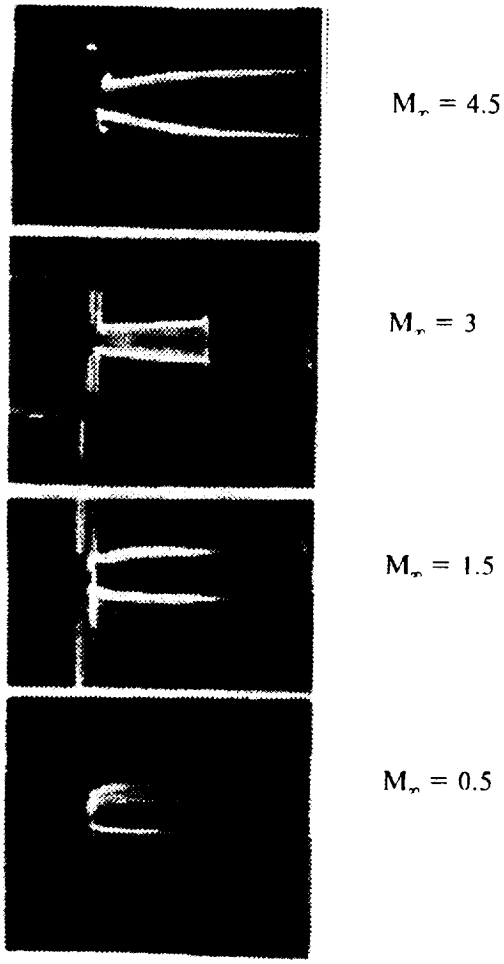

Fig.7. "Gas electrodes" occurring during discharge burning in a supersonic gas flow.

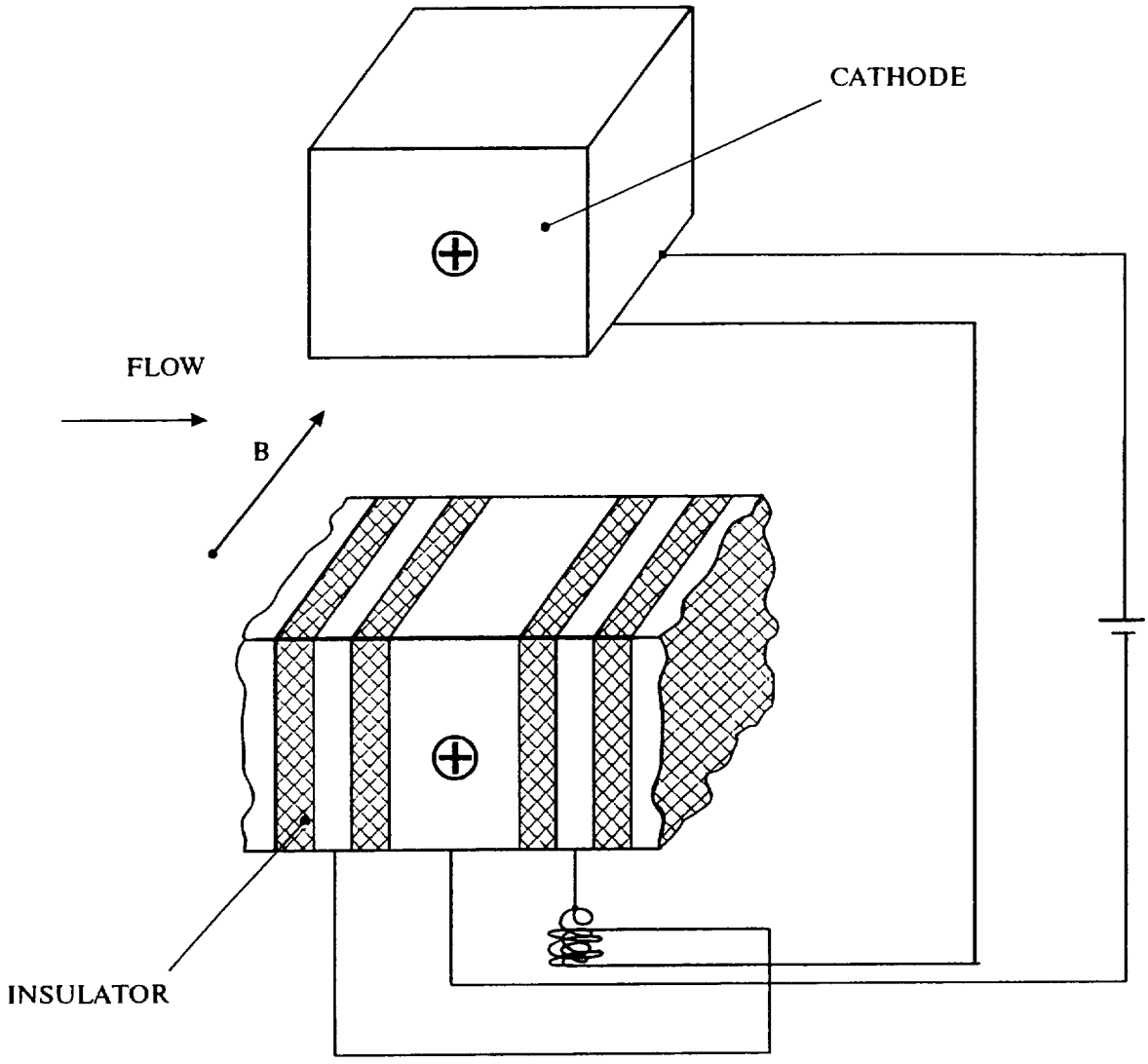

Fig.8. Schematic of device to provide microarc displacements along electrode

E.2.3 Summary

Although not clearly noted in the report the schematic of the experimental rig (Figure E.1- 3) shows the special electrode wall sections installed in the test chamber of the facility with a separate magnet coil for applying the magnetic field. Therefore, the test rig was separate from the MHD channel used for flow acceleration in the TsAGI facility.

The primary objective in these investigations was to investigate the mode of current transport from the hot-core flow through the boundary layer and near-wall sheath layer. The major concern is to understand how the transverse current flows from the hot-core and thermal-overshoot regions, through the cold sublayer, and into the electrodes.

The photographs taken inside the test channel clearly show the presence of a thin, highly luminescent layer close to the wall (Figure E.2- 7). This is caused in part by the intense, local Joule heating, and also by the thermal overshoot phenomenon described in Section E.2.1. The core Mach numbers in the test channel ranged from 2 to 4. At a Mach number of 3, using a recovery factor of 0.9, the estimated ratio Taw/T in Equation (E.2- 5) is 2.6, indicating the temperature within the boundary layer may be substantially higher than in the core. This is entirely consistent with the observation of the luminescent region close to the channel walls. Although the wall is not adiabatic, the regions near the insulator faces are close to adiabatic, and substantial elevation in static temperatures within the boundary layer would be expected.

The results of this experimental work may be summarized as follows:

1. In a high-Mach-number flow through MHD accelerators, the thermal recovery process near the electrode walls in combination with the Joule heating from the injected power can drive a thermal instability that results in the formation of microarcs in the sheath (near-wall) regions. Evidence for this comes from the photographs employing a high-speed framing camera. Estimated current in a typical microarc was 5-10 amps. The number of microarcs grows in rough proportion to the total current.
2. The experiments that employed quadruple segmented electrodes show the current transport in the sheath region on the anodes is primarily due to microarcs that have observed lifetimes in the range 10^{-5} to 0.01 seconds. The microarcs concentrate along the downstream edge near the electrode-insulator interface at the higher currents. At low currents (less than 5 A) the current distribution with respect to streamwise distance is nearly uniform. The microarcs concentrate on the downstream edge of the anodes and on the upstream edge of the cathodes. This arc concentration phenomenon leads to arc erosion of the anodes at the electrode-insulator interfaces. Arc erosion damage was clearly visible in the photograph Figure E.1- 6.
3. Microarcs were also observed at the cathode. In this case the current concentration was along the upstream electrode-insulator interface. The more severe erosion damage appeared to be along the anode as opposed to the cathode face.

4. The application of a magnetic field changes the current distribution on the anode considerably. At a field strength of 2.4 T, most of the current passed through the downstream segment. The report gives an exponential decay law for the current I_i on the i-th segment, in terms of the streamwise coordinate X_i:

$$I_i = I_{i0} \exp\left(-kB^2 X_i\right) \tag{E.2- 8}$$

Therefore, the current decay with an e-folding distance is inversely proportional to the square of the magnetic field.

5. The report indicates that intense Joule heating in the boundary layer can lead to localized gasdynamic flow disturbances including shocks. It is not clear if this is a theoretically predicted or observed result.

APPENDIX E, SECTION E.3

E.3 ENGO REPORT ON THE FEASIBILITY OF MHD FOR SIMULATING FLOWS OVER TRANSATMOSPHERIC VEHICLES

As noted in Appendix F, a major technical issue for MHD accelerators (and other gas acceleration technologies) is the problem of adding sufficient enthalpy to the flow, while maintaining the entropy within the bounds of the targeted flight envelope. Because most MHD accelerators (such as the one at TsAGI) operate close to local thermodynamic equilibrium (LTE), they must rely on thermal ionization of an alkali metal seed to achieve the requisite electrical conductivities. This generally implies that the accelerator must operate at temperatures above 2,500 K.

E.3.1 Overview

A major shortcoming of the present TsAGI facility is the arc heater operates at a maximum stilling chamber pressure of 20 atm and a temperature of about 3,800 K. Figure E.3- 1 shows a typical point on the H-S diagram for the present facility. This point represents the estimated conditions in the test section. Note that it lies well to the right of the target 2,000 pounds force per foot squared (lbf/ft^2) post-bowshock flight envelope, implying that either the either the test section Mach numbers or the test section pressures will be lower than the corresponding post-bowshock values. Because entropy scales inversely with the logarithm of pressure, the easiest way to improve this situation is to either increase the operating pressure of the arc heater (maintaining a fixed temperature), thus reducing the starting entropy; or increase the magnetic field, which will have the effect of increasing the slope of the H-S curves which describe the flow through the accelerator system.

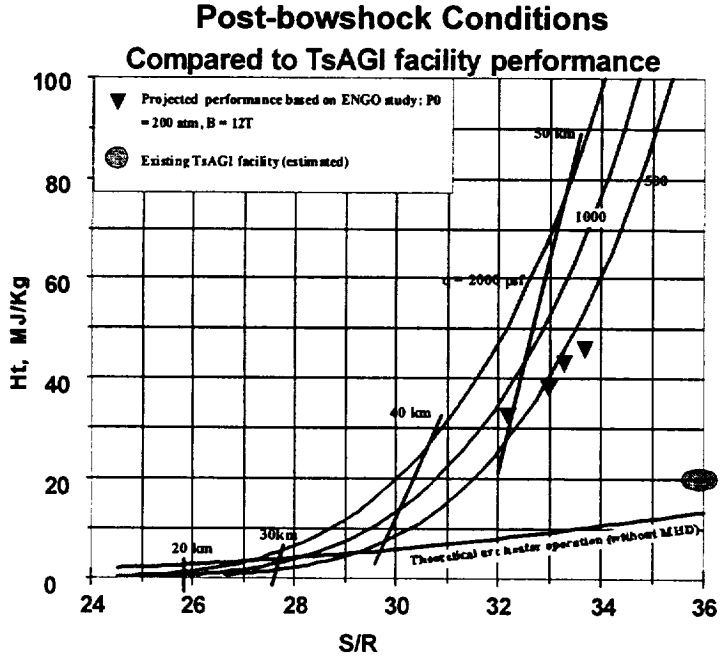

Figure E.3- 1. Post-bowshock conditions.

Both of these strategies were considered in the research described in Section E.3.2 that is the translated ENGO report. This report documents subcontract research conducted by ENGO during 1995-96. The report does not specifically address the TsAGI MHD facility, nor was it intended to develop recommendations for an upgraded Russian MHD test facility. The research is of a more general nature and addresses the question of what performance gains might be realized from a hypothetical "high performance" facility that was assumed to have a 12-T superconducting magnet and an arc heater operating at 200 atm stilling chamber pressure. The purpose of this research was to investigate the current transport across the sheath layers of both anode and cathode components. The goal was to gain understanding of microarcs that propagate across the sheath and boundary layer regions. Special diagnostic electrodes were constructed containing segmented faces. This structure enabled the currents through each electrode segment to be measured, thus providing a quantitative description of how current varies across a typical electrode in the streamwise direction.

A one-dimensional (1-D) computational code was used to model all phases of the problem, including the gas dynamics, the MHD interaction, and the chemical kinetics. The chemistry model included five equations for the chemistry between oxygen (O_2) and nitrogen (N_2) as well as rate equations for ionization, reattachment, and dissociation processes. Vibrational excitation and relaxation appears to have been be simulated only for the lower vibrational states. As noted in the report, the code was run for a range of stagnation conditions, seed fractions, and magnetic fields. It was assumed the seed material was K in all cases. The findings are discussed in the report and commented upon in the Summary (Section E.3.3).

A second parallel study was conducted on the question of the effects of alkali metal seed on scramjet combustion processes. This study relied on a separate chemical kinetics code.

Section 6 of the ENGO report addresses the question of to what degree an alkali metal seed could change the flow chemistry and kinetics through a scramjet combustion chamber. The conclusions are given in the report and are summarized in Section E.3.2. A parallel, yet separately funded effort was conducted by Ohio State University (OSU) and is discussed in Section C.3. These reports are summarized in Section E.3.3.

E.3.2 ENGO Report on the Feasibility of Reproducing Flight Conditions for Transatmospheric Vehicles in Hypersonic MHD-Gas Acceleration Wind Tunnels

(presented in pp. E.3-3 through E.3-13)

ENERGYGO LTD

ON THE POSSIBILITY OF REPRODUCING FLIGHT CONDITIONS FOR TRANSATMOSPERIC VEHICLES IN HYPERSONIC MHD-GAS ACCELERERATION WIND TUNNELS

Final Report

London/Moscow

1996

ON THE POSSIBILITY OF REPRODUCING FLIGHT CONDITIONS FOR TRANSATMOSPHERIC VEHICLES IN HYPERSONIC MHD-GAS ACCELERATION WIND TUNNELS

Abstract

It is universally accepted that the general line of developing aerospace engineering is the construction of a transatmospheric vehicle (TAV) whose flight trajectory features high values of aerodynamic loads and heat fluxes. Even more accute problem is the development and tests of engines for such vehicles. That is why the problem of constructing test rigs for reproducing flight conditions and for verifying computation codes used to calculate flows over the vehicle and processes proceeding in the engines is very urgent.

The report analyzes possible schemes of aerodynamic rigs intended for reproducing gas dynamic parameters (velocity, density, pressure, and temperature) and chemical air composition as applied to the TAV trajectory with the indication of required stagnation parameters (P_0,T_0). Based on the calculation of physico-chemical processes taking place in nozzles of classical facilities it is inferred that the chemical air composition differs noticeably from the natural air composiiton even in solving the problem of producing and retaining the gas in the plenum chamber at ultrahigh temperatures and pressures ($T_0 \geq 7000$K, $P_0 \geq 4000$ atm).

The analysis carried out reveals a distinct advantage of MHD-gas acceleration facilities in solving the stated problem. A set of equations of magnetogasdynamics and multitemperature physico-chemical kinetics which underlie the computation program is presented. The channels of energy transport from the electromagnetic field to the gas at different gas densities are considered. The program was compiled using the experimental data obtained in the TsAGI MHD-gas acceleration hypersonic wind tunnel.

The report presents the calculated data on gas acceleration regimes in a wide spectrum of initial conditions and electrodynamic parameters ($P_0 = 2$–200 atm, $T_0 = 3000$–5000K, K seed fractions are 0.25%–2%, magnetic field induction is 2.4–12 T, current density is 20–200 A/cm^2, channel angles are 0–1.5° etc).

The altitude and velocity ranges are indicated which can be attained in different facility operation conditions. The consideration of nonequilibrium physico-chemical processes in the MHD-channel and in the secondary nozzle makes it possible to state that the nonequilibrium effects facilitate considerably the reproduction of a natural chemical air composition and a static temperature in the facility test section. Other parameters of the facility are given at which it is possible to provide an essentially exact reproduction of gasdynamic parameters in the scramjet combustion chamber in direct-connect mode. The results of the analysis are compared with similar data obtained earlier at UTSI and AEDC.

The influence of alkali seeds on the induction time and hydrogen burning process in the scramjet combustion chamber is evaluated.

Finally, possible technical approaches to the realization of calculated versions of MHD-accelerators are analyzed.

1. Introduction

Reproduction of flight conditions on aerodynamic test rigs is a most complicated challenge of top priority among the problems concerning the construction of transatmospheric vehicles (TAV) which is of particular importance for development of TAV engines. These problems are analyzed in papers[1-5] with the consideration of capabilities of available test rigs to test TAV components.

The work[5] gives a detailed analysis and a general approach to conducting similar tests. It is stated here that in order to obtain most comprehensive data it is necessary to satisfy at least five conditions:

1) correct correlation of flow velocities and real flight;
2) adequacy of thermodynamic gas properties;
3) scale correlation;
4) correlation of characteristic test times, and
5) correlation of test and predicted data.

For aerodynamic characteristics of the vehicle to be estimated it suffices that the model scale be 1–10%, while for studying the operation of a hypersonic engine diffusor the scale must be 5–25%. As for its combustion chamber tested in the direct connection regime, a complete scale correlation is obligatory both in terms of its area and length. The 5–20% – scale is sufficient for testing the engine nozzle integrated with the airframe in the aerospace vehicle.

The aerodynamic characteristics of the airframe can be obtained in wind tunnels using a perfect gas with the application of respective corrections taking account of real gas properties. It concerns also the investigation of characteristics of the hypersonic diffusor and airframe-induced compression wave systems at its entry.

Most complicated in this context is the reproduction of conditions in the scramjet combustion chamber because in this case high flow stagnation parameters and full engine scale should be reproduced.

The TAV flight conditions governed by the vehicle trajectory are such that the velocity increases from supersonic values to orbital ones in a relatively small altitude range of 25–40 km which causes considerable heat fluxes and strong loads on the vehicle components. It is a common practice to consider the climb trajectories with a constant dynamic pressure $q = \rho u^2/2$. In the literature, the dynamic pressure values are different to be between q = 1 atm (or ~2000 PSF) to 0.05 atm (~100 PSF).

Gas dynamic stagnation parameters for the total (pressure P_0 and the total temperature T_0 (enthalpy H_0)) are derived, as a rule, from the condition $H_0 = u^2/2 + h_{st}$ and S = const when u becomes zero.

Fig.1 shows respective values of temperatures T_0 and pressures P_0 as a function of the flight trajectory. Similar figures are contained almost in all papers devoted to this problem.

The stagnation enthalpy values are constant for a specified flight velocity, while the stagnation pressure P_0 depends significantly on the flight reproduction coditions.

The greatest values of P_0 correspond to the reproduction of free flight conditions, slightly smaller values to the region behind the oblique shock near the body and considerably smaller values refer to the scramjet combustion chamber. The gas dynamic conditions in the scramjet combustion chamber are given in table (1) for q = 0.75 atm (1500PSF) depending on free flight Mach number. Respective pressures for smaller dynamic pressure values will be smaller proportionally, but in this case it is necessary to account for the dependence of temperature on the pressure at constant enthalpy. Here M is the flight Mach number, M_2 is the combustion chamber flow Mach number, P_2, T_2, u_2 are, respectively, static pressure, temperature and velocity. P_{0_2}, T_{0_2} are the stagnation pressure and temperature to be reproduced in the direct connection regime [6].

Table 1

M_∞	5	8	10	12	15	20
M_2	1.75	3	3.75	4.4	5.2	6.1
P_2 [bar]	2.5	1.8	1.5	1.15	0.8	0.5
T_2 [K]	800	1100	1400	1500	2000	2250
u_2 [m/s]	978	1900	2720	3270	4480	5500
P_{0_2} [bar]	14	80	100	700	1500	3000
T_{0_2} [K]	1200	2000	3500	5000	7200	9000

Respective stagnation temperatures and pressures are also given in Fig. 1.

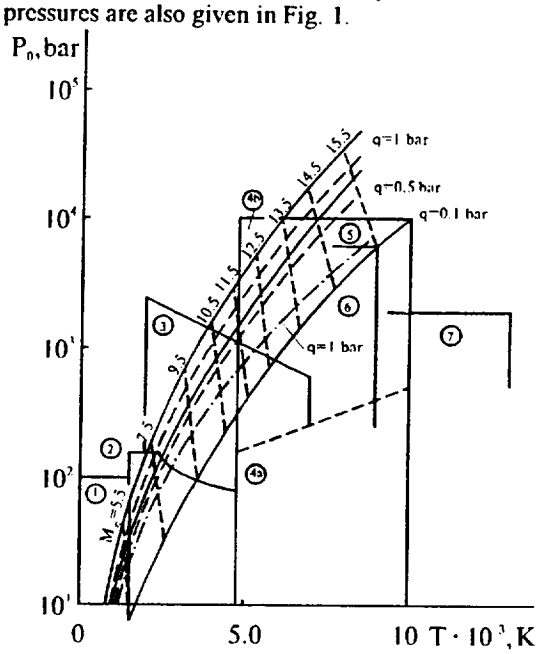

—— TAV flight trajectory based on free-flow parameters

— — - TAV flight trajectory based on flow patameters before diffusor

—·— TAV flight trajectory based on flow parameters in combustion chamber (direct connection), q=1 bar

1 Ts-16VK TsIAM
2 Arc-wind tunnel stand
3 TsAGI hot-shot wind tunnel
4a TsAGI MHD-facility
4b MHD facility (project)
5 Stalker tube (AEDC)
6 Caltex
7 HEG

Fig.1. Stagnation parameters in wind tunnel plenum chamber required for reproduction of TAV flight conditions for different M and modelling zones

The most severe conditions corresponding to the flight velocity, i.e., $M > 12$ ($P_0 > 1500$ atm, $T_0 > 7000$K) can be attained nowadays only in hot-shot facilities (operation time is 2–10 ms). The largest of them are as follows:

1. The piston shock wind tunnel of AEDC[7], previously the ballistic range facility, is used nowadays as a Stalker tube. The acceleration of an expandable piston is provided by gunpowder explosion products. The maximum stagnation parameters are as follows: stagnation enthalpy is 20 mJ/kg, $T_0 \sim 10000$K, $P_0 = 10000$ atm, operation time is 2 ms, nozzle exit diameter is 0.457 m.
2. The piston wind tunnel Caltex[8] (California Institute of Technology). Its parameters are close to those of the wind tunnel of AEDC, the nozzle exit diameter being 0.314 m.
3. The piston wind tunnel HEG, Germany[9]. It is a largest wind tunnel in the world. Its parameters are: $P_0 = 2000$ atm, $T_0 = 13000$K, nozzle exit diameter D = 0.9 m.
4. The facilities with pistons Y-7, Y-11 of TsNIIMASh, Russie[10]. The nozzle exit diameter is 0.4–0.8 m, Mach number M = 6–9. These wind tunnels refer to facilities of adiabatic compression.
5. The expanding wind tunnel GASL[11]. A gas portion being compressed and accelerated in a shock wave expands to vacuum. As a result, it is possible to attain velocities of 5–9 km/s. The nozzle exit diameter is 150 mm, the length of a stationary flow region is ~ 4–10 m.

The most essential shortcomings of the above-listed facilities are a small operation time insufficient for investigating the development of processes in the combustion chamber when its size is ~ 10 m and relatively small exit nozzle section sizes at small

Mach numbers ($M_2 < 6$) required to reproduce gas dynamic parameters T_{st}, P_{st}, M_{st}.

The test time can be increased considerably by applying facilities in which the energy is supplied to the flow behind the nozzle throat. For example, at relatively small static temperatures the energy supply can be accomplished by heating the moving gas by a high-frequency electromagnetic field or by providing the absorption of the laser radiation by the gas. Such heating results, however, in an intense decrease in the total pressure. Therefore, it is necessary to attain high initial stagnation pressures in the plenum chamber $P_0 > 10000$ atm. In MHD-gas acceleration facilities, the total pressure drop can be compensated for by the volume Lorentz force acting on the flow. The positive experience in constructing and operating similar facilities has been gained both in Russia and in the USA[12-13].

The stagnation pressure level in available facilities is, however, insufficient at present for testing scramjet combustion chambers.

The efforts at constructing a MHD-gas acceleration wind tunnel[5] are also considered as most perspective. The paper[2] contains the calculated parameters of such a facility based on the numerical analysis of equations for one-dimensional gas motion in the MHD-channel in which the gas is assumed to be in thermodynamic equilibrium.

In the present paper, a detailed analysis is performed with the consideration of possible deviation from the thermodynamic equilibrium (chemical reactions and vibrational nonequilibrium are taken into account), as well as possible influence of the difference in the chemical gas composition from the real one on the combustion processes in the scramjet combustion chamber is estimated.

A well-known hypersonic MHD-gas acceleration is chosen for the analysis. The wind tunnel consists of an arc heater, a primary supersonic nozzle, a MHD-channel with sectionized electrodes (energized by independent sources), a magnetic system, a secondary nozzle, a test section, supersonic and subsonic diffusors, a cooler, an exhaust system. To provide electric conduction of the gas, some K seeds are injected. The MHD-channel operates in the regime of the Faraday channel. All the facility components are well studied except for the MHD-channel operation. The next section is devoted to the gas acceleration processes in the MHD channel.

2. Sets of equations

The MHD-accelerator was calculated using the following set of one-dimensional equations of gas dynamics:

$$\frac{d}{dx}\left(\rho H_0 u F\right) = \frac{V_k I_k}{S_k} - St\,\rho\left(H_0 - H_w\right) u \Pi$$

$$\frac{d}{dx}\left[\left(P + \rho u^2\right)F\right] = -\frac{C_f}{2}\rho u^2 \Pi + \frac{I_k B h_k}{S_k} + P\frac{dF}{dx}$$

$$\frac{d}{dx}\left(\rho u F\right) = 0 \qquad (1)$$

$$H_0 = \frac{u^2}{2} + H \qquad H = \sum_{i=1}^{6}\frac{\rho_i}{\rho} H_i$$

$$H_i = RT\frac{\Pi_i}{m_i} + \frac{E_{vi}}{m_i} + E_i$$

$$\Pi_i = \frac{7}{2} \quad \text{for } i = 1,3; \qquad \Pi_i = \frac{5}{2} \quad \text{for } i = 4,6.$$

Eqs.1 were solved simultaneously with the equations of vibrational and chemical kinetics [14]:

$$\frac{1}{F}\frac{d}{dx}\left(\frac{E_{v1}}{m_1}\rho_1 uF\right) = \beta\frac{V_k I_k - UBh_k}{S_k F} + z_{1vT} + z_{1vv} + z_{1chem}$$

$$\frac{1}{F}\frac{d}{dx}\left(\frac{E_{v2}}{m_2}\rho_2 uF\right) = z_{2vT} + z_{2vv} + z_{2chem} \qquad (2)$$

$$\frac{1}{F}\frac{d}{dx}\left(\frac{E_{v3}}{m_3}\rho_3 uF\right) = z_{3vT} + z_{3vv} + z_{3chem}$$

Coefficient β in Eqs.2 represents the portion of electron heat energy transferred at collisions to excitation of vibrational levels of N_2 molecules. This parameter was varied within the range of $0 < \beta < 1$.

The equations describing nonequilibrium kinetics of chemical processes account for the following reactions:

$$\begin{aligned} O_2 + M &= O + O + M \\ N_2 + M &= N + N + M \\ NO + M &= N + O + M \\ N + O_2 &= NO + O \\ O + N_2 &= NO + N \end{aligned} \qquad (3)$$

where M is any particle of the i-th species.

The rates of transferring vibration energy at particle collisions required to calculate values of z_i, as well a chemical reaction rates were the same as in paper[14].

The voltage drop V_k was calculated using the relation

$$V_k = \frac{I_k h_k B}{F_k e n_e}\left(\frac{1}{\beta_H a_k} + 1\right) + uBh_k,$$

where the constant a_k depends on the electrode and channel geometry: $a_k \sim S_k/h_k$ at constant conduction and moderate values of $\beta_H \sim 1$[14]. The electron concentration n_e at a specified mole K concentration was calculated in a thermodynamical equilibrium state at $T_e = T_v$ (see Supplement).

Eq.(4) does not include the electrode voltage drops. It was suggested that the energy released in the electrode layers was absorbed by the electrodes.

In accordance with the data of paper[14], the friction coefficient C_f is taken as $C_f = 5 \cdot 10^{-3}$, and $St \sim C_f/2$. The overestimated values of the coefficients C_f and St are justified by the fact that the current concentration at the electrode edges gives rise to a local gas overheating which can be followed by appearance of shocks, as well as by an increased heat transfer to the electrode walls. More correct data on the coefficients C_f and St in the MHD-channel conditions can be obtained only experimentally.

3. Calculation results

The calculations were accomplished for the following channel geometry: the entry channel section is a square with a side of b, the electrode channel walls are at angle α, the side insulating walls remains parallel, the channel section area F increases along the x-axis at a constant derivative dF/dx = const.

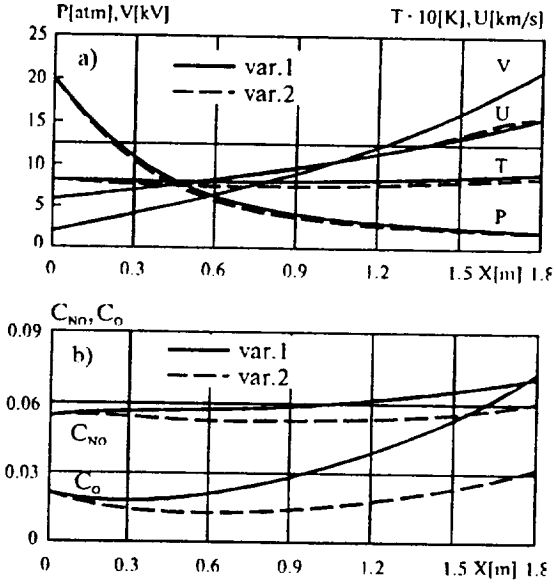

$P_0 = 200$ atm, $T_0 = 4700$K

Fig.2(a,b).

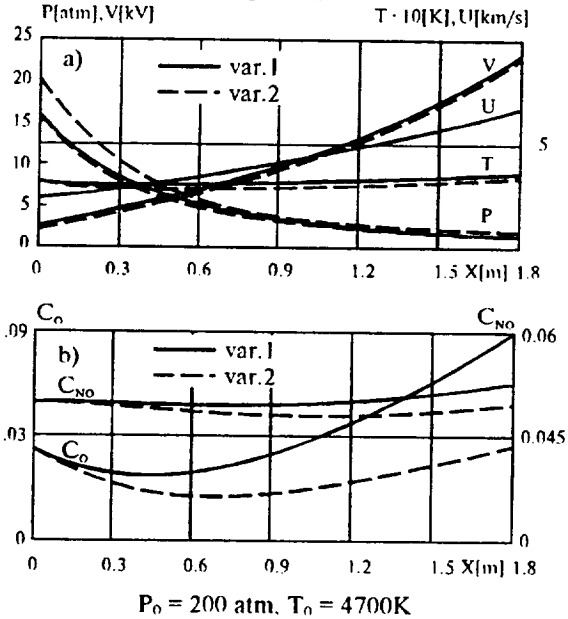

$P_0 = 200$ atm, $T_0 = 4700$K

Fig.3(a,b).

Figs. 2a–3b, as well as tables (2–5) contain the data calculated at the following parameters:

$F_1 = 44 \cdot 10^{-4}$ m^2, $\alpha = 6.8°$, $dF/dx = 7.87 \cdot 10^{-3}$ m, B = 12 T, j = 33 A/cm^2, $L_2 = 0.6$ m.

The version 1 in the figures refers to the condition C_k=0.5%, a_1=0.66, and the version 2 to C_k = 1%, a_1 = 0.15.

The stagnation pressure and temperature at the channel entry (P_0 = 200 atm, T_0 = 4700K) are chosen the same as in work[2]. They seem to correspond to maximum parameter values attained nowadays in wind tunnels with arc heaters at gas mass flow rates up to 20 kg/s.

The chemical gas composition and vibrational temperatures at the channel entry correspond to conditions of thermochemical equilibrium at P_1 and T_1. The magnetic induction B is assumed to be B = 12 T similar to that indicated in work[2].

At B = 12 T and current density ~33 A/cm^2, static pressures at the channel entry P_1 = 16–20 atm prove to be optimum so as to obtain the greatest flow velocities at the least static temperatures T.

As follows from the data given above, the influence of an additional gas heating due to a nonuniform current distribution at the electrode walls represented by the parameter $a_k(x) \sim S_k/h_k(x) \sim 1/F(x)$, contributes to an increase in the static channel temperature. According to the data given in tables (2)–(5), this influence can be compensated for by increased K seed concentration.

P_1 = 20 atm, a_1 = 0.66, C_k = 1% Table 2

L, m	P_L, kPa	T_L, K	U_L, m/s	P_2, kPa	T_2, K	U_2, m/s	C_O, %	C_{NO}, %	F_2, sm^2
1.1	356	3150	4241	83.1	2265	4502	2.23	5.35	380
1.5	246	3306	5224	52.3	2312	5460	3.43	5.70	509
1.7	209	3400	5784	51.0	2448	5990	4.28	5.94	510

P_1 = 20 atm, a_1 = 0.15, C_k = 0.5% Table 3

L, m	P_L, kPa	T_L, K	U_L, m/s	P_2, kPa	T_2, K	U_2, m/s	C_O, %	C_{NO}, %	F_2, sm^2
1.1	345	3058	4235	82.9	2208	4483	1.68	5.25	370
1.5	238	3211	5211	53.0	2262	5434	2.43	5.48	491
1.7	203	3309	5768	50.1	2380	5965	2.99	5.69	506

P_1 = 16 atm, a_1 = 0.15, C_k = 0.5% Table 4

L, m	P_L, kPa	T_L, K	U_L, m/s	P_2, kPa	T_2, K	U_2, m/s	C_O, %	C_{NO}, %	F_2, sm^2
1.0	306	3064	4314	82.1	2267	4542	1.70	5.15	321
1.35	214	3213	5265	53.0	2317	5473	2.35	5.41	426
1.55	181	3320	5880	51.4	2468	6060	2.91	5.63	420

P_1 = 16 atm, a_1 = 0.66, C_k = 1% Table 5

L, m	P_L, kPa	T_L, K	U_L, m/s	P_2, kPa	T_2, K	U_2, m/s	C_O, %	C_{NO}, %	F_2, sm^2
0.95	330	3150	4200	81.2	2290	4455	2.24	5.36	340
1.35	224	3322	5276	53.1	2383	5496	3.44	5.72	436
1.55	187	3415	5890	51.2	2523	6080	4.36	5.97	433

As might be expected, the channel flow turns out to be in equilibrium in terms of vibrational molecule degrees of freedom (vibrational temperatures differ from the static temperature by no more than 10K at β = 1). The chemical equilibrium is not, however, established, therefore, the concentrations of O atoms and NO molecules at the channel exit may be smaller than those in equilibrium (Figs. 2b, 3b). As for the O atoms, the difference is 1.5–2 times.

4. Application to modelling problems

Tables (2)–(5) present the parameters at the MHD-channel exit and the secondary nozzle exit section areas at which the conditions in the direct connection regime are the closest to those at the scramjet entry. At the chosen length of the secondary nozzle L_2 = 0.6 m, the flow in it proves to be similar to a frozen one in terms of chemical composition, while in terms of vibrational degrees of freedom the gas state is close to an equilibrium one.

When the flow accelerated in the MHD-channel expands to full-scale static temperatures of ~250K, it is possible to obtain full-scale Mach numbers corresponding to a free flight at altitudes of ~65–75 km.

The resulting flow differs very slightly from a full-scale one by the presence of NO molecules and atomic oxygen. In this case, the gas density is such

that the chemical processes in flows over bodies may be considered to be frozen.

The secondary nozzle exit section sizes for the above-outlined accelerator sizes are 7×7 m^2.

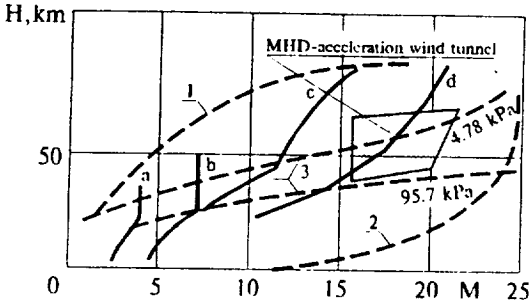

1 Missile start trajectory
2 Atmospheric entry trajectory for ballistic heads
3 Flight corridor for orbiter with scramjet
a) Continuous wind tunnel
b) Intermittent wind tunnel
c) Arc heating wind tunnel
d) Hot-shot wind tunnel

Fig.4. Regions of flight trajectory modelling in wind tunnels of different classes

Fig. 4 taken from work[5], illustrates the region of parameters which can be reproduced using the MHD-facility version given above. When the facility is used in the direct connection regime, considerable part of TAV flight trajectories are overlapped at $M > 15$.

5. Comparison with other methods of obtaining flows

At present, consideration is also given to other methods of obtaining flows to study flows in scramjet. Among them are the method of heating a supersonic flow having high stagnation pressures[4], and the method of adiabatic gas heating to high stagnation parameters using a heavy piston[10] or a light piston to heat the pushing gas in a shock wind tunnel[7].

These methods also disable of providing a gas adequate in terms of chemical composition which may be illustrated by the following examples.

Let us consider the gas expansion in a supersonic nozzle from some initial values of P_1, T_1 to $P_2 = 0.8$ atm, $T_2 = 2000$K, $u_2 \sim 4500$ m/s with due consideration of nonequilibrium chemical kinetics.

The flow velocity u_1 is derived from the condition

$$h_1(P_1, T_1) + U_1^2/2 = h_2(P_2, T_2) + U_2^2/2$$

As examples, two conditions will be considered:

1) $P_1 = 20$ atm, $T_1 = 3600$K
2) $P_1 = 80$ atm, $T_1 = 4650$K

The first condition corresponds to the accelerator exit, and the second one to the pressure higher than the combustion chamber pressure by a factor of 10^2.

Let the initial chemical composition in section 1 be in thermodynamic equilibrium.

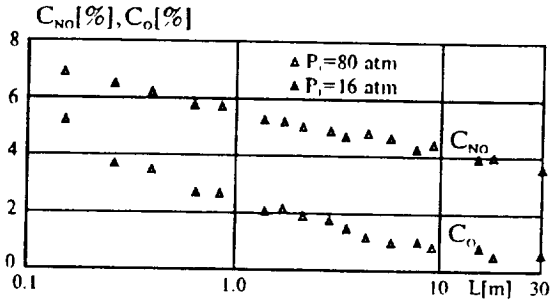

Fig.5.

Fig.5 presents concentrations of NO molecules and O atoms as a function of the length of the nozzle part providing the gas transition from states P_1, T_1, u_1 to states P_2, T_2, u_2. As follows from these dependences, even for nozzles with a very small expansion ratio and having the length of several tens of meters it is impossible to attain the chemical gas composition close to an equilibrium one.

6. Influence of nonequilibrium components O, NO and alkali seeds on hydrogen burning processes

As shown in tables (2)–(5), the MHD-acceleration wind tunnel flow is characterized by an increased concentration of atomic oxygen O and of molecules of NO. Besides, it contains up to 1% of K seeds.

In order to evaluate the influence of these factors on the processes proceeding in the scramjet, a numerical analysis has been carried to consider the following reactions[10]:

(1) $H_2O + H = OH + H$
(2) $O_2 + H = OH + O$
(3) $H_2 + O = OH + H$
(4) $H_2 + O_2 = OH + OH$
(5) $H_2O + O = OH + OH$
(6) $H_2 + M = H + H + M$
(7) $O_2 + M = O + O + M$
(8) $H_2O + M = OH + H + M$
(9) $OH + M = H + O + M$
(10) $H_2O + O = H + HO_2$
(11) $H_2 + O_2 = H + HO_2$
(12) $H_2O + O_2 = OH + HO_2$
(13) $H_2O + OH = H_2 + HO_2$
(14) $OH + OH = H + HO_2$
(15) $OH + O_2 = O + HO_2$
(16) $HO_2 + M = H + O_2 + M$

(17) $H + H_2O_2 = H_2O + OH$
(18) $H + H_2O_2 = HO_2 + H_2$
(19) $HO_2 + HO_2 = H_2O_2 + O_2$
(20) $HO_2 + H_2O = H_2O_2 + OH$
(21) $OH + HO_2 = H_2O_2 + O$
(22) $H_2O + O_2 = H_2O_2 + O$
(23) $H_2O_2 + M = OH + OH + M$
(24) $O + O_3 = O_2 + O_2$
(25) $OH + O_3 = HO_2 + O_2$
(26) $HO_2 + O_3 = OH + O_2 + O_2$
(27) $H + O_3 = OH + O_2$
(28) $O_3 + M = O_2 + O + M$
(29) $O + N_2 = N + NO$
(30) $N_2 + M = N + N + M$
(31) $NO + M = N + O + M$
(32) $O + NO = N + O_2$
(33) $H + NO = N + OH$
(34) $OH + NO = H + NO_2$
(35) $OH + NO_2 = NO + HO_2$
(36) $H_2 + NO_2 = H + HNO_2$
(37) $O_2 + NO = O + NO_2$
(38) $HNO_2 + M = NO + OH + M$
(39) $NO_2 + M = NO + O + M$
(40) $NO_2 + N = NO + NO$
(41) $O_3 + NO = NO_2 + O_2$
(42) $HNO + M = H + NO + M$
(43) $OH + NO_2 + M = HNO_3 + M$

The agreement of the calculation results with the data of other authors employing different combinations of reactions from (1) to (43) was verified by test calculations with the application of
a) reactions (1) – (9);
b) reactions (1) – (23);
c) reactions (1) – (39) and
d) reactions (1) – (43).

The induction length was estimated by attaining a maximum in the distribution of H concentration along the combustion chamber length. The calculation using all four schemes for chosen conditions led to essentially the same data both on the induction length and the gas dynamic parameters.

The reactions (7), (29)–(43) were used for check calculations of NO concentrations in a heated air to be compared with available experimental and calculated data which confirmed the correctness of applying this scheme.

Fig.6 shows the distribution of mole fraction of atomic hydrogen in a flow having the initial parameters corresponding to parameters at the secondary nozzle exit (see table 4): P = 82 kPa, T = 2267K, u = 4542 m/s for two cases:
1) the initial gas composition is a stoihiometric air-oxygen mixture,
2) air containing O atoms to amount of 1.7% (see table 2) and NO molecules (5.15%) and the same mass fraction of H_2 as in the case 1).

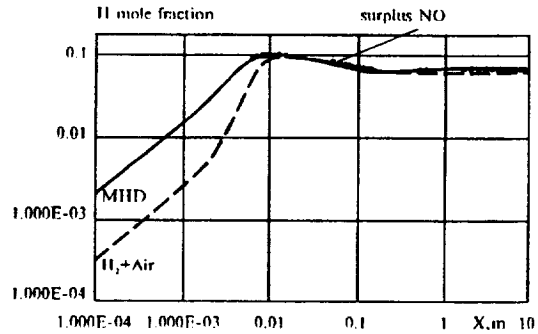

Fig.6 P = 82000 Pa, T = 2267K, U = 4542 m/s

The calculations were performed using a set of kinetic equations (1) to (43). As is seen in Fig.6, an earlier concentration rise in H atoms (solid line) is exhibited in the MHD-flow as compared with a real flow (dashed line). A maximum value of the mole fraction of H atoms is achieved, however, on the same length for these two cases. The doted line indicates the distribution of the mole fraction of H atoms when hydrogen burns in air featuring an increased amount of nitric oxide C_{NO} = 10%.

It is obvious that even a similar excess of NO in a free-stream flow does not exert an appreciable influence on the induction time, but it changes somewhat the burning length. The variation in the specific mass flow rate $\Delta\rho u$, as compared with that of a real air, is not in excess of $\Delta(\rho u)/\rho u < 0.1\%$. Respective variations in the specific mass flow rate for the MHD-flow are still smaller $(\Delta\rho u/\rho u)_{MGD} < 0.02\%$.

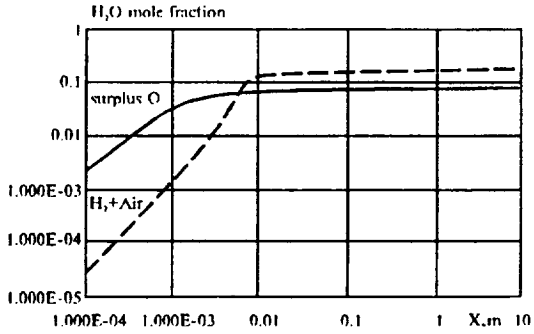

Fig.7 P = 82000 Pa, T = 2267K, U = 4542 m/s.

Fig.7 depicts the function of the mole fraction of water vapors for hydrogen burning in a real air (doted line) and in air characterized by essentially complete dissociation of oxygen ($C_{O_2} = 9 \cdot 10^{-3}$, $C_O = 2.12 \cdot 10^{-1}$, solid line). The initial parameters are the same as in Fig.6. In this case, a notable difference is noted not only in induction times but also in equilibrium fraction of water vapors, as well as in flow parameters P, ρ, T, u. The variation in the specific mass flow rate with respect to that of real air reaches $(\Delta\rho u/\rho u)_O \sim 12\%$.

The seed influence on the burning process was investigated by an example of Na. Its choice as a seed to be investigated (instead of K) is explained by more comprehensive literature data of previous studies. The intermediary position of Na among alkali metals allows an assumption concerning similarity of physico-chemical processes for K, as well.

The composition of hydrocarbon fuel burning products in the presence of alkali seeds was investigated experimentally earlier in view of the development of MHD-generators, powerful lasers, plasma engines etc.

As indicated in works[15]-[18], burning of hydrocarbon fuels in the presence of Na seeds proceeds with the following dominant reactions

(44) $Na + H_2O = NaOH + H$

(45) $Na + O_2 + M = NaO_2 + M$

(46) $Na + OH + M = NaOH + M$

At present, two approaches are applied to the description of kinetic processes for Na atoms. They are the scheme of Jensen and Jones[19,20], as well as the scheme of Hynes at all[21]. A critical analysis of these two approaches to the description of Na kinetics in flames is given in paper[22], where it was inferred that concentrations of neutral flame components were independent of seeds. This finding allowed the authors to exclude reactions with the participation of Na compounds to calculate radicals in the flame of Bunzen burner.

In order to include the influence of Na on oxygen burning, we considered, apart from reactions (44) to (46), the following reactions:

(47) $NaO_2 + H = NaO + OH$

(48) $NaOH + OH = NaO + H_2O$

(49) $NaO_2 + OH = NaOH + O_2$

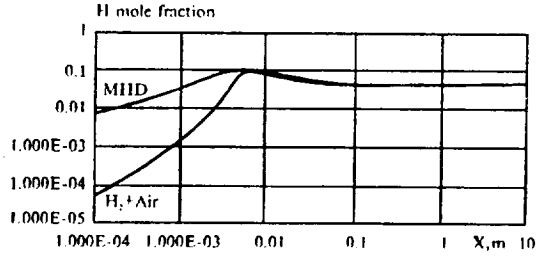

Fig.8 M = 16, P_0 = 21 atm, T_0 = 3400K, B = 7T.

The rate constants for these reactions were taken from works[19-21]. In the calculations of the influence of Na on burning of H_2, the set of reactions (44) to (49) was used simultaneously with the set of (1) to (9). The calculations revealed that the influence of Na on burning processes of H_2 was insignificant (Fig.8), and the function of concentration of radical H $C_H = C_H(x)$ almost coincided with the curve in Fig.6 referring to the flow without Na, which confirms the findings of paper[22].

For the seed influence to be analyzed more completely, it is also necessary to consider plasmachemical reactions in hydrogen burning process, because in this case the seed will supply a considerable amount of electrons and ions. It is suggested this investigation to be conducted later on.

Supplement

The expression for mean energy lost by an electron at one collision with gas particles can be presented as follows:

$$\frac{j^2}{\sigma n_e \tau_e^{-1}} = \frac{j^2 m_e}{n_e^2 e^2} = \frac{3}{2} k \frac{\Sigma_g (T_e - T_g) + \Sigma_v (T_e - T_v) + \Sigma_* (T_e - T_*)}{\Sigma} \quad (A1)$$

where the quantities Σ_g/Σ, Σ_v/Σ, Σ_*/Σ signify the energy part transferred, respectively, to rotational degrees of freedom, molecule vibrations and to excitation of electron states of atoms and molecules, being the Σ – total transport section.

The right-hand side of the expression (A1) can be given as follows:

$$\frac{3}{2} k \frac{(\Sigma_g - \Sigma_v)(T_e - T_v) + \Sigma_g (T_v - T_g) + \Sigma_* (T_e - T_*)}{\Sigma} \quad (A2)$$

The quantity Σ_g can be estimated using the data taken from work[23] on microwave measurements of the time required to ransfer the electron energy to nitrogen molecules at $T < 800K$ when excited vibrations can be neglected and the quantity Σ_v is evaluated from the excitation sections for vibrations of $N_2\sigma(\varepsilon)$ averaged over the Maxwellian distribution of electron energies ε.

Similar estimates made at T = 3000K yield the following values: $\Sigma_g/\Sigma \sim 10^{-3}$, $\Sigma_v/\Sigma \sim 5 \cdot 10^{-4}$.

Considering that $T_e > T_v > T_g$, $T_e > T_*$, we obtain the following estimate: at $j = 33$ A/cm^2, T_g=3000K, $n_e = 2 \cdot 10^{15}$ cm^{-3}.

$$T_e - T_v < \frac{j^2 m_e}{\frac{3}{2} n_e^2 e^2 k \cdot 1.5 \cdot 10^{-3}} \equiv 30K$$

Conclusions

1. At the present time, there are no hypersonic wind tunnels in which it would be possible to reproduce flight conditions at M = 12–20 required to optimize scramjet. A MHD-gas

acceleration wind tunnel is a most promising facility for solving this problem.

2. The acceleration process in the Faraday-type MHD-channel for a thermodynamically nonequilibrium gas model in the presence of alkali seed of K has been analyzed. It is shown that in applying available arc gas heaters at $P_0 = 200$ atm and $T_0 = 4700$K and magnetic fields B = 12 T it is possible to reproduce almost exactly gas dynamic parameters at the scramjet combustion chamber entry within the flight Mach numbers of 15–20 (direct connection regime), the atomic oxygen concentration not exceeding in this case ~ 2%, and NO ~5%.

   For gas expanding in the secondary nozzle up to values of static temperatures corresponding to free flight conditions, the exact flight reproduction can be attained at H = 65–70 km (u = 7.5 km/s, M=20–25).

3. The influence of deviations of the chemical composition of air from a real one due to the presence of NO, atomic oxygen, alkali seeds on hydrogen burning processes has been analyzed. It is revealed that the excess of $\alpha_{NO} = 10\%$ in the oxygen-hydrogen mixture does not vary appreciably the induction time and changes only slightly the specific mass flow rate at the combustion chamber exit ($(\Delta\rho u)/\rho u \sim -0.1\%$).

A small excess of atomic oxygen (C_O~2%) changes the initial stage of burning process, while the induction time, burning time and gas dynamic parameters vary inconsiderably. The concentration of atomic oxygen (C_O~20%) leads to a notable variation in both the initial burning stage and mole fractions of combustion products. Variations in the specific mass flow rate at the combustion chamber exit can attain 12% as compared with a real air.

The presence of seed atoms in the MHD-flow does not change reaction rates and does not exert an appreciable influence on the induction time and gas dynamic parameters in the combustion chamber. For a fundamental conclusion on the seed influence to be made, plasma-chemical reactions should be considered and the results obtained should be verified experimentally.

Nomenclature

B – magnetic induction
b – channel width
C_f – channel drag coefficient
C_i – mole concentration of i-th species particles
E_v – vibration energy
Evi – vibration energy per i-th species particle
E_i generation energy for i-th component
e – electron charge
F – channel cross section area
H – enthalpy
h – channel height
I – current
j – current density
k – Boltzmann constant
L – length
M – Mach number
m – molecular weight
m_e – electron mass
n – particle concentration, $1/m^3$
P – pressure
R – gas constant
S – electrode sectioning step
T – temperature
u – velocity
x – coordinate along the flow
β_H – Hall parameter
ρ – density
Σ – collision section
σ – electrical conduction
τ – collision time

Subcripts

chem – chemical
0 – stagnation parameters
1 – channel entry parameters channel exit parameters
2 – nozzle exit parameters
i – i = 1, 2, 3, 4, 5, 6 refer, respectively, to N_2, O_2, NO, O, N, K
k electrode number
g translational and rotational molecule degrees of freedom
v vibrational molecule degrees of freedom
* electron-excited state
e electron

References

[1] J.Lineberry, and J.Chapmen, "MHD-Acceleration for Hypersonic Applications", AIAA 91-0384.

[2] M.J.Christionsen, H.J.Shmidt, and J.N.Chapmen, "Further Analysis of MHD-Accelerator for Hypersonic Wind Tunnel", 33rd SEAM Proceeding, The University of Tennessee Space Institute, pp.V.5-1–V.5-8, (1995).

[3] Miles,R., Brown,G., Lempert,W., Natelson,D., Vetter,B., Guest.,J., Williams,G., and Bogdonoff,S., "Radiatively Driven Hypersonic Wind Tunnel", AIAA-94-2472.

[4] Williams,G., Comas,G., Menrenven,C., Lempert,W., and Miles,R., "Energy Addition and Thermolization Issues in a Radiatively –

Driven Hypersonic Wind Tunnel by Macheret", AIAA-95-2142.

[5] Boudreau,A., Smith,V., and Daniel,D., "Developmental Testing of Ramjet/Scramjet Propulsion Systems", AJAA-93-5121.

[6]. Alfyorov,V., "On the Problem of Creating the Flow Conditions in Scramjet Combustion Chamber in Wind Tunnels", AIAA-93-1843.

[7] Maus,J.R., Laster,M.L., Hornung,H.G., "The G-Range Impulse Facility of a High-Performance Free-Piston Shock Tunnel", AIAA 92-3946.

[8] Stalker,R.J., "Recent Developments with Free-Piston Drivers". Proceedings of the 17th International Symposium of Shock Tubes", New York AIP. (1990).

[9] Eitelberg,G., "Calibration of the HEG and its use for Verification of Real Gas Effects in High Enthalpy Flows", AIAA-93-5170, AIAA/DGLR International Aerospace Planes and Hypersonics Technologies Conference, Munich, Germany. (1993).

[10] Anfimov,N.A., Kislykh,V.V., Krapivnoy,K.V., "Nonisentropic Multicascade Gas Compression in Piston Gasdynamic Units (PGU) U-11 and RHYEL", Development Outlook. Zeitschrift fur Flugwissenschaften und Weltraumforschung, N16, p.169, (1992).

[11] Bakas,R.I., Tamango,I., Rizkalla,D., Pulsonetty,M.V., Erolos,I.L., "Hypersonic Mixing and Combustion Studies in the GALS HYPULSE Facility", AIAA Paper 90-2095, (1990).

[12] Alfyorov,V., "A Report on the Status of MHD-Hypersonic Ground Test Technology in Russia", AIAA 93-3193.

[13] Tempelmayer,K.E., Rittenhouse,L.E., "Status Report on the Design and Test Experience of Steady-Flow JxB Accelerator for Wind Tunnel", Proceedings of Fifth Symposium on Engineering Aspects of Magnetohydrodynamics. (1967).

[14] Alfyorov,V.I., and all., "Investigation of Physico-chemical Processes in Hypervelocity MHD-GAS Accelerattion Wind Tunnels". 33rd SEAM Proceeding, The University of Tenessee Space Institute. pp.V.I-1-V.I-7, (1995).

[15] Dautov,N.G., Starik,A.M., "On Choice of the Kinetic Scheme to Describe Detonation in H_2+Air Mixture behind Shock Waves", Teplofizika, 31, N2, pp.292-301, (1993) (in Russian)

[16]. Jensen,D.E., Jones,G.A., "Reaction Rate Coefficient for Flame Calculations", Combust. Flame, 32, pp.1., (1978).

[17] Alcemade,C.Th.J., Hollenfer,Tj., Snalleman,W., Zeegorst,P.J.Th., Metal Vapours in Flames, Oxford. Pergamon Press, (1882).

[18] Kelley,R., Podley,P.J., "Photometric Studies in Hydrogen Oxygen Carbon Dioxide Flames. Part I. Metal Hydroxcite Dissociation Energies", Trans. Faraday Soc., 67, N3, pp.740-749, (1971).

[19] Jensen,D.E., Jones,G.A., "Alcali Metal Compounds in Oxygen-rich Flames", J.Chem. Soc. Faraday Trans I,78, N9, pp. 2835-2842, (1982).

[20] Jensen,D.E., Jones,G.A., "Kinetic of Flame Inhibition by Sodium", J.Chem. Soc. Faraday Trans. I. 78, N9, pp.2843- 2850, (1982)

[21] Hynes,A.J., Steinberg,M., Schofield,K., "The Chemical Kinetics and Thermodynamics of Sodium in Oxygen-rich Hydroqen Flames", J. Chem. Phys., 80, N6, pp. 2585-2597, (1984).

[22] Mokhov,A.V., Nefedov,A.P., "Laser Fluorescent Diagnostics of Plasma of Combustion Products with Alkali Seeds", In: Khimiya plazmy, Energoizdat, Moscow, pp. 249-287, (in Russian), (1993).

[23] Smirnov,B.M., Atomic processess in plasma. Atomizdat, pp. 186-191 (in Russian), (1963).

E.3.3 Summary

With respect to the high-speed combustion studies (Section 6), the conclusions were quite similar to those of the OSU study (Section C.3). The study found the presence of small amounts of alkali metal in the flow stream of a supersonic combustion system does not significantly alter the chemical kinetics or the ignition delay times. However, it should be noted that both of these studies made the assumption of a premixed flow stream. Although it seems probable the mixing process would be essentially unaffected by the presence of small amounts of seed material, this question was not investigated in the MARIAH Project. It should also be mentioned that through most of the combustion regimes of interest, the mixing process is the factor that limits ignition.

APPENDIX F

CONTENTS

APPENDIX F

FIGURES

APPENDIX F. MARIAH II CONCEPT

The Magnetohydrodynamic Accelerator Research Into Advanced Hypersonics (MARIAH) Project was undertaken for the purpose of conducting studies into the feasibility of using magnetohydrodynamic (MHD) accelerators to produce true air simulation for hypervelocity propulsion in ground testing facilities. The MARIAH II concept is an outgrowth of that effort and is based upon MHD augmentation of ultra-high-pressure (UHP) drivers with radiative energy addition. This synthesis of the Radiatively Driven Hypersonic Wind Tunnel (RDHWT) with MHD is a hybrid concept which employs the UHP technology with beamed energy addition as the primary driver and MHD as a second-stage driver.

The primary issues addressed in this appendix are: overall conversion efficiencies; potential advantages of the hybrid scheme compared with the stand-alone RDHWT; the optimal range of parameters (pressure, temperature, velocity) for the MHD channel operation in the overall hybrid scheme; the requirements on electric and magnetic fields as well as an ionizer; and the required plenum conditions for the first stage. The key technical issues are identified, and some recommendations for a research and development (R&D) program to further demonstrate the feasibility of the MARIAH II scheme are given.

F.1 OVERVIEW

The problem of duplicating the high-enthalpy, high-dynamic pressure, high-Mach-number regime characteristic of hypervelocity flight in a ground test facility has been a challenge to airframe and engine designers for the past 40 years. For continuous flow testing (i.e., - simulations that last several seconds or more), the primary means of generating such flows has been the arc heater. While arc heater technology has progressed significantly in the last two decades, it continues to be limited to operation at reservoir pressures below 150 atmosphere (atm). Due to the complete addition of energy by Joule dissipation, arc heaters also suffer from high entropy values at the exit. This fact, coupled with a reasonably well-defined hypervelocity flight envelope, imposes second law limitations on the amount by which the total enthalpy can be increased without crossing the targeted flight envelope. These fundamental limitations have prompted researchers to search for alternatives to arc heater technology.

In the recent past, both MHD and UHP drivers with downstream radiative energy addition have been proposed as alternatives for augmenting the total enthalpy of air (Refs. 1, 2, 3, 4, 5, 6, 7, 8, 9). While MHD accelerators have been applied in the past to arc heated flows, they are not intrinsically limited to such flows. The UHP drivers with radiative energy addition, referred to as RDHWT have been described in some detail in References 1 - 3, while MHD augmentation of airflows has been described in References 4 - 9. Each of these technologies has limitations associated with both hardware and fundamental physics. Second law limitations (specifically, limitations due to Joule dissipation or the thermalization of beamed energy) are common to both technologies. However, each offers unique advantages when compared to arc heaters. In the RDHWT scheme the proposed resolution of the entropy problem is to start the process at very low entropy levels by pressurizing the gas in a reservoir to 20,000 atm or more while maintaining temperature at modest levels (below 1,500 Kelvin (K), for instance). For the MHD concept, the problem of Joule heating is mitigated in some sense by the push work done on the gas by the MHD body force. The latter contribution adds no entropy to the flow and this fact constitutes the primary argument for MHD over other energy addition methods.

The MARIAH II concept, which would employ the UHP technology with beamed energy addition as the primary driver and MHD as a second stage driver is investigated in this section. The primary issues which are addressed below include: a) overall conversion efficiencies; b) potential advantages of the MARIAH II scheme compared with the stand-alone RDHWT; c) the optimal range of parameters (pressure, temperature, velocity) for the MHD channel operation in the overall scheme; d) the requirements on electric and magnetic fields on an ionizer; and e) required plenum conditions for the first stage. The key technical issues are identified and some recommendations are given for a R&D program to further demonstrate the feasibility of the MARIAH II scheme.

F.2 BASIS FOR THE MARIAH II CONCEPT

Figure F- 1 is a Mollier diagram showing total enthalpy vs. entropy corresponding to post-bowshock conditions experienced by a hypersonic aircraft at various flight altitudes. The diagram shows that duplicating these conditions in a ground test facility will require the total

enthalpy of the gas to be increased from ambient levels to tens of millions Joules per kilogram (J/kg). The limiting envelope for arc heater operation (Ref. 9) is shown in Figure F- 1.

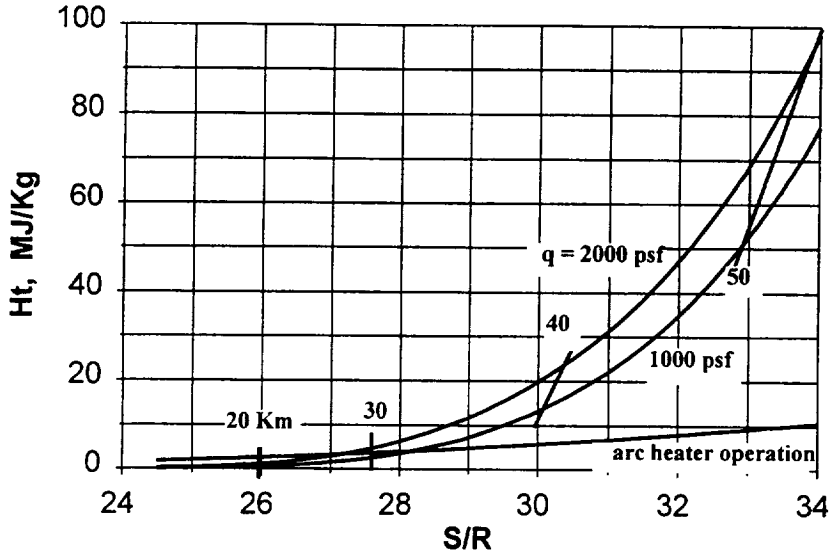

Figure F- 1. Hypersonic test facility performance requirements in terms of entropy, total enthalpy, and dynamic pressure.

Arc heaters have been the primary means of creating high enthalpy continuous flows for hypersonic testing for the past 30 years. These devices operate at relatively low-plenum pressure (below 150 atm) and high temperature and rely on a complete conversion of electrical power to heat by way of Joule dissipation. This results in very high entropy levels at the heater exit. While the total enthalpy is limited only by the amount of electrical power added, the thermodynamic end point is typically too far to the right on the H-S diagram, as can be seen in Figure F- 1. The overall result is that the test section pressures and/or Mach numbers are lower than those corresponding to in-flight, post-bowshock conditions.

This situation has prompted researchers to investigate alternative technologies for simulating hypervelocity flight. One such alternative is the UHP gas piston driver. This technology, originally developed in Russia, relies on the creation of a reservoir of extremely high-pressure gas that is subsequently released through a narrow throat into a downstream expansion region (Refs. 10, 11, 12, and 13). Experience with this technology in both Russia and the U.S. indicates that reservoir pressures of 20,000 atm are attainable. The advantage of using such high-plenum pressures to drive a high-speed flow is the entropy scales as the logarithm of the inverse of the reservoir pressure.

High-plenum pressures thus correspond to greatly reduced starting entropy levels in comparison to arc heaters. The RDHWT concept (Refs. 1, 2, 3) combines the UHP driver with beamed

energy addition in the form of laser, microwave, or relativistic electrons to significantly improve its performance and broaden its capabilities. A key element of the RDHWT concept is that the beamed energy is added to the expanding supersonic flow downstream of the throat. This provides a large increase in the total enthalpy while at the same time greatly reducing the maximum static temperatures attained when compared to more conventional technologies. This in turn alleviates the materials problems downstream of the nozzle throat. The overall thermodynamic process of such a device is illustrated in Figure F- 2, which shows a representative path on the Mollier diagram.

A key idea of the RDHWT concept is that the beamed energy is added to the expanding supersonic flow downstream of the throat. This provides a large increase in the total enthalpy while at the same time greatly reducing the maximum static temperatures attained compared to more conventional technologies. This in turn alleviates the materials problems downstream of the nozzle throat.

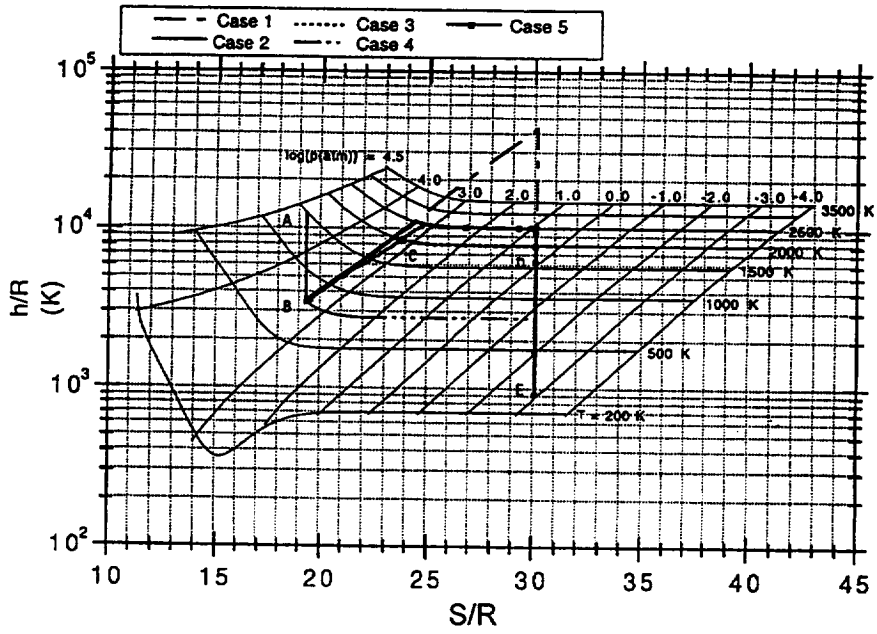

Figure F- 2. Mollier diagram for air, showing typical process paths for the RDHWT (Ref. 2). The baseline Case 3 is the line ABCDE.

MHD is the other driver technology considered. It is worth emphasizing that the important feature that differentiates MHD energy addition from energy addition by means of an arc heater or beamed energy is that an MHD accelerator adds some significant fraction of the input electric power as push work. The latter quantity is defined as the conversion efficiency, η. It follows that the quantity (1 - η) is the fraction of input power added through Joule dissipation. It could be argued that if η is close to zero it might be better to use the much simpler arc heater technology. Therefore, it is of interest to develop some simple ways of estimating η.

Consider an axial flow an MHD channel with velocity u, (in the x direction) with magnetic field B, (in the z direction). The transverse electric field, E_y, causes the transverse current j_y, while the longitudinal component of the electric field E_x, is needed to compensate for the longitudinal (Hall) current j_x (see the discussion of this in References 5 and 14 and later in this section). Since the input electric power per unit volume is $\langle j \cdot E \rangle$, and the push work is $\langle j_y u B \rangle$, η can be expressed as:

$$\eta = \frac{\langle j_y u B \rangle}{\langle j_y E_y + j_x E_x \rangle} \tag{F- 1}$$

where the brackets $\langle\ \rangle$ denote an average across the duct. Recall that for a Faraday accelerator the streamwise current j_x, is zero and the Ohm's Law relations are (Ref. 14):

$$E_y = uB + j_y / \sigma \tag{F- 2}$$

$$E_x = (\Omega / \sigma) j_y \tag{F- 3}$$

where Ω is the Hall parameter defined in Equation (F- 15) below, and σ is the conductivity. These equations can be used to express the input power, $\langle j \cdot E \rangle$ as follows:

$$\left\langle j_y E_y + j_x E_x \right\rangle = \langle j_y^2 / \sigma \rangle + \langle j_y u B \rangle \tag{F- 4}$$

The first term in this equation is the Joule dissipation and the second is the push work. Only the Joule dissipation contributes to entropy production. Equation (F- 1) can be related to the load factor K, by recalling the definition of K:

$$K = \frac{\langle E_y \rangle}{\langle uB \rangle} \tag{F- 5}$$

If it is assumed that the current j_y does not fluctuate too severely across the duct, then one factor of j_y can be canceled in Equation (F- 1) yielding the result:

$$\eta = 1 / K \tag{F- 6}$$

Therefore, in a Faraday accelerator, the conversion efficiency is approximately equal to the reciprocal of the load factor. Equation (F- 6) implies that for high conversion efficiency and low

Joule dissipation, the accelerator should operate at a load factor as close to one as possible. On the other hand, Equation (F- 2) states that for a load factor of one there is no transverse current and hence, no push force ($j_y B$=0). An accelerator operating at maximal theoretical conversion efficiency is one for which both the push work and the input power per unit length have the limiting value of zero. Thus, the requirements of finite push force and finite power addition are incompatible with the requirement of maximum conversion efficiency. In practice, Joule dissipation is always present, and implies the conversion efficiency of any real MHD accelerator will be less than one.

The above reasoning suggests the length of the MHD channel will depend in some way on the load factor or equivalently, on the conversion efficiency. This can be quantified by considering the governing equation for the total enthalpy per unit mass, H. For a quasi-one-dimensional (1-D) linear channel this equation takes the form:

$$\dot{m}\frac{dH}{dx} = -q_w P_{ch}(x) + K(K-1)\sigma u^2 B^2 A(x) \qquad \text{(F- 7)}$$

where q_w is the heat flux to the walls, m is the mass flow rate, $P_{ch}(x)$ the channel perimeter and $A(x)$ the channel cross-section. Viscous dissipation has been neglected. Define $L_{\Delta H}$ as the length of MHD duct required to increase the total enthalpy by an amount ΔH. Then $L_{\Delta H}$ can be estimated from Equation (F- 7) as:

$$L_{\Delta H} = \frac{\dot{m}\Delta H}{\langle K(K-1)\sigma u^2 B^2 A\rangle - \langle q_w P_{ch}\rangle} \qquad \text{(F- 8)}$$

(Although for preliminary qualitative analysis one can disregard the wall heat flux term, the flux can be quite high in typical accelerators, and the term should generally be retained in design calculations). The above relation suggests that for minimum channel length the accelerator should be operated at the maximum possible load factor. However, as noted above, this corresponds to maximum Joule dissipation, an undesirable operating condition. In practice, values of K in the range 1.1 to 3 may represent a reasonable compromise between achieving a workable duct length and minimizing Joule dissipation. It is clear from Equation (F- 8) that to increase the MHD efficiency i.e., to make K close to 1 and to restrict the channel length L for minimizing boundary layer effects, the values of σ, u, and B have to be high. Of course, overly strong magnetic fields and low densities may result in very large Hall parameters (Refs. 5, 14), which is undesirable (see discussion below). The desirability of high velocities (u), in the channel is one of the reasons RDHWT is potentially a good front end for MHD acceleration: the RDHWT can provide much higher gas velocities at the MHD duct entrance than those created by a conventional arc heater with subsequent isentropic expansion. As to the high conductivity required for efficient MHD operation, creating it presents a great challenge, especially at high densities and/or low temperatures.

Potential advantages of the MARIAH II scheme can be better understood by looking at basic thermodynamic constraints imposed on the RDHWT performance envelope. Certainly, the RDHWT modeling performed in References 1 - 3 has demonstrated that the UHP driver combined with laser, microwave, or electron beam (e-beam) heating of the dense supersonic stream is potentially capable of achieving Mach numbers of 12 and above at high dynamic pressures with long run times and relatively low contamination of the flow. However, the concept still has inherent limitations dictated by the second law.

The enthalpy that can be added to the flow by heating, to be then converted into kinetic energy through expansion is obviously related to the average temperature T_a at which the heat is added, and to the entropy increase, Δs ($\Delta H = T_a \Delta s$). Despite the fact it is thermodynamically advantageous to operate at high temperatures, the temperature T_a cannot be very high because of the need to minimize air dissociation and wall erosion. The entropy increase Δs, is also limited since the final entropy is set by required test section conditions, while the minimal initial entropy is essentially defined by the incompressibility of high-density fluids (RDHWT operates close to that limit).

Using MHD acceleration in some portion of the RDHWT expansion nozzle could broaden the performance envelope, thereby increasing Mach number and/or dynamic pressure in the test section. This is due to the fact that at least a part of the energy addition in the MHD channel comes directly in the form of push work by increasing kinetic energy of the flow in a non-entropy-generating way. As can be easily shown, the total enthalpy added in the MHD channel depends on the loading parameter K (Ref. 5):

$$\Delta H_t = \frac{K}{K-1} \cdot T_a \Delta s \qquad \text{(F- 9)}$$

Thus, if a way is found to create a sufficient conductivity to be able to run the MHD channel at K close to 1, a significant augmentation of flow enthalpy, test section Mach number, and dynamic pressure could be expected.

On the other hand, using RDHWT (UHP driver plus radiatively heated supersonic nozzle) as a front end to the MHD channel also has several advantages. Indeed, the RDHWT is a very flexible, multiparametric system (Refs. 1, 3). By varying UHP pressure and temperature, supersonic nozzle geometry, and the heating power, a wide range of conditions can be reached at the MHD channel entrance. For example, velocity and Mach number can be already high, while the gas pressure is not very low. This could be advantageous for the MHD operation and compares favorably with the conventional arc heater where gas parameters at the MHD channel entrance are fixed by the quasi-isentropic expansion from the maximum tolerable pressure and temperature in the arc. An additional advantage for MHD could be provided by pre-ionization of air in the case where high-energy e-beams are used as an energy source for the RDHWT. This version of the MARIAH II wind tunnel facility is shown schematically in Figure F- 3.

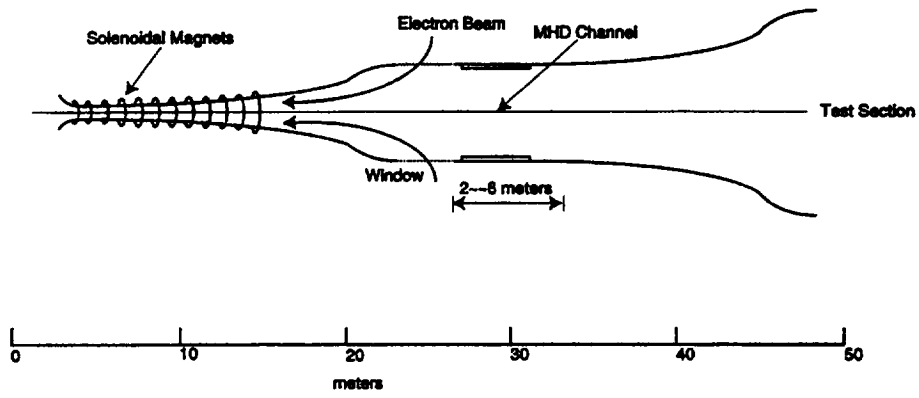

Figure F- 3. A schematic picture of the MARIAH II concept tunnel. Relativistic electron beams focused by solenoidal magnets add energy to air at high pressures, followed by acceleration in an MHD duct at low pressures.

In view of these considerations, for preliminary assessment of the viability and performance advantage of the MARIAH II concept, the following questions must be considered:

1. What is the range of parameters (pressure, temperature, flow velocity, electrical conductivity) where an MHD accelerator would be useful for significantly augmenting total enthalpy?
2. How to achieve these parameters and how UHP driver combined with radiative heating can help?
3. How significantly can RDHWT performance (Mach number, dynamic pressure) be extended by using the MARIAH II concept?
4. Is it possible to relax requirements on the UHP using MHD enthalpy augmentation?

F.3. TWO REGIMES OF MHD CHANNEL OPERATION

Efficient operation of an MHD accelerator requires high values of the electrical conductivity σ, as discussed in the previous section. However, simulation of high-Mach number, high-dynamic-pressure conditions in the test section requires low entropy that in turn requires high pressure and/or low temperature in the MHD channel. For conventional MHD operation [even with potassium (K) or cesium seed (Cs)], the temperature in the channel must be approximately

3,000 K resulting in MHD channel static pressures on the order of tens to hundreds of atmospheres depending on the flight conditions to be simulated. Sufficiently high-electrical conductivity is extremely difficult to achieve under these conditions.

Therefore, two "unconventional" modes of MHD acceleration have been suggested: a) high-pressure operation with highly non-uniform ionization; and b) low-pressure, low-temperature operation with an external ionization source.

F.3.1. MHD Acceleration at High-Pressure: A Guided-Arc Concept

In this regime, the flow exiting the UHP driver will be directly passed into an MHD channel. The pressure in this channel would be high (approximately a few hundred atmospheres), and the temperature (although high) is below that needed for conventional MHD operation. Thus, the flow will have to be ionized and the discharge stabilized in order to develop MHD augmentation. Because it is all but impossible to get a uniformly high conductivity at those conditions, a possible approach may be that of a guided-arc accelerator.

In this case, a bright arc would be initiated across the channel along a line defined by either a laser or an e-beam. This arc will be sustained by two thin linear electrodes on each side of the flow, extending in the flow direction. In the absence of a magnetic field the arc will propagate downstream and move along the electrodes to the end of the channel. It has been shown by Topchiyan et al, (Refs. 10, 11) such arcs can be initiated and maintain their integrity as they move downstream in high-pressure hypersonic flows. In the presence of a magnetic field, the arc will be accelerated due to the high-electric current and will serve as a fluid accelerator.

A single arc will not suffice to accelerate the entire flow. It would be interesting to examine the possibility of initiating an array of arcs as a flow driver, each with its own pair of linear electrodes. The spatial separation between these arcs should be small enough to generate uniform flow acceleration, but large enough to minimize magnetic interaction between them. By segmenting the electrodes, arcs could be passed from one pair of electrodes to the next as the flow moves downstream, and a new set of arcs could be initiated.

Thus, a rapid-fire sequence of arcs can be formed to more effectively drive the flow and to minimize flow nonuniformity. It is understood that the approach will create fundamentally nonuniform air, and the implications of this must be studied. With a high enough repetition rate and close enough separation, this nonuniformity may hopefully thermalize before the air enters the test section. The high pressure also enhances the recombination rate of electric charges and nonequilibrium species, thereby helping to minimize nitric oxide (NO) and ozone formation.

The high temperature in the arc allows the electrical conductivity to be sustained and enhances the $\Delta H/\Delta s$ ratio. Of course, there will be additional entropy generated by the arc moving

through the air that also has to be evaluated in order to determine the actual work-to-heat ratio. These issues need to be addressed in future research.

F.3.2. MHD Acceleration at Low Pressure and Temperature, with E-Beam Ionization

Because of difficulties of sustaining high-uniform conductivity at high densities, it would be advantageous if an acceptable MHD channel performance at low densities could be demonstrated. Again, the second law imposes an important constraint here. The entropy at the channel entrance has to be significantly less than the required entropy at the test section. Since entropy increases with temperature and decreases with pressure, low pressures in the channel would all but preclude operation at high temperatures. This, in turn, creates two difficult problems.

First, low temperatures mean only a small amount of enthalpy can be added in the form of heat, $T\Delta s$. According to Equation (F- 9), this must be compensated by the loading parameter, K (close to 1) so almost all of the enthalpy is added directly as kinetic energy.

Secondly, the low-temperature operation of the MHD channel requires adequate conductivity be created by means other than conventional thermal ionization. Because the requirement $K \approx 1$ restricts the maximum value of electric field E, the effective field $(E - uB)$ in the channel will be small and incapable of sustaining the discharge. This leaves only an external ionization source as a method of creating the conductivity. Specifically, beams of high-energy electrons could be used for the ionization of the gas.

The MARIAH II concept tunnel in this scenario would have an UHP front end. After expansion to supersonic velocity, air will be heated using lasers, microwaves, or relativistic e-beams, and its velocity increased while still at very high-pressure (from thousands of atmospheres down to about 1,000 atm or perhaps, several hundred atmospheres). The air will then be isentropically expanded to low pressure (approximately 0.1 atm) and low temperature (perhaps 300 K). Further acceleration will be provided by the MHD channel, possibly in the form of a Faraday accelerator with ionization sustained by high-energy e-beams injected parallel to the magnetic field. The entropy at the channel exit should match the test section entropy; hence the gas can reach the required conditions by isentropic expansion after the MHD channel. Figure F- 3 is a schematic diagram of such a wind tunnel, and Figure F- 4 shows a representative thermodynamic path of air in the tunnel.

A 1-D analysis and estimates of the performance of the low-pressure MHD accelerator are described below. Approximate analytical solutions of the equations are then used for an example comparison between the MARIAH II tunnel and "pure" RDHWT.

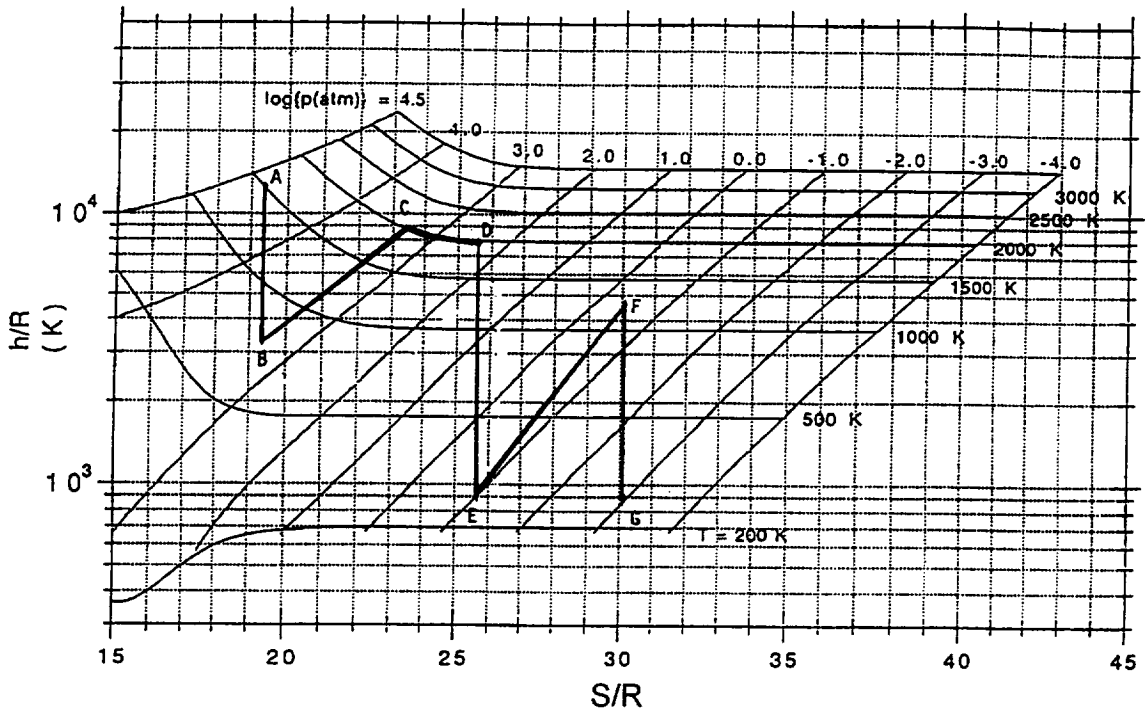

Figure F- 4. Thermodynamic path (ABCDEFG) of the example case of a MARIAH II facility. A – UHP plenum; AB, DE, FG – isentropic expansion regions; BCD – heating by beamed energy sources; EF – low-pressure MHD accelerator; G – test section.

F.4. ONE-DIMENSIONAL ANALYSIS OF LOW-PRESSURE MHD CHANNEL WITH E-BEAM IONIZATION

F.4.1. Basic Flow Equations and Ionization Kinetics

Consider an MHD channel in the form of a rectangular duct with side b, (cross-sectional area $A=b^2$), and length L (with the x axis directed along the duct). Transverse electric, E, and magnetic, B, fields are perpendicular to each other and to the x-axis. An e-beam with current density j_b accelerated by the voltage V_b (to energy eV_b) is injected from the side parallel to the magnetic field. The high-energy electrons ionize the gas while thermalizing, and low-energy thermal electrons determine the conductivity σ, and electric current density j, in the channel. Because a low-pressure, low-temperature regime is assumed, the air can be described as an ideal gas with constant specific heats. Assuming an ideal Faraday accelerator allows one to use quasi-1-D approximation, the set of 1-D steady-state equations for the channel is then (Ref. 14):

$$\rho u = \dot{m}/A = F = const \qquad \text{(F- 10)}$$

$$\rho u\frac{du}{dx}+\frac{dP}{dx}=jB \tag{F- 11}$$

$$\rho u\left(c_p\frac{dT}{dx}+u\frac{du}{dx}\right)=jE+\frac{j_bV_b}{b} \tag{F- 12}$$

$$j=\sigma\left(E-uB\right) \tag{F- 13}$$

$$P=\rho RT \tag{F- 14}$$

To solve these equations, initial conditions, electric and magnetic fields, and the conductivity have to be specified. In an example case considered below, the inlet pressure and temperature in the MHD channel were set at 0.1 atm and 274 K; the inlet velocity is determined by the processes in the RDHWT stage followed by an isentropic expansion.

Magnetic and electric field strengths are chosen to provide predetermined values of the Hall parameter and the loading parameter. The Hall parameter, Ω, is defined as the ratio of the electron cyclotron frequency, ω_H, and electron momentum transfer collision frequency, ν_c (Ref. 14):

$$\Omega=\omega_H/\nu_c \tag{F- 15}$$

where $\omega_H=\frac{eB}{m}$, and the collision frequency can be expressed in terms of the neutral number density n, and the appropriate rate coefficient, k_{en}: $\nu_c = k_{en}n$.

To maximize the acceleration the magnetic field should be as strong as possible. However, increasing B and the Hall parameter would generate strong drift (or Hall) electric current normal to both E and B, along the flow. This would also reduce the transverse current and consequently, decrease the push force. To prevent this from occurring, a longitudinal electric field with the strength $E_x=\Omega\left(E-uB\right)$ is usually created by segmenting the electrodes into many sections, each insulated from its neighbors so it may be maintained at a different potential (Ref. 14). This field reduces the longitudinal current to zero, and the system can then be adequately described as in the low-Ω case with only transverse electric field and current. The practical problem that exists in such high-Ω systems is that in the boundary layer where $u\approx 0$, the electric field $E_{total}=\sqrt{E_x^2+E^2}=E\sqrt{\Omega^2+1}$ is much stronger than in the core flow, which could result in short-circuiting between the electrode segments, thereby destroying the compensating effect of the longitudinal field and sharply reducing MHD acceleration. This problem is most acute at low-

static pressures because the Hall parameter scales inversely with pressure. For subatmospheric MHD channel operation the (theoretically calculated) Hall parameter can exceed 100, even for modest B fields. With this in mind the important issues of boundary layer control and electrode design is left for future research. In this section an ideal quasi-1-D Faraday accelerator with full compensation of the Hall current is assumed.

For ease in the analytic solution of flow equations, it is convenient to assume constant Hall parameter value along the channel. This means the constant ratio B/ρ:

$$\frac{B}{\rho}=\Omega\frac{m}{M}\cdot\frac{k_{en}}{e}=const \qquad \text{(F- 16)}$$

where M is the (average) mass of an air molecule.

In further analysis, a constant loading parameter K will also be assumed. This, together with the earlier assumptions, results in the constancy of the effective field:

$$E-uB=(K-1)uB=(K-1)(\rho u)(B/\rho)=(K-1)F\Omega\frac{m}{M}\cdot\frac{k_{en}}{e} \qquad \text{(F- 17)}$$

To determine the conductivity σ, electron and ion concentrations must be known. Qualitatively, the ionization caused by a high-energy e-beam injected into the channel can be described as follows: high-energy electrons lose their energy primarily on ionization, creating a cascade of lower energy electrons that can create additional ionization. The well-known energy cost of an electron-ion pair created in air by high-energy electrons is about W_i= 34 eV, a factor of 2 - 3 times greater than the ionization energy of molecules. When the energy of the cascade electrons falls below minimum ionization energy, they excite vibrational and electronic molecular states, thermalize in elastic collisions, and gain energy from electric fields. For typical conditions of the MHD channel operation, that is, for air at ≈0.1 atm, E/n≈1 Td (1 Td = 10^{-17} V·cm^2) the field-induced heating of electrons is very weak (Ref. 15), and the thermalization of both electrons and molecular states can be assumed to be fast. Thus, only thermalized electrons will be considered as participating in recombination and attachment processes, as well as in the electric current across the channel.

Thermalized electrons can attach to oxygen (O_2) molecules, forming negative ions (Ref. 16):

$$e+O_2+O_2\xrightarrow{k_a}O_2^-+O_2 \qquad \text{(F- 18)}$$

[Nitrogen (N_2) is less effective than O_2 as an energy-removing third body], or recombine with positive molecular ions. The electron-ion recombination in molecular gases proceeds not as a three-body collision, but predominantly as a dissociative process (Ref. 16), for example:

$$e + NO^+ \xrightarrow{k_{dr}} N + O \tag{F- 19}$$

Negative ions can be destroyed and free electrons recreated in detachment processes, stimulated either thermally:

$$O_2^- + M \xrightarrow{k_d} O_2 + e + M,\ k_d = 10^{-11}\exp\left(-5000/T\right)\mathrm{cm}^3/\mathrm{s} \tag{F- 20}$$

or in collisions with active particles, such as atoms, radicals, and excited molecules (Ref. 16):

$$O_2^- + N \rightarrow NO_2 + e, \tag{F- 21}$$

$$O_2^- + O_2(^1\Delta_g) \rightarrow O_{2+}O_2, k_{act} = (2-5)\times 10^{-10}\ cm^3\ /\ s \tag{F- 22}$$

Positive and negative ions can also recombine with each other. At subatmospheric densities, this is a three-body process whose effective two-body rate coefficient, k_r, is therefore proportional to density.

The set of equations for number densities of charged species is then:

$$\begin{aligned}
\dot{n}_e &= \frac{j_b Y \rho}{e W_i} - k_{dr} n_e n_+ - k_a n_e \left[O_2\right]^2 + k_{d,eff} n_n \\
\dot{n}_+ &= \frac{j_b Y \rho}{e W_i} - k_{dr} n_e n_+ - k_r n_+ n_ \\
\dot{n}_ &= k_a n_e \left[O_2\right]^2 - k_{d,eff}\, n_n
\end{aligned} \tag{F- 23}$$

where Y is the so-called stopping power of the medium with respect to the high-energy electrons of a given energy, and $k_{d,eff}$ is the effective detachment rate coefficient, taking into account both thermal and active-particle-induced detachment. Since the characteristic times of the ionization-recombination processes under typical conditions of interest are orders of magnitude shorter than flow times, the quasi-steady-state approximation is justified:

$$\dot{n}_e = \dot{n}_+ = \dot{n}\_ = 0, \tag{F- 24}$$

which reduces the ionization kinetics to the set of algebraic equations to be solved for each point of the flow. Further simplification can be made if one of the two channels of electron losses, attachment or dissociative recombination, dominates. Simple analysis for the typical conditions (density on the order of 1/10 of the normal atmospheric density, temperature of up to 1,500 K, a considerable concentration of active particles generated by the e-beam) shows in the first approximation attachment can be neglected, and dissociative recombination be considered the dominant channel of electron losses. Thus, the quasi-steady-state electron number density is determined simply as:

$$n_e = \sqrt{\frac{j_b Y \rho}{e W_i k_{dr}}} \tag{F- 25}$$

The electrical conductivity that is due predominantly to thermalized electrons is then:

$$\sigma = \frac{e^2 n_e}{m \nu_c} = \frac{M}{k_{en} m} \sqrt{\frac{j_b Y}{W_i k_{dr} \rho}} = \sigma_o \sqrt{\frac{\rho_o}{\rho}} \tag{F- 26}$$

where

$$\sigma_0 = \frac{e^2 \left(M/m \right)}{\rho_0 K_{en}} \sqrt{\frac{j_b \rho_0 y}{e W_i K_{dr}}} \tag{F- 27}$$

is the conductivity at the reference density ρ_o, which we chose for convenience to be 1.29 kg/m^3 (normal atmospheric density). The values of the rate coefficients are k_{en}=5.8×10^{-9}cm^3/s, and k_{dr}=1.5×10^{-7} cm^3/s (Ref. 16, 17).

F.4.2. Approximate Analytic Solution of the Set of One-Dimensional Flow Equations

Expressing derivatives *dP/dx* and *dT/dx* through *du/dx* from the set of flow equations [(F- 10) through (F- 14), (F- 16), (F- 17), (F- 26), (F- 27)] and denoting $c_p^* = c_p / R$, $c_v^* = c_v / R = c_p^* - 1$, $\gamma = c_p / c_v$, and $M = u / \sqrt{\gamma R T}$ (Mach number), obtained from Equation (F- 12):

$$u \frac{du}{dx} = \frac{\sigma (K-1)\left(c_p^* - K\right) F^2 \left(B/\rho\right)^2 - j_b V_b / b}{c_v^* F \left(1 - 1/M^2\right)} \tag{F- 28}$$

When Mach number at the MHD channel entrance is already high (because of the previous acceleration in the UHP driver and radiative heating), the $1/M^2$ term in the denominator can be dropped. The two terms in the numerator of the Equation (F- 28) represent, respectively, acceleration due to the Lorentz force combined with Joule heating, as well as heat addition due to e-beam. If the MHD efficiency is low, so that the loading parameter K, exceeds c_p^* (for cold air, $c_p^* = 3.5$), both terms in the numerator become negative, and the flow decelerates which is natural for supersonic flow in constant-area duct with heat addition. To accelerate air in the MHD duct, not only should the loading parameter be less than c_p^*, but also the heating by the e-beam has to be less than the energy addition by the Lorentz force. In the following discussion the power deposition by which e-beam in the channel will be neglected will be considered (this is the case in the example calculations below). The Equation (F- 28) can then be integrated to give:

$$u(x) = \left(u_i^{3/2} + \frac{3/2}{c_v^*} \sigma_o \sqrt{\rho_o F} (K-1)\left(c_p^* - K\right)(B/\rho)^2 x \right)^{2/3} \qquad \text{(F- 29)}$$

where u_i is the velocity at the channel entrance. This solution for the velocity distribution allows to immediately obtain distribution of other parameters (temperature, pressure, and density) along the channel. Indeed, the following is obtained:

$$\begin{aligned} \rho(x) &= \frac{F}{u(x)} = F \cdot \left(u_i^{3/2} + \alpha x \right)^{-2/3}, \\ T(x) &= T_i + \frac{j_b V_b x}{c_v F b} + \frac{K-1}{2R\left(c_p^* - K\right)} \left[\left(u_i^{3/2} + \alpha x \right)^{4/3} - u_i^2 \right], \\ \alpha &= \frac{3/2}{c_v^*} \sigma_o \sqrt{\rho_o F}\, (K-1)\left(c_p^* - K\right)(B/\rho)^2, \end{aligned} \qquad \text{(F- 30)}$$

where T_i is the temperature at the MHD channel inlet. The pressure profile along the channel is then easily found from the equation of state.

F.4.3 Example Case of the MARIAH II Concept with Low-Pressure MHD Duct

As a baseline, take the RDHWT parameters corresponding to Case 3 from Reference 3 (shown schematically on Figure F- 4) as a trajectory on the Mollier diagram. In this case, the plenum is at 25,000 atm and 1,500 K. On initial isentropic expansion to Mach 1.5, the gas is radiatively heated as it expands: first at constant pressure, then on reaching T=2,000 K, at constant temperature. When entropy becomes equal to that required at the test section, the heating stops and the gas expands isentropically. In this case, the test section pressure and temperature are

1.29×10^{-3}atm, 274 K, respectively. The gas velocity at the test section reaches 4,180 meters per second (m/s), corresponding to Mach 12.6.

Suppose the isothermal heating is interrupted earlier when the entropy is by $\Delta s/R$=4.4 less than that in the test section, and air is isentropically expanded to P = 0.1 atm, T = 274 K. The velocity at these conditions is easily calculated as u_i=3,525 m/s, corresponding to Mach number M=10.6. Let the air now enter the MHD channel where the ratio B/ρ =59 T·meters cubed per kilogram (m^3/kg), which correspond to Ω =50 and the loading parameter is set to K=1.1, which specifies the electric field, E=29.74 kilovolts per meter (kV/m). The magnetic field in the channel is several Tesla, and the reduced electric field is quite low: $E/n\leq1$ Td. As an example, take the channel width b=15 centimeters (cm), which allows mass flow rate $\dot{m}$ = 10.3 kilograms per seconds (kg/s). According to the data from Reference 18 to penetrate this distance at 0.1 atm, the energy of electrons in the beam has to be around 30 kiloelectronvolt (keV), and the stopping power is Y=0.85 megaelectronvolts times meters squared per kilogram (MeV·m^2/kg). (Should a higher mass flow rate be required, both b and V_b have to be increased; however, the ratio V_b/b does not change much). As can be easily checked, the choice of the beam current density of j_b=0.1 Ampere per centimeter squared (A/cm^2) allows us to neglect the direct energy addition by the beam in the total enthalpy balance.

The MHD channel length L, is found by iterations. Assuming the value of L, analytic expressions for $u(x)$, $P(x)$, $T(x)$, $\rho(x)$ are used to get the air parameters at the channel exit. For isentropic expansion to the test section pressure, the expression $P/\rho^{\gamma} = const$ is used together with the equation of state to calculate the final temperature. Depending on the deviation of this temperature from the required test section temperature of 274 K, the channel length is increased or decreased in the next iteration.

In this specific case, convergence was achieved at the reasonable channel length L=0.95 m. The gas density in the channel somewhat decreased, from ρ_i=0.13 down to ρ_f=0.101 kg/m^3. Temperature, on the other hand, went up significantly to T_f=1,431 K, and the pressure increased to P_f=0.408 atm. Interestingly, despite the increase in static pressure, gas accelerated due to the strong Lorentz force reaching at the channel exit velocity of u_f=4,515 m/s. In the test section, velocity is 4,765 m/s, corresponding to the Mach number M=14.3, which is a significant improvement over M=12.6 in the pure radiative heating Case 3 of Reference 3. Additional (with respect to Case 3) enthalpy added to the flow is 2.6 megajoules per kilogram (MJ/kg).

Another potential advantage of the MARIAH II concept could be the possibility of reducing the plenum pressure in the UHP driver, thus allowing the use of well-developed technologies to simplify the scaling problem. To check this, the plenum pressure in the example case was changed to 10,000 atm at the same entropy (the temperature came down to approximately 1,200 K). Following the same thermodynamic trajectory, a velocity of 3,091.5 m/s at the MHD channel entrance is obtained. The calculations converge at the channel length L=0.92 m, with gas parameters at the channel exit being P_f = 0.393 atm, T_f = 1,407 K, ρ_f = 0.099 kg/m^3, and u_f = 4,045 m/s. The velocity at the test section is 4,317 m/s, corresponding to M = 13. This is still

higher Mach number than in the Case 3 and is achieved with dramatically lower plenum pressure.

Another question to consider is are there any advantages of the MARIAH II scheme in developing a high-dynamic pressure hypervelocity tunnel. Specifically, a baseline case similar to the Case 3 is again considered, only with test section pressure an order of magnitude higher than in the Case 3: 10^{-2} atm. "Dropping" earlier from the 2,000 K isotherm, the test section velocity is calculated at 3,881 m/s. This corresponds to Mach number M=11.7 and dynamic pressure $q=\rho u^2/2$=0.95 atm=1,944 pounds force per foot squared (lbf/ft^2).

In the MARIAH II process case, again a "drop" from the 2,000 K isotherm, down to 0.1 atm, 274 K is made. While maintaining the same Hall and loading parameters as before, iterations yield the channel length: L=0.33 m. At the end of the channel, gas parameters are: P_f= 0.2215 atm, T_f= 668 K, ρ_f= 0.118 kg/m^3, and u_f= 3,883 m/s. The velocity at the test section is 3,983 m/s, corresponding to M = 12 and the dynamic pressure is approximately 1 atm, or slightly above 2,000 lbf/ft^2. The M and q represent only a small improvement over the case of purely radiative heating. The explanation is simple: according to Equation (F- 9) the total enthalpy added in the MHD channel is proportional to $T_a\Delta s$, and both T_a and Δs are smaller than in the previous low-q case. The way to improve performance in the high-q case is to decrease the loading parameter K, making it even less than 1.1 (perhaps K = 1.05), and lengthen the channel accordingly.

F.5. SUMMARY

The preliminary analysis performed in this section shows that a MARIAH II flow train consisting of an UHP driver, beamed energy heating of a supersonic stream, and an MHD accelerator offers interesting possibilities for the future development of high-dynamic pressure, long-run time hypervelocity wind tunnels. The MARIAH II scheme draws upon the strengths of each of the components and benefits from their synergistic action. The UHP driver with radiative heating of supersonic flow (or RDHWT) adds a large amount of enthalpy to air when the density is high and entropy is low. This relaxes requirements on MHD performance and creates favorable gas conditions in the MHD channel. Conversely, an MHD accelerator is capable in principle of significantly extending the performance envelope (Mach number, dynamic pressure, etc.) of the RDHWT. In the present study, these ideas were quantified in 1-D analytical calculations of the representative example cases.

Two major schemes of the MARIAH II facility have been suggested. One is the guided arc concept, which at this time is in its early and qualitative stage. Some of the principal issues to be addressed in experimental and theoretical development of the concept are: a) how well multiple arcs can be controlled and stabilized by lasers or electron beams, and accelerated in crossed electric and magnetic fields; b) how effective is a moving region of hot gas in imparting momentum to the bulk flow; c) what is the efficiency of the scheme in terms of entropy generation; and d) can the resulting flow nonuniformity and chemistry inside arcs be acceptable for test facilities.

The other concept of the MARIAH II facility relies on using an MHD duct as an "afterburner" for the RDHWT. In this scheme, MHD would operate at low pressures and temperatures with ionization created by beams of energetic (30 - 60 keV) electrons. Simple analysis and estimates performed in this section show that such a scheme could indeed significantly augment the Mach number and dynamic pressure as compared with the pure beamed energy case. It is also possible to considerably reduce the UHP in the plenum, thus helping to scale the facility to larger volumes and longer run times. Among many issues to be resolved in developing this concept are: a) coupling of ionizing e-beams into the duct where strong magnetic and electric fields have to be created; b) control of gas flow and ionization processes in the boundary layer (in conjunction with designing a system of segmented electrodes to avoid breakdown and short-circuiting due to high electric fields in the slow-moving gas near the electrodes); and c) chemical quality of the flow subjected to the flux of energetic electrons.

Development of the MARIAH II facility should also address issues related to UHP drivers and beamed energy addition. Scaling of the UHP drivers to very large volumes and long run times, survivability of throat materials, selection of energy sources (lasers, microwaves, or e-beams), and their coupling to dense supersonic flow are among the critical issues. A multidisciplinary effort aimed at resolution of the listed technical issues could result in development of the new advanced concept of hypervelocity test facilities.

F.6 REFERENCES

1. Miles, R.B., Brown, G.L., Lempert, W.R., Yetter, R., Williams, G.J., Jr., Bogdonoff, S.M., Natelson, D., and Guest, J.R., "Radiatively Driven Hypersonic Wind Tunnel," *AIAA Journal*, Vol. 33, No. 8, pp. 1463-1470; see also AIAA Paper 94-2472, 1995.

2. Macheret, S., Meinrenken, C., Williams, G., Gillespie, W., Lempert, W., and Miles, R. "Energy Addition and Thermalization Issues in a Radiatively Driven Hypersonic Wind Tunnel," AIAA Paper 95-2142.

3. Macheret, S., Meinrenken, C., Williams, G., Gillespie, W., Lempert, W., and Miles, R., "Radiative Energy Addition to High Pressure Supersonic Air," AIAA Paper 96-1984.

4. Nelson, G.L., and Simmons, G., "Augmentation of Hypersonic Propulsion Testing Facilities Using MHD," AIAA Paper 95-1937.

5. Adamovich, I.V., Rich, J.W., and Nelson, G.L. "Feasibility Study of MHD Acceleration of Unseeded and Seeded Air Flows," AIAA Paper 96-2347.

6. Crawford, R.A., Chapman, J.N., and Rhodes, R.P., "Potential Applications of Magnetohydrodynamic Acceleration to Hypersonic Environmental Testing," AEDC-TR-90-6, Arnold Engineering Development Center, Aug. 1990.

7. Shair, F.H., and Sherman, A., "Electron Beam Preionization in an MHD Generator," *Sixth Symposium on Engineering Aspects of MHD*, Apr. 1965.

8. Simmons, G.A., Nelson, G.L., and Lee, Y.M., "Analysis of an Unseeded, Nonequilibrium MHD Accelerator Concept for Hypersonic Ground Testing Applications," AIAA Paper 92-3994.

9. Whitehead, G.L., McDermott, W.N., Siler, L.G., and Roepke, R.G., "Assessment of MHD Application to Hypersonic Propulsion Testing Facilities," Arnold Engineering Development Center Report (AEDC), AEDC-TMR-87-V54, 1987, pp. 7-12.

10. Topchiyan, M.E., and Kharitonov, A.M., "Wind Tunnels for Hypersonic Study (Achievements, Problems, Outlooks)," *The Science Report No. 8 - 93 of the International Center of Aerophysical Studies, Institute of Theoretical and Applied Mechanics*, Russian Academy of Sciences Siberian Branch, 1993.

11. Topchiyan, M.E., Rychkov, V.N., Pinakov, V.I. and Meshcheryakov, A.A. "Creation and Use of Adiabatic Compression Units for Producing Dense Hypersonic Flows," *International Symposium IUTAM,* Marseille, France, Sept. 1992.

12. Meshcheryakov, A.A., Pinakov, V.I., and Topchiyan, M.E., "On Stress Distribution in Locking Piston and Tube of an Adiabatic Compression Unit," *Zhurnal Prikladnoi Mekhaniki i Tekhnicheskoi Fiziki (Journal of Applied Mechanics and Technical Physics)*, No. 2, [In Russian], 1980.

13. Pinakov, V.I., Rychkov, V.N., and Topchiyan, M.E., "Simulation of Hypersonic Flows in Gasdynamic Facilities with High Pressure," *Zhurnal Prikladnoi Mekhaniki i Tekhnicheskoi Fiziki (Journal of Applied Mechanics and Technical Physics)*, [In Russian], No. 1, 1981.

14. Jahn, R.G., *Physics of Electric Propulsion*, McGraw-Hill, 1968.

15. Rychkov, V.N., and Topchiyan, M.E. "The Development of Methods and Some Findings of Investigations of a Gas Outflowing Under Pressures up to 10,000 Atm," *Lecture for Workshops under the Program "Windows on Science,"* Princeton University, Livermore National Laboratory, Arnold Engineering Development Center, Wright-Patterson Laboratory, May 1996.

16. Raizer, Y.P., *Gas Discharge Physics*, Springer, Berlin, 1991.

17. Kroll, N. and Watson, K., *Phys. Rev.*, Vol. 5, No. 4, 1972, pp. 1883-1905.

18. Berger, M.J., and Seltzer, S.M., "Tables of Energy Losses and Ranges of Electrons and Positrons," NASA SP-3012, 1964.

REPORT DOCUMENTATION PAGE

Form Approved
OMB No. 07704-0188

1. AGENCY USE ONLY *(Leave blank)*	2. REPORT DATE	3. REPORT TYPE AND DATES COVERED
	October 1997	Contractor Report (April 1995-October 1997)

4. TITLE AND SUBTITLE
Magnetohydrodynamics Accelerator Research Into Advanced Hypersonics (MARIAH) - Final Report

5. FUNDING NUMBERS
PO A45416D

6. AUTHOR(S)
Jack A. Baughman, David A. Micheletti, Gordon L. Nelson, and Gloyd A. Simmons

7. PERFORMING ORGANIZATION NAME(S) AND ADDRESS(ES)
MSE Technology Applications, Inc.
200 Technology Way
P. O. Box 4078
Butte, MT 59702-4078

8. PERFORMING ORGANIZATION REPORT NUMBER
MSE-029

9. SPONSORING/MONITORING AGENCY NAME(S) AND ADDRESS(ES)
U.S. Department of Energy
Federal Energy Technology Center, Pittsburgh, PA and
National Aeronautics and Space Administration
Langley Research Center
Hampton, VA 23681-2199

10. SPONSORING/MONITORING AGENCY REPORT NUMBER
NASA/CR-97-206242/PT2

11. SUPPLEMENTARY NOTES
Technical Monitor: Dennis M. Bushnell, Langley Research Center.
This report was prepared under NASA Ames Research Center Purchase Order A45416D and DOE Contract DE-AC22-96EW96405.

12a. DISTRIBUTION/AVAILABILITY STATEMENT
Unclassified–Unlimited
Subject Category 09 Distribution: Standard
Availability: NASA CASI (301) 621-0390

12b. DISTRIBUTION CODE

13. ABSTRACT *(Maximum 200 words)*
This report documents the activities, results, conclusions and recommendations of the Magnetohydrodynamics Accelerator Research Into Advanced Hypersonics (MARIAH) Project in which the use of magnetohydrodynamics (MHD) technology is investigated for its applicability to augment hypersonic wind tunnels. The long range objective of this investigation is to advance the development of ground test facilities to support the development of hypervelocity flight vehicles. The MHD accelerator adds kinetic energy directly to the wind tunnel working fluid, thereby increasing its Mach number to hypervelocity levels. Several techniques for MHD augmentation, as well as other physical characteristics of the process are studied to enhance the overall performance of hypersonic wind tunnel design. Specific recommendations are presented to improve the effectiveness of ground test facilities. The work contained herein builds on nearly four decades of research and experimentation by the aeronautics ground test and evaluation community, both foreign and domestic.

14. SUBJECT TERMS
MHD; Accelerator; MARIAH; Hypervelocity; Wind tunnel; Propulsion testing; Ground test facilities; Gas dynamics; Shock tunnel; Computational fluid dynamics; Air chemistry; Seeding; Ionization technologies; Foreign MHD activity

15. NUMBER OF PAGES
405

16. PRICE CODE
A18

17. SECURITY CLASSIFICATION OF REPORT	18. SECURITY CLASSIFICATION OF THIS PAGE	19. SECURITY CLASSIFICATION OF ABSTRACT	20. LIMITATION OF ABSTRACT
Unclassified	Unclassified	Unclassified	